

Inhibition and reaction mechanism of

Mycobacterium tuberculosis

anthranilate

phosphoribosyltransferase

A potential target for novel drug design

Preeti Kundu

A thesis

submitted to Victoria University of Wellington

in fulfilment of the requirements for the degree of

Doctor of Philosophy in Chemistry

Supervisor: Prof. Emily Parker

Co-supervisor: Prof. Peter Tyler



Ferrier Research Institute
Te Kāuru

2020

Abstract

Tuberculosis (TB), which is estimated to affect 2 billion individuals worldwide, is an infection predominately caused by *Mycobacterium tuberculosis* (*M. tuberculosis*). Of particular concern is the increasing prevalence of TB, which is becoming resistant to the treatments currently available. Anthranilate phosphoribosyltransferase (AnPRT) catalyses the formation of *N*-(5'-phosphoribosyl)anthranilate (PRA) from 5-phospho- α -ribose-1-diphosphate (PRPP) and anthranilate and plays an important role in the synthesis of an essential amino acid in *M. tuberculosis*. A strain with a genetic knockout of the *trpD* gene, which encodes for the AnPRT enzyme, was unable to cause disease, even in immune-deficient mice. Therefore, this enzyme is a potential drug target for the development of new treatments against TB and other infectious diseases.

This research explores the synthesis of different substrates and potential transition state analogues in order to understand catalysis and inhibition of AnPRT enzymes to aid novel drug design. The first part of this study utilises "bianthranilate-like" phosphonate inhibitors that display effective inhibition of the AnPRT enzyme, with the lowest K_i value being 1.3 μM . It was found strong enzymatic inhibition increases with an increased length of the phosphonate linker that occupies multiple anthranilate binding sites within the anthranilate binding channel of the enzyme. Crystal studies of the enzyme in complex with the inhibitors were carried out in order to expose the binding interactions. The second part of this study investigates several new compounds that target the active site of *M. tuberculosis* AnPRT, based on a virtual screening approach. This approach identified a strong AnPRT inhibitor, which displays an apparent K_i value of $7.0 \pm 0.4 \mu\text{M}$ with respect to both substrates. This study also exposed a conformational change at the active site of the enzyme that occurs on inhibitor binding. The observed conformational changes of the enzyme active site diminish the binding of the substrate PRPP. These pieces of information provide future inhibitor design strategies to aid the development of novel anti-TB agents that target the AnPRT enzyme.

To elucidate the reaction mechanism of *M. tuberculosis* AnPRT, the third part of this study explores the substrate binding sites in detail. This study uses structural analysis,

complemented by differential scanning fluorimetry (DSF) and isothermal titration calorimetry (ITC), to reveal detailed information of the substrate and inhibitor binding sites. The final part of this thesis presents the synthesis of various PRPP analogues and potential transition state mimics that were designed based on the likely reaction mechanism of the enzyme. This set of inhibitors includes a number of iminoribitol analogues that were developed to capture the geometry of the flattened ribose ring and include a nitrogen atom within the ring to mimic the positive charge characteristics that are expected in the oxocarbenium-ion-like transition state predicted for *M. tuberculosis* AnPRT. Additionally, we were able to solve the structure of *M. tuberculosis* AnPRT in complex with one of the potential transition state mimics, which was observed to bind at the active site of the enzyme. This structure provides new insight into the catalytic mechanism of the enzyme and creates an opportunity to develop more specific inhibitors against the *M. tuberculosis* AnPRT enzyme.

Acknowledgements

Many people need to be acknowledged for their unique, direct or indirect, contributions to the work presented in this thesis. First and foremost, I would like to thank Professor Emily Parker for believing in me and for giving me the opportunity to work with you. I have been very grateful for your guidance and support during the toughest time of my life. Thank you for always having an open door when I needed your help with any issues, science and unrelated. Your passion, hard work and dedication to science is really inspiring. In addition, I would like to thank my co-supervisor, Professor Peter Tyler, for your support, calmly chat and your knowledge of anything related to the synthesis of transition state analogues.

Thank you to past and present members of the Parker research group, particularly to Dr Gerard Johan Moggré (GJ) whose work this thesis builds upon in many places. Thank you, GJ for the knowledgeable chat and teaching me the ways of the synthetic chemistry laboratory. To Dr Yu Bai, thank you for making the biochemistry lab a fun place to work with your music. I value your ability to critically discuss results and general insightful discussions of science, history, country and many other interesting topics in coffee breaks. A big thank you to Dr Wanting Jiao for introducing me docking and providing reviews and valuable advice. Many thanks to Dr Oliver Sterritt for the detailed review of my thesis, introducing me to the Australian Synchrotron and for taking my samples there.

Many thanks to Rudranuj Bundela (Rudy) for all of our pleasant or unpleasant debates about research and other subjects, which really has broadened my perspective. Calling me “big sister” means a lot to me. You have helped me a lot to get through the difficult times by discussing issues and providing me with valuable advice. An enormous thank you to Parastoo and Mohammad for all the special memories, help and chat. It has been fantastic to have gone through the PhD experience with both of you.

Thank you, Leyla and Candice for making the lab a pleasant place to work. Thank you, Davey Lim, Govind Pratap, Effie, Sarah Kessans, Nicky, Kyle, Rose, Gerd Mittelstädt and Rosannah Cameron for all of your help and insightful discussion. I would also like thank to Amelia, Matt,

Wayne, Marie and Ian, the technicians from the University of Canterbury and Victoria University of Wellington.

Thank you to the Biomolecular Interaction Centre, Department of Chemical and Physical Science at the University of Canterbury for financial support and Victoria University of Wellington for my doctoral scholarship and travel funding to attend conferences. Also, to the Ferrier Research Institute for providing all of the facilities required to carry out this work.

To my family and friends, thank you for the support you have given me. In particular, this thesis would not have been here without the continuing support of my husband Sandeep. Thank you for motivating me and believing in me when the science and times were hard. Your encouragement brings out the best in me! Lots of love to my lovely kids Pari and Samar Veer. Pari used to say to me “I hope mama you will finish your PhD soon so then you can play with me”. Finally, the day has come, thanks for being so kind. Lastly, I want to dedicate my thesis to my father and brother. Losing both of them in the last two years has been an incalculable lasting blow. They will be forever missed.

Table of content

Abstract	i
Acknowledgements	iii
Table of content	v
List of Figures	xii
List of Tables	xvii
Abbreviations.....	xix
Chapter 1 Introduction	1
1.1 Enzymes.....	2
1.2 <i>Mycobacterium tuberculosis</i>	2
1.3 Tuberculosis.....	3
1.4 New anti-TB drugs	5
1.4.1 SQ109.....	5
1.4.2 TMC207.....	6
1.4.3 OPC-67683	6
1.5 Amino acid biosynthesis as a drug target.....	7
1.6 Tryptophan biosynthesis	9
1.7 Classification of the phosphoribosyltransferase family	10
1.8 Anthranilate phosphoribosyltransferase	13
1.8.1 The structure of AnPRT	14
1.8.2 The PRPP binding of AnPRTs.....	15
1.8.2.1 Detailed binding interactions of PRPP in various AnPRTs	17
1.8.2.2 Detailed binding of PRPP in <i>M. tuberculosis</i> AnPRT.....	20
1.8.3 The binding of anthranilate to AnPRT	21

1.8.3.1 Binding of anthranilate in different AnPRT structures	21
1.8.4 Conformational Changes	26
1.9 The reaction mechanism of AnPRT	29
1.10 Inhibition of AnPRT.....	31
1.11 Thesis objectives.....	35
Chapter 2 Characterisation and inhibition of <i>M. tuberculosis</i> AnPRT.....	36
2.1 Introduction.....	37
2.2 Protein expression and purification	37
2.3 Kinetic Characterisation	38
2.4 Michaelis-Menten kinetics	39
2.5 Inhibition of <i>M. tuberculosis</i> AnPRT	41
2.5.1 Inhibition kinetics.....	45
2.6 Inhibitor in complex with <i>M. tuberculosis</i> AnPRT	48
2.6.1 Crystal conditions	49
2.6.2 Structure refinement	50
2.7 Bianthranilate phosphonate inhibitors bound with AnPRT	50
2.7.1 AnPRT with 2.6.....	51
2.7.2 AnPRT with 2.8 and 2.9.....	52
2.7.3 AnPRT with 2.10.....	54
2.7.4 AnPRT with 2.11.....	57
2.7.5 Conclusion.....	58

2.8 Summary.....	59
Chapter 3 Molecular modelling.....	61
3.1 Overview.....	62
3.2 Virtual screening.....	62
3.3 Virtual screening workflow	62
3.3.1 Grid generation.....	63
3.3.2 Preparation of the compound library.....	65
3.3.3 Docking and scoring.....	65
3.4 Hit validation	73
3.4.1 Kinetic assay.....	73
3.4.2 X-ray crystallography	80
3.4.2.1 AnPRT complexed with ligand 3.5	82
3.4.2.2 AnPRT complexed with ligand 3.9	83
3.5 Differential scanning fluorimetry	88
3.6 Investigating the effect of 3.9 on PRPP binding using ITC	90
3.7 Summary.....	93
Chapter 4 Probing the substrate binding sites	95
4.1 Introduction.....	96
4.2 Insight into the active site of <i>M. tuberculosis</i> AnPRT.....	96
4.2.1 PRPP binding site	96
4.2.2 Binding of metal ions	98
4.2.3 Investigating the binding of PRPP and Mg ²⁺ ions at the active site	100
4.2.4 Diphosphate binding to the active site	102
4.3 An investigation into the nucleophilic binding site	104
4.3.1 Differential scanning fluorimetry (DSF)	107

4.3.2 Detection of anthranilate and anthranilate analogue binding by ITC.....	108
4.4 Inhibition of <i>M. tuberculosis</i> AnPRT	111
4.4.1 Cyclopentane analogue 4.11	111
4.4.1.1 Retrosynthetic analysis for analogue 4.11	112
4.4.1.2 Detailed synthesis of the cyclopentane analogue (4.11)	113
4.4.1.3 AnPRT inhibition study with cyclopentane phosphate (4.11)	117
4.4.2 Cyclopentene analogue 4.12	119
4.4.3 Diphosphorylated iminosugar 4.14	120
4.4.3.1 Detailed synthesis of iminosugar 4.14.....	120
4.4.3.2 AnPRT inhibition with diphosphorylated amine 4.14.....	121
4.4.4 Iminoribitol analogues	123
4.4.4.1 Synthesis of iminoribitol phosphate 4.19	124
4.4.4.2 AnPRT Inhibition studies on iminoribitol analogues.....	125
4.4.5 Crystallisation.....	128
4.5 Docking of substrate mimics	128
4.6 Summary.....	131
Chapter 5 Towards transition state analogues for <i>M. tuberculosis</i> AnPRT	132
5.1 Overview.....	133
5.2 Transition state.....	133
5.3 Tight binding of transition state analogues.....	134
5.4 Transition state analogue design	135
5.5 Synthesis of transition state analogues.....	137
5.5.1 Retrosynthetic analysis	137
5.5.2 Detailed synthesis of phosphorylated amine 5.2	138
5.5.3 Detailed synthesis of iminosugar derivative 5.8.....	139

5.5.4 Detailed synthesis of hydroxymethyl pyrrolidine derivative 5.6.....	141
5.6 Inhibition study of <i>M. tuberculosis</i> AnPRT with analogues.....	142
5.6.1 Steady-state kinetics.....	142
5.7 Crystal structures of inhibitors bound to AnPRT	147
5.7.1 Crystallography	147
5.7.2 Structure determination	147
5.8 The binding mode for inhibitor 5.8 with AnPRT	150
5.8.1 The detailed binding interactions of ligands in the AnPRT/PRPP/4FA/Mg ²⁺ and AnPRT/5.8/diphosphate structures	151
5.8.2 Comparison of the oligomeric state of the AnPRT/PRPP/4FA/Mg ²⁺ and AnPRT/5.8/diphosphate structures	154
5.9 Interpretation of AnPRT/5.8/diphosphate structure	156
5.10 The binding of ligand 5.8 with <i>M. tuberculosis</i> AnPRT	157
5.11 Summary.....	159
Chapter 6 Summary and future directions.....	161
6.1 Inhibition of <i>M. tuberculosis</i> AnPRT	162
6.2 Substrate binding sites	166
6.3 Distinct conformation of flexible loops	167
6.4 The catalytic properties of <i>M. tuberculosis</i> AnPRT	168
6.5 Future directions	169
Chapter 7 Methods and experimental procedures.....	173
7.1 General methods.....	174
7.1.1 pH measurements.....	174
7.1.2 Reagents and solvents	174
7.1.3 Chromatography	174

7.1.4 Spectroscopy.....	174
7.1.5 Mass spectrometry	175
7.1.6 Buffer Preparation	175
7.1.7 Protein expression	175
7.1.8 Autoinduction	175
7.1.9 Cell harvesting.....	176
7.1.10 Cell lysis.....	177
7.1.11 Protein purification.....	177
7.1.11.1 Immobilised metal affinity chromatography (IMAC).....	177
7.1.11.2 Size exclusion chromatography (SEC)	177
7.1.12 Sodium dodecyl sulphate polyacrylamide gel electrophoresis (SDS-PAGE)	178
7.1.13 Concentration and storage of enzymes.....	178
7.1.14 Determination of protein concentration.....	178
7.1.15 Determination of PRPP and anthranilate concentrations	179
7.1.16 Lanzetta phosphate assay.....	179
7.1.17 Standard kinetics assay.....	180
7.1.17.1 Kinetic and Inhibition assay in Chapter 2	180
7.1.17.2 Inhibition assay in Chapter 3	181
7.1.17.3 Inhibition study in Chapter 4	181
7.1.17.4 Inhibition assay in Chapter 5	182
7.1.18 Differential scanning fluorimetry (DSF)	182
7.1.19 Isothermal titration calorimetry	183
7.1.20 Crystallography.....	184
7.1.20.1 Crystal condition for variant <i>M. tuberculosis</i> AnPRTs	184
7.1.20.2 Data collection and processing.....	185

7.2 Synthesis of analogues for Chapter 4.....	186
7.2.1 Synthesis of cyclopentane analogue 4.11	186
7.2.2 Synthesis of iminosugar 4.14	196
7.2.3 Synthesis of iminoribitol phosphate 4.19	198
7.3 Synthesis of transition state analogues for Chapter 5	201
7.3.1 Synthesis of phosphorylated amine 5.2	201
7.3.2 Detailed synthesis of iminosugar derivative 5.6 and 5.8.....	203
Appendix 1	208
Appendix 2	209
Appendix 3	211
Appendix 4	215
Appendix 5	216
References	247

List of Figures

Figure 1.1 The chemical structure of a few first- and second-line drugs.....	4
Figure 1.2 Chemical structures of new anti-TB drug candidates.....	6
Figure 1.3 The shikimate pathway illustrating the branch point, chorismate, with its multiple end-products.....	8
Figure 1.4 The enzyme-catalysed reactions for the formation of L-tryptophan from chorismate.	9
Figure 1.5 Illustration of the monomeric unit of four types of PRTs.....	12
Figure 1.6 The AnPRT catalysed the reaction.	13
Figure 1.7 The oligomeric structure of <i>M. tuberculosis</i> AnPRT.	14
Figure 1.8 The monomer unit of the <i>M. tuberculosis</i> AnPRT (PDB: 1ZVW).....	15
Figure 1.9 The binding mode of PRPP and Mg ²⁺ in different AnPRT structures.....	16
Figure 1.10 The binding mode of PRPP and Mg ²⁺ ions in the <i>M. tuberculosis</i> AnPRT structure (PDB: 1ZVW).....	18
Figure 1.11 The binding mode of PRPP and metal ions in the <i>P. carotovorum</i> (PDB: 1KGZ) and <i>S. solfataricus</i> AnPRT (PDB: 1ZYX) structures.	19
Figure 1.12 PRPP binding in <i>M. tuberculosis</i> AnPRT.....	20
Figure 1.13 The binding sites of anthranilate and an anthranilate analogue (4FA) in different AnPRT structures.....	22
Figure 1.14 The chemical structure of anthranilate and anthranilate analogue (ACS172).....	23
Figure 1.15 ACS172 binding interaction at multiple sites in <i>M. tuberculosis</i> AnPRT structure (PDB: 3QQS).	24
Figure 1.16 The ACS172 bound <i>M. tuberculosis</i> AnPRT structure (PDB: 3QQS) shows a number of binding positions in the substrate-binding tunnel.	25
Figure 1.17 Proposed catalytic cycle for <i>M. tuberculosis</i> AnPRT.....	27

Figure 1.18 A possible reaction mechanism for the AnPRT catalysed reaction.	29
Figure 1.19 The reactions catalysed by NPs, type I and type III PRTs.....	30
Figure 1.20 The chemical structures of <i>M. tuberculosis</i> AnPRT inhibitors.	32
Figure 1.21 The series of inhibitors tested against <i>M. tuberculosis</i> AnPRT.....	32
Figure 1.22 The twisted confirmation for inhibitor 636 observed at binding sites 1–2 in the substrate-binding tunnel.	33
Figure 1.23 The chemical structure of “trianthranilate-like” 644 compound and its binding within the anthranilate substrate-binding tunnel in <i>M. tuberculosis</i> AnPRT (PDB: 4GIU).....	34
Figure 2.1 SDS-PAGE purification gel of <i>M. tuberculosis</i> AnPRT and <i>E. coli</i> PRAI:InGPS.	38
Figure 2.2 The enzyme-coupled assay utilised to get stable InGP product.....	39
Figure 2.3 Michaelis-Menten curves for both substrates of <i>M. tuberculosis</i> AnPRT.	40
Figure 2.4 Structures of the phosphonate moieties attached to the nucleophilic base inhibitors for type I <i>M. tuberculosis</i> HGPRT.....	42
Figure 2.5 <i>M. tuberculosis</i> AnPRT inhibition graphs for both substrates to determine inhibitor K_i values.....	48
Figure 2.6 <i>M. tuberculosis</i> AnPRT co-crystallised with 2.11 and Mg^{2+} , with 0.2 M imidazole malate (pH 6.5), 10% PEG–4000 (w/v).	49
Figure 2.7 The binding interaction of 2.6 with <i>M. tuberculosis</i> AnPRT.	52
Figure 2.8 Two different binding modes for 2.8 and 2.9 bound with AnPRT.....	53
Figure 2.9 The inner side binding mode for ligand 2.10 with <i>M. tuberculosis</i> AnPRT.	55
Figure 2.10 The 2.10 -bound <i>M. tuberculosis</i> AnPRT structure.....	56
Figure 2.11 The binding interaction for the 2.11 -bound AnPRT structures.	57
Figure 3.1 The predicted binding mode and interactions for PRPP as determined by Glide..	64
Figure 3.2 The hierarchical virtual screening workflow.....	65
Figure 3.3 Structures and docking poses of chosen compounds from the virtual screen of the ZINC library against <i>M. tuberculosis</i> AnPRT.....	69

Figure 3.4 The binding sites of 6MI in the AnPRT structure (PDB: 4N93).	72
Figure 3.5 Structures and docking poses of the selected compounds from the virtual screen against <i>M. tuberculosis</i> AnPRT.....	73
Figure 3.6 Kinetics assay graphs in the presence of both substrates for <i>M. tuberculosis</i> AnPRT at various concentrations of the chosen compounds from the docking study.....	79
Figure 3.7 The binding position for ligand 3.5	82
Figure 3.8 Chain C of the AnPRT/ 3.9 bound structure overlaid with chain A of the AnPRT/PRPP/Mg ²⁺ structure.....	84
Figure 3.9 Chain A of the 3.9 bound AnPRT structure.....	85
Figure 3.10 The different conformation of the $\beta 2$ – $\alpha 6$ loop in various <i>M. tuberculosis</i> AnPRT structures.	87
Figure 3.11 Melting temperatures for AnPRT in the presence of various ligands by DSF.	89
Figure 3.12 ITC isotherms displaying the thermodynamics for the binding of 3.9 and PRPP to <i>M. tuberculosis</i> AnPRT	91
Figure 4.1 The binding of ligands at the active site with similar conformation adopted by $\beta 1$ – $\alpha 5$ and $\beta 2$ – $\alpha 6$ loops in various <i>M. tuberculosis</i> AnPRTs.....	97
Figure 4.2 Metal binding features in various <i>M. tuberculosis</i> AnPRT structures.	99
Figure 4.3 ITC experiments display the thermodynamic parameters for the binding of PRPP and Mg ²⁺ ions to <i>M. tuberculosis</i> AnPRT.	102
Figure 4.4 <i>M. tuberculosis</i> AnPRT inhibition graphs in the presence of various concentrations of diphosphate against PRPP.	103
Figure 4.5 <i>M. tuberculosis</i> AnPRT structures displaying the anthranilate binding sites.	105
Figure 4.6 DSF melting temperatures for <i>M. tuberculosis</i> AnPRT in the presence of several ligands.	107
Figure 4.7 Structural representations of anthranilate and 4FA.....	109
Figure 4.8 ITC data for the binding of 4FA to <i>M. tuberculosis</i> AnPRT.	110
Figure 4.9 The chemical structure of R5P and cyclopentane analogue 4.11	112

Figure 4.10 The crystal structure of cyclopentenone 4.7 with the correct stereochemistry.	115
Figure 4.11 Inhibition of <i>M. tuberculosis</i> AnPRT by R5P and cyclopentane 4.11 .	118
Figure 4.12 Cyclopentene phosphate 4.12 was tested as a mimic transition state.	119
Figure 4.13 <i>M. tuberculosis</i> AnPRT inhibition graph for cyclopentene phosphate 4.12 .	119
Figure 4.14 The chemical structure of iminosugar 4.14 .	120
Figure 4.15 The kinetic assay of <i>M. tuberculosis</i> AnPRT for diphosphorylated amine 4.14 .	121
Figure 4.16 Potential transition state and transition state mimics for <i>M. tuberculosis</i> AnPRT.	123
Figure 4.17 The potential inhibitors for <i>M. tuberculosis</i> AnPRT.	124
Figure 4.18 K_i^{app} determination for several analogues tested against <i>M. tuberculosis</i> AnPRT.	126
Figure 4.19 Stereo representation of the best docking poses of the AnPRT inhibitors predicted by induced fit docking.	130
Figure 5.1 Reaction coordinate diagram for an enzyme-catalysed reaction.	133
Figure 5.2 The possible dissociative “ S_N1 -like” reaction mechanism of AnPRT.	135
Figure 5.3 The chemical structures of potential transition state analogues for AnPRT.	136
Figure 5.4 <i>M. tuberculosis</i> AnPRT inhibition graphs for different compounds.	144
Figure 5.5 The apparent K_i values of <i>M. tuberculosis</i> AnPRT inhibitors compared to both substrates.	145
Figure 5.6 Structural superimpositions reveal inhibitor 5.8 and a diphosphate molecule (brown) mimicking the binding mode of PRPP (green) and 4FA (pink).	151
Figure 5.7 The binding interactions of ligands in the AnPRT/PRPP/4FA/Mg ²⁺ (PDB: 4N5V) and AnPRT/ 5.8 /diphosphate structures.	152
Figure 5.8 Inspection of the observed changes in the position of both domains by binding different ligands.	155
Figure 5.9 Structural superimposition of AnPRT/ 5.8 /diphosphate monomers.	156

Figure 5.10 ITC experiments to detect inhibitor 5.8 binding to AnPRT 25 °C.	158
Figure 6.1 The binding of inhibitor 3.9 (yellow) in chain A of the AnPRT/ 3.9 structure.	167
Figure 6.2 Proposed expansion of the iminoribitol inhibitor and the phosphonate isostere.	170
Figure 6.3 Potential improvements to the transition state analogues to expend their binding into the enzyme catalytic site.	171
Figure 6.4 The expanded transition state analogue based on cyclopentane and compounds with a double bond characteristic.	171

List of Tables

Table 2.1 Comparison of kinetic parameters for AnPRT from various organisms.	41
Table 2.2 “bianthranilate”-like inhibitors with apparent K_i values against <i>M. tuberculosis</i> AnPRT.....	44
Table 3.1 Compounds selected from the virtual screening with K_i values and their best-fitted inhibition model for both substrates against <i>M. tuberculosis</i> AnPRT.	75
Table 3.2 Data collection and refinement statistics for AnPRT crystals in complex with ligands 3.9 and 3.5	81
Table 3.3 <i>M. tuberculosis</i> AnPRT melting temperatures in the presence of various ligands..	88
Table 4.1 <i>M. tuberculosis</i> AnPRT melting temperatures in the presence of various ligands.	108
Table 4.2 The type of inhibition and K_i values for different ligands along with both substrates for <i>M. tuberculosis</i>	122
Table 4.3 The K_i values of different iminoribitol analogues along with both substrates for <i>M. tuberculosis</i>	127
Table 4.4 Structural representation of AnPRT inhibitors with their docking scores.	129
Table 5.1 The types of inhibition with the apparent K_i values displayed for AnPRT inhibitors.	146
Table 5.2 Data collection and refinement statistics for AnPRT/ 5.8 /diphosphate structure.	148
Table 5.3 <i>M. tuberculosis</i> AnPRT structures with PDB code, space group and cell parameters.	149
Table 6.1 Inhibitors with the apparent K_i values and their best-fitted inhibition model for both substrates against <i>M. tuberculosis</i> AnPRT.....	164
Table 6.2 The types of inhibition with the apparent K_i values displayed for <i>M. tuberculosis</i> AnPRT inhibitors.....	164
Table 7.1 The culture medium for autoinduction.	176

Table 7.2 Extinction coefficients for both protein	178
Table 7.3 The experimental set-up for ITC	183
Table 7.4 The crystallisation conditions for <i>M. tuberculosis</i> AnPRT crystals with various ligands.	185
Table 7.5 Crystal datasheet for compound 4.7	208

Abbreviations

ADP	Adenosine diphosphate
apo	apoenzyme
AICAR	5-Aminoimidazole-4 carboxamide ribonucleotide
AK	adenylate kinase
AMP	Adenosine monophosphate
AS	anthranilate synthase
AnPRT	Anthranilate phosphoribosyltransferase
ATP	Adenosine triphosphate
ATPPRT	Adenosine triphosphate phosphoribosyltransferase
Boc	<i>tert</i> -butyloxycarbonyl
Cal.	Calculated
CDCl ₃	Chloroform
DCM	Dichloromethane
DMAP	4-(dimethylamino)pyridine
DMSO	dimethyl sulphoxide
DSF	differential scanning fluorimetry
EDTA	Ethylenediaminetetraacetic acid
E	enzyme
EP	enzyme-product
ES	enzyme-substrate
E4P	erythrose-4-phosphate
HIV	human immunodeficiency virus
HMPA	Hexamethylphosphoramide
h	hours
IMAC	Immobilised metal affinity chromatography
InGP	indole glycerol phosphate
InGPS	indole glycerol phosphate synthase
IR	infrared
ITC	isothermal titration calorimetry
<i>k</i> _{cat}	turnover number
kDa	kilodalton
<i>K</i> _i	inhibition constant
KIE	Kinetic isotope effect
<i>K</i> _M	Michaelis-Menten constant
LB	lysogeny broth
LiAlH ₄	Lithium aluminium hydride
<i>m</i> -CPBA	<i>meta</i> -chloroperoxybenzoic acid

Me	Methyl
MWCO	molecular weight cut-off
NaBH ₄	Sodium borohydride
NPs	Nucleoside phosphorylases
<i>n-BuLi</i>	<i>n-butyl lithium</i>
PRA	<i>N</i> -(5'-phosphoribosyl) anthranilate
NaIO ₄	Sodium periodate
NMR	nuclear magnetic resonance
Obsd.	Observed
CDRP	1-(<i>O</i> -carboxyphenylamino)-1'-deoxyribulose-5'-phosphate
PDB	Protein Data Bank
PEP	phosphoenol pyruvate
ProFAR	<i>N'</i> -[(5'-phosphoribosyl)formimino]-5-aminoimidazole-4-carboxamide ribonucleotide
PRPP	Phosphoribosyl pyrophosphate
RMSD	root-mean-square deviation
Rt	Room temperature
S	substrate
SDS-PAGE	sodium dodecyl sulphate polyacrylamide gel electrophoresis
SEC	Size exclusion chromatography
Tris	Tris(hydroxymethyl)aminomethane
TB	Tuberculosis
THF	Tetrahydrofuran
TLC	Thin layer chromatography
TMSCl	Trimethylsilyl chloride
TS	Transition state
TST	Transition state theory
UV	ultraviolet
WHO	World Health Organization

Amino acid three letter codes:

Ala	Alanine	Leu	Leucine
Arg	Arginine	Lys	Lysine
Asn	Asparagine	Met	Methionine
Asp	Aspartate	Phe	Phenylalanine
Cys	Cysteine	Pro	Proline
Gln	Glutamine	Ser	Serine
Glu	Glutamate	Thr	Threonine
Gly	Glycine	Trp	Tryptophan
His	Histidine	Tyr	Tyrosine
Ile	Isoleucine	Val	Valine

Chapter 1 Introduction

1.1 Enzymes

Enzymes are mostly protein molecules that act as catalysts and accelerate chemical reactions. Enzymes differ from most other chemical catalysts by being much more substrate-specific and provide precise stereochemical control. Enzymes are known to accelerate the rate of a chemical reaction by as much as 10^{12} -fold over the spontaneous rate of the uncatalyzed reaction.¹ This incredible rate enhancement results from the juxtaposition of chemically reactive groups at the active site of an enzyme and other groups from the target molecule (substrate), in a way that lowers the activation energy of reaction, so that the reaction steps required to convert the substrate into the reaction product occur more readily.

Enzymatic catalytic power facilitates life processes in all life-forms, from viruses to humans. Enzymes are also of fundamental interest in the health sciences since many diseases can be linked to the aberrant activities of one or a few enzymes.¹ The modulation of the rate of enzyme activity allows an organism to control the production of metabolites in response to cellular needs.² Many enzymes catalyse a single reaction; therefore, the reaction specificity of an enzyme allows for its selective targeting without impacting other vital processes.³ The ability to alter the function of an enzyme through inhibition also forms the basis of many drugs. Hence, a significant amount of modern pharmaceutical research is based on the search for potent and specific inhibitors of essential enzymes.

1.2 *Mycobacterium tuberculosis*

Mycobacterium tuberculosis (*M. tuberculosis*) is the primary causative agent of tuberculosis (TB).⁴ However, *Mycobacterium bovis* (*M. bovis*), *Mycobacterium africanum* (*M. africanum*), *Mycobacterium canetti* (*M. canetti*) are also responsible for TB.⁵ *Mycobacterium* species persist in fish, amphibians, reptiles, birds, and mammals and they are omnipresent in organisms, soil and the water.⁶ *M. tuberculosis* is a metabolically flexible aerobic pathogen that has the tremendous ability to adapt to the continuously changing host environment experienced during decades of persistent infection.⁷ It is hypothesised that through their evolution, mycobacteria had to face nutrient depletion or poisonous environments resulting in their complex cell wall.⁶ The molecular complexity of the mycobacterium cell envelope is

structurally distinct from most other prokaryotes. Although *M. tuberculosis* is classified as a Gram-positive organism, its envelopes have prominent features of Gram-negative cell walls, such as an outer permeability barrier acting as a pseudo-outer membrane.⁷ Additionally, *M. tuberculosis* has developed specific mechanisms to protect itself against endogenously and exogenously produced oxidants and reductants found specifically within the lung.⁸ *M. tuberculosis* uses many biosynthetic pathways that are not present in mammalian organisms. These pathways have important roles in the synthesis of necessary cell wall components, amino acids and sugars.⁸ These essential pathways provide an important focus for the development of new anti-TB chemotherapies.

1.3 Tuberculosis

TB is a major health threat. Although, multiple drugs and vaccines have been developed, TB is still the second most common cause of death worldwide.⁹ The World Health Organization (WHO) 2018 report shows that around 1.6 million people have died from TB and new infections occurred in 10 million people in 2017 alone.¹⁰

In 1882, *M. tuberculosis* was first identified by Robert Koch.¹¹ The organism is a rod-shaped bacterium and has a distinctive lipid-rich cell wall structure, which contributes to the pathogenicity and drug resistance of this human pathogen. Infection with *M. tuberculosis* follows a series of events.¹² The infectious bacilli are inhaled by potential human host as droplet nuclei that have been exhaled into the atmosphere from TB patient. These nuclei are able to survive for a few hours in the atmosphere. The bacteria are phagocytosed by alveolar macrophages and the appearance of *M. tuberculosis* lymphocytes approximately 2–3 weeks post-infection marks the end of the phase of rapid bacterial replication. TB infections are generally found in the lungs, but infections of other parts of the body, such as the spine and lymph nodes, are also possible. However, in the last stage, the disease may also contribute to tissue damage and the dissemination of infectious bacteria into the airways. In addition, the features that enable *M. tuberculosis* to persist within the tissues of its host have also allowed TB to remain one of the world's great killers, even into the 21st century.¹²

In the early 1950s, when more effective drugs such as isoniazid (INH), rifampicin (RIF), ethambutol (EMB), streptomycin (SM) and pyrazinamide (PZA) were introduced for the

treatment of TB infections (Figure 1.1)¹³, the incidence of mortality dramatically decreased from approximately 75% to 20%. However, the safety of these drug agents was uncertain as a combination of these drugs needs to be taken over a long period of time which increase the risk of drug-resistance in TB.

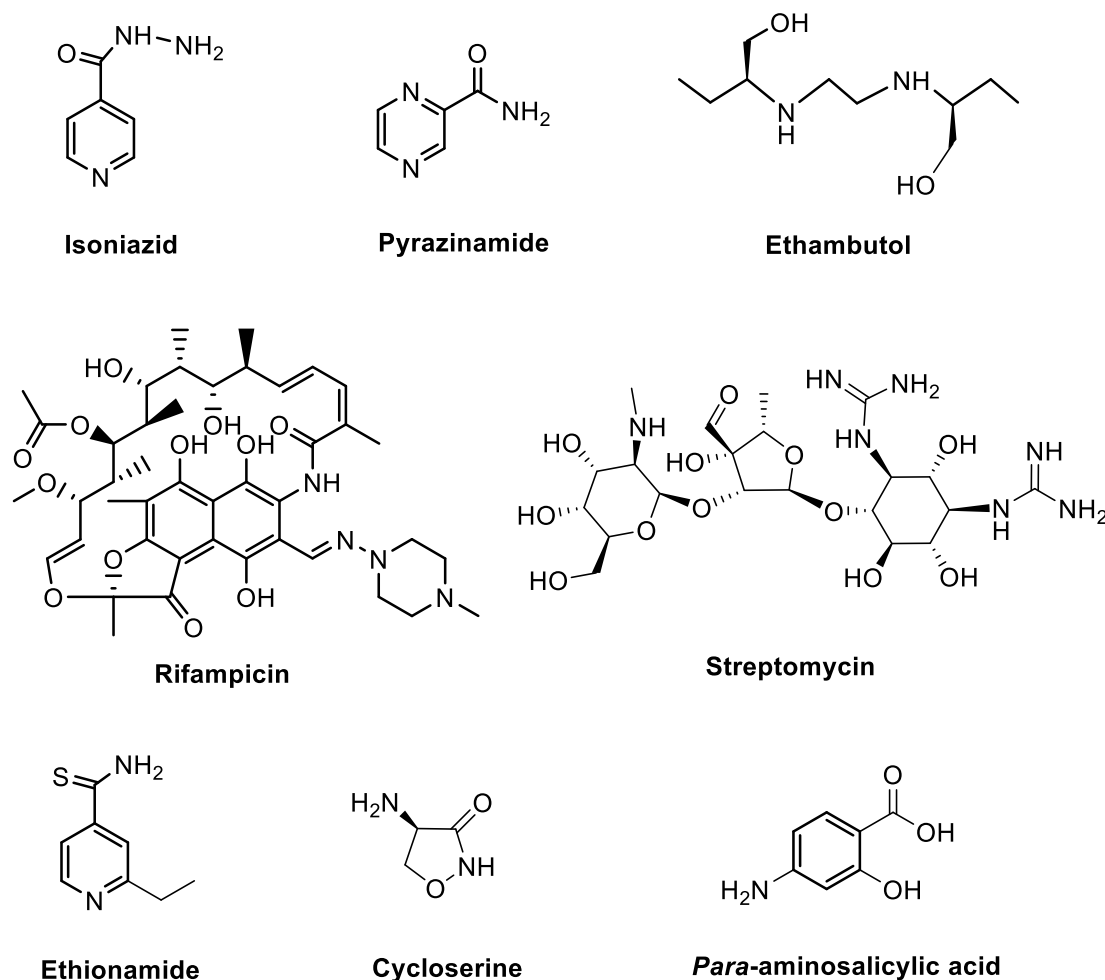


Figure 1.1 The chemical structure of a few first- and second-line drugs.

Second-line drugs, such as ethionamide (ETH), cycloserine (CS), fluoroquinolones (FQs), aminoglycosides (kanamycin, amikacin and capreomycin), and *para*-aminosalicylic acid (PAS), are also used to treat TB (Figure 1.1).¹⁴ Although protracted, a six-month course of these drugs is cheap and effective to treat the disease. However, the current treatment regime is being undermined by a number of factors, including increasing resistance to current TB drugs, intolerance, an increase in human immunodeficiency virus (HIV) associated TB and the emergence of multiple drug resistance (MDR) and extreme drug-resistant (XDR) TB.¹⁵

In 2015, drug-resistant TB had widely emerged, particularly MDR-TB. Six per cent of new cases of MDR-TB have been reported. This means that the *M. tuberculosis* pathogen is resistant to most common TB drugs. Proper TB care and control averted up to 6 million deaths and cured 36 million people between 1995 and 2008.¹⁶ Yet, TB remains a severe global public health threat. The effective treatment of persistent infections, such as MDR and XDR-TB, is one of the major goals for researchers and pharmaceutical companies.

1.4 New anti-TB drugs

TB has been more prevalent worldwide in the last decades than at any other time in human history.¹⁷ The emergence of MDR-TB strains of *M. tuberculosis* makes the discovery of new molecular scaffolds with anti-TB properties a priority and the current situation even necessitates the re-engineering and repurposing of some old drugs to achieve effective treatments for TB. A new TB drug should not have side effects, exhibit excellent activity against *M. tuberculosis* and require a short treatment duration. The growing awareness around TB in recent years has led to an increase in research into the development of anti-TB drugs.¹⁸ Currently, a number of new anti-TB drugs are in the pipeline.¹⁹ A few effective drugs are listed in Sections 1.4.1–1.4.3.

1.4.1 SQ109

The synthesis and screening of diamine analogues of EMB have provided a variety of compounds with better activity against *M. tuberculosis* compared to that of EMB.¹⁹ The most effective compound, SQ109, exhibits excellent *in vitro* activity against *M. tuberculosis*, including strains resistant to EMB, INH and RIF drugs (Figure 1.2).²⁰ SQ109 is a new anti-TB drug candidate in the ethylenediamine class that inhibits the synthesis of the *M. tuberculosis* cell wall. SQ109 was safe and well-tolerated in Phase I and early Phase II clinical trials.²¹ A particularly potent combination is SQ109/RIF displaying inhibition of *M. tuberculosis* growth greater than 99% at very low concentrations, while also being effective against RIF-resistant strains.²²

1.4.2 TMC207

A series of diarylquinolines have been developed that exhibit potent *in vitro* and *in vivo* activity against *M. tuberculosis*.¹⁸ The most potent molecule (Figure 1.2), TMC207 exhibits excellent activity against drug-susceptible, MDR and XDR *M. tuberculosis* strains, with no cross-resistance to current first-line drugs.²³ TMC207 has a unique mechanism of action where a molecule of TMC207 binds to an adenosine triphosphate synthase (ATP synthase) enzyme, the “energy currency” for bacterium cells. The binding of TMC207 inhibits the enzymatic reaction of ATP synthase by blocking proton transformation leading to insufficient amounts of the reaction product, ATP. Based on clinical evaluations of safety, tolerability and efficacy, TMC207 has recently received accelerated approval for the treatment of pulmonary MDR-TB in adults.²⁴ TMC207 has now become a new anti-TB drug and has been named Bedaquiline (Figure 1.2).²⁵

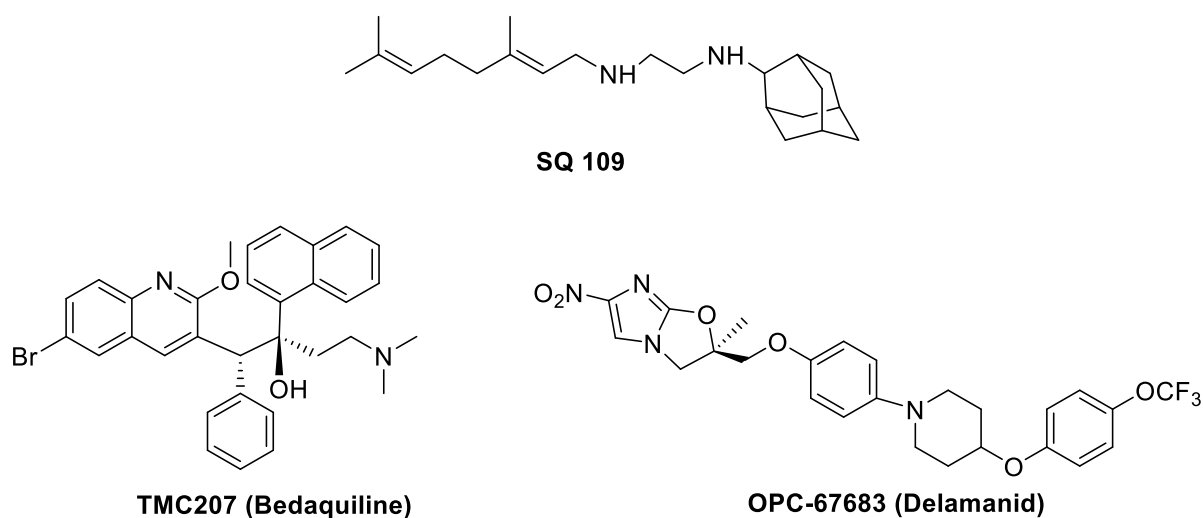


Figure 1.2 Chemical structures of new anti-TB drug candidates.

1.4.3 OPC-67683

Investigations into another class of nitroimidazoles compounds resulted in the discovery of OPC-67683.²⁶ Recently completed phase II clinical trials of OPC-67683 have been successful, and this compound has been named delamanid (Figure 1.2).²⁷ Mycolic acid is an essential component of the cell walls of Mycobacterium that is present only in mycobacteria not in mammals cell.²⁸ Delamanid blocks the biosynthesis of mycolic acid. It also exhibits excellent *in vitro* activity against drug-susceptible and resistant *M. tuberculosis* strains and does not

show antagonistic activity in combination with most common anti-TB drugs such as INH, RIF, EMB or SM.²⁸ The long half-life of delamanid and its efficacy in immunocompromised mice suggest that this drug may be useful for the treatment of co-infected TB/HIV patients.²⁹ Its bactericidal activity was also demonstrated in individuals with drug-susceptible and drug-resistant MDR and XDR-TB.³⁰ Its safety and tolerability profile and ongoing clinical trials have also demonstrated its efficacy in the paediatric population.³⁰

SQ109, bedaquiline and delamanid are the most promising new drugs since these are highly active against drug-resistant and susceptible strains and demonstrate excellent sterilising power of TB. These and other developments in anti-TB drug therapies give hope that within the next decade an effective anti-TB regimen of shorter duration may be achieved.

1.5 Amino acid biosynthesis as a drug target

M. tuberculosis uses many biosynthetic pathways that are essential for the survival of *M. tuberculosis* and present only in bacteria, fungi and plants but absent in humans. One of these pathways is the shikimate pathway in which chorismate acts as a branch point for the biosynthesis of the aromatic amino acids; phenylalanine, tyrosine and tryptophan (Figure 1.3).³¹ Important compounds such as folate, vitamin K and E are also known to be generated by the shikimate pathway. The pathway commences with phosphoenol pyruvate (PEP) and erythrose 4-phosphate (E4P) and leads to the formation of chorismate in multiple steps with the involvement of seven distinct enzymes. After the synthesis of chorismate, the pathway splits in two directions, where one branch leads to the formation of prephenate, the precursor for L-phenylalanine and L-tyrosine, and the other branch leads to anthranilate, from which L-tryptophan is synthesized. Enzymes, which are specific to this biosynthetic pathway, are therefore very important targets for the synthesis of inhibitory drugs.³² For example, *M. tuberculosis* tryptophan and histidine auxotrophs were not able to survive long-term starvation of single amino acids.³³ Several studies have also shown that leucine, tryptophan, and arginine auxotrophs do not multiply or even survive in macrophages if these amino acids are not present within the compartment of the macrophage where the TB bacteria reside.^{34–36} These studies support that the enzymes of this pathway are potential drug targets for the treatment of mycobacterial diseases.

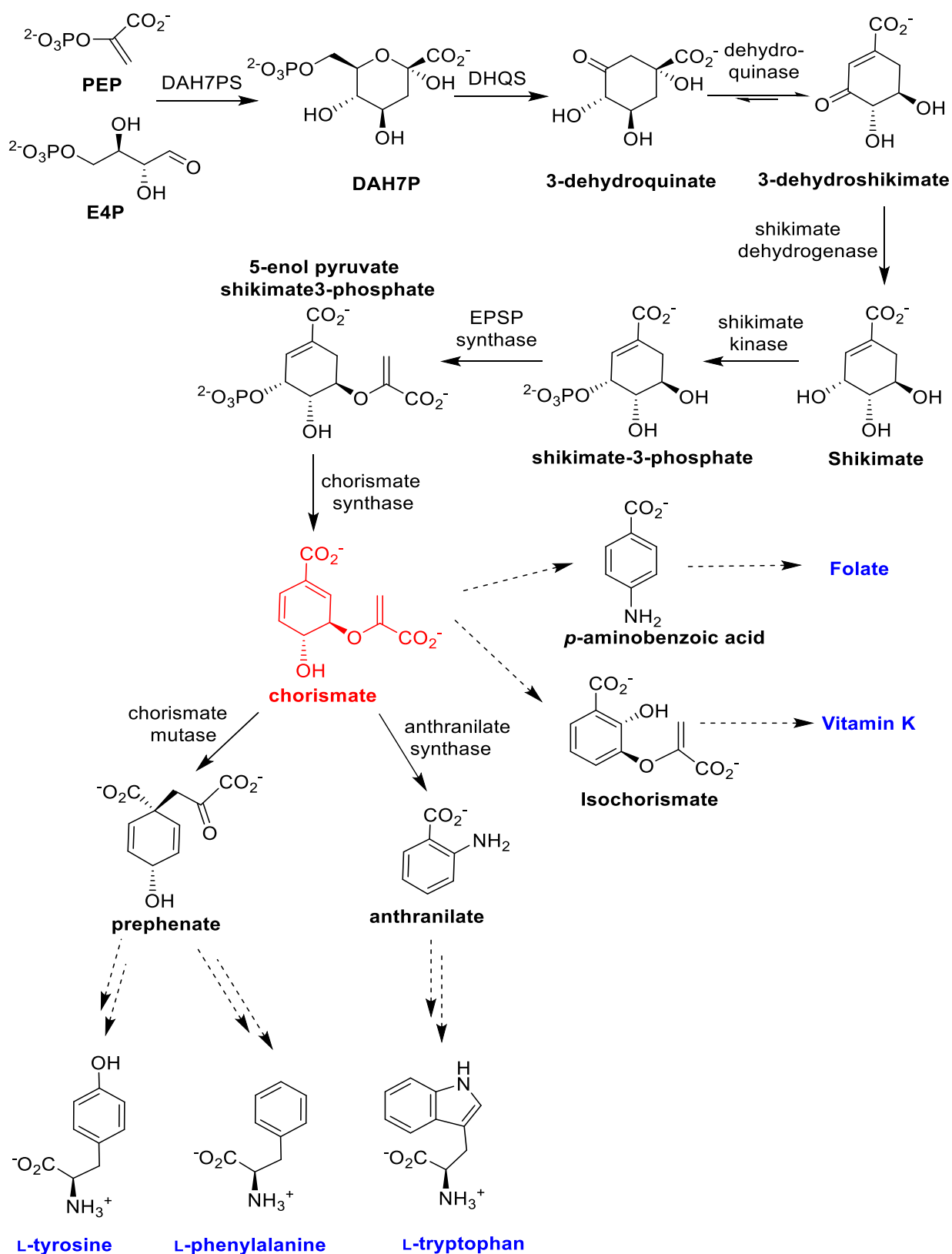


Figure 1.3 The shikimate pathway illustrating the branch point, chorismate, with its multiple end-products.

1.6 Tryptophan biosynthesis

Enzymes which are specific to the biosynthesis of L-tryptophan are very important targets for the design and synthesis of anti-TB drugs. The biosynthesis of the amino acid tryptophan from chorismate has been shown to be very important for the survival of *M. tuberculosis*.³⁷ In *E. coli*, a genetic knockout of the *trpD* gene, which encodes the anthranilate phosphoribosyltransferase (AnPRT) enzyme, was unable to cause disease even in immune-deficient mice,³⁸ demonstrating that this pathway may be a useful target for the design and synthesis of drugs.

Tryptophan biosynthesis in different microbes involves a series of six chemical reactions, beginning with chorismate as an initial precursor (Figure 1.4). The initial enzyme specific to the tryptophan pathway is anthranilate synthase (AS), which converts chorismate and glutamine into anthranilate and also liberates pyruvate and glutamate as by-products. AS is a heterodimeric enzyme which is encoded by the *trpE* and *trpG* genes.³⁹

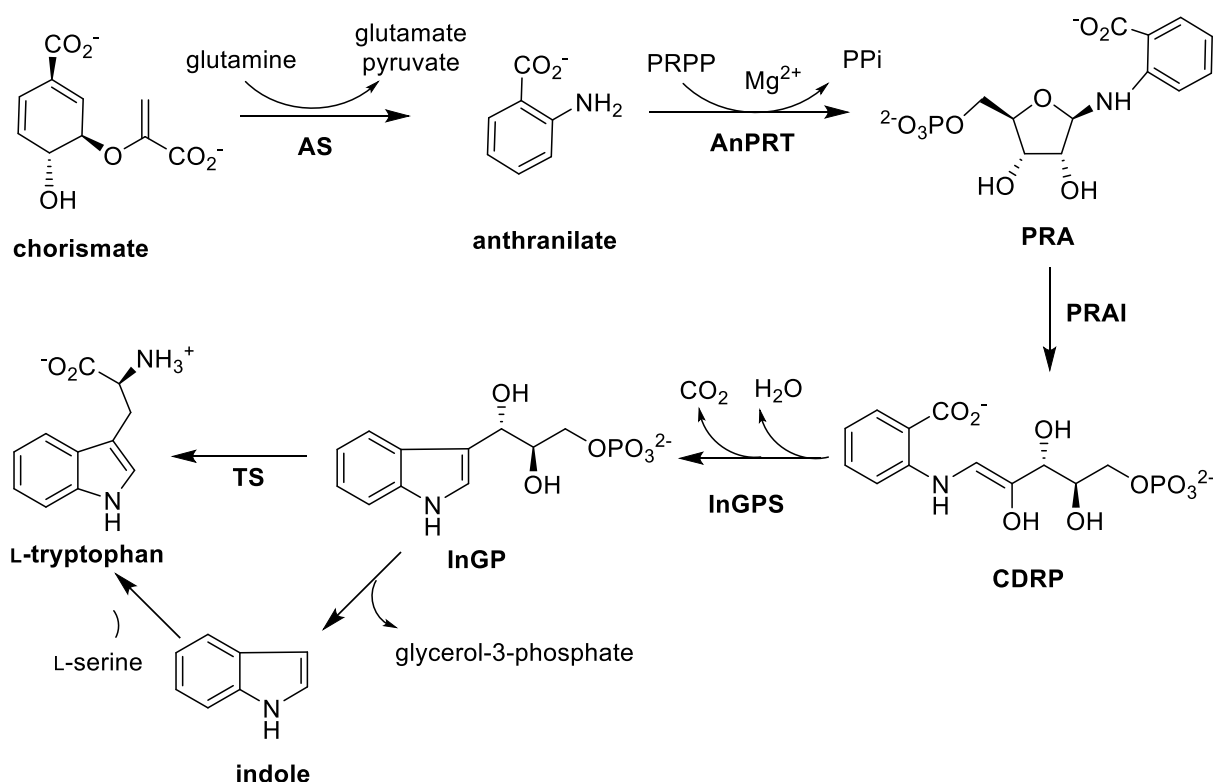


Figure 1.4 The enzyme-catalysed reactions for the formation of L-tryptophan from chorismate.

The *trpD* gene encodes AnPRT, the second enzyme which catalyses the nucleophilic addition of 5-phospho- α -ribose-1-diphosphate (PRPP) to anthranilate in the presence of metal ions to form *N*-(5'-phosphoribosyl) anthranilate (PRA). However, the *trpD* and *trpG* genes are found fused only in *E. coli*⁴⁰ and *Thermotoga maritima* species.⁴¹ The AnPRT catalysed product, PRA is then isomerised to 1-(*O*-carboxyphenylamino)-1'-deoxyribulose-5'-phosphate (CDRP). In a few species, PRA isomerisation is carried out by the PRA isomerase (PRAI) enzyme, which is encoded by the *trpF* gene. However, the *trpF* gene has not been identified in the *Mycobacterium* genome⁴² and, therefore, isomerisation of PRA to CDRP is speculated to be catalysed by the *N'*-[(5'-phosphoribosyl)formimino]-5-aminoimidazole-4-carboxamide ribonucleotide (ProFAR) isomerase enzyme.⁴³ ProFAR isomerase is encoded by the *hisA* gene that participates in the biosynthesis of L-histidine.⁴³

The *trpC* gene, encoding the fourth enzyme in the pathway, encodes for indole glycerol phosphate synthase (IGPS) which converts CDRP to indole-3-glycerol phosphate (InGP) and also releases CO₂ and H₂O as by-products. In *E. coli*, the *trpF* and *trpC* genes are also fused.⁴⁰ Tryptophan synthase (TS), the final enzyme in the tryptophan pathway, is a heterodimeric protein encoded by the *trpA* and *trpB* genes. The *trpA* gene is responsible for the cleavage of glyceraldehyde-3-phosphate from the indole moiety and *trpB* is responsible for a further reaction of the indole with L-serine to form L-tryptophan.

1.7 Classification of the phosphoribosyltransferase family

A family of phosphoribosyltransferase (PRT) enzymes catalyses the transfer of the phosphoribosyl group of PRPP to a nitrogen-containing nucleophile, generally an aromatic base.⁴⁴ The PRT proteins play an important role in several biosynthetic pathways such as in the synthesis of tryptophan, histidine and pyrimidine along with their involvement in the nucleotide salvage pathway.^{44,45} However, not all PRT proteins play a role in biosynthesis; they can also be involved in the regulation of the expression of purine and pyrimidine biosynthetic genes in some bacteria. AnPRT enzymes are part of the PRT family which is divided into four subtypes: type I, type II, type III and type IV.

The type I enzymes were first described at a sequence and structural level in the PRT family and these enzymes are mainly part of the nucleotide synthesis and salvage pathways. Examples include orotate PRT,⁴⁶ hypoxanthine-guanine PRT⁴⁷ and uracil PRT.⁴⁸ The type I PRT enzymes are a homologous group of enzymes that share a common structural core consisting of a five-stranded parallel β sheet ($\beta 2$ - $\beta 1$ - $\beta 3$ - $\beta 4$ - $\beta 5$) surrounded by three α -helices (Figure 1.5, **A**). A thirteen-amino acid sequence motif serves as a conserved PRPP binding loop. This flexible loop acts as a gate for the active site and changes the conformational state of the protein to facilitate catalysis. Allosteric regulation is also observed in some type I PRTs, such as glutamine PRPP aminotransferase, which is inhibited by the end products of the purine biosynthetic pathway: adenosine monophosphate, adenosine diphosphate, guanosine monophosphate and guanosine diphosphate.⁴⁹

Type II PRTs are classified based on the novel fold found for quinolinic acid PRT⁵⁰ and nicotinic acid PRT⁵¹ (Figure 1.5, **B**). The type II PRTs do not display the unique protein fold with the 13-residue sequence characteristic of type I PRTs. Members of this subfamily lack the conserved PRPP binding site. This family exhibits a novel N-terminal open-faced β -sandwich domain and a unique seven-stranded α/β barrel-like domain.⁵¹ There are also differences in the oligomeric structures of type II PRTs: hexameric (*Homo sapiens* quinolinic acid PRT),⁵² dimeric (*Salmonella typhimurium* quinolinic acid PRT),⁵⁰ and monomeric (*Saccharomyces cerevisiae* nicotinic acid PRT)⁵¹ species have been reported.

Type III PRTs enzymes are represented by AnPRT (Figure 1.5, **C**).⁵³ AnPRT catalyses the second step in the tryptophan biosynthesis pathway. AnPRT is a homodimer, with an active site located in the hinge region of a large C-terminal domain and a smaller N-terminal domain. The catalytic site is mostly accommodated within the C-terminal domain. The substrate binding mode at the catalytic site of AnPRT is distinct to type I, II and III PRTs.⁵⁴ Structures of AnPRT from different organisms, such as *Sulfolobus solfataricus* (*S. solfataricus*),⁵⁵ *Pectobacterium carotovorum* (*P. carotovorum*)⁵⁶ and *M. tuberculosis*,^{53,57} have a well-defined novel protein fold that is also different from other types of PRT enzymes.

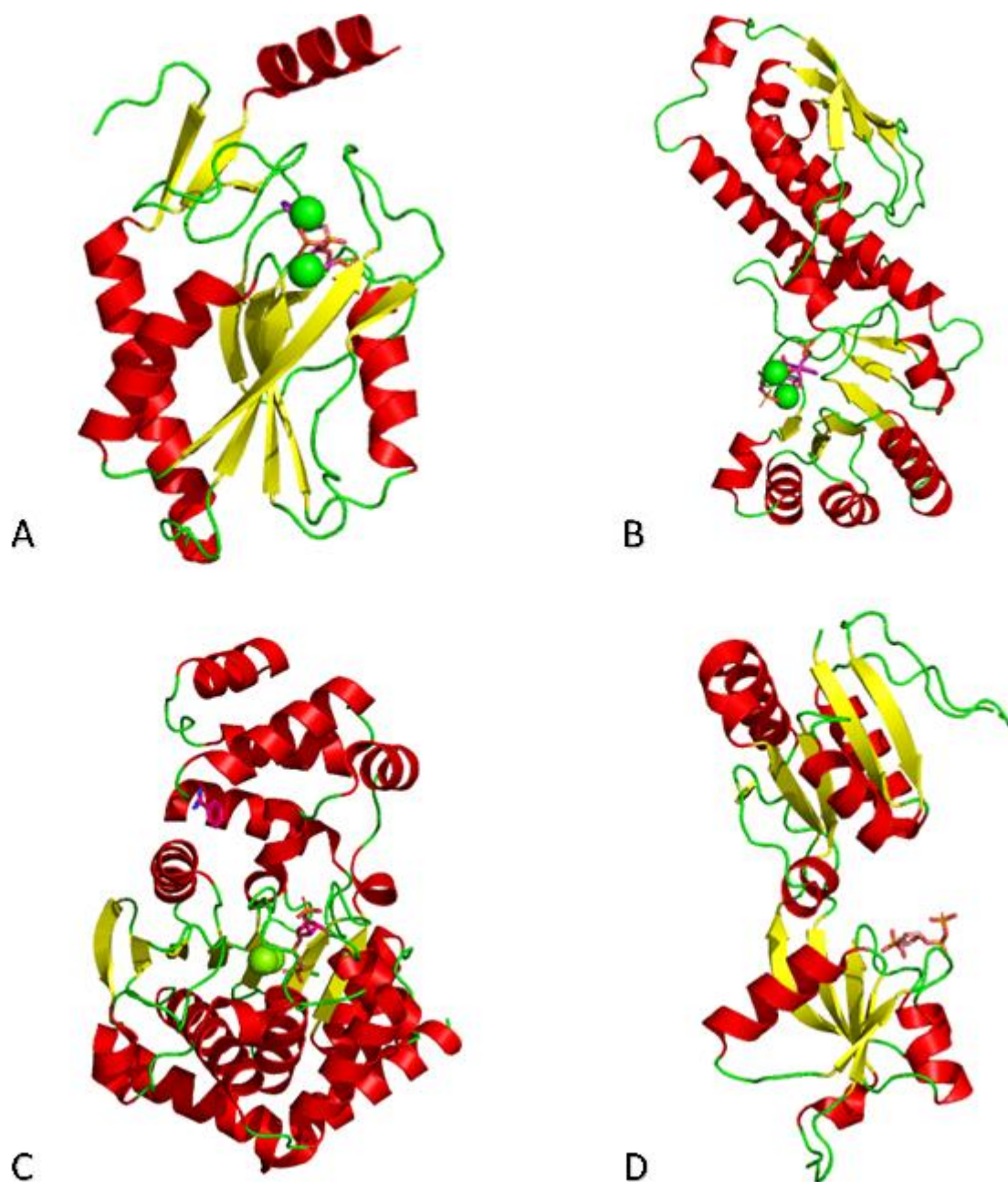


Figure 1.5 Illustration of the monomeric unit of four types of PRTs.

(A) Type I hypoxanthine PRT from *Trypanosoma cruzi* (PDB: 1TC2).⁵⁸ (B) Type II quinolinate PRT from *M. tuberculosis* (PDB: 1QPR).⁵⁹ (C) Type III AnPRT from *M. tuberculosis* (PDB: 1ZVW).⁶⁰ (D) Type IV ATP-PRT from *Lactococcus lactis* (PDB: 1Z7N).⁶¹ Types I, II and III are represented by their chain B and Type IV is shown as chain G. α -Helices are shown in red, β -sheets in yellow, flexible loops in green, metal ions in green spheres and PRPP as pink sticks.

Type IV PRTs are solely exemplified by adenosine triphosphate PRT (ATP-PRT), which catalyses the first step of the histidine biosynthetic pathway (Figure 1.5, **D**).⁶² These enzymes are highly regulated by histidine, the end product of the pathway. ATP-PRT enzymes are also structurally diverse, which allows for different allosteric regulation mechanisms. Based on their different quaternary structures, type IV enzymes are divided into two sub-families. The first sub-family is called the long form ATP-PRTs. Long form ATP-PRTs are homohexameric with each chain consisting of a mixed α/β bilobal domain containing the active site and a C-terminal domain for allosteric histidine binding. The second sub-family is known as the short form ATP-PRTs. Short form ATP-PRTs are heterooctameric and consist of four HisG₅ catalytic subunits and four regulatory HisZ subunits.⁶³ In short form ATP-PRTs, an active site is found in a cleft in the catalytic core (consisting of domains I and II) forming the ATP binding site and domain II which accommodates the PRPP binding site. The PRPP binding site in type IV PRTs and domain II with a five-stranded parallel β sheet surrounded by three α -helices are structurally similar to the equivalent regions in type I PRTs. However, the flexible hood domain, which sits over the PRPP binding site in type I enzymes, is not present in type IV PRTs.

1.8 Anthranilate phosphoribosyltransferase

AnPRTs are responsible for the second committed step in tryptophan biosynthesis. AnPRTs catalyse the magnesium-dependent substitution reaction between anthranilate and PRPP to form PRA and diphosphate (Figure 1.6).

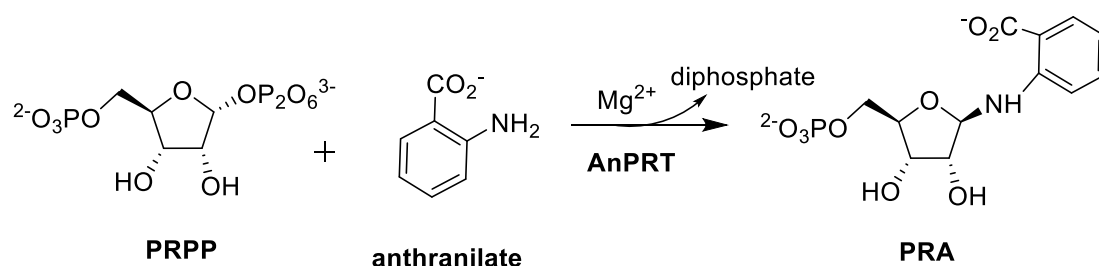


Figure 1.6 The AnPRT catalysed the reaction.

Catalysis by *M. tuberculosis* AnPRT does not take place in the absence of Mg²⁺ ions, and no significant inhibition has been observed at higher concentrations of Mg²⁺ ions up to 10 mM.⁵⁷ However, this observation is dissimilar to the metal dependency reported for the thermophilic *S. solfataricus* AnPRT enzyme, where enzymatic activity decreases as the

concentration of Mg^{2+} ions increases (more than 0.1 mM).^{55,64} *Thermococcus kodakarensis* (*T. kodakarensis*) AnPRT from a hyperthermophilic archaeon also provides contrary results to the previously characterised AnPRTs that displayed the maximum activity of enzyme only with Mg^{2+} ions. However, the maximum activity of *Thermus thermophilus* (*T. thermophilus*) AnPRT was observed in the presence of the divalent Zn^{2+} cation followed by Ca^{2+} rather than Mg^{2+} .⁶⁵

1.8.1 The structure of AnPRT

Crystal structures of AnPRT enzymes have been solved from eight different organisms: *M. tuberculosis*,^{60,66} *T. kodakarensis*,⁶⁵ *P. carotovorum*,⁵⁶ *S. solfataricus*,⁵⁵ *T. thermophilus* (PDB: 1V8G), *Xanthomonas campestris* (*X. campestris*, PDB: 4HKM), *Acinetobacter baylyi* (*A. baylyi*, PDB: 4GTN) and *Nostaceae* (PDB: 1VQU). The AnPRT enzyme crystal structures have revealed the oligomeric form consisting of two chains (Figure 1.7, shown in green and blue). The inter-chain interactions are mainly dominated by hydrophobic interactions and a few hydrogen bonds. No salt bridge interactions are observed at the interface in the oligomeric form of AnPRT.

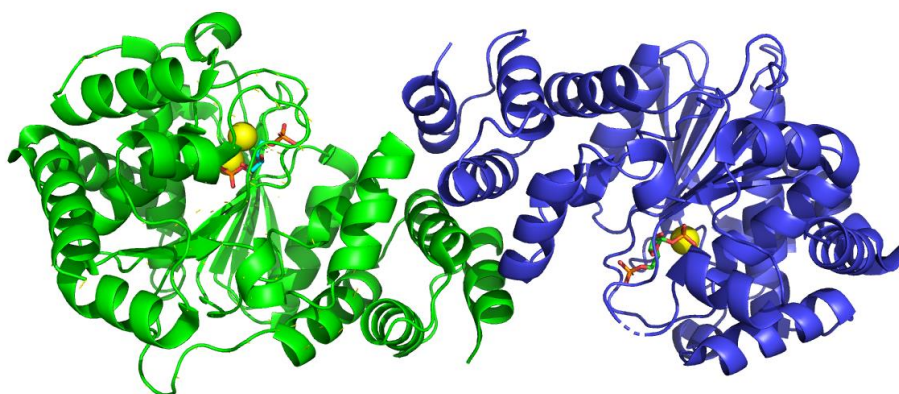


Figure 1.7 The oligomeric structure of *M. tuberculosis* AnPRT.

Both monomeric chains are shown in blue and green. The ligands are present in each catalytic site and can be seen as yellow spheres and brown sticks.

The role of dimerisation was studied by mutating interface residues of *S. solfataricus* AnPRT.⁶⁷ The dimer oligomeric state was disrupted to form a monomer by replacing two non-polar interface residues with negatively charged residues. This double mutant of *S. solfataricus* AnPRT was observed as a mixture of monomeric and dimeric forms in equilibrium and demonstrated similar catalytic activity to the wild type dimer, although it had reduced

thermal stability. This study suggested that dimerisation of AnPRT is only important for its high intrinsic stability and does not directly support catalytic activity.

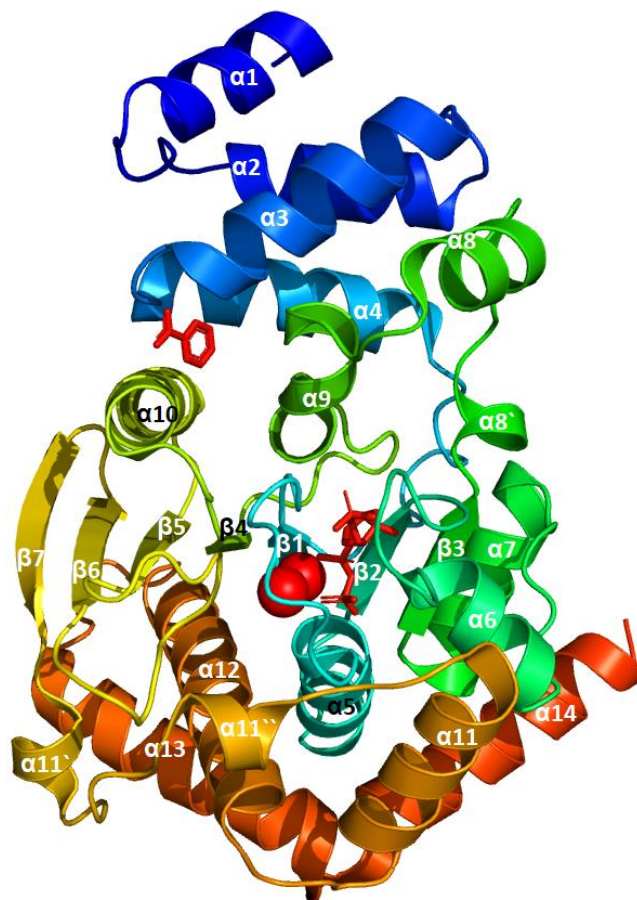


Figure 1.8 The monomer unit of the *M. tuberculosis* AnPRT (PDB: 1ZVW).

PRPP and benzamidine are shown as red sticks and Mg^{2+} ions are shown as red spheres.

Each monomeric unit of the protein comprises two domains—a smaller N-terminal domain consisting of six α -helices ($\alpha 1$ – $\alpha 4$, $\alpha 8$ and $\alpha 9$) and a larger α/β C-terminal domain with a seven-stranded β -sheet (six parallel and one antiparallel strand) surrounded by several α -helices (Figure 1.8). The smaller N-terminal domain is connected to the larger C-terminal domain via a hinge region incorporating the $\alpha 4$ – $\beta 1$, $\beta 3$ – $\alpha 8'$ and $\alpha 9$ – $\beta 4$ joining residues.

1.8.2 The PRPP binding of AnPRTs

The AnPRT active site is found in a deep cleft between the N-terminal α -helical domain (residues 1–95 and 180–210) and the larger C-terminal α/β domain. The overall conformation of the PRPP binding site is similar in different structures of *P. carotovorum* AnPRT (PDB: 1KGZ),⁵⁶ *S. solfataricus* AnPRT (PDB: 1ZXY),⁶⁷ *T. thermophilus* AnPRT (PDB: 1VG8) and over 28

published structures of *M. tuberculosis*.^{53,54,57,60,66,68,69} The *M. tuberculosis* AnPRT structure (PDB: 1ZVW) contains PRPP coordinated in an “extended” form between the $\beta 1$ – $\alpha 5$ and $\beta 2$ – $\alpha 6$ loops, with the diphosphate group buried the most deeply (Figure 1.9, **A**).

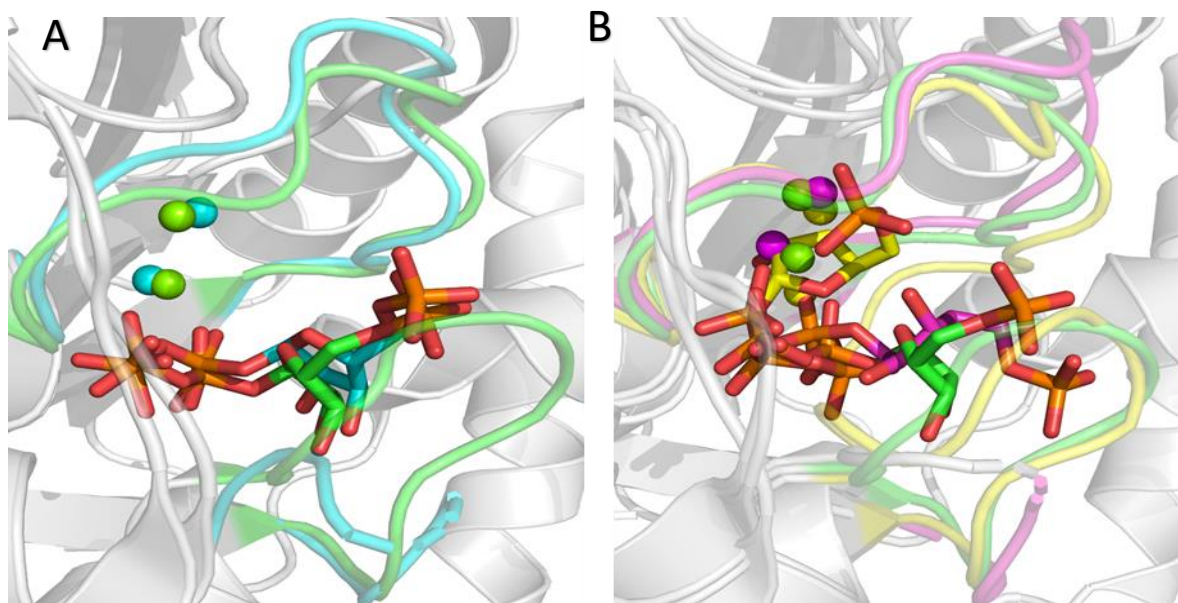


Figure 1.9 The binding mode of PRPP and Mg^{2+} in different AnPRT structures.

(**A**) Structural superposition of chain A of *M. tuberculosis* AnPRT (PDB: 1ZVW) bound with PRPP (green) and Mg^{2+} (green spheres) with chain A of *P. carotovorum* AnPRT (PDB: 1KGZ) bound with PRPP (cyan) and Mn^{2+} (cyan spheres). (**B**) An overlay of chain A of *M. tuberculosis* AnPRT (PDB: 1ZVW) bound with PRPP (green) and Mg^{2+} (green spheres) with chain A of *S. solfataricus* AnPRT (PDB: 1ZXY) bound with PRPP (pink) and Mn^{2+} (pink spheres) and chain A of *S. solfataricus* AnPRT mutant (PDB: 3GBR) bound with PRPP (yellow) and Mn^{2+} (yellow spheres).

A similar extended binding mode of PRPP is also observed in *P. carotovorum* AnPRT structure (PDB: 1KGZ, Figure 1.9, **A**). Two Mg^{2+} ions are present at the active site of AnPRT. Both of these ions are octahedrally coordinated and help in the binding of PRPP at the enzyme active site. The positions of one Mg^{2+} ion and the pyrophosphate moiety are highly similar in all AnPRT structures due to the conserved residues that form the metal binding sites across the family. Notable points of difference are observed in the binding of PRPP by overlaying the *M. tuberculosis* AnPRT structure (PDB: 1ZVW) with *S. solfataricus* AnPRT structures (PDB: 1ZXY and PDB: 3GBR, figure 1.9, **B**). PRPP is bound at the same position in the *M. tuberculosis* 1ZVW

and *S. solfataricus* 1ZXY structures but PRPP accommodates itself into an “S”-shaped arrangement in the *S. solfataricus* 1ZXY structure. It is likely that this ligand has been modelled incorrectly in the *S. solfataricus* AnPRT structure (PDB: 1ZXY) resulting from model bias⁵⁷ and analysis with the CheckMyMetal web tool.⁷⁰ Furthermore, the structure (PDB: 3GBR) of the PRPP/Mn²⁺ bound double mutant (Asp83Gly/Phe149Ser) of *S. solfataricus* AnPRT exhibits electron density that supports the extended conformation that contrasts remarkably with the “S”-shaped arrangement observed in wild type *S. solfataricus* AnPRT (Figure 1.9, **B**). The extended PRPP conformation resembles (but is not identical to) *M. tuberculosis* AnPRT. The observed distinct conformation of PRPP could be the reason for mutating Asp83 and Phe149 residues, located adjacent to the PRPP binding site of *S. solfataricus* AnPRT.

1.8.2.1 Detailed binding interactions of PRPP in various AnPRTs

In wild type *M. tuberculosis* AnPRT (PDB: 1ZVW), two Mg²⁺ ions are coordinated octahedrally (Figure 1.10) with individual ions contacting two water molecules, two oxygen atoms of diphosphate and side chain oxygen atoms of Ser119 and Glu252. In contrast, the other Mg²⁺ ion interacts with four water molecules and the amino acids Asp251 and Glu252. Both Mg²⁺ ions share two bridging ligands—Glu252 and a water molecule—forming a distorted octahedral arrangement. The diphosphate group of PRPP co-ordinates to an Mg²⁺ ion and makes hydrogen bonds with the side chain of Gly107, Lys135 and the backbone of Asn117, Ser119, Thr120 residues and various surrounding water molecules. The phosphate group of PRPP makes hydrogen bonds with the backbone of Ala141, Ser142, Ser143, and Gly110 residues and the ribose ring interact with the C3 hydroxyl group of the side chain of Asn138 found on the β2–α6 loop. Most of the water molecules form interactions with the side chains of residues of the β1–α5 loop, generating a network of hydrogen bonds between amino acids, diphosphate and metal ions to place ribose in a favourable position for the reaction to occur; the C1 carbon is accessible to the anthranilate binding site between the two subdomains of the protein.

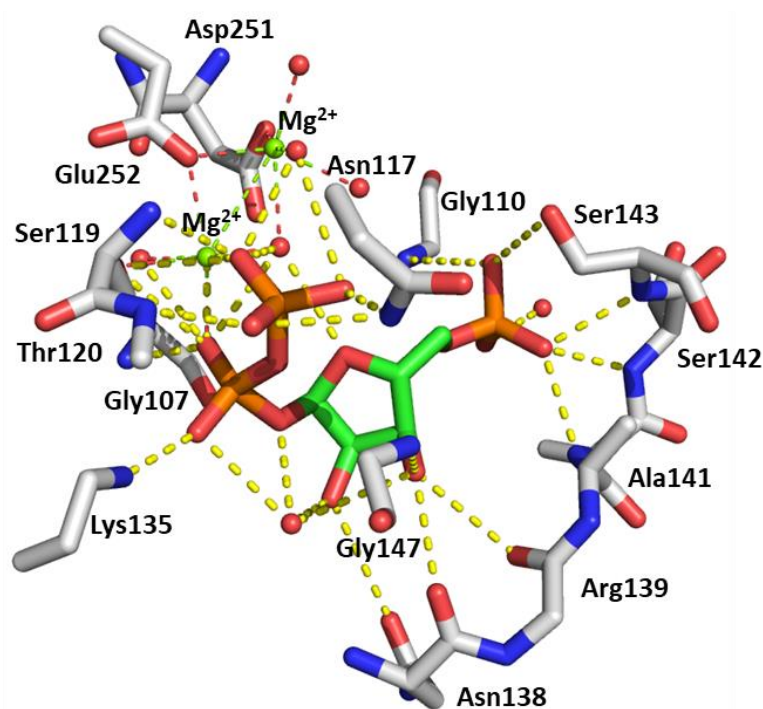


Figure 1.10 The binding mode of PRPP and Mg^{2+} ions in the *M. tuberculosis* AnPRT structure (PDB: 1ZVW).

PRPP and protein residues are shown as green and grey sticks respectively. Mg^{2+} and water molecules are shown as green and red spheres respectively. Covalent bonds and probable hydrogen bonds are shown as broken lines. Water is represented as red spheres.

In chain A of the *P. carotovorum* AnPRT structure (PDB: 1KGZ), the diphosphate group of PRPP is co-ordinated to the Mn^{2+} ion and makes hydrogen bonds with the backbone of Gly91, Asn101, Ser103, Thr104, Ser132 and various surrounding water molecules (Figure 1.11, **A**). The phosphate group of PRPP only makes contacts with amino acid Gly94 while the ribose ring does not make any contacts with the side chain of any amino acid due to the disordered nature of the $\beta 2$ - $\alpha 6$ loop in chain A. However, the PRPP molecule makes slightly different contacts in chain B of the *P. carotovorum* AnPRT structure. The C2 hydroxyl group of the ribose ring and diphosphate group make extra hydrogen bonds to Ser132 and Lys119 respectively. Mn^{2+} ions generate a network of hydrogen bonds linking water molecules, the diphosphate group and the side chains of amino acids such as Ser103, Glu237 and Asp236.

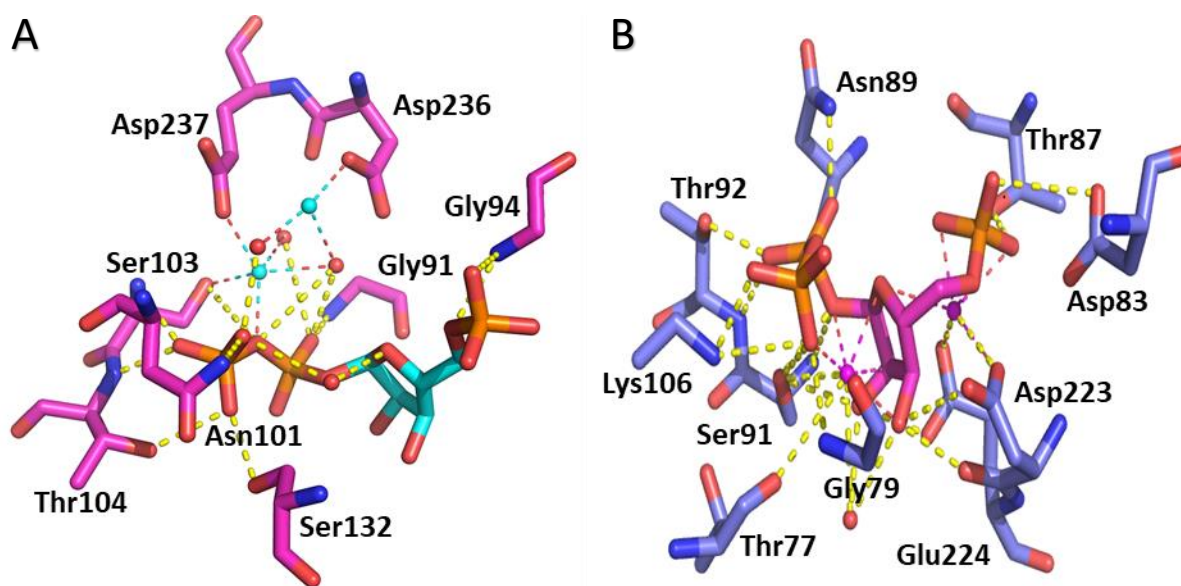


Figure 1.11 The binding mode of PRPP and metal ions in the *P. carotovorum* (PDB: 1KGZ) and *S. solfataricus* AnPRT (PDB: 1ZYX) structures.

(A) *P. carotovorum* AnPRT chain A (pink) bound with PRPP (cyan) and Mn^{2+} (cyan spheres).

(B) *S. solfataricus* AnPRT chain A (blue) bound with PRPP (pink) and Mg^{2+} (pink spheres).

Covalent bonds and probable hydrogen bonds are represented as broken lines. Water is represented as red spheres.

In all chains of the *S. solfataricus* AnPRT structure (PDB: 1ZXY), the diphosphate group of PRPP is stabilised by hydrogen bonds with Gly79, Asn89, Ser91, Thr92, Lys106 and its coordination to Mg^{2+} (Figure 1.11, B). However, the ribose ring and phosphate moieties of PRPP bind in a completely different position. The ribose ring makes hydrogen bonds with Ser91, Asp223, Glu224, a water molecule and Mg^{2+} ; the phosphate group hydrogen bonds are formed with Asp83, Thr87 and Mg^{2+} . The first Mg^{2+} atom is coordinated to one water molecule, the side chain of Thr77, Ser91, the C2 and C3 hydroxyl groups of the ribose ring and one oxygen atom of the diphosphate group in distorted octahedral coordination. The second Mg^{2+} ion binds to the side chains of Asp223, Glu224 and to the phosphate group of PRPP.

In the *S. solfataricus* mutant (Asp83Gly/Phe149Ser) structure (PDB: 3GBR), the position of the diphosphate moiety of the PRPP molecule is similar to all other AnPRT structures. However, the position of the ribose 5-phosphate moiety of PRPP is in an “extended” conformation (Figure 1.11, B). The mutated residues Asp83Gly and Phe149Ser were present in the $\beta 1$ – $\alpha 5$ and $\beta 3$ – $\alpha 8'$ loops that undergo a major positional change upon binding of PRPP compared to

the apo *S. solfataricus* (PDB: 1ZXY) structure.⁵⁵ In the wild type *S. solfataricus* AnPRT enzyme, the phosphate group of the PRPP is stabilised by a hydrogen bond with Asp83 and coordination with Mg²⁺. However, this hydrogen bond is lost in the double mutant of *S. solfataricus* AnPRT and metal ions are located too far apart to contribute to the binding of PRPP. As a result, the extended conformation of PRPP is present in the double mutant *S. solfataricus* AnPRT.

1.8.2.2 Detailed binding of PRPP in *M. tuberculosis* AnPRT

An identical binding mode of PRPP is observed in various *M. tuberculosis* AnPRT structures.^{53,66,71} In *M. tuberculosis* AnPRT, PRPP binds between the $\beta 1$ – $\alpha 5$ (residues 107–117) and $\beta 2$ – $\alpha 6$ loops (residues 138–146), with the diphosphate group buried the most deeply and the phosphate group facing out towards the solvent.

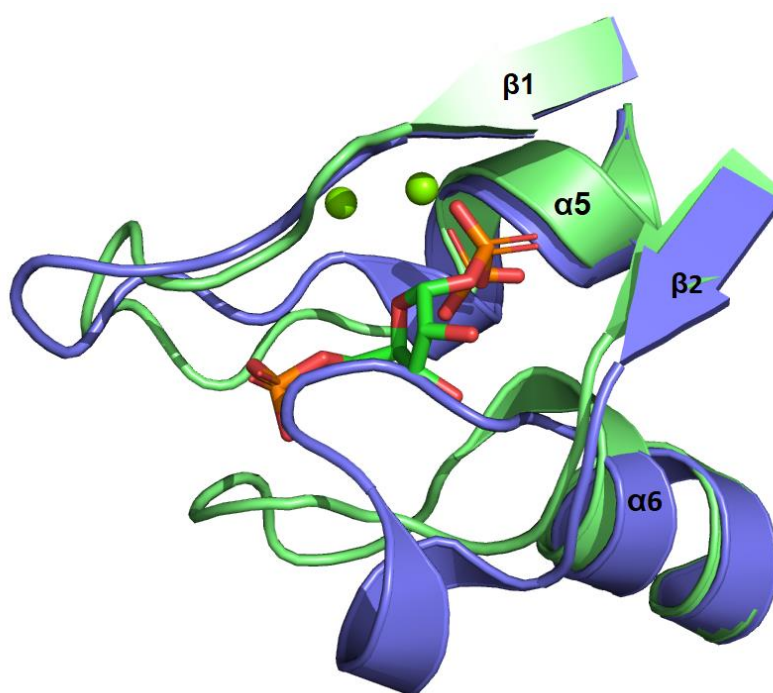


Figure 1.12 PRPP binding in *M. tuberculosis* AnPRT.

The movement of the $\beta 1$ – $\alpha 5$ and $\beta 2$ – $\alpha 6$ loops induced by PRPP binding. The apo enzyme (PDB: 1ZVW) is shown in blue and the PRPP-bound form (PDB: 2BPQ) in green. The PRPP molecule is shown as green sticks and Mg²⁺ ions are shown as green spheres.

To accommodate the binding of PRPP and the Mg²⁺ ions, two flexible loops ($\beta 1$ – $\alpha 5$ and $\beta 2$ – $\alpha 6$) are observed to adopt significantly different conformations in the ligand bound (PDB:

1ZVW) and ligand free (PDB: 2BPQ) structures indicating that this conformational change occurs on ligand binding (Figure 1.12). In the apo AnPRT structure (PDB: 2BPQ), the $\beta 2$ – $\alpha 6$ loop is in the “closed” conformation as it partially fills the PRPP binding site. In contrast, in the PRPP bound structure (PDB: 1ZVW), the $\beta 2$ – $\alpha 6$ loop moves out by about 8–9 Å into an “open” conformation to assist the binding of the ribose-5-phosphate moiety of PRPP. In addition, the $\beta 1$ – $\alpha 5$ loop undergoes a movement of 3–4 Å to make room for the diphosphate group of PRPP. The flexible $\beta 2$ – $\alpha 6$ loop of *M. tuberculosis* AnPRT suggests that the $\beta 2$ – $\alpha 6$ loop adopts the “open” conformation to allow PRPP binding before shuffling to the “closed” conformation when PRPP adopts the appropriate binding position within the active site of the enzyme.

1.8.3 The binding of anthranilate to AnPRT

AnPRT enzyme activity is subject to substrate inhibition by anthranilate. *M. tuberculosis* AnPRT activity is significantly reduced by increasing the anthranilate substrate concentration above 15 μM .⁵⁷ Similarly, an anthranilate concentration above 4 μM reduces the activity of *T. kodakarensis* AnPRT.⁶⁵ AnPRT activity from *Salmonella typhimurium* is also subject to feedback inhibition (inhibition of the enzyme by both substrates in the presence of tryptophan).⁷² The inhibition of the AnPRT enzyme by anthranilate means to reduce the production of AnPRT and tryptophan, the end product of the pathway. However, the anthranilate is an intermediate of the pathway and accumulation of metallic intermediates within the cell has not been reported previously.⁷³ Furthermore, the concentration of anthranilate within the cell is also unknown and, therefore, cellular anthranilate inhibition is still hard to verify.

1.8.3.1 Binding of anthranilate in different AnPRT structures

Initially, two distinct binding sites for the anthranilate substrate were predicted for *M. tuberculosis* AnPRT bound with PRPP and Mg^{2+} (PDB: 1ZVW) using the docking tool GOLD by Lee *et al.*⁶⁰ The first, and presumably catalytic, binding site (binding site 1) was identified close to PRPP, with the amino group of anthranilate adjacent to the anomeric carbon of PRPP. The second anthranilate binding site (binding site 2) was located distally from PRPP in the middle of the substrate-binding tunnel.

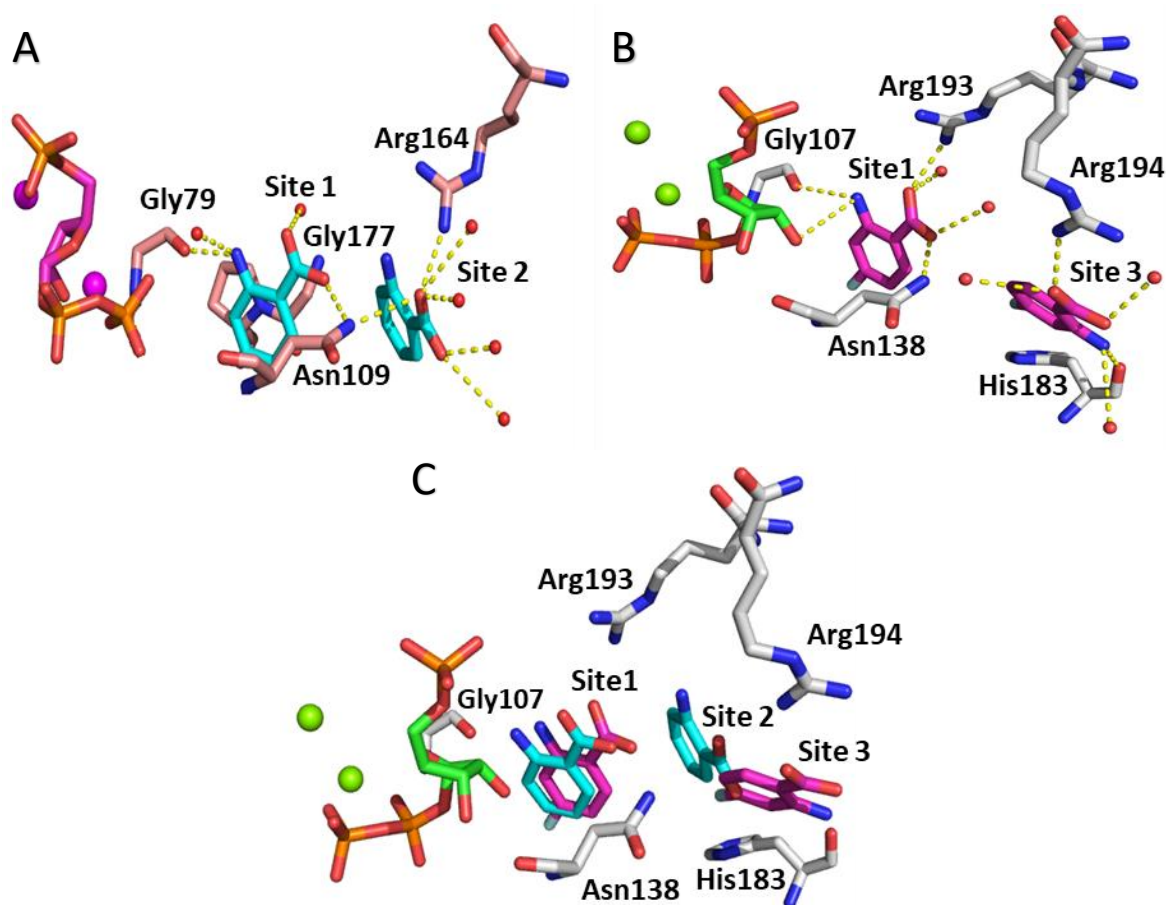


Figure 1.13 The binding sites of anthranilate and an anthranilate analogue (4FA) in different AnPRT structures.

(A) Anthranilate (cyan) bound at site 1 and site 2 in chain D (misty rose) of *S. solfataricus* AnPRT (PDB: 1ZXY). PRPP (pink) and Mg^{2+} (pink spheres) ligands are also shown in the diagram. (B) Chain A (grey) of *M. tuberculosis* AnPRT (PDB: 4N5V) structure bound with 4FA (pink), PRPP (green) and Mg^{2+} (green spheres). Polar contacts of anthranilate and 4FA are shown as yellow dashes. (C) An overlay of chain A (grey) of *M. tuberculosis* AnPRT (PDB: 4N5V) and chain D of *S. solfataricus* AnPRT (PDB: 1ZXY) display three binding sites for anthranilate substrate within the tunnel.

Experimentally, anthranilate binding sites similar to the predicted binding sites 1 and 2 were observed in all monomeric units of ligand bound *S. solfataricus* AnPRT (PDB: 1ZYK and 2GVQ) with the exception of only an anthranilate molecule at site 2 in chain A of 2GVQ.⁵⁵ At site 1, an anthranilate molecule makes hydrogen bonds with its amino group to Gly79 and the carboxylate group of anthranilate contacts Asn109, and a water molecule. The anthranilate is stacked parallel to Gly177 (Figure 1.13, A). Anthranilate molecule at site 2 makes contacts

with its carboxylate group to Asn109 and Arg164 and interacts with Ala150 and His154 hydrophobically.

Recently, the binding of an anthranilate-like inhibitor, 4-fluoroanthranilate (4FA), by *M. tuberculosis* AnPRT (PDB: 4N5V) revealed a new binding site (binding site 3) near the entrance to the anthranilate substrate tunnel (Figure 1.13, **B** and **C**).⁷⁴ In the *M. tuberculosis* AnPRT structure (PDB: 4N5V), the site 1 4FA ligand makes hydrogen bonds with its amino group to Gly107 and a C2 hydroxy group of PRPP and the 4FA carboxylate group makes contacts with Asn138, Arg193 and two water molecules. In site 3, the 4FA ligand forms hydrogen bonds, via its carboxylate group, with Arg194 and two water molecules, and via its amino group to a water molecule and His183. Similar binding modes for binding various anthranilate analogues are observed in the 5-fluoroanthranilate (5FA), 6-fluoroanthranilate (6FA) and 6-methyl anthranilate (6MA) bound AnPRT structures.⁷⁴ Similarly, the *M. tuberculosis* AnPRT R194A mutant crystal structure (PDB: 4X5E) shows three different binding sites for anthranilate substrates.⁶⁶ Each chain of the crystallised protein has two anthranilate molecules bound within the anthranilate tunnel, occupying sites 1 and 2 in chain A and sites 2 and 3 in chain B.

The bianthranilate-like inhibitor (ACS172) bound in the *M. tuberculosis* AnPRT (PDB: 3QQS) structure shows ACS172 bound to the enzyme at a number of binding sites.⁵³ ACS172 is an anthranilate analogue that consists of two benzoic acids which are joined via a secondary amine (Figure 1.14). It is the one of strongest inhibitor for *M. tuberculosis* AnPRT (apparent $K_i^{\text{anth}} = 16 \pm 10 \mu\text{M}$, $K_i^{\text{PRPP}} = 6.8 \pm 0.6 \mu\text{M}$ and $\text{IC}_{50} = 40 \pm 2 \mu\text{M}$).⁶⁹



Figure 1.14 The chemical structure of anthranilate and anthranilate analogue (ACS172).

The four chains in the asymmetric unit are associated as two dimers in the ACS172 bound structure (PDB: 3QQS). In chains A and B, the ligand ACS172 was refined with full occupancy and was found at site 2 of the anthranilate binding channel. The carboxylate group on the innermost aromatic ring of ACS172 forms hydrogen bonds with Arg193 and a water molecule

whereas the carboxylate group on the outermost ring interacts with Arg138, Arg194 in both chains and a water molecule in chain B only (Figures 1.1,5 **A** and 1.16, **A**).

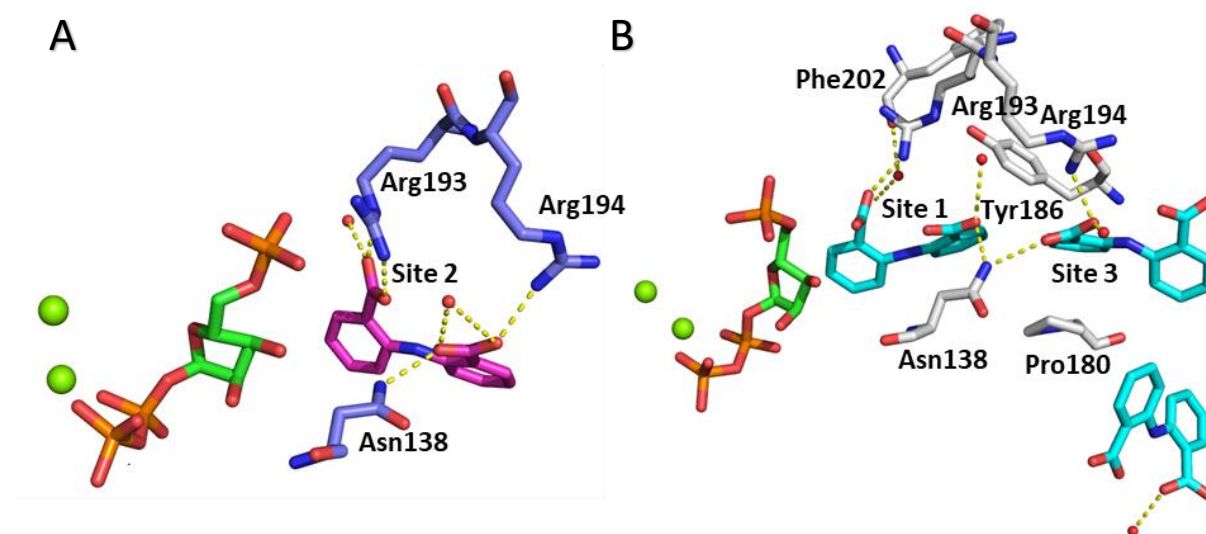


Figure 1.15 ACS172 binding interaction at multiple sites in M. tuberculosis AnPRT structure (PDB: 3QQS).

(A) Chain B (blue) bound with ACS172 (pink), PRPP (green) and Mg²⁺ ions (green). **(B)** ACS172 (cyan) bound at distinct sites in chain C (grey). PRPP and metals ions are shown as green sticks and green spheres respectively. Water molecules are shown as red spheres and hydrogen bonds are represented as yellow broken lines.

In chains C and D, ACS172 ligands were modelled at 0.6 occupancy at site 1 and site 3 into the anthranilate binding tunnel. In addition, chain C bound a third ACS172 molecule that was detected near the entrance of the anthranilate binding tunnel (Figures 1.15, **B** and 1.16, **B**). This ligand at the outermost site does not make any contacts to protein residues and it was, therefore, speculated to not represent a possible binding site for the ligand in solution.⁵³ In both chains, site 1 ACS172 molecules form hydrogen bonds with the inner ring carboxylate group and Arg193 and Phe202 via an ordered water molecule. However, the outer ring of the site 1 ligand contacts Asn138 and a water molecule via its carboxylate group. The outer ring binding mode of the site 1 ACS172 molecule suggests π interactions by binding in a plane-to-edge conformation against the aromatic ring of Tyr186. At site 3, the inner ring of ACS172 makes interactions between its carboxylate group and Asn138, Arg194 and a water molecule.

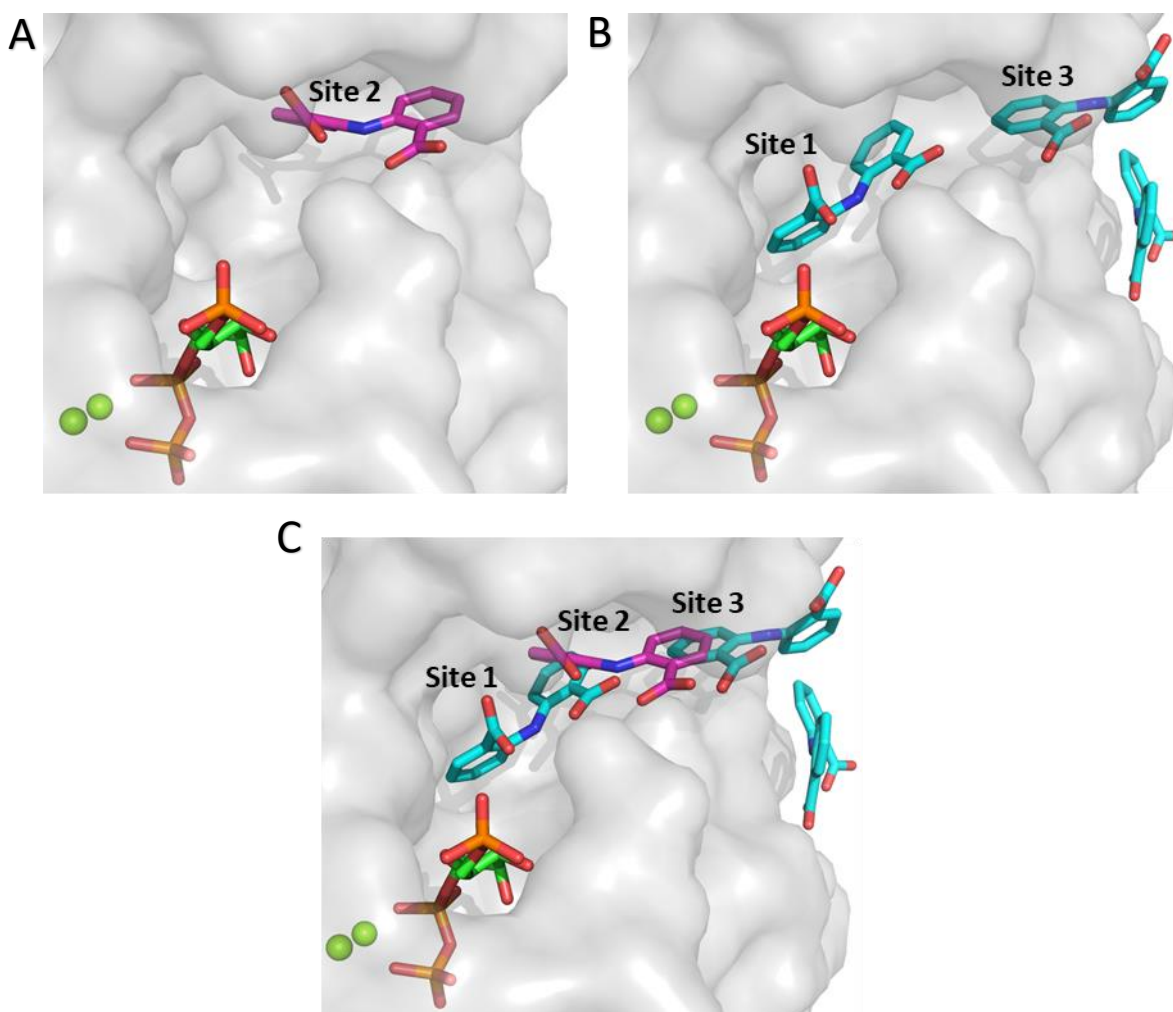


Figure 1.16 The ACS172 bound M. tuberculosis AnPRT structure (PDB: 3QQS) shows a number of binding positions in the substrate-binding tunnel.

(A, B) Site 2 binding position of ACS172 (pink) observed in chain B, and site 1 and site 3 binding positions of ACS172 (cyan) detected in chain C of the PDB: 3QQS structure. (C) An overlay of chain B and chain C shows the multiple binding sites for ACS172 (pink and cyan respectively) in the substrate-binding tunnel. PRPP (green) and Mg²⁺ ions (green spheres) are present at the active site of the M. tuberculosis AnPRT enzyme.

Furthermore, the inner ring of the site 3 ACS172 is stacked parallel with Pro180 and makes weak hydrogen bonds between the hydrogens of the proline ring of Pro180 and the π -electron cloud of the aromatic ring of ACS172. The inner ring of ACS172 located at site 3 packs against the aromatic ring of Tyr186 suggesting a role of the π interactions in the binding of the aromatic ring (Figure 1.15, B). The overlay of chain B and chain C shows a number of

positions for the binding of an inhibitor throughout the substrate-binding tunnel (Figure 1.16, C). It is predicted that the anthranilate substrate moves to site 1 for the catalytic activity of the enzyme, suggesting a number of positions for the binding of anthranilate within the anthranilate binding tunnel. The outer binding site molecule at the entrance to the anthranilate-binding tunnel is presumed to prevent enzyme activity by blocking anthranilate from reaching the catalytic site deeper inside the enzyme. This could also be the reason for the observed substrate inhibition at a high concentration of anthranilate, presumably via the binding of another anthranilate molecule at the outer site of the tunnel and subsequent disruption of anthranilate reaching site 1 for catalysis.

1.8.4 Conformational Changes

The conformational arrangements of an enzyme are critical for its catalytic activity and are also important for drug design as different conformations of the enzyme may have different binding affinities for specific molecules. An overlay of the apo structure (PDB: 1KHD) with the PRPP/Mn²⁺ (PDB: 1KGZ) bound structures of *P. carotovorum* AnPRT indicates little overall conformation change on substrate binding, presumably due to the disordered β 2– α 6 loop. The β 2– α 6 loop was not modelled due to the unclear charge density of a few residues. An overlay of the apo (PDB: 1O17) structure with ligand bound *S. solfataricus* AnPRT structures (either with PRPP and Mg²⁺ (PDB: 1ZYK) or PRPP, Mg²⁺ and anthranilate (PDB: 1ZXY)) shows the “closed” conformation of the β 2– α 6 loop. However, the “open” conformation of the β 2– α 6 loop was only observed in the anthranilate bound *S. solfataricus* structure (PDB: 2GVQ).

The different crystal structures of *M. tuberculosis* AnPRT variants capture the different conformations of the enzyme that presumably facilitate the different stages of catalysis. A comparison of these different conformations asserts a possible binding order of the ligands (Figure 1.17).⁶⁶

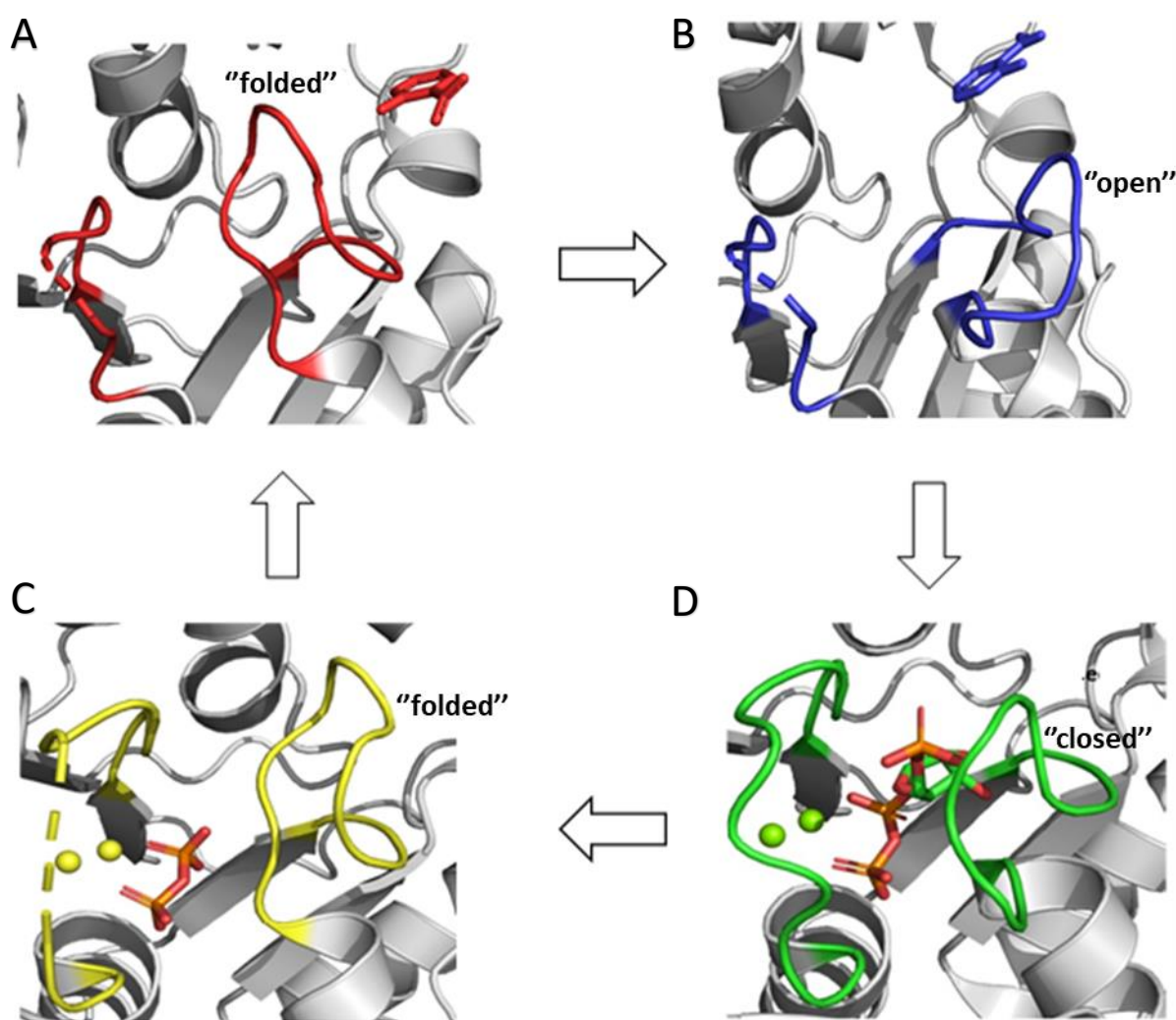


Figure 1.17 Proposed catalytic cycle for *M. tuberculosis* AnPRT.

The $\beta 2$ - $\alpha 6$ loop is coloured throughout the cycle to highlight its position. (A) Anthranilate (red) bound at site 3 with the $\beta 2$ - $\alpha 6$ loop in the “folded” conformation (PDB: 4X5D). (B) The movement of the $\beta 2$ - $\alpha 6$ loop to the “open” position to accommodate the binding of PRPP/ Mg^{2+} (PDB: 4OWV). (C) The $\beta 2$ - $\alpha 6$ loop in the “closed” conformation with the binding of PRPP and Mg^{2+} ions (PDB: 1ZVW). (D) Catalysis occurs, PRA leaves and diphosphate- Mg^{2+} remains at the active site; the $\beta 2$ - $\alpha 6$ loop returns to the “folded” conformation (PDB: 4X5C).

EmilyThe *M. tuberculosis* R193A anthranilate bound structure (PDB: 4X5D) has illustrated that anthranilate can only bind at site 3 of the anthranilate binding tunnel without PRPP and Mg^{2+} . Moreover, it has previously been suggested that anthranilate binds first at the outer site followed by the binding of PRPP.⁷⁴ The “folded” conformation of the $\beta 2$ - $\alpha 6$ loop within the anthranilate tunnel has been associated with the binding of anthranilate (PDB: 4X5D) and 4FA

(PDB: 4N8Q) ligands at site 3 of the tunnel, without PRPP binding (Figure 1.17, **A**). This folded conformation may block the anthranilate substrate from binding close to the active site without PRPP binding. However, the exact role of the “folded” conformation during catalysis is unclear, as it could facilitate the movement of anthranilate into the anthranilate binding tunnel after PRPP binding or it could also play a role in helping to release the product PRA. Previously, the flexible $\beta 2$ – $\alpha 6$ loop of *M. tuberculosis* has been observed to occupy either the “open” or “closed” conformation with and without PRPP binding, respectively (Figure 1.17, **B** and **C**).⁶⁰ The PRPP and Mg^{2+} bound structures of various variants of *M. tuberculosis* AnPRT (PDB: 4X58, 4X59 and 4X5B) and chain B of wild type (PDB: 1ZVW) AnPRT show the “closed” conformation of the $\beta 2$ – $\alpha 6$ loop with an observed binding of PRPP at the active site of the enzyme.

However, chain A of wild type (PDB: 1ZVW) AnPRT shows the “open” conformation of the $\beta 2$ – $\alpha 6$ loop without any ligands bound to the subunit. The careful observation of these structures suggests that the “open” conformation of the $\beta 2$ – $\alpha 6$ loop may allow the binding of PRPP at the active site and the “closed” conformation of the $\beta 2$ – $\alpha 6$ loop is only adopted after the proper binding of PRPP at the catalytic site of the enzyme. Additionally, the “open” to “closed” conformational transition of the $\beta 2$ – $\alpha 6$ loop may help to transfer anthranilate from site 3 to the catalytic site of the enzyme. The *M. tuberculosis* anthranilate bound AnPRT structure (PDB: 4OWV) shows the binding of anthranilate at site 3 in the tunnel with an “open” conformation of the $\beta 2$ – $\alpha 6$ loop and the AnPRT/PRPP/FA/ Mg^{2+} structure (PDB: 4N5V) shows the “closed” conformation of the loop with an observed binding of 4FA at site 1, near the enzyme catalytic site.

For catalysis of the AnPRT enzyme, it was predicted that the “folded” conformation of the $\beta 2$ – $\alpha 6$ loop, which is also associated with the movement of anthranilate from the distant site to the catalytic site, is a precatalytic event for the enzyme. The “open” conformation of the $\beta 2$ – $\alpha 6$ loop allows PRPP binding and the “closed” conformation is the actual catalytic state of the enzyme when PRPP is already bound at the active site and anthranilate is at site 1, near to the actual catalytic site. After this, enzyme catalysis occurs, and the products of the reaction leave the active site. This is followed by the return of the $\beta 2$ – $\alpha 6$ loop to a more open “folded” conformation while the diphosphate- Mg^{2+} complex remains at the active site. This post catalytic event with the more open “folded” conformation is supported by the *M.*

tuberculosis R193L mutant with diphosphate-Mg²⁺ bound structure (PDB: 4X5C, Figure 1.17, D) diphosphate-Mg²⁺ is released from the complex.

1.9 The reaction mechanism of AnPRT

M. tuberculosis AnPRT catalyses the substitution of the diphosphate of PRPP by nucleophilic attack of anthranilate in the presence of Mg²⁺ ions to form PRA and diphosphate (Figure 1.18). Though, it is still unclear whether the reaction of AnPRT proceeds via a dissociative or an associative mechanism. In a dissociative “S_N1-like” mechanism, the diphosphate group of PRPP fully dissociates first, forming an oxocarbenium ion intermediate, before nucleophilic attack by another substrate. However, both of these steps (the addition of anthranilate and removal of the diphosphate group) take place simultaneously, forming a highly coordinated transition state during the possible associative “S_N2-like” mechanism of AnPRT. The reaction mechanism of AnPRT has not been studied in detail so far.

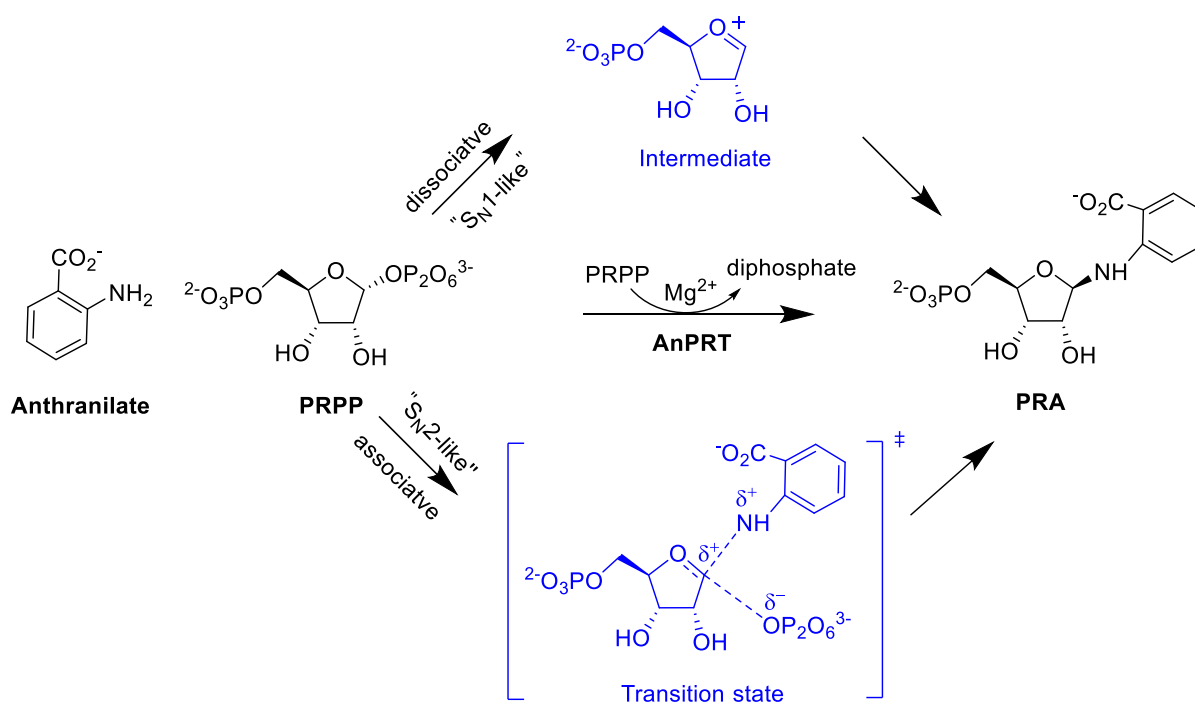


Figure 1.18 A possible reaction mechanism for the AnPRT catalysed reaction.

The dissociative “S_N1-like” reaction mechanism of AnPRT has been proposed based on the available structures of various PRTs.⁵⁷ The mechanism for AnPRT is predicted to be similar to that determined for nucleoside phosphorylase (NPs) due to the common ancestry and structural resemblance. (Figure 1.19).^{75,76} NPs catalyse a reversible phosphorolysis reaction where ribose 1-phosphate is removed from the nucleoside through the cleavage of the *N*-1-glycosidic bond (Figure 1.19, **A** and **B**).⁷⁷

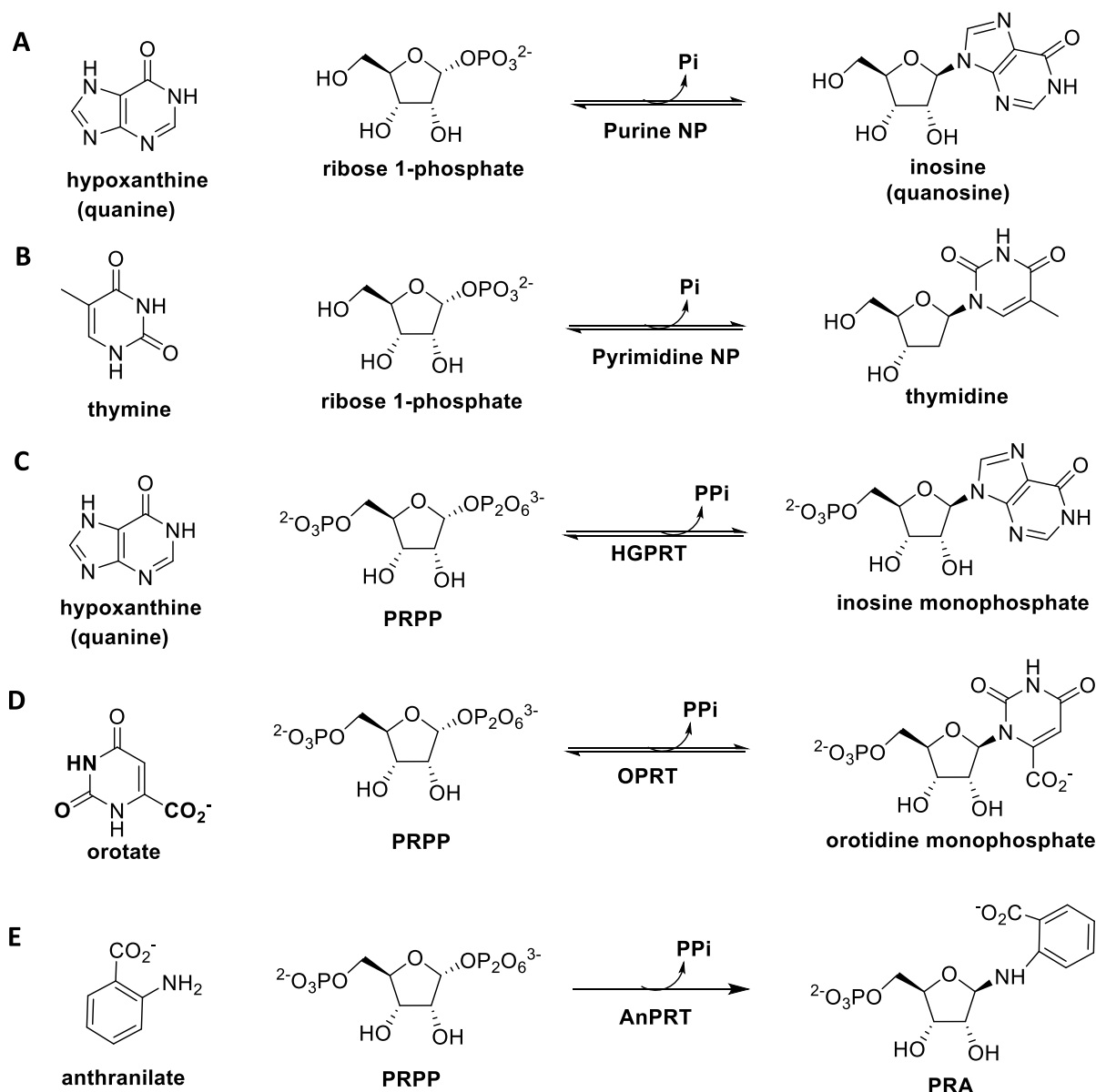


Figure 1.19 The reactions catalysed by NPs, type I and type III PRTs.

In the purine/pyrimidine NPs, the mobile ribosyl-oxocarbenium ion intermediate of the dissociative “S_N1-like” reaction mechanism was proposed to be generated as the phosphate moiety of PRPP and the nucleoside ring are anchored by a number of interactions with

adjacent protein residues and the ribose ring of PRPP is the least interactive portion. The proposed reaction mechanism of NPs is also supported by a structure in complex with a transition state mimic (PDB: 1B8O) solved for purine NP.⁷⁷ Similarly, based on structural and kinetic isotope effect (KIE) studies of orotate/guanine PRTs, type I PRTs are also reported to follow a dissociative “S_N1-like” mechanism where the diphosphate group dissociates first, before the ribose ring of PRPP is transferred to guanine/orotate to form inosine/orotidine monophosphate (Figure 1.19, **C** and **D**).^{77,78}

Likewise, similar binding modes for the natural substrates and their analogues have been observed in various structures of *M. tuberculosis* AnPRT.^{53,54,57,74} In detail (Section 1.8.2), the diphosphate moiety of PRPP is buried most deeply at the active site and makes numerous hydrogen bonds to adjacent protein residues and metal ions. Hence, it is presumed that the diphosphate moiety of PRPP does not move very much during catalysis. The phosphate group of PRPP also interacts with several protein residues. However, the ribose ring of PRPP only forms a few hydrogen bonds to side chains of protein residues. Therefore, the flexibility of the ribose ring is evident in various AnPRT structures,⁵⁴ which supports the formation of a mobile ribosyl-oxocarbenium ion intermediate of a dissociative “S_N1-like” reaction mechanism (Figure 1.18, 1.19, **E**).⁵⁷

1.10 Inhibition of AnPRT

A range of different substrate analogues has been reported for *M. tuberculosis* AnPRT.^{53,66,69,74} These analogues were shown, through X-ray crystallography, to bind into the anthranilate-binding tunnel with no observed binding in the PRPP binding site of the enzyme. There are several compounds (6FA, ACS142, ACS145, ACS174 and ACS179) that were found to be strong inhibitors of *M. tuberculosis* AnPRT with observed K_i values of less than 50 μ M (Figure 1.20). However, the best hit from miscellaneous compound library screens was the “bianthranilate”-like compound ACS172, which provides significant inhibition to the enzyme (apparent K_i values of $K_i^{\text{anth}} = 16 \pm 10 \mu\text{M}$, $K_i^{\text{PRPP}} = 6.8 \pm 0.6 \mu\text{M}$ and $\text{IC}_{50} = 40 \pm 2 \mu\text{M}$). Additionally, ACS172 reduces cell growth of *Mycobacterium marinum* (*M. marinum*) at a concentration between

25 and 600 $\mu\text{g/mL}$.⁶⁹ *M. marinum* causes disease in fish and responds to the anti-TB drugs RIF and SM in a similar way to the *M. tuberculosis* pathogen.

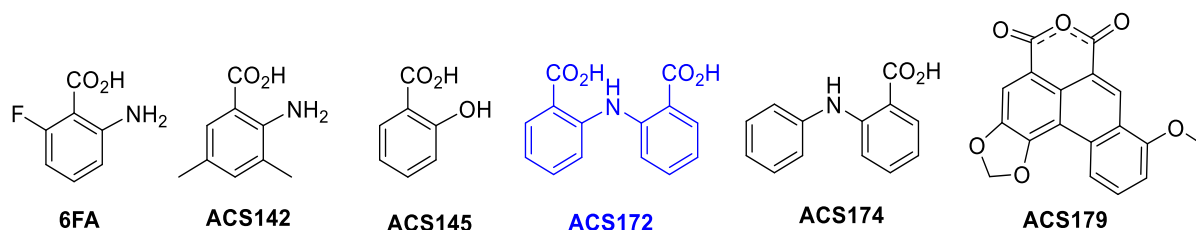


Figure 1.20 The chemical structures of *M. tuberculosis* AnPRT inhibitors.

The promising results observed for ACS172 encouraged the synthesis of further analogues for the design of more potent anthranilate analogues for *M. tuberculosis* AnPRT inhibition. The first series of benzoic acid derivatives of ACS172 was screened using a dose-response assay of AnPRT and these compounds were found to be weaker inhibitors for the enzyme compared to ACS172 (Figure 1.21).⁶⁹ These results indicate that all functional groups of ACS172 are crucial for enzyme inhibition.

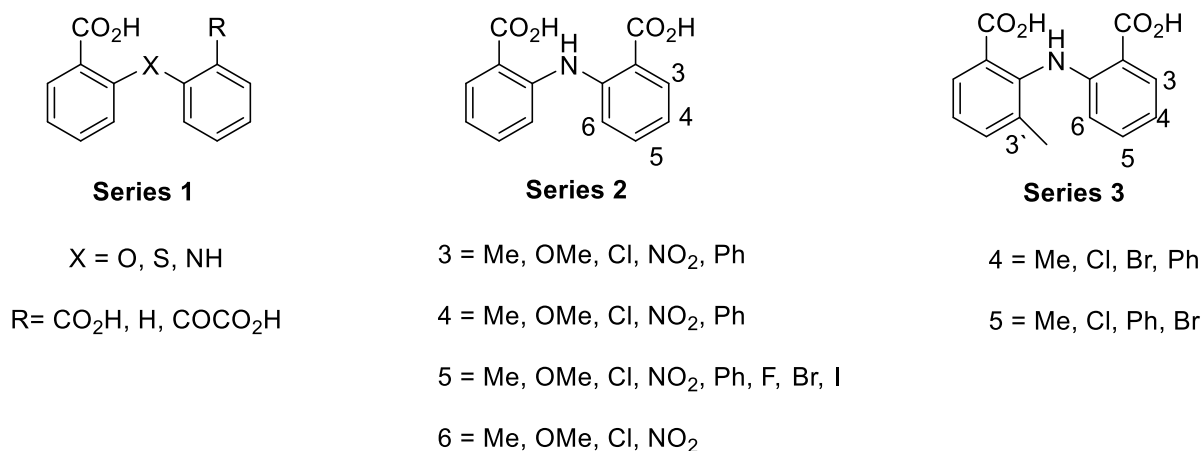
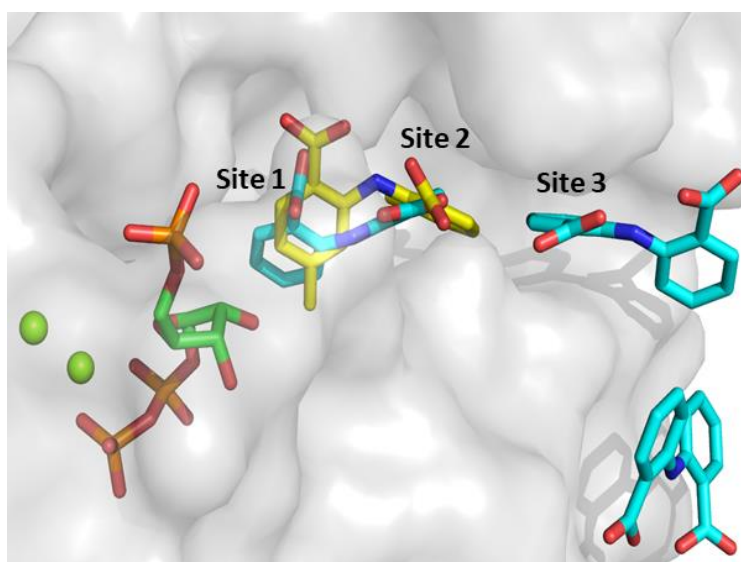


Figure 1.21 The series of inhibitors tested against *M. tuberculosis* AnPRT.

Subsequently, the second series of ACS172 derivatives, with a single substitution of hydrophobic, electron-withdrawing or electron-donating groups, were tested against *M. tuberculosis* AnPRT (Figure 1.21).⁶⁹ From the second series, the highest level of inhibition resulted from the presence of substituents at positions 4 and 5. Interestingly, instead of a Ph group, the substitution at position 4 for all functional groups (Me, MeO, Cl, NO₂) exhibited stronger enzymatic inhibition. The most active inhibitors of the second series contained Me and Cl substituents at position 4 with IC₅₀^{abs} values four times higher than ACS172. Hence, the

additional methyl group at the 3'-position in the second ring with substituents at positions 4 and 5 was considered for testing in series 3.

Interestingly, the introduction of the additional methyl group at position 5 resulted in five to 10 times stronger enzymatic inhibition compared to a singly substituted inhibitor from series 3. Surprisingly, the 3'-methylated analogues bearing another hydrophobic substituent at position 4 were weaker inhibitors than the related analogues with a substituent at position 4 only, that were identified as the best inhibitors from series 3. The reason for this trend is still unclear. However, on the basis of the crystallographic observations (PDB: 3QQS and 4GIU, Figure 1.22), it has been hypothesised that 3'-methyl and 5-methyl substituents cause steric hindrance, which allows the molecule to adopt a “twisted” conformation that enables these substituted compounds to bind deeper into the anthranilate binding tunnel and disfavours these compounds binding at site 2 and site 3.⁶⁹



*Figure 1.22 The twisted confirmation for inhibitor **636** observed at binding sites 1–2 in the substrate-binding tunnel.*

*Chain B (PDB: 4GIU) bound with 3'-methyl and 5-methyl analogue **636** (yellow) is overlaid with chain C (PDB: 3QQS) bound with ACS172 (cyan). The PRPP and metal ions are also shown as green sticks and green spheres respectively.*

Another extended scaffold of ACS172, “trianthranilate-like” compound **644**, has been reported as an inhibitor of *M. tuberculosis* AnPRT (Figure 1.23).⁶⁹ Inhibitor **644** consists of three benzoic acids that are bridged by two secondary amines and is the best inhibitor for *M.*

tuberculosis AnPRT that has been described to date. It shows competitive inhibition with respect to PRPP with a 40-fold increase in potency ($K_i^{\text{PRPP}} = 0.86 \pm 0.1 \mu\text{M}$) and non-competitive inhibition with respect to anthranilate ($K_i^{\text{anth}} = 6.2 \pm 0.5 \mu\text{M}$) compared to ACS172 ($K_i^{\text{anth}} = 16 \pm 10 \mu\text{M}$, $K_i^{\text{PRPP}} = 6.8 \pm 0.6 \mu\text{M}$). Additionally, it inhibits enzymatic activity almost completely with an IC_{50} value of $1.9 \pm 0.1 \mu\text{M}$).

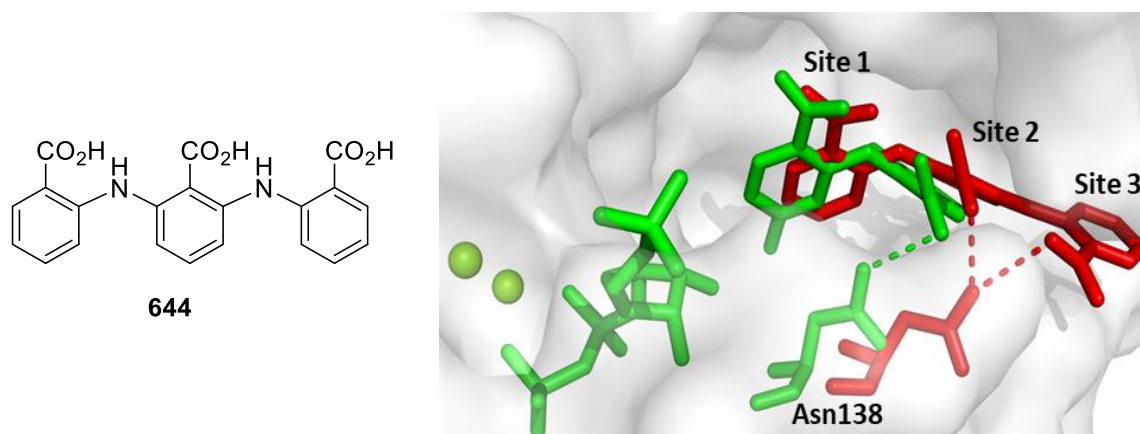


Figure 1.23 The chemical structure of “trianthranilate-like” **644** compound and its binding within the anthranilate substrate-binding tunnel in *M. tuberculosis* AnPRT (PDB: 4GIU). The repurposing of Asn138 by binding **644** is detected in an overlay of chain A of the **644**-bound (PDB: 14JI1, red) and chain A of the **636**-bound structure (PDB: 4GIU, green). The PRPP and metal ions are also shown as green sticks and green spheres respectively. The ligand interactions with Asn138 are shown as dashed lines.

An important difference noticed in the **644**-bound (PDB: 14JI1) and the **636**-bound (PDB: 4GIU) *M. tuberculosis* structures is that Asn138 has moved 3.6 \AA away from PRPP to the anthranilate binding tunnel (Figure 1.23, **B**). Asn138 assists in the binding of PRPP and the movement of this residue causes competitive inhibition by **644** with respect to PRPP. Recently, Zhang *et al.* reported that if the tryptophan biosynthetic pathway of *M. tuberculosis* can be interrupted, either chemically or genetically, then human macrophages are able to kill the bacterium both in vivo and during infection.⁷⁹ This provides further validation and interest to target the tryptophan biosynthetic pathway for the design of novel antimicrobial drugs.

1.11 Thesis objectives

AnPRT is involved in the biosynthesis of the essential aromatic amino acid tryptophan. This enzyme is not present in humans and the obligatory role of this pathway in *M. tuberculosis* makes this enzyme an interesting drug target. Current knowledge regarding the catalytic mechanism of the enzyme is limited. This project aims to gain further understanding of the transition states involved during catalysis and the inhibition of AnPRT through the study of non-natural inhibitors in order to aid anti-TB drug design.

The specific research objectives of each chapter of this thesis are below:

Chapter 2 describes the kinetic and structural characterisation of *M. tuberculosis* AnPRT using a range of further extended analogues based on lead ACS172.

Chapter 3 discusses computer-assisted drug design modelling used to find non-natural inhibitors that can bind within the catalytic site of *M. tuberculosis* AnPRT. X-ray crystallography, DSF and ITC techniques are applied to explain the binding of the ligands to AnPRT in detail.

Chapter 4 explores the substrate binding sites to elucidate the reaction mechanism of the enzyme. Ligands capable of binding at the catalytic site of *M. tuberculosis* AnPRT are also explored via crystallography, DSF and ITC.

Chapter 5 presents the design, synthesis and characterisation of potential transition state analogues. Potential reaction and catalytic mechanisms for the enzyme are also proposed.

Chapter 6 overviews the key findings of this thesis, discusses the overall conclusions and presents opportunities for future research into the inhibition of AnPRT.

Chapter 2 Characterisation and inhibition of *M. tuberculosis* AnPRT

2.1 Introduction

This chapter discusses the purification and general characterisation of wild type *M. tuberculosis* AnPRT. Prior to undertaking the studies reported in this chapter, the physical characteristics of this enzyme were examined by Drs C. E. Lee and T. M. V. Cookson.^{57,80} The work described in this chapter involved an investigation into the purification, molecular mass and kinetic characteristics of *M. tuberculosis* AnPRT, prior to commencing inhibition studies of this enzyme. This chapter also reports the purification of another enzyme, *E. coli* PRAI:InGPS (PRA isomerase (PRAI) and indole-3-glycerol phosphate synthase (InGPS) fused as single protein in *E. coli*), which was necessary for carrying out the inhibition studies of *M. tuberculosis* AnPRT through coupled enzyme assays.

The inhibition of the AnPRT enzyme was characterised kinetically, using a range of different compounds which were synthesised and provided by the University of Auckland. In addition, structural studies of AnPRT co-crystallised with these inhibitors were carried out.

2.2 Protein expression and purification

Expression and purification of both *M. tuberculosis* AnPRT and *E. coli* PRAI:InGPS (Figure 2.1) were carried out following a similar protocol to that reported by a previous member of the Parker group.⁵⁷ The *M. tuberculosis trpD* and *E. coli trpFC* genes had already been cloned into the expression vectors pET-23a (+) (Novagen) and pProEX-HTb (Invitrogen™) respectively. *E. coli*/BL21 (DE3)/Chap3 cells were used for the expression of both proteins. Autoinduction was used for protein expression in culture as detailed fully in Section 7.1.8. Both soluble proteins were purified as stated in Section 7.1.11.

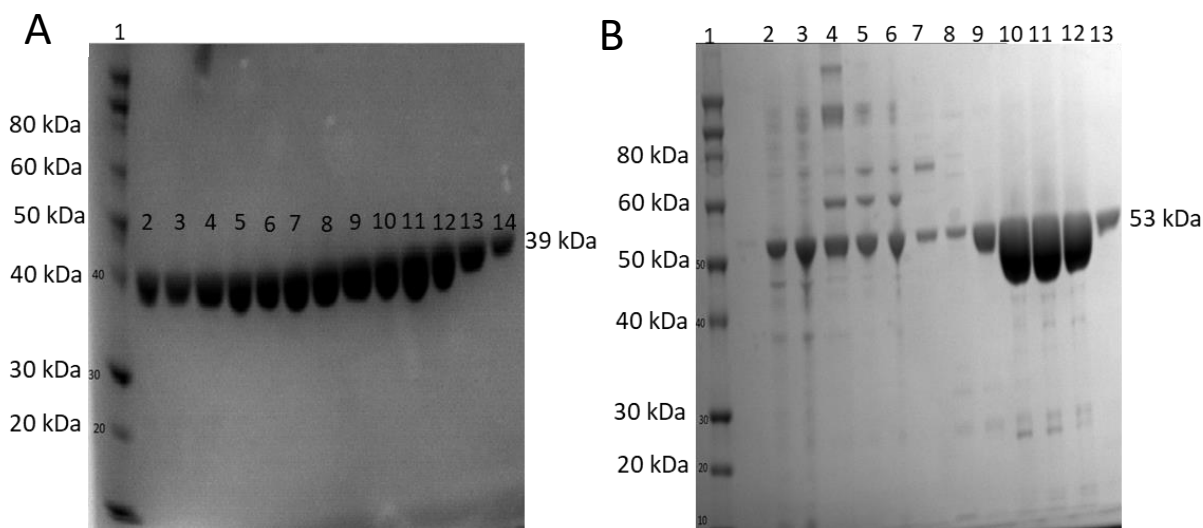


Figure 2.1 SDS-PAGE purification gel of *M. tuberculosis* AnPRT and *E. coli* PRAI:InGPS.

(A) Lane 1: Protein ladder with molecular weights defined to the left. Lanes 2–14: Purified *M. tuberculosis* AnPRT at 39 kDa. The different fractions of the elution peak collected from the SEC. (B) Lane 1: The protein ladder with molecular weights defined to the left. Lanes 2–13: Several fractions of the elution peak for *E. coli* PRAI:InGPS (53 kDa) collected from IMAC.

The masses of both purified His-tagged proteins were confirmed by mass spectrometry. The masses obtained by ESI-MS for *M. tuberculosis* AnPRT and *E. coli* PRAI:InGPS were 38674.4 Da and 52734.4 Da respectively, which is in agreement with the calculated masses (38673.7 Da and 52732.7 Da), including their His tags, calculated from the amino acid sequence using ProtParam.⁸¹ The value obtained for *M. tuberculosis* AnPRT is similar to the calculated value of 38673.7 Da without the starting methionine amino acid as the deletion of methionine is possible with methionine aminopeptidase in *E. coli* cells.⁸²

2.3 Kinetic Characterisation

The kinetic features of *M. tuberculosis* AnPRT have been studied in detail previously.⁵⁷ In order to study potential inhibitors for *M. tuberculosis* AnPRT, an enzyme-coupled UV absorbance-based assay was utilised with slight modification to the previously established protocol.⁵⁷ The assay utilises two enzymes from the tryptophan biosynthetic pathway; *M. tuberculosis* AnPRT, in order to convert anthranilate and PRPP into PRA; *E. coli* PRAI:InGPS in order to convert PRA into the stable InGP product (Figure 2.2).

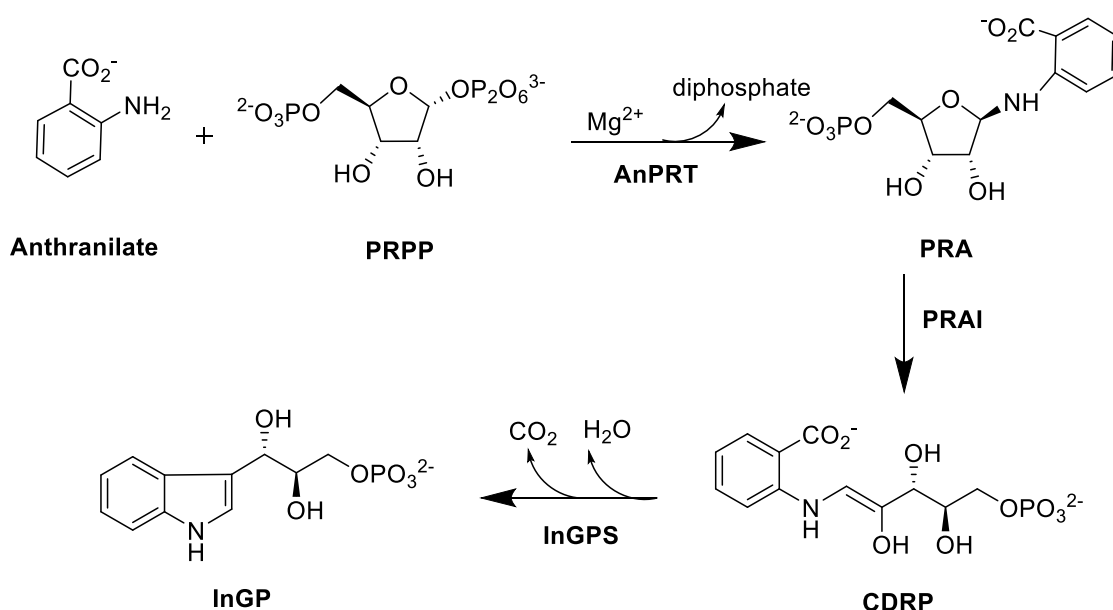


Figure 2.2 The enzyme-coupled assay utilised to get stable InGP product.

In *E. coli*, PRAI is fused together with InGPS and converts PRA into InGP. The presence of *E. coli* PRAI:InGPS is necessary to remove the build-up of the unstable *M. tuberculosis* AnPRT reaction product, as the break-down of the unstable PRA to ribose 5-phosphate and anthranilate would alter the known concentration of both substrates, complicating the kinetic analysis. *E. coli* PRAI:InGPS is present in excess of *M. tuberculosis* AnPRT to ensure that the AnPRT catalysed reaction is the rate-limiting step. The conversion of PRA to InGP, catalysed by PRAI-InGPS, is monitored spectrophotometrically at 270 nm in order to detect the formation of the InGP product. Using known concentrations of substrates, the extinction coefficient for InGP production from anthranilate and PRPP was determined to be 7500 L mol⁻¹ cm⁻¹ at 270 nm at 25 °C.

2.4 Michaelis-Menten kinetics

The experimental set up to determine the kinetic parameters of *M. tuberculosis* AnPRT are described in detail in Section 7.1.17. The experimentally determined apparent K_M values of 1.6 ± 0.1 μM for anthranilate and 49 ± 2 μM for PRPP are comparable to those recorded for this enzyme previously (Figure 2.3).⁵⁷ The turnover number of 1.2 ± 0.2 s⁻¹ also compares well to values determined for other AnPRT enzymes (Table 2.1).^{48,57,67,80,83,84}

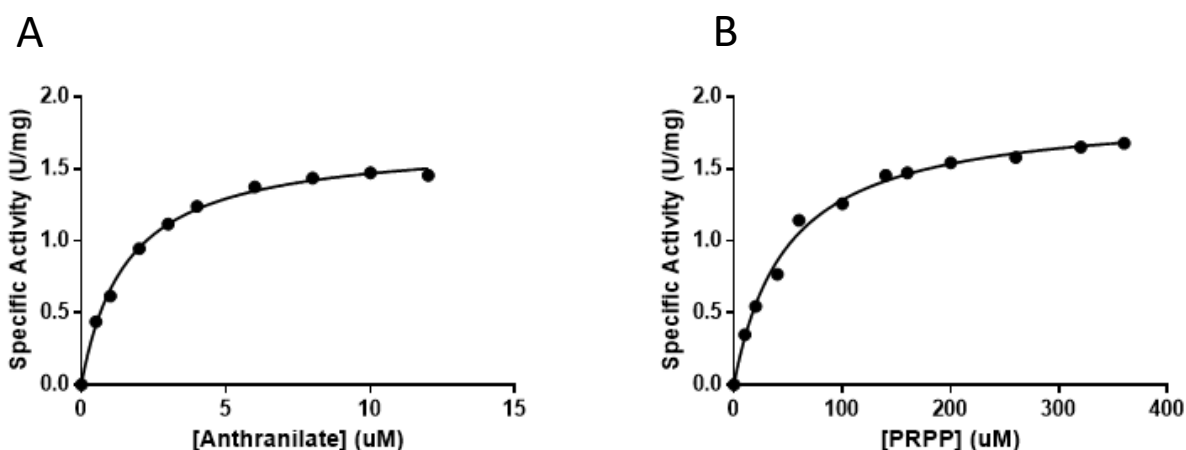


Figure 2.3 Michaelis-Menten curves for both substrates of *M. tuberculosis* AnPRT.

(A) For the anthranilate curve, PRPP was held at a concentration of 0.4 μM . (B) For the PRPP curve, anthranilate was held at a concentration of 15 μM . All data monitored at a wavelength of 270 nm at 25 °C in 50 mM Tris.HCl, pH 8.0, 150 mM NaCl, 1 mM MgCl_2 buffer components and fitted to the Michaelis-Menten equation using GraphPad Prism 7.

For the *M. tuberculosis* AnPRT enzyme, the K_M value for PRPP is in agreement with recorded literature values for *E. coli* AnPRT.⁸³ However, the *M. tuberculosis* AnPRT had the lowest catalytic efficiency (k_{cat}/K_M) value for PRPP compared to other AnPRT enzymes. The modest differences noted in the kinetic parameters for AnPRT from different organisms may be due to different experimental conditions such as variation in pH, temperature and buffer components.

At 60 °C, PRPP has a half-life of 56 min and at 80 °C its half-life is 2 min.⁸⁵ The PRPP substrate is hydrolysed to ribose 5-phosphate and diphosphate in the presence of metal ions at a higher temperature.⁸⁶ Therefore, it is not surprising that the binding affinity is lowest for PRPP and highest for the anthranilate substrate for the enzyme from the thermophile *S. solfataricus*.⁸⁵ However, this seems not to be the case for recorded mesophilic organisms including *E. coli*, *S. typhimurium* and *Saccharomyces cerevisiae* (*S. cerevisiae*).

Table 2.1 Comparison of kinetic parameters for AnPRT from various organisms.

Organism source	K_M (μM) PRPP	K_M (μM) Anthranilate	k_{cat} (s^{-1})	k_{cat}/K_M ($\mu\text{M}^{-1}\text{s}^{-1}$) (PRPP)	k_{cat}/K_M ($\mu\text{M}^{-1}\text{s}^{-1}$) (anthranilate)
<i>M. tuberculosis</i> (this study)	49 ± 4	1.6 ± 0.1	1.2 ± 0.02	0.03 ± 0.005	0.76 ± 0.2
<i>M. tuberculosis</i> ⁵⁷	48 ± 2	2 ± 0.2	1.9 ± 0.06	0.04 ± 0.003	0.95 ± 0.13
<i>M. tuberculosis</i> ⁸⁰	1.3 ± 0.2^a	3.3 ± 0.2^a	1.1 ± 0.02^a	0.08 ± 0.1^a	0.03 ± 0.03^a
<i>S. typhimurium</i> ⁸⁴	6.7	8.3	4.1	0.61	0.5
<i>E. coli</i> ⁸³	50 ^b	0.3 ^b	4.4 ^b	0.088 ^b	15.7 ^b
<i>S. solfataricus</i> ⁶⁷	180	0.1	0.41 ± 0.04	2.3×10^{-3}	4.8
<i>S. cerevisiae</i> ⁵²	22.4 ± 2.6	1.6 ± 0.5	2.9 ± 0.5	0.13 ± 0.04	1.8 ± 0.9

^a Data determined using fluorescence assay.

^b AnPRT in complex with anthranilate synthase.

2.5 Inhibition of *M. tuberculosis* AnPRT

The main objective of this thesis is to explore the mechanism and inhibition of the *M. tuberculosis* AnPRT enzyme in order to aid anti-TB drug design. Previously, a range of different compounds and substrate analogues (detailed in Section 1.10) have been screened and tested against the *M. tuberculosis* AnPRT enzyme. Most of these compounds were found to be competitive inhibitors, but only with respect to the anthranilate substrate.^{57,69,71,74,80} All of these analogues were shown, through X-ray crystal structures, to bind into the anthranilate binding tunnel with no observed binding at the PRPP binding site or the actual catalytic site of the enzyme (Section 1.8 and 1.10). The main goal of this work is to design and synthesise analogues that can bind to the enzyme at the catalytic site in order to understand the reaction mechanism and to assist with the design of more potent inhibitors.

Various types of inhibitors have been studied against PRTs enzymes.^{87,88} The inhibition of PRTs with phosphonate-containing compounds has been well studied.^{89,90} Phosphonate-containing prodrugs (Figure 2.4) exhibit low K_i values (as low as $0.69 \mu\text{M}$) against type I *M. tuberculosis* hypoxanthine-guanine PRT.⁹¹ These prodrugs have low cytotoxicity and high anti-TB activity.

The inhibitor-bound HGPRT structures show that these compounds bind to both the PRPP substrate binding site and the nucleophilic substrate binding site.⁹⁰ The nucleophilic substrate mimic is linked via a flexible acyclic chain of different lengths, which bears a phosphonate group. It is hypothesised that the approaches of analogues with a flexible linker to target these type I PRTs may be applicable to all PRT types, irrespective of the shape of their PRPP binding site.⁵⁴

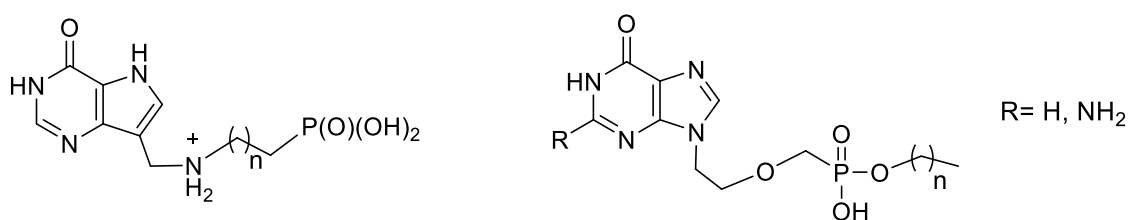


Figure 2.4 Structures of the phosphonate moieties attached to the nucleophilic base inhibitors for type I M. tuberculosis HGPRT.

In type III *M. tuberculosis* AnPRT, the buried PRPP binding site is approached by the nucleophilic base, anthranilate, through the long substrate-binding tunnel. There are multiple binding sites for anthranilate in the substrate-binding tunnel that the molecule can interact with en route to the actual catalytic site of the enzyme. The “bianthranilate”-like compound (ACS172) had the lowest K_i values ($K_i^{\text{anth}} = 16 \pm 10 \mu\text{M}$, $K_i^{\text{PRPP}} = 6.8 \pm 0.6 \mu\text{M}$) identified from a library of inhibitors tested against *M. tuberculosis* AnPRT.⁶⁹ ACS172 was found to bind to multiple sites along the anthranilate binding tunnel (Section 1.8.3). However, no inhibitors have been found to bind in the PRPP binding site of AnPRT. The main goal of the work presented in this chapter was to probe the possibility of any ligand binding at the PRPP binding site; hence a series of compounds (Table 2.2, 2.3 and 2.4) was designed and synthesised by the Brimble lab at the University of Auckland. The “bianthranilate”-like mimicking component of these substrate analogues aimed to be an anchor that linked to a potential flexible linker “hook” for approaching the binding sites of PRPP.⁵⁴ These compounds had previously undergone testing against *M. tuberculosis* AnPRT to record either IC_{50} values or the percentage of enzyme Inhibition by Dr G. L. Evans⁵⁴ and were provided for further inhibition testing in this study against *M. tuberculosis* AnPRT.

An initial group of compounds (**2.1**, **2.2** and **2.3**) containing an “anthranilate-like” moiety adjacent to an aromatic ring with ether linkers of various lengths coupled to a carboxylate

group was tested and these compounds were found to be much weaker inhibitors of *M. tuberculosis* AnPRT compared to ACS172 (Table 2.2, and Figure 2.5). Interestingly, the compound with the longest linker (**2.3**) showed slightly better inhibition against AnPRT among these carboxylate linker inhibitors and had the lowest K_i value of $30 \pm 2 \mu\text{M}$. It is possible that ligands with longer linkers could position into multiple binding sites of the substrate binding tunnel and block the access of anthranilate effectively.

Following this preliminary study, a series of compounds (**2.4**, **2.5**, **2.6** and **2.7**) containing an “anthranilate-like” moiety adjacent to an aromatic ring with ether linkers of various lengths coupled to phosphonate groups were tested (Table 2.2 and Figure 2.5). This group of compounds was identified as better inhibitors for the enzyme compared to the group of inhibitors coupled to a carboxylate group. Similarly, compounds with a longer linker corresponded to lower K_i values with the exception of **2.5**. Compound **2.5**, possessing the longest linker attached to the *meta* position relative to the amine group had the weakest inhibition (K_i^{anth} value of $9 \pm 1 \mu\text{M}$ and K_i^{PRPP} value of $53 \pm 3 \mu\text{M}$) for AnPRT among these inhibitors. This might be due to steric hindrance caused by the presence of longer linker at the *meta* position that causes the molecule to adopt a twisted conformation of ligand that disfavours binding sites 2–3 as noticed previously for *meta* substituted ACS172 analogues.⁶⁹ Contradictorily, compound **2.4**, with a four-atom linker had strong inhibition, with respect to both substrates (K_i^{anth} value of $5 \pm 0.4 \mu\text{M}$ and K_i^{PRPP} value of $11 \pm 1 \mu\text{M}$). However, compound **2.7** with a five-atom long linker attached to the *para* position relative to the amine group had the lowest K_i values with respect to anthranilate (K_i^{anth} value of $4 \pm 0.4 \mu\text{M}$ and K_i^{PRPP} value of $23 \pm 1 \mu\text{M}$) and almost double the value of **2.6**, which possessed the 4-atom linker (K_i^{anth} value of $7 \pm 1 \mu\text{M}$ and K_i^{PRPP} value of $63 \pm 2 \mu\text{M}$). These inhibitors (**2.4**, **2.5**, **2.6** and **2.7**) showed significant inhibition with respect to anthranilate substrate and fitted best with a competitive inhibition model.

Table 2.2 “bianthranilate”-like inhibitors with apparent K_i values against *M. tuberculosis* AnPRT.

Code	Structure	Apparent K_i (μ M) with anthranilate	Apparent K_i (μ M) with PRPP
ACS172		6.8 ± 1^a	16 ± 10^a
2.1		41 ± 3	108 ± 4
2.2		39 ± 4	175 ± 10
2.3		30 ± 2	130 ± 10
2.4		5 ± 0.4	11 ± 1
2.5		9 ± 1	53 ± 3
2.6		7 ± 1	63 ± 2
2.7		4 ± 0.4	23 ± 1
2.8		4.4 ± 0.4	15 ± 1
2.9		3.5 ± 0.5	13 ± 1
2.10		2.8 ± 0.5	12 ± 1
2.11		1.3 ± 0.1	5.4 ± 0.3

^a The K_i values for ACS172 are from Evan et al.⁶⁹

For the determination of apparent K_i values, assays with respect to anthranilate were performed in a final volume of 1 mL and consisted of 50 mM Tris.HCl, pH 8.0, 150 mM NaCl,

1 mM MgCl₂, 2.0 μg·mL⁻¹ (0.05 μM) AnPRT, 0.026 mg·mL⁻¹ (0.5 μM) *E. coli* PRAI-InGPS, 103 μM PRPP ($\approx 2 \times K_M$), anthranilate from 0 to 8 μM and inhibitors at various concentrations.

For assays testing inhibition with respect to PRPP, the concentration of PRPP was varied from 0 to 250 μM and anthranilate was held at constant 3.2 μM ($\approx 2 \times K_M$). Initial rate data were fitted to either competitive or non-competitive inhibition equations using GraphPad

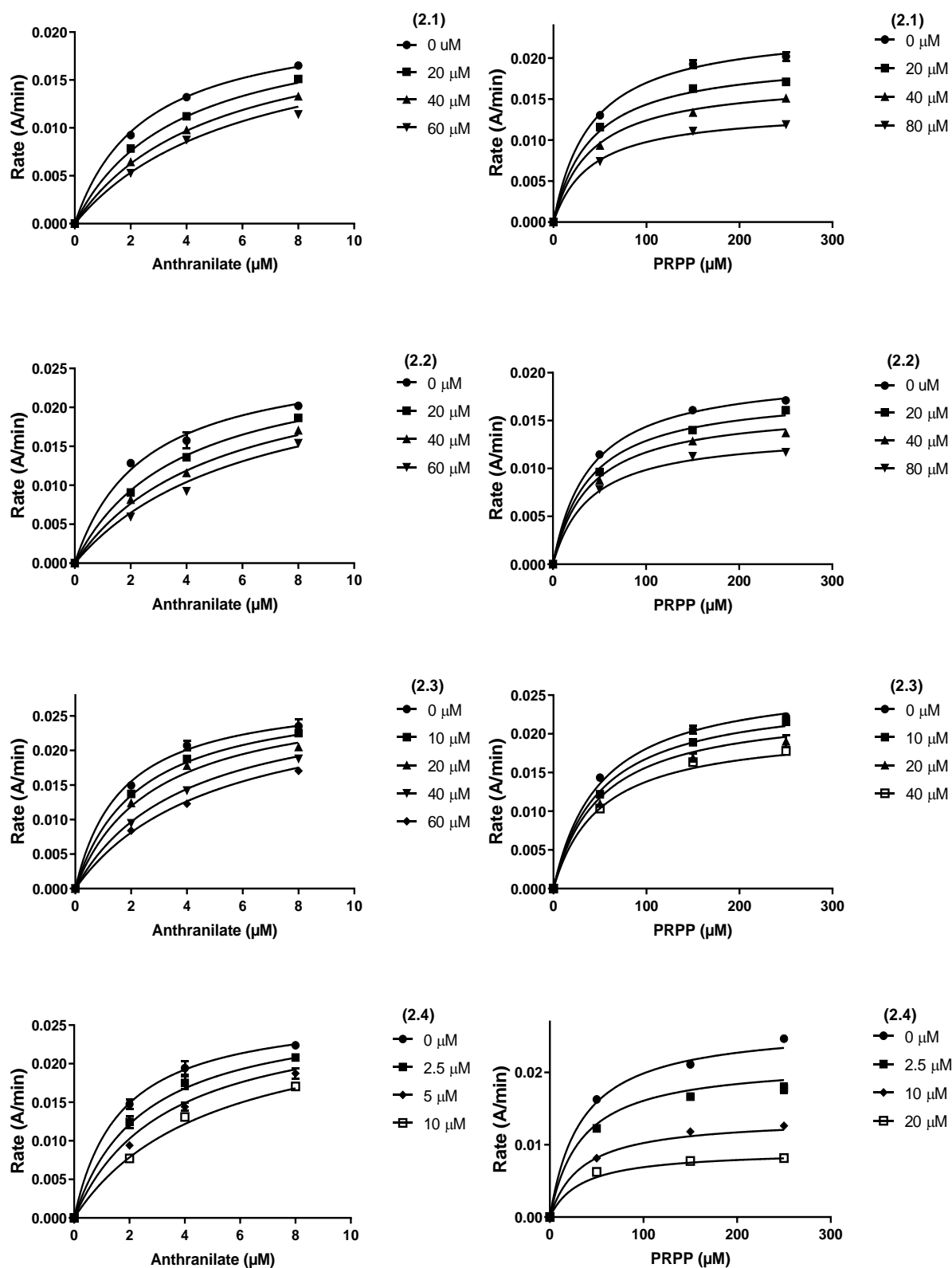
Prism 7.0.

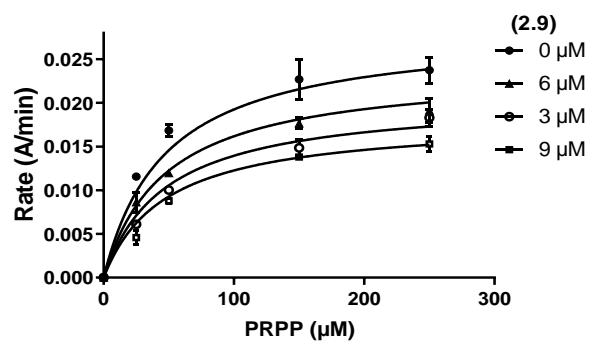
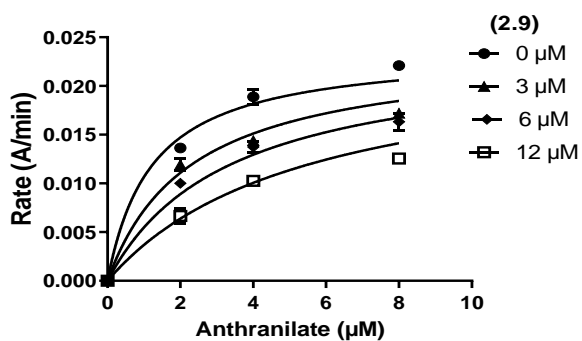
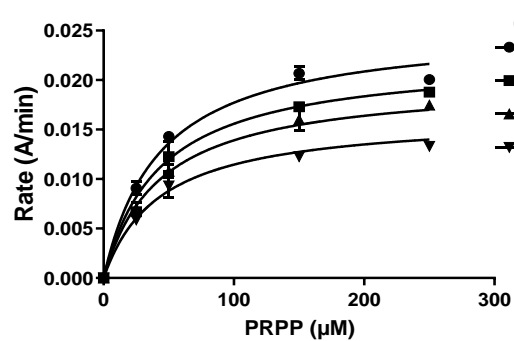
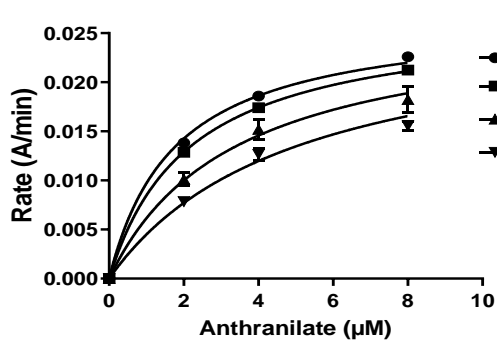
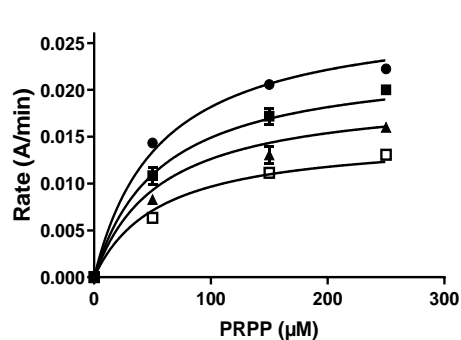
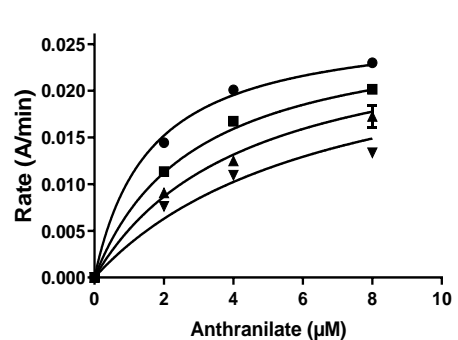
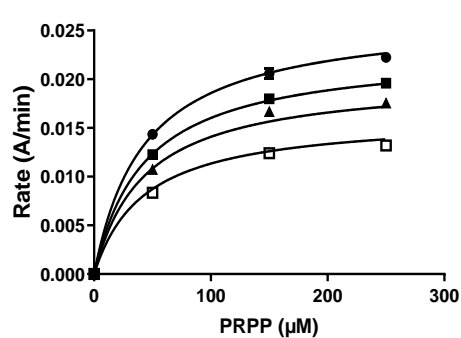
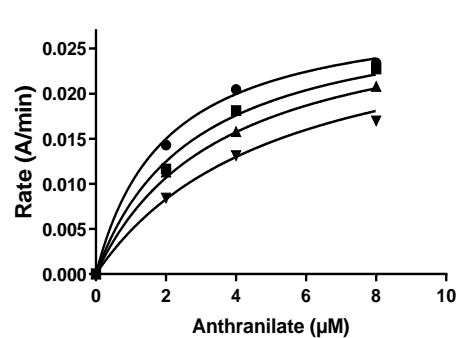
Following this preliminary study, four compounds (**2.8**, **2.9**, **2.10** and **2.11**) containing a “bianthranilate”-like component with an ether linker to phosphonate groups were tested and found to be the best inhibitors against *M. tuberculosis* AnPRT described to date (Table 2.2 and Figure 2.5). The increased affinity of these compounds may be due to the fact that the additional carboxylate group can form specific interactions with polar amino acid side chains, e.g., Arg194 and Asn138. This is discussed further below in Section 2.7. Similarly, to the other compound set, an increase in the inhibition of AnPRT was noticed with an increase in the length of the attached linker. Among all compounds tested, **2.11** was the most potent inhibitor for both substrates (K_i^{anth} value of 1.3 ± 0.1 μM and K_i^{PRPP} value of 5.4 ± 0.3 μM). The strong inhibition of inhibitor **2.11** may be attributed to the additional triazole ring that is part of the phosphonate tail being able to block the access of anthranilate into tunnel more effectively. Another compound, **2.10**, had almost half the potency of **2.11** with almost double the K_i values (K_i^{anth} value of 2.8 ± 0.5 μM and K_i^{PRPP} value of 12 ± 1 μM). The compound **2.9** (K_i^{anth} value of 3.5 ± 0.5 μM and K_i^{PRPP} value of 13 ± 1 μM) was almost similar in its potency to **2.8** (K_i^{anth} value of 4.4 ± 0.4 μM and K_i^{PRPP} value of 15 ± 1 μM). These phosphonate compounds had better K_i values than the “bianthranilate”-like compound, ACS172. This increased affinity could, therefore, be due to the addition of the phosphonate linker.

2.5.1 Inhibition kinetics

To characterise these compounds, steady-state kinetic parameters were obtained by holding one substrate at a low fixed concentration ($2 \times K_M$) while varying the concentrations of both the other substrate and the inhibitor. The concentration of one substrate was kept low ($2 \times K_M$) to avoid saturation of the enzyme with that substrate whilst allowing the inhibitor to have better access to compete with the other substrate. Inhibitor stocks were prepared by dilution in 2% DMSO in water and were added accordingly to achieve the desired concentration in the

assay. No change in the reaction rate of *M. tuberculosis* AnPRT was observed in the presence of 1% DMSO. The reactions were initiated with PRPP or anthranilate. All measurements were carried out in triplicate. Initial rate data were fitted to either competitive or non-competitive inhibition equations using GraphPad Prism 7.





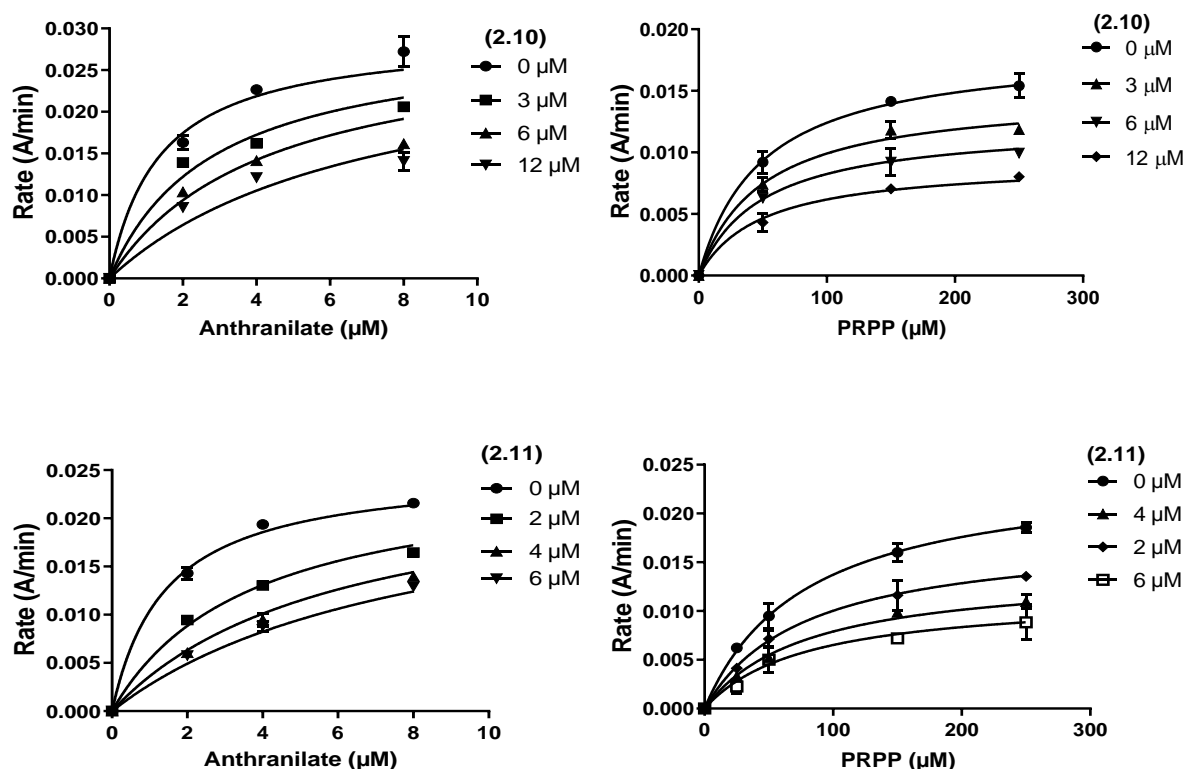


Figure 2.5 *M. tuberculosis* AnPRT inhibition graphs for both substrates to determine inhibitor K_i values.

Error bars represent the standard deviation of triplicate measurements. Where error bars are not visible, they are contained within the symbol.

Data obtained for the various inhibitors when varying the anthranilate concentration best fit the competitive inhibition model, whereas data obtained when varying PRPP concentration best fit the non-competitive inhibition model. The inhibition models of the various inhibitors that were fitted to the kinetic data suggest that these inhibitors bind at the same site as anthranilate does, but not at the PRPP binding site. Lower apparent K_i values were obtained against anthranilate compared to the higher K_i values obtained against PRPP.

2.6 Inhibitor in complex with *M. tuberculosis* AnPRT

Crystal structures of *M. tuberculosis* AnPRT complexed with these phosphonate inhibitors were solved to shed light on the binding of these inhibitors as well as to investigate the extent to which the phosphonate moiety could reach into the PRPP binding site of the enzyme. The crystal structure of *M. tuberculosis* AnPRT in complex with a bianthranilate phosphonate

inhibitor was obtained using the soaking method published by Evan *et al.*⁶⁸ As soaked inhibitors may cause conformational changes in the protein leading to disruption in crystal contacts, phosphonate inhibitors were co-crystallised successfully with *M. tuberculosis* AnPRT enzyme. These structures allow us to interpret the differences that occurred in the enzyme by introducing the inhibitor using either a ligand soaking or co-crystallisation method.

2.6.1 Crystal conditions

Identified conditions were further optimised using the hanging drop vapour diffusion method in 24-well VDX plates to give crystals of uniform shape and size (detailed in Section 7.1.20.1). Freshly purified or frozen *M. tuberculosis* AnPRT enzyme (6 mg mL⁻¹) was used to grow crystals. Typically, crystals were fully formed overnight and generally grew as a rectangular-shaped crystal (Figure 2.6). Droplet sizes were 3 µL.

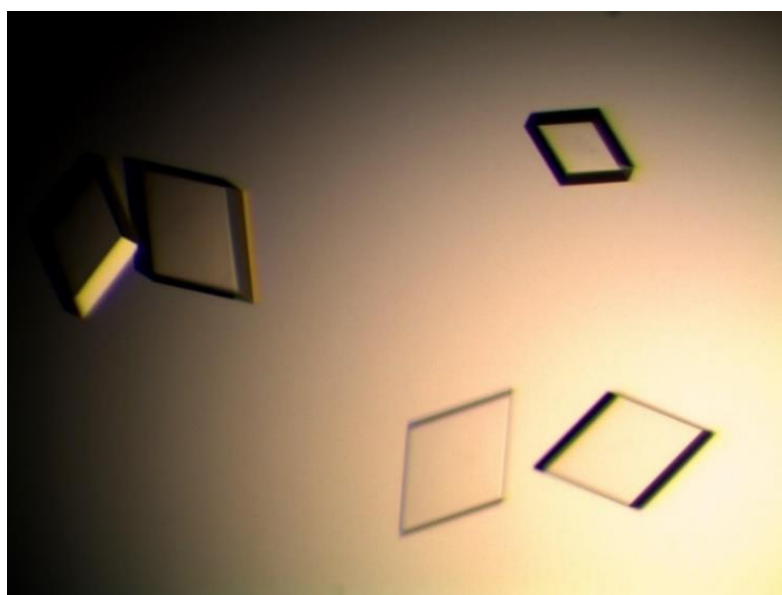


Figure 2.6 M. tuberculosis AnPRT co-crystallised with 2.11 and Mg²⁺, with 0.2 M imidazole malate (pH 6.5), 10% PEG-4000 (w/v).

The best method for cryoprotection of the crystals was found to be either 25% glycerol or 10% PEG-4000 in mother liquor. Crystals were flash-frozen using liquid nitrogen directly or after protection with the cryo-protectant solution. Data collection was carried out on the MX beamlines at the Australian Synchrotron. Datasets were collected and inspected for density corresponding to the introduced ligand.

2.6.2 Structure refinement

The crystal structures in complex with various inhibitors were solved using molecular replacement (*CCP4* suite)⁹² as detailed in Section 7.1.20.2. A molecular replacement strategy using the monomer unit of wild type *M. tuberculosis* AnPRT (PDB: 3QR9) was applied to solve the crystal structures in complex with the inhibitors of interest. Finding the true space group for the inhibitor-bound crystal structures proved challenging. Crystallographic refinement was complicated due to pronounced pseudo-translational symmetry and ambiguous space-group determination, leading to an apparent primitive orthorhombic ($P2_12_12_1$) space group and absences that were consistent with previously solved structures. However, no solution was found within the possible space groups determined by *pointless*⁹³ for a few datasets. Data-quality assessments in the alternative monoclinic $P2_1$ space group were better and produced a high-quality structural model that refined to acceptable values of R and R_{free} . *Zanuda*⁹⁴ also indicated that $P2_1$ was the correct space group for these datasets. The superpositions of the $P12_11$ and $C121$ structures indicate that the lattice in the $P12_11$ structure corresponds to an intermediate position between the lattice observed for the $C121$ structures.⁶⁸ This also supports the hypothesis that the subunits that are related by crystallographic symmetry elements in the $C121$ or $P2_12_12_1$ structures are related by pseudosymmetry elements in the $P12_11$ structure. Pseudosymmetry occurs where a non-crystallographic symmetry element within the asymmetric unit is close to a crystallographic symmetry operator.⁹⁵ Thus, the $P12_11$ space group has been correctly assigned, even though the unit cell has a β of approximately 90°.

Structures were solved by molecular replacement using *PhaserMR*⁹⁶ and refinement using *Refmac5*.⁹⁷ In the refinement of the ligand-bound structures, the model of the protein in the absence of any ligand was solved and ligands bound to the enzymes were added last in the refinement process to avoid the introduction of model bias. Information on data collection and refinement parameters can be found in detail in the experimental section (Appendix 1).

2.7 Bianthranilate phosphonate inhibitors bound with AnPRT

This section outlines five additional inhibitor-bound AnPRT structures. Three crystal structures in complex with **2.8** (PDB: 5BO2), **2.9** (PDB: 5BO3), **2.10** (PDB: 5BNE) bound to *M.*

tuberculosis AnPRT were already solved by Dr G. L. Evans at the School of Biological Sciences, University of Auckland.^{54,68} These inhibitor-bound crystals were grown using inhibitor soaking or streak-seeding using wild-type AnPRT. Hence, these three structures complement the information found via enzymology in this study and provide a comparison to the five new structures complexed with the phosphonate ligands obtained by the co-crystallisation method, in the presence or absence of the PRPP substrate.

2.7.1 AnPRT with 2.6

The structure of *M. tuberculosis* AnPRT was obtained in complex with ligand **2.6** and solved in the space group $P2_12_12_1$, the most common space group for this protein.⁶⁸ Two monomeric units were present in the asymmetric unit. Both monomers have a similar binding mode for phosphonate inhibitor **2.6** in which aromatic rings moiety of **2.6** bind between sites 2 and 3 (site 2–3) within substrate binding tunnel (Figure 2.7, **A**). The binding site 2–3 of **2.6** ligand is identical to the ACS172 molecule bound at the similar site in the AnPRT 3QQS structure. The $\beta 1$ – $\alpha 5$ and $\beta 2$ – $\alpha 6$ loops are observed in the open conformation as expected without the binding of the PRPP substrate. The ACS172 molecule makes hydrogen bonds with its inner carboxylate to Arg193 and a water molecule and with its outer carboxylate group to Asn138 and Arg194 and a water molecule (Figure 2.7, **B**). However, the inhibitor **2.6** forms contacts to Arg193 and Tyr186 with its inner carboxylate group and the phosphonyl linker interacts with only Arg187 (Figure 2.7, **C**). The ligand **2.6** does not make any contacts with Asn138 and Arg194 due to the absence of an outer carboxylate group. The lack of a strong interaction by the inhibitor resulted in weaker enzyme inhibition (K_i^{anth} value of $7 \pm 1 \mu\text{M}$ and K_i^{PRPP} value of $63 \pm 2 \mu\text{M}$) than ACS172

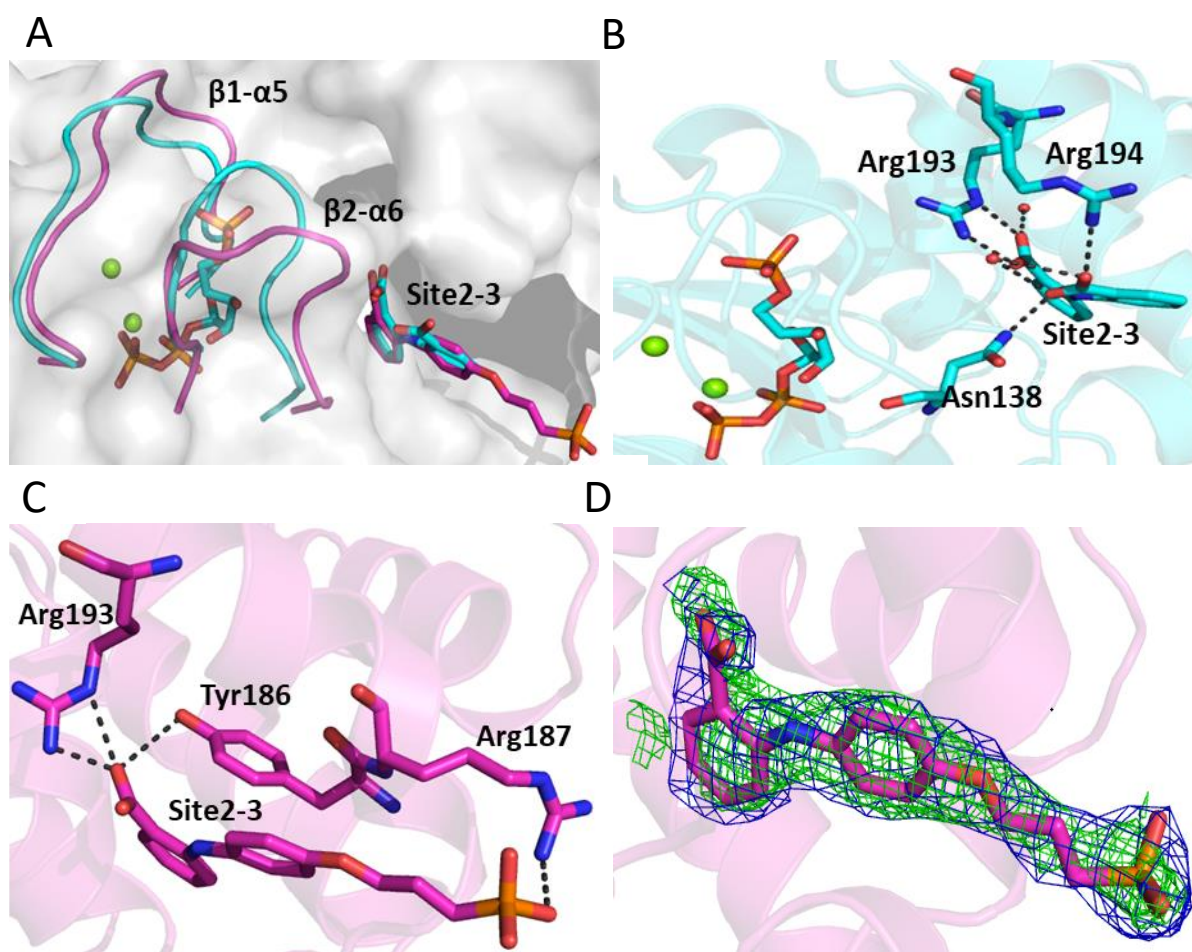


Figure 2.7 The binding interaction of **2.6** with *M. tuberculosis* AnPRT.

(A) Structural superimposition of Chain A (pink) bound with **2.6** (pink) with chain B (PDB: 3QQS, cyan) bound with Mg^{2+} ions (green), PRPP (green) and ACS172 (cyan). (B and C) ACS172 and **2.6** ligands bound at site 2–3 and established polar contacts to the side chain residues present at the anthranilate binding tunnel. Hydrogen bonds of ACS172 and **2.6** ligands are represented as yellow and black broken lines respectively. (D) Omit map showing the density into which ligand **2.6** was modelled. 2Fo-Fc omit map contoured at $1.0\ \sigma$ (blue mesh) and Fo-Fc omit map contoured at $3.0\ \sigma$ (green mesh).

2.7.2 AnPRT with **2.8** and **2.9**

Compounds **2.8** and **2.9**, containing 4 and 5 atoms linkers, adopt two distinct binding modes in the different monomeric units of the obtained ligand-bound structures of *M. tuberculosis* AnPRT (PDB: 5BO2 and 5BO3, Figure 2.8). Both structures were obtained using the ligand soaking method and were solved in the C121 space group.

In the inner side binding mode of the inhibitor (Figure 2.8, **A** and **B**), the phosphonyl anchor of the inhibitor positions itself at the site 2 of the substrate binding tunnel. However, the binding mode of the inhibitor does not overlay with either the position of ribose-5-phosphate or the diphosphate moiety within the PRPP binding site.

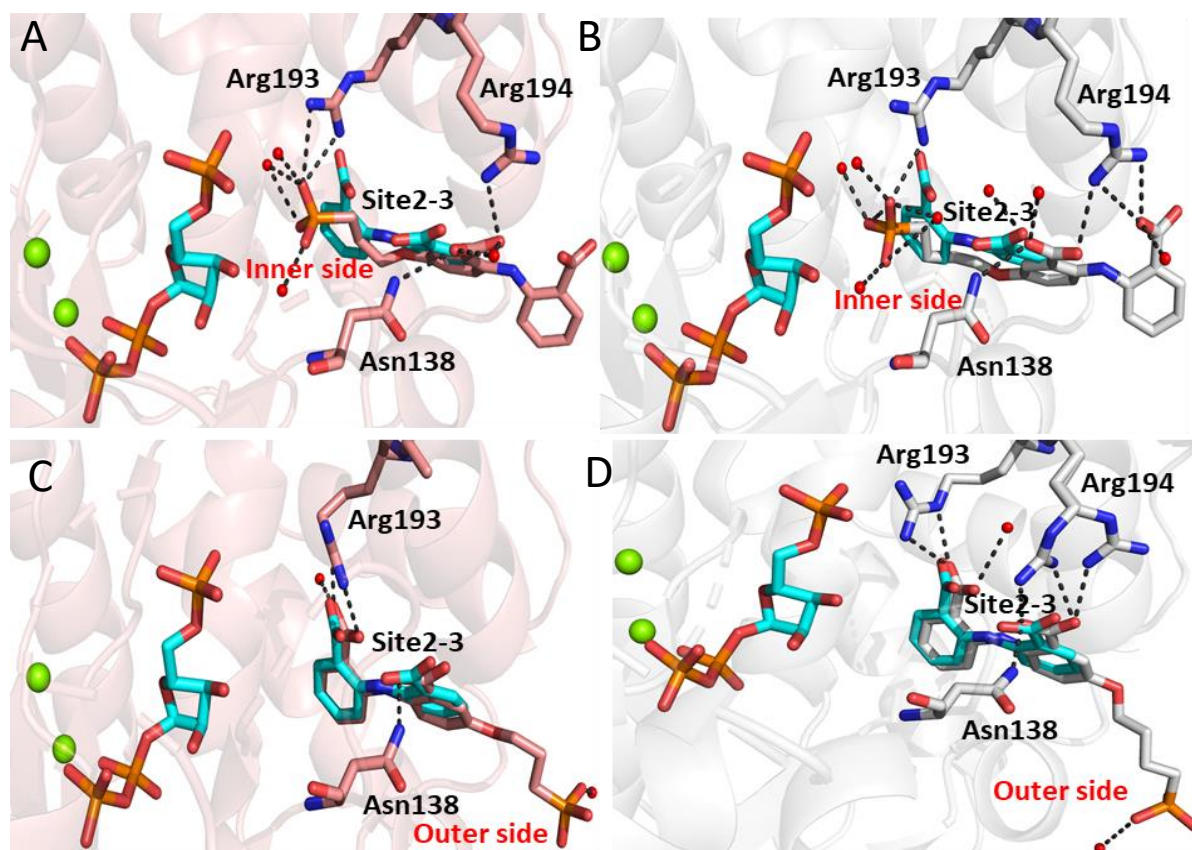


*Figure 2.8 Two different binding modes for **2.8** and **2.9** bound with AnPRT. (**A**, **B**) the structural superposition of chain B (PDB: 3QQS) bound with Mg^{2+} ions (green), PRPP and ACS172 (cyan), chain A of **2.8** (PDB: 5BO2, red) and chain A of **2.9** (PDB: 5BO3, grey). The AnPRT structures show the inner side binding mode of the phosphonate inhibitors. (**C**, **D**) The overlay of chain B (PDB: 3QQS) bound with Mg^{2+} ions (green), PRPP and ACS172 (cyan), chain B of **2.8** (PDB: 5BO2, red) and chain B of **2.9** (PDB: 5BO3, grey). The AnPRT structures represent the binding site and outer side binding mode for the **2.8** and **2.9** ligands. Hydrogen bonds of **2.8** and **2.9** ligands are represented as black dashes.*

The **2.8** bound structure shows the phosphonate group forms contacts with Arg193 and three water molecules, whereas the bianthranilate moiety interacts only with Asn138, Arg194 and one water molecule. Similarly, ligand **2.9**, with a longer linker, interacts with identical residues

(Asn138, Arg193 and Arg194) and water molecules. There are additional polar contacts to three water molecules via the phosphonyl group and its carboxylate groups present on both aromatic rings of ligand **2.9**. In both inhibitor-bound structures, the repositioning of the bianthranilate moiety to occupy site 3 rather than site 2–3 in the substrate binding tunnel may be due to Arg193, a key residue of binding site 2, shifting to make a hydrogen bond with the phosphonyl group. However, in the outer side binding mode (Figure 2.8, **C** and **D**), the phosphonyl anchor of the inhibitor positions itself at the entrance of the substrate binding tunnel and does not make any contacts except with water molecules. In the outer binding mode of both inhibitors, “bianthranilate”-like moiety of **2.8** and **2.9** bound at a similar site 2–3 position compared to ACS172 bound structure and interacts with identical side chains of Asn138, Arg193 and Arg194. Therefore, the AnPRT inhibition values for both inhibitors (**2.8** and **2.9**) are similar (Table 2.2) with respect to both substrates due to the identical binding mode observed for both ligands.

2.7.3 AnPRT with **2.10**

The structure of the enzyme bound to the second most potent inhibitor in the list, the 6–atom linker compound (**2.10**), shows the inhibitor bound similarly to other phosphonate inhibitors (**2.6**, **2.8** and **2.9**) to the anthranilate binding tunnel but reaching beyond to the edge of the PRPP binding site (Figure 2.9). A new AnPRT structure co-crystallised with ligand **2.10** has been solved in the C121 space group, different from the previous **2.10** bound AnPRT structure (PDB: 5BNE) in a lower symmetry group, *P*12₁1. The “bianthranilate”-like moiety of **2.10** occupies site 3 and the entrance of the tunnel, identical to the binding mode of **2.8** and **2.9** (Figure 2.9, **A**). The ligand **2.10** binds in a similar manner to **2.8** and **2.9**, with the phosphonate group in and close to the PRPP binding site in both structures apart from chain A of the structure solved in the C121 space group. The ligand **2.10** forms hydrogen bonds with protein residues; Asn138, Arg193 and Arg194 (Figure 2.9, **B**).

Interestingly, chain A of this co-crystallised structure displays the opposite conformation for compound **2.10**, with the flexible phosphonate anchor of the inhibitor present at the outer side of the substrate binding tunnel. A similar outside binding mode was also observed for ligand **2.10** in another AnPRT structure bound with PRPP and Mg²⁺ ions and refined in the

$P12_11$ space group (Figure 2.10). This outer binding mode of the phosphonate anchor implies a high degree of flexibility and does not show any contacts with the protein backbone except for hydrogen bonding with Arg187 only in chain D of the PRPP complex structure. The “bianthranilate”-like moiety within this ligand occupies site 2–3 in the anthranilate binding tunnel in a fashion similar to the “bianthranilate”-like inhibitor ACS172 (PDB: 3QQS; Figure 2.10).

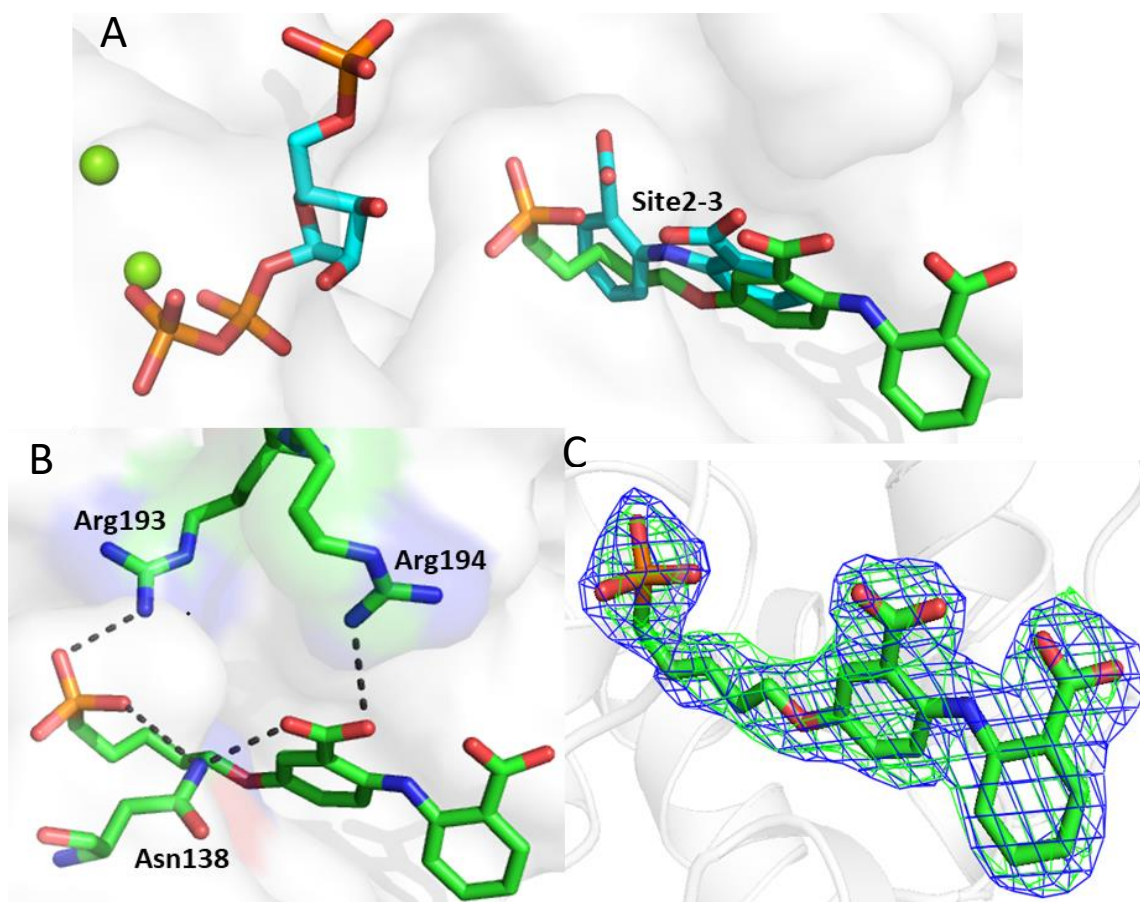


Figure 2.9 The inner side binding mode for ligand **2.10** with *M. tuberculosis* AnPRT. (A) Overlay of chain B bound with **2.10** (green) and chain B of ACS172, PRPP and two Mg^{2+} (PDB: 3QQS, cyan) bound AnPRT structures. (B) The binding interactions of **2.10** (green) in chain B (green) of the **2.10**-bound AnPRT structure. Hydrogen bonds are represented as black dashed lines. (C) Omit map showing the density into which ligand **2.10** was modelled. 2Fo-Fc omit map contoured at 1.0 σ (blue mesh) and Fo-Fc omit map contoured at 3.0 σ (green mesh).

However, the bianthranilate-like moiety of **2.10** also forms hydrogen bonds with the backbone of protein residues Asn138, Arg193 and Arg194 in all three **2.10** bound AnPRT structures. AnPRT Inhibition values for **2.10** (K_i^{anth} value of $2.8 \pm 0.5 \mu\text{M}$ and K_i^{PRPP} value of $12 \pm 1 \mu\text{M}$) are low as recorded for ligands **2.8** and **2.9** due to the similar binding fashion observed for inhibitor **2.10** with or without PRPP.

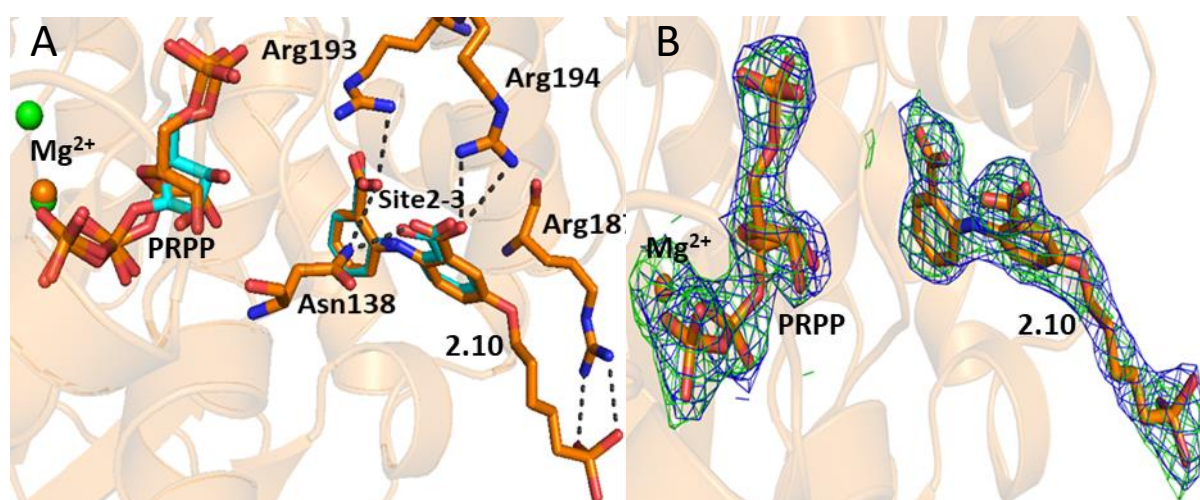


Figure 2.10 The **2.10**-bound *M. tuberculosis* AnPRT structure.

(A) Overlay of chain B (orange) bound with **2.8**, PRPP and one Mg²⁺ and chain B (PDB: 3QQS, cyan) of the ACS172, PRPP and two Mg²⁺ bound AnPRT structure. Mg²⁺ ions of **2.10** and ACS 172 bound structures are represented as orange and green spheres respectively. Polar contacts are shown as black broken lines. (B) Omit map showing the density into which ligand **2.10**, PRPP and one Mg²⁺ ion were modelled. 2Fo-Fc omit map contoured at 1.0 σ (blue mesh) and Fo-Fc omit map contoured at 3.0 σ (green mesh).

Further to this, **2.10**, PRPP and Mg²⁺ co-crystallised with AnPRT show similar binding modes for the PRPP substrate (Figure 2.10). However, only one Mg²⁺ ion is present in the **2.10** ligand-bound structure. In all **2.10** bound structures, the β1–α5 and β2–α6 loops adopt distinct conformations depending on the absence or presence of PRPP like other inhibitor-bound structures. However, there was no interconnection between the type of space group, the binding ligand mode and the method by which the ligand was introduced.

2.7.4 AnPRT with 2.11

The strongest inhibitor of the series (**2.11**; K_i^{anth} value of $1.3 \pm 0.1 \mu\text{M}$ and K_i^{PRPP} value of $5.4 \pm 0.3 \mu\text{M}$) has a triazole component in the linker, which will introduce conformational restraints that are not present in other inhibitors on the list. AnPRT was successfully co-crystallised only with **2.11** and **2.11**, PRPP and Mg^{2+} metal ions (Figure 2.11, A–E).

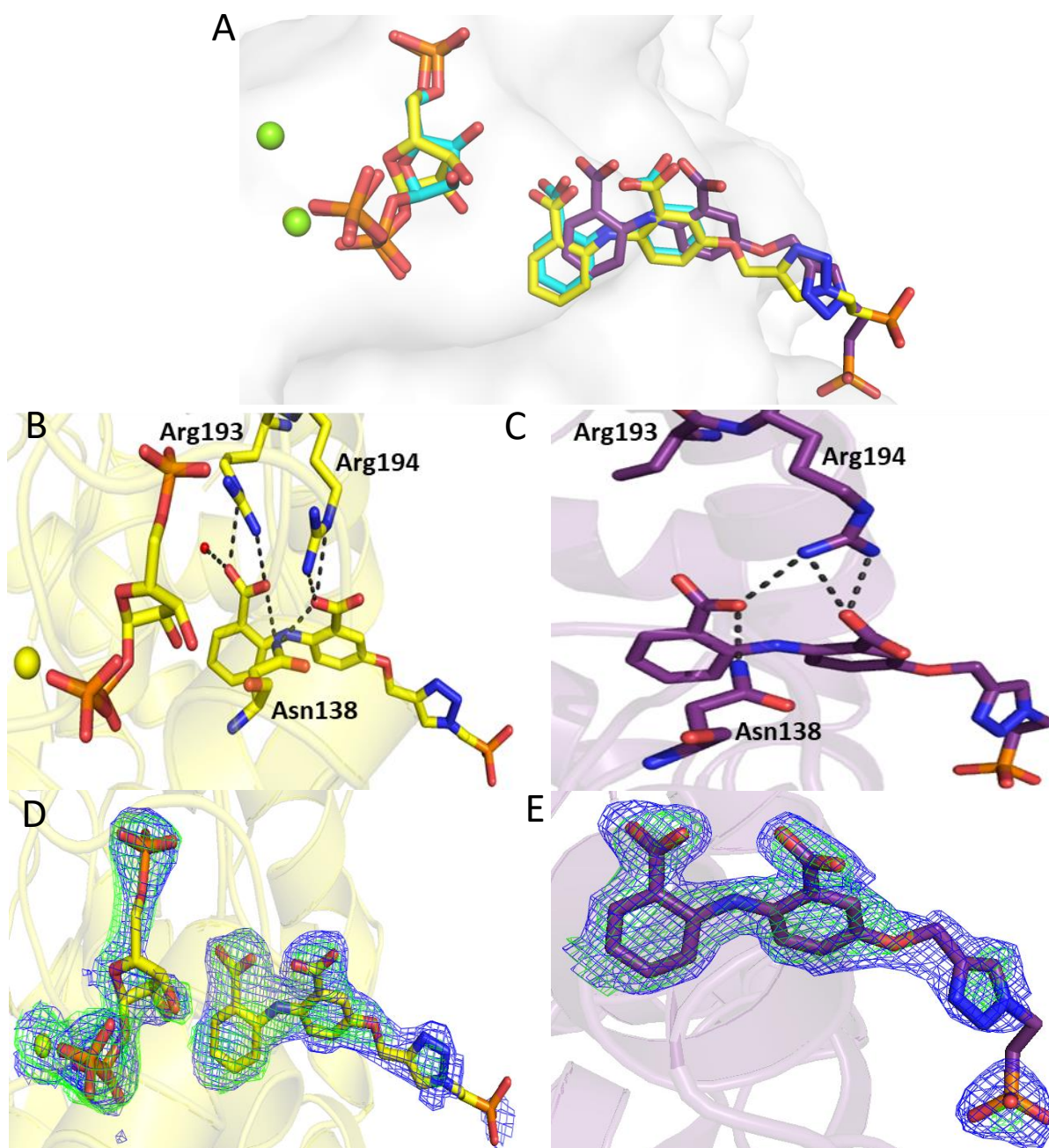


Figure 2.11 The binding interaction for the **2.11**-bound AnPRT structures.

(A) Superposition of chain C (yellow), of **2.11**, PRPP and one Mg^{2+} , chain B (purple) of **2.11** and chain B of ACS172, PRPP and two Mg^{2+} (PDB: 3QQS, cyan) bound AnPRT structures. (B,

*C) The binding interactions of **2.11** (yellow and purple) in chain C (yellow) and chain B (purple) in the **2.11**-bound AnPRT structures respectively. Hydrogen bonds are represented as black dashed lines. (D, E) Omit map showing the density into which ligand **2.11** was modelled in chain C (yellow) and chain B (purple) of the AnPRT structures. 2Fo-Fc omit map contoured at 1.0 σ (blue mesh) and Fo-Fc omit map contoured at 3.0 σ (green mesh).*

Both structures have been solved in the $P12_11$ space group. X-ray crystallographic data for both structures indicated a clear charge density for the bianthranilate-like moiety and the triazole component. Unfortunately, no charge density was observed for the flexible phosphonyl group linker. Presumably, the flexible phosphonyl group adopted more than one conformation. Hence, this group is modelled with zero occupancy in both **2.11** bound structures (Figure 2.11, **D, E**). Both structures show an almost identical binding mode for binding the bianthranilate-like moiety, similar to the “bianthranilate”-like inhibitor ACS172 (PDB: 5BNE) but reaching far into the PRPP binding site (Figure 2.11, **A**). The long flexible linker of the inhibitor was designed to bind within the PRPP binding site but it was bound to the opposite side in the outermost side of the substrate binding tunnel. Compound **2.11** forms hydrogen bonds with the backbone of protein residues Asn138, Arg193 and Arg194 (Figure 2.11, **B, C**). Furthermore, one Mg^{2+} ion (yellow sphere) was found only in the **2.11**, PRPP and Mg^{2+} bound structure.

2.7.5 Conclusion

All phosphonate-bound *M. tuberculosis* AnPRT structures described in this chapter show that none of the inhibitors occupy the PRPP binding site. In addition, there are no specific differences in the binding of the inhibitors observed in the PRPP:inhibitor complex structures and only inhibitor bound AnPRT structures. This is also consistent with these compounds being competitive inhibitors with respect to anthranilate, but not with respect to PRPP, as shown by the steady-state kinetics. These data are also consistent with these compounds being partial inhibitors: at no concentration measured were the compounds able to completely inhibit enzymatic activity as noticed in the dose-response curves and maximal % inhibition.⁵⁴ These inhibitors were more accessible to the solvent-exposed binding modes at the anthranilate binding sites rather than the catalytic site of the enzyme. The effect of conformational constraints of the enzyme on the binding affinity of the inhibitors acts as an

entropic barrier which restrains the binding of inhibitors to the PRPP binding site. The repositioning of the protein side chains Arg187, Arg193 and Arg194—the key residues for binding ligands into substrate binding tunnel—offered hydrogen bonding partners to the inhibitors.

While **2.8**, **2.9** and **2.11** only form a few hydrogen bonds to the protein, they display the strongest inhibition with low K_i values for the enzyme. However, the inhibitor-bound AnPRT structure shows the intramolecular hydrogen bonding is present within the “bianthranilate”-like inhibitors that compel a chemical scaffold which was also important for inhibiting the enzyme strongly as well.⁶⁹ Moreover, the ligands **2.8**, **2.9** and **2.11** with elongated linkers occupy multiple anthranilate sites within the channel and display low K_i values. The K_i values decreased with an increase in the length of the linkers. This observation indicates that stronger inhibition is obtained when multiple anthranilate sites are occupied by inhibitors.

Further to this, using co-crystallization or soaking methods, the generation of these phosphonate inhibitor bound structures found no correlation between space group, the mode of ligand binding and the method by which the ligand was introduced to the enzyme (either by soaking or co-crystallization).

2.8 Summary

Both *M. tuberculosis* AnPRT and *E. coli* PRAI:InGPS proteins were successfully expressed. Both proteins were purified with expected sizes as confirmed by mass spectrometry. *M. tuberculosis* AnPRT was kinetically characterised using a UV enzyme-coupled assay. The apparent K_M values for PRPP and anthranilate were $49 \pm 4 \mu\text{M}$ and $1.6 \pm 0.1 \mu\text{M}$ respectively, with a k_{cat} value of $1.9 \pm 0.02 \text{ s}^{-1}$. These values correlated well to the values reported previously for *M. tuberculosis* AnPRT.

A set of anthranilate and “bianthranilate”-like compounds with flexible linkers were tested against *M. tuberculosis* AnPRT using an enzyme-coupled assay. The bianthranilate moiety compounds, with phosphonate linkers, were the most effective at inhibiting the enzyme and the compounds with an “anthranilate-like” moiety adjacent to an aromatic ring with carboxylate group linkers had the least effect on the reaction kinetics of AnPRT. All

compounds were competitive with respect to anthranilate and non-competitive with respect to PRPP. K_i values against the anthranilate substrate ranged from 1.3 to 41 μM while K_i values against PRPP varied between 5.4 and 175 μM . The most potent inhibitor was **2.11** with respect to both substrates (K_i^{anth} value of $1.3 \pm 2.5 \mu\text{M}$ and K_i^{PRPP} value of $5.4 \pm 0.3 \mu\text{M}$) of AnPRT.

In conjunction with the inhibition enzymology studies, structures of *M. tuberculosis* co-crystallised only with the inhibitor or the inhibitor complexed with PRPP, Mg^{2+} ions were obtained. These structures were also compared with the structures obtained in different space groups, using a distinct method by Dr G. L. Evans. These structures showed the inhibitors bind only in the anthranilate channel but do not reach into PRPP binding site, the actual catalytic site of the enzyme. Ligands **2.8**, **2.9** and **2.10** displayed two different binding modes in individual monomeric units. Additionally, in this study, no link between the space group, the binding mode of the ligand and the method of ligand introduction into the protein crystal was found.

Chapter 3 Molecular modelling

3.1 Overview

Chapter 3 describes the computer-assisted drug design to predict the predominant binding mode of ligands within the catalytic site of *M. tuberculosis* AnPRT. The virtual screening approach screened a ZINC library of commercially available compounds, scored the results, and has informed new structural hypotheses of how inhibitors bound to the enzyme. A number of compounds were selected for testing AnPRT inhibition using an enzyme-coupled kinetic assay. X-ray crystallography, DSF and ITC techniques were applied to explain the binding of the ligands to AnPRT in detail.

3.2 Virtual screening

Computational approaches have had a major role in many drug discovery studies, from hit identification to lead optimisation.^{98–100} Methodologies such as virtual screening are extensively used in various discoveries, where small molecules are docked into macromolecule structures to identify those structures which are most likely to bind tightly to the receptor macromolecule.^{101,102} Virtual screening results provide a target-focussed subclass of molecules from bigger libraries and subsequently lessens the number of compounds that are experimentally tested. This computational approach is a key tool for searching for lead compounds as it is expeditious and less resource demanding compared to experimental methods such as high-throughput screening.¹⁰³ In fact, the development of several drugs has been based on these structure-based design, such as HIV protease inhibitors,^{104–106} tyrosine kinase inhibitors¹⁰⁷ and anti-depressants drugs.¹⁰⁸ Therefore, the *M. tuberculosis* AnPRT active site was deemed a suitable target for this approach in order to find novel scaffolds that may bind at the active site for further elucidation of the reaction mechanism and inhibition of AnPRT, in order to aid the development of anti-TB drugs.

3.3 Virtual screening workflow

Structure-based virtual screening was performed using the virtual screening workflow in Schrödinger Suite 2017-1, with the following steps:¹⁰⁹

- Grid generation: The generation of the receptor grid is the first step in modelling, which identifies a three-dimensional description of the binding site that allows Glide to search for favourable contacts between the ligand and receptor binding site. The shape and properties of the binding site are exemplified on a set of calculated grids, which significantly speeds up for positioning and scoring ligand poses.¹¹⁰
- Ligand preparation: The compound library was prepared using selection methods focusing on maximising the diversity and drug-likeness of compounds. A set of three PAINS filters was used to eliminate the compounds that include common functional groups that likely result in false positives in ligand screening calculations.
- Virtual screening: There are three main stages with increasing precision in Glide dock.¹¹⁰ Scoring is carried out during each docking stage and after each screening stage, the compounds are filtered so that only the ones with high docking scores are kept for the next stage. First, the high throughput virtual screening (HTVS) mode is used to identify and rank the binding energies of potential drug candidates from a library that has millions of compounds. Second, the standard precision (SP) function is mainly used for standard docking for a smaller number of compounds. Third, the extra precision (XP) is used for precise, narrow screening and employs a larger penalty for poses that disrupts physical properties. The SP GlideScore scoring function is lighter and maximizes false positives and is used to rank compounds docked by HTVS or SP Glide. Whereas the XP GlideScore scoring function is used for XP Glide.

3.3.1 Grid generation

The preparation of the receptor grid was done by Dr Wanting Jiao. It has been previously demonstrated that the conformation of the ligand-bound receptor provides a better model for molecular docking compared to the *apo* or homology-modelled receptors.¹¹¹ Therefore, chain A of *M. tuberculosis* AnPRT (PDB: 4N93) bound to the PRPP, Mg²⁺ and 6MI ligands was chosen as the receptor for docking. The anthranilate analogue, 6MI, is accepted as an alternative substrate for AnPRT.⁷⁴ The receptor was prepared by the standard protocol in the protein preparation wizard. Both Mg²⁺ ions and three water molecules that have key roles in PRPP binding were included in the receptor grid (Section 1.8.2). One water molecule directly contacts the anomeric oxygen of the ribose ring and the other two water molecules are

coordinated to the Mg^{2+} ions and the diphosphate moiety of PRPP in the original structure. The missing hydrogens were added to the targeted site and the hydrogen bonds were optimised. The receptor grid was then generated using the prepared structure with the software Glide.¹⁰⁹ The centre of the grid was defined as the centroid of residues within 5 Å of the PRPP molecule. The PRPP was docked into the prepared grid by XP rigid docking to validate the docking protocol. A similar binding mode was observed for the docked PRPP molecule as compared to the crystallographically observed binding mode of PRPP (Figure 3.1, A).

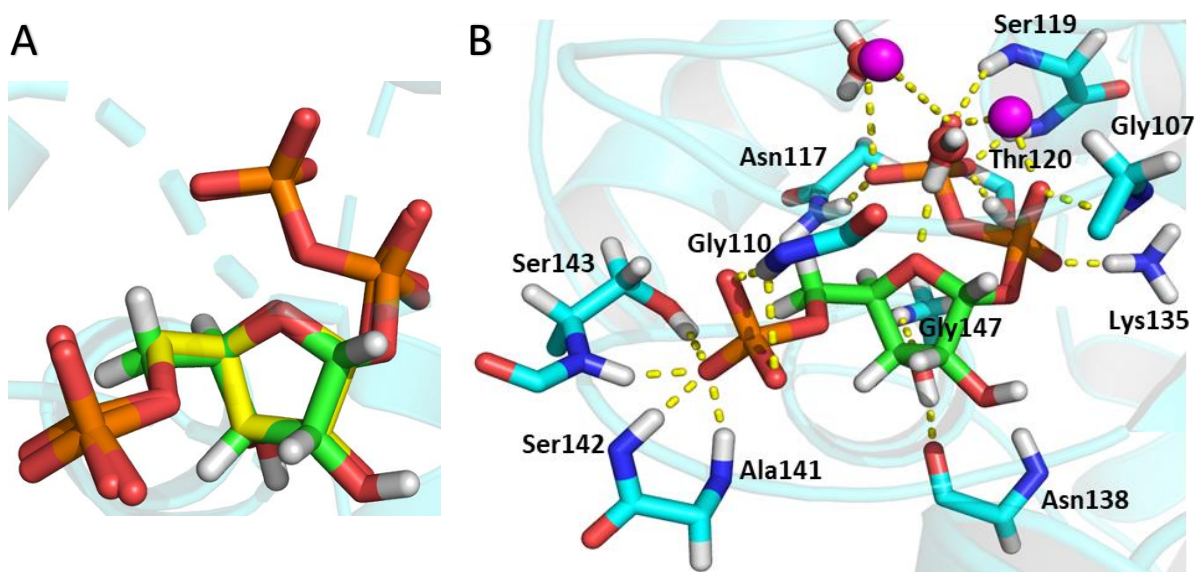


Figure 3.1 The predicted binding mode and interactions for PRPP as determined by Glide.

(A) The overlay of the Glide predicted PRPP docking pose (green carbons, white hydrogen atoms) with the observed PRPP binding mode in the original structure (PDB: 4N93, yellow carbons). **(B)** The predicted binding interactions observed for the docked PRPP molecule (green) within the receptor grid. The side chain residues are shown in cyan. The spheres of Mg^{2+} and water molecules are represented in pink and red, respectively. The hydrogen atoms are represented as white sticks. Interactions are shown as yellow dashes.

The residues that are important for binding PRPP at the catalytic site of the enzyme, detailed in Section 1.8.2, are almost identical as observed for the docked PRPP molecule (Figure 3.1, B). The active site residues Gly107, Asn117, Ser119, Thr120 and Lys135 along with a water molecule form contacts with the diphosphate moiety of PRPP. The phosphate moiety of PRPP forms hydrogen bonds with residues Ala141, Ser142, Ser143 and Gly110. The ribose ring

oxygen interacts with a water molecule and its C3 hydroxyl group forms contacts with Asn138 and Gly147 located on the $\beta 2$ – $\alpha 6$ loop. These residues interacting with PRPP are taken into account to validate docking poses for selected compounds from the virtual screen.

3.3.2 Preparation of the compound library

A ZINC library of commercially available compounds was obtained from the ZINC database.¹¹² The original library contained over 1,000,000 lead-like compounds and ligands were selected with suitable pharmacological properties in the Schrödinger Suite (Figure 3.2). The selected compounds were then prepared using LigPrep from the Schrödinger Suite, with the following settings: Force field OPLS3, generate possible states at pH range 7.5 ± 0.5 using Epik and generate at most 1 stereoisomer per ligand. The filtered library contained 461,163 compounds which were filtered by the three PAINS filters which rapidly identify drug molecules by QikProp, prefilter by Lipinski's rule, and filter reactive functional groups by Ligfilter in the Schrödinger Suite.

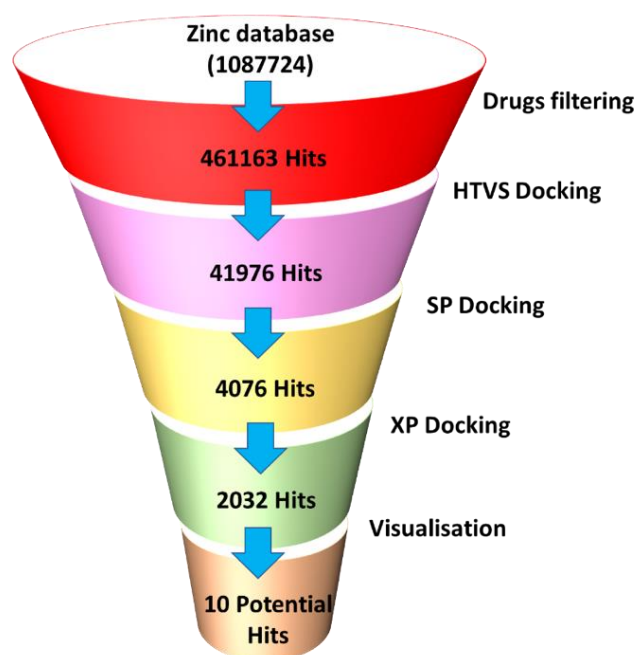


Figure 3.2 The hierarchical virtual screening workflow.

3.3.3 Docking and scoring

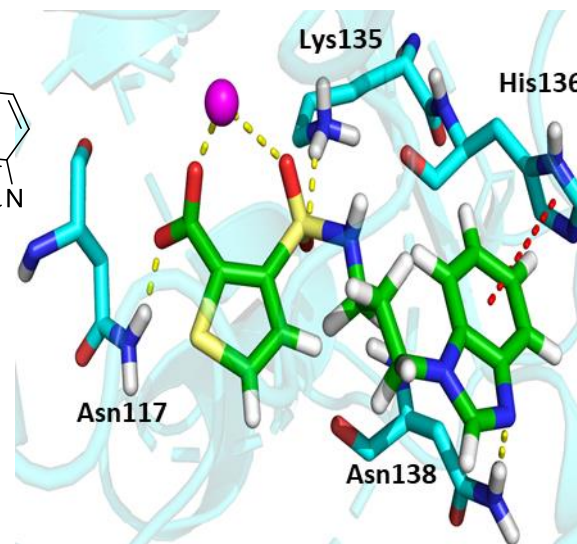
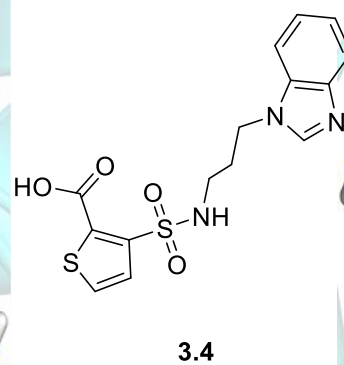
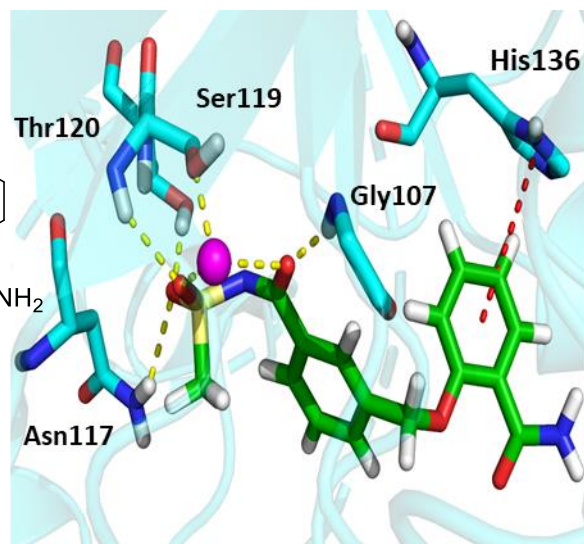
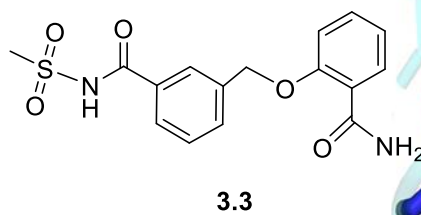
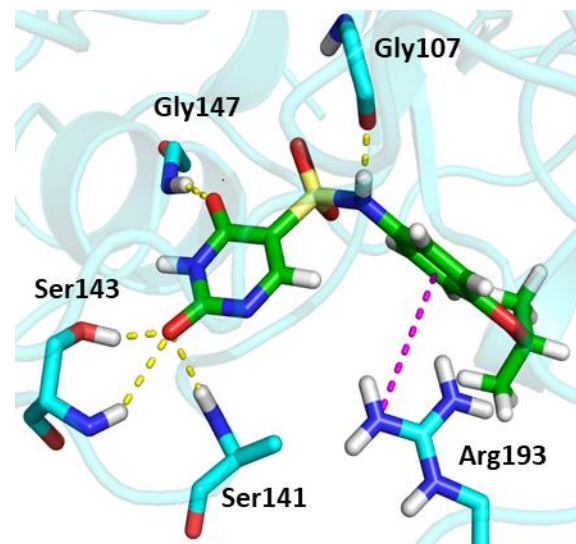
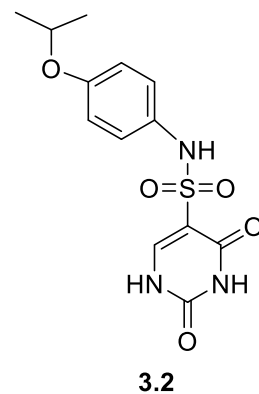
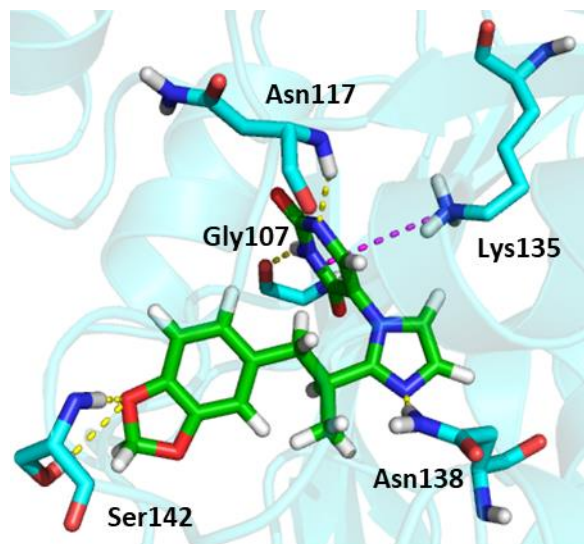
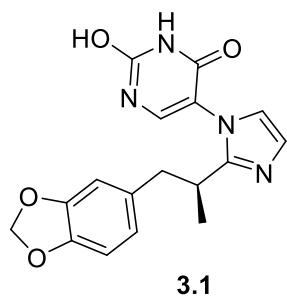
The compound library was screened using HTVS, SP and XP docking methodologies (Figure 3.2). Glide HTVS and SP were set to save 10% of the high scoring ligands and XP Glide was run

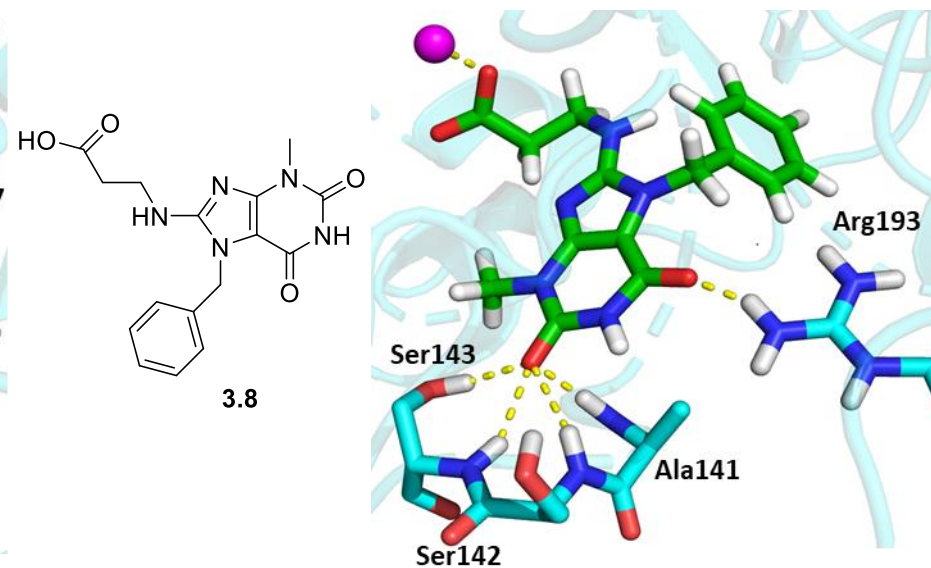
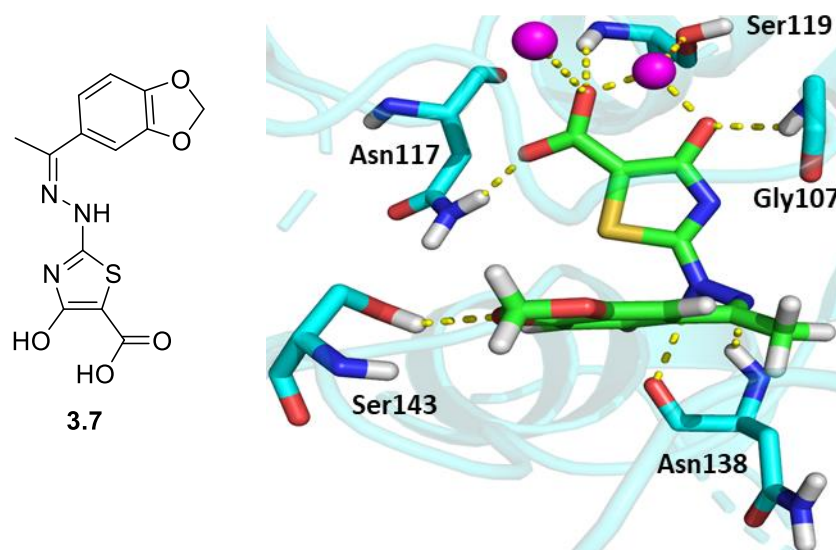
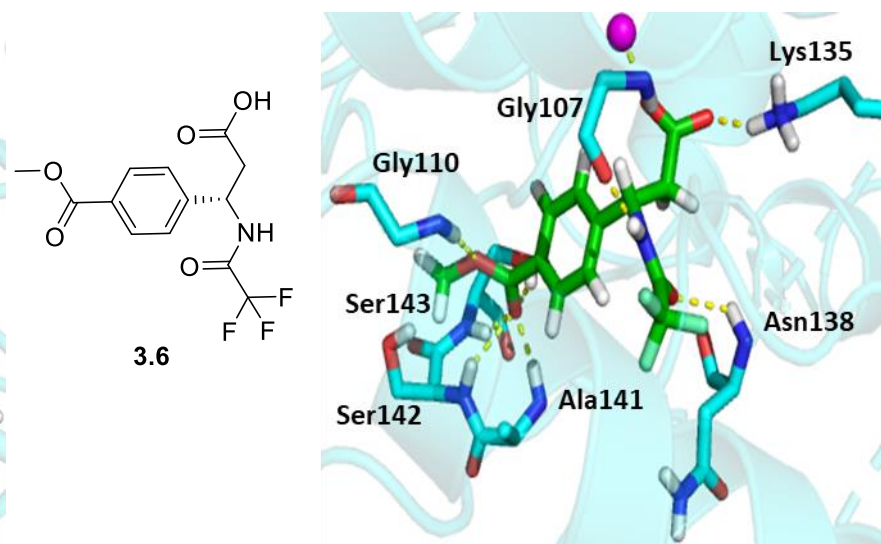
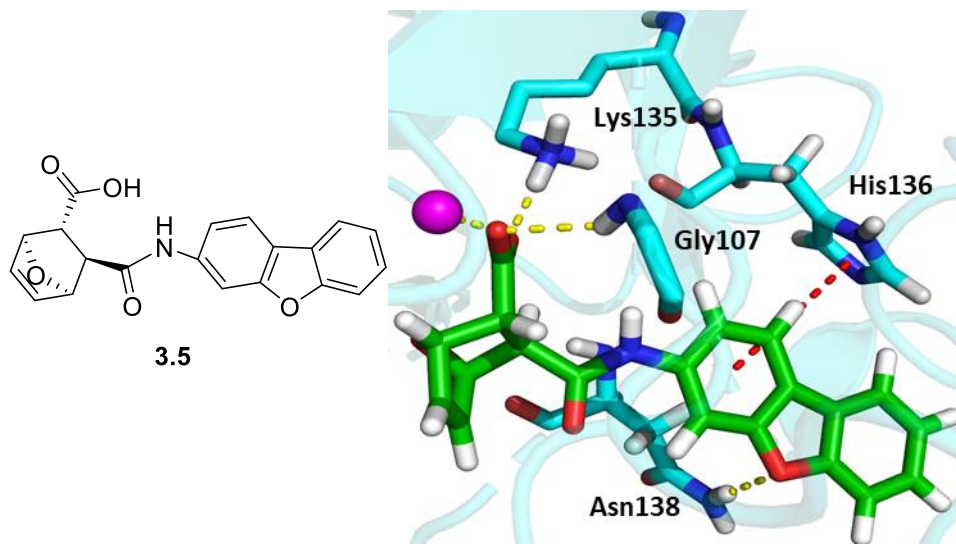
with set parameters and generated only a maximum of one pose per compound state. Of the 50% of the best scoring compounds, 2032 compounds remained with a XP Glide score. The top 1200 poses with docking scores above -8.50 and ligands forming minimum four hydrogen bonds into the receptor grid were examined based on the following criteria:

- Ligand interactions with key residues: The residues present at the active site (see Figure 3.1, **B**) were considered important for ligand binding. Docked compounds forming contacts with these residues were selected preferentially. Ligands with a minimal amount of steric hindrance around the active site and a high number of hydrogen bonds with key active site residues were considered for further evaluation.
- Ligands that were easily available for purchase and had potential for modification with extra functional groups to enhance binding were further selected with higher priority.

On the basis of the selection criteria, 10 compounds available for purchase were chosen for direct investigation. Based on the predicted binding positions and interactions, the selected compounds can be separated into three groups. Compounds **3.1** and **3.2** fit into the PRPP binding site and display π -cation interactions with two active-site residues, Lys135 and Arg193. Compounds **3.3**, **3.4**, and **3.5** reach the anthranilate binding site 1 within the tunnel and also display binding within the active site. These compounds also explore the predicted π - π stacking interaction with the aromatic ring of His138. The remaining compounds (**3.6**, **3.7**, **3.8**, **3.9** and **3.10**) bind to the PRPP binding site and interact with most of the residues that assist with the binding of PRPP substituents.

The predicted ligand interactions of the selected compounds are shown below in Figure 3.3; the yellow dashed lines show the H-bonding, the π -cation and π - π stacking interactions are shown in pink and red broken lines, respectively. To display ligand interactions distinctly, only protein residues that interact with the ligands are displayed and labelled.





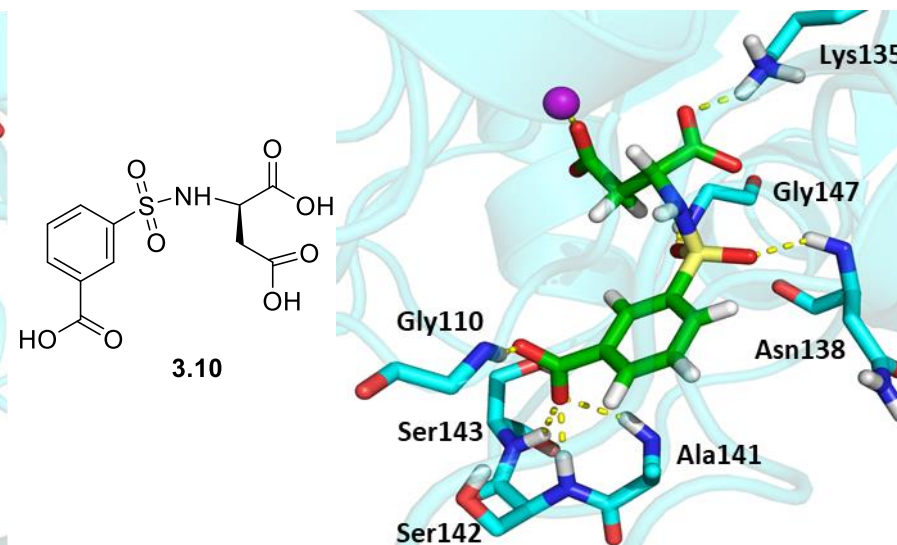
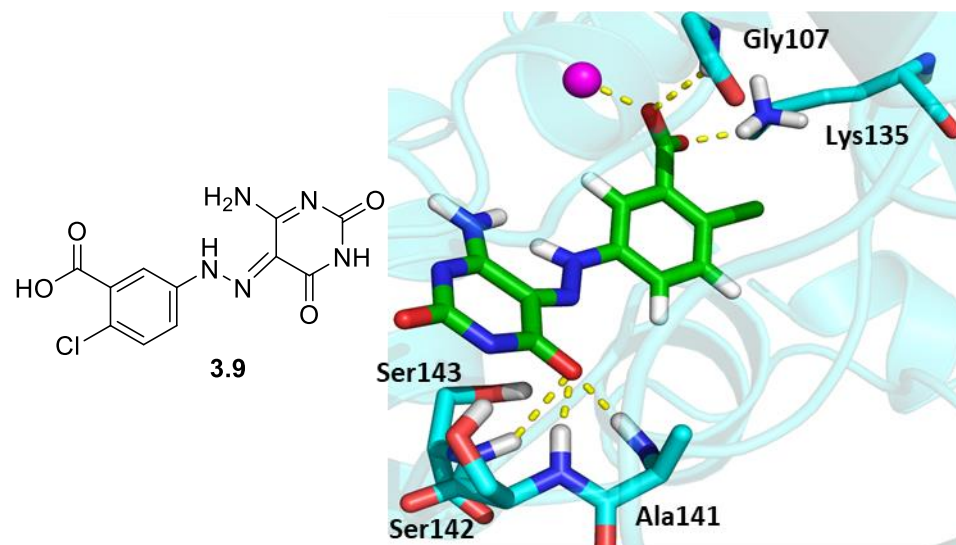


Figure 3.3 Structures and docking poses of chosen compounds from the virtual screen of the ZINC library against *M. tuberculosis* AnPRT.

A more detailed evaluation of the selected compounds (Figure 3.3) is presented here.

3.1—this ligand was selected for its fit into the PRPP binding site and the pyrrole nitrogen provides an easy way to further functionalise this molecule. Additionally, the pyrimidine ring of this ligand displays π -cation interaction with Lys135 and makes this an interesting ligand to investigate.

3.2—the sulphonamide group resembles the natural ribose-5-phosphate group. The sulfonamide group with the pyrimidine ring of **3.2** produces a complementary fit to the ribose-5-phosphate site. The aromatic phenyl ring also shows π -cation interactions with Arg193.

3.3—the *N*-methylsulfonyl benzamide moiety is predicted to bind to the PRPP binding site and the carbamoylphenoxy group is predicted to reach into the anthranilate binding site 1. The methylsulfonyl is predicted to form H-bonding interactions with the diphosphate moiety and Mg^{2+} , and its benzamide ring binds closely to the position of the ribose ring in PRPP. A π - π interaction is predicted to occur at site 1 with the aromatic ring of carbamoylphenoxy and His136. The binding of **3.3** at the catalytic site by covering both the PRPP and the anthranilate binding sites makes this an interesting ligand to investigate.

3.4 and **3.5**— these ligands have a similar charged head group and were chosen for their fit into the PRPP site and anthranilate binding site 1. The substituted aromatic rings were also selected to explore the effect of a π - π stacking interaction with His136.

3.6—this is a fascinating compound for further testing due to the presence of an electronegative trifluoro acetyl group. In addition, multiple H-bonding interactions for **3.6** are predicted with the residues present at the enzyme active site.

3.7—this ligand is predicted to bind to the PRPP binding site and the thiazole moiety forming H-bonding interactions with both Mg^{2+} ions and binds closely to the position of the ribose ring in PRPP.

3.8—the predicted docking pose of **3.8** forms multiple H-bonding interactions. The propanoic acid moiety is placed at the binding position observed for the diphosphate group of PRPP and forms interactions with a metal ion, Gly107 and Lys135. The purine ring has a complementary

fit within the active site at the position of the ribose ring and the phosphate group of PRPP and interacts with several of the phosphate-binding residues Ala141, Ser142, and Ser143.

3.9—the presence of two six-membered rings in this compound provides a favourable geometry for binding and these rings occupy the space between loops $\beta 2$ – $\alpha 6$ and $\beta 1$ – $\alpha 5$ in the PRPP pocket. The carboxylate group is placed at the binding position of the diphosphate moiety of PRPP and interacts with a metal ion, Gly107, and Lys135. The purine ring of **3.9** is bound at the position of the ribose ring and the phosphate group of PRPP and interacts with the phosphate-binding residues Ala141, Ser142, and Ser143. The ligand also has the potential for further functionalisation.

3.10—**3.10** reached all the way across to the PRPP binding site and formed H-bonding interactions with a metal ion, diphosphate and phosphate binding residues. Additionally, H-bonding to the backbone residues Asn138 and Gly147, located on the $\beta 2$ – $\alpha 6$ loop, was also observed in the predicted docking pose. The sulphate group along with the aromatic ring of this compound produced a complementary fit to the ribose-5-phosphate site. The size and magnitude of H-bonding and the fitting of two carboxyl groups into the buried diphosphate site made this an interesting ligand to investigate.

The structures of the selected compounds indicate that these compounds may have the ability to bind within the anthranilate binding tunnel, as demonstrated by other similar compounds tested against AnPRT in Chapter 2. Therefore, these compounds and 50 compounds with high docking scores from the virtual screen of the PRPP site were also docked into the anthranilate binding channel. Chain A of the original AnPRT structure (PDB: 4N93, Figure 3.4), which shows the anthranilate analogue 6MI binding at sites 1 and 3, was used for generating the receptor grid.

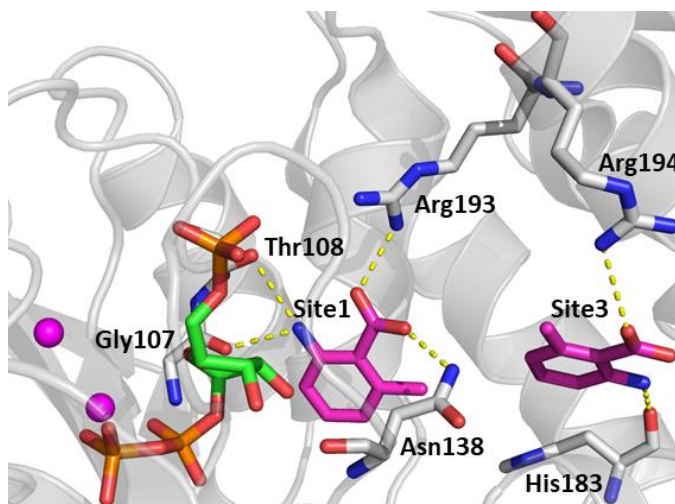


Figure 3.4 The binding sites of 6MI in the AnPRT structure (PDB: 4N93).

Chain A of AnPRT structure bound with PRPP (green), 6MI (pink) and metal ions (pink spheres). The binding positions and protein residues interacting with 6MI are labelled.

Interactions are shown as yellow dashed lines.

Due to licencing restrictions of Schrödinger Suite, the docking of these compounds within the tunnel was performed by Dr Wanting Jiao. The docking calculation predicted identical preferred positions for most of the compounds in the PRPP binding site with a span over to site 1 into the tunnel. Interestingly, three compounds could span over to the anthranilate binding tunnel and reach to PRPP binding site. Therefore, two compounds were purchased for further evaluation against *M. tuberculosis* AnPRT. A detailed evaluation of the selected compounds (Figure 3.5) is described below.

3.11—the presence of three rings made this compound long enough to span over into the PRPP and anthranilate binding sites. The furan ring with the carboxylate group was positioned in the buried pocket for the diphosphate moiety of PRPP while its carboxylate group interacts with both metal ions found in the active site. The phenyl and pyrazole rings are accommodated in the anthranilate binding sites 1 and 2. The amine group of the pyrazole ring interacts with the side chain of Asn138 while the carbamonyl group is predicted to form hydrogen bonds with the backbone amide of Asn138.

3.12—similar to **3.11**, **3.12** consists of three aromatic rings. However, all rings sit only within the tunnel and form π - π interactions with the phenyl and furyl moieties of **3.12** to the aromatic rings of His136 and Tyr186, respectively. The butanoic group of **3.12** could still reach

into the buried site of diphosphate and interact, via its carboxylate group, with the Mg^{2+} ion and the side chain of Lys135. Furthermore, the additional hydrogen bonds formation is predicted via its amide moiety to Gly107 and Asn138.

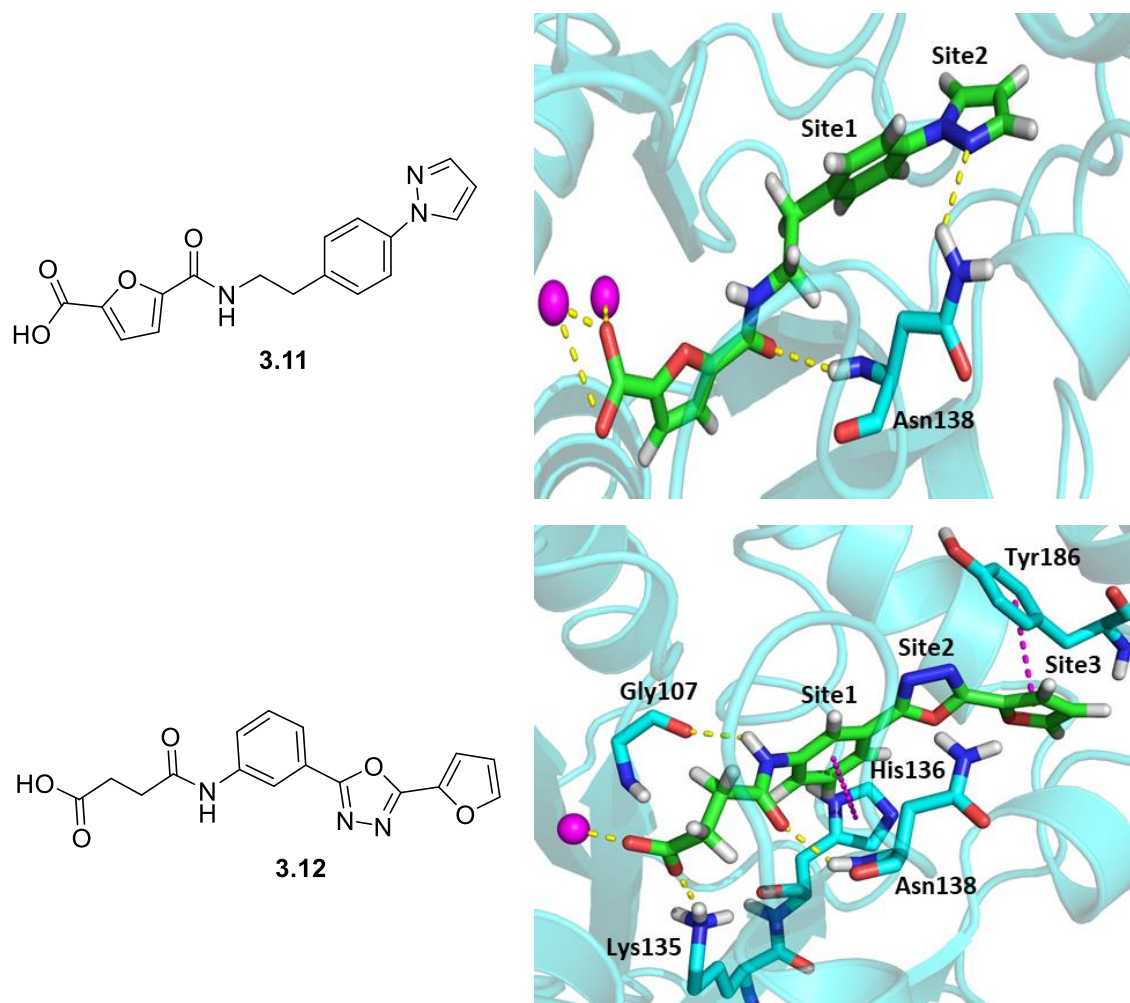


Figure 3.5 Structures and docking poses of the selected compounds from the virtual screen against *M. tuberculosis* AnPRT.

3.4 Hit validation

The chosen compounds from the virtual screening were purchased. The virtual screening hits were inspected via two approaches: kinetic assays and X-ray crystallography.

3.4.1 Kinetic assay

The inhibition of *M. tuberculosis* AnPRT activity with selected compounds (**3.1–3.12**) was determined using the standard enzyme coupled kinetic assay (detailed in Section 7.1.17).

Stock solutions of all compounds were prepared either in water or 2% DMSO. No change in the initial rates of enzyme reaction was observed for control reactions in the presence of up to 5% DMSO (v/v), which is higher than the amount of DMSO ($\leq 1\%$) used in inhibition studies. The selected compounds were predicted to bind both the PRPP and anthranilate sites. Therefore, these compounds were assayed with both substrates in order to assess whether these compounds could compete with both substrates of AnPRT simultaneously. Therefore, apparent K_i values were determined when one of the two substrates was varied while the other substrate was held at a constant concentration ($2 \times K_M$).

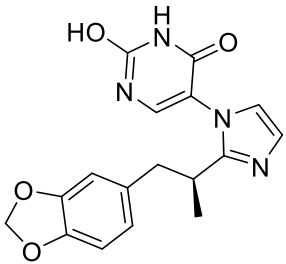
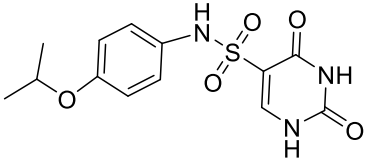
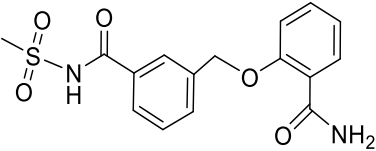
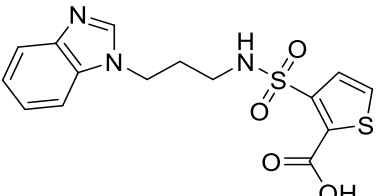
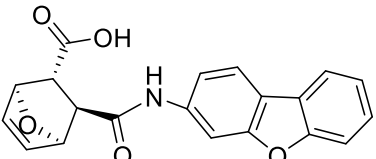
The kinetic results show that most of the compounds selected from the virtual screen could inhibit the activity of *M. tuberculosis* AnPRT (Table 3.1 and Figure 3.6). Interestingly, **3.9** shows the highest inhibitory activity against AnPRT with respect to both substrates, inhibiting in a competitive manner with a similar apparent K_i value of $7.0 \pm 0.4 \mu\text{M}$ with respect to both substrates. The second inhibitor is **3.5**, which shows moderate competitive inhibition only with respect to the anthranilate substrate (K_i value of $41 \pm 4 \mu\text{M}$) and weaker non-competitive inhibition with respect to PRPP (the K_i value of $350 \pm 28 \mu\text{M}$). The remaining selected compounds (**3.1–3.4**, **3.7**, **3.8** and **3.10–3.12**) are either moderate or weak inhibitors with apparent K_i values above $100 \mu\text{M}$. However, no enzymatic inhibition was observed (up to a concentration of $240 \mu\text{M}$) for compound **3.6**, which possesses an electronegative trifluoro group.

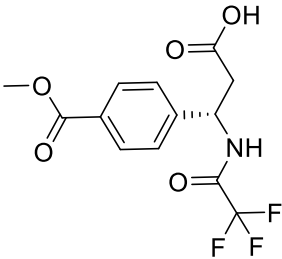
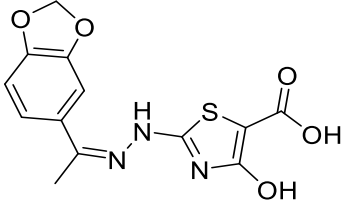
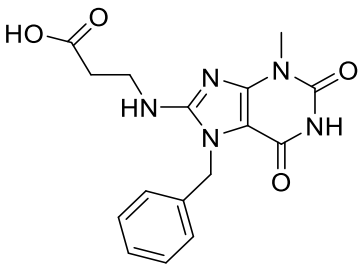
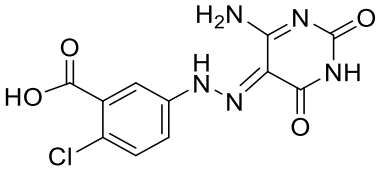
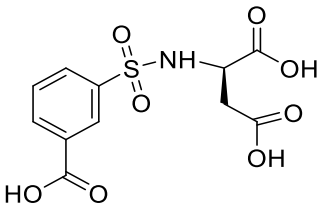
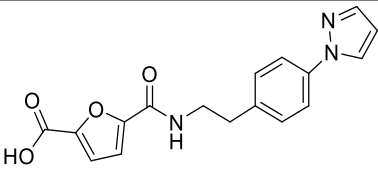
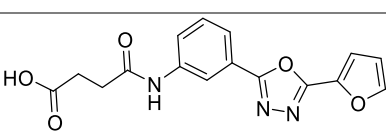
In addition, the predicted three-site binding compounds, **3.11** (K_i^{PRPP} value of $952 \pm 57 \mu\text{M}$ and K_i^{anth} value of $116 \pm 10 \mu\text{M}$) and **3.12** (K_i^{PRPP} value of $950 \pm 51 \mu\text{M}$ and K_i^{anth} value of $191 \pm 15 \mu\text{M}$) cause the enzymatic activity to decrease more effectively with respect to the anthranilate as compared to PRPP. These compounds cause an inhibitory effect with respect to the anthranilate substrate in a competitive manner and display a non-competitive effect with respect to PRPP. Similarly, **3.1** (K_i^{PRPP} no inhibition up to $240 \mu\text{M}$ and K_i^{anth} value of $104 \pm 13 \mu\text{M}$), **3.3** (K_i^{PRPP} value of $313 \pm 29 \mu\text{M}$ and K_i^{anth} value of $116 \pm 10 \mu\text{M}$) and **3.7** (K_i^{PRPP} value of $166 \pm 10 \mu\text{M}$ and K_i^{anth} value of $137 \pm 11 \mu\text{M}$) are stronger inhibitors with respect to anthranilate than PRPP. In contrast, the compounds **3.2** (K_i^{PRPP} value of $180 \pm 17 \mu\text{M}$ and K_i^{anth} value of $422 \pm 21 \mu\text{M}$) and **3.8** (K_i^{PRPP} value of $133 \pm 12 \mu\text{M}$ and K_i^{anth} value of $695 \pm 30 \mu\text{M}$),

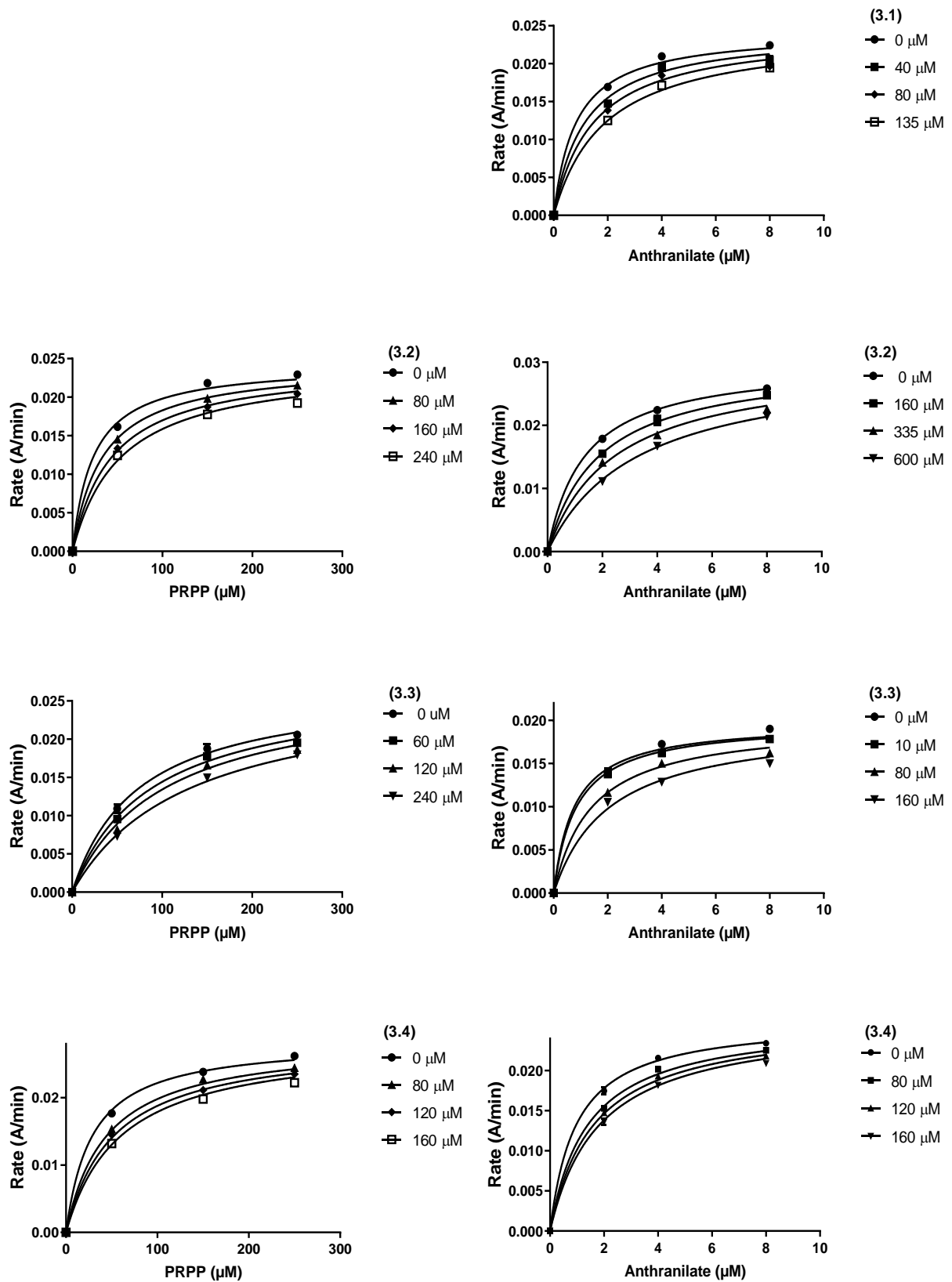
along with the sulphonyl compound **3.4** (K_i^{PRPP} value of $148 \pm 12 \mu\text{M}$ and K_i^{anth} value of $180 \pm 13 \mu\text{M}$) show higher AnPRT inhibition with respect to PRPP compared to anthranilate.

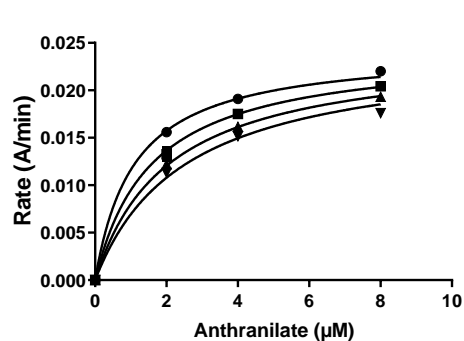
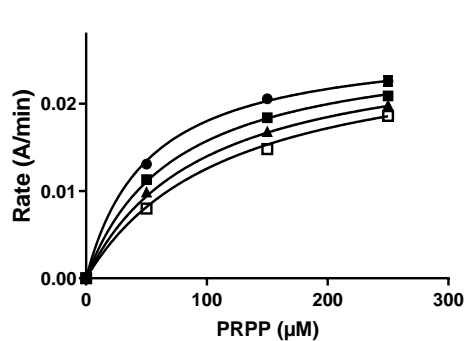
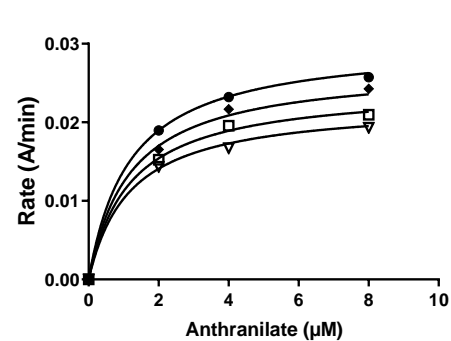
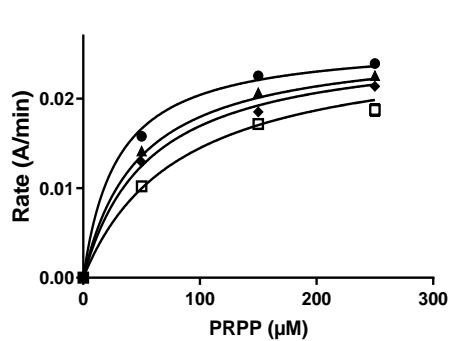
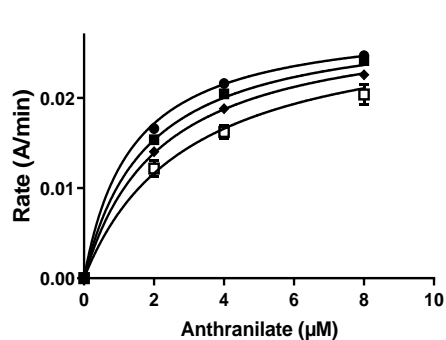
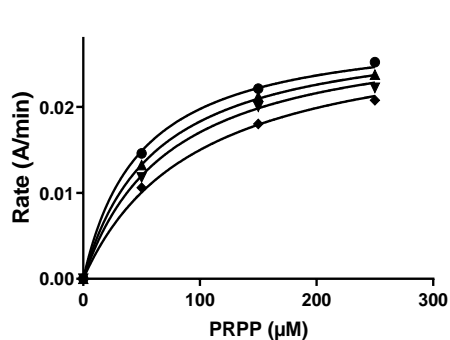
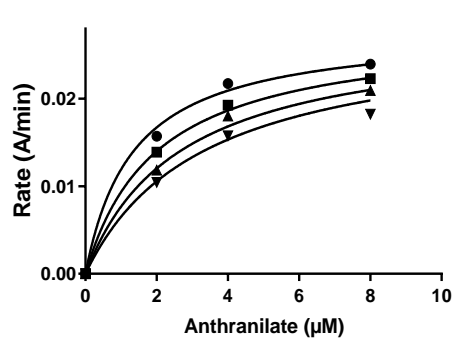
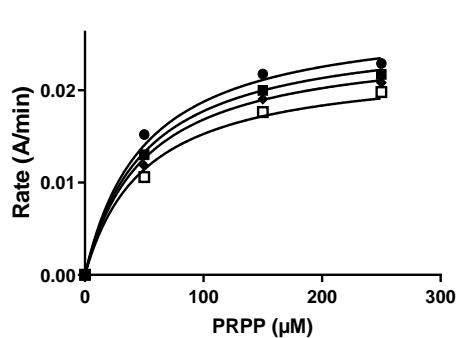
Furthermore, the pyrimidine ring containing compound **3.10** has predicted binding interactions with most of the residues that assist the binding of PRPP. It is the second inhibitor from the selected virtual screen compounds that competes to the same extent with respect to both substrates (the K_i value of $201 \pm 15 \mu\text{M}$); although it is not a potent inhibitor of AnPRT.

*Table 3.1 Compounds selected from the virtual screening with K_i values and their best-fitted inhibition model for both substrates against *M. tuberculosis* AnPRT.*

No.	Structure	Type of inhibition with respect to PRPP	App. K_i (μM) with PRPP	Type of inhibition with respect to anthranilate	App. K_i (μM) with anthranilate
3.1		No inhibition up to $240 \mu\text{M}$	No inhibition up to $240 \mu\text{M}$	competitive	104 ± 13
3.2		competitive	180 ± 17	competitive	422 ± 21
3.3		competitive	313 ± 29	competitive	92 ± 10
3.4		competitive	148 ± 12	competitive	180 ± 13
3.5		Non-competitive	350 ± 28	competitive	41 ± 4

3.6			No inhibition up to 240 μ M		No inhibition up to 240 μ M
3.7		competitive	166 \pm 10	competitive	137 \pm 11
3.8		competitive	133 \pm 12	Non-competitive	695 \pm 30
3.9		competitive	7.0 \pm 0.3	competitive	7.0 \pm 0.5
3.10		competitive	201 \pm 18	competitive	201 \pm 12
3.11		Non-competitive	952 \pm 57	competitive	116 \pm 10
3.12		Non-competitive	950 \pm 40	competitive	191 \pm 15





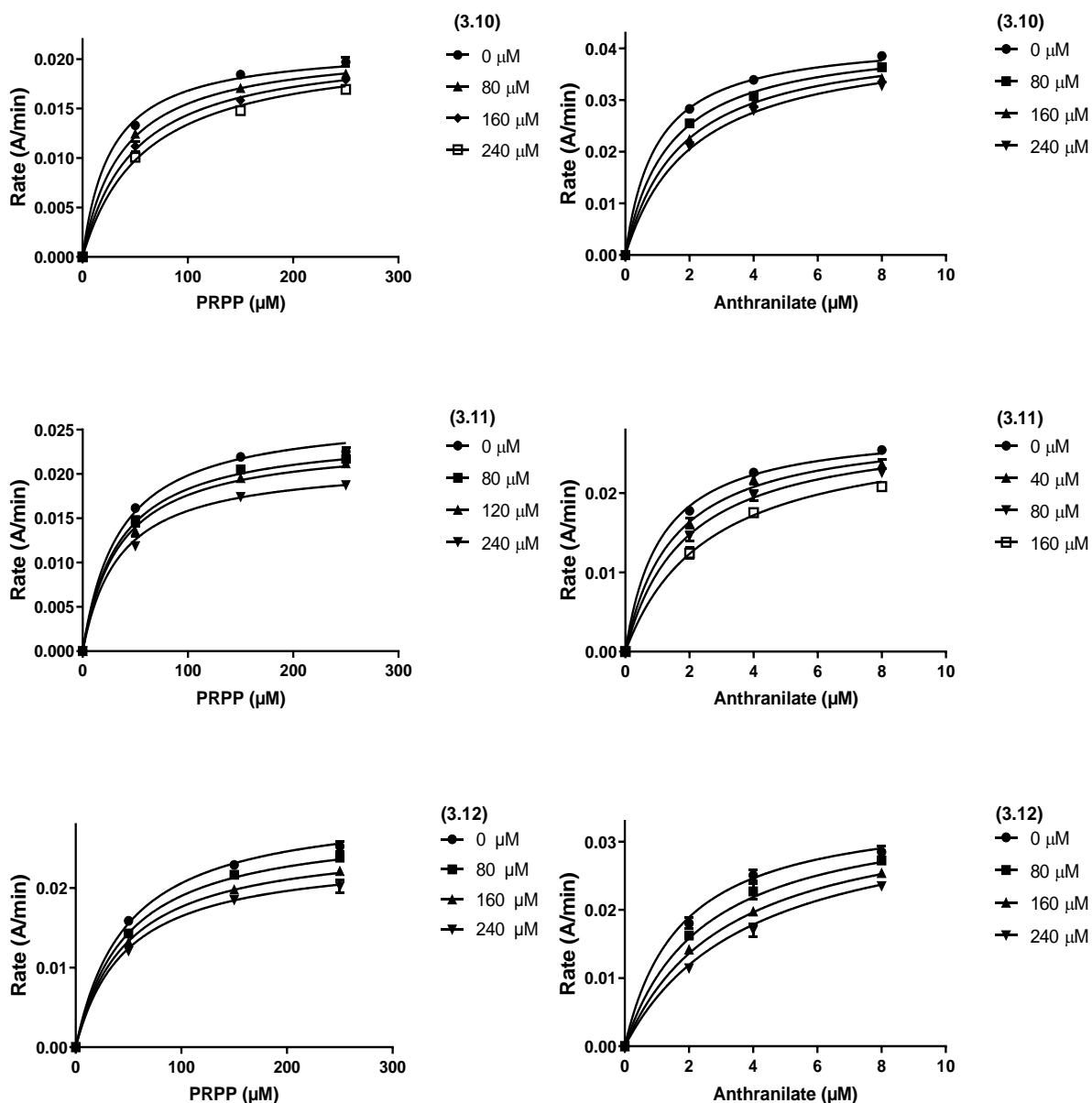


Figure 3.6 Kinetics assay graphs in the presence of both substrates for *M. tuberculosis* AnPRT at various concentrations of the chosen compounds from the docking study. For the determination of the K_i values, assays contained 50 mM Tris.HCl (pH 8.0), 150 mM NaCl, 1 mM $MgCl_2$, 0.04 μM AnPRT, 0.6 μM *E. coli* PRAI:InGPS, PRPP varied from 0 to 250 μM while anthranilate ($\approx 2 \times K_M$) was kept constant at 3.2 μM, anthranilate varied from 0 to 8 μM when PRPP ($\approx 2 \times K_M$) was kept constant 100 μM and inhibitors were used at various concentrations. The apparent K_i values were calculated by plotting a graph using competitive and non-competitive inhibition equations in GraphPad Prism 7.0.

3.4.2 X-ray crystallography

X-ray crystallography provides detailed information about the ligand-binding site along with binding conformation for the ligands. The analysis of protein crystals complexed with ligands can also be used to validate the binding poses from the docking. Therefore, the *M. tuberculosis* AnPRT enzyme complexes with selected compounds from the virtual screen were further inspected using X-ray crystallographic analysis.

AnPRT crystals were grown using established conditions (Section 7.1.20.1) and ligands were either co-crystallised or soaked into apo crystals at concentrations varying from 2 to 50 mM, depending on the solubility of the ligand. Then, crystals were looped and flash frozen directly or using 25% glycerol as a cryoprotectant. Numerous crystal diffraction datasets were obtained for *M. tuberculosis* AnPRT enzyme complexed with selected compounds (**3.2**, **3.3**, **3.4**, **3.5**, **3.8**, **3.9** and **3.11**) from the virtual screen. However, ligand density was observed only for compounds **3.5** and **3.9**. Data were solved using the standard protocol mentioned in Section 7.1.20.2. Data collection and refinement statistics for both solved AnPRT crystal structures are shown in Table 3.2.

Table 3.2 Data collection and refinement statistics for AnPRT crystals in complex with ligands 3.5 and 3.9.

AnPRT structures with ligands	3.5	3.9
Data Collection		
Space group	<i>P</i> 12 ₁ 1	<i>P</i> 12 ₁ 1
Cell dimensions		
a, b, c (Å)	78.7, 79.5, 117.9	77.4, 79.9, 116.6
α, β, γ (°)	90.0, 90.4, 90.0	90.0, 90.6, 90.0
No. of unique reflections	45,031 (4387)	25,811 (4559)
Resolution range (Å) ^a	47.3–2.6 (2.7–2.6)	46.8–3.1
R _{merge} ^a	0.105 (0.410)	0.110 (0.292)
R _{p.i.m.} ^a	0.046 (0.182)	0.046 (0.128)
CC _{1/2} ^a	0.991 (0.743)	0.994 (0.669)
I/σ(I) ^a	12.5 (2.61)	13.6 (3.10)
Completeness ^a (%)	99.9 (99.6)	99.1 (97.5)
Redundancy ^a	7.0 (6.9)	6.5 (5.7)
Wilson B-factor (Å ²)	37.6	50.9
Refinement		
No. of atoms, B factor ^b		
Protein	9507, 40.0	9226, 42.8
Ligands	26, 60.7	84, 59.6
water	32, 25.8	NA
R _{work} /R _{free} (%/%) ^{a,c}	0.204/0.254 (0.305/0.343)	0.209/0.256 (0.288/0.392)
Residues in most favored region of Ramachandran plot (%)	0.30	0.38
RMSD of		
Bond lengths (Å) ^d	0.012	0.010
Bond angles (°) ^d	1.5	1.47
PDB code	Not deposited	Not deposited

^a Outer resolution shell is shown in parentheses.

^b The average atomic temperature factor.

^c $R_{work} = (|F_{obs}| - |F_{calc}|) / |F_{obs}|$ and $R_{free} = \sum T (|F_{obs}| - |F_{calc}|) / \sum T |F_{obs}|$, where *T* is a test data set of 5% of the total reflections randomly chosen and set aside before refinement.

^d RMSD from ideal geometry values from Engh and Huber (1991).¹¹³

NA- Not available

3.4.2.1 AnPRT complexed with ligand 3.5

The crystal structure of *M. tuberculosis* AnPRT complexed with the virtual screen ligand **3.5** was solved at 2.6 Å resolution in the $P12_11$ space group and contained four monomeric chains in the asymmetric unit. Even though a high concentration of ligand **3.5** (8.75 mM) was used during crystallisation, the uptake of ligand by the enzyme is low as four monomeric units are present in the asymmetric unit and the binding of the ligand is observed only in one monomeric chain. This might be reason of poor enzyme inhibition observed by the ligand (K_i^{anth} value of $41 \pm 4 \mu\text{M}$ and K_i^{PRPP} value of $350 \pm 28 \mu\text{M}$). In addition, the monomeric fold of the protein in the structure was unaffected by the binding of ligand **3.5** as demonstrated by the low RMSD value of 0.48 Å obtained by superimposing chain A of the **3.5** ligand-bound AnPRT structure with chain A of the AnPRT structure bound with natural ligands (PDB: 4N93).

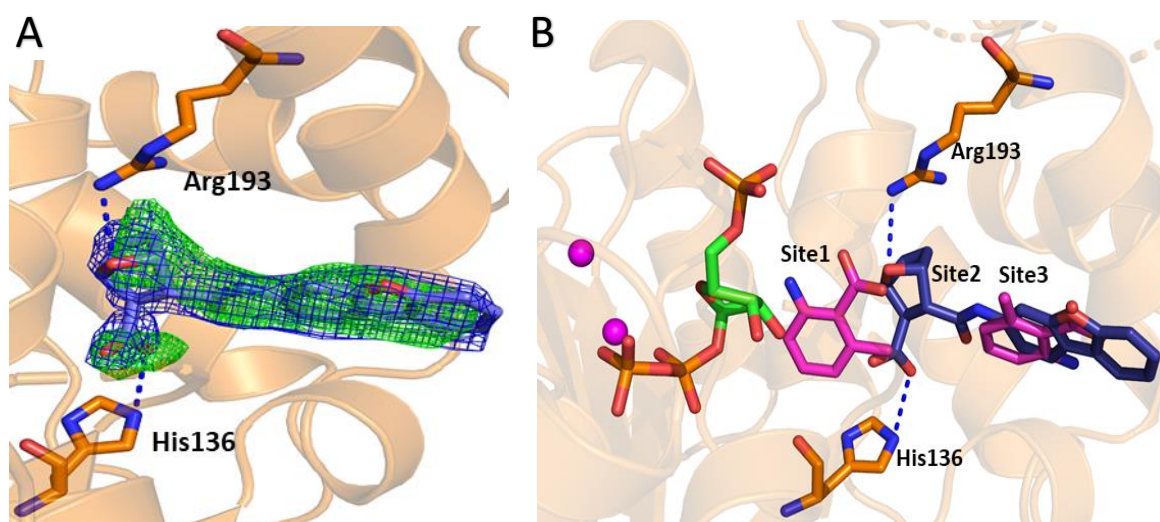


Figure 3.7 The binding position for ligand **3.5**.

(A) Omit map showing the density into which the **3.5** ligand was modelled. 2Fo-Fc omit map contoured at 1.0 σ (blue mesh) and Fo-Fc omit map contoured at 3.0 σ (green mesh). (B) Chain A (brown) bound with **3.5** (blue) is overlaid with PRPP (green), 6MA (pink) and Mg^{2+} (pink sphere) molecules from chain A of AnPRT (PDB: 4N93). The binding interactions of ligand **3.5** are shown in blue dashed line.

3.5 was selected based on the predicted docking poses within the PRPP site and anthranilate binding site 1. However, the AnPRT/**3.5** structure shows that the ligand **3.5** binds only within the anthranilate binding channel and does not reach to the PRPP binding site (Figure 3.7). The

binding of **3.5** was observed closer to site 1 compared to the entire substrate-binding tunnel. The observed binding in the crystal structure is consistent with the kinetic results as **3.5** is non-competitive with respect to PRPP and competitive with respect to anthranilate. The ligand **3.5** establishes direct contacts to the enzyme by interacting with His136 and Arg193. However, the conformations of the $\beta 1$ – $\alpha 5$ and $\beta 2$ – $\alpha 6$ loops are unclear due to missing charge density for a few residues on the $\beta 2$ – $\alpha 6$ loop.

3.4.2.2 AnPRT complexed with ligand 3.9

The crystal structure of *M. tuberculosis* AnPRT bound with ligand **3.9** was solved in the $P12_11$ space group at a resolution of 3.1 Å. The structure contained four separate monomers in the asymmetric unit and the two dimers could be generated via crystallographic symmetry. The ligand **3.9** was modelled with an occupancy of one in all chains. Monomeric units of ligand **3.9** bound AnPRT structures overlaid with chain A of the PRPP and 6MI AnPRT structure (PDB: 4N93) gave an RMSD value of between 0.50 and 0.67 Å.

The highest difference in the RMSD values (0.67 Å) is observed when chain C of AnPRT/**3.9** is overlaid with chain A of AnPRT/PRPP/6MI (PDB: 4N93 and Figure 3.8, **A**). Chain C of AnPRT/**3.9** has a distinct conformation of the *N*-terminal domain—particularly the $\alpha 1$, $\alpha 3$, $\alpha 8$ and $\alpha 8'$ helices compared to chain A of AnPRT/PRPP/6MI. It appears that the *N*-terminal domain is shifted towards the tunnel due to the binding of **3.9**. In addition, the position of helices $\alpha 6$, $\alpha 11$ and $\alpha 11'$ along with the $\alpha 11$ – $\alpha 11'$ loop have also been repositioned towards the active site due to the binding of **3.9**. However, the position of the $\beta 2$ – $\alpha 6$ loop is not clear due to the missing charge density of a few residues while the conformation of the $\beta 1$ – $\alpha 5$ loop is shifted towards the active site (Figure 3.8, **B**). In chain C, **3.9** forms contacts only via its carboxylate group to Arg194 (Figure 3.8, **C, D**). Virtual screening has assumed the preferred binding position for **3.9** at the PRPP site. However, the solved structure of AnPRT/**3.9** shows that the **3.9** molecule reaches into site 2 of the substrate-binding channel and is distant to the PRPP binding site in all monomeric chains.

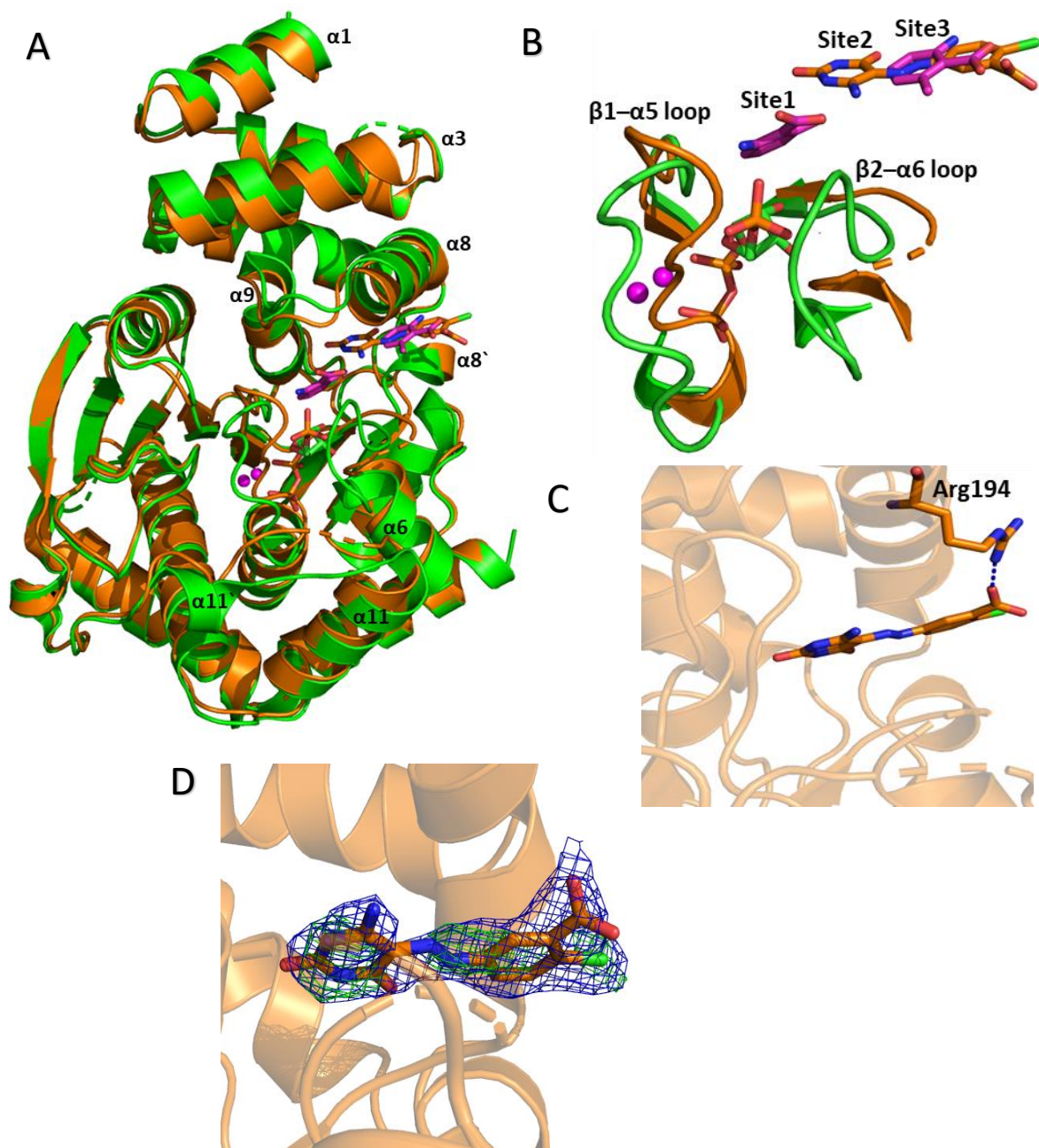


Figure 3.8 Chain C of the AnPRT/**3.9** bound structure overlaid with chain A of the AnPRT/PRPP/Mg²⁺ structure.

(A, B) Chain C of the AnPRT/**3.9** and chain A of AnPRT/PRPP/Mg²⁺ (PDB: 4N93) structures are shown in brown and green respectively. PRPP is shown as green, 6MI is shown as pink and **3.9** is shown as brown sticks respectively. Mg²⁺ ions are represented as pink spheres. (C) The binding interaction of **3.9** (brown) in chain C of AnPRT/**3.9** (brown) is represented as blue dashed lines. (D) the electron density map showing the 2Fo-Fc map contoured at 1 σ shown as blue mesh, the Fo-Fc map contoured at 3 σ shown as green mesh.

A similar binding position is observed for ligand **3.9** in chain B and chain D of the AnPRT/**3.9** structure and no notable hydrogen bonding interactions are observed for **3.9** both chains (Appendix 3). In addition, the conformation of the $\beta 1$ – $\alpha 5$ and $\beta 2$ – $\alpha 6$ loops is not clear due to missing charge density for few residues in chains B and D.

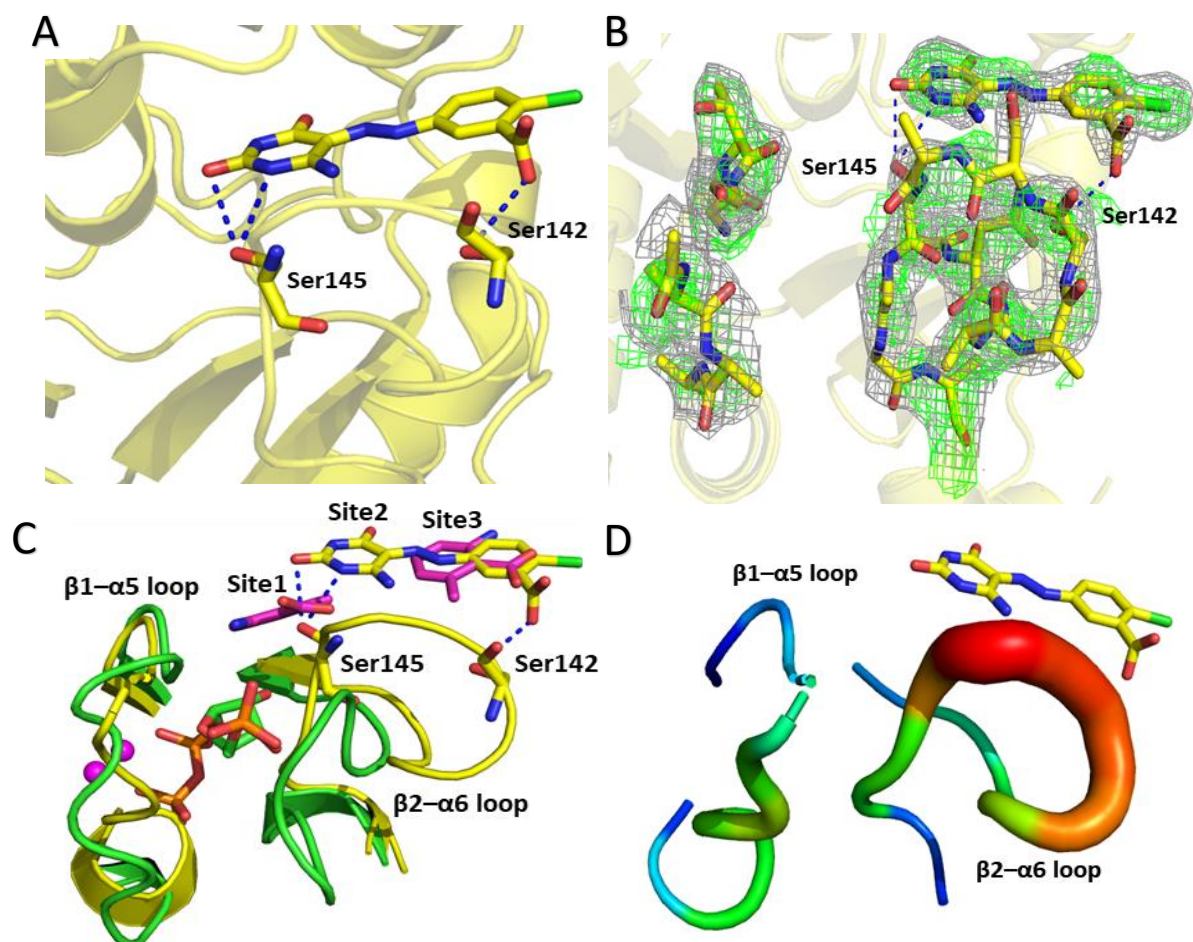


Figure 3.9 Chain A of the **3.9** bound AnPRT structure.

(A) The binding of inhibitor **3.9** in chain A (yellow) of the AnPRT/**3.9** structure. (B) Part of the electron density map showing the conformation of the $\beta 1$ – $\alpha 5$ and $\beta 2$ – $\alpha 6$ loops and difference electron density into which **3.9** ligand was modelled. 2Fo-Fc map contoured at 1 σ shown as grey mesh, Fo-Fc map contoured at 3 σ shown as green mesh (C) Chain A (yellow) of the AnPRT/**3.9** bound structure overlaid with chain A of the AnPRT/PRPP/Mg²⁺ structure (green, PDB: 4N93). (D) B-factor putty model showing for the $\beta 1$ – $\alpha 5$ (residues 106–119) and $\beta 2$ – $\alpha 6$ (residues 136–149) loops of chain A of AnPRT/**3.9** structure. The ligand **3.9** (yellow) exhibited 60.2 average B-factors and the residues present on $\beta 1$ – $\alpha 5$ and $\beta 2$ – $\alpha 6$ loops displayed average B-factors 46.6 and 54.5 respectively. Larger red regions show high B-factor residues and lighter blue regions show low B-factor residues.

Interestingly, in chain A, **3.9** forms contacts with the residues present in the $\beta 2$ – $\alpha 6$ loop via the amine functionality while the carbonyl group and the carboxylate moiety interact with Ser145 and Ser142, respectively (Figure 3.9, **A**, **B**). Structural superposition of chain A bound with ligand **3.9** and chain A of ligands bound AnPRT structure (PDB: 4N93) shows that **3.9** binds to sites 2 and 3 within the anthranilate binding tunnel and the position of the ligand appears to affect the PRPP binding site by a dramatic movement in the position of $\beta 2$ – $\alpha 6$ loop (Figure 3.9, **C**, **D**). Loops $\beta 1$ – $\alpha 5$ and $\beta 2$ – $\alpha 6$ appear to be in the closed conformation in the AnPRT/PRPP/Mg²⁺ structure and this conformation has a key role in allowing PRPP binding to the active site.⁵⁷ However, in the AnPRT/**3.9** structure, it seems that the binding of the inhibitor **3.9** causes significant displacement and destabilisation of the $\beta 1$ – $\alpha 5$ and $\beta 2$ – $\alpha 6$ loops which can interfere with the binding of PRPP to the active site of the enzyme. This also accounts for the results of the kinetic assays, as inhibitor **3.9** is competitive with respect to PRPP and anthranilate and gave a similar K_i value of $7.0 \pm 0.4 \mu\text{M}$ with respect to both substrates.

The rearrangement of the $\beta 2$ – $\alpha 6$ loop caused by the binding of **3.9** in chain A has not been previously reported in any other *M. tuberculosis* AnPRT structures (Figure 3.10, **A–D**). The different conformations of the $\beta 2$ – $\alpha 6$ loops are detailed in Section 1.8.4.

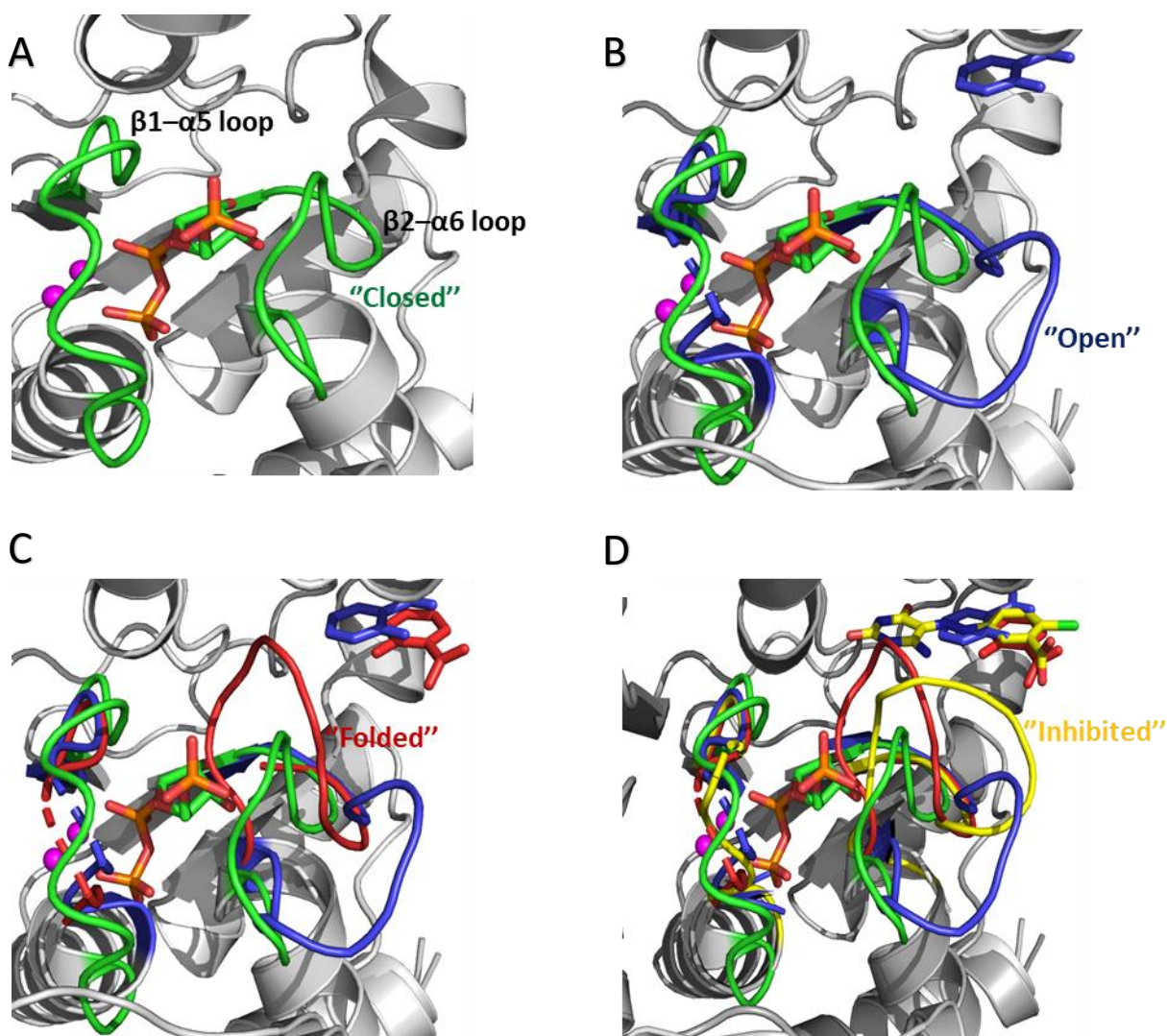


Figure 3.10 The different conformation of the $\beta 2$ - $\alpha 6$ loop in various *M. tuberculosis* AnPRT structures.

The $\beta 1$ - $\alpha 5$ and $\beta 2$ - $\alpha 6$ loops are coloured to highlight its position and similar colours to the loop are used to emphasize the loop conformation. **(A)** The $\beta 2$ - $\alpha 6$ loop in the "closed" conformation with the binding of PRPP and Mg^{2+} ions (PDB: 1ZVW, green). **(B)** The movement of the $\beta 2$ - $\alpha 6$ loop to the "open" position (PDB: 4OWV, blue). **(C)** In the anthranilate (red) bound AnPRT structure, the $\beta 2$ - $\alpha 6$ loop is in the "folded" conformation (PDB: 4X5D, Red). **(D)** The $\beta 2$ - $\alpha 6$ loop in the "inhibited" conformation with the binding of inhibitor **3.9** (yellow) in the AnPRT/**3.9** structure (yellow).

3.5 Differential scanning fluorimetry

Differential scanning fluorimetry (DSF) is a rapid and low-cost screening assay to identify ligands that bind and stabilize (or otherwise) a protein. Interactions between a ligand and a protein change the protein thermal stability and alter the melting temperature (T_m) of the protein. DSF experiments probe the changes in melting temperature, which indicates the strength of ligand binding by stabilisation or destabilisation of the protein.¹¹⁴ Enthalpically-driven ligand binding processes lead to a more thermally stable protein in drug screening.¹¹⁵ When the enthalpy change is positive, binding is entropically driven and when the enthalpy of binding is negative, binding is enthalpically driven. Therefore, DSF was employed to determine whether the thermal stability of *M. tuberculosis* AnPRT was affected by varying concentrations of **3.9**.

DSF experiments were carried out as outlined in Section 7.1.18 and the raw data from the DSF scans can be viewed in the Appendix 4. The stability of *M. tuberculosis* AnPRT was also determined in the presence of its natural ligands in order to compare the binding effect of inhibitor **3.9** (Figure 3.11 and Table 3.3). The melting temperature (T_m) for apo AnPRT was observed to be 67.9 ± 0.3 °C, which is higher than the reported value of 54.1 ± 0.3 °C.⁵⁷ The melting point of a protein can be influenced by various factors such as buffers, salts etc., whose interactions with the protein are nonspecific and may change protein stability. Therefore, the melting temperature of the same protein possesses a degree of heterogeneity in varying assay conditions that can cause distinct Boltzmann sigmoidal fitting.¹¹⁶

Table 3.3 *M. tuberculosis* AnPRT melting temperatures in the presence of various ligands.

Ligand	T_m B (°C)
AnPRT	67.9 ± 0.2
AnPRT/PRPP	67.6 ± 0.2
AnPRT/Mg ²⁺	70.1 ± 0.1
AnPRT/Mg ²⁺ /50 μ M 3.9	72.7 ± 0.1
AnPRT/Mg ²⁺ /350 μ M 3.9	75.2 ± 0.1
AnPRT/Mg ²⁺ /PRPP	77.6 ± 0.1
AnPRT/Mg ²⁺ /PRPP/50 μ M 3.9	78.4 ± 0.1
AnPRT/Mg ²⁺ /PRPP/350 μ M 3.9	77.1 ± 0.1

The presence of metal ions with AnPRT had a notable effect on the melting temperature, elevating it from 67.9 ± 0.3 °C to 70.1 ± 0.1 °C. However, no changes were observed in the stability of AnPRT ($T_m = 67.6 \pm 0.2$ °C) in the presence of PRPP.⁵⁴ Interestingly, the binding of ligand **3.9** had a stabilising effect on the protein and changed the melting temperature by up to 5 °C. A protein solution containing 1 mM metal ions in the presence of 50 µM or 350 µM **3.9** gave a melting temperature of 72.7 ± 0.1 °C and 75.2 ± 0.1 °C, respectively.

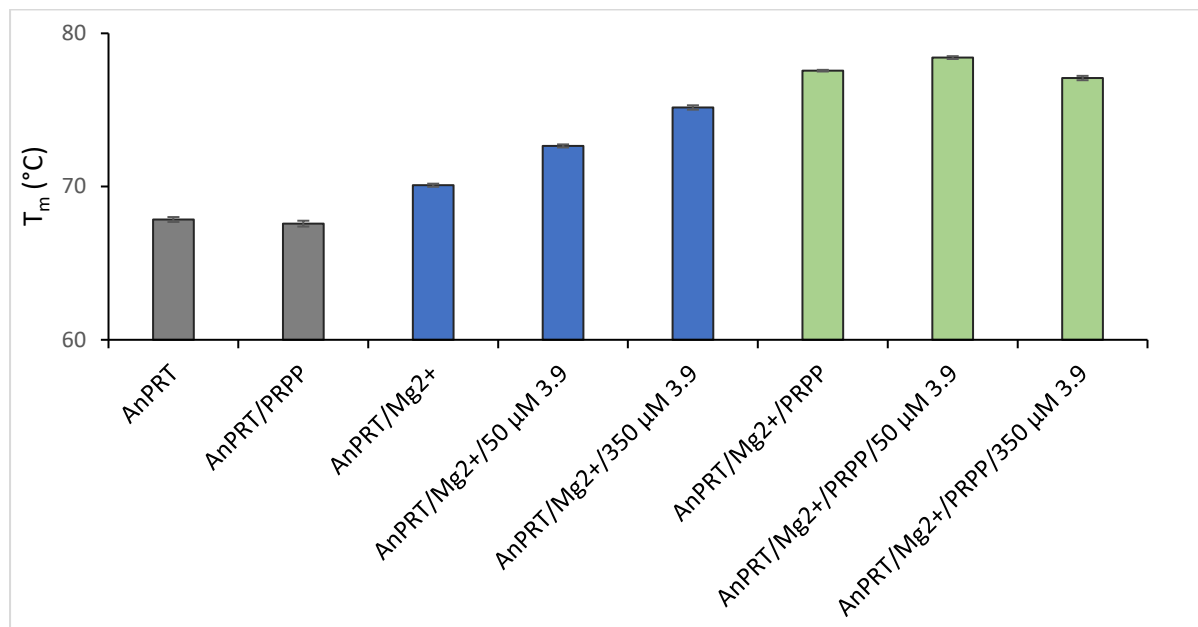


*Figure 3.11 Melting temperatures for AnPRT in the presence of various ligands by DSF. The final concentration of the ligands was 1 mM Mg²⁺, 0.5 mM PRPP, 50 µM or 350 µM **3.9**. AnPRT was present at a concentration of 1 mg/mL in 50 mM Tris-HCl and 150 mM NaCl buffer (pH 8.0). The distinct colour is used to see the change in temperature clearly for the different groups of the ligands. All data are collected in triplicate, and error bars correspond to the standard error of the mean.*

The combination of PRPP and metal ions had a significant effect on protein stability as the melting temperature increased by approximately 10 °C. The change in the conformation of the $\beta 1$ – $\alpha 5$ and $\beta 2$ – $\alpha 6$ loops occurred upon the binding of ligands at the enzyme active site might be the reason for this global change in protein stability. A small change of less than 1 °C in melting temperature was observed by the addition of **3.9** in the presence of PRPP and Mg²⁺ ions. The melting temperature of the protein with PRPP increased by 0.8 °C with the addition of **3.9** at a low concentration (50 µM). However, an increase in the concentration of

3.9 (350 μ M) in the presence of PRPP decreased the melting temperature of the protein by 0.5 °C. The binding of **3.9** together with PRPP may affect protein stability as ligand **3.9** competes with PRPP for binding at the PRPP site in a competitive manner as observed in the kinetic studies (Section 3.4.1). DSF is only a crude indicator for binding and one of the challenges associated with DSF is that small changes in T_m (0.5 to 2 °C) may not be noticeable from the melting profile of a protein if the protein progresses through a slow transition or multiple small denaturing events.¹¹⁷ Instead, the thermodynamic event associated with ligand binding is better investigated by ITC.

3.6 Investigating the effect of **3.9** on PRPP binding using ITC

ITC allows for the determination of protein–ligand interactions by measuring heat changes related to ligand binding that allow for the calculation of the dissociation constant (K_d) or binding affinity (K_a), binding stoichiometry (n) and enthalpy changes (ΔH). From the enthalpy changes, the other thermodynamic parameters (the Gibbs free energy (ΔG) and entropy (ΔS)) can be calculated using the equations $\Delta G = \Delta H - T\Delta S = -RT\ln K_d$ (where R is the gas constant and T is the absolute temperature). These thermodynamic quantities also provide insight into the type of noncovalent forces responsible for binding; polar interactions tend to contribute favourably to the enthalpic component, whereas hydrophobic interactions tend to be more entropically driven.¹¹⁸ However, the binding stoichiometry (n) can be easily erroneous, since the concentration of active macromolecules and ligands is harder to know precisely.

The kinetic study revealed that **3.9** is competitive with respect to both substrates of AnPRT. In addition, the structural investigation of AnPRT/**3.9** revealed that the binding of **3.9** likely interferes with the binding of PRPP by the dramatic change in the conformation of the $\beta 1$ – $\alpha 5$ and $\beta 2$ – $\alpha 6$ loops even though **3.9** was bound in substrate binding tunnel. In addition, it can be observed by DSF that the thermal stability of *M. tuberculosis* AnPRT changes due to the binding of **3.9**. To understand whether the binding of **3.9** influences the binding of PRPP directly, ITC experiments were carried out to gain an understanding of the binding of **3.9** to AnPRT (Figure 3.12, **A–E**).

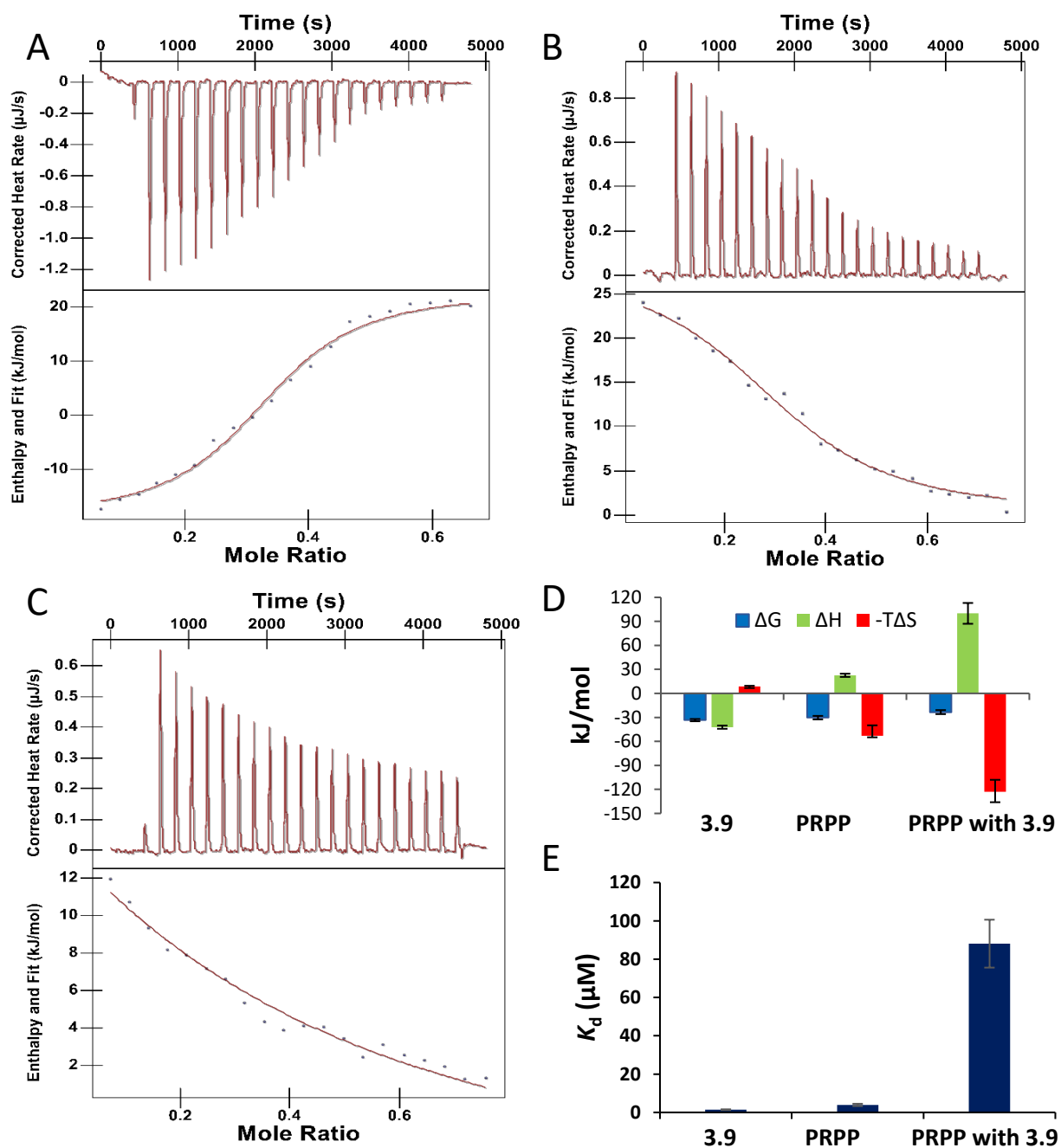


Figure 3.12 ITC isotherms displaying the thermodynamics for the binding of **3.9** and PRPP to *M. tuberculosis* AnPRT.

(A) ITC isotherm obtained from the titration of 350 μM **3.9** into a cell containing 60 μM AnPRT. (B, C) Comparison of ITC experiments involving the titration of 500 μM PRPP into 60 μM AnPRT in the absence or presence of 350 μM **3.9** respectively. Mg^{2+} ions (1 mM) were present in all ITC runs and raw data from the ITC experiments fit an independent model. (D, E) comparison between K_d and the thermodynamic parameters obtained for the binding of 350 μM **3.9**, 500 μM PRPP and 500 μM PRPP in the presence of 350 μM **3.9**.

Only the binding of ligand **3.9** stabilises the AnPRT enzyme as evidenced by the higher melting temperature of the enzyme recorded by DSF. Therefore, titration was performed by titrating 350 μM **3.9** into 60 μM *M. tuberculosis* AnPRT in the presence of 1 mM Mg^{2+} (Figure 3.12, **A**). The obtained data were fitted to an independent model and a K_d value of 1.4 ± 0.2 μM was obtained (Figure 3.12, **D**). The ITC binding isotherms signify that the binding events of **3.9** form a 1:2 ligand/AnPRT complex with the number of binding sites being 0.380 ± 0.007 . The process of ligand binding to AnPRT is exothermic as the heat change is negative. The inspection of the thermodynamic parameters for **3.9** indicates that binding of this ligand may involve dynamic changes as indicated by the unfavourable entropy in addition to hydrogen bonding (ΔH). The favourable hydrogen bonds may contribute to the greater K_d value by binding inhibitor **3.9** to the enzyme. Therefore, **3.9** may be taken as an indicator for hit selection and further modifications.

Although, it is ideal to improve the enthalpy and the entropy contribution to binding simultaneously for binding a drug candidate. Enthalpically favourable hit binding is important in the initial stage of drug discovery as the entropic contribution can be enhanced more easily than the enthalpic contribution in the later stage of lead discovery.¹¹⁹ The entropic contribution of the hit could be increased by rigidifying the conformation of the ligand with the addition of lipophilic groups. Additionally, the enthalpically favourable interactions are important for the selective enhancement of a hit and the best-in-class drugs are generally more enthalpically favourable such as HIV protease and the hydroxymethylglutaryl coenzyme A reductase.¹²⁰ Hence, the enthalpic contribution is a key factor during hit-to-lead optimisation, which also indicates that ligand **3.9** is a hit candidate for further optimisation.

Two other sets of ITC experiments were carried out by titrating 500 μM PRPP into 60 μM *M. tuberculosis* AnPRT either in the presence or absence of 350 μM **3.9** (Figure 3.12, **B, C**). Both data sets were fitted to an independent model. Mg^{2+} ions (1 mM) were present in both titrations as metal ions play a key role in allowing the binding of PRPP to the active site of the enzyme. PRPP binds to the enzyme with a high affinity and gave a K_d value of 3.9 ± 0.6 μM . The ITC binding isotherms signify that the binding events of PRPP form a 1:2 ligand/AnPRT complex with the number of binding sites being 0.4 ± 0.008 . The ITC experiments indicate that the affinity of the enzyme for PRPP is greatly affected when **3.9** was present. The addition of

350 μM **3.9** reduced the binding affinity for PRPP by multiple times and gave a K_d value of $88.1 \pm 12.5 \mu\text{M}$ for PRPP.

The thermodynamic parameters obtained for the binding of PRPP alone were very different compared to the binding of only **3.9** to AnPRT (Figure 3.12, E). Intriguingly, the inspection of the thermodynamic parameters indicates that the binding of PRPP is dominated by hydrophobic interactions and driven by entropy; this process is endothermic as the heat change is negative. The binding of PRPP to the enzyme in the presence of **3.9** was even more entropically driven. Therefore, the ITC results suggest that the binding affinity of AnPRT for PRPP is significantly reduced in the presence of **3.9**. These results are consistent with the information obtained from the kinetic study, crystallography and DSF (Sections 3.4, and 3.5). Hence, it can be concluded that the binding of **3.9** is competitive with respect to PRPP presumably through significant $\beta 1$ – $\alpha 5$ and $\beta 2$ – $\alpha 6$ loop displacement, which interferes with the binding of PRPP to the active site of the enzyme.

3.7 Summary

Several new ligands were discovered to target the *M. tuberculosis* AnPRT active site from virtual screening. A few selected compounds were tested against the enzyme using the enzyme-coupled assay and most of these compounds were found to be either moderate or poor inhibitors. Interestingly, the compound **3.9** was the strongest inhibitor. This inhibitor competes with PRPP and anthranilate substrates to the same extent and displays the lowest K_i value of $7.0 \pm 0.4 \mu\text{M}$. Another inhibitor, **3.5**, was competitive with respect to anthranilate (the K_i value of $41 \pm 4 \mu\text{M}$) and non-competitive with respect to PRPP (the K_i value of $350 \pm 28 \mu\text{M}$). The binding modes of both inhibitors were elucidated by X-ray crystallography. Structural insight into the binding modes of the ligands was correlated with their inhibitory activity. However, the binding sites of the ligands and their interactions with the protein were distinct from their positions predicted by modelling.

Interestingly, the AnPRT structure complexed with inhibitor **3.9** revealed a significant effect of the inhibitor on the conformation of loops that are important in the binding of PRPP. The recorded DSF and ITC data for **3.9** binding with AnPRT verify that the binding of ligand **3.9**

changes the binding affinity for PRPP at the active site. Together, these pieces of evidence can be useful to further explicate the inhibition and mechanism of *M. tuberculosis* AnPRT including knowledge for the development of future inhibition strategies aiming to disrupt the binding of PRPP at the active site of the enzyme.

Chapter 4 Probing the substrate binding sites

4.1 Introduction

Most of the enzyme-catalysed biological reactions are crucial for the physiological activity of an organism. An understanding of the transformations of these enzyme-catalysed reactions is significant since the insights gained from these strategies may facilitate the development of methods to mimic or control their action. The event to control enzymatic reaction in the biological system can be valuable. Over the last decade, the specific inactivation of some target enzymes has been noticed with a great variety of molecules.^{121,122} The molecular basis of the knowledge of these phenomena in chemical terms can aid in the rational design of drugs with maximal *in vivo* specificity. A common approach to study enzyme catalysis is to use naturally occurring and synthetic substrate analogues for mechanistic studies.^{123,124} The use of substrate analogues has enabled researchers to obtain important information regarding the catalytic mechanisms of enzymatic reactions. Many of these compounds are good enzyme inhibitors and have been developed into clinically useful chemotherapeutic agents. The main objective of this thesis is to explore the mechanism and inhibition of *M. tuberculosis* AnPRT in order to aid anti-TB drug design. This has been done by synthesising substrate analogues to investigate the features of both substrate binding sites to probe the reaction mechanism of *M. tuberculosis* AnPRT. The detailed study of both substrate binding sites was done to generate key information to design drug-like molecules to target TB.

4.2 Insight into the active site of *M. tuberculosis* AnPRT

4.2.1 PRPP binding site

The first crystal structure previously solved for *M. tuberculosis* AnPRT, which was complexed with PRPP and Mg^{2+} (PDB: 1ZVW), was crystallised under benzamidine conditions (detailed in Section 1.8.1). However, the presence of benzamidine leads to structural changes of AnPRT—as noticed by overlaying the apo structure obtained in the presence (PDB: 2BPQ) and absence of benzamidine (PDB: 3QR9). The presence of benzamidine also changes the physiological function of the enzyme—as the addition of benzamidine (100 mM) at the concentration used during crystallisation completely inhibits the AnPRT activity.⁸⁰ Recently, the structure of *M. tuberculosis* AnPRT (PDB: 5C7S) complexed with PRPP and Mn^{2+} was determined without

using benzamidine in the crystallisation conditions. No difference was observed in the binding of PRPP by superimposing the AnPRT/PRPP/Mn²⁺ structure with the AnPRT/PRPP/Mg²⁺/benzamidine structure (PDB: 1ZVW, Figure 4.1).

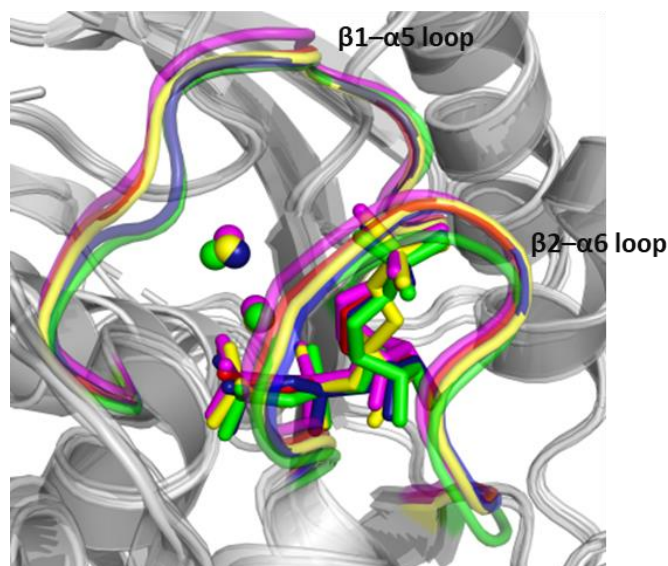


*Figure 4.1 The binding of ligands at the active site with similar conformation adopted by $\beta 1\text{--}\alpha 5$ and $\beta 2\text{--}\alpha 6$ loops in various *M. tuberculosis* AnPRTs.*

*Structural superposition of the *M. tuberculosis* AnPRT/PRPP/2 \times Mg²⁺ (yellow) onto various AnPRT structures; AnPRT/PRPP/2 \times Mg²⁺/benzamidine (PDB: 1ZVW, red), AnPRT/PRPP/2 \times Mn²⁺ (PDB: 5BYT, pink), AnPRT/PRPP/1 \times Mg²⁺ (PDB: 5C7S, blue) and AnPRT/PRPP/Mg²⁺/4FA (PDB: 4N5V, green).*

In this work, we have obtained another *M. tuberculosis* AnPRT structure bound with PRPP and two Mg²⁺ ions without any additives using the standard crystallisation conditions used for AnPRT crystallisation (Section 7.1.19). The structure was determined at 2.0 Å in a C121 space group (Appendix 2). There are no differences observed in the binding mode of PRPP and binding positions of both Mg²⁺ ions when this structure is superimposed onto various previously solved AnPRT structures; AnPRT/PRPP/2 \times Mg²⁺/benzamidine (PDB: 1ZVW), AnPRT/PRPP/2 \times Mn²⁺ (PDB: 5BYT), AnPRT/PRPP/1 \times Mg²⁺ (PDB: 5C7S) and AnPRT/PRPP/Mg²⁺/4FA (PDB: 4N5V). Similarly, the $\beta 1\text{--}\alpha 5$ and $\beta 2\text{--}\alpha 6$ loops are observed in the “closed” conformation due to the binding of PRPP at the active site of the enzyme. Thus, the observed binding of PRPP with either one or two metal ions and in the presence of an

anthranilate analogue, 4FA, within the tunnel does not introduce any notably conformational or positional changes in the catalytic site of the enzyme.

4.2.2 Binding of metal ions

The activity of the *M. tuberculosis* AnPRT enzyme depends on Mg^{2+} ions.⁸⁰ The AnPRT reaction does not proceed when Mg^{2+} ions are absent (see details in Section 1.8). The recorded *M. tuberculosis* AnPRT/PRPP/ $1 \times Mg^{2+}$ structure (PDB: 5BYT) that was crystallised in a 3:1 concentration ratio of PRPP and Mg^{2+} shows that the second Mg^{2+} ion is absent in the structure while the first Mg^{2+} ion is coordinated to the diphosphate moiety of PRPP. No changes were noticed in the AnPRT structure when the second metal ion was absent. A water molecule is observed to occupy that second metal ion position as seen in the AnPRT/PRPP/ $2 \times Mg^{2+}$ (PDB: undeposited) and AnPRT/PRPP/ $2 \times Mn^{2+}$ (PDB: 5BYT, blue) structures (Figure 4.2, **A**). Similarly, the $\beta 1-\alpha 5$ and $\beta 2-\alpha 6$ loops are observed in the “closed” conformation in both AnPRT structures.

Similarly, the binding of a single Mg^{2+} ion is also observed in AnPRT structures bound with PRPP and phosphonate inhibitors **2.10** or **2.11** (Section 2.7). The binding of one Mg^{2+} ion that is coordinated to the diphosphate moiety of PRPP has been examined by NMR in solution.¹²⁵ It has been observed that the enzyme activity depends on the PRPP- $1 \times Mg^{2+}$ ion complex since the activity of *M. tuberculosis* AnPRT decreases as the concentration of PRPP- $1 \times Mg^{2+}$ complex increases above 2 mM.⁵⁴ However, this observation is not consistent with the metal ion inhibition reported for *S. solfataricus* AnPRT.⁶⁴ Additionally, the *M. tuberculosis* AnPRT structure (PDB: 5C2L) bound solely with Mg^{2+} ions shows the binding of only one metal ion at the active site (Figure 4.2, **B**, cyan). However, the binding position for this Mg^{2+} ion is distinct from that observed in the other AnPRT structures bound with Mg^{2+} ions in the presence of PRPP. The binding position of Mg^{2+} in the AnPRT/ $1 \times Mg^{2+}$ structure (PDB: 5C2L) is 1.8 Å away from the binding site of the second metal ion present in the presence of PRPP (AnPRT/PRPP/ $2 \times Mg^{2+}$ (PDB: undeposited), presumably due to the altered position of the $\beta 1-\alpha 5$ loop when PRPP is absent. It has been hypothesised that *M. tuberculosis* AnPRT binds a single PRPP/ Mg^{2+} complex first, followed by the binding of the second Mg^{2+} ion.⁵⁴ Therefore,

binding of PRPP with both metal ions is observed at the active site of most *M. tuberculosis* AnPRT structures.

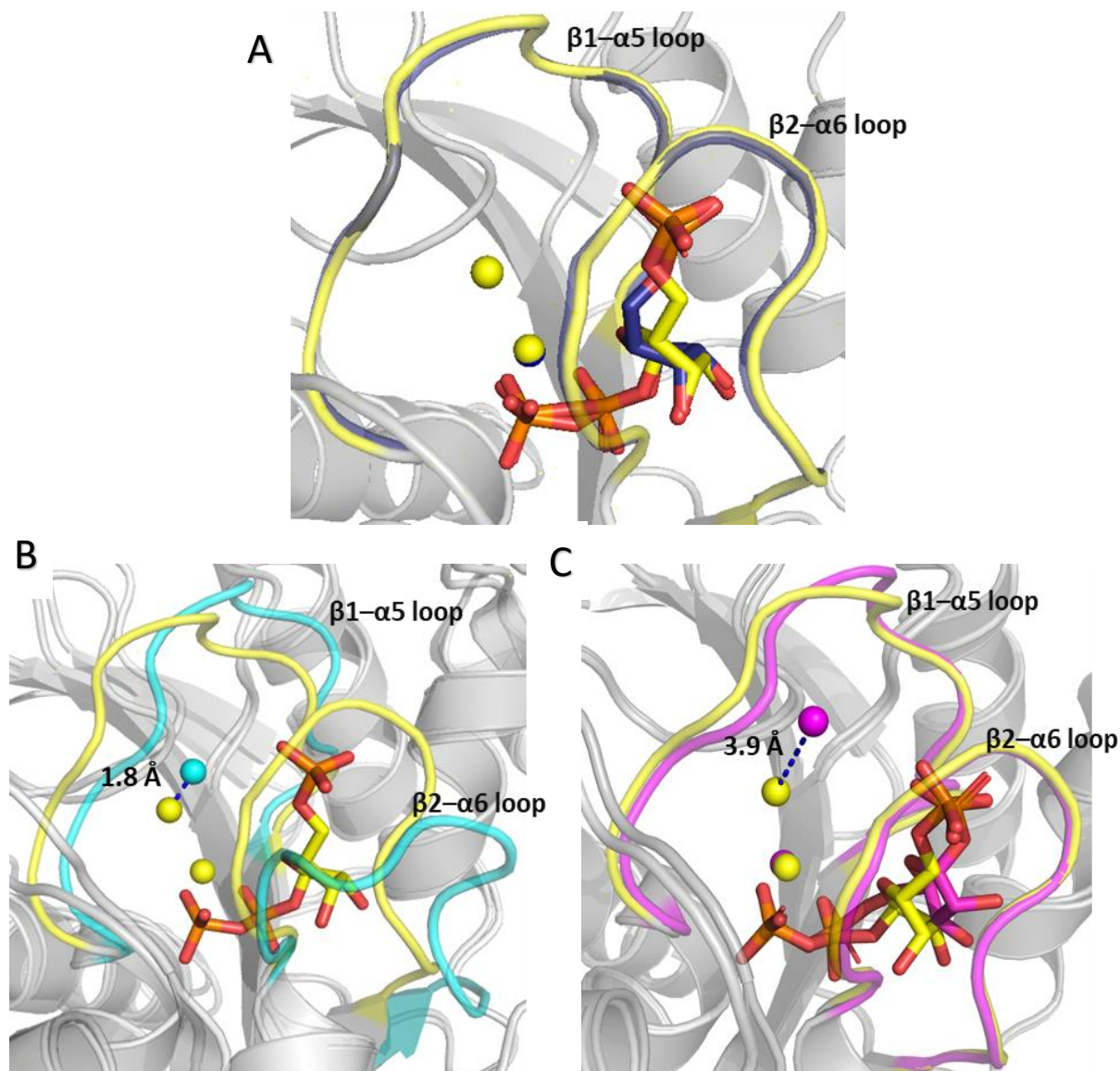


Figure 4.2 Metal binding features in various *M. tuberculosis* AnPRT structures.

(A) Structural superposition of a new AnPRT/PRPP/2xMg²⁺ structure (yellow) onto an AnPRT structure bound with a single Mg²⁺ ion ; AnPRT/PRPP/1xMg²⁺ (PDB: 5BYT, tint). (B) Structural superposition of a new AnPRT/PRPP/2xMg²⁺ structure (yellow) onto AnPRT/1xMg²⁺ (PDB: 5C2L, cyan). (C) The overlay involves a new AnPRT PRPP bound structure (yellow) with the 1PR5PP bound structure (PDB: 5C1R, pink). The distance between the metal ions is shown as blue dashes.

Another AnPRT structure (PDB: 5C1R) bound with a stereoisomer of PRPP, 1'-phospho- α -ribosyl-5'-pyrophosphate (1PR5PP), shows that the binding position of the second metal ion is shifted towards the β 1- α 5 loop due to the repositioning of the phosphoribosyl moiety (Figure 4.2, C).⁵⁴ The structural superposition of AnPRT/1PR5PP/2 \times Mg²⁺ (PDB: 5C1R) to AnPRT/PRPP/2 \times Mg²⁺ (PDB: undeposited) shows that the second metal has migrated 3.9 Å towards the β 1- α 5 loop. The metal ion migration is associated with the movement of the phosphoribosyl moiety, although the diphosphate molecule remains bound to a deeply buried pocket at the active site of the enzyme. The flexibility of the ribose ring has also been noticed previously and the conformation of the β 1- α 5 and β 2- α 6 loops is dependent upon the substrate binding to the active site, which supports the dissociative "S_N1-like" mechanism.

4.2.3 Investigating the binding of PRPP and Mg²⁺ ions at the active site

Metal ions play important roles in the biological function of *M. tuberculosis* AnPRT (Section 4.2.2). Therefore, ITC experiments were carried out to determine the binding affinity of AnPRT for these metal ions. To determine the effect of Mg²⁺ ions on PRPP binding, ITC titrations with PRPP were performed in the presence or absence of metal ions.

The standard ITC assay is described in detail in Section 7.1.17. Initially, ITC experiments were performed by titrating Mg²⁺ ions into 90 μ M AnPRT (Figure 4.3, A). However, no detectable binding was observed for Mg²⁺ ions up to a concentration of 5 mM in the absence of PRPP. There is not an enthalpy change associated with the binding of Mg²⁺ ions with the enzyme. The collected data clearly indicate that the affinity of AnPRT for Mg²⁺ ions is either too weak or the heat changes that occur during the binding of Mg²⁺ ions cannot be detected by ITC. It is highly possible that the binding for the Mg²⁺ ion seen in the AnPRT structure (PDB: 5C2L) is due to the higher, non-physiological concentration of Mg²⁺ ions (10 mM) in the crystallisation condition.

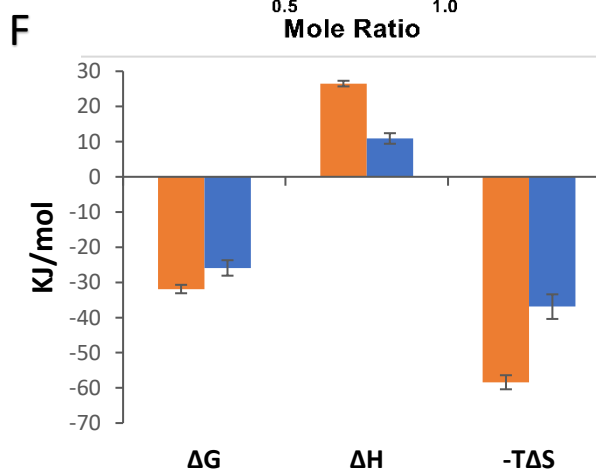
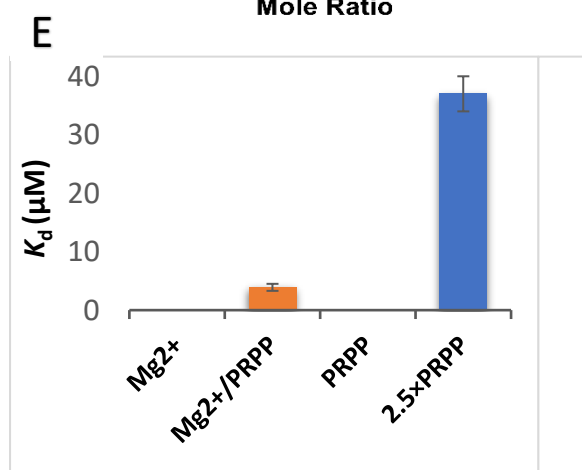
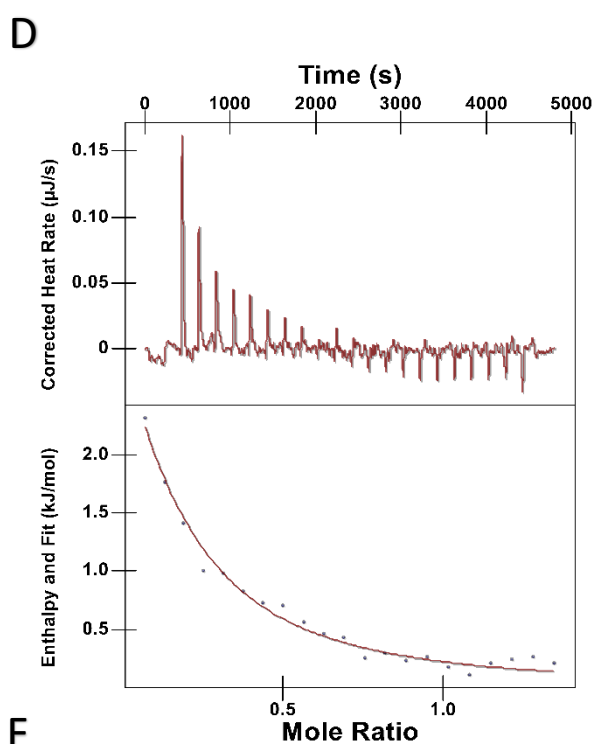
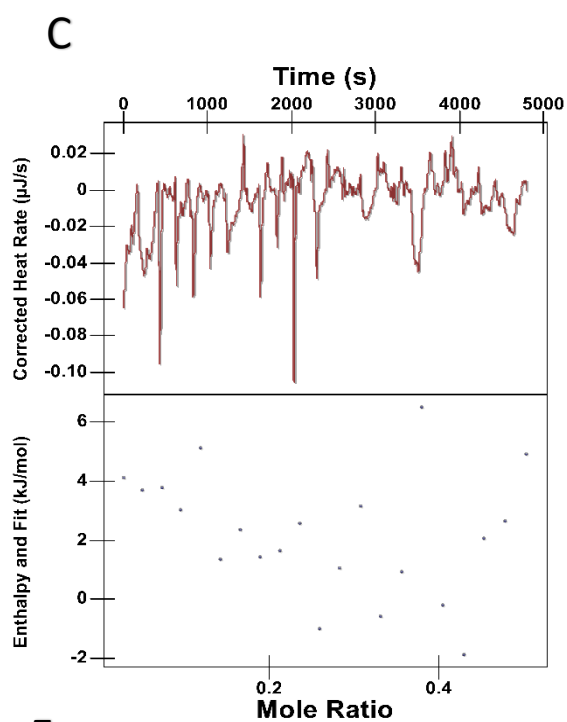
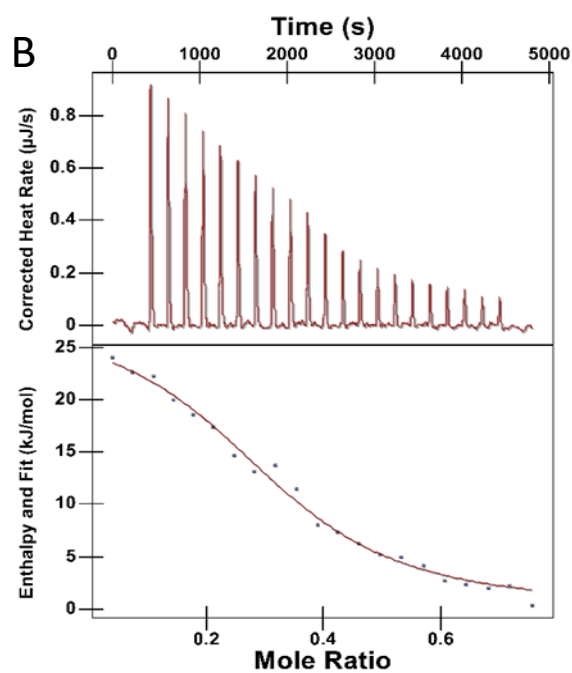
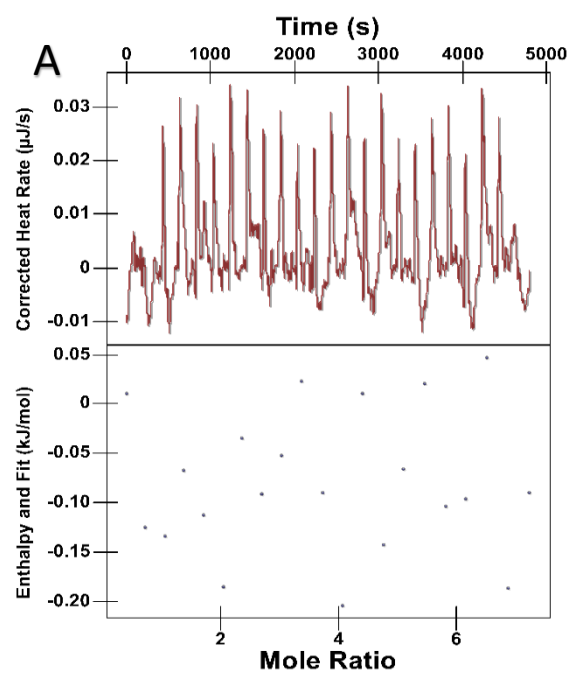


Figure 4.3 ITC experiments display the thermodynamic parameters for the binding of PRPP and Mg²⁺ ions to M. tuberculosis AnPRT.

(A) Raw data from ITC experiments involving the titration of 5 mM Mg²⁺ into a cell containing 60 μM AnPRT. (B, C) ITC isotherm from the titration of 500 μM PRPP into 60 μM AnPRT in the presence and absence of 1 mM Mg²⁺ ions. (D) Raw data from titrating 1mM PRPP into 60 μM AnPRT in the absence of Mg²⁺ ions. (E, F) Comparison between K_d values and thermodynamic parameters for binding 500 μM PRPP with 1 mM Mg²⁺ ion (orange) and 2.5-fold PRPP (1.25 mM) in the absence of metal ions (blue) to AnPRT.

Next, two sets of ITC experiments were carried out by titrating 500 μM PRPP into a 60 μM solution of AnPRT either in the presence or absence of Mg²⁺ ions to investigate the effect of the ions on PRPP binding. The ITC isotherms for titrating 500 μM PRPP in the presence of 1 mM Mg²⁺ fitted excellently to an independent binding model (Figure 4.3, B) and gave a K_d value of 3.9 ± 0.6 μM (Figure 4.3, E). The thermodynamic parameters obtained from the binding isotherms indicate that the binding of PRPP in the presence of Mg²⁺ is an endothermic process and thus binding is being driven entropically (Figure 4.3, F).

M. tuberculosis AnPRT did not undergo any heat change during the titration of 500 μM PRPP in the absence of Mg²⁺ ions (Figure 4.3, C). However, a 2.5-fold increase in the concentration of PRPP (1.25 mM) shows very weak PRPP binding with an almost 10-fold increment in the K_d value (37 ± 3.0 μM) (Figure 4.3, D–F). The obtained ITC data clearly indicate that the binding of PRPP was strengthened enormously by the presence of Mg²⁺. A higher concentration of PRPP can still lead to PRPP binding at the active site of the enzyme but the affinity of AnPRT for PRPP is very weak when Mg²⁺ is absent. The obtained ITC data also indicate that the binding of PRPP and Mg²⁺ complex is likely to occur during enzyme catalysis at their physiological concentrations.

4.2.4 Diphosphate binding to the active site

In most *M. tuberculosis* AnPRT structures complexed with PRPP, the diphosphate moiety of PRPP is found buried deep into the active site of the enzyme. The binding of the diphosphate–Mg²⁺ complex independently into the active site observed in the *M. tuberculosis* AnPRT structure (PDB: 4X5C) shows similar binding of the diphosphate molecule compared to the

diphosphate moiety of PRPP in the PRPP-bound AnPRT structures.⁵⁷ Thus, it is hypothesised that the binding of the diphosphate–Mg²⁺ complex is a post catalytic event where the diphosphate–Mg²⁺ complex remains in the active site (Section 1.8.4).⁶⁶ It is also postulated that either the diphosphate–Mg²⁺ complex or the charge in the ribosyl ring of PRPP makes diphosphate a better leaving group, which could have potential implications for the design of novel anti-TB drug candidates. Therefore, to check the binding of the diphosphate molecule and whether the diphosphate molecule can inhibit enzyme activity even though PRPP is present, a kinetic assay was performed.

The standard enzyme-coupled inhibition assay for *M. tuberculosis* AnPRT was performed to determine the effect of several constant concentrations of diphosphate on the rate of the reaction in the presence of varying concentrations of PRPP. Interestingly, diphosphate was found to be a strong competitive inhibitor with respect to PRPP for AnPRT and gave an apparent K_i value of $46 \pm 4.0 \mu\text{M}$ (Figure 4.4).

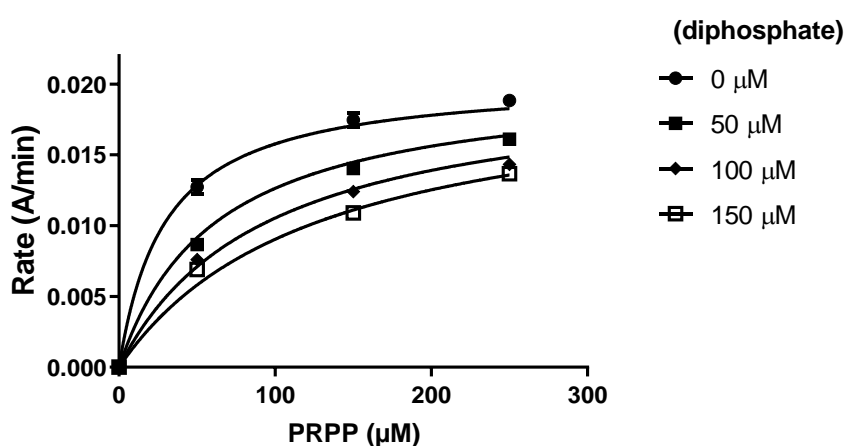


Figure 4.4 *M. tuberculosis* AnPRT inhibition graphs in the presence of various concentrations of diphosphate against PRPP.

The kinetic assay was performed in buffer containing 50 mM Tris.HCl (pH 8.0), 150 mM NaCl, 1 mM MgCl₂, 0.04 μM AnPRT, 0.6 μM *E. coli* PRAI:InGPS, 10 μM anthranilate; PRPP was varied from 0 to 250 μM. The sodium diphosphate dibasic was used at various concentrations.

In contrast, no enzyme inhibition was exhibited up to a concentration of 1 mM of monophosphate in the presence of PRPP. Hence, the results of the kinetic assay suggest that the diphosphate molecule can compete with PRPP to bind at the active site of the enzyme.

The binding of diphosphate or diphosphate–Mg²⁺ at a deeply buried position of the active site can also be seen through X-ray crystallography.⁷¹ Thus, with a view of designing novel drug candidates, the introduction of a diphosphate group or a bioisostere of the diphosphate–Mg²⁺ complex may lead to strong inhibition of *M. tuberculosis* AnPRT.

4.3 An investigation into the nucleophilic binding site

There are many reported *M. tuberculosis* AnPRT structures where the enzyme is bound to several distinct anthranilate analogues.^{54,57,66,68,69,71,74} The binding of the anthranilate analogues within the substrate binding tunnel is explained in detail in Sections 1.8.3 and 1.8.4. In brief, there are two anthranilate binding sites observed in the *S. solfataricus* AnPRT structures, either in the presence (PDB: 1ZYK) or absence of PRPP (PDB: 2GVQ). Similarly, two sites—site 1 and site 3 are observed for anthranilate analogues in the tunnel in distinct *M. tuberculosis* AnPRT structures with an observed binding of either PRPP (PDB: 4N5V, 3QQS) or diphosphate (PDB: 4OWN and 4X5E) at the active site of the enzyme. Another structure of *M. tuberculosis* AnPRT (PDB: 4X5D) shows the binding of anthranilate only at site 3 when none of the other ligands are bound at the catalytic site of the enzyme. Based on the available *M. tuberculosis* AnPRT crystal structures (Section 1.8.4), the catalytic cycle of AnPRT has been hypothesised to begin with the binding of the anthranilate substrate at site 3 with an “open” conformation of the $\beta 1$ – $\alpha 5$ and $\beta 2$ – $\alpha 6$ loops, followed by the binding of PRPP at the active site and a subsequent switching of the conformation of both loops to the “closed” conformation. The “closed” conformation of the loops facilitates the movement of anthranilate from site 3 to site 1, ready for nucleophilic attack in order to facilitate catalysis.⁷¹ After the completion of the enzymatic reaction, diphosphate still remains in a deeply buried position at the active site and the $\beta 2$ – $\alpha 6$ loop adopts a “folded” conformation in order to release the reaction product. However, this proposed catalytic cycle is based on the crystal structures of the enzyme.

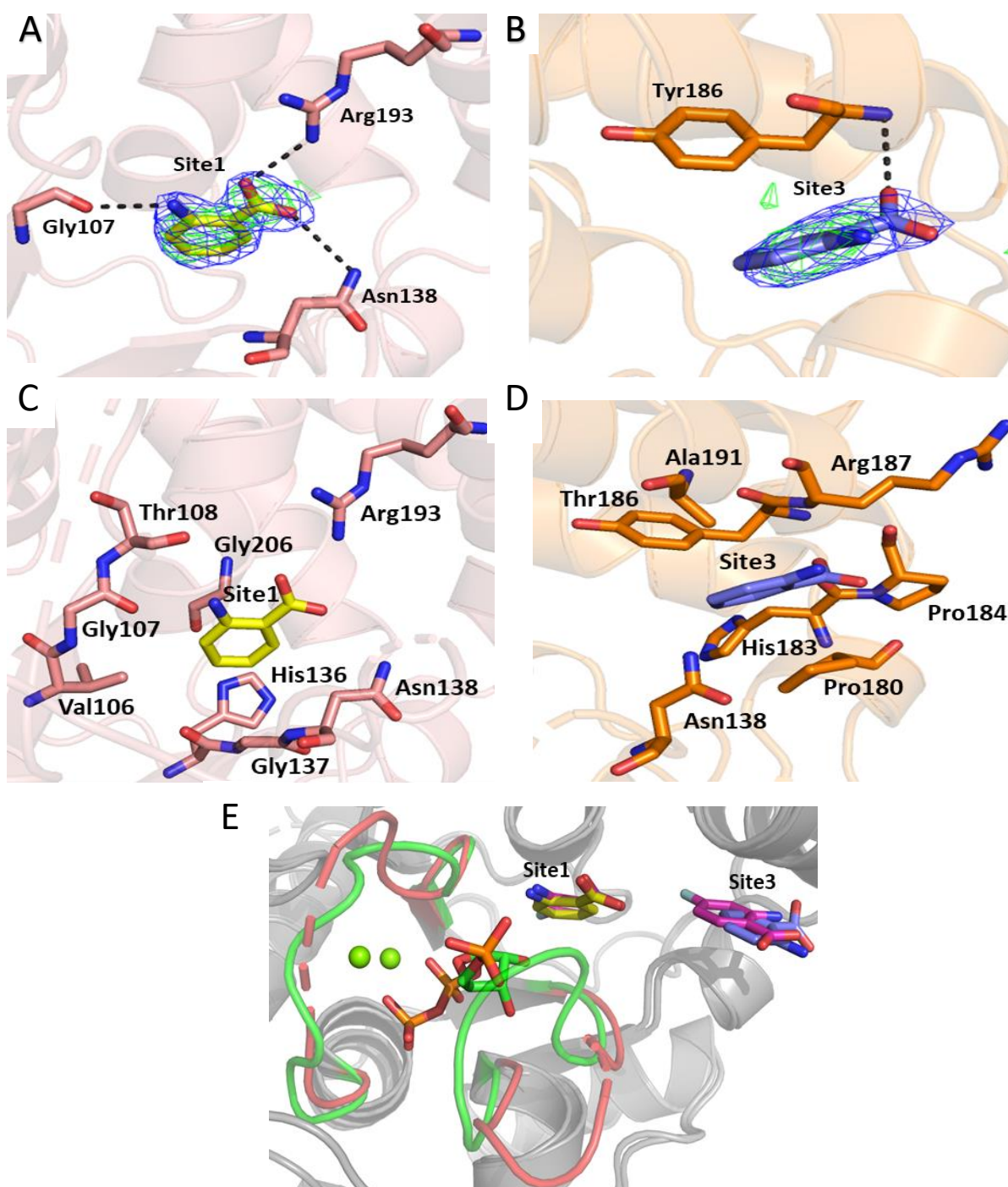


Figure 4.5 *M. tuberculosis* AnPRT structures displaying the anthranilate binding sites. (A, B) chain A (tint) and chain B (orange) of the anthranilate bound structure showing the binding of anthranilate (yellow in chain A and blue in chain B). Polar contacts of anthranilate are shown as black dashes. Part of the electron density map into which anthranilate (yellow and blue) was modelled in chain A (tint) and chain B (orange) respectively. 2Fo-Fc map contoured at 1 σ shown as a blue mesh, Fo-Fc map contoured at 3 σ shown as a green mesh. (C, D) chain A (tint) and chain B (orange) of the anthranilate

bound structure showing the residues involved in the binding of anthranilate (yellow in chain A and blue in chain B). (E) An overlay of chain A of the AnPRT structure (PDB: 4N5V) bound with PRPP (green), Mg^{2+} (green sphere) and 4FA (pink) with the structure with chain A bound with anthranilate (yellow) at site 1 and chain B bound with anthranilate (blue) at site 3. The distinct positions of the loops in the absence (red) and presence of PRPP (green) are shown with dissimilar colours.

Recently, we have managed to solve the *M. tuberculosis* AnPRT/anthranilate structure at 2.31 Å. This crystal was obtained using standard crystallisation conditions (Section 7.1.20). Data collection and refinement statistics are shown in Appendix 2. The structure was solved in the C121 space group with two distinct monomeric units present in the asymmetric unit, although the dimer could be generated via crystallographic symmetry. In chain A, anthranilate makes polar contacts with Arg193 and Asn138 via its carboxylate group and its amino group interacts with only Gly107 (Figure 4.5, **A**). However, in chain B, anthranilate is hydrogen bonded to Tyr186 only via its carboxylate group (Figure 4.5, **B**). The binding of anthranilate at both sites is mostly of hydrophobic nature. The residues such as Val106, Thr108, Gly206, His136 and Gly137 are involved in hydrophobic interactions at site 1 in chain A while Asn138, Pro183, His180, Pro184, Arg187 and Ala191 residues are contributed to hydrophobic interactions (Figure 4.5, **C**, **D**).

Structural superimposition of chain A of a PRPP and anthranilate-analogue, 4FA, bound AnPRT structure (PDB: 4N5V) onto both chains of the new anthranilate bound structure shows the binding of anthranilate at site 1 in chain A and site 3 in chain B without the binding of any ligand at the active site of the enzyme (Figure 4.5, **E**). The $\beta 1-\alpha 5$ and $\beta 2-\alpha 6$ loops are in the “open” conformation though a few residues of the loops are missing due to poor density. In the absence of a ligand at the catalytic site, the binding of anthranilate or anthranilate mimics at site 1 has not been seen in previously solved structures of *M. tuberculosis* AnPRT. However, similar binding for anthranilate has been observed in *S. solfataricus* AnPRT (PDB: 2GVQ). The binding of the nucleophilic anthranilate closer to the PRPP site indicates the possibility for anthranilate to bind at multiple sites within the tunnel prior to the binding of PRPP at the active site of AnPRT. However, this hypothesis is also based on crystallographic observations. Therefore, the binding of anthranilate or anthranilate analogues was studied in solution using DSF and ITC.

4.3.1 Differential scanning fluorimetry (DSF)

DSF was used to determine the thermal stability of *M. tuberculosis* AnPRT in the presence of ligands at various concentrations (Figure 4.6 and Table 4.1). The melting temperature of AnPRT in the presence of 1 mM Mg^{2+} was found to be 67.9 ± 0.3 °C. The melting temperature of AnPRT increased as the concentration of anthranilate or the anthranilate analogue increased. These results, in combination with the crystallographic observations, indicate that the binding of anthranilate might occur throughout the tunnel prior to the binding of PRPP as protein stability is strengthened by increasing concentrations of anthranilate and the anthranilate mimic, ACS172. However, the ligand binding constants may well be different depending on conformation of loops and binding positions of ligands.

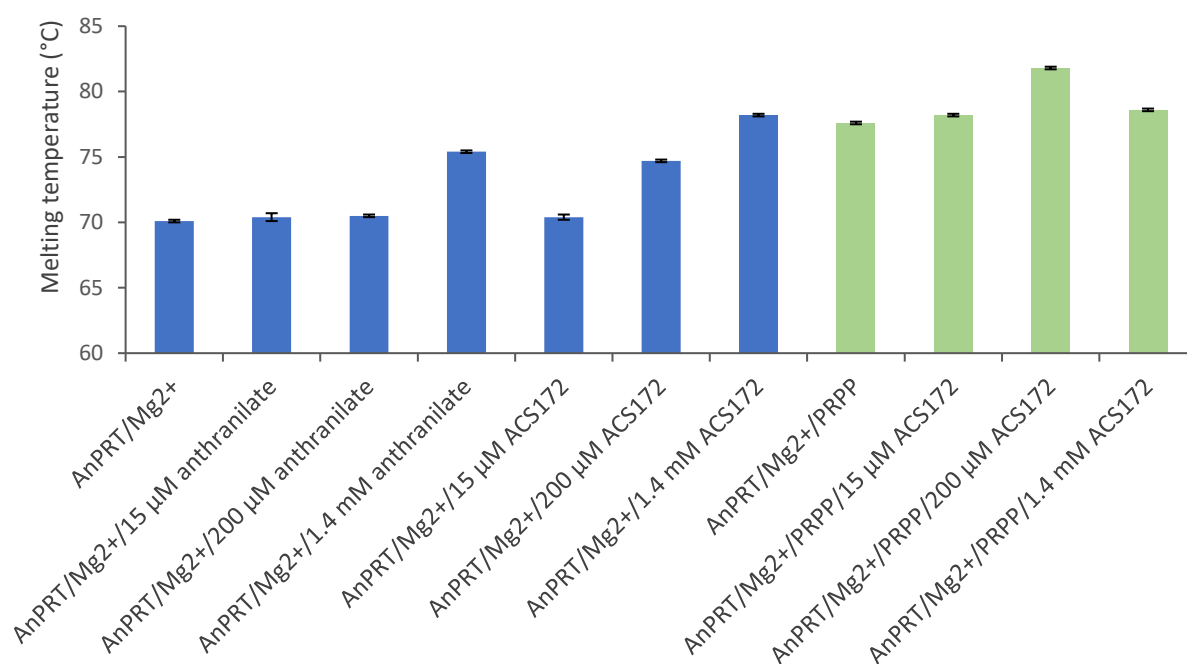


Figure 4.6 DSF melting temperatures for *M. tuberculosis* AnPRT in the presence of several ligands.

M. tuberculosis AnPRT with 1 mM Mg^{2+} in the absence (blue) or presence (green) of PRPP either with 15 µM, 200 µM and 1.4 mM anthranilate or ligand ACS172. The enzyme was analysed in 50 mM Tris.HCl, 200 mM NaCl buffer (pH 8.0) at a concentration of 1 mg/mL.

Table 4.1 *M. tuberculosis* AnPRT melting temperatures in the presence of various ligands.

Ligand	T_m (°C)
AnPRT	67.9 ± 0.4
AnPRT/Mg ²⁺	70.1 ± 0.1
AnPRT/Mg ²⁺ /15 µM anthranilate	70.4 ± 0.3
AnPRT/Mg ²⁺ /200 µM anthranilate	70.5 ± 0.1
AnPRT/Mg ²⁺ /1.4 mM anthranilate	75.4 ± 0.1
AnPRT/Mg ²⁺ /15 µM ACS172	70.4 ± 0.2
AnPRT/Mg ²⁺ /200 µM ACS172	74.7 ± 0.1
AnPRT/Mg ²⁺ /1.4 mM ACS172	78.2 ± 0.1
AnPRT/Mg ²⁺ /PRPP	77.6 ± 0.1
AnPRT/Mg ²⁺ /PRPP/15 µM ACS172	78.2 ± 0.1
AnPRT/Mg ²⁺ /PRPP/200 µM ACS172	81.8 ± 0.1
AnPRT/Mg ²⁺ /PRPP/1.4 mM ACS172	78.6 ± 0.1

The binding of PRPP with metal ions has a significant effect on protein stability as the melting temperature of the enzyme (77.6 ± 0.1 °C) in the presence of PRPP is elevated by 7.5 °C compared to AnPRT/Mg²⁺. The addition of 15 µM ACS172 did not change the melting temperature of AnPRT/PRPP/Mg²⁺. Interestingly, the melting temperature of the protein by the addition of 200 µM ACS172 (T_m = 81.8 ± 0.1) was elevated by 3.2 °C compared to AnPRT/PRPP/Mg²⁺. However, protein stability decreased (78.6 ± 0.1 °C) in the presence of a higher concentration of ACS172 (1.4 mM). The lower melting temperature of AnPRT in the presence of ACS172 (1.4 mM) and PRPP might be the reason of the change in protein stability as the conformation of the β 2– α 6 loop is “closed” when PRPP itself binds into the active site and “opened” when only ACS172 binds into the tunnel. Since DSF is only a crude indicator of protein–ligand binding, the thermodynamic events associated with ligand binding were characterised in detail by ITC.

4.3.2 Detection of anthranilate and anthranilate analogue binding by ITC

ITC experiments were employed to determine the binding of anthranilate into the substrate binding channel of *M. tuberculosis* AnPRT. Thus, the experiment was performed by titrating anthranilate into 1 mM AnPRT in the absence of PRPP. No heat changes were observed during this titration, even at concentrations as high as 5 mM for anthranilate. The collected data

clearly indicate that the heat changes that occur during anthranilate binding are too weak to detect by ITC.

Then, the anthranilate analogue 4FA (Figure 4.7), which is also accepted as a substrate for AnPRT, was used as an alternative to anthranilate to determine the substrate binding sites in the tunnel. Thus, the binding isotherm of 4FA was obtained by titrating 6 mM 4FA into 1 mM *M. tuberculosis* AnPRT (Figure 4.8, **A**).

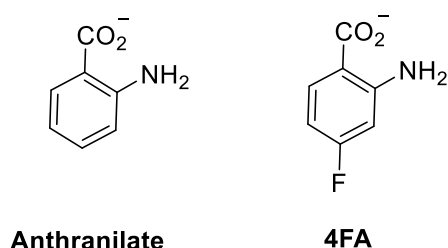


Figure 4.7 Structural representations of anthranilate and 4FA.

The obtained data were best fitted to a two-site sequential binding model; the process of ligand binding to AnPRT being exothermic (Figure 4.8, **B**). The binding of 4FA to *M. tuberculosis* had a K_d value of 38 ± 7.6 mM at the first binding site and a K_d of 171 ± 11 mM for the second site (Figure 4.8, **C**). This indicates that the binding of 4FA occurs at the two sites in the tunnel and that binding occurs in an un-cooperative manner, where binding at the first available site decreases binding affinity at the second site. The thermodynamic parameters obtained from the binding isotherm indicate that the binding at this first site appears to have a larger entropic contribution to the ligand binding at the second site (Figure 4.8, **D**). The obtained two-site sequential binding model indicates that the anthranilate analogue binds at two sites in the tunnel in the absence of PRPP at the active site, in agreement with the crystallographic observations in the AnPRT/anthranilate structures.

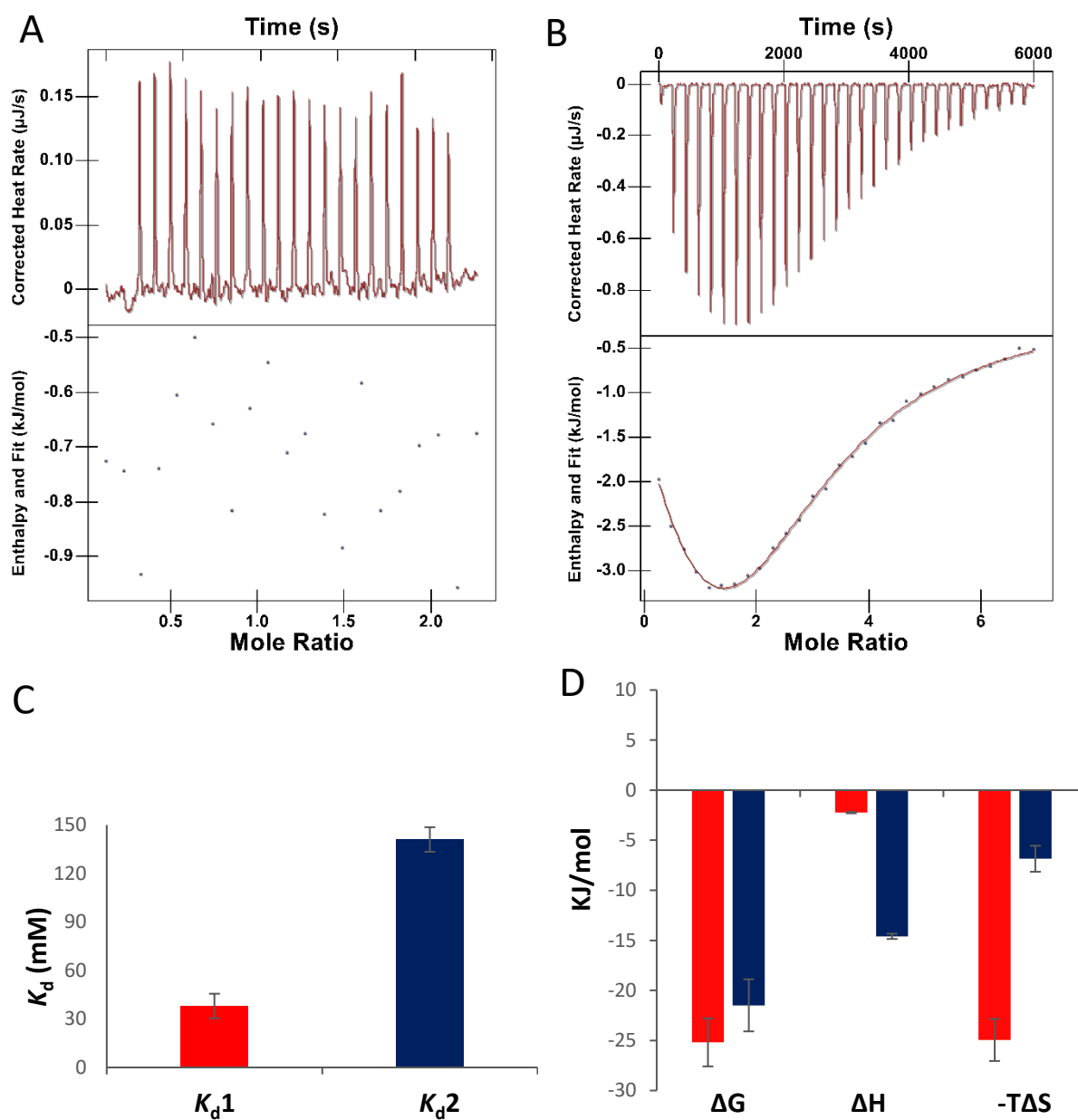
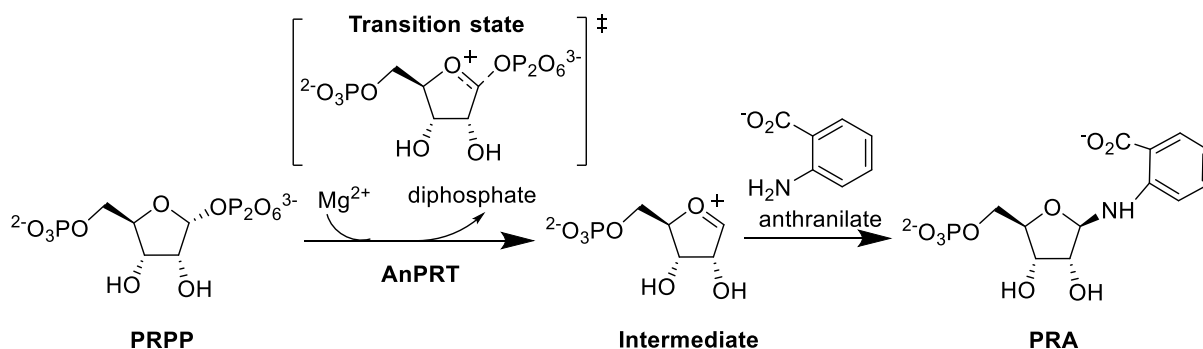


Figure 4.8 ITC data for the binding of 4FA to *M. tuberculosis* AnPRT.

(A) Raw data from ITC experiments involving the titration of 5 mM anthranilate into a cell containing 1 mM AnPRT. (B) ITC raw data for the titration of 4 mM 4FA into 1 mM *M. tuberculosis* AnPRT fitted into a two-site sequential binding model. (C, D) Comparison of the K_d values and thermodynamic parameters for both binding sites of the multiple site binding model. The red and blue colours correspond to the first and second binding site data, respectively.

4.4 Inhibition of *M. tuberculosis* AnPRT

As mentioned previously in Section 1.9, the reaction mechanism of *M. tuberculosis* AnPRT is proposed to proceed via a dissociative “S_N1-like” mechanism, where the diphosphate group of PRPP fully dissociates first, forming an oxocarbenium ion intermediate, before the nucleophilic attack by another substrate (Scheme 4.1).



Scheme 4.1 The possible catalytic states for dissociative “S_N1-like” mechanism of AnPRT.

Based on possible catalytic states of the enzymatic reaction, a number of compounds that were available or easily accessible through synthesis were tested against *M. tuberculosis* AnPRT.

4.4.1 Cyclopentane analogue 4.11

In an S_N1 like mechanism, the formation of the positive charge at the anomeric carbon by the departure of the diphosphate group is stabilised through the lone pair of the oxygen atom. In order to probe this involvement in the reaction, it would be interesting to see the behaviour of the *M. tuberculosis* AnPRT enzyme in the presence of a substrate analogue without the ring oxygen atom. Cyclopentane compound **4.11** (Figure 4.9) is an easily accessible, interesting compound for mechanistic and inhibitory studies for all PRT enzymes. This analogue **4.11**, without the ring oxygen, allows for comparison with R5P inhibitor to determine the effect of replacing the anomeric oxygen with a carbon atom on enzyme inhibition (Figure 4.9). R5P is a weak competitive inhibitor with respect to PRPP with a K_i value of 1 ± 0.1 mM for *M. tuberculosis* AnPRT.⁵⁷ This comparison could be helpful in

obtaining insight into the role of the anomeric ring oxygen in order to understand PRPP binding and inhibition of the enzyme.

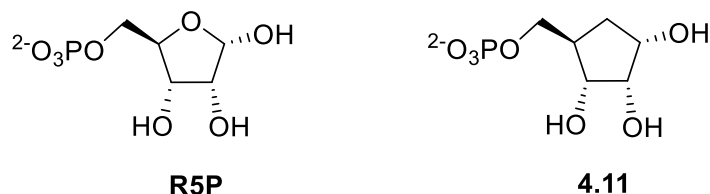
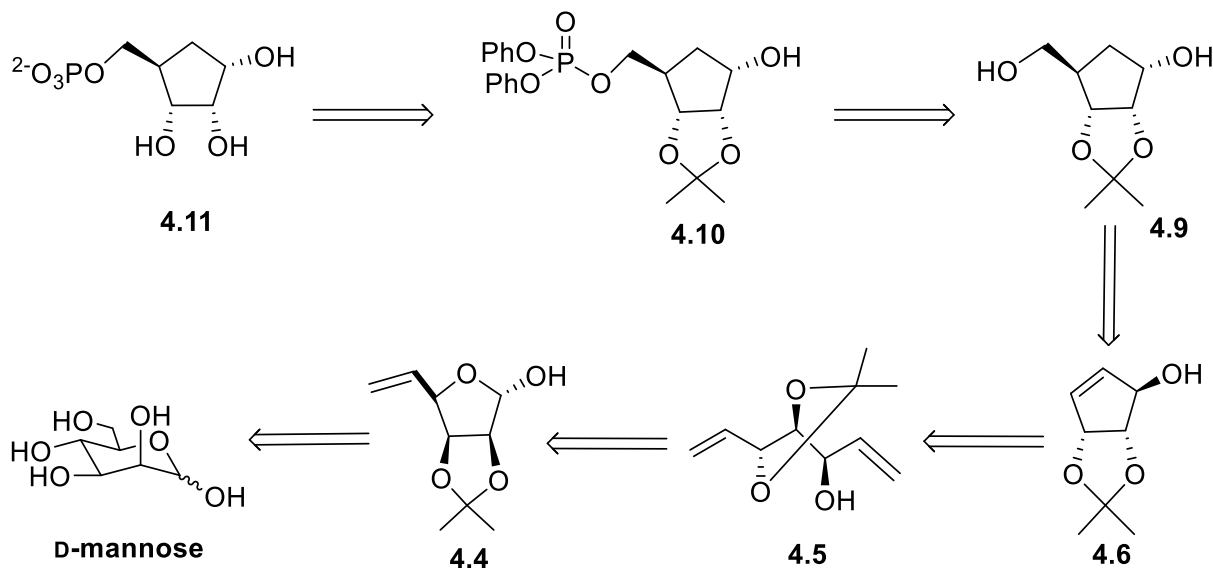


Figure 4.9 The chemical structure of R5P and cyclopentane analogue **4.11**.

4.4.1.1 Retrosynthetic analysis for analogue **4.11**

A scheme for the synthesis of cyclopentane derivative **4.11** was designed in ten steps from D-mannose (Scheme 4.2). It was imagined that compound **4.11** could be obtained from protected cyclopentane **4.10** in two steps via deprotection of the isopropylidene group in an acidic environment followed by catalytic hydrogenation using platinum oxide (PtO_2) as a catalyst and hydrogen gas as a hydrogen donor to cleave the phenyl ester.¹²⁶ Selective primary phosphorylation of **4.10** could be achieved by using diphenyl phosphoryl chloride.



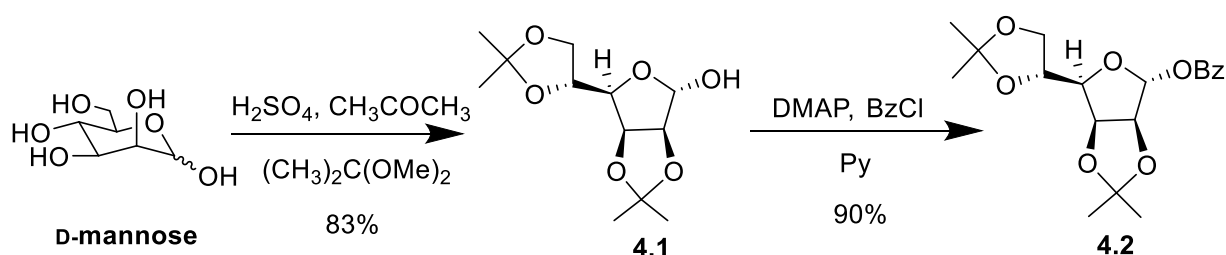
Scheme 4.2 Retrosynthetic analysis for the synthesis of the cyclopentane **4.11**.

Cyclopentane **4.9** can be synthesised from cycloalkene **4.6** using the mild oxidation of an alcohol to a carbonyl, followed by the benzophenone-initiated photochemical addition of methanol to get desired regiochemistry of hydroxymethyl adduct, followed by reduction of

carbonyl to get the alcohol with the desired stereochemistry. Ring-closing metathesis could be achieved to get cycloalkene **4.6** from dialkene **4.5**. Dialkene **4.5** can be obtained from the protected alkene **4.4** followed by de-benzoylation and Wittig olefination. Alkene **4.4** could be obtained from protected mannose followed by acid catalysed thermal rearrangement of D-mannose.

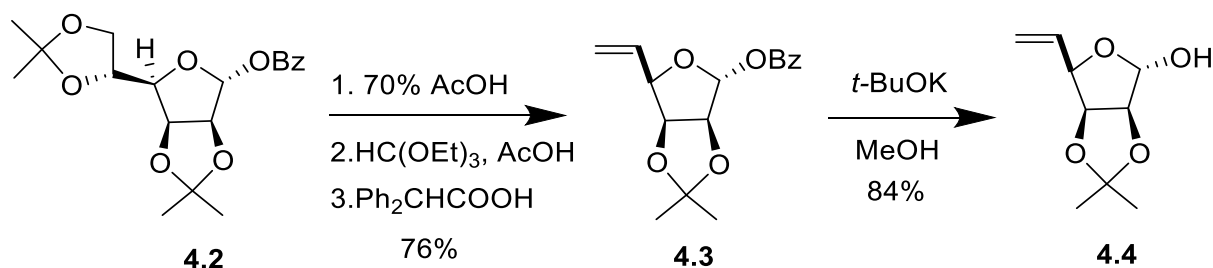
4.4.1.2 Detailed synthesis of the cyclopentane analogue (4.11)

Protected mannose **4.2** was synthesised in 2 steps from D-mannose (Scheme 4.3). The acetonide protecting group was used to lock the mannose ring in its furanose form and for its flexibility in oxidising the 5,6-isopropylidene protecting group selectively to an alkene, which is required at a later stage of the synthesis. D-Mannose was condensed with 2,2-dimethoxypropane in acetone and H_2SO_4 was used as a catalyst to give di-acetonide mannose derivative **4.1** (83%). Then, benzoylation was achieved at the anomeric position with benzoyl chloride in dry pyridine with a catalytic amount of 4-dimethylamino pyridine (DMAP) to give the fully protected compound **4.2** in 90% yield.



*Scheme 4.3 Synthesis of benzoyl 2,3,5,6-di-O-isopropylidene- α -D-mannose **4.2**.*

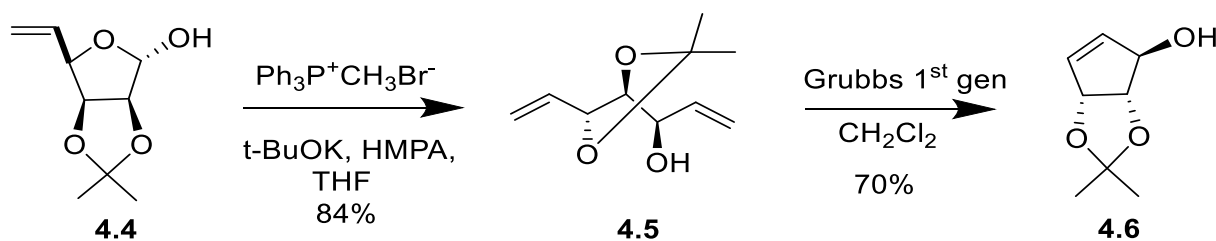
Selective removal of the 5,6-di-O-isopropylidene group of compound **4.2** was achieved, followed by reprotection and thermal rearrangement at the 5,6-position¹²⁷ to give alkene **4.3** in 76% yield over three steps (Scheme 4.4). The regioselective removal of the 5,6-isopropylidene was monitored carefully since prolonged reaction time can cause the loss of the 2,3 acetonide. Anomeric debenzoylation of compound **4.4** was successfully achieved using *t*-BuOK in methanol in 84% yield.



*Scheme 4.4 Synthesis of 2,3-O-isopropylidene- α -D-lyxo-hex-5-enofuranose **4.4**.*

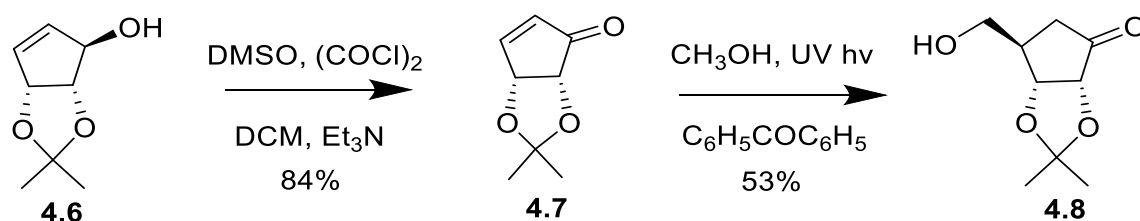
After synthesising compound **4.4**, a Wittig olefination was used to get diene **4.5** (Scheme 4.5). The reagents required for this literature procedure,¹²⁷ Wittig reagent and *n*-butyl lithium (*n*-BuLi) in THF were used at 78 °C. The concentration of *n*-BuLi changes over time and old bottles of *n*-BuLi available nullified the chances of product formation. *t*-BuOK in THF and hexamethylphosphoramide (HMPA) were then used with the Wittig reagent, methyl triphenylphosphonium bromide, at -20 °C in order to generate the ylide intermediate.¹²⁸ However, the formation of the desired product was not observed due to the formation of the unstable ylide at -20 °C.

After that, *t*-BuOK in THF/HMPA was used to generate a stable ylide at -78 °C followed by the addition of compound **4.4** with an additional hour of stirring at -20 °C. The reaction was then kept at room temperature in order to get complete conversion to product **4.5**. However, product **4.5** was volatile under reduced pressure. Therefore, a cold trap was used with the rotary evaporator to trap any product coming through. Compound **4.5** was successfully obtained in excellent yield (84%). The ring-closing metathesis (RCM) was performed with Grubbs 1st generation catalyst in order to give cyclopentene **4.6** in reasonable yield (70%) from dialkene **4.5**.



*Scheme 4.5 Synthesis of cyclopentene **4.6**, using Wittig olefination and ring-closing metathesis.*

Oxidation of cyclopentene **4.6** was performed with oxalyl chloride (COCl_2) in dimethyl sulphoxide (DMSO),¹²⁹ which gave cyclopentenone **4.7** in 84% yield (Scheme 4.6).



*Scheme 4.6 Oxidation and photochemical addition of methanol leading to hydroxymethylcyclopentenone **4.8**.*

The structure of compound **4.7** was confirmed by X-ray crystallography with a flack value of 0.1 ± 0.4 (Figure 4.10, Appendix 1). The benzophenone initiated photochemical addition of methanol to 1-4 enone can be achieved readily in a stereo-controlled manner.¹³⁰ The photoaddition of methanol to cyclopentenone **4.7** (Scheme 4.6) gave compound **4.8** (53%), which is highly unstable in acidic conditions so purification was done using florisil chromatography, which is less acidic and non-polar than silica-based chromatography.¹³¹

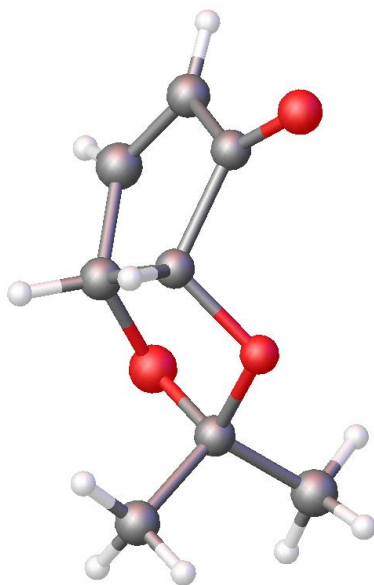
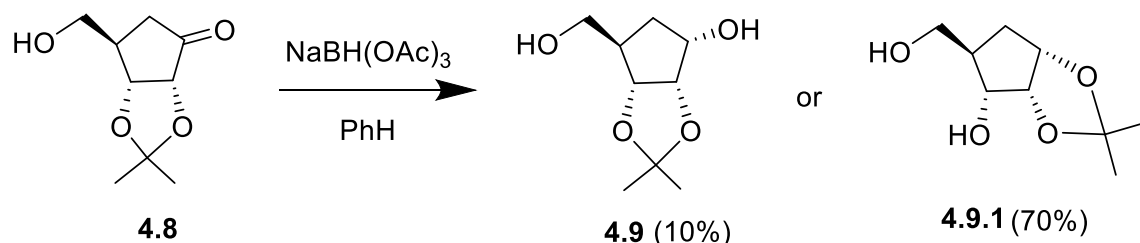


*Figure 4.10 The crystal structure of cyclopentenone **4.7**.*

Reduction of ketone **4.8** using sodium triacetoxyborohydride (Scheme 4.7) was first attempted with toluene instead of benzene due to the carcinogenicity of benzene. However, the reaction did not work. The reaction was successfully performed in benzene but product

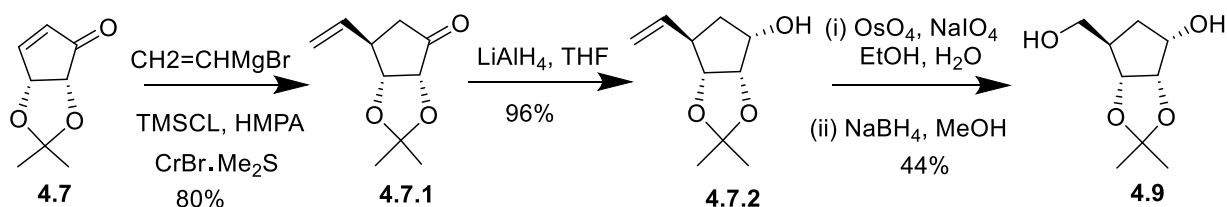
4.9, with the desired configuration and regioselectivity, was achieved in very poor yield (10%) due to its high susceptibility to acidic conditions of the silica column. Unfortunately, the epimerised compound **4.9.1** (70%) was the major product even though triethylamine was used in the silica column to offset the acidity.



Scheme 4.7 Anomeric reduction with a bulky reducing agent.

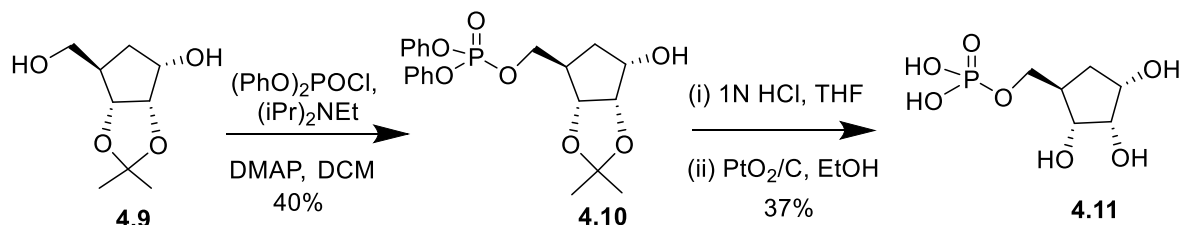
Due to the unavailability of the appropriate UV lamp at Victoria University of Wellington, adding methanol to compound **4.7** photochemically was not possible. Therefore, a chemical approach was attempted. The work done by Schneller *et al.*¹³² was used in order to add the vinyl moiety as the source of C-5 hydroxymethylene **4.7.1** from compound **4.7** (Scheme 4.8). Compound **4.7.1** was readily afforded in 80% yield.

With compound **4.7.1** in hand, reduction with lithium aluminium hydride (LiAlH_4), a stronger reducing agent, was accomplished and **4.7.2**, with the α -configuration at the C1 position, was obtained in excellent yield (96%). Furthermore, the ethylene group of **4.7.2** was transformed to the hydroxymethyl group of **4.9** in two steps; oxidation of the double bond with osmium tetroxide (OsO_4) and sodium periodate (NaIO_4) followed by reduction with sodium borohydride (NaBH_4) to afford **4.9** in 44% yield. Extreme care is necessary during the isolation and purification of each step due to the alacrity with which the compound is rearranged to the alcoholic epimers.



Scheme 4.8 Another approach for the synthesis of cyclopentane 4.9.

The primary hydroxyl group of **4.9** (Scheme 4.9) was selectively phosphorylated by using diphenyl chlorophosphate in the presence of DMAP and the hindered base *N,N*-diisopropylethylamine [(iPr)₂NEt]. The resulting phosphate ester **4.10** was produced in 40% yield.



*Scheme 4.9 phosphorylation and deprotection of phosphocyclopentane **4.11**.*

The final steps for synthesis of compound **4.11** involved the removal of the isopropylidene group from **4.10** using 1 M HCl to produce the triol, followed by catalytic reduction with PtO₂ in an atmosphere of H₂ gas to give **4.11**. The crude product **4.11** was loaded on a RESOURCE Q column and eluted with a linear gradient of H₂O/0.2 M NH₄HCO₃. Fractions containing the desired product were identified by a phosphate colourimetric assay and lyophilised to give **4.11** as a white powder (37% over two steps).

4.4.1.3 AnPRT inhibition study with cyclopentane phosphate (**4.11**)

The exact concentration of cyclopentane phosphate **4.11** was measured using a phosphate colourimetric assay. The substrate analogue inhibition study for the *M. tuberculosis* AnPRT enzyme was done using the standard protocol (Section 7.1.17). The commercially available R5P was tested against AnPRT using similar assay conditions in order to compare how the enzyme inhibition is affected by replacing the endocyclic oxygen with a carbon atom in analogue **4.11**. Enzyme catalysis was measured at various concentrations of both compounds along with varying concentrations of PRPP (0–250 μM) while the concentration of anthranilate was kept constant at 10 μM (≈6 × K_M). All measurements were carried out in triplicate.

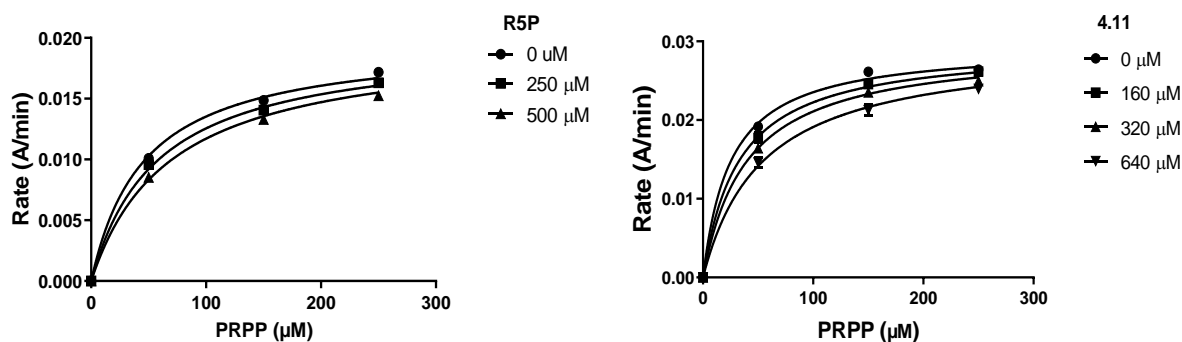


Figure 4.11 Inhibition of *M. tuberculosis* AnPRT by R5P and cyclopentane **4.11**.

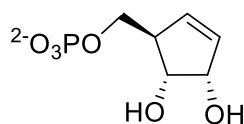
For the determination of the K_i values, assays contained 50 mM Tris.HCl (pH 8.0), 150 mM NaCl, 1 mM $MgCl_2$, 0.95 mg/mL (0.04 μM) AnPRT, 11.0 mg/mL (0.6 μM) *E. coli* PRAI: InGPS. PRPP varied from 0 to 250 μM while anthranilate was kept constant (10 μM) and inhibitors were used at various concentrations.

R5P acted as a competitive inhibitor against PRPP and gave an apparent K_i value of 1.0 ± 0.1 mM (Figure 4.11) which is similar to the recorded value.⁵⁷ Similarly, PRPP analogue **4.11** was also found to be competitive with respect to PRPP with an apparent K_i value of 555 ± 46 μM. Since cyclopentane analogue **4.11** turned out to be an inhibitor of AnPRT, this would indicate that replacing the anomeric oxygen with a carbon atom doubled the potency of inhibition of the compound. However, it can be noted that both PRPP analogues are poor inhibitors for *M. tuberculosis* AnPRT.

Moreover, the activity of the AnPRT enzyme did not change with respect to anthranilate as compound **4.11** is not expected to bind at the anthranilate binding site of AnPRT. Diphosphate plays a key role in the binding of PRPP at the active site of the enzyme and the binding of diphosphate itself reduces enzymatic activity by virtue of steric occlusion. Therefore, it would be interesting to check the inhibition of the enzyme with PRPP analogue **4.11** in the presence of diphosphate at the active site of the enzyme. To this end, the concentration of diphosphate was held constant at 100 μM in the assay while the concentration of analogue **4.11** was varied. However, no difference in the activity of AnPRT was observed with cyclopentane **4.11** in the presence of diphosphate under the tested conditions.

4.4.2 Cyclopentene analogue 4.12

The PRPP analogue **4.12** (Figure 4.12) was synthesised and provided by Gerard Johan Moggré.¹²⁸ Cyclopentene **4.12** was chosen to be tested as a competitive inhibitor with respect to PRPP for AnPRT in order to capture the geometry of the flattened ribose ring due to the double bond characteristics, which is expected to be similar to the double bond characteristics in the oxocarbenium ion present in the transition state of the S_N1 -like mechanism. Hence, this analogue might be useful to understand the reaction mechanism of AnPRT.



4.12

Figure 4.12 Cyclopentene phosphate **4.12** was tested as a mimic transition state.

The PRPP mimic **4.12** was tested against *M. tuberculosis* AnPRT using the standard kinetic assay employed for the PRPP analogue (Section 7.1.17). Compound **4.12** was able to inhibit *M. tuberculosis* AnPRT with respect to PRPP (Figure 4.13). However, the apparent K_i value for cyclopentene phosphate was $313 \pm 19 \mu\text{M}$, which suggests this analogue is only a modest competitive inhibitor for *M. tuberculosis* AnPRT. Interestingly, the double bond characteristics of cyclopentene showed stronger enzymatic inhibition compared to cyclopentane **4.11** and R5P.

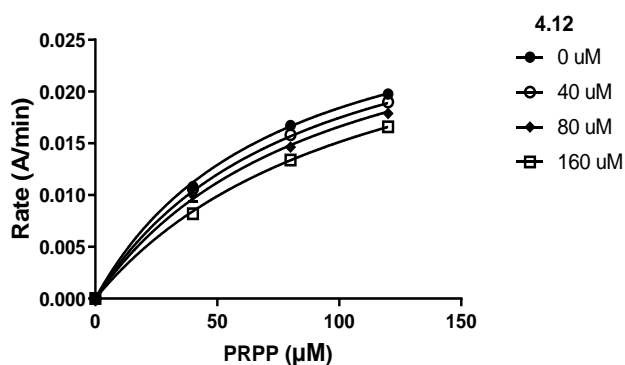


Figure 4.13 *M. tuberculosis* AnPRT inhibition graph for cyclopentene phosphate **4.12**.

Inhibition was measured by varying the concentration of the inhibitor at 25 °C at pH 8.0 with varying PRPP concentrations from 0 to 250 μM , while the concentration of anthranilate was held constant (10 μM). Assays were carried out in 50 mM Tris.HCl (pH 8.0), 150 mM NaCl, 1 mM MgCl_2 , 1.12 mg/mL (0.04 μM) AnPRT, 18.8 mg/mL (0.6 μM), *E. coli* PRAI: InGPS.

4.4.3 Diphosphorylated iminosugar **4.14**

The PRPP binding site of the enzyme is mostly dominated by polar amino acids. In order to target the PRPP binding site, our designed analogue contains two-phosphate groups to enhance the binding of the analogue into the PRPP binding site of the enzyme (Figure 4.14). Additionally, the compound was synthesised to capture the geometry of the flattened ribose ring and include a nitrogen atom within the ring to mimic the positive charge characteristics (when it is protonated) that are expected in the oxocarbenium-ion-like transition state.

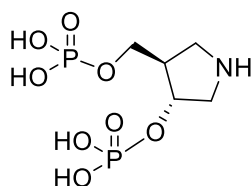
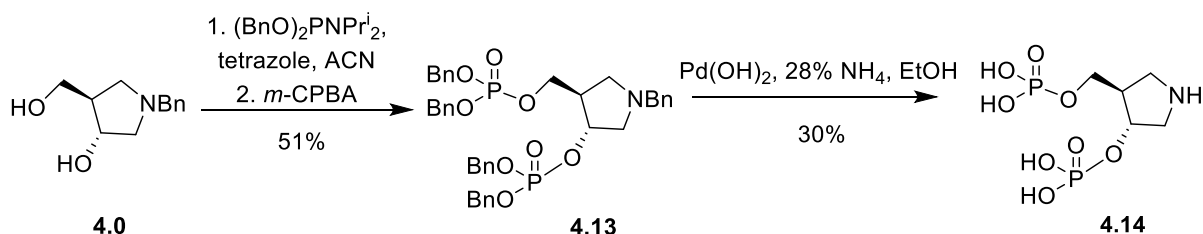


Figure 4.14 The chemical structure of iminosugar **4.14**.

4.4.3.1 Detailed synthesis of iminosugar **4.14**

Diphosphorylated amine **4.14** was expected to be easily accessible in two steps from pyrrolidine **4.0** via phosphorylation of the hydroxyl group of **4.0** using dibenzyl *N,N*-diisopropyl-phosphoramidite followed by global hydrogenation using a metal catalyst (Scheme 4.10). The pyrrolidine **4.0** is the common precursor for the synthesis of transition state mimics in Chapter 5. In detail, the common precursor hydroxymethyl benzylamine **4.0** was subjected to dibenzyl *N,N*-diisopropyl-phosphoramidite and 1H-tetrazole, followed by oxidation with *meta*-chloroperoxybenzoic acid (*m*-CPBA)¹³³ to give the primary phosphorylated compound in 40% yield and the diphosphorylated **4.13** in 51% yield.



Scheme 4.10 Phosphorylation of cyclopentane amine derivative **4.14**.

The protected diphosphate **4.13** was hydrogenated with Pd/C in ethanol overnight. However, this only resulted in the loss of the *O*-benzyl ester and unprotected *N*-benzyl amine. Instead, hydrogenation of the crude product with Pearlman's catalyst and 28% aqueous ammonia gave the fully deprotected desired analogue **4.14** in 30% yield.

4.4.3.2 AnPRT inhibition with diphosphorylated amine **4.14**

The iminosugar **4.14** was tested against *M. tuberculosis* AnPRT using the standard kinetic assay employed for the PRPP analogue (Table 4.2 and Figure 4.15). Compound **4.14** was a competitive inhibitor with respect to PRPP with a K_i value of $541 \pm 66 \mu\text{M}$. No inhibition was observed with respect to anthranilate up to a concentration of $250 \mu\text{M}$. Interestingly, the results indicate that replacing the anomeric oxygen of the ribose ring of PRPP by a carbon atom in PRPP mimic **4.11**, and introducing an amine group in the di phosphorylated cyclopentane ring **4.14**, causes a similar level of AnPRT inhibition with K_i values of $541 \pm 66 \mu\text{M}$ and $555 \pm 46 \mu\text{M}$ respectively.

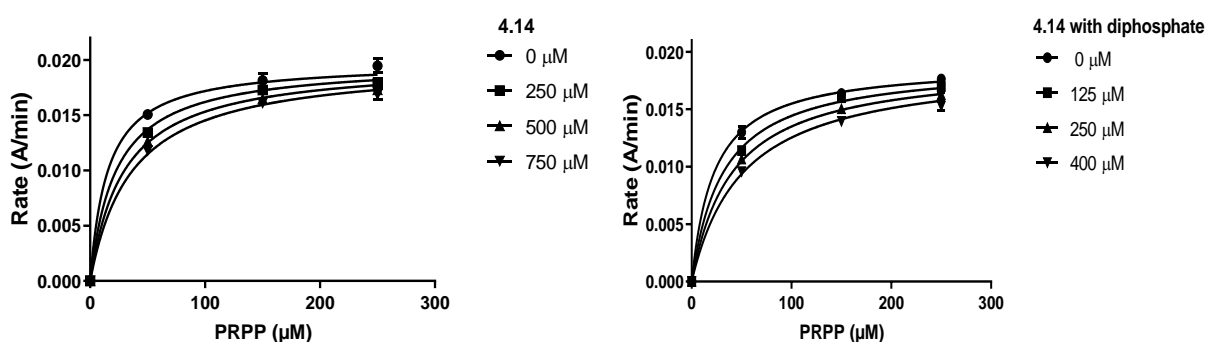
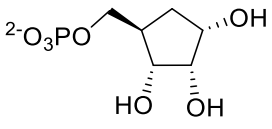
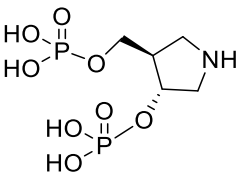
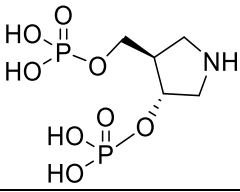


Figure 4.15 The kinetic assay of *M. tuberculosis* AnPRT for diphosphorylated amine **4.14**. The final volume of 1 mL of the cuvette consisted of 50 mM Tris.HCl, pH 8.0, 150 mM NaCl, 1 mM MgCl₂, 1.12 mg/mL⁻¹ (0.04 μM) *M. tuberculosis* AnPRT, 11 mg/mL (0.6 μM) *E. coli* PRAI: InGPS, anthranilate 10 μM, PRPP varied from 0 to 250 μM. Diphosphate was kept constant at 100 μM and inhibitors were present at various concentrations.

Table 4.2 The type of inhibition and K_i values for different ligands along with both substrates for *M. tuberculosis*.

Code	Chemical structure	K_i (μM) against PRPP	Type of inhibition with PRPP	K_i (μM) against anthranilate
4.11		555 ± 46	competitive	No inhibition up to 250 μM
4.14		541 ± 66	competitive	No inhibition up to 250 μM
4.14 with diphosphate		311 ± 26	competitive	No inhibition up to 250 μM

Moreover, PRPP mimic **4.14** was also tested against AnPRT in the presence of diphosphate to determine whether the diphosphorylated amine **4.14** could still bind into the active site when diphosphate is already present in the active site. Interestingly, with respect to PRPP, inhibitor **4.14** in the presence of 100 μM of diphosphate reduced the activity of AnPRT in a competitive manner almost to half (K_i value of 311 ± 26 μM) compared with only compound **4.14**. No enzymatic inhibition was observed for **4.14** with respect to anthranilate in the presence of diphosphate. Hence, the inhibition assay suggests that the phosphorylation of the secondary hydroxyl group of analogue **4.14** causes no steric hindrance and the inhibitor is able to decrease enzyme activity more strongly due to the binding of diphosphate at the active site.

4.4.4 Iminoribitol analogues

Iminoribitols act as transition state mimics for PRTs and are found to be strong inhibitors with lower K_i values in the range of pM or nM.^{90,134–136} In order to generate strong PRTs inhibitors, the addition of a diphosphate group together with an iminosugar generated an unstable mimic. Therefore, the Ferrier Research Institute approached the synthesis of bis-phosphorylated derivatives of 2,5-dideoxyaltritol (**4.15** and **4.16**, Figure 4.16) by the insertion of a methylene bridge between the anomeric carbon and phosphate group.¹³⁴ These transition state mimics resulted in strong inhibitors for *Plasmodium falciparum* orotate PRT and *Saccharomyces cerevisiae* adenine PRT.¹³⁴

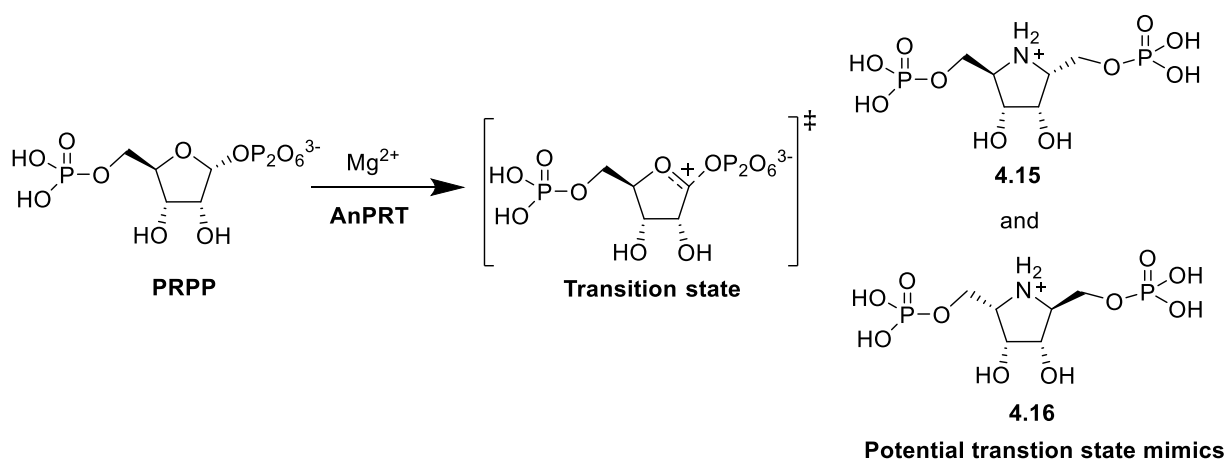


Figure 4.16 Potential transition state and transition state mimics for *M. tuberculosis* AnPRT.

The nitrogen atoms of these iminoribitol compounds are protonated at physiological pH. In addition, these analogues may act as transition state mimics for *M. tuberculosis* AnPRT (Figure 4.17). The analogues D-2,5-dideoxy-2,5-imino-altritol 1,6-bisphosphate (**4.15**) and L-2,5-dideoxy-2,5-imino-altritol 1,6-bisphosphate (**4.16**) were synthesised and kindly provided by Dr Lawrence Harris from the Ferrier Research Institute. The iminoribitol compounds in Figure 4.17 display a tight binding affinity for *Plasmodium falciparum* and human orotate PRTs.^{136–138} The cyclic iminoribitols **4.18** and **4.19** mimic the ribocation characteristic of the transition states and the pyrimidine or aromatic ring with the carboxylic acid moiety was included to mimic the attacking nucleophile that interacts with amino acids during catalysis. A direct linking of the ribocation mimic and the nucleophilic derivative can enhance the binding of an analogue to the catalytic site of the enzyme. These PRT transition state mimics were also tested against *M. tuberculosis* AnPRT in order to provide insight into potential anti-TB agents.

The following analogues were synthesised in Prof. Peter Tyler's laboratory: **4.17**, **4.18** and precursor **19.1** for the synthesis of analogue **4.19**.

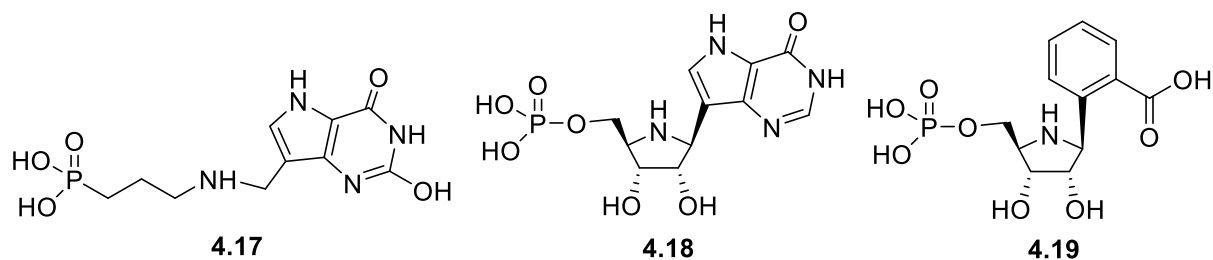
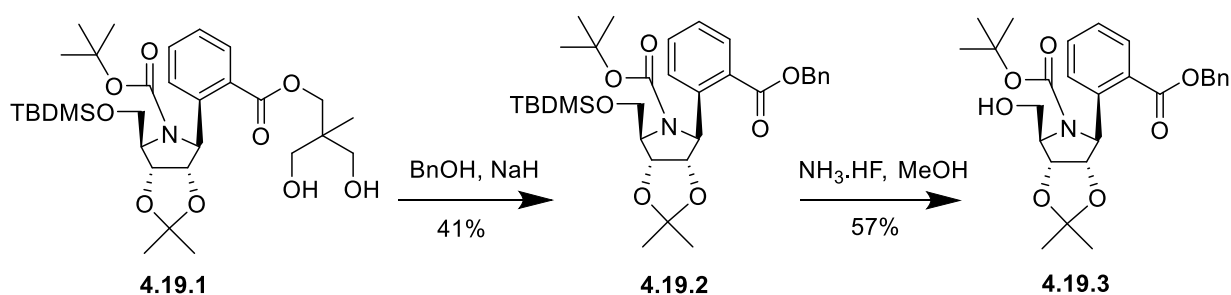


Figure 4.17 The potential inhibitors for *M. tuberculosis* AnPRT.

4.4.4.1 Synthesis of iminoribitol phosphate 4.19

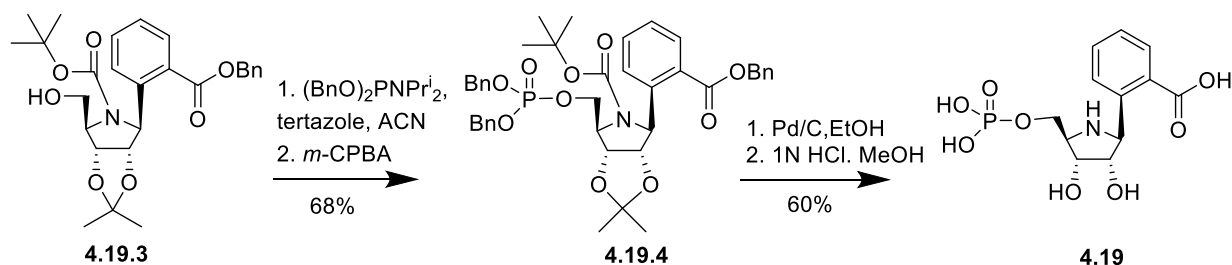
The synthesis of the transition state mimic **4.19** from precursor **4.19.1** was carried using a published procedure.¹³⁷ 3-Bromo-4-(4-methyl-2,6,7-trioxabicyclo[2.2.2]octan-1-yl)pyridine and 5-*O*-*tert*-butyldimethylsilyl-1,*N*-dehydro-1,4-dideoxy-1,4-imino-2,3-*O*-isopropylidene-D-ribitol were transformed in a suitably protected ester **4.19.1** using *n*-butyllithium and tin (IV) chloride, followed with BOC protection and aqueous acidic acid treatment. The benzyl protection of the carboxylate group, followed by the cleavage of the butyl group in **4.19.1**, was successfully achieved using sodium benzyl oxide to afford **4.19.2** in 41 % yield (Scheme 4.11). Then, the removal of *tert*-butyldimethylsilyl (TBDMS) from the primary hydroxyl was done with ammonium fluoride in methanol to give **4.19.3** (57 %).



Scheme 4.11 Synthesis of primary hydroxyl and benzyl protected carboxylate **4.19.3** from ribitol **4.19.1**.

After that, the primary phosphorylation of **4.19.3** was achieved using dibenzylphosphor-*N,N*-diisopropylamidite $[(\text{BnO})_2\text{PNPr}_2]$ and *meta*-chloroperoxybenzoic acid (*m*-CPBA) oxidation to

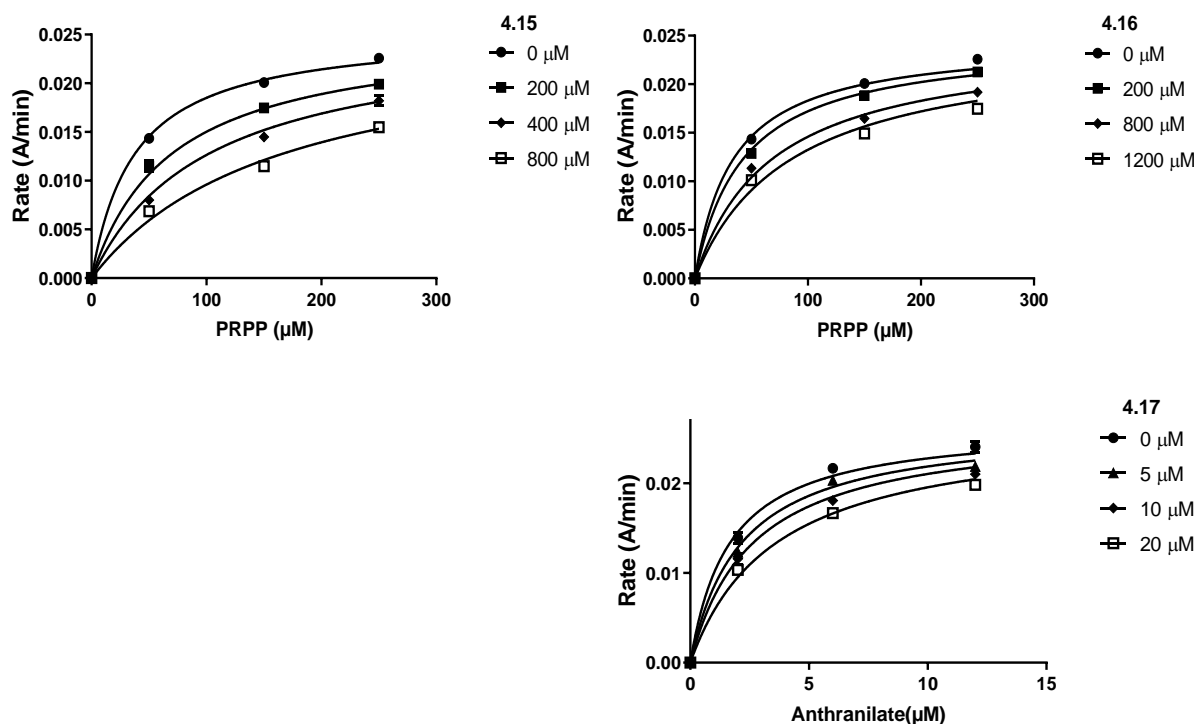
produce **4.19.4** in 68% yield (Scheme 4.12). The final global deprotection of the benzyl, *tert*-butyloxycarbonyl and isopropylidene groups was done by catalytic hydrogenolysis with Pd/C in EtOH followed by 1 M HCl in MeOH to afford **4.19** in reasonable yield (60%).



Scheme 4.12 Phosphorylation and deprotection steps for the synthesis of Iminoribitol **4.19**.

4.4.4.2 AnPRT Inhibition studies on iminoribitol analogues

M. tuberculosis AnPRT activity in the presence of iminoribitol analogues was assessed using the standard enzyme coupled assay (Section 7.1.17) and the results fitted best with the competitive inhibition model (Figure 4.18 and Table 4.3).



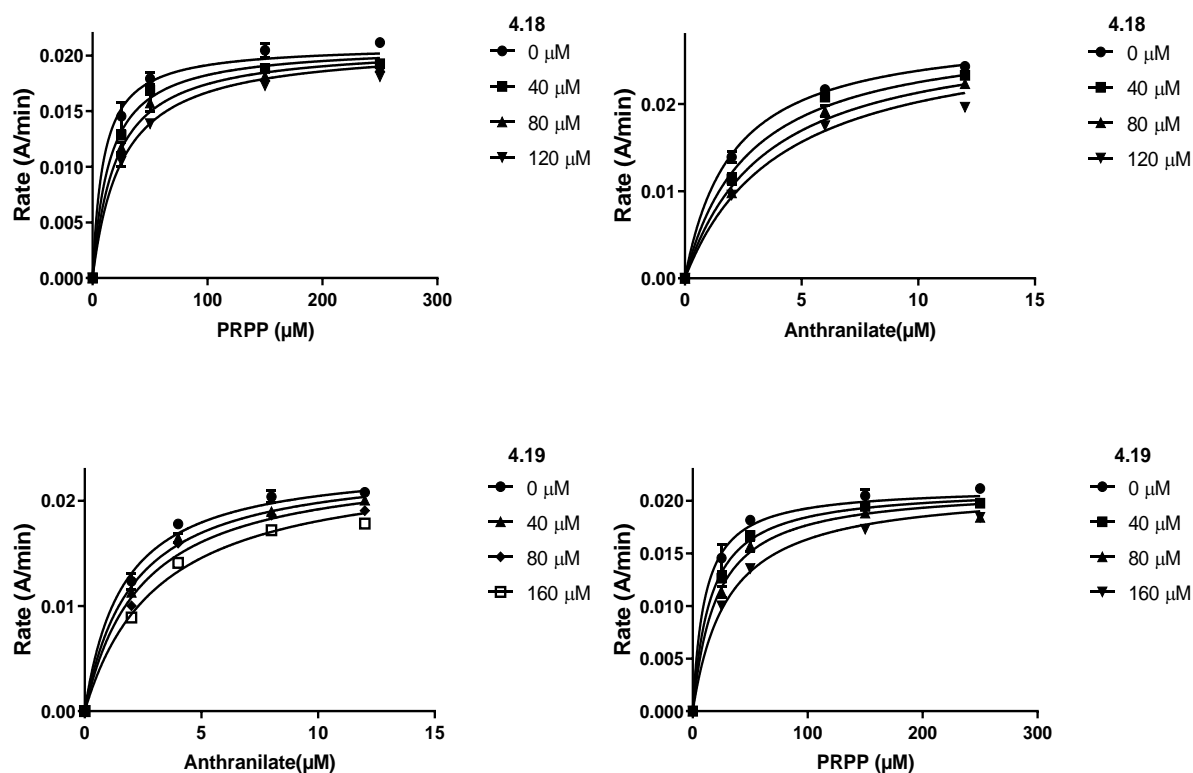


Figure 4.18 K_i^{app} determination for several analogues tested against *M. tuberculosis* AnPRT.

Kinetic assays were performed in a final volume of 1 mL and consisted of 50 mM Tris.HCl (pH 8.0), 200 mM NaCl, 1 mM $MgCl_2$, 1.12 mg/mL (0.05 μM) TrpD, 18.84 mg/mL (0.6 μM) *E. coli* PRAI: InGPS. For assays with respect to anthranilate, the assays contained 100 μM PRPP ($\approx 2 \times K_M$), anthranilate from 0 to 8 μM, 4 μM anthranilate ($\approx 2 \times K_M$) and PRPP was varied from 0 to 250 μM for the various concentration of inhibitors, **4.17** to **4.19**. However, iminoribitol analogues **4.15** and **4.16** were only tested with PRPP at concentrations between 0 and 250 μM; anthranilate was kept at constant 10 μM ($\approx 5 \times K_M$).

The bis-phosphates **4.15** and **4.16** are either moderate or weak inhibitors of AnPRT and display K_i values of 235 ± 16 μM and 794 ± 76 μM, respectively (Table 4.3). The D-isomer **4.15** is a 3-fold stronger inhibitor of AnPRT than the L-isomer **4.16**. This might be due to the unfavourable configuration of the L-isomer **4.16** compared to the natural substrate PRPP. No enzymatic inhibition was observed for analogue **4.17** up to a concentration of 250 μM along with the PRPP substrate. The ligand **4.17** is likely to bind in the anthranilate tunnel and may not reach the PRPP binding site as observed for phosphonate analogues in Chapter 2 and the docked compounds in Chapter 3. However, the pyrimidine analogue **4.17** was a strong inhibitor with a K_i value of 17 ± 2 μM with respect to the anthranilate substrate for AnPRT.

Interestingly, the pyrimidine ring bonded directly with the iminoribitol ring in analogue **4.18** boosted AnPRT inhibition with respect to PRPP with a K_i value of $70 \pm 9 \mu\text{M}$ and weakened the enzymatic activity with respect to the anthranilate substrate with a K_i value of $114 \pm 12 \mu\text{M}$. Therefore, these results indicate that the pyrimidine analogue can also be considered in order to generate stronger AnPRT inhibitors in the future.

Table 4.3 The K_i values of different iminoribitol analogues along with both substrates for M. tuberculosis.

Code	Chemical structure	K_i (μM) against PRPP	K_i (μM) against anthranilate
4.15		235 ± 16	NA
4.16		794 ± 76	NA
4.17		No inhibition up to $250 \mu\text{M}$	17 ± 2
4.18		70 ± 9	114 ± 12
4.19		22 ± 4	93 ± 11

Instead of pyrimidine, the fusing of benzoate directly to the iminoribitol ring in mimic **4.19** strongly enhanced the inhibition of the enzyme with respect to the PRPP substrate (K_i value of $22 \pm 4 \mu\text{M}$) and weakened inhibition with respect to anthranilate (K_i value of $93 \pm 11 \mu\text{M}$). Based on the AnPRT inhibition assay, it can be concluded that the mimicking of the ribocation

characteristic with the insertion of a nucleophilic moiety may enhance the binding of analogues to catalytic sites of the enzyme as these iminoribitol analogues are competitive with respect to the PRPP and anthranilate substrates.

4.4.5 Crystallisation

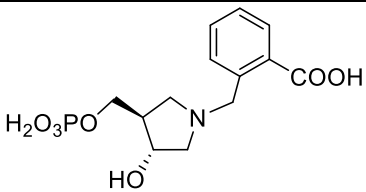
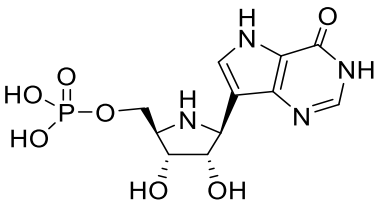
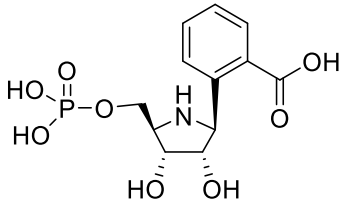
M. tuberculosis AnPRT was crystallised according to standard procedures; 3–5 mg/mL AnPRT in 50 mM Tris.HCl (pH 8.0), 150 mM NaCl and 5% glycerol (v/v)) were mixed 1:1 (v/v) with a reservoir solution containing 200 mM sodium imidazole malate (pH 6.5–8.0), 5%–15% PEG-4000. Analogues were either co-crystallised or the *apo* crystal was soaked in the presence of the ligand at concentrations varying from 10 to 50 mM. Several datasets were collected and refined for AnPRT, but no ligand density was observed for any inhibitors.

4.5 Docking of substrate mimics

Since no ligand density was observed for *M. tuberculosis* AnPRT complexed with the analogues, molecular modelling was used to determine the binding mode of the stronger inhibitors **4.18** and **4.19** to the catalytic site of the enzyme. The AnPRT/diphosphate/**5.8** structure (detailed in Chapter 5) was chosen to perform molecular modelling due to the similarity of the designed mimics to the transition state mimic **5.8**. Additionally, this is the only available *M. tuberculosis* AnPRT complexed with the potential transition state mimic **5.8** that binds at the enzyme catalytic site. Molecular modelling was performed by Dr Wanting Jiao using a standard induced fit protocol in the Schrödinger Suite, 2019. The receptor grid was centroid with ligand **5.8** within 5 Å of ligand **5.8** and the original diphosphate molecule kept at the active site of the enzyme. The ligand **5.8** was docked back into the receptor grid to validate the docking results.

The predicted docking poses of the ligands reveal that the binding positions of ligands **4.18** and **4.19** are almost similar to ligand **5.8**; binding into the PRPP and anthranilate binding site 1 (Figure 4.19, **A**). However, there are a number of distinct interactions observed for each ligand that may produce different docking scores and may also be a reason for the distinct enzyme inhibition with these ligands (Table 4.2 and Table 4.4).

Table 4.4 Structural representation of AnPRT inhibitors with their docking scores.

Code	Chemical structure	Docking score
5.8		-13.04
4.18		-11.32
4.19		-13.75

In detail, the phosphate group of **5.8** interacts with Ala141, Ser142, Gly110, Ser143, Asn203 residues and the C3 hydroxy group forms hydrogen bonds with Gly147 and the diphosphate molecule. However, the anthranilate moiety of mimic **5.8** interacts with Asn138 and Arg193 (Figure 4.19, **B**). Similarly, the iminoribitol ring of the docked ligand **4.18** makes contacts to identical residues, with an additional hydrogen bond to Thr108 being made with its amine group (Figure 4.19, **C**). However, the pyrimidine ring of **4.18** only makes a hydrogen bond to Asn138. The interaction of ligands with Arg193 is very crucial for AnPRT inhibition and the absence of an interaction with Arg193 in the predicted binding pose may be the reason for poor enzyme inhibition and the lower docking score observed for ligand **4.18**.

Moreover, the ligand **4.19** forms almost identical hydrogen bonds to transition state mimic **5.8** (Figure 4.19, **D**). However, the presence of the additional C2 hydroxyl group, along with changes in the position of the amine group in iminoribitol **4.19**, leads to additional interactions to Asn138 and Tyr108, respectively. Additionally, the C3 hydroxyl group of **4.19** makes hydrogen bonds to the diphosphate molecule instead of residue Gly147, as observed for analogue **5.8**. The shortened bond between the iminoribitol ring and the benzoate moiety in **4.19**, the presence of the additional C2 hydroxyl group, and the additional amine interactions drag the benzoate moiety of ligand **4.19** more inwards into the enzyme active

site compared to the transition state mimic **5.8**. This may explain strong enzyme inhibition of ligand **4.19** along with PRPP and the inhibition to weaken with respect to anthranilate.

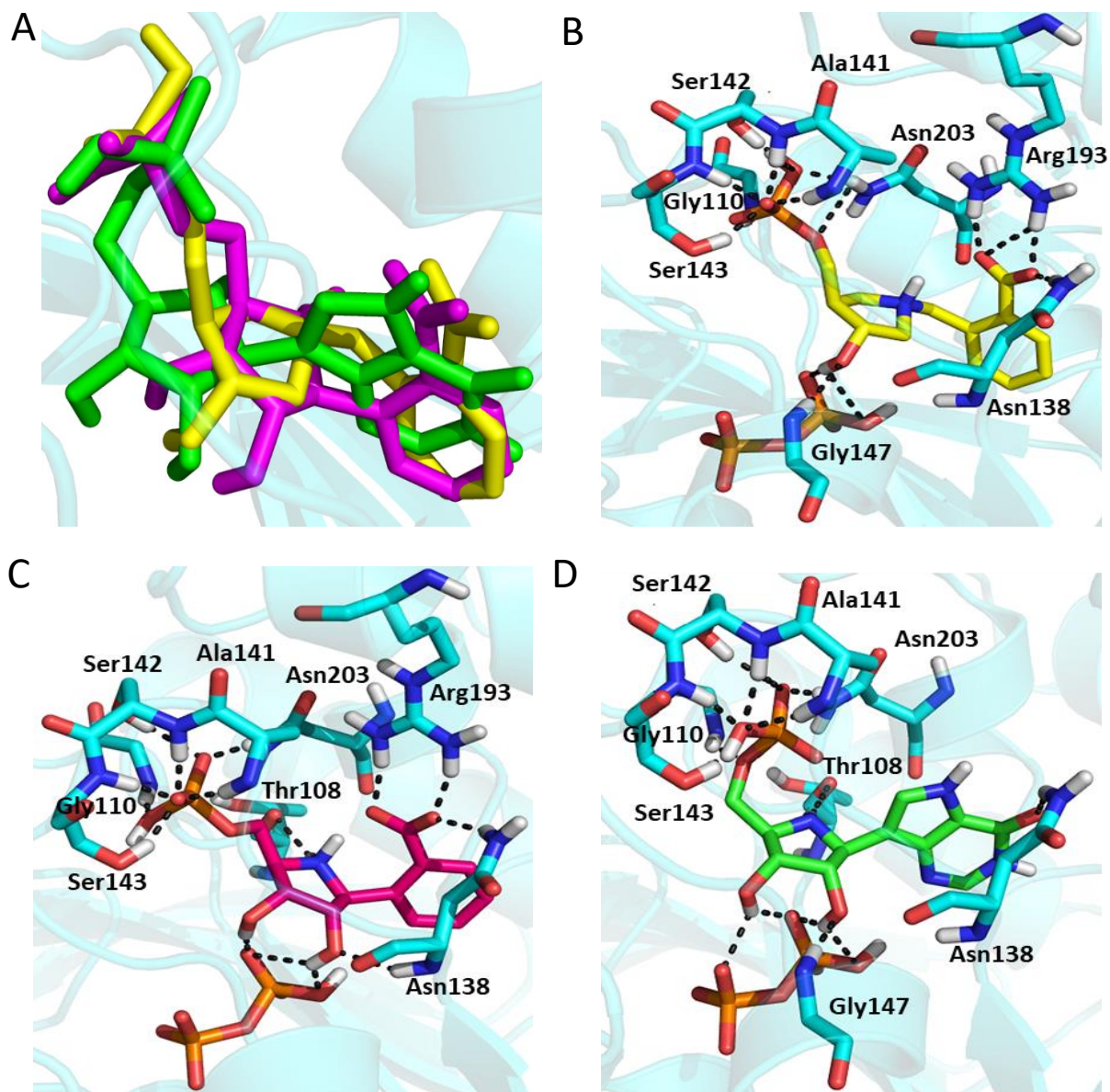


Figure 4.19 Stereo representation of the best docking poses of the AnPRT inhibitors predicted by induced fit docking.

(A) The overlay of the predicted docking poses of all the iminoribitol ligands, **5.8** (yellow), **4.18** (green) and **4.19** (pink). (B–D) The predicted binding interactions are displayed for each ligand individually. The active site residues are shown in cyan and the docked ligands are shown with distinct colours; **5.8** in yellow, **4.18** in pink and **4.19** in green. The diposphate groups are also present as brown sticks and polar contacts are represented by black dashed lines.

4.6 Summary

The active site of *M. tuberculosis* AnPRT was successfully explored in depth to understand the binding of substrates to the enzyme. The ligand binding to the enzyme was examined by structural analysis of *M. tuberculosis* AnPRT crystals, which were complemented by DSF and ITC studies. The obtained results indicate that the binding of PRPP and Mg^{2+} complexes is likely to occur during enzyme catalysis and the anthranilate substrate can bind at multiple sites within the tunnel without the binding of PRPP at the active site of the enzyme.

AnPRT can be inhibited strongly by the binding of a diphosphate molecule to the active site of the enzyme. Therefore, the introduction of a diphosphate group or a bioisostere of the diphosphate- Mg^{2+} complex may lead to strong inhibition of *M. tuberculosis* AnPRT. This hypothesis was supported by the doubling of the inhibitory effect of compound **4.14** in the presence of 100 μ M sodium diphosphate dibasic.

The analogues **4.11** and **4.14** were successfully synthesised using established strategies. Several analogues were tested against *M. tuberculosis* AnPRT and were found to be competitive inhibitors with respect to PRPP for the *M. tuberculosis* AnPRT enzyme. These results indicate that these analogues may have some characteristics of the transition state analogues. The stronger inhibition competency for the cyclopentene phosphate **4.12** suggests that the double bond characteristic around the reaction centre is an important aspect for inhibition. Interestingly, D-isomer **4.15** is a 3-fold stronger inhibitor for AnPRT than the L-isomer **4.16**. This suggests that the unfavourable configuration of the L-isomer **4.16** compared to the natural substrate PRPP may have an effect on its potency as a potential inhibitor to AnPRT. The iminoribitol analogues **4.18** and **4.19**, mimicking the ribocation characteristic of the natural substrate along with the insertion of a nucleophilic moiety, strongly enhanced enzyme inhibition. These results indicate that the nitrogen atoms of iminoribitol compounds can be protonated at physiological pH and act as a positive charge characteristic of the transition state mimic. The pyridine or benzoate moiety may occupy the nucleophilic binding position during catalysis. This hypothesis is further supported by molecular modelling, which predicted the binding of these analogues to the enzyme catalytic site with a high score. Therefore, these analogues may act as transition state mimics for *M. tuberculosis* AnPRT and can also be considered in order to generate stronger AnPRT inhibitors in the future.

Chapter 5 Towards transition state analogues for *M. tuberculosis* AnPRT

5.1 Overview

This chapter explores the inhibition of the *M. tuberculosis* AnPRT enzyme using putative transition state mimicking compounds to aid anti-TB drug design. Several compounds were chosen to be synthesised based on the likely reaction mechanism of the enzyme. The inhibition of the enzyme was successfully characterised using an enzyme-coupled assay and the compounds were found to be strong inhibitors of AnPRT. AnPRT was co-crystallised successfully with one of the strongest inhibitors among the tested compounds. Lastly, ITC analysis is presented; which was performed to reveal the stoichiometry of ligand binding to the enzyme.

5.2 Transition state

Transition state theory (TST) was first developed in 1935 and has been accepted as a tool for the interpretation of a wide variety of reaction rates of chemical reactions.^{139,140} It postulates that the substrates (S) are in equilibrium with the transition state (TS) and an enzyme (E) shifts this equilibrium through specific tight binding interactions to the TS in order to stabilise the transition state complex.¹⁴⁰ Energetically, the TS is the point on the reaction coordinate profile with the highest energy and this high energy barrier is the rate-determining step for the overall reaction (Figure 5.1).^{141,142}

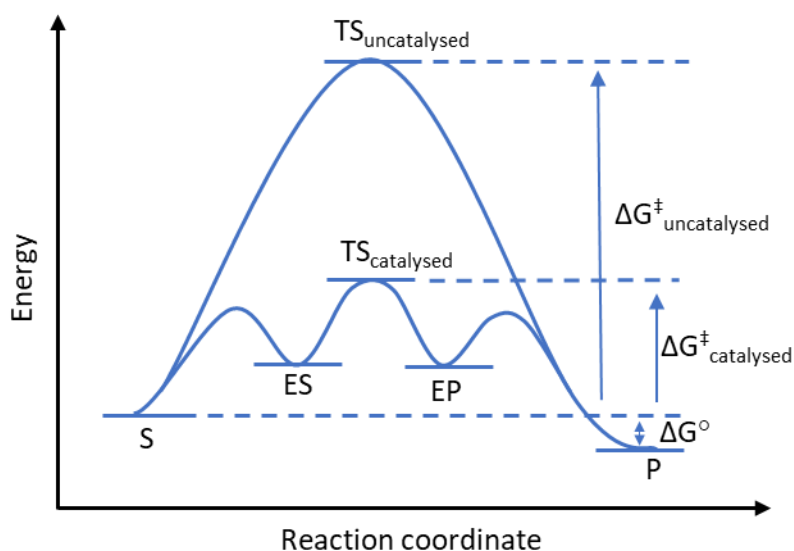


Figure 5.1 Reaction coordinate diagram for an enzyme-catalysed reaction involving the formation of enzyme-substrate (ES) and enzyme-product (EP) complexes.

The activation energy (ΔG^\ddagger), relative to the uncatalysed reaction, is decreased by the enzyme, resulting in a higher reaction rate. An enzyme-catalysed reaction is a multistep reaction and enzymes reach their enzyme-TS complex by dynamic conformational changes on the femtosecond to picosecond time scale.¹⁴³ However, these time scales are 10^8 to 10^{12} -fold slower than the lifetime of the TS.¹⁴⁴

5.3 Tight binding of transition state analogues

The tight binding of stable compounds that mimic the TS of an enzyme-catalysed reaction was first hypothesised based on TS theory (TST) in 1946 by Linus Pauling.¹⁴⁵ He states that during an enzyme-catalysed reaction, the substrate molecule binds to the enzyme and introduces the forces of attraction required to stabilise the transition state ($TS_{\text{catalysed}}$) in order to proceed the chemical reaction (Figure 5.1). Although the TS of an enzyme-catalysed reaction generally has a short lifetime ($\sim 10^{-15}$ s), a TS analogue can bind to an enzyme more tightly than a substrate by orders of magnitude - up to 10^{10} to 10^{18} times.¹⁴⁶ The binding energy of the TS analogue is proportional to the catalytic rate enhancement.¹⁴⁷

A TS analogue is a molecule that mimics the TS geometry, charge distribution and chemical functionality, delivering strong interactions at an enzyme binding site and resulting in a powerful inhibition.¹⁴⁸ The development of TS analogues as therapeutic agents requires characterisation of each specific TS of the enzyme-catalysed reaction, as a more complicated reaction progress profile for even a basic enzyme-catalysed reaction occurs compared to the uncatalysed reaction as binding steps are involved. Kinetic isotope effect (KIE) and quantum mechanics/molecular mechanics (QM/MM) methods can provide chemical models of the TS of enzyme-catalysed reactions. However, Wolfenden speculated in 1972 that it would be unrealistic to propose that an ideal transition state mimic, perfectly resembling the properties of the TS, could ever be synthesised.¹⁴⁸ The search for TS analogues grew rapidly after that, and by 1975 almost 60 putative analogues had been described.¹⁴⁹ Moreover, academic research groups have made an important contribution to the discovery of TS analogues and tight binding TS analogues are now well described in the literature.^{77,135,137,150} This chapter discusses work towards finding an alternative means to target the *M. tuberculosis* AnPRT

enzyme. Work involving the design and synthesis towards a putative TS analogue for this enzyme is described here.

5.4 Transition state analogue design

As discussed above, knowledge of the precise nature of the TS can guide the design of inhibitors, which may lead to very potent inhibitors. However, synthesis of these inhibitors is challenging and time-consuming. In a collaborative effort the Albert Einstein College of Medicine (USA) and Ferrier Research Institute (NZ) have been working on the design of TS analogues, in order to aid drug discovery.¹⁵¹ This collaboration has pursued iminosugar targets, where the anomeric oxygen of ribose is substituted by a nitrogen atom that can be protonated at biological pH. This protonated nitrogen would represent the positive charge at the TS, which should be able to exploit ionic interactions at the active site that are important for stabilising the TS. These particular derivatives have been shown to have high potency for nucleoside processing enzymes of human cancer cells and *Plasmodium falciparum* parasites and one compound has received market approval for the treatment of peripheral T-cell lymphoma in Japan.^{136,137}

At present, a model of the TS structure for AnPRT enzymes is unavailable. KIE analysis of the enzyme can give a direct manifestation of the TS. However, KIE studies on AnPRT are challenging due to the instability of the reaction substrate PRPP and the product PRA.¹⁵² Based on work done on other PRT enzymes and crystal structures solved for AnPRT, a dissociative “S_N1-like” reaction mechanism has been predicted for *M. tuberculosis* AnPRT (Section 1.9 and Figure 5.2).

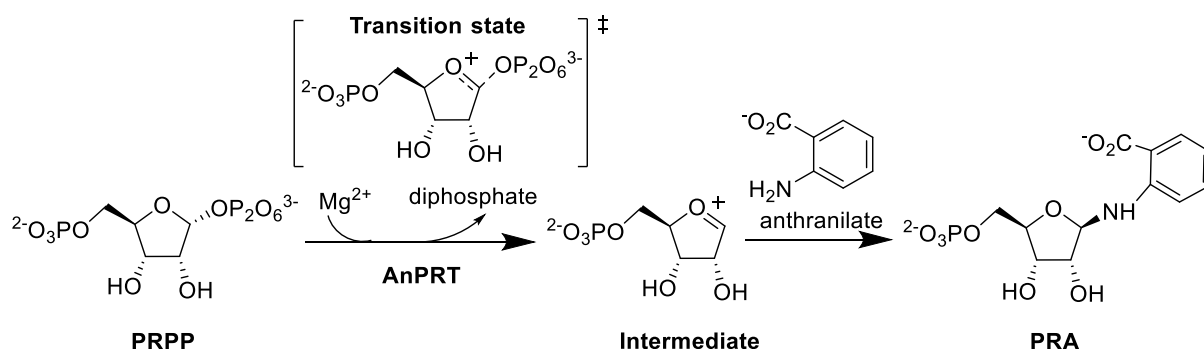


Figure 5.2 The possible dissociative “S_N1-like” reaction mechanism of AnPRT.

This mechanism suggests a TS with a positive charge at the ring oxygen atom and the geometry of the anomeric carbon centre that is altered from sp^3 (tetrahedral geometry) to sp^2 (trigonal planar geometry) character. An enzyme-catalysed reaction with an altered geometry or charge at a potential TS is an ideal target to design TS mimics.

Based on the earlier work of similar enzyme-catalysed reactions,^{136,137} three iminosugar derivatives (**5.2**, **5.6** and **5.8**) are proposed inhibitor designed for AnPRT (Figure 5.3).

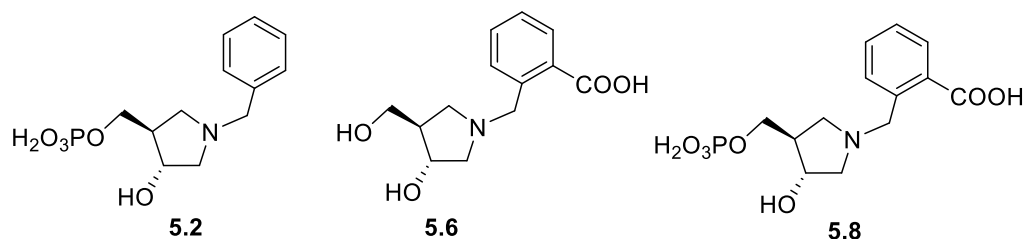


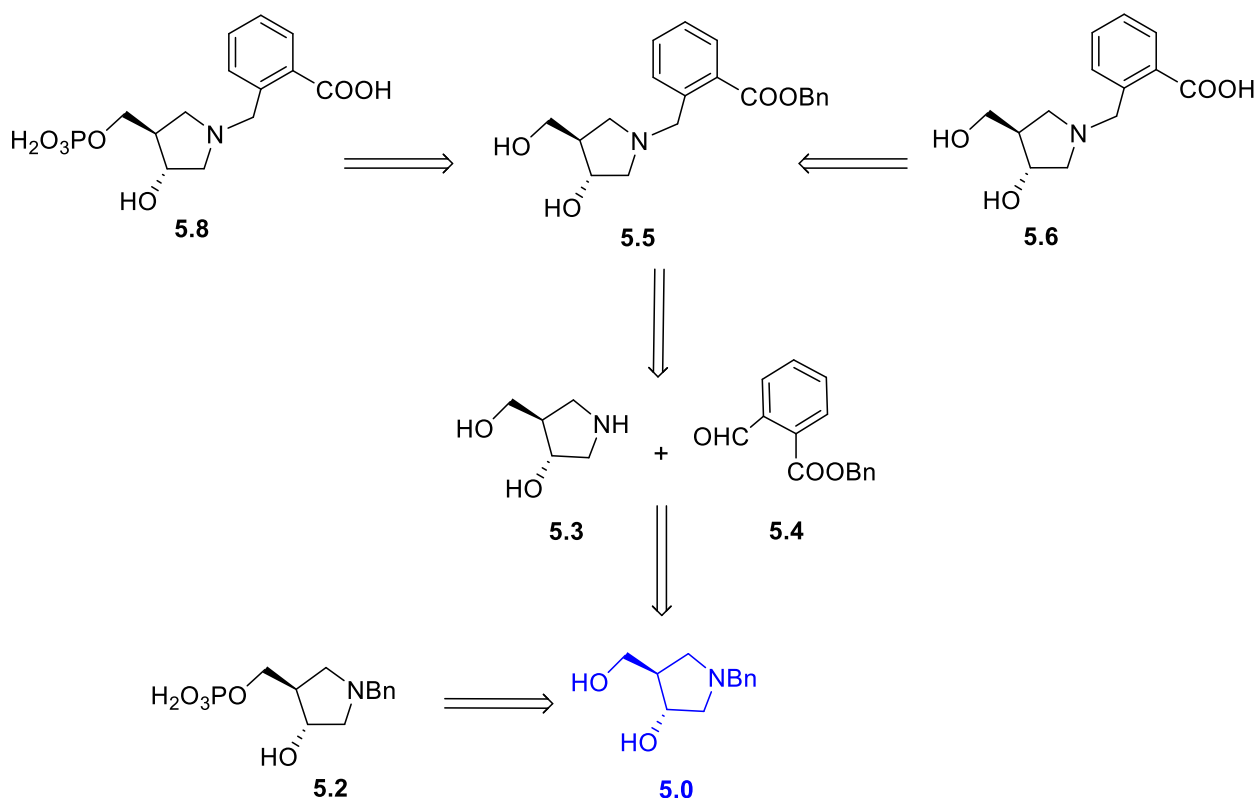
Figure 5.3 The chemical structures of potential transition state analogues for AnPRT.

These compounds are supposed to capture the geometry of the flattened ribose ring and include a nitrogen atom within the ring to mimic the positive charge characteristics that are expected in the oxocarbenium-ion-like TS. The carboxylate group plays a major role in the binding of ligands to the anthranilate binding tunnel of AnPRT, as discussed in Chapter 2. Therefore, analogue **5.2**, characterised by the absence of the carboxylate group, was chosen to favour the binding of the ligand within the PRPP binding site of the enzyme. The ribose phosphate group plays an important role in PRPP binding, so it was therefore included in compound **5.2**. To determine the effect of ligand binding without the phosphate moiety, the phosphate moiety was excluded in analogue **5.6**. In compounds **5.6** and **5.8**, the ribosyl mimic and the anthranilate-like moiety are joined through the insertion of a methylene bridge along with the replacement of the amine group of the anthranilate part of the molecule. The aim of introducing the anthranilate-like moiety is to mimic the characteristics of the anthranilate substrate that may also act as a potential hook to facilitate the binding of the ribosyl mimic of analogues **5.6** and **5.8** to the catalytic site of AnPRT.

5.5 Synthesis of transition state analogues

5.5.1 Retrosynthetic analysis

A scheme for the synthesis of all iminosugar derivatives was designed from a common precursor (3*R*,4*R*)-1-benzyl-4-(hydroxymethyl)pyrrolidin-3-ol **5.0** (Scheme 5.1), which was provided by Professor Peter Tyler (Ferrier Research Institute, NZ).



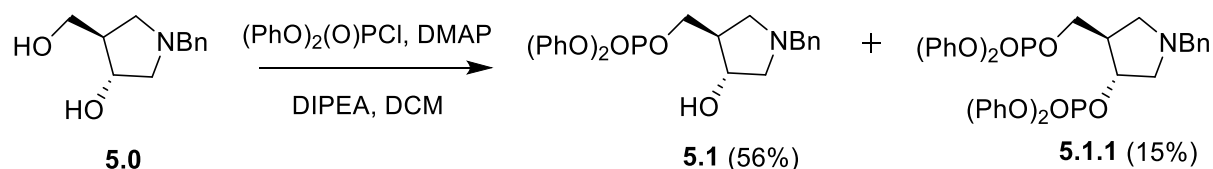
*Scheme 5.1 Retrosynthetic analysis for different analogues from precursor **5.0**.*

It was envisaged that compound **5.8** could be derived from cyclopentane **5.0** in five steps. It was predicted that phosphorylated cyclopentane **5.8** could be obtained from protected cyclopentane **5.5** in two steps via the selective primary phosphorylation with trimethyl phosphite, followed by global deprotection of the ester groups. The reduced amine **5.5** could be obtained with amine **5.3** and aldehyde **5.4**. The amine **5.3** could be synthesised by hydrogenation of benzyl protected pyrrolidine **5.0**. However, another building unit, aldehyde **5.4**, could be obtained by selective acid group protection of 2-formylbenzoic acid through a benzylation reaction. The alternate target **5.6** could be easily achieved with de-esterification

from **5.5** by hydrogenation and additional target **5.2** could be obtained from common precursor **5.0** in two steps; primary phosphorylation with diphenyl phosphoryl chloride followed by Birch reduction.

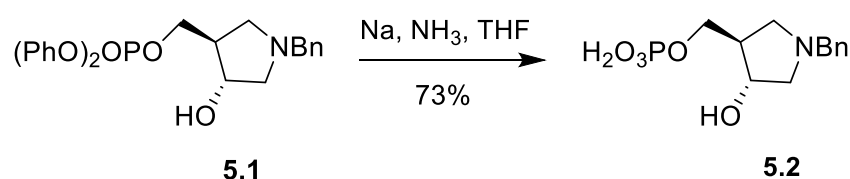
5.5.2 Detailed synthesis of phosphorylated amine **5.2**

To synthesise analogue **5.2**, the phenyl protected phosphate was chosen as the starting product because it can be readily deprotected using a Birch reduction. Hydroxymethyl **5.0** was subjected to 1.2 equivalents of diphenyl phosphoryl chloride and a poor nucleophilic base, diisopropylethylamine (Hünig's base) in DCM (Scheme 5.2). DMAP was used as a catalyst. The reaction yielded primary phosphorylated **5.1** as a major product (56%) and diphosphorylated benzylamine **5.1.1** (15%) as a minor product, which were easily separated using a silica column.



Scheme 5.2 The synthesis of phosphorylated cyclopentane benzylamine.

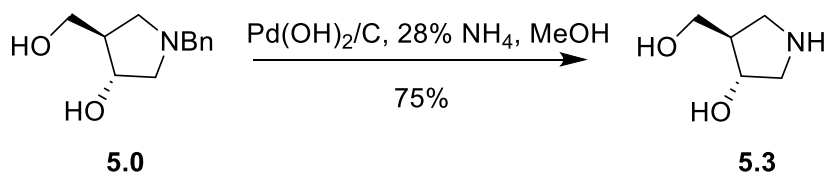
After that, a Birch reduction was performed (Scheme 5.3) and the crude product was purified on a Bio-Gel P2 SEC column with ammonium acetate (100 mM) and a water gradient to give phosphocyclopentane benzylamine **5.2** in 73% yield (Section 7.3.1).



*Scheme 5.3 The formation of the targeted cyclopentane benzylamine **5.2** using a Birch reduction.*

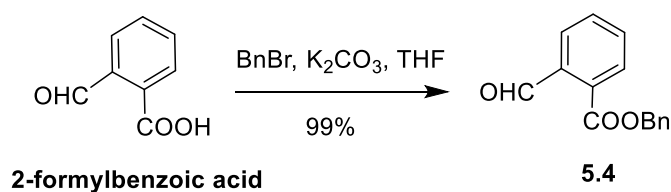
5.5.3 Detailed synthesis of iminosugar derivative 5.8

To synthesise target **5.8**, debenzylation of the benzyl protected pyrrolidine **5.0** was conducted. The most common method in the literature for debenzylation of a secondary amine has been reported with 10% Pd/C at 50 °C for 3 days in an atmosphere of H₂ gas.¹⁵³ However, this is a time-consuming process even at high temperatures, therefore, other approaches were examined in order to achieve the reaction efficiently. Deprotection of *N*-benzyl amine **5.0** was attempted using 10% Pd/C in the presence of ammonium formate in methanol with reflux of the reaction mixture for 2 h. However, no desired product was obtained. Another literature approach was trialled¹⁵⁴ by treating pyrrolidine **5.0** with Pearlman's catalyst (Pd(OH)₂/C) and 28% aqueous ammonia in methanol and the desired product **5.3** was achieved in good yield (75%) without further purification (Scheme 5.4).



Scheme 5.4 Synthesis of reduced iminosugar 5.3.

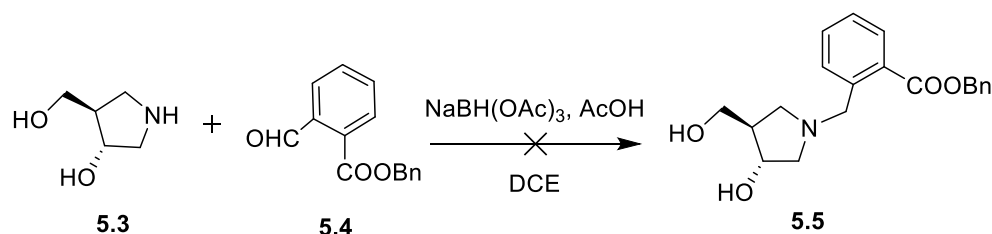
To synthesise building block **5.4** (Scheme 5.5), the ester group of 2-formylbenzoic acid was selectively protected with benzyl bromide in the presence of potassium carbonate, which afforded benzyl 2-formylbenzoate **5.4** in excellent yield (99%).



Scheme 5.5 Esterification for benzyl 2-formylbenzoate 5.4.

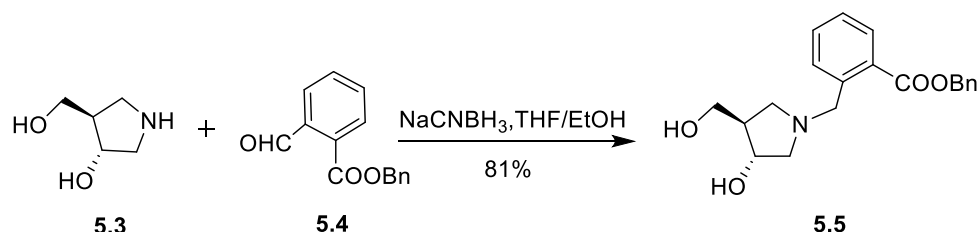
After that, a reduction reaction of secondary amine **5.3** and benzyl 2-formylbenzoate **5.4** was performed to achieve the tertiary amine **5.5**. To work on hydride-induced reductive aminations of aldehydes, sodium triacetoxyborohydride [NaBH(OAc)₃] was selected as this bulky borohydride reagent is mild, safe and exhibits remarkable activity with imines than aldehydes.¹⁵⁵ 1,2-Dichloroethane (DCE) was used as the reaction solvent and acetic acid was

chosen as a catalyst. Usually, these types of reactions are perceived faster in DCE than THF.¹⁵⁵ Unfortunately, no desired product formation was observed under these conditions (Scheme 5.6). The steric factors associated with using the secondary amine may have been the reason for no product being formed.



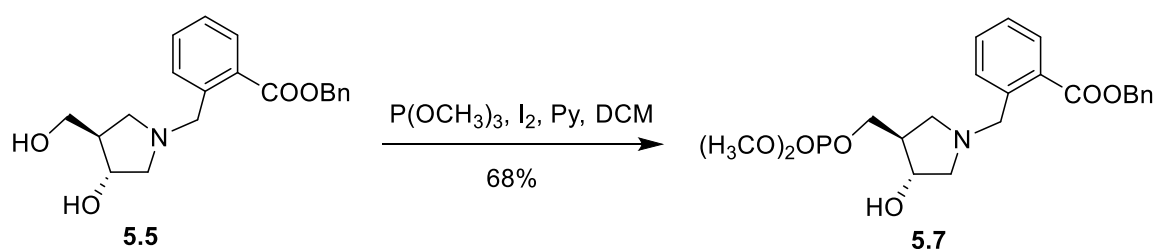
*Scheme 5.6 The reduction reaction did not yield the desired product **5.5**.*

Sodium cyanoborohydride (NaCNBH_3) was used as an alternative reducing agent as this reagent displays greater stability in acidic conditions and solubility in aprotic solvents.¹⁵⁶ The reduced product **5.5** was successfully achieved using NaCNBH_3 in a 3:1 ratio of THF/EtOH solvent in 81% yield (Scheme 5.7).



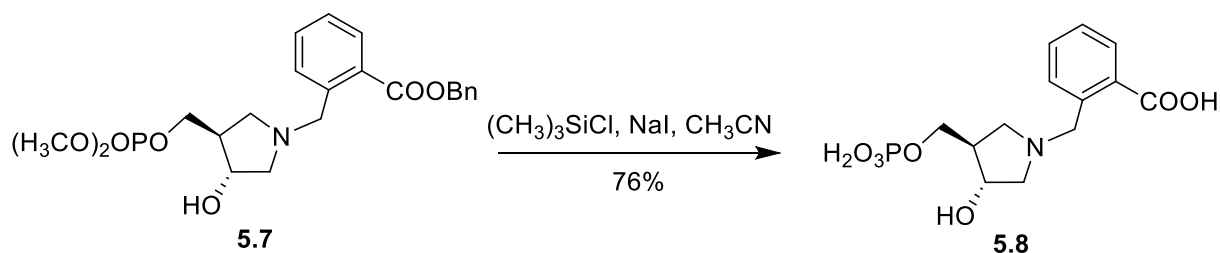
*Scheme 5.7 Synthesis of reduced iminosugar derivative **5.5**.*

Furthermore, for the synthesis of the methyl phosphorylated amine derivative **5.7** (Scheme 5.8), the primary alcohol of iminosugar **5.5** was selectively phosphorylated¹⁵⁷ using one equivalent of trimethyl phosphite in DCM, followed by oxidation with iodine. The reaction was quenched by pyridine to successfully produce **5.7** in 68% yield.



*Scheme 5.8 The primary phosphorylation of hydroxymethyl **5.7**.*

For the global deprotection of ester **5.7** (Scheme 5.9), iodotrimethylsilane was generated *in situ*, to avoid the formation of undesirable by-products, by treating trimethylsilyl chloride with anhydrous sodium iodide (NaI) in dry acetonitrile (CH₃CN).¹⁵⁸ A yellow coloured solution was obtained with the immediate formation of a white precipitate of sodium chloride. The reaction was monitored by TLC and the crude product of **5.8** was purified on a cation exchange column.

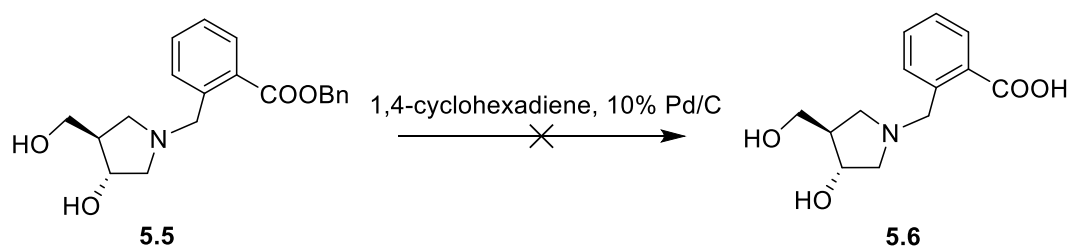


Scheme 5.9 The deprotection step to afford final product 5.8.

Unfortunately, the product was not pure enough to be used in bioassays. The eluent from the cation exchange column was therefore further purified using a SOURCE Q anion exchange column with a linear gradient of H₂O/0.1 M NH₄HCO₃ to achieve **5.8** successfully in 76% yield (Section 7.3.2).

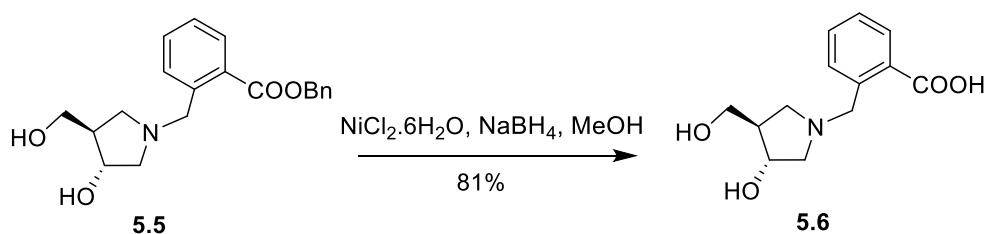
5.5.4 Detailed synthesis of hydroxymethyl pyrrolidine derivative 5.6

To achieve the synthesis of target **5.6**, selective hydrogenation of benzyl ester **5.5** was required but the literature lacks reports on selective hydrogenolysis of benzyl esters in the presence of benzylamines. There are only a few examples in which a benzyl ester has been cleaved in the presence of benzyl ether.^{159,160} The catalytic transfer hydrogenation using various hydrogen donors such as 1,4-cyclohexadiene,¹⁶⁰ formic acid¹⁶¹ and ammonium formate^{162–164} is a general method for the reduction reaction. Partial debenzylation of tertiary and secondary amines can also be achieved using an oxidizing agent such as ceric ammonium nitrate.¹⁶⁵ Firstly, debenzylation of **5.5** was tried with 1,4-cyclohexadiene and Pd/C. Unfortunately, *N*-debenzylolation also occurred with cleavage of benzyl ester (Scheme 5.10).



*Scheme 5.10 De-esterification with 1,4-cyclohexadiene did not yield the desired product **5.6**.*

Another approach for cleaving the ester group chemo-selectively was tried using nickel chloride.¹⁶⁶ Benzyl ester **5.5** was refluxed in methanol to which $\text{NiCl}_2 \cdot 6\text{H}_2\text{O}$ was added. This was followed by the addition of NaBH_4 , which resulted in the formation of black precipitates of nickel boride and the desired product **5.6** (Scheme 5.11).



Scheme 5.11 De-esterification with nickel chloride and NaBH_4 .

Size exclusion chromatography using a Bio-Gel P2 SEC column was performed with ammonium acetate (25 mM) and a water gradient to afford clean product **5.6** in 81% yield (Section 7.3.2).

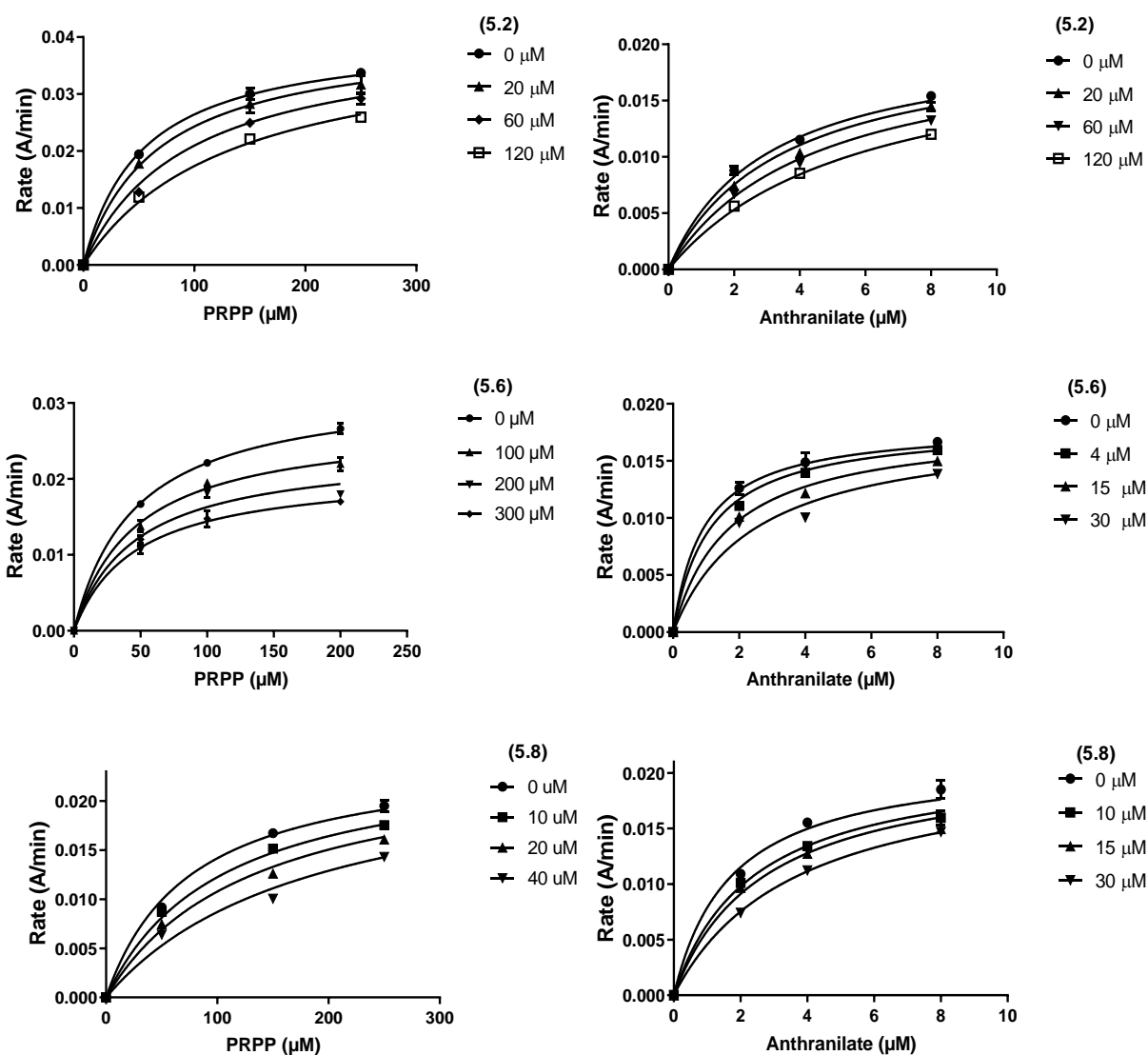
5.6 Inhibition study of *M. tuberculosis* AnPRT with analogues

5.6.1 Steady-state kinetics

The synthesised compounds were tested against *M. tuberculosis* AnPRT enzyme (Section 7.1.17.4). The actual concentration of these compounds was measured using Lanzetta assay, excluding compound **5.6** (which does not contain a phosphate group) which was calculated using weight/volume measurements. The steady-state kinetic parameters were obtained by holding one substrate at a low concentration ($2 \times K_M$) while varying the concentrations of the other substrate and an inhibitor (Figure 5.4, 5.5 and Table 5.1). As the proposed inhibitors were designed to fit into both substrate binding sites, the concentration of one substrate was

kept low ($2 \times K_M$) to avoid substrate saturation of the enzyme. This, in turn, would allow the inhibitors to have better access to compete with the other substrate in varying concentrations.

Previously, the Schramm group reported that phosphate groups have improved the binding of TS inhibitors to the purine NP enzyme.^{151,167} Therefore, it would be interesting to examine the activity of *M. tuberculosis* AnPRT with analogue **5.8** in the presence and absence of diphosphate or monophosphate. Hence, the additive assay was performed with diphosphate held at a concentration of 100 μM or monophosphate retained at 1 mM to avoid enzyme inhibition.



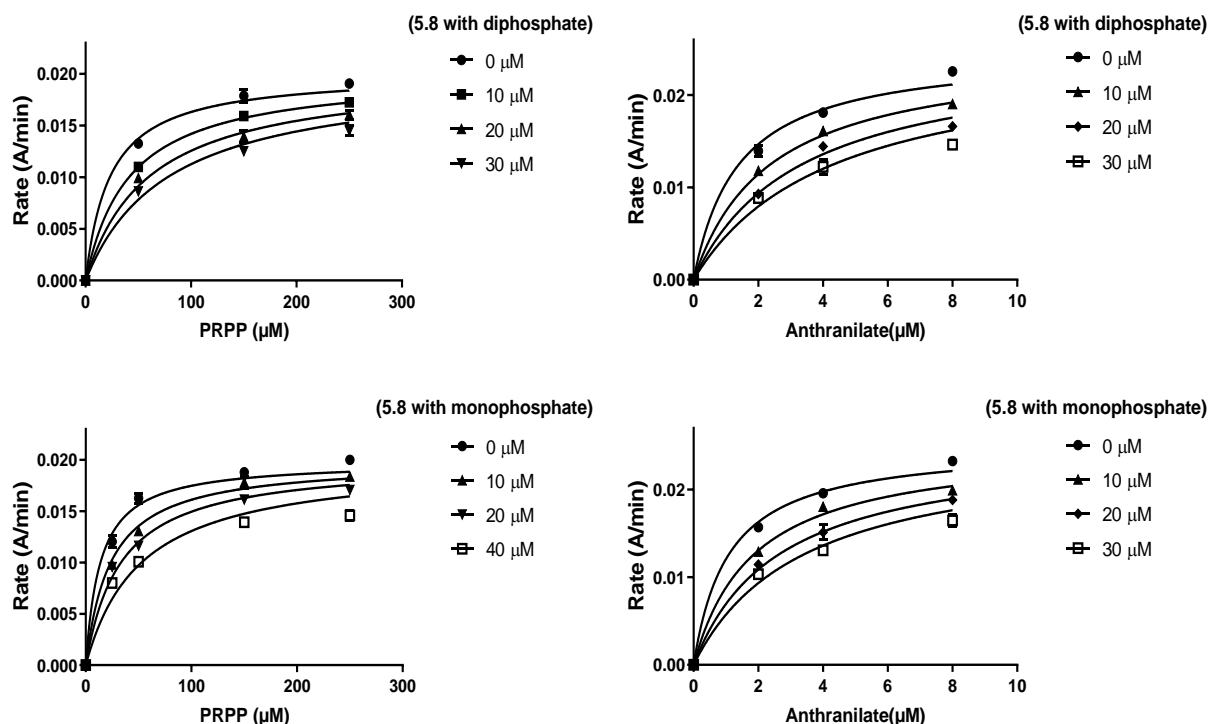


Figure 5.4 *M. tuberculosis* AnPRT inhibition graphs for different compounds.

For the determination of the K_i values, assays contained 50 mM Tris. HCl (pH 8.0), 150 mM NaCl, 1 mM $MgCl_2$, 0.04 μM AnPRT, 0.6 μM *E. coli* PRAI: InGPS, anthranilate varied from 0 to 8 μM, PRPP varied from 0 to 250 μM while the other substrate was kept constant ($\approx 2 \times K_M$) and inhibitors were used at various concentrations. The K_i values were calculated using graphing software GraphPad Prism7.

Interestingly, the kinetic studies show that all compounds could inhibit *M. tuberculosis* AnPRT (Figure 5.5 and Table 5.1). With respect to PRPP, analogue **5.2** proved to be a stronger inhibitor with an apparent K_i value of 80 ± 6 μM than compound **5.6**, which was weaker, with a K_i value of 561 ± 48 μM. Inhibitor **5.6** is less likely to compete with PRPP without the phosphate moiety. Accordingly, the kinetic data for compound **5.6** was fitted best with non-competitive inhibition with respect to PRPP and competitive inhibition with respect to anthranilate.

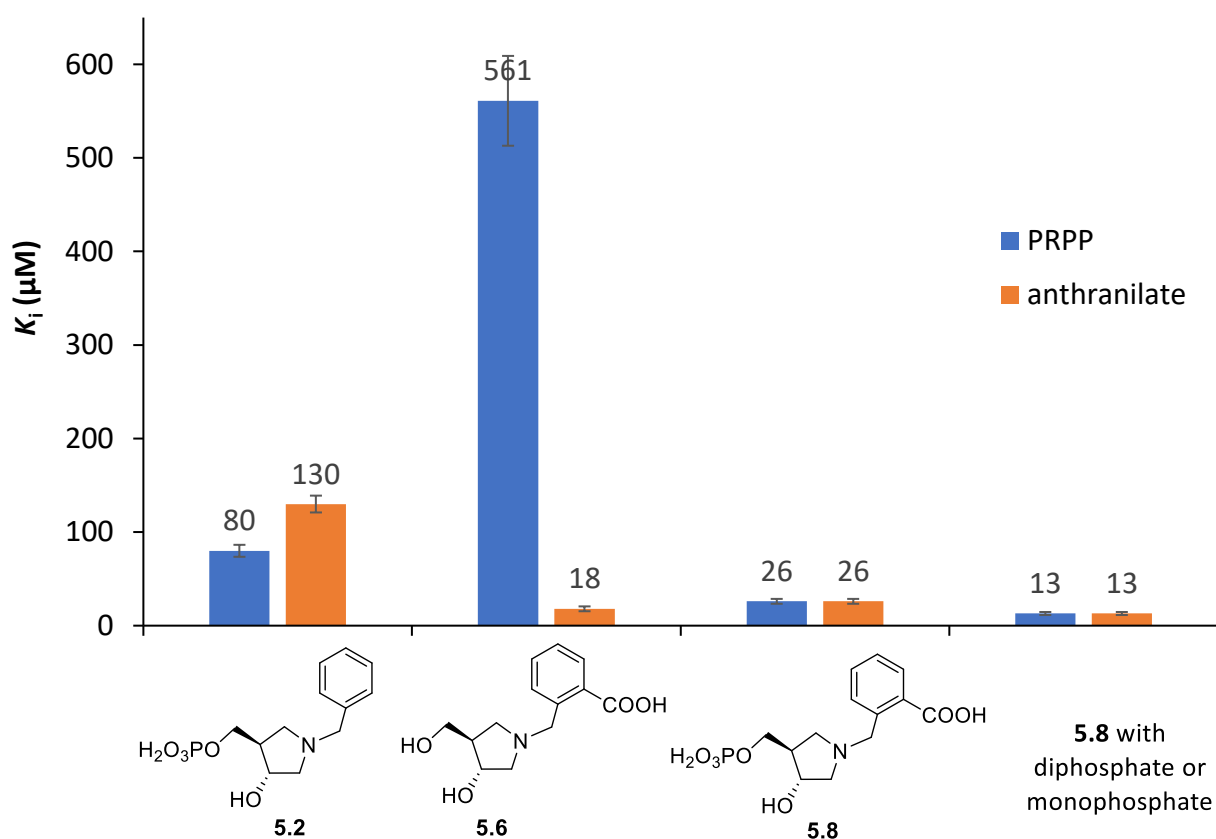
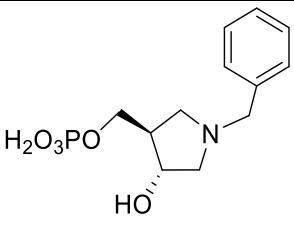
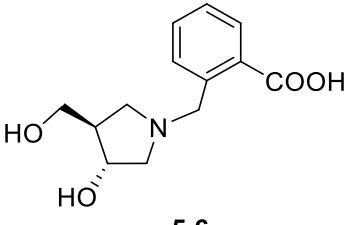
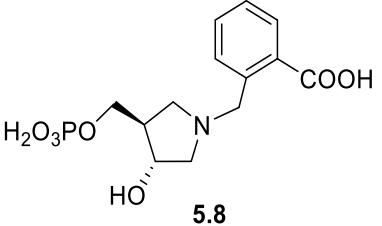


Figure 5.5 The apparent K_i values of *M. tuberculosis* AnPRT inhibitors compared to both substrates.

Inhibition with respect to the anthranilate substrate, the introduction of the carboxylate group in compound **5.6** has a high impact on the K_i value; an almost 7-fold decrease is observed for compound **5.6** (K_i^{anth} value of 18 ± 2.6 μ M), compared to analogue **5.2** where the carboxylate group is absent (K_i^{anth} value of 80 ± 6.4 μ M). These results also indicate, as expected, that the carboxylic acid functionality plays a crucial role in binding anthranilate within the substrate binding tunnel. This role has also been supported by observations from X-ray crystal structures of AnPRT.^{57,71,74} Consequently, the kinetic parameters for inhibitor **5.6** fitted best to a non-competitive inhibition model with respect to PRPP and competitive inhibition with respect to anthranilate.

Table 5.1 The types of inhibition with the apparent K_i values displayed for AnPRT inhibitors.

Chemical structure with code	Type of inhibition with PRPP	Apparent K_i (μM) with PRPP	Type of inhibition with anthranilate	Apparent K_i (μM) with anthranilate
 <p>5.2</p>	competitive	80 ± 6	Non-competitive	130 ± 9
 <p>5.6</p>	Non-competitive	561 ± 48	competitive	18 ± 3
 <p>5.8</p>	competitive	26 ± 3	competitive	26 ± 3
5.8 with diphosphate or monophosphate	competitive	13 ± 2	competitive	13 ± 2

Interestingly, the ribosyl and anthranilate mimic **5.8** is the strongest inhibitor among these compounds with an apparent K_i value of $26 \pm 3 \mu\text{M}$ with respect to both substrates of *M. tuberculosis* AnPRT. Correspondingly, compound **5.8** was fitted to a competitive inhibition model with respect to both substrates. Remarkably, *M. tuberculosis* AnPRT had apparent K_i values of $13 \pm 2 \mu\text{M}$ with respect to both substrates for compound **5.8** in the presence of either $100 \mu\text{M}$ diphosphate or 1 mM monophosphate. These results provide an indication that diphosphate and phosphate molecules can block the active site of AnPRT effectively along with the binding of analogue **5.8**.

5.7 Crystal structures of inhibitors bound to AnPRT

5.7.1 Crystallography

Crystal structures of *M. tuberculosis* AnPRT in complex with the synthesised ribosyl mimics were pursued using X-ray diffraction methods in order to rationalise structurally the characteristics of the ligand binding and the kinetic properties observed for these inhibitors. The enzyme crystals were grown in complex with the tested inhibitors using the procedure described in Section 7.1.19. The AnPRT crystals were either co-crystallised with synthesised analogues **5.2** and **5.6** at concentrations varying from 5 mM to 10 mM with 20 mM Mg^{2+} or an apo crystal of AnPRT was soaked with compounds **5.2** or **5.6** at a concentration of 10 mM. Generally, crystals that did not break up or dissolve during this treatment were looped, cryoprotected and flash frozen. Several datasets were collected for enzymes in complex with analogues **5.2** and **5.6**; however, no density was observed for these compounds for any of these crystals. This observation might be indicative of a weak binding affinity to the enzyme for these analogues. However, several attempts at varying the concentration of ligand **5.8** from 5 mM to 20 mM with 20 Mg^{2+} either failed to produce AnPRT crystals or the apo crystals cracked when attempts were made to soak in ligand **5.8** at concentrations of 10 mM and 20 mM. Ultimately, *M. tuberculosis* AnPRT crystals grew after 4 months with inhibitor **5.8** (10 mM), MgCl_2 (20 mM) and diphosphate (5 mM) using standard reservoir conditions (Table 7.3). X-ray diffraction data for this crystal was collected at the Australian Synchrotron using the MX2 beamline.

5.7.2 Structure determination

The crystal structure of *M. tuberculosis* AnPRT bound with inhibitor **5.8** was refined to a resolution of 2.34 Å. Data were solved using a protocol explained in Section 7.1.19. Data collection and refinement statistics are shown in Table 5.2.

Table 5.3 Data collection and refinement statistics for AnPRT/5.8/diphosphate structure.

<i>M. tuberculosis</i> AnPRT complexed with 5.8/diphosphate	
Data Collection	
Space group	<i>P</i> 2 ₁ 2 ₁ 2 ₁
Cell dimensions	
a, b, c (Å)	56.4, 89.9, 140.1
α, β, γ (°)	90.0, 90.0, 90.0
No. of unique reflections	30,537
Resolution range (Å) ^a	75.67–2.34 (2.42–2.34)
R _{merge} ^a	0.084 (0.396)
R _{p.i.m.} ^a	0.025 (0.12)
CC _{1/2} ^a	0.999 (0.782)
I/σ(I) ^a	14.9 (4.2)
Completeness ^a (%)	99.1 (100)
Redundancy ^a	12.7 (12.6)
Wilson B-factor (Å ²)	38.4
Refinement	
R _{work} /R _{free} (%/%) ^{a,c}	0.207/0.237 (0.214/0.276)
No. of atoms and B factor ^b (Å ²)	
Protein	4868, 41.0
Solvent	51,34.7
Ligands	22,39.6
Ligand (diphosphate)	9 at 0.5 occupancy, 56.3
Ramachandran	
Preferred (%)	98.24
Allowed (%)	1.47
outliers (%)	0.29
RMSD of	
Bond lengths (Å) ^d	0.010
Bond angles (°) ^d	1.34

^a Outer resolution shell is shown in parentheses.

^b The average atomic temperature factor.

^c $R_{work} = (|F_{obs}| - |F_{calc}|) / |F_{obs}|$ and $R_{free} = \sum T (|F_{obs}| - |F_{calc}|) / \sum T |F_{obs}|$, where *T* is a test data set of 5% of the total reflections randomly chosen and set aside before refinement.

^d RMSD from ideal geometry values from Engh and Huber (1991).¹¹³

M. tuberculosis AnPRT in complex with ligand **5.8** crystallised in an orthorhombic space group (*P*2₁2₁2₁), the most common space group recorded for this enzyme. Over 40 structures have been reported for *M. tuberculosis* AnPRT. However, the unit cell dimensions for the AnPRT/**5.8**/diphosphate structure were distinctive from any previously reported *M. tuberculosis* AnPRT structures (Table 5.3). The distinctive unit cell dimensions for this AnPRT/**5.8**/diphosphate structure could be due to a change in the conformation of the enzyme that occurred by the binding of ligands (detailed in Section 5.7).

Table 5.3 M. tuberculosis AnPRT structures with PDB code, space group and cell parameters.

PDB code	Space group	Cell dimensions (Å)	Unit cell angle β (°)	Reference
AnPRT/ 5.8 /diphosphate	<i>P</i> 2 ₁ 2 ₁ 2 ₁	56, 90, 140	90	This study
5C2L, 4N8Q, 4ZTV, 4N93, 4ZTV, 4X58, 4X59, 4X5D	<i>P</i> 2 ₁ 2 ₁ 2 ₁	79, 91, 120	90	66,74
3QR9, 4M0R, 4MOV	<i>P</i> 2 ₁ 2 ₁ 2 ₁	79, 92, 120	90	69,74
4OWU, 4OWO, 4OWM	<i>P</i> 2 ₁ 2 ₁ 2 ₁	79, 92, 121	90	74
4OWQ	<i>P</i> 2 ₁ 2 ₁ 2 ₁	79, 92, 122	90	74
4X5D, 4OWS, 4OWN	<i>P</i> 2 ₁ 2 ₁ 2 ₁	80, 92, 121	90	66
4N5V	<i>P</i> 2 ₁ 2 ₁ 2 ₁	80, 93, 121	90	74
2BPQ, 1ZVW	<i>P</i> 2 ₁ 2 ₁ 2 ₁	81, 82, 118	90	60
4ZOJ	<i>P</i> 2 ₁ 2 ₁ 2	79, 111, 79	90	-
4GIU, 4GKM	<i>P</i> 2 ₁ 2 ₁ 2	111, 80, 79	90	69
5BYT	<i>P</i> 2 ₁ 2 ₁ 2	112, 81, 79	90	54,68
5BNE	<i>P</i> 12 ₁ 1	77, 78, 117	90	54,68
3QS8	<i>P</i> 12 ₁ 1	78, 81, 111	90	71
3TWP, 3UU1	<i>P</i> 12 ₁ 1	79, 111, 81	90	71
3QQS, 4ZOK	<i>P</i> 12 ₁ 1	95, 78, 102	111	71
1ZYK	<i>P</i> 121	93, 66, 117	108	55
5C1R, 5C7S, 3R88, 5BO2, 4ZOF	<i>C</i> 121	94, 78, 100	110	54,68
4X59, 4X5A, 4X5B, 4X5C, 3R6C, 4X5E, 5BO3	<i>C</i> 121	95, 78, 102	112	66,74

5.8 The binding mode for inhibitor 5.8 with AnPRT

In the AnPRT/Mg²⁺/diphosphate structure, two separate monomers are present within the asymmetric unit, though a homodimer can be generated via crystallographic symmetry. Chain A crystallised in an apo form, with no ligands present, whereas chain B displayed clear density for inhibitor **5.8**, modelled with an occupancy of 1. A diphosphate molecule was also found trapped at this active site; this was modelled with an occupancy 0.5. The occupancies of the **5.8**/diphosphate ligands were similar to the concentration ratio (1:0.5) of **5.8**/diphosphate ligands that were present in the crystallisation condition. However, intriguingly, no clear density was observed for Mg²⁺ ions, which were available in the crystallisation condition at a high concentration of 20 mM. The *M. tuberculosis* AnPRT (PDB: 4N5V) structure containing PRPP, Mg²⁺ and 4FA ligands, the most likely structure to accurately represent the binding state of the natural ligands, was chosen to compare with the AnPRT/**5.8**/diphosphate structure. 4FA is accepted as an alternate substrate by *M. tuberculosis* AnPRT and binds at the anthranilate site within the substrate binding tunnel.⁵⁷

The AnPRT/PRPP/4FA/Mg²⁺ structure shows two 4FA molecules bound to each chain of the dimer, with one bound at site 1 and the other bound at site 3. The position of 4FA at site 1 is the closest position observed for the binding of a nucleophilic anthranilate analogue to the binding position of PRPP. An overlay of chain A (PDB: 4N5V) accommodating PRPP, 4FA, Mg²⁺ and chain B containing **5.8** and diphosphate shows that ligand **5.8** binds at the catalytic site of AnPRT (Figure 5.6). The anthranilate-like moiety of compound **5.8** occupies the same position as the 4FA molecule at site 1 within the anthranilate binding tunnel. Interestingly, the 'ribose' ring of analogue **5.8** is observed shifted towards the nucleophile binding site, relative to its position in PRPP. However, variability in the positioning of the ribose ring of the PRPP molecule has been recorded previously.⁵⁷ The trace diphosphate molecule can also be spotted at the active site and overlays well with the diphosphate moiety of the PRPP molecule. It is speculated that the binding of diphosphate mimics the role of PRPP binding that is required in the reaction.

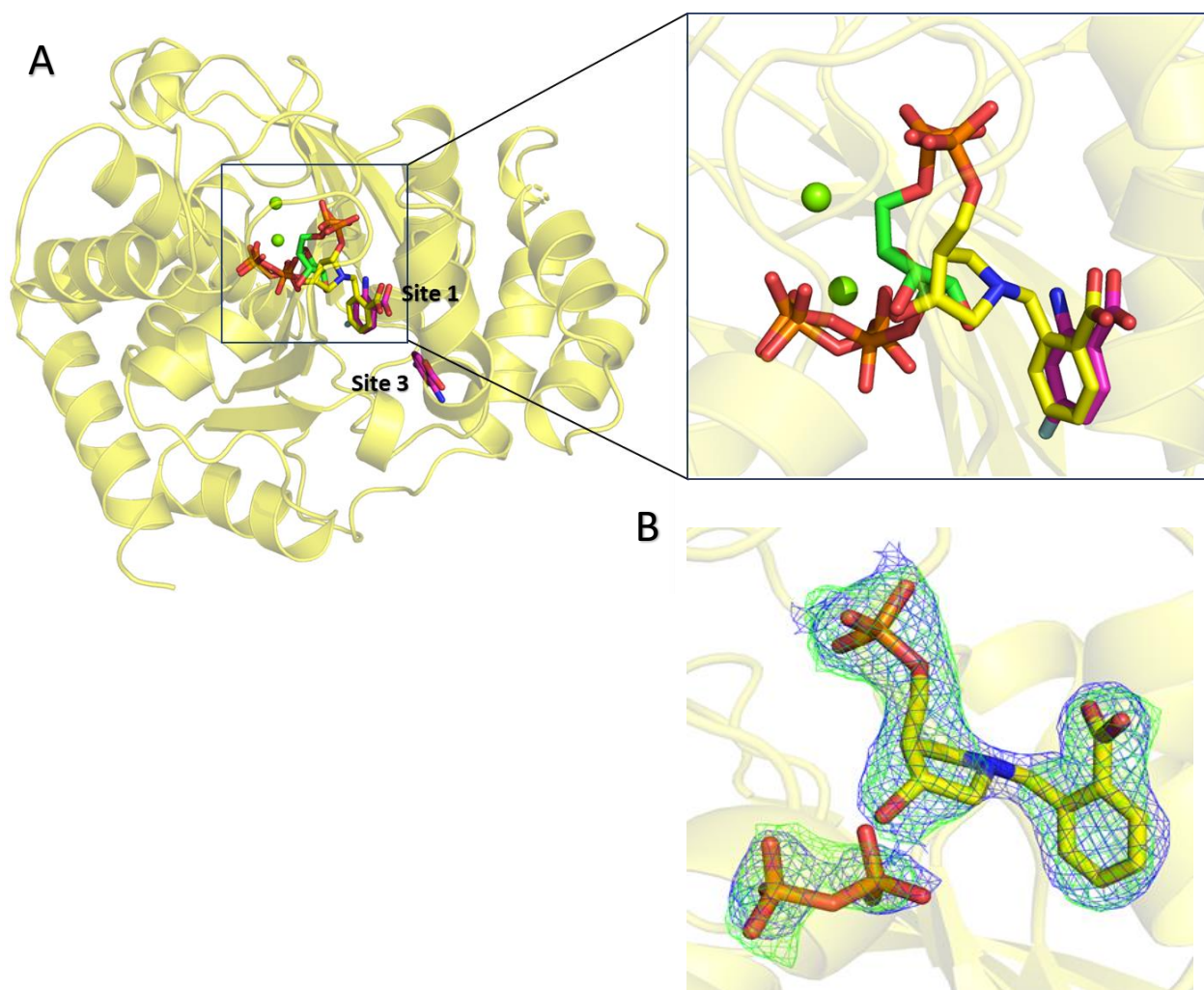


*Figure 5.6 Structural superimpositions reveal inhibitor **5.8** and a diphosphate molecule (brown) mimicking the binding mode of PRPP (green) and 4FA (pink). (A) An overlay of chain A (PDB: 4N5V) accommodating PRPP (green), 4FA (pink), Mg²⁺ (green spheres) with chain B (yellow) containing **5.8** and diphosphate (yellow). (B) Fo-Fc map (green) contoured at 3.0 σ and 2Fo-Fc map (blue) contoured at 1.0 σ to illustrate the presence of **5.8** (yellow) at full occupancy and diphosphate (brown) at 0.5 occupancy in chain B of the AnPRT/**5.8**/diphosphate structure.*

5.8.1 The detailed binding interactions of ligands in the AnPRT/PRPP/4FA/Mg²⁺ and AnPRT/5.8**/diphosphate structures**

In chain A of the AnPRT/PRPP/4FA/Mg²⁺ structure, the 4FA molecule located at site 1 resides 4.2 Å away from the amino group of the C1 atom of PRPP, in a favourable orientation for the nucleophilic attack, which results in the anticipated β -PRA product. The 4FA molecule, located

at site 1, forms hydrogen bonds via its carboxylate group with the side chains of Asn138, Arg193 and two water molecules, and with its amine group to the backbone of Gly107 (Figure 5.7, A).

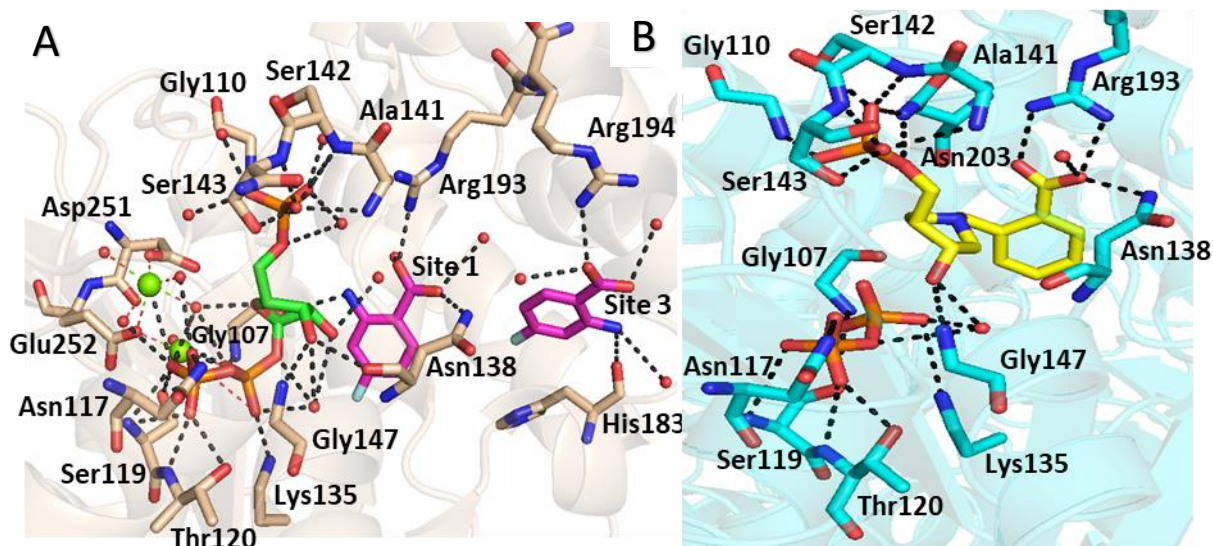


Figure 5.7 The binding interactions of ligands in the AnPRT/PRPP/4FA/Mg²⁺ (PDB: 4N5V) and AnPRT/5.8/diphosphate structures.

(A) Chain A (misty rose) bound with PRPP (green), 4FA (pink) and Mg²⁺ (green spheres) in the AnPRT/PRPP/4FA/Mg²⁺ structure (PDB: 4N5V). (B) Chain B (cyan) containing 5.8 (yellow) and diphosphate (brown) in the AnPRT/5.8/diphosphate structure. Polar contacts and metal coordination bonds are shown as black and red dashes respectively. Water molecules are shown as red spheres.

In addition, another 4FA molecule is bound at site 3 in the channel and forms hydrogen bonds via its carboxylate group to the side chain of Arg194, the backbone of His183 and three water molecules. Similarly, the AnPRT/5.8/diphosphate structure shows the anthranilate-like moiety of analogue 5.8 hydrogen-bonding at site 1 via its carboxylate group to the side chains of Arg193, Asn138 and a water molecule (Figure 5.7, B). The labile primary amine group is absent in the 5.8 bound AnPRT structure, while the secondary amine included in the amine ring of analogue 5.8 does not make any interactions with protein residues.

Additionally, chain A of the AnPRT/PRPP/4FA/Mg²⁺ shows that the phosphate group of PRPP forms polar contacts with the backbone nitrogen atoms of Ala141, Ser142, and Gly110, the side chain hydroxyl of Ser143 and four water molecules. The C3 hydroxyl group of PRPP makes polar contacts with the side chain of Asn138 and Gly147, present on the β2–α6 loop. In

addition, two water molecules form polar contacts with the C2 and C3 hydroxyl groups of the ribose ring. The diphosphate group of PRPP co-ordinates to an Mg^{2+} ion and makes hydrogen bonds to the backbone nitrogen atoms of Gly107, Ser119, Thr120, and the side chains of Asn117, Lys135 and various surrounding water molecules. Additionally, two Mg^{2+} ions are coordinated octahedrally. The first Mg^{2+} ion forms contacts with two water molecules, two oxygen atoms of the diphosphate group and side chain oxygen atoms of Ser119 and Glu252. The second Mg^{2+} ion interacts with four water molecules and side chain oxygen atoms of Asp251 and Glu252. Similarly, the phosphate group of analogue **5.8** in chain B of the AnPRT/**5.8**/diphosphate structure interacts with the nitrogen atoms of the backbone of residues Ala141, Ser142, Gly110, and the side chain hydroxyl of Ser143. An additional contact of the phosphate group of ligand **5.8** is observed with the side chain nitrogen atom of Asn203 by shifting the phosphate group of **5.8** towards anthranilate binding site 1. The C3 hydroxyl group of the ribosyl mimic of **5.8** forms hydrogen bonds with the side chain nitrogen atom of Gly147 and a water molecule. The diphosphate molecule forms contacts with the backbone of residues Gly107, Ser119, Thr120, the side chains of Asn117, Ser119, Lys135 and a water molecule.

The binding modalities of the ribosyl and anthranilate mimic **5.8** along with the binding of diphosphate might be indicative of a cleaved diphosphate moiety from PRPP and the subsequent generation of a mobile oxocarbenium ion characteristic of a dissociative “ $\text{S}_{\text{N}}1$ -like” mechanism, as opposed to an immobile carbon position necessitated by an associative “ $\text{S}_{\text{N}}2$ -like” mechanism. However, the absence of a diphosphate group directly linked to the ribose ring of analogue **5.8** could be another reason for the ribose ring being transferred towards the nucleophilic anthranilate. To release the diphosphate moiety during the catalytic process, loop $\beta 2$ – $\alpha 6$ is required to fold into the anthranilate channel. However, the binding of ligand **5.8** at the catalytic site would prevent this loop movement from occurring. Hence, the position of the $\beta 2$ – $\alpha 6$ loop is in the closed conformation. It is possible that the diphosphate molecule is wedged in the active site for this reason. The detached diphosphate molecule has been spotted at a similar position previously within *M. tuberculosis* AnPRT (PDB: 4X5E) and it has been hypothesised that the diphosphate moiety of the PRPP molecule does not move during catalysis.⁵⁷ If this hypothesis is correct, this AnPRT/**5.8**/diphosphate structure may have potentially captured the catalytic state of the enzyme.

If the factor of relative binding affinities of ligand **5.8** to AnPRT is taken into consideration, then it is quite possible that the binding of ligand **5.8** might occur preferentially at the anthranilate site. It may be that the position of the diphosphate ensures the ribose ring of analogue **5.8** cannot reach to the PRPP binding site. The ribosyl mimic and the anthranilate-like moiety of inhibitor **5.8** were joined through the insertion of a single methylene bridge and this single methylene bridge might not be long enough for the ribosyl mimic of analogue **5.8** to reach its preferred position. Hence, the transfer of the ribosyl mimic of **5.8** towards the anthranilate binding site is noticed. The observed binding of analogue **5.8** suggests that the right bond distance between the ribosyl mimic and the anthranilate-like moiety could lead us to design strong AnPRT inhibitors that bind at the PRPP and anthranilate binding sites properly.

5.8.2 Comparison of the oligomeric state of the AnPRT/PRPP/4FA/Mg²⁺ and AnPRT/5.8/diphosphate structures

Again, the PRPP with anthranilate analogue, 4FA bound structure (PDB: 4N5V) was chosen for comparison with the AnPRT/**5.8**/diphosphate structure to analyse any differences in the overall protein conformation in the presence of mimic **5.8** at the catalytic site of the enzyme. The inhibitor **5.8**-bound AnPRT structure was determined with two non-associated monomers in the asymmetric unit and a dimer could be generated via crystallographic symmetry.

No ligand binding was detected in chain A, whereas chain B is bound with inhibitor **5.8** and diphosphate. The apo subunit of the AnPRT/**5.8**/diphosphate structure shows similar overall protein fold compared to chain A of the AnPRT/PRPP/4FA/Mg²⁺ structure and the comparison gave an RMSD value of 0.72 Å. In comparison, there are significant differences in the AnPRT structures when overlaying the ligand bound subunit of the AnPRT/**5.8**/diphosphate structure either to chain A (the RMSD values 1.67 Å) or chain B (the RMSD values 1.72 Å) of the AnPRT/PRPP/4FA/Mg²⁺ structure. Also, the overlay of the AnPRT/**5.8**/diphosphate and AnPRT/PRPP/4FA/Mg²⁺ dimers gave the RMSD values of 1.86 Å. The conformation changes noticed in the ligand bound subunit of the AnPRT/**5.8**/diphosphate structure compared to the AnPRT/PRPP/4FA/Mg²⁺ structure is the main contributor to the observed high RMSD values of 1.86 Å. In detail (Figure 5.8, **A**), a notable difference in the position of both the N-terminal

and C-terminal domains is evident from an overlay of chain B bound with inhibitor **5.8** and diphosphate with chain A containing PRPP, 4FA, Mg^{2+} (RMSD = 1.67 Å).

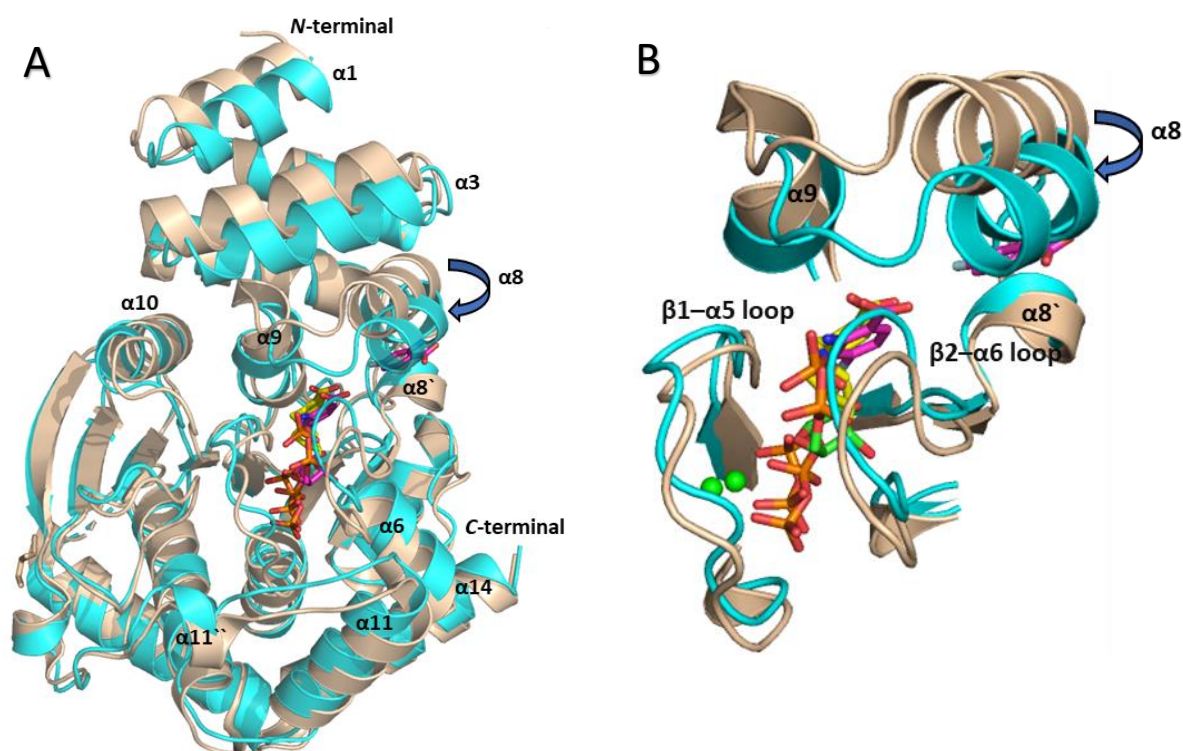


Figure 5.8 Inspection of the observed changes in the position of both domains by binding district ligands.

(A) An overlay of chain A (PDB: 4N5V, tint) bound with PRPP (green), 4FA (pink), Mg^{2+} (green sphere) with chain B (cyan) containing **5.8** and diphosphate. **(B)** A closer view of the active site showing the differences that occur upon the binding of ligand **5.8**.

Remarkably, a distinct conformation of the N-terminal domain, particularly the α1, α3, α8, α8' and α9 helices, is observed. However, the C-terminal domain (α6, α10, α11, α11'' and α14 helices) is shifted towards the active site; this is likely to be caused by the binding of ligand **5.8** at the catalytic site of the enzyme. Additionally, the β1-α5 and β2-α6 loops are altered and projected into the catalytic site during binding of analogue **5.8** at the catalytic site of the enzyme (Figure 5.8, **B**). Interestingly, the shift of the α8 helix into the anthranilate binding tunnel is noticed upon the binding of ligand **5.8** to AnPRT. This particular AnPRT structure might have captured a conformational state during enzyme catalysis in which the substrate binding tunnel is blocked by the shifted N-terminal domain position in order to prevent the migration of another substrate molecule into the tunnel during the act of enzyme

catalysis (Figure 5.8, **B**). The blocking of the anthranilate binding tunnel during enzyme catalysis could be a reason for the substrate-inhibition of the enzyme noticed with by anthranilate.⁵⁷ The movement of the N-terminal domain might prevent If the concentration of anthranilate is too high (more than 15 μ M).

5.9 Interpretation of AnPRT/5.8/diphosphate structure

In the *M. tuberculosis* AnPRT/5.8/diphosphate structure, the apo and ligand-bound chains do not align well and resulted in an RMSD of 1.2 Å over 2234 atoms. Each chain of AnPRT/5.8/diphosphate structure consists of two domains (N-terminal and C-terminal). These domains are joined by a hinge region ($\alpha 4$ – $\beta 1$, $\alpha 8$ – $\beta 3$ and $\alpha 9$ – $\beta 4$, Figure 5.9, **A**). To analyse intrachain differences, N-terminal and C-terminal domains of apo and ligand-bound chains are distinct by the hinge region. The smaller N-terminal domain consists of residues 25–103 and residues 181–216, while the remaining residues (other than the hinge region) contribute to the larger C-terminal domain (Figure 5.9, **B** and **C**).

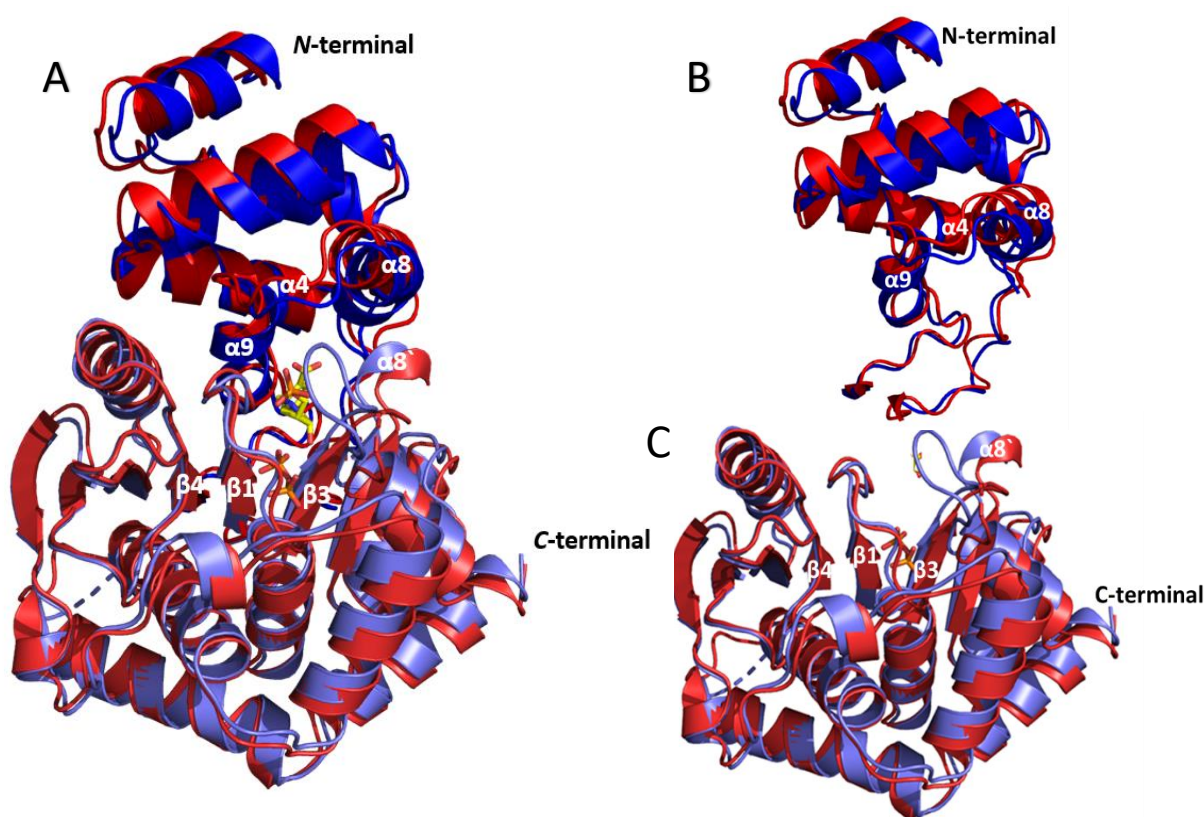


Figure 5.9 Structural superimposition of AnPRT/5.8/diphosphate monomers.

(A) Overlay of apo (Red) and ligand-bound chains (blue) of AnPRT/5.8/diphosphate structure. (B, C) Each chain is distinct into N-terminal and C-terminal domains. Both domains for each chain are distinguished by contrasting colour.

As calculated by PISA,¹⁶⁸ the interdomain interface for ligand-bound chain involves 53 and 42 residues of N-terminal and C-terminal domains respectively and $\sim 3382.8 \text{ \AA}^2$ or 42.0 % of the total potential surface area is buried by these interdomain interactions. The interdomain interface for the apo chain is weaker and consists of 46 and 42 residues of N-terminal C-terminal domains respectively and buries only $\sim 3070 \text{ \AA}^2$ or 39.1 % of the total potential surface area is buried in the intrachain interactions.

However, the dimer interface (between the apo and ligand-bound chains) of the AnPRT/5.8/diphosphate structure is dominated by hydrophobic residues, involving 26 residues per chain and burying $\sim 1752 \text{ \AA}^2$ or 13.2% of the total potential surface area of both chains. This value is similar to the previously solved structures of *M. tuberculosis* AnPRT, for example the interchain interface involves 25 residues per chain and buries $\sim 1722.9 \text{ \AA}^2$ or 12.2 % of the total potential surface area for the AnPRT/PRPP/4FA/Mg²⁺ structure. The theoretical solvation free energy gain is almost similar for the formation of the dimer interface for AnPRT/PRPP/4FA/Mg²⁺ and AnPRT/5.8/diphosphate structures, -18.5 kcal/mol and -18.0 kcal/mol respectively. Therefore, PISA analysis indicates that the dimer interface is not substantially changed despite the change in conformation of the ligand-bound chain in AnPRT/5.8/diphosphate structure.

5.10 The binding of ligand 5.8 with *M. tuberculosis* AnPRT

Analysis of the AnPRT/5.8/diphosphate structure shows the binding of inhibitor 5.8 and diphosphate to only one chain of the dimeric enzyme and displays the significant overall conformational changes. This structure suggests the possibility of asymmetric catalysis by the enzyme (Section 5.9). To determine the binding affinity and binding stoichiometry of analogue 5.8 in solution, ITC experiments were carried out. The standard ITC assay is described in detail in Section 7.1.19.

Charge density for the diphosphate molecule was discovered in the inhibitor **5.8**-bound AnPRT structure. Therefore, titrations were performed in either the presence or absence of diphosphate molecules to determine the effect of diphosphate on the binding of inhibitor **5.8** to the enzyme. No detectable binding was observed for ligand **5.8** up to a concentration of 5 mM without the addition of diphosphate. The collected data clearly show that the heat change for ligand **5.8** is too small to measure when diphosphate is absent (Figure 5.10, **A**).

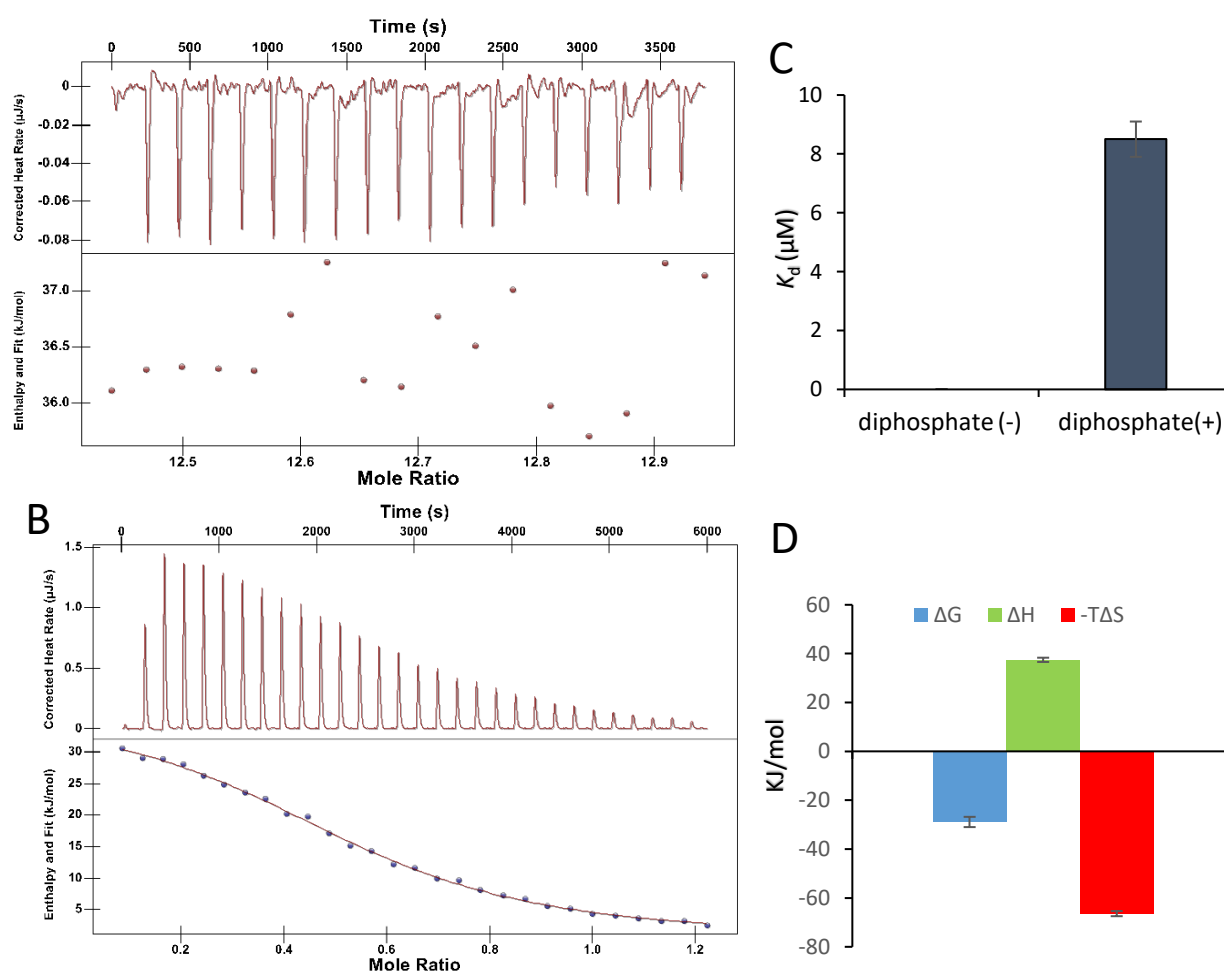


Figure 5.10 ITC experiments to detect inhibitor **5.8** binding to AnPRT 25 °C.

(**A**) Raw data from ITC experiments involving the titration of 5 mM **5.8** into a cell containing 83 μM AnPRT in the absence of diphosphate. (**B**) Raw data from ITC experiments involving the titration of 6 mM **5.8** into a cell containing 83 μM AnPRT in the presence of 500 μM diphosphate. (**C**) A comparison of the K_d values for the binding of **5.8** to AnPRT in the absence and presence of 500 μM diphosphate. No binding was observed when diphosphate was absent. (**D**) The thermodynamic parameters for the data observed (Figure **B**) for binding ligand **5.8** to AnPRT in the presence of 500 μM diphosphate.

Interestingly, the binding of ligand **5.8** was strengthened significantly by the addition of 500 μM diphosphate (Figure 5.10, **B**). The binding isotherms for titrating a solution of 600 μM ligand **5.8** in the presence of 500 μM diphosphate and 1 mM MgCl_2 fitted excellently to an independent binding model and resulted in a K_D value of $8.5 \pm 0.6 \mu\text{M}$ (Figure 5.10, **C**). The thermodynamic parameters obtained from the binding isotherm indicate that the binding of inhibitor **5.8** to AnPRT in the presence of Mg^{2+} and diphosphate is an endothermic process; that is, the process is being driven by favourable entropic changes (Figure 5.10, **D**).

The ITC experiment was consistent with a stoichiometry of 1:2 ligand/AnPRT complex with the number of binding sites being 0.547 ± 0.008 per monomer. This data can be supported by the AnPRT/**5.8**/diphosphate structure, which represents ligand **5.8** binding at a single catalytic site, although the homodimeric AnPRT enzyme appears to contain two catalytic sites, as observed in several AnPRT structures.^{54,60,66,68,69,71,74} It can be speculated that this data implying that asymmetric catalysis may be a feature of the *M. tuberculosis* AnPRT enzyme, or at least the binding sites are not independent.

5.11 Summary

Several compounds were chosen to be synthesised based on the putative reaction mechanism of the AnPRT enzyme. The proposed transition state mimics, compounds **5.2**, **5.6** and **5.8**, were successfully synthesised and tested against *M. tuberculosis* AnPRT using an enzyme-coupled assay. All of these compounds inhibit the AnPRT enzyme with the ribosyl and anthranilate mimic **5.8** displaying the lowest K_i value of $13 \pm 2 \mu\text{M}$ with respect to both substrates in the presence of diphosphate and monophosphate.

A crystal structure of AnPRT was obtained in complex with inhibitor **5.8**. Interestingly, the binding of ligand **5.8** was observed in only one chain of the homodimeric protein, with a trapped diphosphate molecule. The inhibitor was found to be bound at the catalytic site of one chain of the homodimeric protein. The anthranilate moiety of inhibitor **5.8** is bound at site 1, the binding site for the attacking nucleophile. The pyrrolidine ring with an attached phosphate group of inhibitor **5.8** is bound at the position of the ribose 5-phosphate moiety of PRPP and was found to be shifted towards the anthranilate binding site 1. The diphosphate

molecule precisely mimics the binding site of the diphosphate group of PRPP at the active site of the enzyme. The binding of inhibitor **5.8** to AnPRT is associated with a shift of the N-terminal domain to the anthranilate binding channel and it is possible that this structure has captured the enzyme in its catalytic state, in which the substrate-binding tunnel is blocked in order to prevent the migration of anthranilate into the tunnel during the act of enzyme catalysis.

That inhibitor **5.8** was bound to only one monomeric unit of the AnPRT structure, may indicate unpreviously recognised asymmetry for this enzyme. The recorded ITC data for ligand **5.8** binding with AnPRT indicates the inhibitor only binds to a single chain, meaning that solution binding mirrors the binding observed in the crystal structure. Therefore, the AnPRT/**5.8**/diphosphate structure may represent a previously unobserved catalytic state of the enzyme.

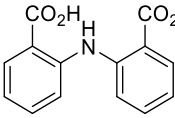
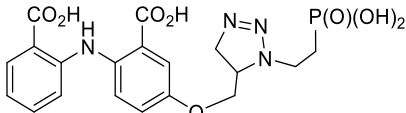
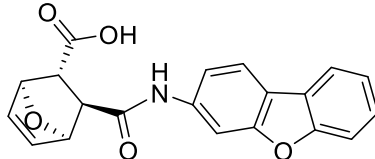
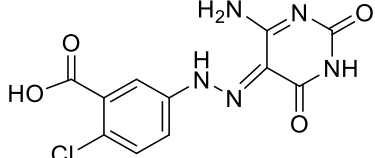
Chapter 6 Summary and future directions

This thesis aimed to contribute to the existing comprehensive knowledge of the *M. tuberculosis* AnPRT enzyme in order to aid novel anti-TB drug design. The thesis aims were achieved with detailed characterisation of the substrate binding sites and inhibition of *M. tuberculosis* AnPRT to unravel the catalytic properties of the enzyme. The key findings of this thesis are outlined below.

6.1 Inhibition of *M. tuberculosis* AnPRT

In previous reports, a “bianthranilate-like” inhibitor, ACS172, was one of the most potent inhibitors for *M. tuberculosis* AnPRT (Table 6.1).⁵⁷ We have studied “bianthranilate-like” phosphonate inhibitors that display the strongest enzyme inhibition to date. The K_i values were observed to decrease with an increase in the length of the phosphonate linkers; the lowest K_i value observed for *M. tuberculosis* AnPRT being inhibitor **2.11** ($K_i^{\text{anth}} = 1.3 \pm 0.1 \mu\text{M}$, $K_i^{\text{PRPP}} = 5.4 \pm 0.3 \mu\text{M}$, Table 6.1). A number of *M. tuberculosis* AnPRT crystal structures complexed with these phosphonate inhibitors were solved. These structures show that the inhibitors with elongated phosphonate linkers occupy multiple anthranilate binding sites within the channel. These results indicate that stronger inhibition is obtained when multiple anthranilate sites are occupied by the inhibitors. However, these inhibitors do not affect the binding of PRPP as no differences in the binding of the inhibitor were observed in AnPRT structures complexed with the inhibitor and PRPP. These inhibitors preferred binding with solvent-exposed binding modes at the anthranilate binding site rather than the catalytic site of the enzyme. These findings are also corroborated by the steady-state kinetic experiments, as these compounds were shown to be competitive inhibitors with respect to anthranilate but non-competitive with respect to PRPP.

Table 6.1 Inhibitors with the apparent K_i values and their best-fitted inhibition model for both substrates against *M. tuberculosis* AnPRT.

Chemical structure with code	K_i (μM) against PRPP	Type of inhibition against PRPP	K_i (μM) against anthranilate	Type of inhibition against anthranilate
 ACS172	6.8 ± 1^a	non-competitive	16 ± 10^a	uncompetitive
 2.11	1.3 ± 0.1	competitive	5.4 ± 0.3	non-competitive
 3.5	41 ± 4	competitive	350 ± 28	non-competitive
 3.9	7.0 ± 0.4	competitive	7.0 ± 0.4	competitive

^a The K_i values for ACS172 are from Evan et al.⁶⁹

Furthermore, several new ligands were predicted to target the active site of *M. tuberculosis* AnPRT using a virtual screening investigation. Compound **3.9**, the strongest inhibitor identified from this virtual screen, is a competitive inhibitor with respect to both PRPP and anthranilate with the K_i values of $7.0 \pm 0.4 \mu\text{M}$ recorded with respect to each substrate (Table 6.1). The second strongest inhibitor from the virtual screen, **3.5**, showed significant competitive inhibition with respect to anthranilate ($K_i = 41 \pm 4 \mu\text{M}$) and weaker non-competitive inhibition with respect to PRPP ($K_i = 350 \pm 28 \mu\text{M}$). The remaining compounds from the screen were shown to be moderate or weak inhibitors with apparent K_i values of $100 \mu\text{M}$ or higher.

Additionally, the active site of *M. tuberculosis* AnPRT was explored with various PRPP analogues or potential transition state mimics that were designed based on the possible reaction mechanism of the enzyme. A number of compounds were successfully synthesised, tested and these were found to be moderate or strong competitive inhibitors with respect to PRPP for *M. tuberculosis* AnPRT (Table 6.2).

*Table 6.2 The types of inhibition with the apparent K_i values displayed for *M. tuberculosis* AnPRT inhibitors.*

Code	Chemical structure	K_i (μM) against PRPP	K_i (μM) against anthranilate
R5P		1000 ± 100	NA
4.11		555 ± 46	No inhibition up to 250 μM
4.12		313 ± 19	NA
4.15		235 ± 16	NA
4.16		794 ± 76	NA
4.18		70 ± 9	114 ± 12
4.19		22 ± 4	93 ± 11

4.14		541 ± 66	No inhibition up to 250 μ M
4.14 with diphosphate		311 ± 26	No inhibition up to 250 μ M
5.8		26 ± 3	26 ± 3
5.8 with diphosphate or monophosphate		13 ± 2	13 ± 2

The stronger inhibition for the cyclopentene phosphate compound **4.12**, compared to the cyclopentane phosphate compounds **4.11** and R5P suggests that the double bond characteristic around the reaction centre is an important aspect for inhibition. Interestingly, the D-isomer **4.15** was found to be a 3-fold stronger inhibitor of AnPRT than the L-isomer **4.16**. This suggests that the unfavourable configuration of the L-isomer **4.16** has less affinity for the enzyme. The iminoribitol analogues **4.18** and **4.19**, mimicking the ribocation characteristic and the directly bonded nucleophilic moiety, exhibited strong enzymatic inhibition. These results indicate that, as expected, the nitrogen atoms of the iminoribitol compound are likely to be protonated at physiological pH and possibly act as a positive charge mimic of the transition state, whereas the pyridine or benzoate moiety may position itself near the nucleophilic anthranilate binding site during enzyme catalysis. The predicted binding position of the iminoribitol analogues with molecular modelling depicts their strong interactions to the catalytic site of the enzyme.

Based on the proposed reaction mechanism, a number of compounds towards potential transition state mimics for AnPRT were successfully synthesised. In the case of these analogues, the iminophosphate ring mimic and the anthranilate-like moiety were joined

through the insertion of a methylene bridge along with the replacement of the amine group of anthranilate. Interestingly, mimic **5.8** was shown to be one of the strongest competitive inhibitors of the enzyme with a K_i value of $13 \pm 2 \mu\text{M}$ with respect to both substrates in the presence of diphosphate and monophosphate. Additionally, AnPRT can also be inhibited with diphosphate itself with an apparent K_i value of $46 \pm 4.0 \mu\text{M}$. The presence of diphosphate at the active site of the enzyme doubled the inhibitory effect as observed in the kinetic assay of iminosugar analogues **4.14** and **5.8**. This observation indicates that the introduction of a diphosphate group or bioisostere of the diphosphate– Mg^{2+} complex can lead to strong inhibition of *M. tuberculosis* AnPRT.

6.2 Substrate binding sites

The substrate binding sites of *M. tuberculosis* AnPRT were successfully explored in depth to understand enzyme inhibition and catalysis. Ligand binding to the enzyme was primarily examined by structural analysis of *M. tuberculosis* AnPRT and further explored by DSF and ITC studies. *M. tuberculosis* AnPRT does not catalyse the reaction in the absence of metal ions. This is further evidenced by ITC where PRPP binding was too weak to detect in the absence of metal ions whereas a strong binding constant for PRPP is obtained in the presence of Mg^{2+} . Therefore, the binding of the PRPP– Mg^{2+} complex is likely to occur during enzyme catalysis under physiological conditions.

Furthermore, the AnPRT/anthranilate structure shows the binding of anthranilate within the tunnel at site 1 and site 3 without PRPP binding at the active site. Similarly, “bianthranilate-like” phosphonate inhibitors in Chapter 2 bound within the tunnel at site 2 and site 3 without the binding of PRPP at the active site of the enzyme. This indicates that anthranilate can bind at multiple sites within the tunnel and reach the attacking site before PRPP binding occurs. This hypothesis is further supported by DSF and ITC studies. DSF data shows protein stability is increased as the concentration of anthranilate is increased (suggesting binding of anthranilate) and ITC data for the titration of anthranilate into a solution of the enzyme (in the absence of PRPP) fits well with a sequential binding site model.

6.3 Distinct conformation of flexible loops

The $\beta 1-\alpha 5$ and $\beta 2-\alpha 6$ loops have been shown to act as a gate for substrate binding and progression of the reaction. Therefore, depending on the substrates, and their binding positions, distinct conformations of both loops have been noticed in various AnPRT structures. Based on the available *M. tuberculosis* AnPRT structures, the conformation of the $\beta 1-\alpha 5$ and $\beta 2-\alpha 6$ loops is in the “open” position only when anthranilate or an anthranilate analogue is bound to the tunnel. However, both loops are observed in the “closed” conformation when PRPP is bound to the active site. The $\beta 2-\alpha 6$ loop adopts a “folded” conformation when diphosphate binds to a buried position of the active site.

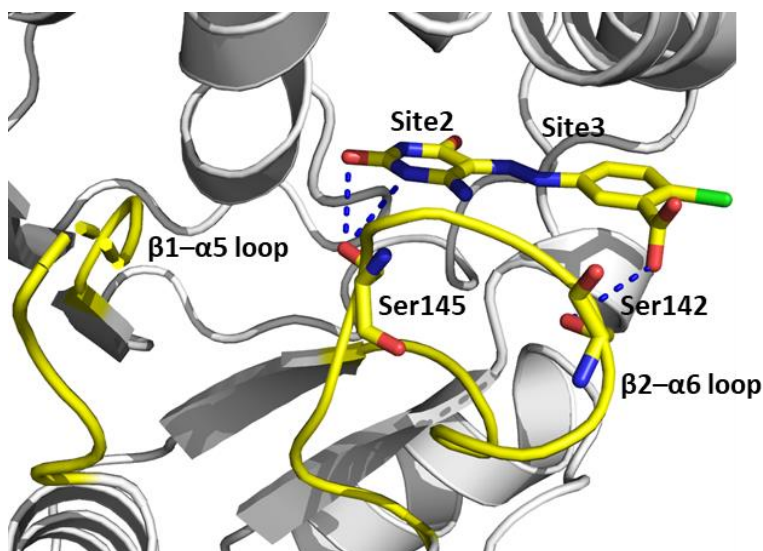


Figure 6.1 The binding of inhibitor **3.9** (yellow) in chain A of the AnPRT/**3.9** structure.

The $\beta 1-\alpha 5$ and $\beta 2-\alpha 6$ loops are coloured to highlight its position. The binding interaction of **3.9** (yellow) in chain A of AnPRT/**3.9** is represented as blue dashed lines.

Interestingly, a new AnPRT/**3.9** structure reveals significant changes in the conformation that these flexible loops adopt. The ligand **3.9** is positioned within the tunnel at sites 2-3 and interacts with the $\beta 2-\alpha 6$ loop that transfers the conformation of the loop within the tunnel (Figure 6.1). Changes in the position of the $\beta 2-\alpha 6$ loop diminish the binding of PRPP. The recorded DSF and ITC data also verify that the binding of ligand **3.9** alters the binding affinity of PRPP to the enzyme. Together, these pieces of evidence may be useful to further explicate the inhibition of *M. tuberculosis* AnPRT including the knowledge for future inhibitor design strategies that target the PRPP binding site of the enzyme.

6.4 The catalytic properties of *M. tuberculosis* AnPRT

A crystal structure of AnPRT with mimic **5.8** and diphosphate bound was solved; although the binding of ligand **5.8** can only be observed for one monomer of the oligomeric enzyme. This is the first structure solved for *M. tuberculosis* AnPRT in which an analogue is bound at the catalytic site of the enzyme, mimicking the nucleophilic portion of the reaction at binding site 1 along with mimicking the binding of the R5P moiety of PRPP. Interestingly, a trapped diphosphate molecule was also found at the buried position of the active site, which is likely imitating the diphosphate portion of PRPP. The iminophosphate ring of analogue **5.8** is observed shifted towards the nucleophile binding site 1. The flexibility of the ribose ring of PRPP has been noted in various AnPRT structures.⁵⁷ Together, the binding mode of mimic **5.8**, along with the binding of the diphosphate, may have captured the cleavage of the diphosphate moiety from PRPP and the subsequent generation of a mobile oxocarbenium ion, characteristic of a dissociative “S_N1-like” mechanism. This is opposed to an immobile carbon position, which is required for an S_N2 mechanism. However, the absence of the diphosphate group in mimic **5.8** may also explain the observation that the iminophosphate ring is shifted towards the nucleophilic binding site 1.

Additionally, to release the diphosphate group during the catalytic process, loop β 2– α 6 is likely to be required to adopt the “folded” conformation, as observed in the diphosphate bound AnPRT structure (PDB: 4X5D).⁷⁴ The observed “closed” conformation of the β 2– α 6 loop, by binding ligand **5.8** at the catalytic site, would prevent the loop movement from occurring, thus holding the diphosphate molecule at the active site. In addition, the detached diphosphate molecule has been observed previously within the structure of *M. tuberculosis* AnPRT (PDB: 4X5E) and aligns well with the diphosphate moiety of PRPP.⁶⁶ It has been speculated that the diphosphate remains at its position during the act of enzyme catalysis.⁵⁷ If this hypothesis is correct, it is quite possible that the AnPRT/**5.8**/diphosphate structure represents a state of enzyme catalytic cycle.

Additionally, the inhibitor **5.8** was shown to be bound to only one monomeric unit of the AnPRT structure. The recorded ITC data for ligand **5.8** binding to AnPRT verify that binding events of **5.8** form a 1:2 ligand:AnPRT complex, suggesting that asymmetric catalysis may be a feature of this enzyme. There might be communication between the different catalytic sites,

which may be transmitted via interface changes. Furthermore, the binding of analogue **5.8** had a significant change in the enzyme conformation compared to various previously obtained AnPRT structures. The binding of inhibitor **5.8** to AnPRT causes a shift of the N-terminal domain to the anthranilate binding channel and raises the possibility of capturing the enzyme in its catalytic state, in which the substrate-binding tunnel is blocked in order to prevent the migration of anthranilate into the substrate-binding tunnel during the act of enzyme catalysis. This blocking of the anthranilate tunnel during catalysis could be a reason for the enzyme inhibition noticed at high concentrations of anthranilate.⁵⁷ Therefore, the AnPRT/**5.8**/diphosphate structure might be representative of the catalytic state of the enzyme.

However, it is also possible that the binding affinity for ligand **5.8** might be more favourable towards the anthranilate binding site than the PRPP site. If the anthranilate site is the preferred binding site for analogue **5.8** then the binding mode may arise as the ribosyl mimic and the anthranilate-like moiety of **5.8** are bridged only by a single methylene bond. The distance of single methylene bond seems to be not long enough for the ribosyl mimic of analogue **5.8** to reach to the PRPP site. Additionally, it may be the position of the bound diphosphate molecule that ensures the ribose ring of analogue **5.8** cannot access to the PRPP site. Hence, the transfer of the ribosyl mimic of **5.8** towards the anthranilate binding site is observed in the AnPRT/**5.8**/diphosphate structure. If this assumption is true, the observed binding of analogue **5.8** suggests that the correct bond distance of the ribosyl mimic and the anthranilate-like moiety bridge can lead us to design AnPRT inhibitors that bind into the PRPP and anthranilate binding sites strongly.

6.5 Future directions

In order to aid anti-TB drug design, transition state mimicry or a drug that will block the active site and anthranilate channel could be useful strategies to target *M. tuberculosis* AnPRT. In Chapter 2, the inhibition study and various AnPRT structures indicate that stronger enzyme inhibition is observed with “bianthranilate-like” analogues with longer elongated phosphonate linkers, which occupy multiple anthranilate sites within the channel. If anthranilate analogue approaches are used, then the multiple binding sites characterised by

several flexible key residues—Asn138, Pro180, Arg193 and Arg194—that are involved with inhibitor binding need to be targeted. However, it is difficult to target the PRPP site due to the long flexible anthranilate binding tunnel in which a number of analogues can bind to different extents but are unable to reach the PRPP binding site.

To target the PRPP binding site, various AnPRT structures show the details of the PRPP binding site, which is buried at the bottom of the anthranilate tunnel and is fenced by two flexible loops that act as a gate. One major challenge for targeting the PRPP binding site is that this site is mainly dominated by polar residues and PRPP binding seems to be driven by interactions with residues present on flexible loops. Therefore, to target both the substrate binding sites together, the most potent inhibitor from molecular modelling, **3.9**, could prove more fruitful. Inhibitor **3.9** has high potency for AnPRT inhibition and it is seen to target both substrate binding sites together by blocking the anthranilate channel and introducing changes in the loop conformations, which reduce the binding affinity for PRPP to the enzyme (Figure 6.1, 3.9 and Section 3.5.2.2). To achieve the aim of targeting both substrate binding sites together and increasing the inhibition potency, further substitutions or additions of chemical groups to inhibitor **3.9** would be a valuable approach for anti-TB drug design.

The analogues studied in Chapters 4 and 5 are either competitive inhibitors with respect to PRPP or both substrates. The observed competitive inhibition behaviour and strong potency of these analogues are fascinating. These analogues are a good starting point in the search of an anti-TB prodrug. The docking of iminoribitol compounds predicted binding with a high docking score at the enzyme catalytic site. It would be valuable to extend these analogues by the addition of methylene or ethylene bridges between the iminoribitol ring and an aromatic ring (Figure 6.2). The use of the phosphonate isostere (as a stable analogue of the phosphate group) of these analogues can also be interesting to understand the reaction mechanism and inhibition of AnPRT enzyme.

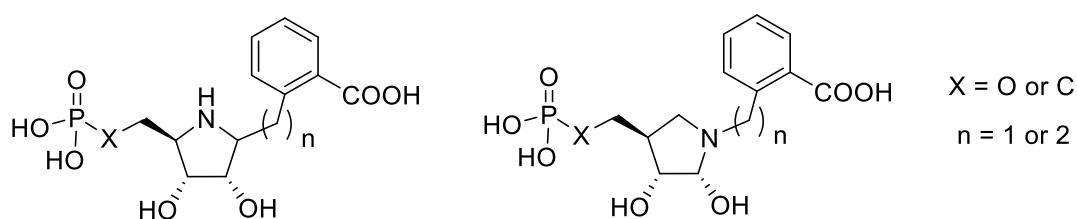


Figure 6.2 Proposed expansion of the iminoribitol inhibitor and the phosphonate isostere.

The AnPRT/**5.8**/diphosphate structure shows the binding of analogue **5.8** at the catalytic site of the enzyme. The obtained structure validates the binding of the iminophosphate ring towards the nucleophilic site along with a fully dissociated diphosphate molecule. The diphosphate molecule has good potency to inhibit AnPRT and the presence of diphosphate or monophosphate also boosts the inhibitory effect and binding affinity of the analogues, evidenced by the kinetic assay and ITC. Therefore, the addition of a diphosphate, monophosphate or an isostere of diphosphate–Mg²⁺ might enhance inhibitor binding affinity for the enzyme catalytic site (Figure 6.3).

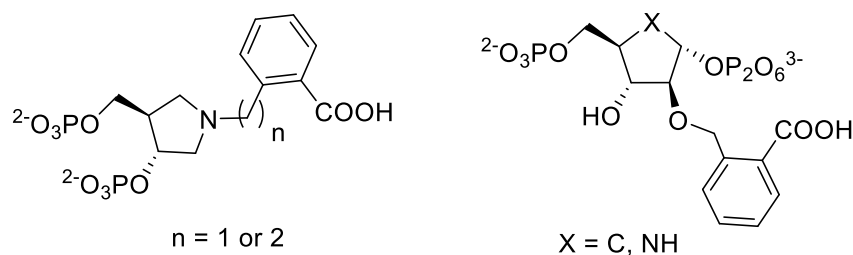


Figure 6.3 Potential improvements to the transition state analogues to expend their binding into the enzyme catalytic site.

The double bond characteristic around the reaction centre and replacing the anomeric oxygen of PRPP with a carbon or nitrogen atom would also be worthwhile investigating for the inhibition of *M. tuberculosis* AnPRT (Figure 6.4).

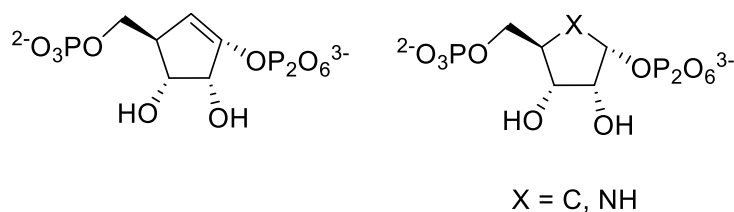


Figure 6.4 The expanded transition state analogue based on cyclopentane and compounds with a double bond characteristic.

To study the reaction mechanism of *M. tuberculosis* AnPRT, the use of KIE methods to predict the transition state of the enzyme are particularly challenging due to the instability of the reaction substrate PRPP and the product PRA.¹⁵² Crystallography is a useful tool to determine binding sites and pinpoint key residues involved in ligand binding. However, the exact reaction mechanism of the enzyme is unable to be determined directly by crystallography as this only

provides a snapshot that captures the state of the enzyme at a single point in time. However, QM/MM computational modelling may be valuable to predict the reaction mechanism of the AnPRT enzyme accurately.

Chapter 7 Methods and experimental procedures

7.1 General methods

7.1.1 pH measurements

The pH of all buffers and other aqueous solutions was determined using a Denver Instruments UB-10 Ultra-Basic pH meter, with a standard probe. The pH of the solution was adjusted by the addition of hydrochloric acid, 1 M or 12 M, or sodium hydroxide, 1 M or 10 M.

7.1.2 Reagents and solvents

Reagents were purchased from commercial suppliers and used without further purification unless stated otherwise.

7.1.3 Chromatography

Thin-layer chromatography (TLC) to monitor chemical reactions was run using Merck Kieselgel 60F254 pre-coated aluminium. The UV traced chemical product was visualised using a UV lamp at 254 nm and further stained with cerium molybdate stain (Hanessian's Stain) and dried with a heat gun. Ninhydrin stain was used to visualise amine compounds. Flash chromatography was carried out on silica gel, 230–400 mesh and florisil gel with 200–400 mesh for unstable organic compounds. The flash chromatography column solvents petroleum ether (petrol), ethyl acetate, diethyl ether, toluene, methanol and ethanol were used. Analytical grade solvents were used without further purification while petroleum ether and ethyl acetate were distilled on a rotary evaporator prior to use.

7.1.4 Spectroscopy

NMR spectroscopy was carried out on Agilent 400 NMR, JEOL 500, and JEOL 600 spectrometers. ^1H -NMR, ^{13}C -NMR and ^{31}P -NMR spectra were calibrated to the signal of the residual protons, carbons and phosphorous in the reported deuterated solvents. The chemical shifts δ_{H} and δ_{C} were calculated relative to tetramethylsilane while the chemical shifts δ_{P} were calculated relative to an external standard of 85% phosphoric acid. All chemical shifts are reported in parts per million (ppm) and coupling constants (J) are reported in Hertz.

7.1.5 Mass spectrometry

The molecular masses of molecules and proteins were determined by electrospray ionisation mass spectrometry (ESI-MS) using a Micromass LCT Classic, Bruker Maxis 3G UHF-TOF tandem. Protein samples were prepared in MilliQ to a concentration of 1 mg/mL. Organic compounds were dissolved in methanol, water or a drop of DCM in methanol depending on compound solubility.

7.1.6 Buffer Preparation

All buffers were prepared with water that was purified with a Milli-Q® Integral Water Purification system from Merck Millipore. After preparation and pH adjustments, all buffers were filtered through a 0.2 µm Durapore® filter.

7.1.7 Protein expression

Expression of both *M. tuberculosis* AnPRT and *E. coli* PRAI:InGPS was carried out using a previously reported protocol.⁵⁷ The TrpD (Rv2192c) and TrpFC genes had already been cloned into the expression vector pET-23a (+) (Novagen) and pProEX-HTb (Invitrogen™). *E.coli*/BL21 (DE3)/Chap3 cells were used for the expression of both proteins. These cells were grown in autoclaved LB (Lennox LB) at a concentration of 20 g/L containing 1 mL spectinomycin (100 mg/mL), 100 µL of ampicillin (100 mg/mL) and chloramphenicol (25 mg/mL). The preculture was grown overnight with shaking (180 rpm) at 37 °C.

7.1.8 Autoinduction

Auto induction of protein expression was carried out using 1 L cultures. For 1 L of culture, 10 mL of overnight preculture was added to an autoclaved solution ZY containing 10 g tryptone and 5 g yeast extract in 958 mL in a 3 L baffled conical flask. Then, 20 mL of stock solution of 50 × M and 50 × 5052 was added followed by the addition of 1 mL of MgSO₄, 0.2 mL of 1000 × trace metal elements stock solution and 1 mL of each antibiotic (Table 7.1). Subsequently, the complete autoinduction media was incubated at 37 °C with shaking at 180 rpm for 4–6 h until the culture was visibly turbid. After that time, the culture was transferred to 20 °C in a shaking incubator (180 rpm) for 24–36 h. Cells were harvested by centrifugation (14,000 g

for 30 min at 4 °C) and the cell pellet was flash-frozen in liquid nitrogen and stored at –80 °C for later use.

Table 7.1 The culture medium for autoinduction.

ZY	958 mL	tryptone	1%
		yeast extract	0.5%
50 x M	20 mL	Na ₂ HPO ₄	1.25 M
		KH ₂ PO ₄	1.25 M
		NH ₄ Cl	2.5 M
		Na ₂ SO ₄	0.25 M
50 x 5052	20 mL	glycerol	25% (w/v)
		glucose	25% (w/v)
		α-lactose	10% (w/v)
1 M MgSO ₄	2 mL	MgSO ₄	2 mM
1000 x trace metal in 60 mM HCl	0.2 mL	FeCl ₃	50 mM
		CaCl ₂	20 mM
		ZnSO ₄	10 mM
		CoCl ₂	2 mM
		CuCl ₂	2 mM
		NiCl ₂	2 mM
		NaMoO ₄	2 mM
		H ₃ BO ₃	2 mM
Antibiotics	1 mL (each)	ampicillin	(100 mg/mL)
		chloramphenicol	(25 mg/mL)

7.1.9 Cell harvesting

Large cell cultures were harvested in 1 L centrifugation bottles at 14,000 *g* for 30 min at 4 °C using a Fiberlite™ F9-6x1000 LEX fixed-angle rotor (Thermo Fisher Scientific). Small cultures were harvested in 50 mL centrifuge tubes at 12,000 *g* for 10 min at 4 °C using a Fiberlite™ F14-14x50cy fixed-angle rotor (Thermo Fisher Scientific). Harvested cell pellets were either immediately lysed or stored at –80 °C.

7.1.10 Cell lysis

Protein cells were lysed either by sonication or using a homogeniser. Sonication was performed using an Omni-Ruptor 4000 Ultrasonic Homogeniser (Omni International). Cell pellets were resuspended in 20–50 mL lysis buffer (50 mM Tris.HCl, 200 mM NaCl and 25 mM imidazole, pH 8.0). The suspended cells were placed in a beaker surrounded with ice and sonicated in 4–5 multiplies of 5 min, at 70% power with the pulse set at 40. Alternatively, large-volume cell lysis was done using a Microfluidics Lab Homogeniser M-110P. Cell pellets were suspended in lysis buffer and passed through the homogeniser twice for complete lysis. The clarified cell lysate was obtained after centrifugation at 12,000 *g* for 30 min at 4 °C.

7.1.11 Protein purification

7.1.11.1 Immobilised metal affinity chromatography (IMAC)

Cell supernatants (*M. tuberculosis* AnPRT and *E. coli* PRAI:InGPS) were filtered and loaded onto a 5 mL HisTrap™ HP column (packed with Ni Sepharose™ High-Performance resin, GE Healthcare). The chromatography was performed on a GE Healthcare ÄKTApurifier™ 10 machine at 4 °C. All buffers and samples were filtered (0.2 µm) prior to use. Samples were loaded using either a 50 mL or 200 mL Superloop™ (GE Healthcare). Protein which bound to the column was eluted using an increasing gradient of low to high imidazole buffer (50 mM to 500 mM imidazole, 50 mM Tris. HCl, 200mM NaCl buffer at pH 8.0) and fractions containing the enzyme of interest were pooled together for further purification.

7.1.11.2 Size exclusion chromatography (SEC)

Purified protein from IMAC was further purified based on molecular weight at 4 °C. SEC was performed using a HiLoad™ 26/60 Superdex™ 200 prep grade column (GE Healthcare) at a flow rate of 0.5 mL/min either in crystal buffer (50 mM Tris.HCl, 150 mM NaCl and 5% glycerol) or low imidazole buffer (50 mM Tris.HCl, 200 mM NaCl and 25 mM imidazole) depending on the intended use of the protein.

7.1.12 Sodium dodecyl sulphate polyacrylamide gel electrophoresis (SDS-PAGE)

Fractions containing the enzyme of interest were analysed by SDS-PAGE, which was performed using pre-cast gels using either Bolt® 10% Bis-Tris Plus 1.0 mm 15-well pre-cast protein gels (Life Technologies) with Bolt® MES SDS running buffer (Life Technologies). Samples were mixed with 1× Bolt® LDS sample buffer, DTT and boiled before loading. Electrophoresis was carried out at 200 V for 32 min. Novex® Sharp pre-stained protein standards (Invitrogen) were also run as the marker in one lane of each gel.

All SDS-PAGE gels were stained using a hot solution containing 0.1% (w/v) coomassie brilliant blue R-250, 10% (v/v) glacial acetic acid and 40% (v/v) methanol for 30 min with gentle shaking. Gels were de-stained with a hot solution containing 10% (v/v) glacial acetic acid and 40% (v/v) methanol. A white light transilluminator was used for photographing the gels.

7.1.13 Concentration and storage of enzymes

Protein solutions were concentrated using a 10 kDa molecular weight cut off (MWCO) Vivaspin® Turbo 15 device (Sartorius) via centrifugation at 4000 *g*, 4 °C to achieve the desired concentration. Concentrated protein solutions were divided into 200 µL aliquots, flash-frozen with liquid N₂ and stored at –80 °C.

7.1.14 Determination of protein concentration

The concentration of both proteins was measured by absorption at 280 nm on a Nanodrop ND-1000 spectrophotometer. The protein-specific molar extinction coefficient (ϵ_{280}) or 1% absorbance values were calculated for each protein from the protein sequences using the ProtParam tool (Table 7.2).⁸¹

Table 7.2 Extinction coefficients for both proteins.

Protein	ϵ_{280} (M ⁻¹ cm ⁻¹)	Absorbance (1%) (=1 mg/mL)
<i>M. tuberculosis</i> AnPRT	34,615	8.94
<i>E.coli</i> PRAI:InGPS	40,715	7.72

7.1.15 Determination of PRPP and anthranilate concentrations

The concentrations of the stock solution of the natural substrates for AnPRT were determined using an enzyme coupled assay.⁵⁷ The concentration of PRPP was measured by limiting the concentration of PRPP while anthranilate was present in excess (at a maximum concentration of 15 mM to avoid enzyme inhibition by anthranilate); at least 20 times the concentration of that expected for PRPP. The change in absorbance, before initiation of the reaction by PRPP and at completion, was measured as ΔA_2 . For a control reaction, without the addition of enzyme, the change in absorbance due to the addition of PRPP in the reaction mixture was measured as ΔA_1 . The total change in absorbance ΔA ($\Delta A_2 - \Delta A_1$) was converted using Beer's Law to obtain the concentration of the product, using the molar extinction coefficient of $7500 \text{ M}^{-1} \text{ cm}^{-1}$, in the cuvette. Then, the substrate concentration in the stock solution was calculated. A similar method was used to calculate the exact concentration of anthranilate.

7.1.16 Lanzetta phosphate assay

The exact concentration of the synthesised phosphate-containing compounds was determined using the Lanzetta assay.¹⁶⁹ Lanzetta reagent was prepared fresh as required from the following components: 3 parts 0.045% w/v malachite green in water, 1 part 4.2% w/v ammonium molybdate in 4 M HCl, 0.1 parts 1.5% v/v Triton X-100 in water. The components were mixed in the dark and stirred for 1 h before the solution was filtered through a $0.45 \mu\text{m}$ syringe filter. For the qualitative detection of phosphate-containing compounds, a $20 \mu\text{L}$ sample of each fraction was mixed with $250 \mu\text{L}$ of Lanzetta reagent and the colour change was judged by optical inspection. For the quantitative determination of inhibitor concentration, $300 \mu\text{L}$ of the inhibitor solution was incubated with $10 \mu\text{L}$ calf alkaline phosphatase solution (5 units/mL in 4 mM MgCl_2) for at least 2 h. To $100 \mu\text{L}$ of the digested sample, $700 \mu\text{L}$ Lanzetta reagent was added and the absorbance at 630 nm was determined after 20 min. A calibration curve for the determination of phosphate concentration was obtained from an analogous analysis of solutions of appropriate concentrations (6–150 μM) of KH_2PO_4 , which had been dried in a high vacuum for at least 3 h before use. As a control, a glucose-6-phosphate solution of known concentration was also digested with calf alkaline phosphatase and analysed.

7.1.17 Standard kinetics assay

All stocks solutions for assay were prepared with Milli-Q water, which was treated with Chelex® 100 resin (Bio-Rad) to remove metal ions from the water. All kinetic assays were carried out using an enzyme coupled assay.⁵⁷ The kinetic measurements monitored the formation of the InGP product at 270 nm on a Varian Cary 300 UV-visible spectrophotometer. All enzymatic reactions were carried out at 25 °C in quartz cuvettes with a path length of 1 cm in Tris buffer (50 mM Tris.HCl, 150 mM NaCl, pH 8.0). All assay solutions and baseline absorbance values were equilibrated at 25 °C and then the reactions were initiated by the addition of *M. tuberculosis* AnPRT or PRPP. In all assay, *E.coli* PRAI:InGPS was kept at a concentration 10 to 15-fold higher compared to *M. tuberculosis* AnPRT to ensure that *M. tuberculosis* AnPRT was the rate determining step. The reactions were initiated either with PRPP or anthranilate. All measurements were carried out in triplicate and averaged. Initial rates of reaction were determined using a least-square fit of the initial rate data, which was used to calculate kinetic parameters using the software Graphpad Prism 7.0

7.1.17.1 Kinetic and Inhibition assay in Chapter 2

The assays for determining the kinetic parameters held the concentration of one substrate constant while varying that of the other substrate and vice versa. The reaction mixture for determining the kinetic parameters for *M. tuberculosis* AnPRT contained 1 mM MgCl₂, 0.04 μM *M. tuberculosis* AnPRT, 0.4 μM *E. coli* PRAI:InGPS in 50 mM Tris.HCl, 150 mM NaCl at pH 8.0. To determine K_M (anthranilate), the PRPP concentration was held at 400 μM. The concentration of anthranilate was varied from 0.5 to 12 μM. To determine K_M (PRPP), the anthranilate concentration was held at 15 μM and the PRPP concentration was varied from 5 to 380 μM.

For the determination of apparent K_i values, assays with respect to anthranilate were performed in a final volume of 1 mL and consisted of 50 mM Tris.HCl (pH 8.0), 150 mM NaCl, 1 mM MgCl₂, 0.05 μM AnPRT, 0.5 μM *E. coli* PRAI-InGPS, 103 μM PRPP ($\approx 2 \times K_M$), while anthranilate was varied from 0 to 8 μM at various concentrations of inhibitor. For assays testing inhibition with respect to PRPP, the concentration of PRPP was varied from 0 to 250 μM and anthranilate was held constant at 3.2 μM ($\approx 2 \times K_M$). Inhibitor stocks of 4 mM (w/v) in

2% DMSO were diluted to create inhibitor solutions at various concentrations. The control reaction for *M. tuberculosis* AnPRT was performed with 5% DMSO.

7.1.17.2 Inhibition assay in Chapter 3

Stock solutions (50 mM, w/v) of all compounds were prepared either in water or 2% DMSO. Inhibitor stocks of 50 mM (w/v) in 2% DMSO were diluted to create inhibitor solutions at various concentrations. Therefore, the final concentration of DMSO in the assays was less than 1%. The control reaction for *M. tuberculosis* AnPRT was performed with 5% DMSO. For the determination of apparent K_i values, assays with respect to anthranilate were performed in a final volume of 1 mL and consisted of 50 mM Tris.HCl (pH 8.0), 150 mM NaCl, 1 mM $MgCl_2$, 0.04 μM AnPRT, 0.6 μM *E. coli* PRAI-InGPS, 103 μM PRPP ($\approx 2 \times K_M$), while anthranilate was varied from 0 to 8 μM at various concentrations of inhibitor. For assays testing inhibition with respect to PRPP, the concentration of PRPP was varied from 0 to 250 μM and anthranilate was held constant at 3.2 μM ($\approx 2 \times K_M$).

7.1.17.3 Inhibition study in Chapter 4

For the determination of apparent K_i values of AnPRT with PRPP analogues (R5P, **4.11**, **4.12**, **4.14**, **4.15** and **4.16**), assays with respect to PRPP were performed in a final volume of 1 mL and consisted of 50 mM Tris.HCl (pH 8.0), 150 mM NaCl, 1 mM $MgCl_2$, 0.04 μM AnPRT, 0.6 μM *E. coli* PRAI-InGPS. Anthranilate was held constant at 10 μM and the concentration of PRPP was varied from 0 to 250 μM . The concentration of inhibitors was varied from 0 to 500 μM for R5P, 0 to 640 μM for analogue **4.11**, 0 to 160 μM for cyclopentene phosphate **4.12**, 0 to 750 μM for diphosphorylated amine **4.14**, 0 to 800 μM for iminoribitol analogue **4.15** and 0 to 1200 μM for **4.16**. The inhibition of AnPRT with respect to PRPP for analogues **4.11** and **4.14** was also determined in the presence of 50 μM sodium diphosphate dibasic additive using similar assay conditions. The concentration of analogues **4.11** and **4.14** was varied from 0 to 400 μM . For analogues **4.11** and **4.14**, inhibition assays with respect to anthranilate were carried out with the concentration of anthranilate varying from 0 to 8 μM while PRPP was held constant at 400 μM .

For the determination of the apparent K_i (PRPP) for the iminoribitol analogues **4.17**, **4.18** and **4.19**, the assays contained 4 μM anthranilate ($\approx 2 \times K_M$) while PRPP was varied from 0 to 250 μM . The concentration of inhibitors was varied from 0 to 250 μM for **4.17**, 0 to 120 μM for **4.18** and 0 to 40 μM for **4.19**. For assays with respect to anthranilate, the assays contained 100 μM PRPP ($\approx 2 \times K_M$) and anthranilate from 0 to 8 μM . The concentration of inhibitors was varied from 0 to 20 μM for **4.17**, 0 to 120 μM for **4.18** and 0 to 120 μM for **4.19**.

7.1.17.4 Inhibition assay in Chapter 5

For the determination of the K_i (PRPP) values for analogues **5.2**, **5.6** and **5.8**, the assays contained 50 mM Tris.HCl (pH 8.0), 150 mM NaCl, 1 mM MgCl_2 , 0.04 μM AnPRT, 0.6 μM *E. coli* PRAI: InGPS, anthranilate 3 μM ($\approx 2 \times K_M$), while PRPP was varied from 0 to 250 μM . The concentration of inhibitors was varied from 0 to 120 μM for **5.2**, 0 to 300 μM for **5.6** and 0 to 40 μM for **5.8**. For assays with respect to anthranilate, the concentration of anthranilate was varied from 0 to 250 μM and PRPP was held constant at 100 μM ($\approx 2 \times K_M$). The concentration of inhibitors was varied from 0 to 120 μM for **5.2**, 0 to 30 μM for **5.6** and 0 to 30 μM for **5.8**. The inhibition of AnPRT for analogues was also determined in the presence of a constant concentration of sodium diphosphate (50 μM) and monophosphate (1 mM) using similar assay conditions. The concentration of analogue **5.8** was varied from 0 to 40 μM .

7.1.18 Differential scanning fluorimetry (DSF)

Melting temperatures of *M. tuberculosis* AnPRT in the presence of various additives were measured by DSF, using an iCycler iQ5 multicolour real-time PCR detection system (Bio-Rad). The obtained result was analysed using Protein Thermal Shift™ Software 1.3. The procedure used by a previous member of the group⁵⁷ was utilised for the DSF experiments. Each sample (triplicate measurements) and reference were scanned from 15–95 °C at a rate of 0.2 °C every 20 s. Each sample and reference were made with 100 μL of buffer (50 mM Tris.HCl, 200 mM NaCl, pH 8.0, including any ligands) and 5 μL of 250 \times SYPRO orange dye. To determine the T_m , the reference cell was prepared with 21 μL of the sample condition and 4 μL of water. After that, 16 μL of 1 mg/mL protein was added to the remaining sample condition and 25 μL of the sample condition was transferred into each sample cell. The melting temperature of

the protein was determined in the presence of various concentrations of several ligands: Mg^{2+} (1 mM), PRPP (0.5 mM), **3.9** (50 μM , 350 μM), anthranilate and ACS172 (15 μM , 200 μM and 1.4 mM).

7.1.19 Isothermal titration calorimetry

Isothermal titration calorimetry (ITC) experiments were performed on a Nano Isothermal Titration Calorimeter (TA Instruments) at 278 K. All experiments consisted of 22 or 30 injections: one 0.42 μL injection and 21 or 29 subsequent 2.02 μL injections. Every titration measured the heat change generated by each injection of ligand from the syringe into 400 μL of protein solution in the sample cell. Buffer constituents and pH values were well matched for ligand and protein solutions. The cell and syringe were washed and cleaned several times prior to use. All solutions were filtrated and degassed before loading into the sample cell and syringe. The initial data point was excluded from the model due to ligand diffusion across the needle tip during the equilibration period. Heats of dilution experiments were measured independently for each experiment and subtracted from the integrated data before curve fitting to the appropriate model using NanoAnalyze (TA Instruments). The experimental set-up for each ITC experiment is listed in Table 7.3.

Table 7.3 The experimental set-up for ITC

	Buffer	Concentration of <i>M. tuberculosis</i> AnPRT (sample cell)	Ligand (syringe)
Chapter 3	50 mM Tris.HCl (pH 8.0), 150 mM NaCl and 1 mM MgCl_2	60 μM	350 μL 3.9
	50 mM Tris.HCl (pH 8.0), 150 mM NaCl and 1 mM MgCl_2	60 μM	400 μL PRPP
	50 mM Tris.HCl (pH 8.0), 150 mM NaCl, 1 mM MgCl_2 and 350 μL 3.9	60 μM	400 μL PRPP
Chapter 4	50 mM Tris.HCl (pH 8.0) and 150 mM NaCl	60 μM	5 mM MgCl_2

	50 mM Tris.HCl (pH 8.0), 150 mM NaCl and 1 mM MgCl ₂	60 μ M	400 μ L PRPP
	50 mM Tris.HCl (pH 8.0) and 150 mM NaCl	60 μ M	400 μ L PRPP
	50 mM Tris.HCl (pH 8.0) and 150 mM NaCl	60 μ M	1 mM PRPP
	50 mM Tris.HCl (pH 8.0), 150 mM NaCl and 1 mM MgCl ₂	1 mM	5 mM anthranilate
	50 mM Tris.HCl (pH 8.0), 150 mM NaCl and 1 mM MgCl ₂	1 mM	4 mM 4FA
Chapter 5	50 mM Tris.HCl (pH 8.0), 150 mM NaCl, 1 mM MgCl ₂	83 μ M	5 mM 5.8
	50 mM Tris.HCl (pH 8.0), 150 mM NaCl, 1 mM MgCl ₂ and 500 μ M sodium diphosphate dibasic	83 μ M	5 mM 5.8

7.1.20 Crystallography

7.1.20.1 Crystal condition for variant *M. tuberculosis* AnPRTs

Crystals of *M. tuberculosis* AnPRTs were grown, under previously published conditions, by hanging-drop vapour diffusion.⁵⁷ Protein solutions (5–6 mg/mL) including the desired concentration of ligand in 50 mM Tris.HCl, 150 mM NaCl, 5% glycerol (v/v), pH 8.0 were mixed (1:1 v/v) with a reservoir solution containing 200 mM sodium imidazole malate (pH 6.0–8.0), 6%–20% PEG-4000 and Milli-Q. Droplet sizes were either 2 or 3 μ L. Crystals grew overnight at 20 °C as rectangular crystals of various sizes. Crystals were flash-frozen directly using liquid nitrogen or cryoprotected first by dipping the crystal in a cryoprotectant solution containing 25% glycerol and mother liquor. The reported structures in the thesis are listed with the additive concentration and reservoir conditions in Table 7.4.

Table 7.4 The crystallisation conditions for M. tuberculosis AnPRT crystals with various ligands.

	Ligand concentration	Reservoir condition
Chapter 2	10 mM 2.6	200 mM sodium imidazole malate (pH 6.5) and PEG 8 %,
	2 mM 2.10	200 mM sodium imidazole malate (pH 7.0) and PEG 10 %
	2 mM 2.10 , 10 mM PRPP, 10 mM Mg ²⁺	200 mM sodium imidazole malate (pH 7.0) and PEG 10 %
	2.73 mM 2.11	200 mM sodium imidazole malate (pH 6.5) and PEG 12%
	2.73 mM 2.11 , 10 mM PRPP, 20 mM Mg ²⁺	200 mM sodium imidazole malate (pH 7.0) and PEG 10%
Chapter 3	8.75 mM 3.5 , 20 mM Mg ²⁺	200 mM sodium imidazole malate (pH 6.0) and PEG 8 %
	3.5 mM 3.9 , 20 mM Mg ²⁺	200 mM sodium imidazole malate (pH 6.5) and PEG 16%
Chapter 4	10 mM PRPP, 20 mM Mg ²⁺	200 mM sodium imidazole malate (pH 7.0) and PEG 10%
	6mM anthranilate, 20mM Mg ²⁺	200 mM sodium imidazole malate (pH 6.5) and PEG 16%
Chapter 5	10 mM 5.8 , 20 mM Mg ²⁺ and 5 mM sodium diphosphate dibasic	200 mM sodium imidazole malate (pH 6.5) and PEG 14%

7.1.20.2 Data collection and processing

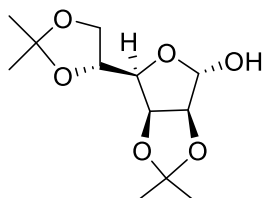
All single-crystal X-ray diffraction data were collected at the Australian Synchrotron either on Macromolecular Crystallography (MX1)¹⁷⁰ or Micro Crystallography (MX2) beamlines.¹⁷¹ Data were processed using X-ray Detector Software (XDS), iMosflm, aimless and truncate (CCP4 suite).^{172–175} Resolution cut-offs were decided based on a CC½ value of >0.5.⁹³ The initial

phases of various *M. tuberculosis* structures were calculated by molecular replacement with chain A of an apo AnPRT (PDB: 3QQS) search model using MolRep¹⁷⁶ or Phaser⁹⁶ in the CCP4 suite. The search model was prepared by deleting all ligands and waters from the structure prior to use. The initial structural model was then refined with Refmac5 using rigid-body refinement and restrained refinement.^{97,177} Coot was used to analyse the electron density map for building the iterative model.¹⁷⁸ After the model and electron density was judged to be in good agreement in all regions apart from the ligand binding site, the electron density in the ligand binding site was examined. If appropriate electron density was displayed, ligand, waters and potential other molecules were added to the model with further refinement with Refmac5. Omit maps ($2|F_o - F_c|$ and $|F_o - F_c|$) were generated using the program FFT (CCP4 program suite) prior to the addition of the ligands. The MolProbity and PDB validation server were used to validate all structures.^{179,180}

7.2 Synthesis of analogues for Chapter 4

7.2.1 Synthesis of cyclopentane analogue 4.11

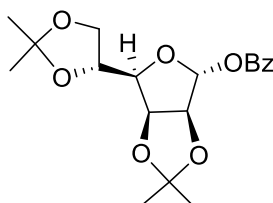
2,3,5,6-di-*O*-Isopropylidene- α -D-mannose (**4.1**)¹²⁸



D-Mannose (40.00 g, 222.00 mmol) was suspended in anhydrous acetone (400 mL). Sulfuric acid (2.80 mL, 55.6 mmol) was added, followed by dropwise addition of 2,2-dimethoxy propane (60 mL, 488 mmol) and the mixture was stirred at rt under an atmosphere of nitrogen. After 6 h, TLC (petrol:ethyl acetate 1:1) indicated the formation of a major product (R_f 0.40) and complete consumption of the starting material (R_f 0.0). The reaction mixture was quenched with triethylamine (16.8 mL, 120.00 mmol) and concentrated *in vacuo*. The residue was purified by flash chromatography (5/1 to 2/1) to afford 2,3,5,6-di-*O*-isopropylidene- α -D-mannose **4.1** (48.00 g, 83%) as a white crystalline solid. IR (ν): 514.4, 683.2, 837.7, 974.6, 1058.9, 1162.8, 3431.0 cm^{-1} ; $[\alpha]_D^{20}$ +46 (c , 1.0 in CHCl_3); δ_H (400 MHz, CDCl_3)

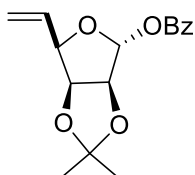
1.32, 1.37, 1.45, 1.46 (12H, 4 × s, 4 × CH₃, iso prop), 2.90 (1H, bs, 1-OH), 4.04 (1H, dd, *J* 8.7, 5.0 Hz, H-6'), 4.08 (1H, dd, *J* 8.7, 6.2 Hz, H-6), 4.18 (1H, dd, *J* 7.1, 3.6 Hz, H-4), 4.40 (1H, dd, *J* 11.7, 6.2 Hz, H-5), 4.61 (1H, d, *J* 5.9 Hz, H-2), 4.80 (1H, dd, *J* 5.9, 3.6 Hz, H-3), 5.37 (1H, s, H-1); δ_C (101 MHz, CDCl₃) 24.63, 25.33, 26.00, 27.00 (4 × Me iso prop), 66.73 (C6), 73.40 (C5), 79.81 (C3), 80.51 (C4), 85.64 (C2), 101.46 (C1), 109.24, 112.82 (2 × Cq iso prop);¹²⁸ HRMS (ESI) calcd. for C₁₂H₂₀NaO₆⁺ [M+H]⁺: 283.1152, obsd.: 283.1152.

Benzoyl 2,3,5,6-di-*O*-isopropylidene-α-D-mannofuranose (**4.2**)¹²⁸



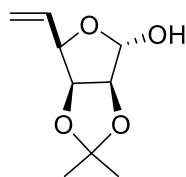
Isopropylidene **4.1** (10.0 g, 38.40 mmol) was dissolved in dry pyridine (100 mL) and cooled to 0 °C. Benzoyl chloride (9.0 mL, 76.8 mmol) was added dropwise over 2 min followed by *p*-dimethylamino pyridine (DMAP) (1.00 g, 8.00 mmol); the resulting reaction mixture was allowed to warm to room temperature. After 2.5 h, TLC analysis (petrol:ethyl acetate, 2:1) showed complete disappearance of the starting material and the formation of a higher running product (*R*_f 0.53). The reaction was poured onto saturated aq. NaHCO₃, diluted with ethyl acetate and the organic layers were washed with saturated aq. NaHCO₃ (2 × 100 mL), H₂O (1 × 100 mL) and brine (1 × 100 mL). The organic layer was dried over MgSO₄, filtered, and concentrated *in vacuo*. The residue was crystallised (petrol/ethyl acetate) to afford benzoyl 2,3,5,6-di-*O*-isopropylidene-α-D-mannofuranose **4.2** as a white crystalline solid (0.90 g, 90%). IR (ν): 517.2, 709.0, 847.0, 963.6, 1023.2, 1038.3.0, 1082.0, 1206.9, 1253.8, 1289.5, 1721.4 cm⁻¹; [α]_D²⁰ +149 (*c*, 0.99 in CHCl₃), δ_H (400 MHz, CDCl₃) 1.37, 1.45, 1.44, 1.52 (12H, 4 × s, Me iso prop), 4.05 (1H, dd, *J* 8.9, 4.4 Hz, H-6'), 4.10–4.13 (2H, m, H-4, H-6), 4.42 (1H, m, H-5), 4.86 (1H, d, *J* 5.9 Hz, H-2), 4.92 (1H, dd, *J* 5.8, 3.6 Hz, H-3), 6.36 (1H, s, H-1), 7.42–7.46 (2H, m, 2H, O-Bz), 7.56–7.58 (1H, m, O-Bz), 7.99–8.01 (2H, m, O-Bz); δ_C (100 MHz, CDCl₃) 25.00, 25.42, 26.29, 27.28 (4 × Me iso prop), 67.19 (C6), 73.12 (C5), 79.70 (C3), 82.90 (C4), 85.54 (C2), 101.83 (C1), 109.67, 113.67 (Cq iso prop) 128.77, 130.12, 133.79 (C_{arom} O-Bz), 165.06 (C=O, O-Bz);¹²⁸ HRMS (ESI) calcd. for C₁₉H₂₄O₇⁺ [M+Na]⁺: 387.1414, obsd.: 387.1406.

Benzoyl 2,3-*O*-isopropylidene- α -D-lyxo-hex-5-enofuranose (**4.3**)³



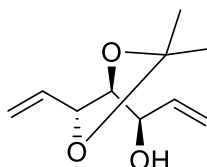
2,3,5,6-Di-*O*-Isopropylidene- α -D-mannofuranose **4.2** (0.50 g, 1.37 mmol) was dissolved in glacial acetic acid (8.50 mL) before water (3.60 mL) was added and the resulting mixture was stirred at 55 °C. After 5 h, TLC analysis (petrol:ethyl acetate, 2:1) showed complete disappearance of the starting material and the formation of a lower running product (R_f 0.0). The reaction mixture was concentrated *in vacuo*. The crude material was suspended in triethyl orthoformate (7.00 mL) and glacial acetic acid (0.04 mL, 0.70 mmol) was added and the reaction mixture was stirred at 80 °C. After 2 h, full conversion was observed by TLC analysis (R_f 0.76, petrol:ethyl acetate, 2:1). The solution was concentrated and heated to 170 °C in an open flask, diphenyl acetic acid (1.75 mg, 0.01 mmol) was added. After 4 h, all starting material had been transformed into a higher running product (R_f 0.55, petrol:ethyl acetate, 4:1). The resulting brown oil was allowed to cool to room temperature. The reaction was poured onto saturated aq. NaHCO₃, diluted with ethyl acetate and the organic layers were washed with H₂O (2 × 25 mL) and brine (2 × 25 mL). The organic layer was dried over MgSO₄, filtered, and concentrated in *vacuo*. Purification by flash chromatography (silica gel, petrol:ethyl acetate, 8:1) gave homogenous product **4.3** (0.22 g, 76%). $[\alpha]_D^{20}$ -99 (*c*, 0.99 in CHCl₃); δ_H (400 MHz, CDCl₃) 1.37, 1.52 (6 H, 2 × s, Me iso prop), 4.62-4.65 (1H, m, H-2), 4.82-4.84 (1H, m, H-3, H-4), 4.88 (1H, m), 5.34 (1H, d, *J* 10.4 Hz, H-6_{cis}), 5.44 (1H, d, *J* 17.2 Hz, H-6_{trans}), 5.93-6.04 (1 H, m, *J* 17.2, 10.4 Hz, H-5), 6.41 (1H, s, H-1), 7.42-7.45 (2H, m, Ar), 7.55-7.57 (1H, m, Ar), 8.00-8.02 (2H, m, Ar); δ_C (101 MHz, CDCl₃) 25.00, 26.10 (2 × CH₃ iso-prop), 81.20, 83.54, 85.42 (C2, C3, C4), 101.34 (C1), 113.26 (Cq iso prop), 119.70 (C6), 128.40, 129.73, 131.47 (C-Ar), 133.36 (C5), 164.98 (CO);¹²⁸ HRMS (ESI) calcd. for C₁₆H₁₈O₅⁺ [M+Na]⁺: 313.1046, obsd.: 313.1046.

2,3-*O*-Isopropylidene- α -D-lyxo-hex-5-enofuranose (**4.4**)¹²⁸



Benzoyl 2,3-*O*-isopropylidene- α -D-lyxo-hex-5-enofuranose **4.3** (8.00 g, 27.55 mmol) was dissolved in 20 mL methanol, *t*-BuOK was added until a pH of 12–14 and the reaction mixture was stirred at rt. After 4 h, TLC analysis (petrol:ethyl acetate, 1:1) showed complete consumption of the starting material and the formation of a lower running product (R_f 0.66). DOWEX H⁺ was added until the solution was neutral (pH 7); the resin was filtered and the filtrate was concentrated *in vacuo*. The residue was purified by flash chromatography (petrol:ethyl acetate, 10:1 to 7.5:1) to give 2,3-*O*-isopropylidene- α -D-lyxo-hex-5-enofuranose **4.4** (4.2 g, 84%) as a clear oil. δ_H (400 MHz, CDCl₃) 1.31, 1.46 (6H, 2 \times s, 3H, Me iso-prop), 4.59–4.67 (2H, m, H-2, H-4), 4.73 (1H, dd, *J* 3.6, 5.6 Hz, H-3), 5.32 (1H, d, *J* 10.2 Hz, H6_{cis}), 5.36–5.54 (2H, m, H-1, H6_{trans}), 5.94–6.1 (1H, m, H-5); δ_C (101 MHz, CDCl₃) 24.85, 26.04 (2 \times Me iso-prop), 81.67, 81.70 (C3, C4), 85.75 (C2), 109.19 (C1), 112.62 (Cq iso-prop), 119.18 (C6), 132.17 (C5).¹²⁸

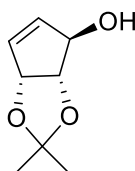
(3*R*,4*S*,5*R*)-3,4-*O*-Isopropylidene-hepta-1,6-diene-3,4,5-triol (4.5)¹²⁷



Methyl triphenylphosphonium bromide (19.30 g, 54.00 mmol) in THF/HMPA (50 mL, 3/1, v/v), *t*-BuOK (6.10 g, 54.0 mmol) was added at -78 °C. The resulting solution was stirred for an additional hour at -20 °C. A solution of 2,3-*O*-isopropylidene- α -D-lyxo-hex-5-enofuranose **4.4** (5.0 g, 27.1 mmol) in THF (10 mL) was added, stirred for 10 min at -20 °C and the solution was allowed to warm to rt. After 16 h, all starting material had been converted into a slightly higher running product (R_f 0.69, petrol:ethyl acetate, 2:1). The reaction mixture was quenched with aq. sat. NH₄Cl and extracted with ethyl acetate. The organic layer was washed with NH₄Cl and water. The organic layer dried with MgSO₄, filtered and concentrated. Purification by flash chromatography (silica gel, petrol:ethyl acetate, 10:1 to 8:1) gave compound (3*R*,4*S*,5*R*)-3,4-*O*-isopropylidene-hepta-1,6-diene-3,4,5-triol **4.5** as a yellow liquid (4.72 g, 87%). $[\alpha]_D^{20}$ -64 (*c*, 1.0 in CHCl₃); δ_H (400 MHz, CDCl₃) 1.38, 1.52 (3H, 2 \times s, Me iso-prop), 4.03–4.15 (2H, m), 4.49 (1H, t, *J* 7.04 Hz), 5.17 (4H, m, H-1, H-7) 5.84 (1H, ddd, *J* 5.1, 10.6, 17.1 Hz) 6.00 (1H, ddd, *J* 7.8, 9.9, 17.4 Hz); δ_C (101 MHz, CDCl₃) 24.97, 27.36 (2 \times Me iso-prop), 70.58, 78.91, 80.63 (C-3, C-4, C-5), 108.76 (Cq iso-prop), 116.98, 119.30 (C-1, C-7),

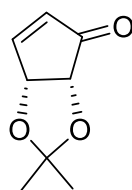
133.92, 136.72 (C-2, C-6);¹²⁷ HRMS(ESI) calcd. for C₁₀H₁₆O₃⁺ [M+Na]⁺: calcd. 207.0992, obsd. 207.0986.

(3*R*,4*S*,5*R*)-3,4-*O*-Isopropylidene-cyclopentene-3,4,5-triol (4.6)¹²⁷



(3*R*,4*S*,5*R*)-3,4-*O*-Isopropylidene-hepta-1,6-diene-3,4,5-triol **4.5** (4.51 g, 24.48 mmol) was dissolved in DCM (15.00 mL), the solution was degassed by passing through a stream of nitrogen for 15 min and 104 mg (0.5 mol%) of Grubbs^{1st} generation catalyst was added under an atmosphere of nitrogen. After 14 h, TLC analysis indicated complete conversion of the starting material (*R_f* 0.47, petrol:ethyl acetate, 3:1). The reaction mixture was purified by flash chromatography (10% ethyl acetate in petrol) to give compound **4.6** (2.7 g, 70%) as a brown oil. δ_{H} (400 MHz, CDCl₃) 1.33, 1.38 (6H, 2 × s, Me iso-prop), 1.80 (1H, bs., OH), 4.50 (1H, d, *J* 6.0 Hz, H-3), 4.78 (1H, s, H-5), 5.27 (1H, d, *J* 5.2 Hz, H-4), 5.88–5.90 (1H, m, H-3) 6.02 (d, *J* 6.0, 1H); δ_{C} (101 MHz, CDCl₃) 25.64, 27.22 (Me iso-prop), 80.61(C-5), 84.23 (C-4), 85.22 (C-3), 111.64 (Cq iso-prop), 134.73, 135.09 (C-1, C-2).¹²⁷

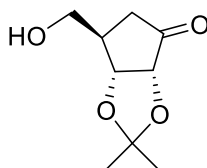
(2*R*,3*R*)-2,3-*O*-Isopropylidene-4-cyclopenten-1-one (4.7)¹³¹



Oxalyl chloride (0.27 mL, 3.20 mmol) was dissolved in DCM (6.00 mL); the solution was stirred at -60 °C. DMSO (0.23 mL, 3.20 mmol) was also dissolved into DCM (2 mL) at -60 °C and added dropwise into the oxalyl chloride solution in cal. 5 min. Stirring was continued for 15 min followed by the addition of compound **4.6** (0.50 g, 3.20 mmol) in cal. 5 min. The reaction mixture was stirred for 15 min and triethylamine (0.99 mmol) was added in cal. 2 min. with stirring at -60 °C. The cooling bath was removed, followed by the addition of water at rt. Stirring was continued for 10 min and the organic layer was extracted with DCM. The organic layer was washed four times with water to remove DMSO and dried over Na₂SO₄, filtered and

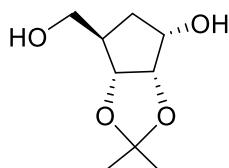
concentrated. Purification by flash chromatography (8% ethyl acetate in petrol) was carried out to give compound (2*R*,3*R*)-2,3-*O*-isopropylidene-4-cyclopenten-1-one **4.7** (4.71 g, 95%) as white crystals. $[\alpha]_D^{20} -39$ (*c*, 0.99 in CHCl₃), Lit. $[\alpha]_D - 65.5$ (*c*, 1.02, CHCl₃);¹³¹ δ_H (400 MHz, CDCl₃) 1.39 (6H, 2 × *s*, Me iso-prop), 4.44 (1H, *d*, *J* 5.2, H-2,) 5.24 (2H, *dd*, *J* 2.4, 5.6, H-3) 6.20 (1H, *d*, *J* 6.0 Hz, H-5), 7.58 (1H, *dd*, *J* 2.0, 6.0 Hz, H-4); δ_C (101 MHz, CDCl₃) 26.12, 27.38 (2 × Me iso-prop), 76.58 (C2), 78.56 (C3), 115.52 (Cq iso-prop), 134.30 (C5), 159.53 (C4), 202.5(C1);¹³¹ HRMS (ESI) calcd. for C₈H₁₀O₃⁺ [M+H]⁺: calcd. 155.0703, obsd. 155.0703 and HRMS (ESI) calcd. for C₈H₁₀O₃⁺ [M+Na]⁺: calcd. 177.0522, obsd. 177.0528. **Crystallography:** Single crystals of C₈H₁₀O₃ were selected and mounted on a nylon loop on a SuperNova Dual, Cu at zero, Atlas diffractometer. The crystals were kept at 120.01(2) K during data collection. The structure was solved (Figure 4.10 and appendix 1) by Dr Matthew Polson using Olex with the SHELXL refinement program.^{181,182}

(2*R*,3*R*,4*R*)-2,3-*O*-Isopropylidene-4-hydroxymethylcyclopentan-1-one (4.8)¹³¹



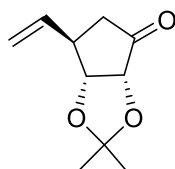
A solution (50.00 mg 0.32 mmol) of (2*R*,3*R*)-2,3-*O*-isopropylidene-4-cyclopenten-1-one **4.7** and 36 mg benzophenone in 25 mL MeOH was degassed by flushing with nitrogen for 1 h. The solution was taken into a Pyrex tube and irradiated at 371 nm in a UV LED chamber. After 90 min, TLC analysis (petrol:ethyl acetate, 3:1) showed complete consumption of the starting material and formation of a lower running product (*R_f* 0.2). The crude product was purified by column chromatography (Florisil, 10% Ethyl acetate in petrol) to give compound **4.8** (30 mg, 53%) as a colourless oil. $[\alpha]_D^{20} -132$ (*c*, 1.0 in MeOH), Lit. $[\alpha]_D - 148.9$ (*c*, 1.00, MeOH);¹³¹ δ_H (400 MHz, CDCl₃) 1.34, 1.42 (6H, 2 × *s*, Me iso-prop), 2.20 (1H, *d*, *J* 18.0 Hz, H-5), 2.56 (1H, *t*, *J* 4.0 Hz, H-4), 2.71–2.78 (1H, *dd*, *J* 9.2, 18.4, Hz H-5), 3.70, 3.83, (2H, *abq*, *J* 10.4 Hz, CH₂OH), 4.28 (1H, *dd*, *J* 5.2 Hz, H-3), 4.70 (1 H, *d*, *J* 5.6 Hz, H-2); δ_C (101 MHz, CDCl₃) 24.61, 26.71 (2 × Me iso-prop), 37.15 (C2), 38.79 (C3), 64.15 (Cq iso-prop), 76.72 (C5), 78.89 (C4), 81.35 (C6), 214.24 (C1);¹³¹ HRMS (ESI) calcd. for C₉H₁₄O₄⁺ [M+Na]⁺: calcd. 209.0784, Obsd. 209.0781.

(1*S*,2*S*,3*R*,4*R*)-2,3-*O*-Isopropylidene-4-hydroxymethylcyclopentan-1-ol (4.9)¹²⁶



(2*R*,3*R*,4*R*)-2,3-*O*-Isopropylidene-4-hydroxymethylcyclopentan-1-one **4.8** (2.5 g, 13 mmol, 1.0 eq.) was dissolved in benzene (40 mL). The reaction was allowed to cool to 0 °C and sodium triacetoxyborohydride (5 g, 22.8 mmol, 1.8 eq.) was added. The reaction was stirred at rt. After 17 h, TLC analysis (petrol:ethyl acetate, 1:2) showed complete conversion into the product (R_f 0.20). The reaction mixture was concentrated and then washed with saturated NH_4Cl , water, followed by extraction twice with CDCl_3 and then once with ethyl acetate. The organic layer was combined and washed twice with 2N HCl to remove the boron ester, extracted first with CDCl_3 and then with ethyl acetate. The combined organic layers were washed with brine, dried and concentrated. The crude product was purified by column chromatography (silica, ethyl acetate:petrol: Et_3N , 2:1:0.1) gave **4.9.1**¹⁸³ (1.96 g, 70%) and **4.9** (0.28 g, 10%) as a colourless oil. **4.9**: δ_{H} (400 MHz, CDCl_3) 1.35, 1.51 (6H, 2 \times s, iso-prop), 1.75 (1H, m, H-5), 1.92 (1H, m, H-5), 2.29 (1H, t, J 4.0 Hz, H-4), 3.51, 3.63 (2H, m, CH_2OH), 3.70, 3.83 (2H, abq, J 10.4 Hz, CH_2OH), 4.12 (1H, dd, J 5.2 Hz, H-3), 4.52 (2 H, m, H-2, H-1); δ_{C} (101 MHz, CDCl_3) 24.35, 26.15 (2 \times Me iso-prop), 34.92 (C2), 44.38 (C3), 63.99 (Cq iso prop), 71.27 (C5), 79.71 (C4), 82.59 (C6), 111.91 (C1);¹²⁶ HRMS (ESI) calcd. for $\text{C}_9\text{H}_{16}\text{O}_4^+$ $[\text{M}+\text{Na}]^+$: calcd. 211.0941, obsd. 211.0943.

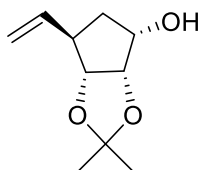
(-)-2*R*,3*R*,4*R*)-2,3-Dihydroxy-2,3-*O*-isopropylidene-4-vinylcyclopentan-1-one (4.7.1)¹³²



Vinylmagnesium bromide solution (1 M) in THF (35 mL, 26 mmol) was added dropwise to a solution of $\text{CuBr}_2\text{Me}_2\text{S}$ (0.35 g, 1.7 mmol) in THF (80 mL) at -78 °C. The reaction mixture was stirred for 10 min before being added dropwise to a solution of **4.7** (3.0 g, 19.5 mmol), TMSCl (5 mL, 40 mmol) and HMPA (9 mL, 51.2 mmol) in THF (20 mL). The reaction mixture was stirred

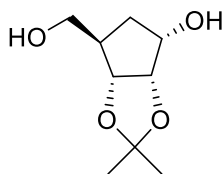
at -78 °C for 5 h under an atmosphere of argon. After this time, TLC (petrol:ethyl acetate, 3:1) indicated the formation of a major product (R_f 0.6) and complete consumption of the starting material (R_f 0.3). The reaction mixture was warmed to 0 °C, quenched by saturated NH_4Cl (30 mL) and the resulting mixture was stirred for 30 min. The organic layer was extracted with ethyl acetate (3 × 100 mL) and washed with H_2O (2 × 100 mL) and brine (100 mL), dried (MgSO_4), filtered and concentrated *in vacuo*. The residue was purified by silica gel flash chromatography (petrol:ethyl acetate, 3:1) to afford product **4.7.1** (2.82 g, 80%) as a yellow oil. δ_{H} (500 MHz, CDCl_3) 1.31 (3H, s, CH_3), 1.40 (3H, s, CH_3), 2.26 (1H, d, J 15.0 Hz, H-5), 2.80 (1H, dd, J 5.0, 15.0 Hz, H-5'), 3.07 (1H, m, H-4), 4.16 (1H, d, J 5.0, H-3), 4.60 (1H, d, J 5.0 Hz, H-2), 5.09 (2H, m, H-7, H-7'), 5.79 (1H, ddd, J 5.0, 10.0, 15.0, H-6); δ_{C} (101 MHz, CDCl_3) 24.88, 26.81 (2 × Me iso prop), 38.48 (C5), 39.70 (C4), 77.81 (C3), 81.33 (C2), 112.36 (Cq iso prop), 116.38 (C7), 137.13 (C6), 213.19 (CO);¹³² HRMS (ESI) calcd. for $\text{C}_{10}\text{H}_{14}\text{O}_3^+$ $[\text{M}+\text{H}]^+$: 183.1016, obsd.: 183.1022.

(-)-(1S,2S,3R,4R)-2,3-Dihydroxy-2,3-O-isopropylidene-4-vinylcyclopentan-1-ol (4.7.2)¹³²



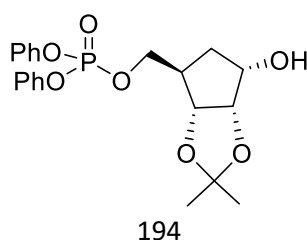
LiAlH_4 (1.05 g, 28 mmol) was suspended in THF (10 mL), the solution was added dropwise into compound **4.7.1** (2.82 g, 15.5 mmol) in THF (60 mL) at 0 °C. The reaction mixture was stirred at room temperature under an atmosphere of argon. After 3 h, TLC (petrol:ethyl acetate, 3:1) indicated the formation of a major product (R_f 0.3) and complete consumption of the starting material (R_f 0.6). The reaction was quenched by sequentially adding water (2 mL), aqueous NaOH (15%, 1 mL) and water (3 mL). The resulting solid was removed by filtration and the filtrate was concentrated *in vacuo* to afford sufficiently pure compound **4.7.2** (2.75 g, 96%) as a colourless liquid. δ_{H} (500 MHz, CDCl_3) 1.33 (3H, s, CH_3), 1.49 (3H, s, CH_3), 1.87 (2H, m, H-5), 2.43 (1H, brs, H-4), 2.72 (1H, m, OH), 4.05 (1H, m, H-1), 4.45 (2H, m, H-2, H-3), 5.05 (2H, m, H-7, H-7'), 5.72 (1H, ddd, J 5.0, 10.0, 15.0, H-6); δ_{C} (101 MHz, CDCl_3) 24.30, 26.06 (2 × Me iso prop), 35.96 (C5), 44.31 (C4), 71.08 (C1), 78.98 (C2), 84.28 (C3), 111.57 (Cq iso prop), 115.23 (C7), 138.01 (C7);¹³² HRMS (ESI) calcd. for $\text{C}_{10}\text{H}_{15}\text{O}_3^+$ $[\text{M}+\text{H}]^+$: 184.1099, obsd.: 184.1095.

(1*S*,2*S*,3*R*,4*R*)-2,3-*O*-Isopropylidene-4-hydroxymethylcyclopentan-1-ol (4.9)¹³²



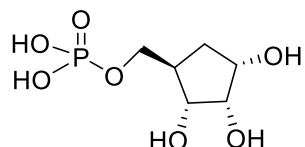
(-)-(1*S*,2*S*,3*R*,4*R*)-2,3-Dihydroxy-2,3-*O*-isopropylidene-4-vinylcyclopentan-1-ol **4.7.2** (1 g, 1.4 mmol, 1.0 eq.) was dissolved in MeOH (15 mL) and H₂O (7 mL). The reaction was allowed to cool to 0 °C. After that, NaIO₄ (0.12 g, 2.0 mmol) and OsO₄ (12 mg, 0.01 mmol) were added. The reaction mixture was stirred at the same temperature for 1 h and then at rt for 2.5 h. After this time, TLC analysis (petrol:ethyl acetate, 3:1) showed complete conversion into the product (*R_f* 0.2). The white solid reaction mixture was filtrated and concentrated. The residue was dissolved in CDCl₃, washed with water, brine, dried and concentrated. The residue was dissolved in MeOH (16 mL) and cooled to 0 °C. NaBH₄ (0.5 g, 3.2 mmol) was added portionwise and stirred at the same temperature. After 3 h, TLC analysis (petrol:ethyl acetate, 1:3) showed complete conversion into the product (*R_f* 0.2). The solvent was removed, and the residue was dissolved in DCM (150 mL) and washed with water, brine and dried over MgSO₄. The crude was purified by a short silica gel column chromatography. The residue was purified by florisil gel flash chromatography (petrol:ethyl acetate, 3:1) to afford the product **4.9** (0.45 g, 44%) as a colourless oil. [α]_D²⁴ +0.86 (*c*, 3.46 in CHCl₃); δ _H (500 MHz, CDCl₃) 1.35, 1.51 (6H, 2 × *s*, Me iso prop) 1.75 (1H, *m*, H-5) 1.92 (1H, *m*, H-5), 2.29 (1H, *t*, *J* 4.0 Hz, H-4) 3.51, 3.63 (2H, *m*, CH₂OH), 3.70, 3.83 (2H, *abq*, *J* 10.4 Hz, CH₂OH), 4.12 (1H, *dd*, *J* 5.2 Hz, H-3), 4.52 (2 H, *m*, H-2, H-1); δ _C (101 MHz, CDCl₃) 24.35, 26.15 (2 × Me iso prop), 34.92 (C2), 44.38 (C3), 63.99 (Cq iso prop), 71.27 (C5), 79.71 (C4), 82.59 (C6), 111.91 (C1);¹³² HRMS (ESI) calcd. for C₉H₁₆O₄⁺ [*M*+Na]⁺: calcd. 211.0941, obsd. 211.0943 and HRMS (ESI) calcd. for C₉H₁₆O₄⁺ [*M*+H]⁺: calcd. 189.1121, obsd. 189.1118.

(-)-(1*S*,2*S*,3*R*,4*S*)-2,3-Dihydroxy-2,3-*O*-isopropylidene-4-diphenylphosphoryloxymethyl cyclopentan-1-ol (4.10)¹³¹



(1*S*,2*S*,3*R*,4*R*)-2,3-*O*-Isopropylidene-4-hydroxymethylcyclopentan-1-ol **4.9** (179 mg, 0.95 mmol) was dissolved in DCM (8 mL), cooled to 0 °C. Diphenyl phosphoryl chloride (230 μ L, 1.1 mmol), diisopropylethylamine (435 μ L, 2.5 mmol) and DMAP (2 mg, 0.02 mmol) were added under an atmosphere of nitrogen and the reaction mixture was stirred at rt overnight. After this time, TLC analysis (petrol:ethyl acetate, 3:1) indicated the complete consumption of the starting material (R_f 0.2) and the formation of higher running product (R_f 0.5). The reaction was quenched with trimethylamine (2 mL). The residue was dissolved in DCM, washed with water, brine, dried and concentrated *in vacuo*. The residue was purified by flash column chromatography (petrol:ethyl acetate, 1:1) to afford major product **4.10** as a light-yellow liquid (0.12 g, 40%). δ_H (500 MHz, $CDCl_3$) 1.32, 1.46 (6H, 2 \times s, Me iso prop), 1.38 (1H, d, J 5.0, 15.0 Hz, H-5), 1.84 (1H, d, J 5.0, 15.0 Hz, H-5), 2.17 (1H, m, H-4), 3.59 (1H, dd, J 5.0, 10.0 Hz, H-3), 4.37–4.56 (4H, m, CH_2OH , H-2, H-1), 7.19–7.35 (10H, Ar-H); δ_C (101 MHz, $CDCl_3$) 24.02, 25.84 (2 \times Me iso prop), 30.50 (C5), 43.00 (d, J_{cp} 6.06 Hz, C4), 68.55 (d, J_{cp} 5.05 Hz, C6), 72.97 (C3), 77.62 (C2), 78.23 (C1), 110.33 (Cq iso prop), 120.05, 120.06, 120.08, 120.09, 125.39, 125.40, 129.75, 129.78, 129.80, 150.50 (d, J_{cp} 6.06 Hz, Ar-C); δ_P -11.69;¹³¹ HRMS (ESI) calcd. for $C_{21}H_{25}O_7P^+$ [M+H]⁺: 421.1411, obsd.: 421.1415.

(+)-(1*S*,2*S*,3*R*,4*R*)-1,2,3-Trihydroxy-4-cyclopentanemethanol-6-dihydrogen phosphate **(4.11)**¹³¹

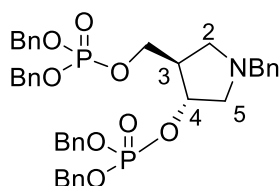


(-)-(1*S*,2*S*,3*R*,4*S*)-2,3-Dihydroxy-2,3-*O*-isopropylidene-4-diphenylphosphoryloxymethylcyclopentan-1-ol **4.10** (61 mg, 0.14 mmol) was dissolved in THF (3.0 mL) and cooled to 0 °C. The reaction mixture was treated with 1 N HCl (5 mL) and allowed to warm to rt and the reaction mixture was stirred at the same temperature for 21 h. After this time, TLC analysis (petrol:ethyl acetate, 3:1) showed the complete formation of a major product (R_f 0.0) and complete consumption of the starting material (R_f 0.6). The reaction was quenched by the addition of amberlite (OH form) anion exchange resin until the mixture was neutral. The resin was removed by filtration and thoroughly washed with THF and deionized water. The filtrate was evaporated to give a colourless product, which was dissolved in EtOH (4 mL) and before the addition of PtO_2 (25 mg). The reaction mixture was hydrogenated with H_2 for overnight.

The mixture was filtered through celite and evaporated. The sample was dissolved in 5 mL of Milli-Q water, loaded on a RESOURCE Q column and eluted with a linear gradient of H₂O/0.2 M NH₄HCO₃. Fractions containing the desired product were recognised using Lanzetta phosphate assay and lyophilised to give **4.11** (12 mg, 37%) as a white powder. δ_{H} (500 MHz, D₂O) 1.60–1.74 (2H, m, H-5), 2.19 (1H, m, H-4), 4.37–4.56 (4H, m, CH₂OH, H-2, H-3), 3.97 (1H, m, H-1); δ_{C} (101 MHz, D₂O) 31.28 (C5), 43.02(d, *J*_{cp} 8.08 Hz, C4), 66.50 (d, *J*_{cp} 4.04 Hz, C6), 70.78 (C1), 72.79 (C3), 74.11 (C2); δ_{P} 0.46;¹³¹ HRMS (ESI) calcd. for C₆H₁₃O₇P⁺ [M+H]⁺: 229.0472, obsd.: 229.0466.

7.2.2 Synthesis of iminosugar 4.14

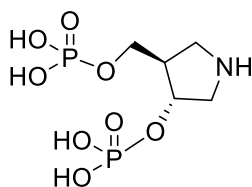
(((3*R*,4*R*)-1-Benzyl-4-((dibenzoyloxy)phosphoryl)oxy)pyrrolidin-3-yl)methyl) phosphate (4.13)



(3*R*,4*R*)-1-Benzyl-4-(hydroxymethyl)pyrrolidin-3-ol **5.0** (255 mg, 1.23 mmol) was suspended in anhydrous acetonitrile (5 mL). 1*H*-Tetrazole (1.1 mL, 0.5 mmol) was added, followed by dropwise addition of dibenzylphosphor-*N,N*-diisopropylamidite (0.52 mL, 1.4 mmol) and the mixture was stirred at rt under an atmosphere of argon. After 3 h, TLC analysis (DCM:Methanol, 8:0.1) indicated the complete consumption of the starting material (*R*_f 0.0). Then, *m*-CPBA (0.8 g, 5 mmol) was added to the reaction mixture and stirred overnight. After this time, TLC analysis (DCM:methanol, 9:0.2) indicated two major running products were present (*R*_f 0.6 and 0.4). The reaction solvent was removed, and the residue was dissolved in DCM (150 mL) and washed with 10 wt% sodium sulfite (50 mL). The combined organic layers were washed with satd. NaHCO₃ (100 mL), dried (MgSO₄), filtered and concentrated *in vacuo*. The residue was purified by flash chromatography (florisil, 1% methanol in DCM) to afford major product **4.13** (0.45 g, 51%) and minor product **4.13.1** (0.22 g, 40%) as an orange oil. **4.13**: δ_{H} (600 MHz, CDCl₃) 2.39 (1H, s, H-2), 2.61 (1H, m, H-3), 2.73, 2.87 (2H, m, H-5), 3.01 (1H, s, H-2), 3.69 (2H, m, CH₂Ph), 3.99 (2H, m, H-6), 4.66 (1H, m, H-4), 4.99 (6H, m, CH₂Ph), 7.25–7.51 (21H, m, Ar-H), 7.94 (1H, d, *J* 12.0 Hz Ar-H), 7.93–8.05 (1H, m, Ar-H); δ_{C} (101 MHz, CDCl₃) 46.25 (C3), 54.06

(C2), 59.25 (C5), 66.58 (C6), 69.51 (CH₂Ph), 78.09 (C4), 127.99, 128.01, 128.51, 128.56, 128.61, 128.68, 129.28, 129.59, 130.03, 132.77, 132.80, 134.40, 135.54, 135.57, 135.60, 135.64, 135.68, 168.59 (Ar-C); δ_P -2.07, 1.17; HRMS (ESI) calcd. for C₄₀H₄₃NO₈P₂⁺ [M+H]⁺: 728.2531, obsd.: 728.2535. **4.13.1**: δ_H (500 MHz, CDCl₃) 2.55 (1H, m, H-2), 2.67 (1H, brs, H-3), 2.75, 3.26 (2H, dd, *J* 5.0, 10.0 Hz, H-5), 3.44 (1H, d, *J* 10.0 Hz, H-2), 3.93 (3H, m, CH₂Ph, H-6), 4.06 (1H, m, H-6), 4.13 (1H, m, H-4), 5.05 (4H, m, CH₂Ph), 7.31–8.05 (15H, m, Ar-H); δ_C (101 MHz, CDCl₃) 46.60 (C3), 53.73 (C2), 58.66 (CH₂Ph), 61.23 (C5), 66.39 (C6), 69.82, 69.85 (CH₂Bn), 72.08 (C4), 127.82, 127.97, 128.18, 128.24, 128.60, 128.78, 128.96, 129.17, 129.30, 129.51, 129.89, 130.11, 131.56, 134.06, 135.45 (Ar-C); δ_P -0.77; HRMS (ESI) calcd. for C₂₆H₃₀NO₅P⁺ [M+H]⁺ 468.1934, obsd.: 468.1941.

((3*R*,4*R*)-4-(Phosphonooxy)pyrrolidin-3-yl)methyl dihydrogen phosphate (4.14)

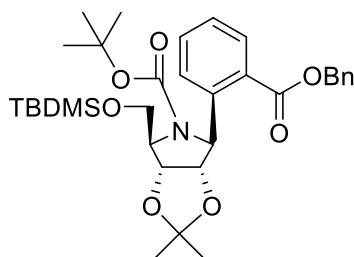


(((3*R*,4*R*)-1-benzyl-4-((bis(benzyloxy)phosphoryl)oxy)pyrrolidin-3-yl)methyl) phosphate **4.13** (450 mg, 0.62 mmol) was dissolved in ethanol (11 mL) and before the addition of Pd/C (220 mg). The reaction mixture was hydrogenated with H₂ for overnight. After this time, TLC analysis (DCM:methanol, 9:0.2) indicated the formation of a lower running product (*R_f* 0.0) and complete consumption of the starting material (*R_f* 0.3). The mixture was filtered through celite and evaporated. NMR of the crude product showed the deprotection of two benzyl group and the presence of a secondary benzyl group. The crude product was again dissolved in ethanol (10 mL). Pearlman's catalyst (150 mg, 1.6 mmol) and aqueous ammonia (90 μ L, 28%, 4.3 mmol) were added. The reaction mixture was stirred under a hydrogen atmosphere overnight. The reaction mixture was filtered through celite and concentrated *in vacuo* to afford **4.14** as a yellow syrup. The sample was dissolved in 35 mL of Milli-Q water, loaded on to a RESOURCE Q column and eluted with a linear gradient of H₂O/0.5 M NH₄HCO₃. Fractions containing the desired product were recognised using Lanzetta phosphate assay and lyophilised to afford **4.14** (51 mg, 30%) as an orange oil. δ_H (500 MHz, D₂O) 2.65 (1H, m, H-3), 3.25–3.27 (1H, m, H-2), 3.33 (1H, m, H-5), 3.41 (1H, m, H-5), 3.49 (1H, m, H-2), 3.71 (2H, m, H-

6), 4.57 (1H, m, H-4); δ_c (101 MHz, D₂O) 43.73 (C3), 44.05 (C2), 50.14 (C5), 61.41 (C6), 73.55 (C4); δ_p -0.03, 1.02; HRMS (ESI) calcd. for C₅H₁₃NO₈P₂⁺ [M+H]⁺: 278.0189, obsd.: 278.0186.

7.2.3 Synthesis of iminoribitol phosphate 4.19

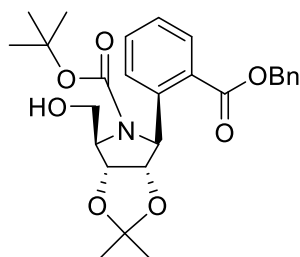
***tert*-Butyl(3a*S*,4*R*,6*R*,6a*R*)-4-(2-((benzyloxy)carbonyl)phenyl)-6-(((*tert*-butyldimethylsilyl)oxy)methyl)-2,2-dimethyltetrahydro-5H-[1,3]dioxolo[4,5-*c*]pyrrole-5-carboxylate (4.19.2)¹³⁷**



Sodium benzyloxide was prepared under an atmosphere of nitrogen by the addition of sodium hydride (95%, 400 mg, 15.83 mmol) in four portions to benzyl alcohol (10 mL) at 0 °C. The reaction mixture was further stirred at rt for 1 h and the resulting solution became clear and was held under an atmosphere of nitrogen. *tert*-Butyl(3a*R*,4*R*,6*R*,6a*S*)-4-(((*tert*-butyldimethylsilyl)oxy)methyl)-6-(2-((3-hydroxy-2-(hydroxymethyl)-2-methylpropoxy)carbonyl)phenyl)-2,2-dimethyltetrahydro-5H-[1,3]dioxolo[4,5-*c*]pyrrole-5-carboxylate **4.19.1** (170 g, 1.123 mmol) was azeotroped with toluene (3 × 10 mL) and dissolved in benzyl alcohol (7.5 mL) and sodium benzyloxide (0.84 mL, 1.0 M, 3 eq.). After this time, TLC analysis (petrol:ethyl acetate, 1:1) indicated the formation of a major product (*R_f* 0.60) and the complete consumption of the starting material (*R_f* 0.2). The reaction mixture was quenched with water (40 mL) and extracted with DCM (3 × 50 mL). The combined organic layers were washed with brine (50 mL), dried (MgSO₄), filtered and concentrated *in vacuo*. The residue was purified by flash chromatography (petrol:ethyl acetate, 8:1) to afford the product **4.19.2** (41 mg, 41 %) as a colourless oil. $[\alpha]_D^{20}$ -46.0 (*c*, 1.97 in CHCl₃); δ_H (500 MHz, CDCl₃) 0.10 (6H, m), 0.93 (9H, s), 1.10 (7H, brs, BOC), 1.33 (3H, s), 1.41 (2H, s, BOC), 1.50 (3H, s), 3.91 (1H, dd, *J* 5.0, 15.0 Hz, H-5'), 4.07 (1H, m, H-4), 4.32–4.36 (1H, m, H-5), 4.46 (1H, d, *J* 10.0 Hz, H-2), 4.78 (1H, brs, H-3), 5.35–5.42 (2H, m, CH₂Ph), 5.91 (1H, brs, H-1), 7.33–7.56 (6H, m, Ar-H), 7.88–8.01 (2H, m, Ar-H); δ_c (126 MHz, CDCl₃) -5.20, -5.22, 18.60, 26.01, 26.13 (3C), 28.12 (3C), 62.50 (CH₂), 64.70 (C1'), 65.55 (C4'), 66.92 (CH₂, Bn), 79.90 (N-CO₂, BOC), 80.25 (C3'), 86.42 (C2'), 112.03, 126.80, 127.16, 128.35, 128.59, 128.67, 129.16, 130.28, 132.57,

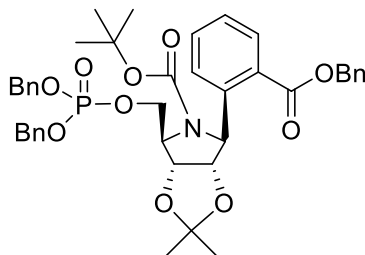
136.38, 144.59, 154.75, 166.45;¹³⁷ HRMS (ESI) calcd. for C₃₃H₄₇NO₇Si⁺ [M+Na]⁺: 620.3014, obsd.: 620.3030.

***tert*-Butyl(3*aS*,4*S*,6*R*,6*aR*)-4-(2-((benzyloxy)carbonyl)phenyl)-6-(hydroxymethyl)-2,2-dimethyltetrahydro-5H-[1,3]dioxolo[4,5-*c*]pyrrole-5-carboxylate (**4.19.3**)**¹³⁷



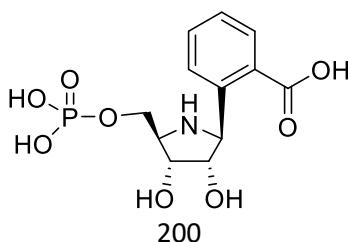
tert-Butyl(3*aS*,4*R*,6*R*,6*aR*)-4-(2-((benzyloxy)carbonyl)phenyl)-6-(((*tert*-butyldimethyl-silyl)oxy)methyl)-2,2-dimethyltetrahydro-5H-[1,3]dioxolo[4,5-*c*]pyrrole-5-carboxylate **4.19.2** (45 mg, 0.08 mmol) was dissolved in anhydrous methanol (1 mL). Ammonium fluoride (40 mg, 1.08 mmol) was added and the mixture was heated to reflux at 60 °C. After 3 h, TLC analysis (petrol:ethyl acetate, 3:2) indicated the formation of a major product (*R_f* 0.4) and complete consumption of the starting material (*R_f* 0.5). The reaction mixture was concentrated *in vacuo*. The residue was purified by flash chromatography (petrol:ethyl acetate, 3:2) to afford **4.19.3** (20 mg, 57%) as a colourless oil. [α]_D²⁰ -23.1 (*c*, 1.60 in CHCl₃); δ _H (500 MHz, CDCl₃) 1.18 (9H, brs, BOC), 1.31 (3H, s, CH₃), 1.62 (3H, s, CH₃), 3.90–3.94 (1H, m, H-5), 4.06 (1H, brs, H-5'), 4.20–4.23 (1H, m, H-4), 4.33 (1H, brs, H-3), 4.45 (1H, d, *J* = 5.0 Hz, H-2) 4.63 (1H, s, OH) 5.37–5.47 (2H, abq, *J* = 15.0, CH₂Bn) 5.98 (1H, brs, H-1), 7.34–7.42 (4H, m, Ar-H), 7.46–7.57 (4H, m, Ar-H), 8.00 (1H, *J* = 10.0 Hz Ar-H). δ _C (126 MHz, CDCl₃) 25.70, 27.70, 28.89 (2CH₃, BOC), 65.55 (C1), 65.61 (C5), 66.93 (CH₂Ph), 67.11 (C4), 81.14 (C3), 85.58 (C2), 112.36 (C-CH₃), 125.97, 127.3, 128.32, 130.93, 132.47, 135.91 (Ar-C), 142.33 (CO), 156.65, 166.84 (CO);¹³⁷ HRMS (ESI) calcd. for C₂₇H₃₃NO₇⁺ [M+H]⁺: 484.2330, obsd.: 484.2339.

***tert*-Butyl(3*aS*,4*R*,6*R*,6*aR*)-4-(2-((benzyloxy)carbonyl)phenyl)-6-(((bis(benzyloxy)phoryl)oxy)methyl)-2,2-dimethyltetrahydro-5*H*-[1,3]dioxolo[4,5-*c*]pyrrole-5-carboxylate**
(4.19.4)¹³⁷



tert-Butyl(3*aS*,4*S*,6*R*,6*aR*)-4-(2-((benzyloxy)carbonyl)phenyl)-6-(hydroxymethyl)-2,2-dimethyltetrahydro-5*H*-[1,3]dioxolo[4,5-*c*]pyrrole-5-carboxylate **4.19.3** (40.0 mg, 0.08 mmol) was suspended in anhydrous acetonitrile (1 mL). 1*H*-tetrazole (70 μ L, 0.03 mmol) was added, followed by dropwise addition of dibenzylphosphor-*N,N*-diisopropylamidite (37.5 μ L, 0.10 mmol) and the mixture stirred at rt under an atmosphere of nitrogen. After 30 mins, TLC (petrol:ethyl acetate, 3:2) indicated the complete consumption of starting material (*R*_f 0.7). Then, *m*-CPBA was added to the reaction mixture. After 30 mins, TLC (petrol:ethyl acetate, 3:2) indicated the lower running product (*R*_f 0.6). The reaction mixture was diluted with DCM, washed with 10 wt% sodium sulfite (10 mL, 8 mmol). The combined organic layers were washed with satd. NaHCO₃ (10 mL), dried (MgSO₄), filtered and concentrated *in vacuo*. The residue was purified by flash chromatography (petrol:ethyl acetate, 9:1) to afford **19.4** (120 mg, 68 %) as a white crystalline solid. [α]_D²⁰ -14.0 (*c*, 1.51 in CHCl₃); δ_{H} (600 MHz, CDCl₃) 1.12 (12H, m, BOC), 1.62 (3H, s, CH₃), 4.12 (1H, brs, H-4), 4.30-4.60 (4H, m, H-2, H-3, H-5, H-5'), 4.99-5.09 (4H, m, 2CH₂-Bn), 5.30 (1H, d, *J* 12.0 Hz, CH₂-Bn), 5.42 (1H, d, *J* 12.0 Hz, CH₂-Bn), 5.86 (1H, brs, H-1), 7.16-8.10 (20H, m, Ar-H); δ_{C} (126 MHz, CDCl₃) 25.63, 27.59, 28.91 (2CH₃, BOC), 64.09 (C4), 64.99 (C1), 66.82 (C5), 69.45 (CH₂), 69.49 (CH₂), 69.52 (CH₂), 80.15 (C3), 86.38 (C2), 112.13 (C-CH₃), 127.26, 128.18, 128.23, 128.25, 128.40, 128.52, 128.57, 128.69, 128.83, 129.78, 130.20, 131.09, 133.58, 135.64, 136.02 (Ar-C), 154.51 (CO), 167.05 (CO); δ_{H} -0.96;¹³⁷ HRMS (ESI) calcd. for C₄₁H₄₆NO₁₀P⁺ [M+H]⁺: 744.2932, obsd.: 744.2954.

2-((2*R*,3*S*,4*R*,5*R*)-3,4-dihydroxy-5-((phosphonoxy)methyl)pyrrolidin-2-yl) benzoic acid
(4.19)¹³⁷

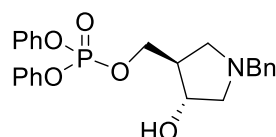


tert-Butyl (3*aS*,4*R*,6*R*,6*aR*)-4-(2-((benzyloxy)carbonyl)phenyl)-6-(((bis(benzyloxy)phosphoryl)oxy)methyl)-2,2-dimethyltetrahydro-5*H*-[1,3]dioxolo[4,5-*c*]pyrrole-5-carboxylate **4.19.4** (89.0 mg, 0.12 mmol) was dissolved in ethanol (4 mL). Palladium on carbon (55 mg, 51.6 μ mol) was added and the reaction mixture was stirred at rt under an atmosphere of hydrogen gas. After 2 h, TLC analysis (petrol:ethyl acetate, 1:1) indicated the complete consumption of the starting material (R_f 0.7). The reaction mixture was filtrated through a celite pad on a sintered funnel, washed with ethanol and concentrated *in vacuo*. The crude product was again dissolved in 4 mL methanol before the addition of HCl (1*M*, 4 mL) and the solution was stirred at rt. After 6 h, TLC analysis (dioxane:7*N* NH₃, 1:1) indicated a lower running product at the baseline (R_f 0.0). The reaction mixture was concentrated *in vacuo* to afford **4.19** (25 mg, 60%) as a light-yellow oil. $[\alpha]_D^{20}$ -37.0 (*c*, 1.06 in H₂O); δ_H (500 MHz, D₂O) 3.85 (1*H*, *m*, H-4), 4.06–4.09 (2*H*, *m*, H-5), 4.36 (1*H*, *m*, H-3), 4.62–4.68 (1*H*, *m*, H-2, partially concealed by D₂O), 5.08 (1*H*, *d*, *J* 10.0 Hz, H-1), 7.41–7.45 (3*H*, *m*, Ar-*H*), 7.72 (1*H*, *m*, Ar-*H*); δ_C (126 MHz, CDCl₃) 62.03 (C5), 64.01 (C1), 64.58 (C4), 69.65 (C3), 72.51 (C2), 129.41, 130.20, 130.54, 130.88, 131.29, 136.76 (Ar-*C*), 174.93 (CO);¹³⁷ δ_P -0.12; HRMS (ESI) calcd. for C₁₂H₁₆NO₈P⁺ [M+H]⁺: 334.0686, obsd.: 334.0691.

7.3 Synthesis of transition state analogues for Chapter 5

7.3.1 Synthesis of phosphorylated amine 5.2

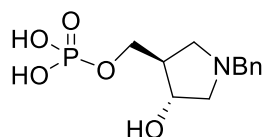
(3*R*,4*R*)-1-Benzyl-4-(hydroxymethyl)pyrrolidin-3-yl)methyl diphenyl phosphate (5.1)



(3*R*,4*R*)-1-Benzyl-4-(hydroxymethyl)pyrrolidin-3-ol **5.0** (101 mg, 0.49 mmol) was dissolved in DCM (2.5 mL) and cooled to 0 °C. Diphenyl phosphoryl chloride (124 μ L, 0.58 mmol), diisopropylethylamine (435 μ L, 2.5 mmol) and DMAP (12 mg, 0.10 mmol) were added under an atmosphere of nitrogen and the reaction mixture stirred at rt for 3 h. After this time, TLC analysis (1% MeOH in DCM) indicated the complete consumption of the starting material (R_f

0.2) with the formation of higher running products (R_f 0.6 and R_f 0.7). The reaction was quenched with water (5 mL). The organic layer was extracted with DCM (2×20 mL). The combined organic layer was washed with NaHCO_3 , brine, dried over Na_2SO_4 , filtered and concentrated *in vacuo*. The residue was purified by flash column chromatography (MeOH:DCM, 0.5:50) to afford major product **5.1** (110 g, 56 %) as a light-yellow liquid. $[\alpha]_D^{24} +10.59$ (c , 0.85 in CHCl_3); δ_H (400 MHz, CDCl_3) 2.18 (2H, dd, J 6.0, 3.2 Hz, H-2), 2.42 (1H, m, H-3), 2.62 (2H, d, J 4.8 Hz, H-5), 2.89 (1H, t, J 9.2 Hz, H-2), 3.56 (1H, s, CH_2Ph), 4.06 (1H, m, H-4), 4.24 (2H, t, J 7.2 Hz, H-6), 7.30–7.45 (15H, m, $5 \times \text{Ar-H}$); δ_C (101 MHz, CDCl_3) 48.49 (C3), 54.96 (C2), 59.81 (CH_2Bn), 61.84 (C5), 69.69 (C6), 73.16 (C4), 120.02, 120.07, 125.59, 127.24, 128.33, 128.37, 128.62, 128.63, 128.80, 129.80, 129.85, 137.92, 150.41, 150.48; δ_P 12.06; HRMS (ESI) calcd. for $\text{C}_{24}\text{H}_{26}\text{NO}_5\text{P}^+$ $[\text{M}+\text{H}]^+$: 440.1621, obsd.: 440.1627.

((3*R*,4*R*)-4-Hydroxypyrrolidin-3-yl)methyl dihydrogen phosphate (5.2)

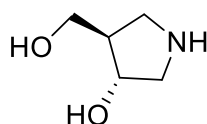


(3*R*,4*R*)-1-Benzyl-4-hydroxypyrrolidin-3-yl)methyl diphenyl phosphate **5.1** (86 mL, 0.19 mmol) was taken up in THF (10 mL) and cooled down to -78°C . A flow of ammonium gas was blown over the flask until approximately 20 mL was collected. Sodium metal (5–10 mg cubes) was added until a dark blue colour persisted. This was maintained for 30 min after which NH_4Cl was added (3 mL) and the ammonia blown off under a flow of nitrogen at rt. The reaction mixture was concentrated *in vacuo*. The crude product was dissolved in isopropyl alcohol and filtered to remove any extra NH_4Cl . The filtrate was concentrated *in vacuo* and the residue was dissolved in H_2O . The eluent was applied to a Bio-Gel P2 SEC column and eluted with a linear gradient of $\text{H}_2\text{O}/0.1 \text{ M } \text{NH}_4\text{HCO}_3$. Fractions containing the desired product were pooled and lyophilised to give ((3*R*,4*R*)-4-hydroxypyrrolidin-3-yl)methyl dihydrogen phosphate **5.2** (40 mg, 76 %) as a white powder. $[\alpha]_D^{27} -3.95$ (c , 0.76 in CHCl_3); δ_H (400 MHz, D_2O) 2.52 (1H, brs, H-3), 3.22 (2H, m, H-2, H-5), 3.45 (1H, m, H-5'), 3.61 (1H, m, H-2), 3.64 (1H, apt, J 8.8, 7.6 Hz, H-6), 3.75–3.87 (2H, m, H-6, H-6'), 4.33 (2H, m, CH_2Bn), 4.40 (1H, m, H-4) 7.41 (5H, m, H-Ar); δ_C (101 MHz, D_2O) 46.38 (C3), 54.27 (C2), 58.91 (CH_2Bn), 60.12 (C5), 63.55 (C6), 73.16

(C4), 128.74, 129.25, 129.54, 129.99, 130.48, 132.09; δ_P 0.73; HRMS (ESI) calcd. for $C_{12}H_{18}NO_5P^+$ $[M+H]^+$: 288.0995, obsd.: 288.0992.

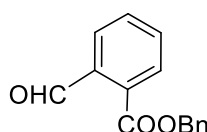
7.3.2 Detailed synthesis of iminosugar derivative 5.6 and 5.8

(3*R*,4*R*)-4-(Hydroxymethyl)pyrrolidin-3-ol (5.3)¹⁸⁴



(3*R*,4*R*)-1-Benzyl-4-(hydroxymethyl)pyrrolidin-3-ol **5.0** (35 mg, 0.17 mmol) was dissolved in methanol (2.5 mL). Pearlman's catalyst (25 mg, 0.17 mmol) and aqueous ammonia (25 μ L, 28%, 0.17 mmol) were added. The reaction mixture was stirred under a hydrogen atmosphere. After 14 h, TLC analysis (ninhydrin, DCM:MeOH:EtOH:NH₄, 3:3:3:1) indicated the formation of a major product (R_f 0.12) and the complete consumption of the starting material (R_f 0.85). The reaction mixture was filtered through celite, washed with 3 M HCl (3 mL) and concentrated *in vacuo* to afford **5.3** as a crude syrup. $[\alpha]_D^{26} +9.09$ (c, 0.33 in CHCl₃); δ_H (400 MHz, D₂O) 1.10 (1H, t, J 7.6 Hz), 2.33 (1H, m), 3.02 (1H, dd, J 5.6 Hz, J 11.6 Hz), 3.13 (1H, dd, J 2.4, 12.8 Hz), 3.27 (1H, dd, J 5.2 12.0 Hz), 3.44–3.51 (3H, m), 4.25–4.28 (1H, m); δ_C (100 MHz, D₂O) 46.79 (C4), 47.21 (C3), 52.72 (C5), 61.91 (C1), 71.53 (C2);¹⁸⁴ HRMS (ESI) calcd. for $C_5H_{12}O_2^+$ $[M+H]^+$: 118.0863, obsd.: 118.0857.

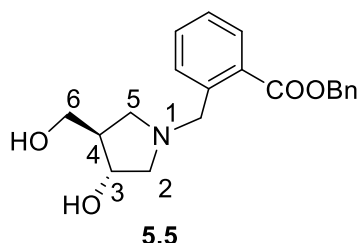
Benzyl 2-formylbenzoate (5.4)



2-Formylbenzoic acid (0.50 g, 3.33 mmol) was dissolved in anhydrous DMF (3 mL). Potassium carbonate (0.55 mg, 4.00 mmol) was added, followed by the dropwise addition of benzyl bromide (0.4 mL, 3.33 mmol). The mixture was stirred at rt under an atmosphere of nitrogen. After 2 h, TLC analysis (petrol:ethyl acetate 2:1) indicated the formation of a major product (R_f 0.6) and the complete consumption of the starting material (R_f 0.3). The reaction mixture was concentrated *in vacuo* and diluted with ethyl acetate. The organic layer was

washed with water (3 × 20 mL) and a saturated solution of sodium chloride (3 × 20 mL). The combined organics were dried (Na₂SO₄), filtered and concentrated *in vacuo*. The residue was purified by flash column chromatography (petrol:ethyl acetate, 10:1) to afford benzyl 2-formylbenzoate **5.4** (0.79 g, 99%) as a colourless liquid. [α]_D²⁷ +30 (c, 0.20 in CHCl₃); δ_{H} (400 MHz, CDCl₃) 5.41 (2 H, s, CH₂) 7.33–7.49 (5 H, m, Ar) 7.61–7.66 (2 H, m, Ar H-3, Ar H-4) 7.94 (1 H, d, *J* 7.43 Hz, Ar H-5) 8.00 (1 H, d, *J* 7.04 Hz, Ar H-2) 10.62 (1 H, s, CHO). δ_{C} (100 MHz, CDCl₃) 67.60 (CH₂), 128.42, 128.47 (2C), 128.58, 128.73 (2C), 130.41, 131.94, 132.44, 132.94, 135.37, 137.13 (Ar-C), 166.01 (CO), 191.96 (CHO); HRMS (ESI) calcd. for C₁₅H₁₃O₃⁺ [M+H]⁺: 241.0859, obsd.: 241.0867.

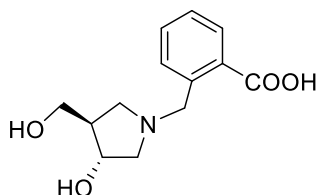
Benzyl 2-((3*R*,4*R*)-3-hydroxy-4-(hydroxymethyl)pyrrolidin-1-yl)methyl)benzoate (5.5)



Benzyl 2-formylbenzoate **5.3** (61 mg, 0.25 mmol) and (3*R*,4*R*)-4-(hydroxymethyl)pyrrolidin-3-ol **5.4** (20 mg, 0.17 mmol) were dissolved in THF/EtOH (3:1, 1.2 mL). Sodium cyanoborohydride (16 mg, 0.25 mmol) was added and the reaction mixture was stirred overnight at rt under an atmosphere of nitrogen. After this time, TLC analysis (DCM:MEOH, 8:1) indicated the complete consumption of the starting material **5.3** (*R*_f 0.3) with some traces of starting material **5.4** remaining and the formation of a product (*R*_f 0.6). Concentrated HCl was added to the reaction mixture until pH 2 was achieved. The reaction mixture was concentrated *in vacuo*, the residue was diluted in DCM (100 mL) and washed with water (2 × 100 mL). The combined organics were dried (Na₂SO₄), filtered and concentrated *in vacuo*. The residue was purified by flash column chromatography (DCM:methanol, 10:1) to afford **5.5** (94 mg, 81%) as a brown liquid. [α]_D²⁷ +8.5 (c, 0.47 in MEOH); δ_{H} (400 MHz, CDCl₃) 2.45 (1H, m, H-4), 2.92 (1H, s), 3.92 (1H, dd, *J* 6.0, 10.8 Hz, H-5), 3.07 (1H, d, *J* 8 Hz, H-2), 3.28 (1H, dd, *J* 5.2, 15.2 Hz, H-2), 3.37 (1H, t, *J* 8 Hz, H-5), 3.61 (1H, dd, *J* 5.2, 4.8 Hz, H-6), 3.70 (1H, dd, *J* 6.0, 4.0 Hz, H-6), 4.45 (1H, m, H-3), 4.43 (4H, bs, N-CH₂,

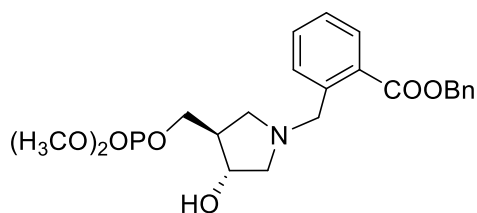
2 × OH), 5.33 (2H, s, CH₂Ph), 7.30–7.45 (5H, m, 5 × Ar-H), 7.52 (1H, t, *J* 6.4 Hz, 1 × Ar-H), 7.64 (1H, d, *J* 3.6 Hz, 1 × Ar-H), 8.97 (1H, d, *J* 6.8 Hz, 1 × Ar-H); δ_c (100 MHz, CDCl₃) 49.10 (C4), 55.50 (C6), 57.27 (CH₂), 61.52 (C2), 62.25, 67.50 (CH₂), 72.89 (C3), 128.48(2C), 128.67(2C), 129.17, 130.04, 131.22, 132.21, 132.94, 134.38 135.43 (Ar-C), 167.40 (CO); HRMS (ESI) calcd. for C₂₀H₂₄NO₄⁺ [M+H]⁺: 342.1716, obsd.: 342.1717.

2-(((3*R*,4*R*)-3-Hydroxy-4-(hydroxymethyl)pyrrolidin-1-yl)methyl)benzoic acid (5.6**)**



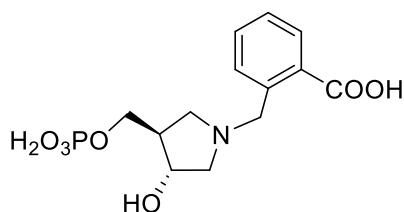
Benzyl 2-(((3*R*,4*R*)-3-hydroxy-4-(hydroxymethyl)pyrrolidin-1-yl)methyl)benzoate **5.5** (10 mg, 0.03 mmol) was dissolved in MeOH (1 mL). NiCl₂·6H₂O (21.0 mg, 0.09 mmol) was added followed by NaBH₄ (10 mg, 0.27 mmol). The reaction mixture was stirred at rt under an atmosphere of nitrogen. After 2 h, TLC analysis (DCM:MeOH, 1:0.5) indicated the complete consumption of the starting material (R_f 0.60) with the formation of a lower running product (R_f 0.0). The reaction was quenched with MeOH (5 mL) and filtered through a celite pad. The filtrate was filtered and concentrated *in vacuo*. The residue was first purified by flash column chromatography (DCM:MeOH, 5:0.5) and then 2%–4% water in CH₃CN to afford product **5.6**. However, the obtained product was purified further using P-2 size exclusion chromatography with ammonium acetate (25 mM) volatile buffer to afford pure **5.6** (94 mg, 81%) as a brown liquid. δ_H (400 MHz, D₂O) 2.34 (1H, brs, H-4), 3.03 (2H, m Hz, H-5, H-2), 3.25–3.36 (1H, m, H-2), 3.45 (1H, t, *J* 6.8 Hz, H-5), 3.52 (2H, m, H-6, H-6'), 4.23–4.27 (3H, m, N-CH₂, H-3), 7.31–7.39 (3H, m, Ar-H), 7.52 (1H, t, *J* 6.8 Hz, Ar-H); δ_c (100 MHz, D₂O) 36.49 (C4), 48.58 (C5), 55.44 (C6), 57.46 (CH₂), 61.32 (C2), 67.85 (CH₂), 72.45 (C3), 129.48, 130.23, 130.22, 130.79, 131.62, 132.27, 136.07 (Ar-C), 174.51 (CO); HRMS (ESI) calcd. for C₁₃H₁₇NO₄⁺ [M+H]⁺: 252.1230, obsd.: 252.1233.

Benzyl-2-((3*R*,4*R*)-3-hydroxy-4-(dimethoxyphosphoryl)oxymethyl)pyrrolidin-1-yl)methyl)benzoate (5.7)



Distilled trimethyl phosphite (48 μ L, 0.40 mmol) was added to Iodine (94 mg, 0.37 mmol) in DCM (1 mL) at 0 °C. After 5 min, the colourless solution was added to a solution of benzyl 2-((3*R*,4*R*)-3-hydroxy-4-(hydroxymethyl)pyrrolidin-1-yl)methyl)benzoate **5.5** (106 mg, 0.31 mmol) and pyridine (210 μ L, 2.4 mmol) in DCM (2.5 mL) at 40 °C. The reaction mixture was stirred at rt under an atmosphere of nitrogen and the formation of a white precipitate was observed. After 15 min, TLC analysis (ninhydrin, DCM:MeOH, 9:1) indicated the formation of a higher running product (R_f 0.77) with some traces of the starting material **5.5**. The reaction mixture was again cooled to 40 °C and 1eq of $I(O)P(OMe)_2$ was added. After 15 min, TLC analysis showed the complete consumption of the starting material (R_f 0.6). The reaction was quenched with $NaHCO_3$. The organic layer was extracted with DCM (2 \times 20 mL). The combined organic layers were washed with brine, dried over Na_2SO_4 , filtered and concentrated *in vacuo*. The residue was purified by flash column chromatography (DCM:MeOH, 9:1) to afford major product **5.7** (88 mg, 64%) as an orange liquid. δ_H (400 MHz, $CDCl_3$) 2.25 (1H, m, H-2), 2.39 (1H, m, H-4), 2.64–2.71 (2H, abq, H-5), 2.90 (1H, t, J 8.8 Hz, H-2), 3.69–3.76 (6H, m, 2 \times CH_3), 3.85–3.91 (2H, m, H-6), 3.97–4.04 (4H, m, H-3, N- CH_2 , OH), 5.26 (2H, s, CH_2Ph), 7.31–7.85 (7H, m, 5 \times Ar-H), 7.78 (1H, d, J 7.6 Hz, Ar-H); δ_C (100 MHz, $CDCl_3$) 48.33 (C4), 54.40 (CH_3), 54.44 (CH_3), 54.96 (C2), 57.19 (C6), 61.54 (C5), 66.89 (CH_2Ph), 68.30 (N CH_2), 72.96 (C3), 127.38, 128.32 (2C), 128.62 (2C), 128.62, 129.95, 130.08, 130.70, 131.64, 135.79, 138.66 (Ar-C), 168.18(CO); δ_P 1.01; HRMS (ESI) calcd. for $C_{22}H_{28}NO_7P^+$ [$M+H$] $^+$: 450.1676, obsd.: 450.1691.

2-(((3*R*,4*R*)-3-Hydroxy-4-((phosphonoxy)methyl)pyrrolidin-1-yl)methyl)benzoic acid (5.8)



Benzyl-2-((3*R*,4*R*)-3-hydroxy-4-(dimethoxyphosphoryl)oxymethyl)pyrrolidin-1-yl)methyl) benzoate **5.7** (0.70 g, 1.56 mmol) was dissolved in anhydrous CH₃CN (2 mL). Sodium iodide (0.48 g, 3.02 mmol) was added, followed by the dropwise addition of TMSCL (0.48 g, 3.02 mmol) at 35°C. A yellow solution was obtained, and the immediate formation of a white precipitate was observed. The mixture was stirred at rt under an atmosphere of nitrogen. After 6 h, TLC analysis (DCM:MeOH, 9:1) indicated the formation of a major product (*R_f* 0.0) and the complete consumption of the starting material (*R_f* 0.77). The reaction mixture was concentrated *in vacuo*, diluted with 1M KOH and stirred for another 30 min. Then, it was applied to a cation exchange column and eluted with water until neutral pH was achieved. The eluent was applied to a SOURCE Q column and eluted with a linear gradient of H₂O/0.1 M NH₄HCO₃. Fractions containing the desired product were pooled and lyophilised to give **5.8** (0.35 g, 68%) as a white powder consisting of the product and residual NH₄HCO₃. [α]_D²⁵ –1.75 (*c*, 0.57 in MeOH); δ_{H} (400 MHz, CDCl₃) 2.51 (1H, m, H-4), 3.05 (1H, dd, *J* 8.0, 11.6 Hz, H-2), 3.32 (2H, m, H-5), 3.64 (1H, t, *J* 8 Hz, H-2), 3.80 (1H, m, H-6), 3.89 (1H, m, H-6), 4.43 (3H, m, N-CH₂, H-3), 7.43–7.50 (3H, m, 3 \times Ar-H), 7.83 (1H, m, 1 \times Ar-H); δ_{C} (100 MHz, CDCl₃) 46.13 (C4), 52.98 (C2), 57.65 (C6), 59.72 (C5), 63.76 (CH₂), 71.32 (C3), 129.48, 130.22, 130.79, 131.62, 132.27, 136.07 (Ar-C), 174.51 (CO); δ_{P} 0.124; HRMS (ESI) calcd. for C₁₃H₁₈NO₇P⁺ [M+H]⁺: 332.0894, obsd.: 332.0893 and HRMS (ESI) calcd. for C₁₃H₁₈NO₇P⁺ [M+Na]⁺: 354.0713, obsd.: 354.0711.

Appendix 1

Table 7.5 Crystal datasheet for compound **4.7**

Identification code	4.7
Empirical formula	C ₈ H ₁₀ O ₃
Formula weight	154.17
Temperature/K	120.0(2)
Crystal system	monoclinic
Space group	<i>P</i> 2 ₁
<i>a</i> /Å	6.0692(3)
<i>b</i> /Å	7.5130(4)
<i>c</i> /Å	8.6308(4)
α /°	90
β /°	101.525(4)
γ /°	90
Volume/Å ³	385.61(3)
<i>Z</i>	2
ρ_{calc} /cm ³	1.3276
μ /mm ⁻¹	0.849
<i>F</i> (000)	164.6
Crystal size/mm ³	0.5073 × 0.0984 × 0.0755
Radiation	Cu K α (λ = 1.54184)
2 θ range for data collection/°	10.46 to 136.36
Index ranges	-7 ≤ <i>h</i> ≤ 7, -8 ≤ <i>k</i> ≤ 9, -10 ≤ <i>l</i> ≤ 10
Reflections collected	4634
Independent reflections	1394 [<i>R</i> _{int} = 0.0257, <i>R</i> _{sigma} = 0.0188]
Data/restraints/parameters	1394/0/101
Goodness-of-fit on <i>F</i> ²	1.068
Final <i>R</i> indexes [<i>I</i> ≥ 2 σ (<i>I</i>)]	<i>R</i> ₁ = 0.0286, <i>wR</i> ₂ = 0.0759
Final <i>R</i> indexes [all data]	<i>R</i> ₁ = 0.0290, <i>wR</i> ₂ = 0.0764
Largest diff. peak/hole / e Å ⁻³	0.20/-0.16
Flack parameter	0.1(4)

Appendix 2

This appendix contains the data and refinement statistics for each crystal structure solved in this thesis, obtained from structure processing and refinement using CCP4 software.

Data collection			
AnPRT complexed with	2.6	2.10	2.10/PRPP/Mg ²⁺
Space group	<i>P</i> 2 ₁ <i>P</i> 2 ₁ <i>P</i> 2 ₁	<i>C</i> 121	<i>P</i> 12 ₁ 1
Cell dimensions			
a, b, c (Å)	79.5, 91.9, 119.9	94.7, 78.3, 102.6	78.0, 80.5, 111.7
α, β, γ (°)	90.0, 90.0, 90.0	90.0, 111.2, 90.0	90.0, 90.0, 90.0
No. of unique reflections	34,248	30,417	62,472
Resolution range (Å) ^a	39.95–2.42 (2.59–2.42)	47.84–2.32 (2.52–2.43)	111.47–2.29 (2.35–2.29)
R _{merge} ^a	0.088 (0.293)	0.033 (0.522)	0.059 (0.093)
R _{p.i.m.} ^a	0.024 (0.08)	0.033 (0.177)	0.024 (0.037)
CC _{1/2} ^a	0.999 (0.878)	0.998 (0.654)	0.996 (0.990)
I/σ(I) ^a	8.66 (2.4)	9.3 (1.23)	12.81 (2.3)
Completeness ^a (%)	100 (100)	100 (100)	100 (100)
Redundancy ^a	14.2 (14.1)	6.5 (6.4)	7.1 (7.3)
Wilson B-factor (Å ²)	21.9	31.6	23.6
Refinement			
No. of atoms, B factor ^b			
Protein	4961, 22.9	4810, 36.3	9842, 25.7
Solvent	183, 18.9	47, 26.0	202, 23.0
Ligands	48.0, 49.4	68, 46.7	228, 34.3
R _{work} /R _{free} (%/%) ^{a,c}	0.190/0.230 (0.198/0.230)	0.189/0.221, (0.195/0.227)	0.189/0.229 (0.196/0.241)
Ramachandran outliers (%)	0.15	0.29	0.11
R.m.s.d. of			
Bond lengths (Å) ^d	0.010	0.009	0.013
Bond angles (°) ^d	1.40	1.465	1.66
PDB code	Not deposited	Not deposited	Not deposited

AnPRT complexed with	Data collection			
	2.11/PRPP/Mg ²⁺	2.11/Mg ²⁺	PRPP/2×Mg ²⁺	Anthranilate
Space group	<i>P</i> 12 ₁ 1	<i>P</i> 12 ₁ 1	<i>C</i> 121	<i>C</i> 121
Cell dimensions				
a, b, c (Å)	78.7, 72.0, 111.3	45.6, 79.1, 91.4	94.3, 78.6, 99.9	95.0, 78.4, 102.8
α, β, γ (°)	90.0, 90.0, 90.0	90.0, 90.0, 90.0	90.0, 109.9, 90.0	90.0, 111.4, 90.0
No. of unique reflections	44,283	37,503	63447 (6334)	31379 (3130)
Resolution range (Å) ^a	48.07–2.43 (2.35–2.29)	90.45–2.10 (2.10–2.16)	31.0–2.0 (1.9–2.0)	47.3–2.3 (2.4–2.3)
R _{merge} ^a	0.059 (0.093)	0.12 (0.511)	0.165 (0.316)	0.124 (0.667)
R _{p.i.m.} ^a	0.024 (0.037)	0.049 (0.199)	0.084 (0.159)	0.050 (0.265)
CC½ ^a	0.997 (0.665)	0.946 (0.517)	0.975 (0.519)	0.997 (0.509)
I/σ(I) ^a	12.9 (4.0)	13.7 (2.1)	5.9 (3.7)	10.5 (3.7)
Completeness (%) ^a	100 (100)	100 (100)	99.8 (99.9)	100 (100)
Redundancy ^a	7.1 (7.3)	7.5 (7.6)	4.7 (4.9)	7.1 (6.3)
Wilson B-factor (Å ²)	26.6	19.6	16.0	30.2
Refinement				
No. of atoms, B factor ^b				
Protein	9709, 28.8	4857, 22.7	4960, 15.4	4766, 34.3
Solvent	153, 22.9	58, 20.4	44, 18.3	20, 56.9
ligands	362, 37.7	66, 37.9	414, 21.5	57, 29.0
R _{work} /R _{free} (%/%) ^{a,c}	0.186/0.241 (0.195/ 0.250)	0.204/0.231 (0.213/ 0.239)	0.221/0.237 (0.238/0.304)	0.194/0.213 (0.228/0.261)
Ramachandran outliers (%)	0.3	0.18	0.29	0.30
R.m.s.d. of				
Bond lengths (Å) ^d	0.015	0.008	0.01	0.01
Bond angles (°) ^d	1.63	1.32	1.22	1.37
PDB code	Not deposited	Not deposited	Not deposited	Not deposited

^a Outer resolution shell is shown in parentheses.

^b The average atomic temperature factor.

^c $R_{work} = (|F_{obs}| - |F_{calc}|) / |F_{obs}|$ and $R_{free} = \sum T (|F_{obs}| - |F_{calc}|) / \sum T |F_{obs}|$, where *T* is a test data set of 5% of the total reflections randomly chosen and set aside before refinement.

^d RMSD from ideal geometry values from Engh and Huber (1991).¹¹³

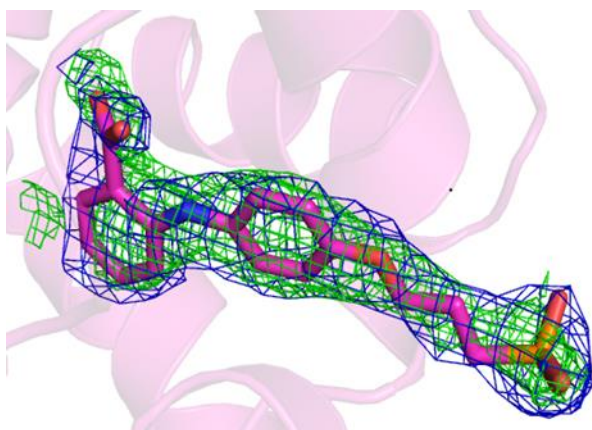
Appendix 3

Omit Maps for ligands

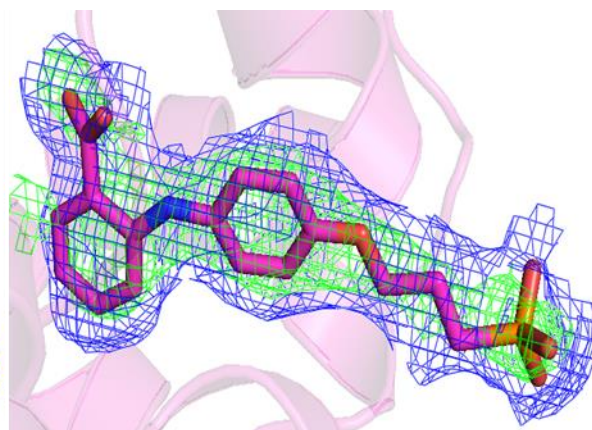
The electron density omit maps for all ligands bound to *M. tuberculosis* AnPRTs. The *Fo-Fc* maps are contoured at 3.0 σ and shown in green for positive and red for negative charge density. The *2Fo-Fc* maps are contoured at 1.0 σ and shown in blue for positive and red for negative charge density. The negative charge density is not observed in these regions of maps.

M. tuberculosis AnPRT/2.6

Chain A – 2.6 (pink)

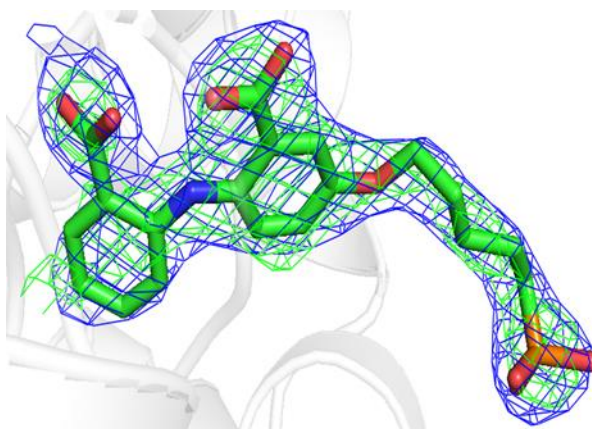


Chain B – 2.6 (pink)

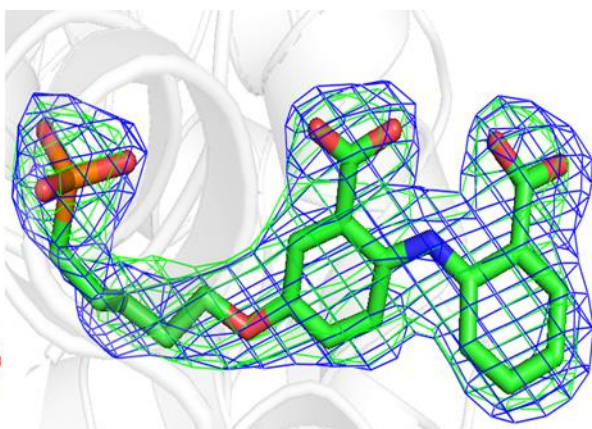


M. tuberculosis AnPRT/2.10

Chain A – 2.10 (green)

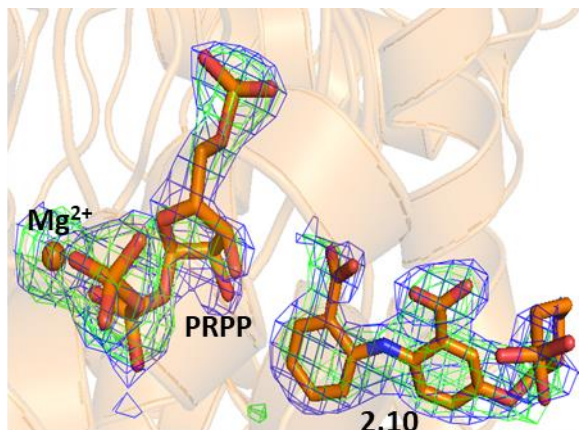


Chain B – 2.10 (green)

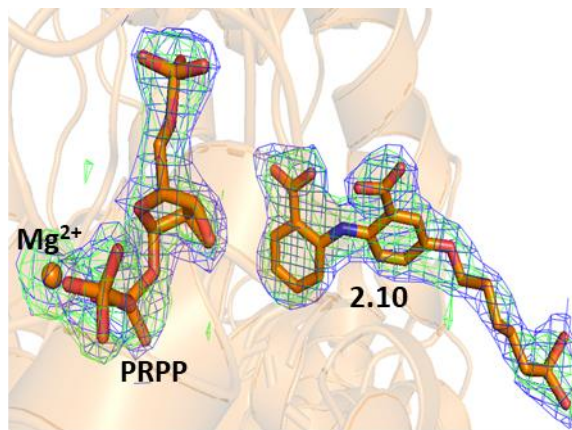


***M. tuberculosis* AnPRT/PRPP/2.10/Mg²⁺**

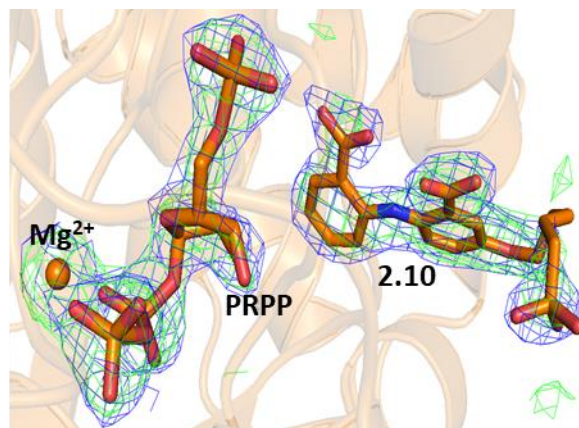
Chain A – PRPP, **2.10** (brown),
Mg²⁺ (brown sphere)



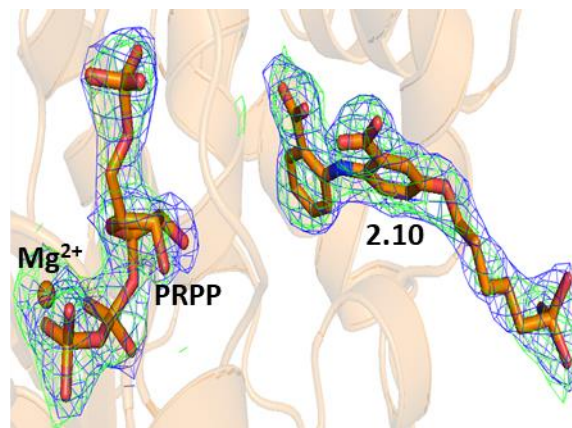
Chain B – PRPP, **2.10** (brown),
Mg²⁺ (brown sphere)



Chain C – PRPP, **2.10** (brown),
Mg²⁺ (brown sphere)

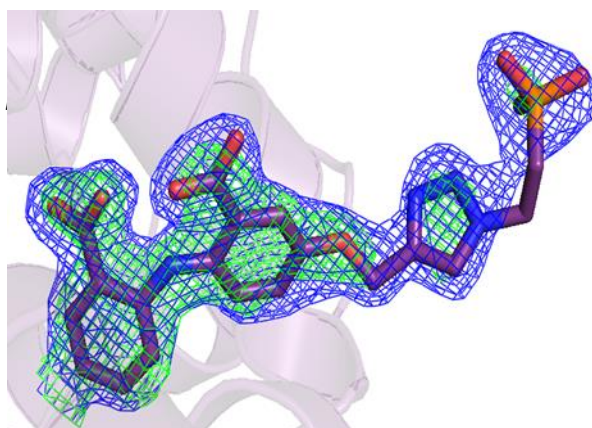


Chain D – PRPP, **2.10** (brown),
Mg²⁺ (brown sphere)

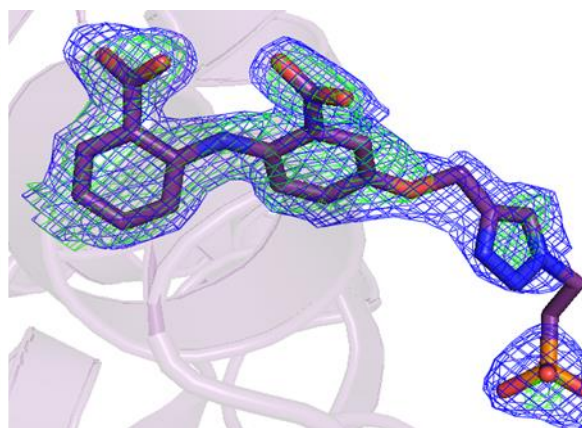


***M. tuberculosis* AnPRT/2.11**

Chain A – **2.11** (purple)

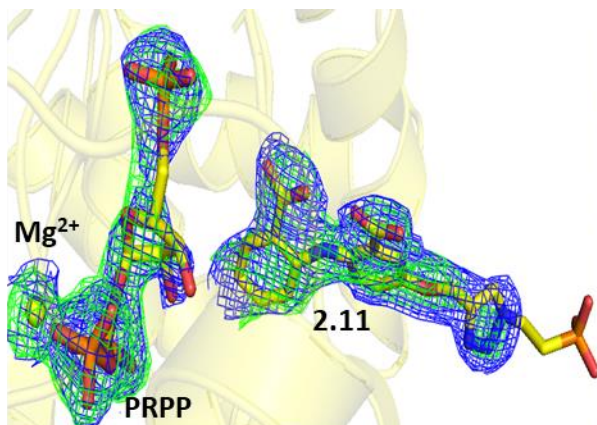


Chain B – **2.11** (purple)

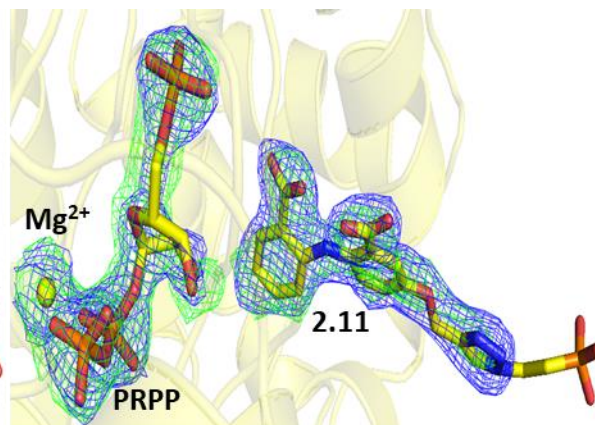


***M. tuberculosis* AnPRT/PRPP/8k/Mg²⁺**

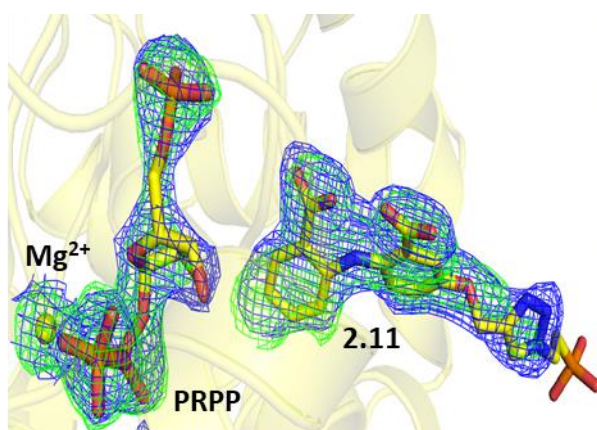
Chain A – PRPP, **2.11** (yellow),
Mg²⁺ (yellow sphere)



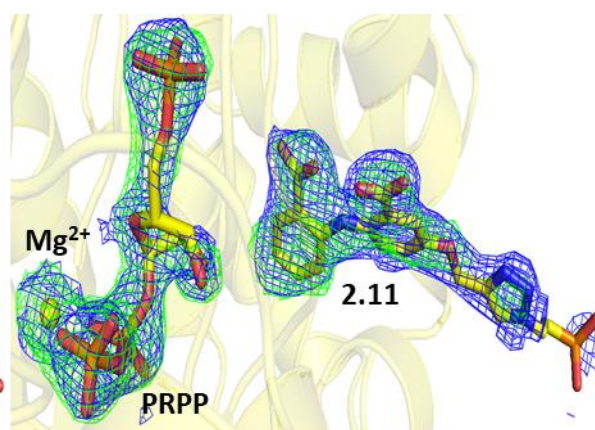
Chain B – PRPP, **2.11** (yellow),
Mg²⁺ (yellow sphere)



Chain C – PRPP, **2.11** (yellow),
Mg²⁺ (yellow sphere)

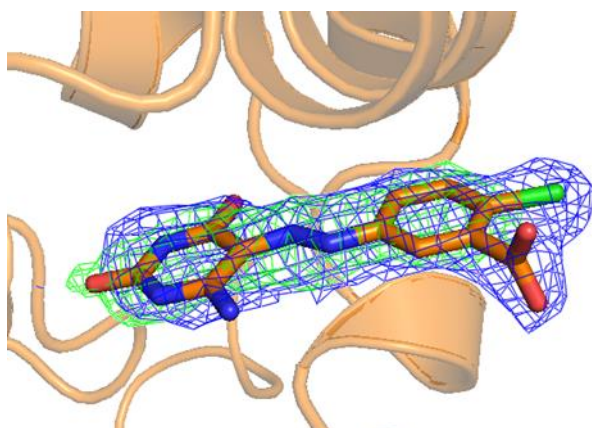


Chain D – PRPP, **2.11** (yellow),
Mg²⁺ (yellow sphere)

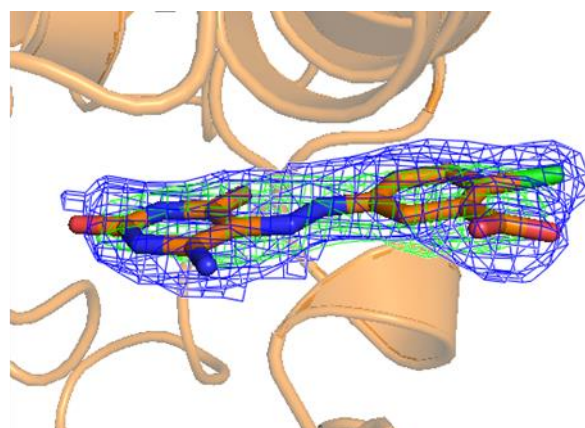


***M. tuberculosis* AnPRT/3.9**

Chain B – **3.9** (brown)

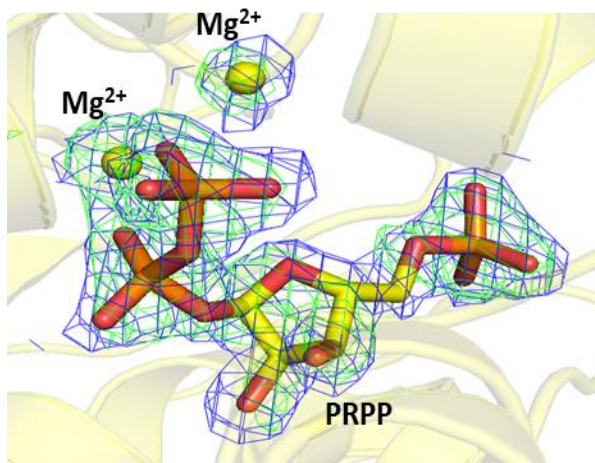


Chain B – **3.9** (brown)

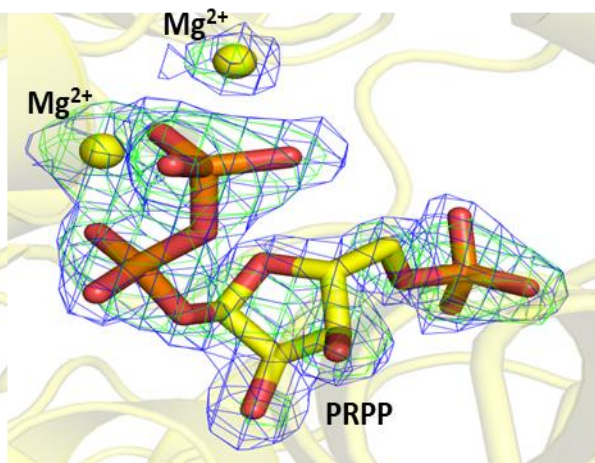


***M. tuberculosis* AnPRT/PRPP/2×Mg²⁺**

Chain A – PRPP (yellow stick),
2×Mg²⁺ (yellow spheres)



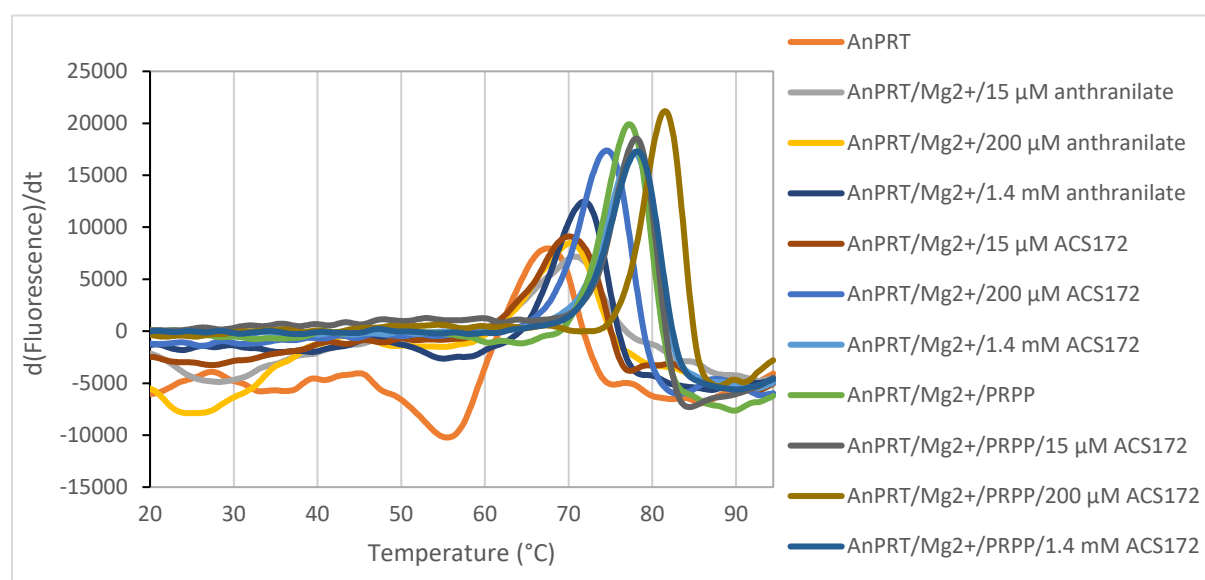
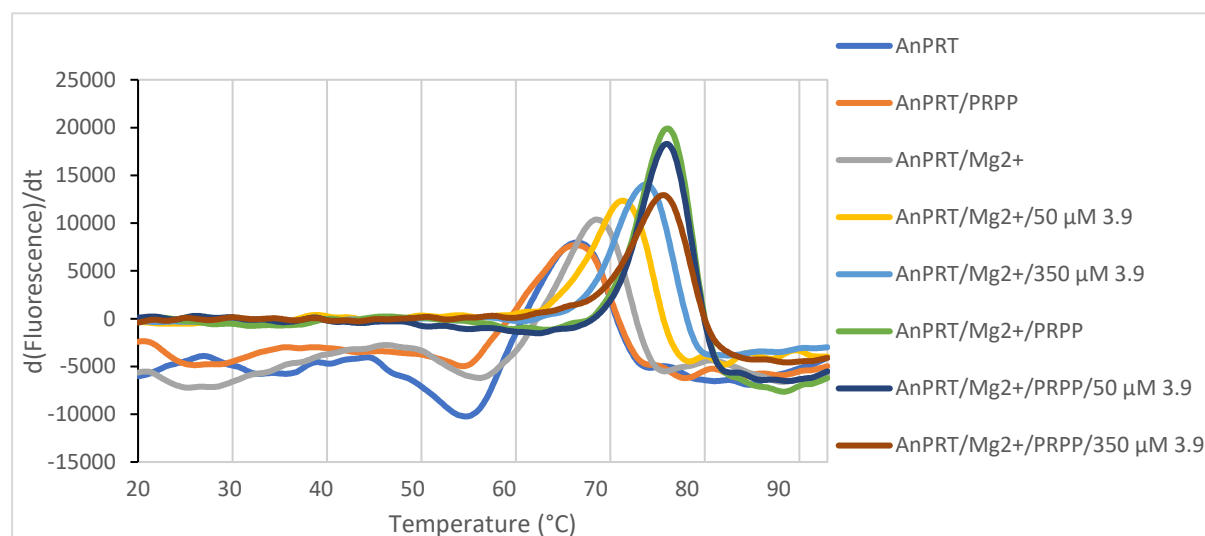
Chain B – PRPP (yellow stick),
2×Mg²⁺ (yellow spheres)



Appendix 4

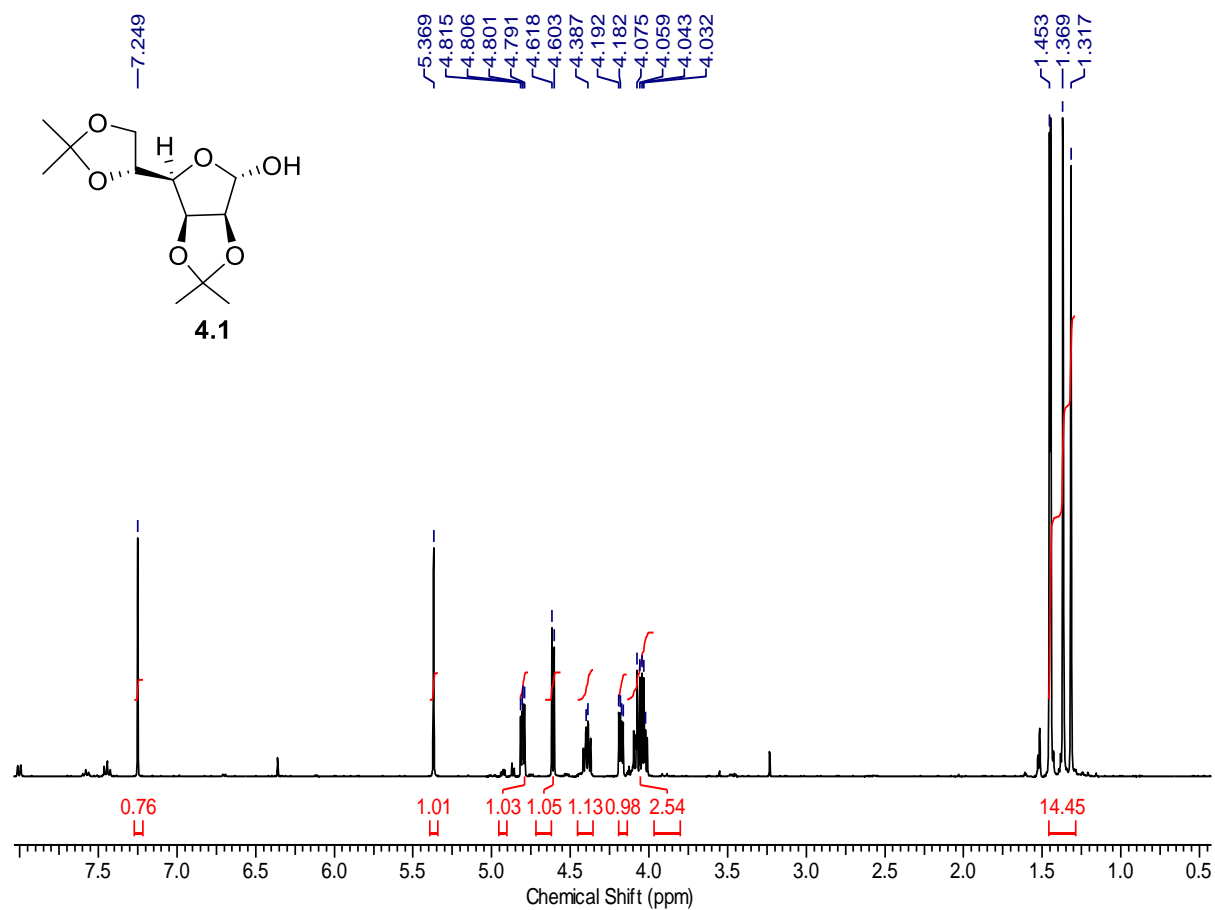
DSF Raw Data

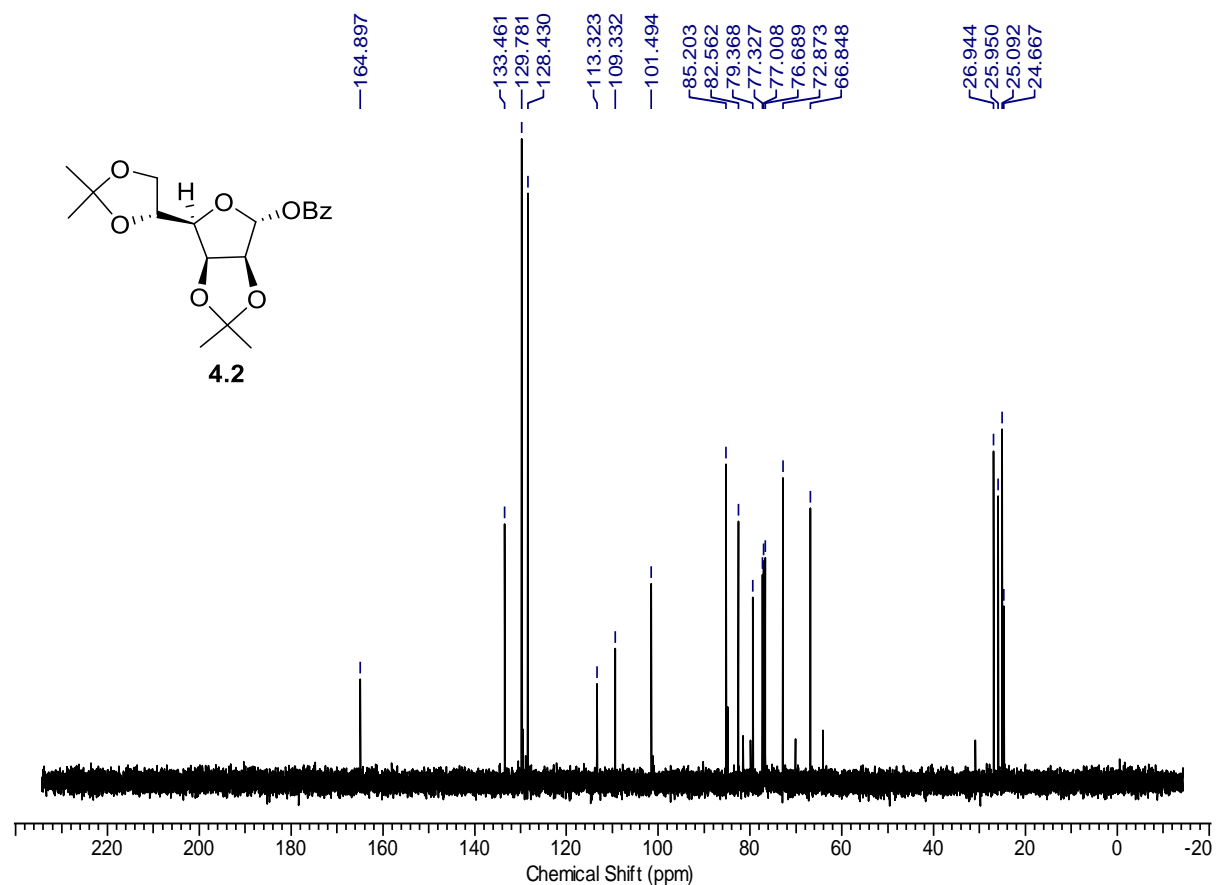
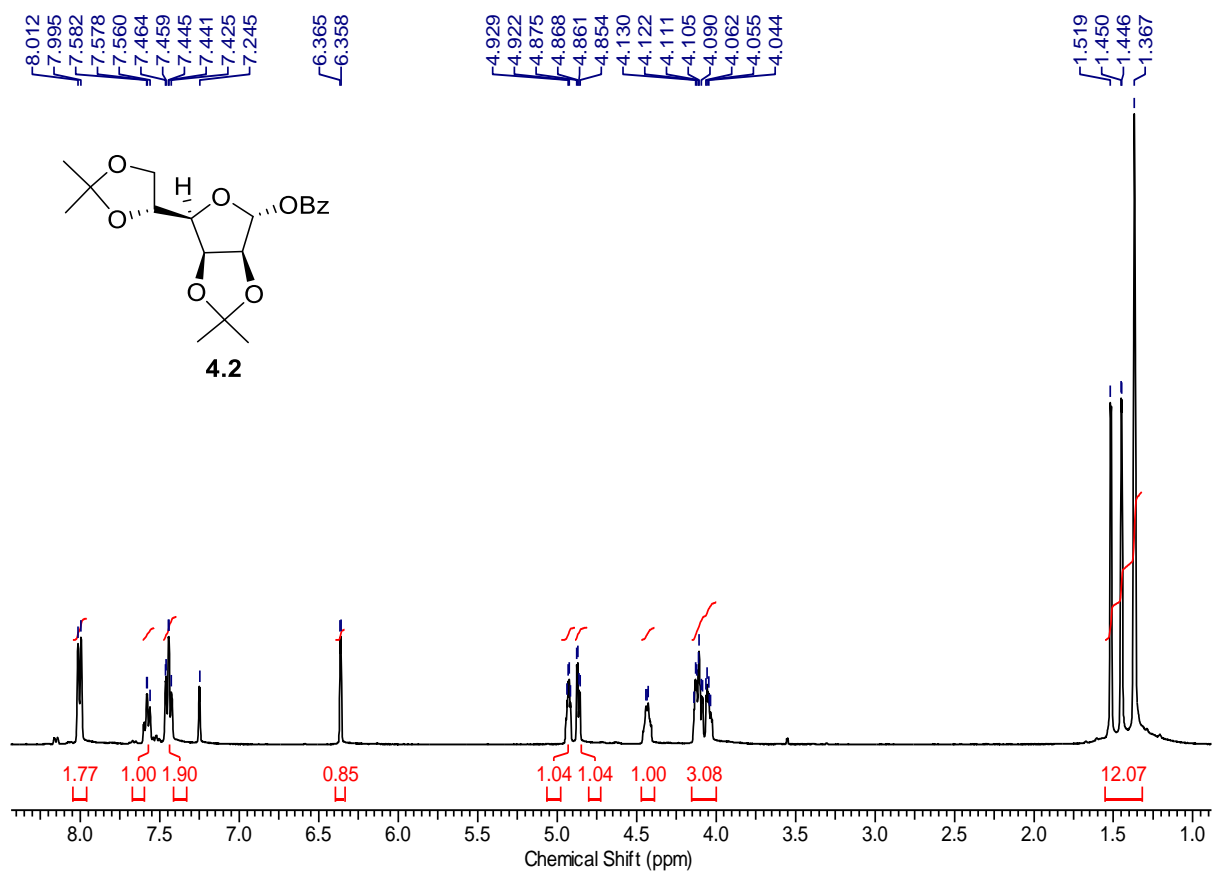
Both graphs represent the raw DSF datasets for *M. tuberculosis* AnPRT melting temperatures in the presence of various ligands. The differentiated fluorescence units (RFU) are plotted against temperature in °C. The denaturation temperature is derived from the local minimum for each data set.

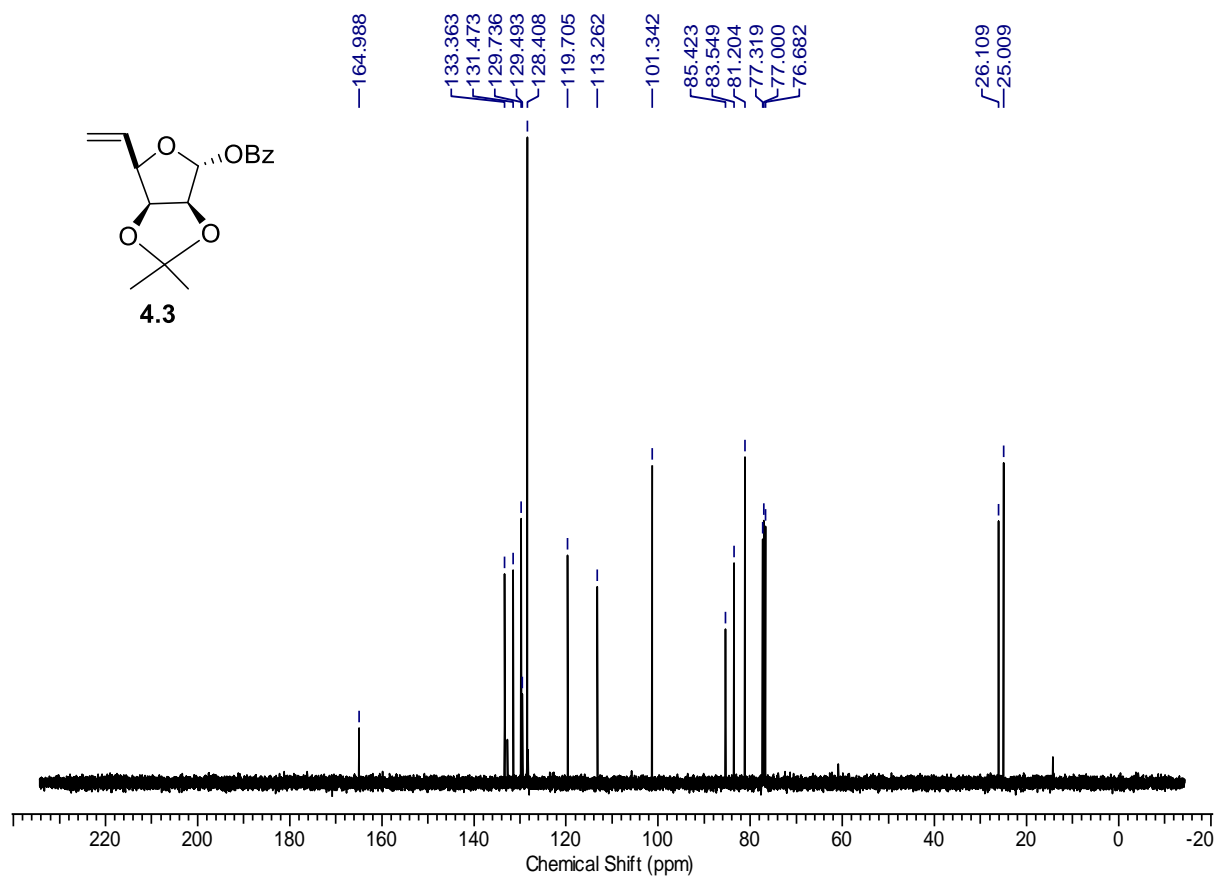
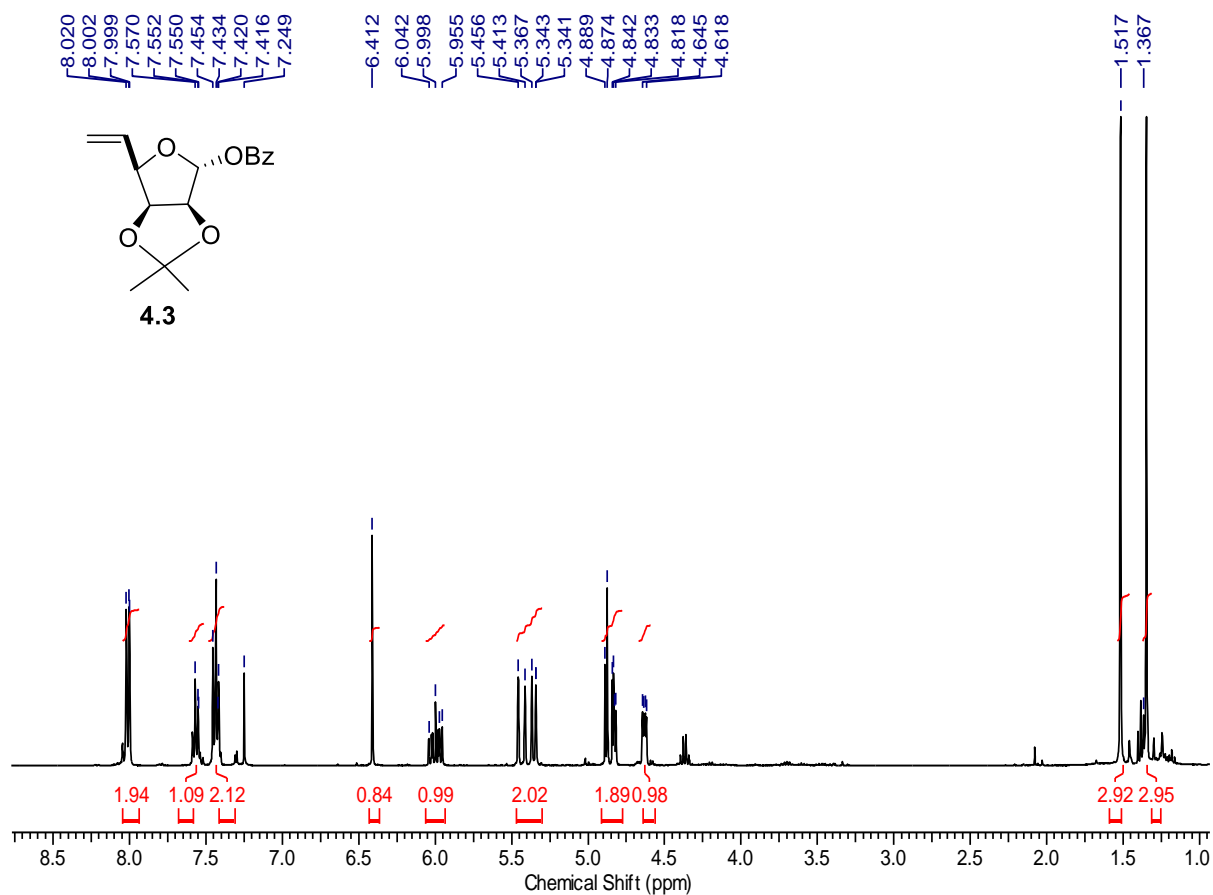


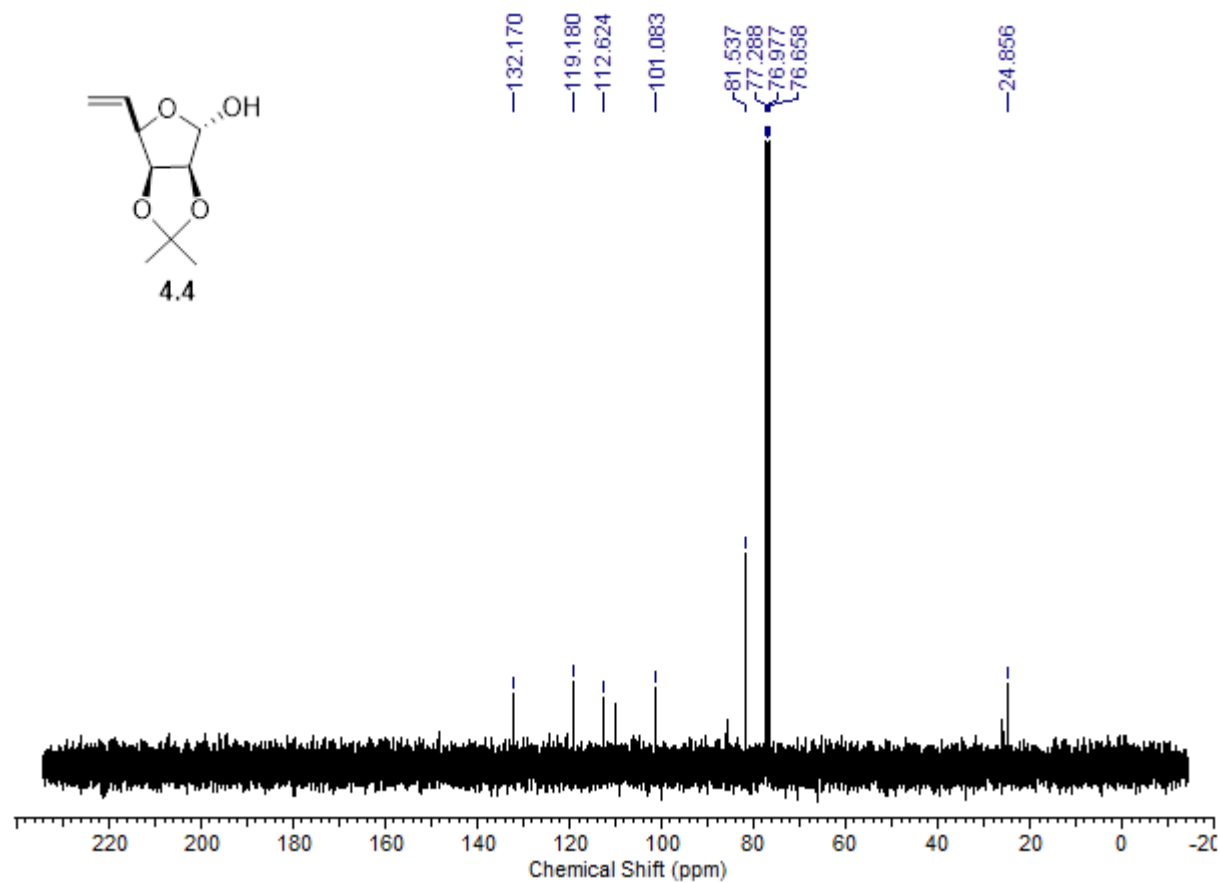
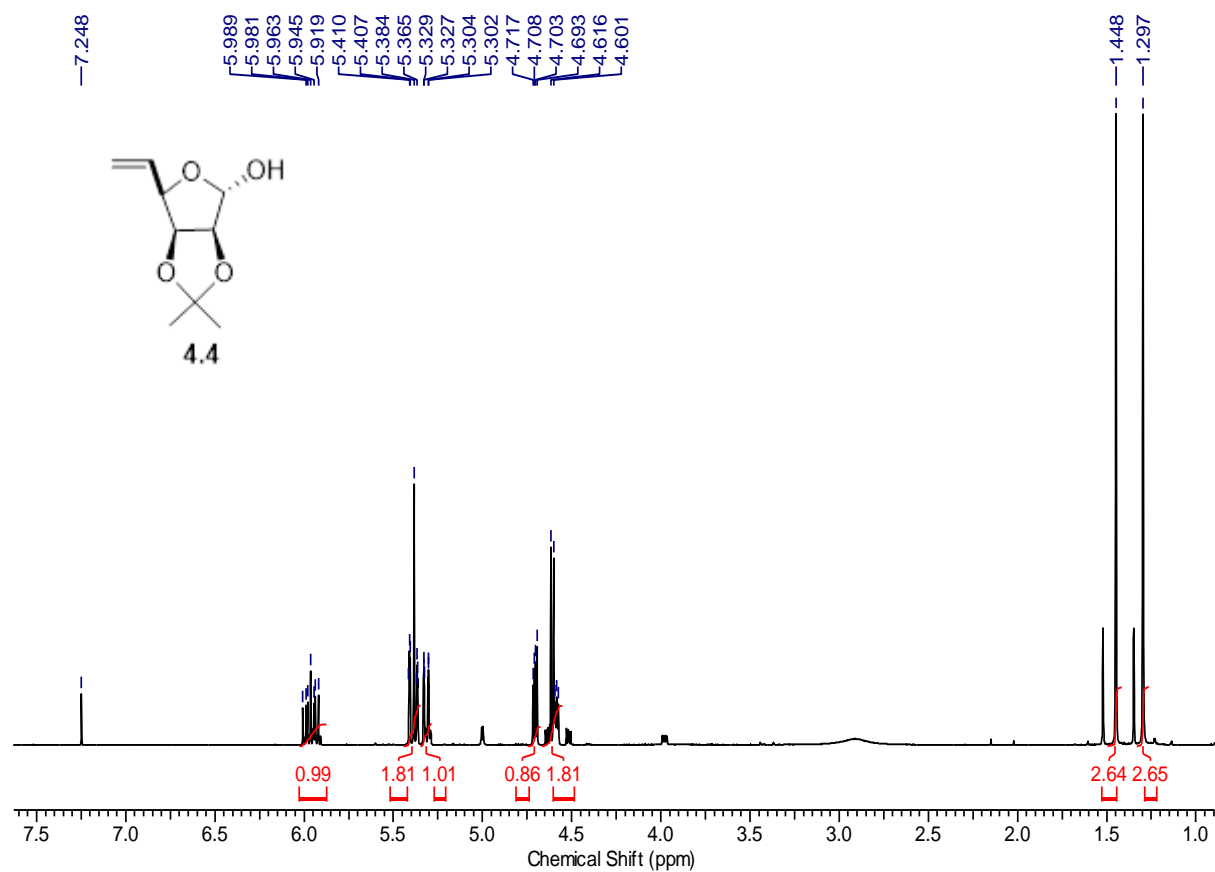
Appendix 5

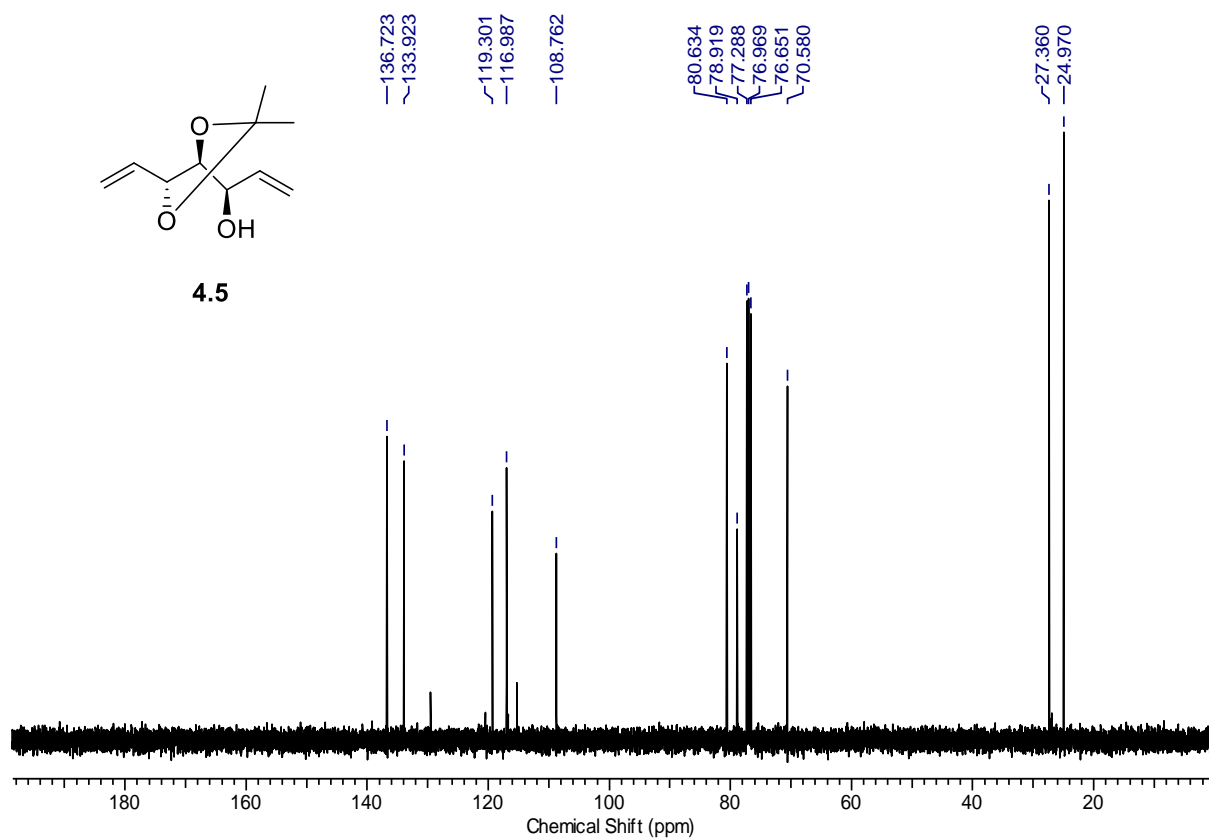
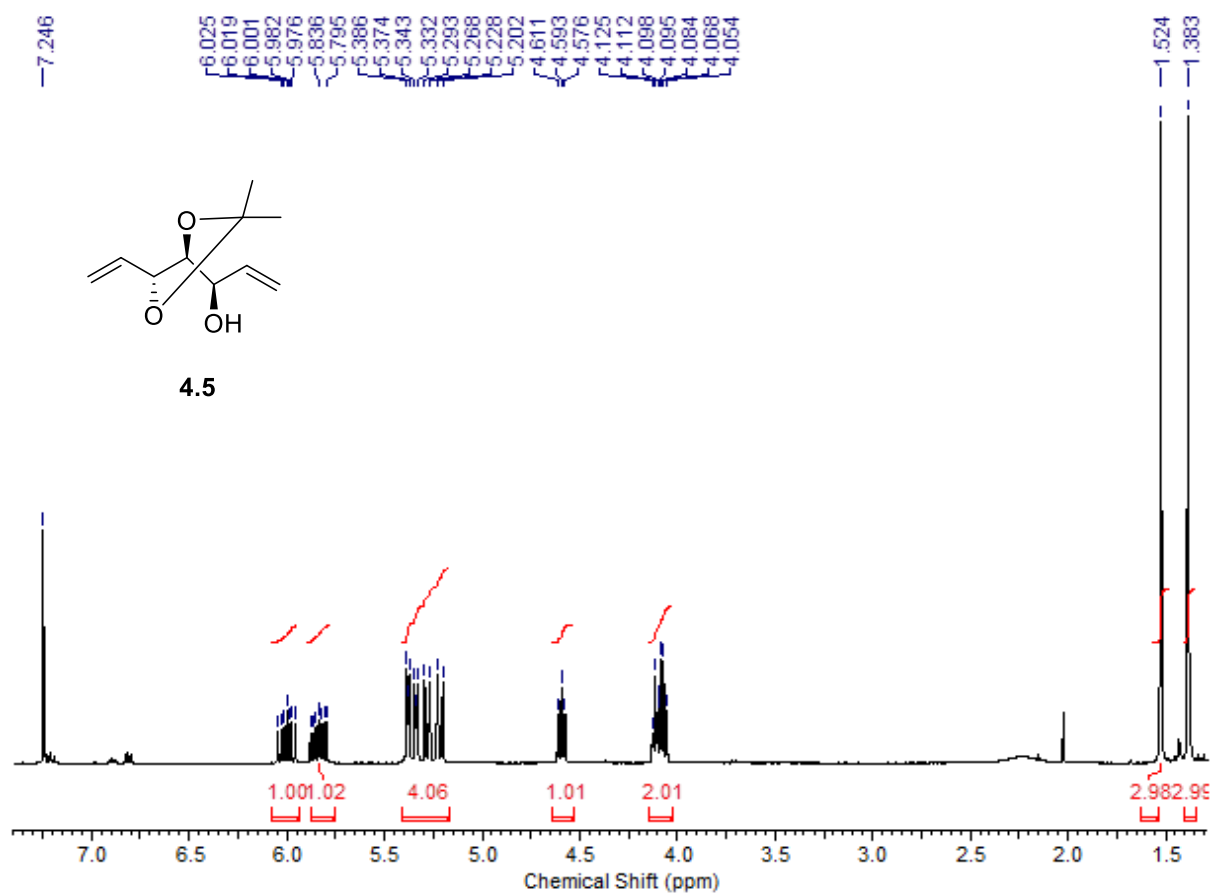
^1H , ^{13}C and ^{31}P NMR spectra for synthesised compounds

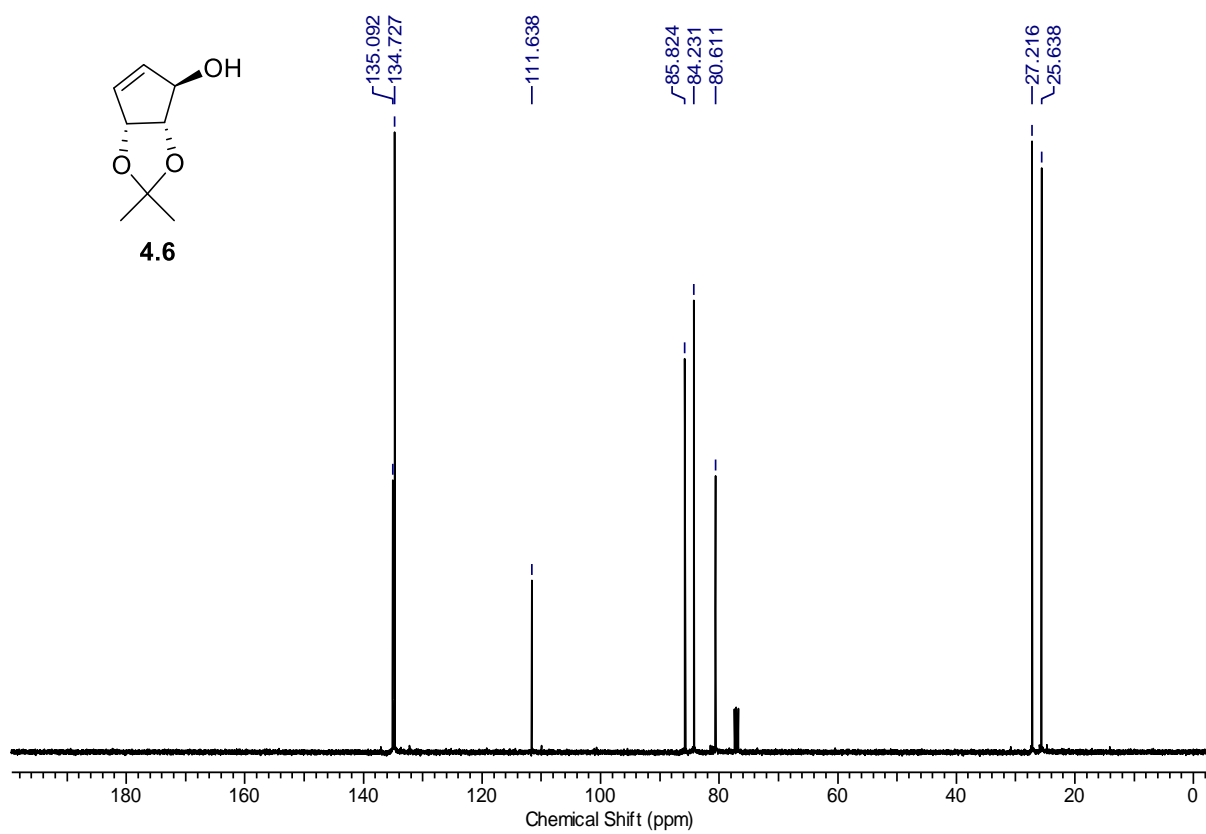
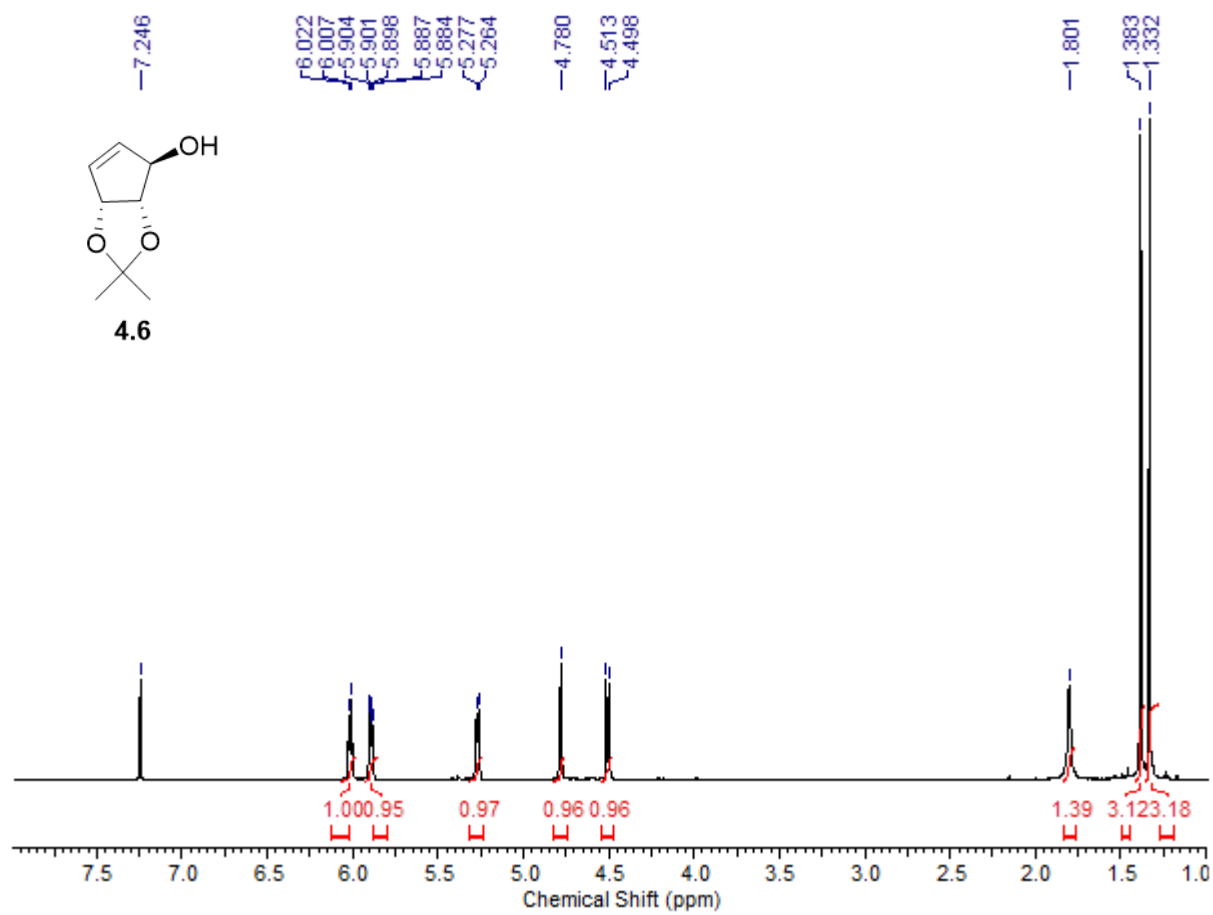


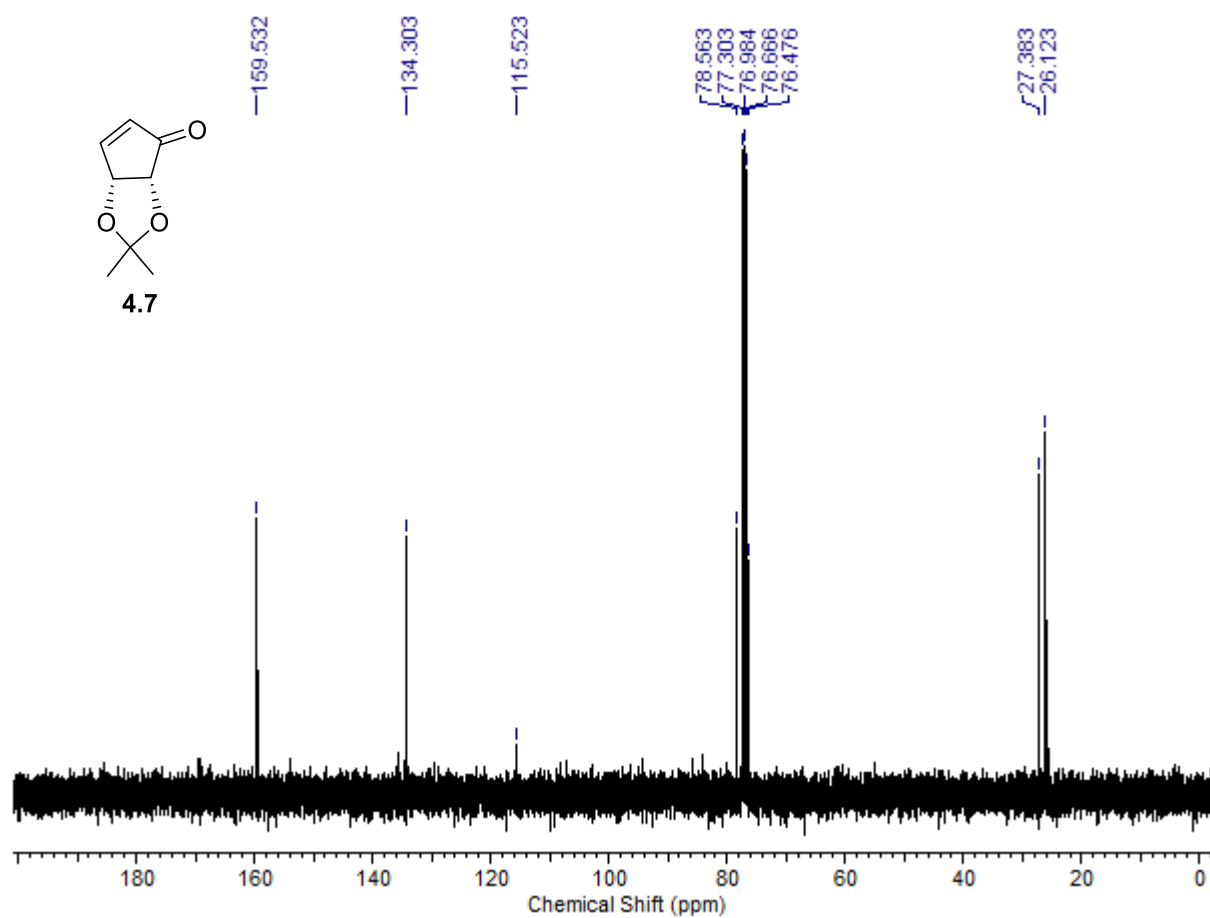
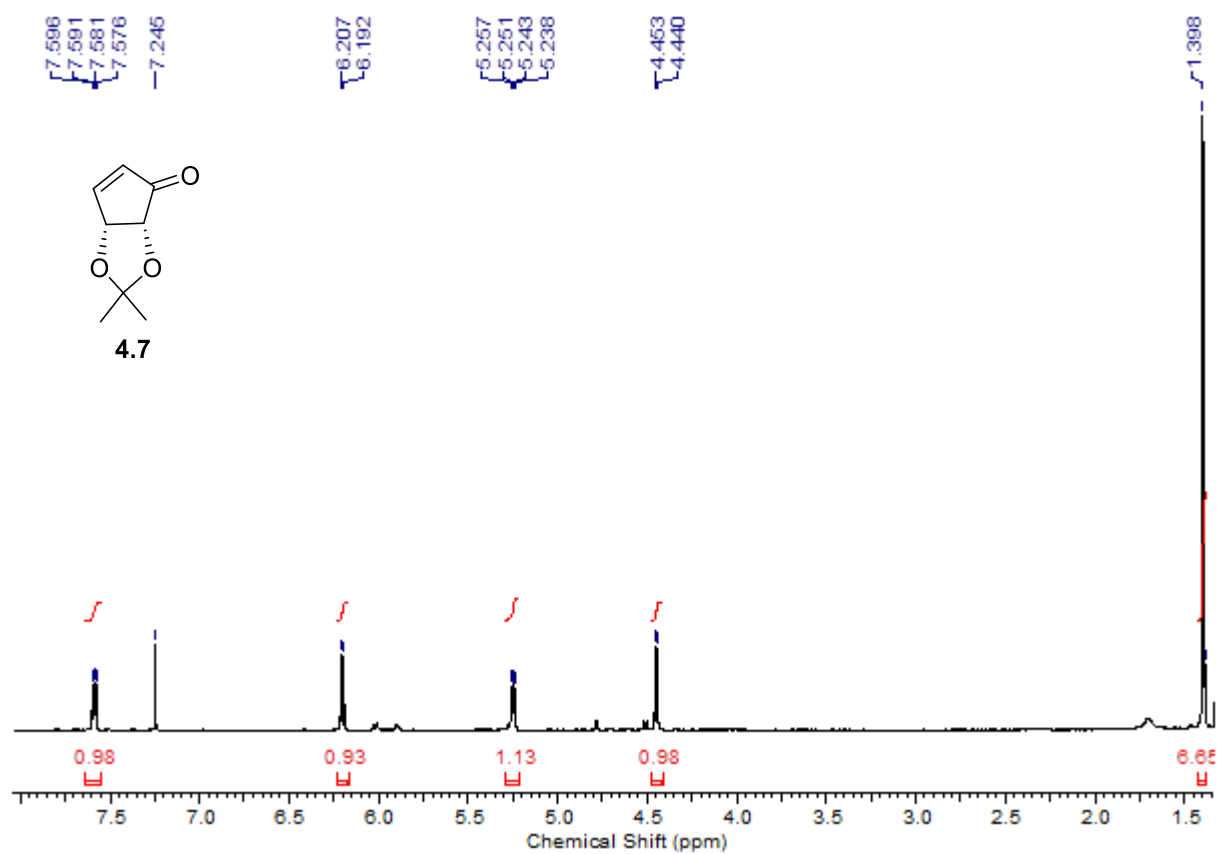


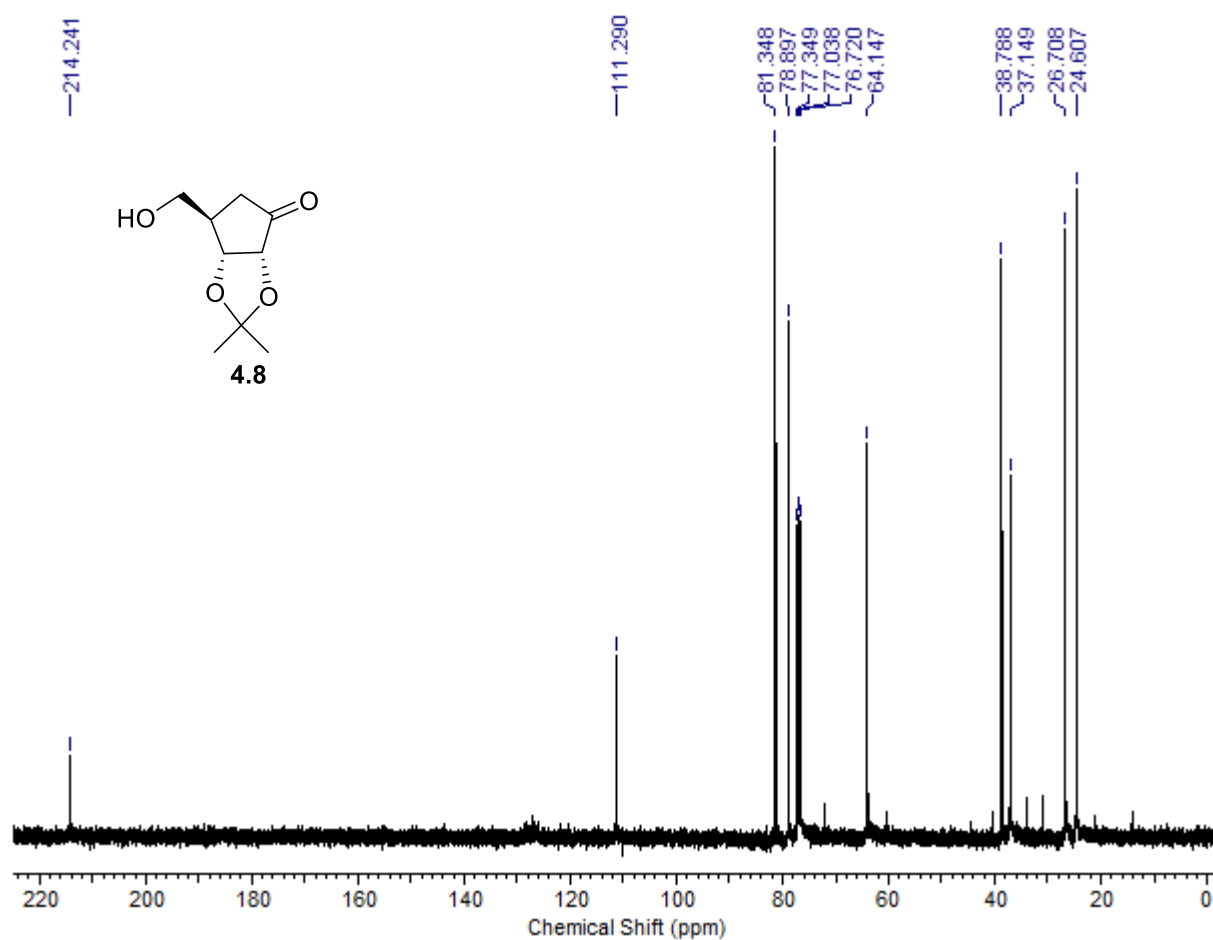
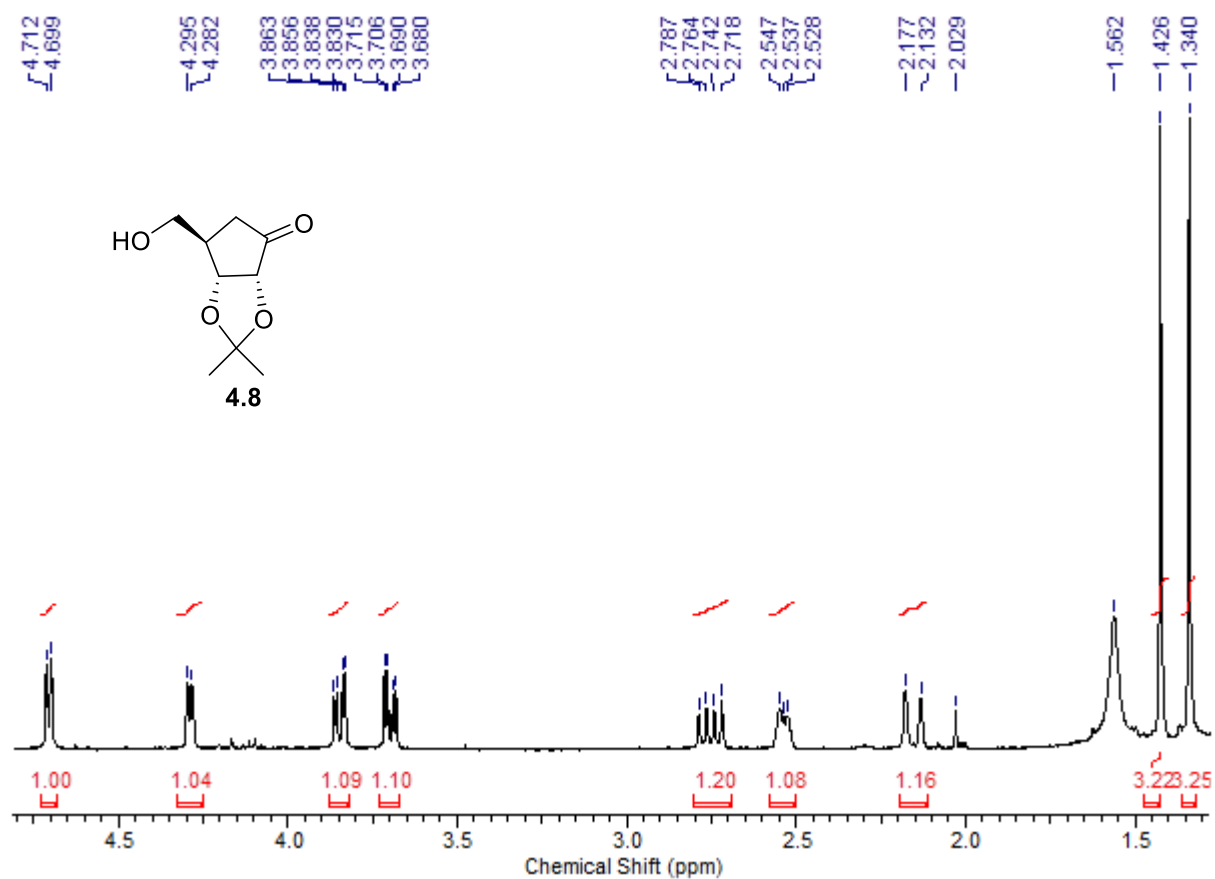


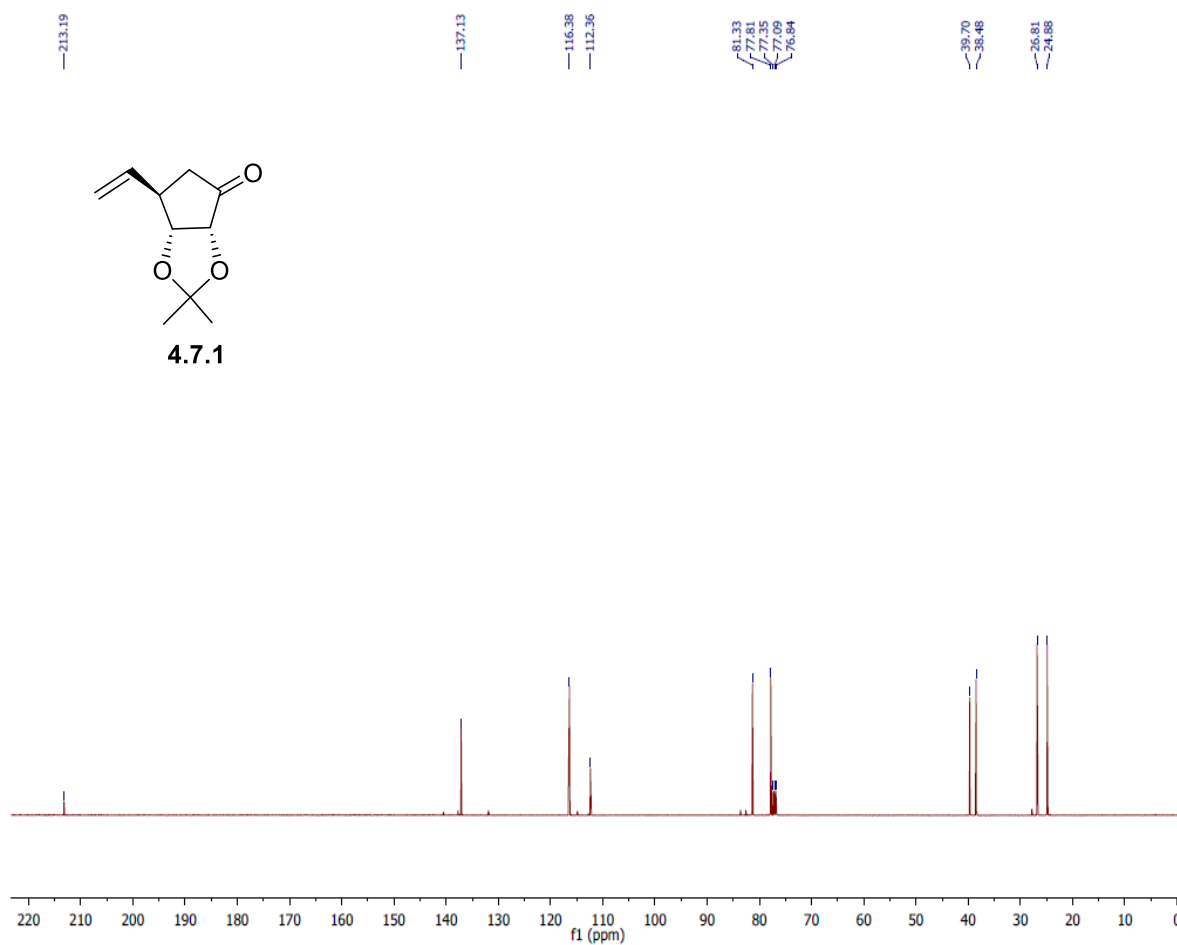
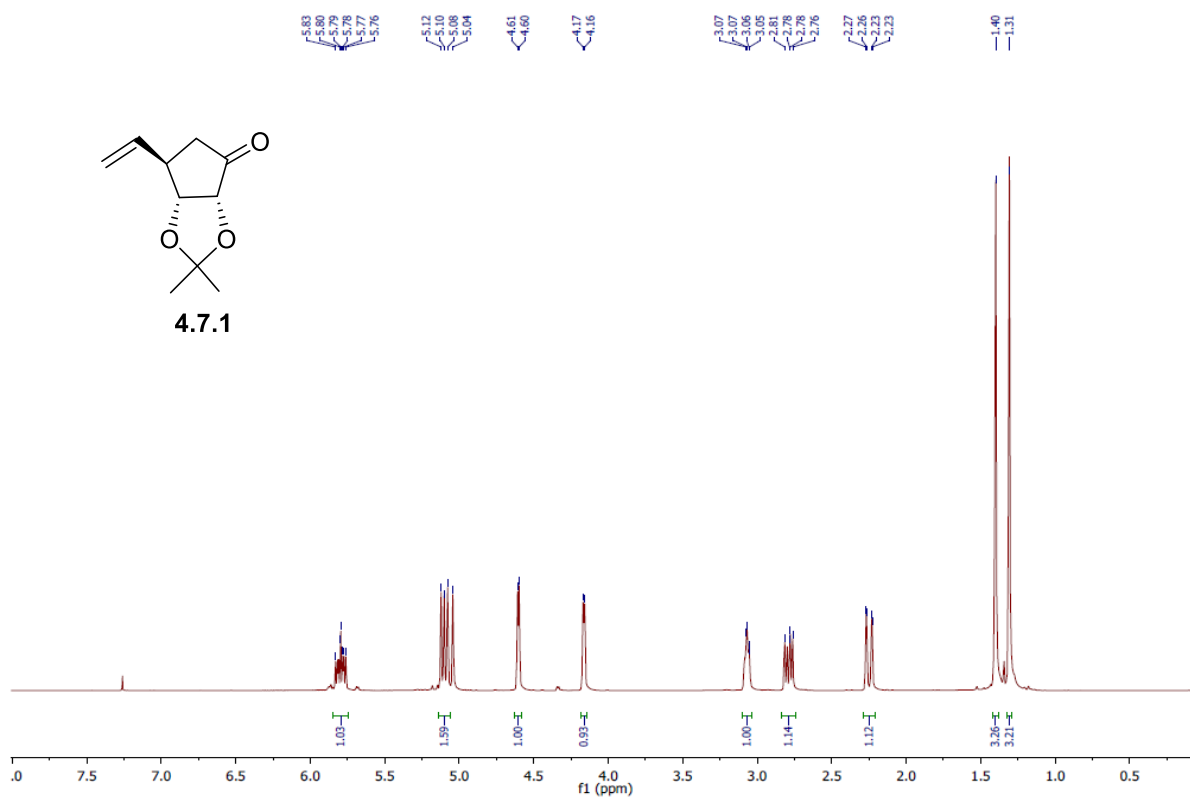


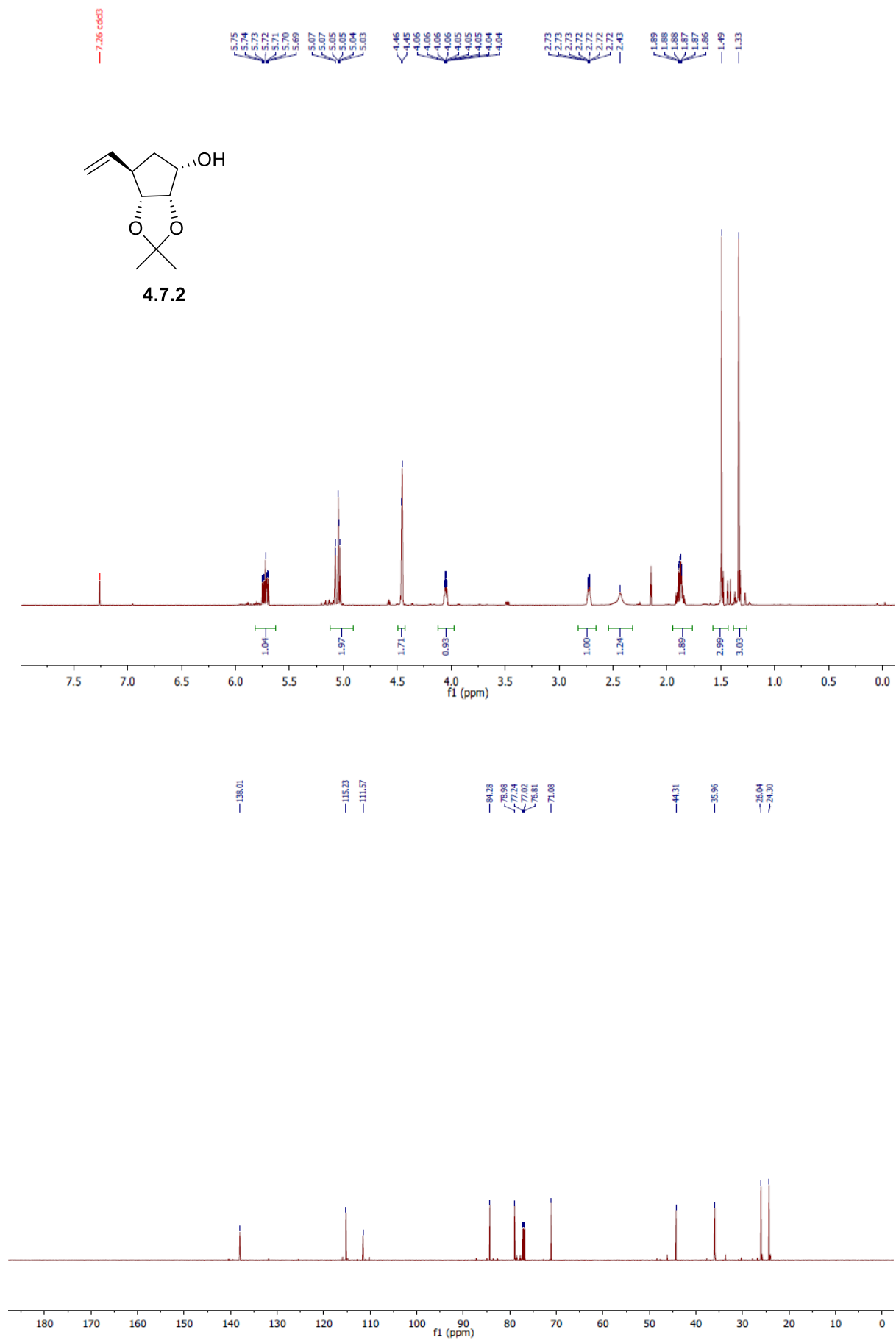


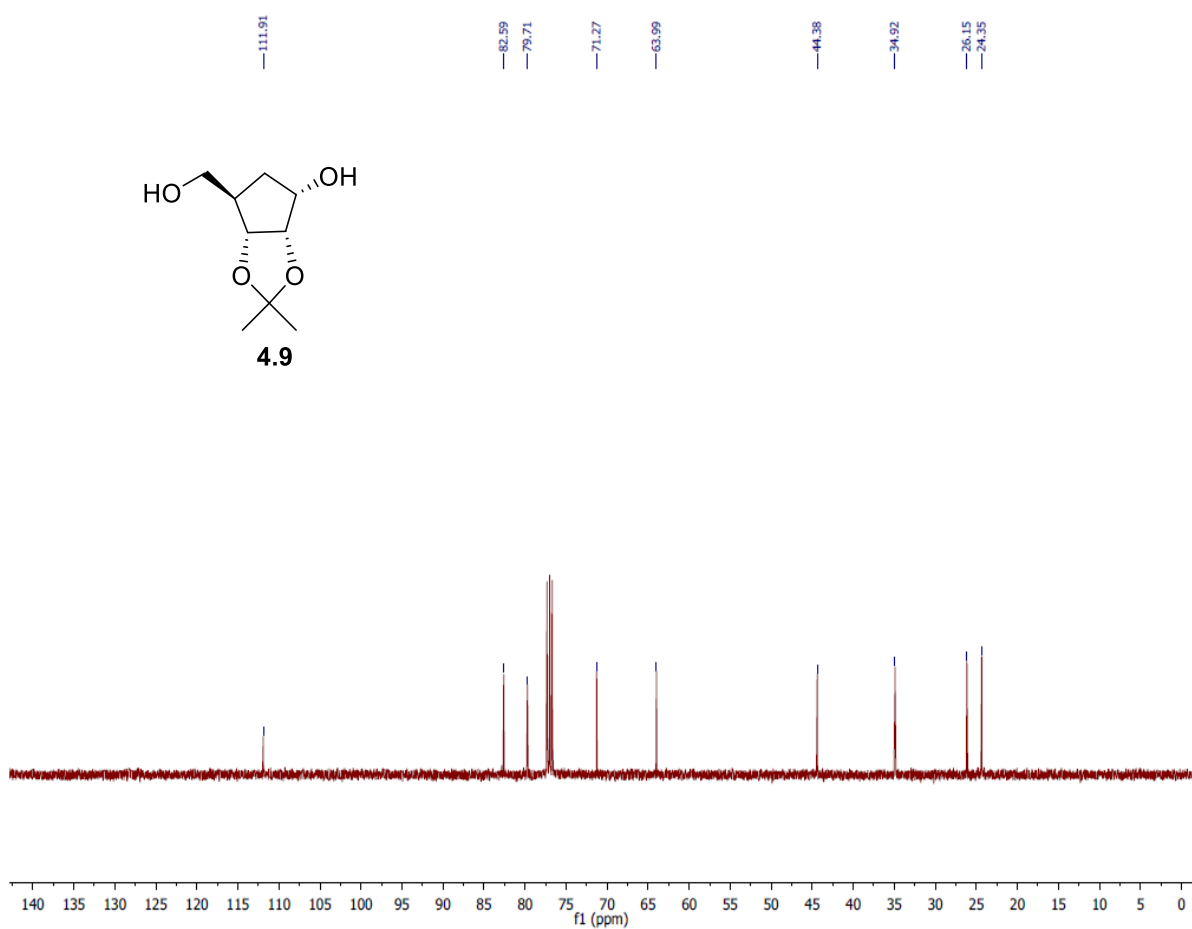
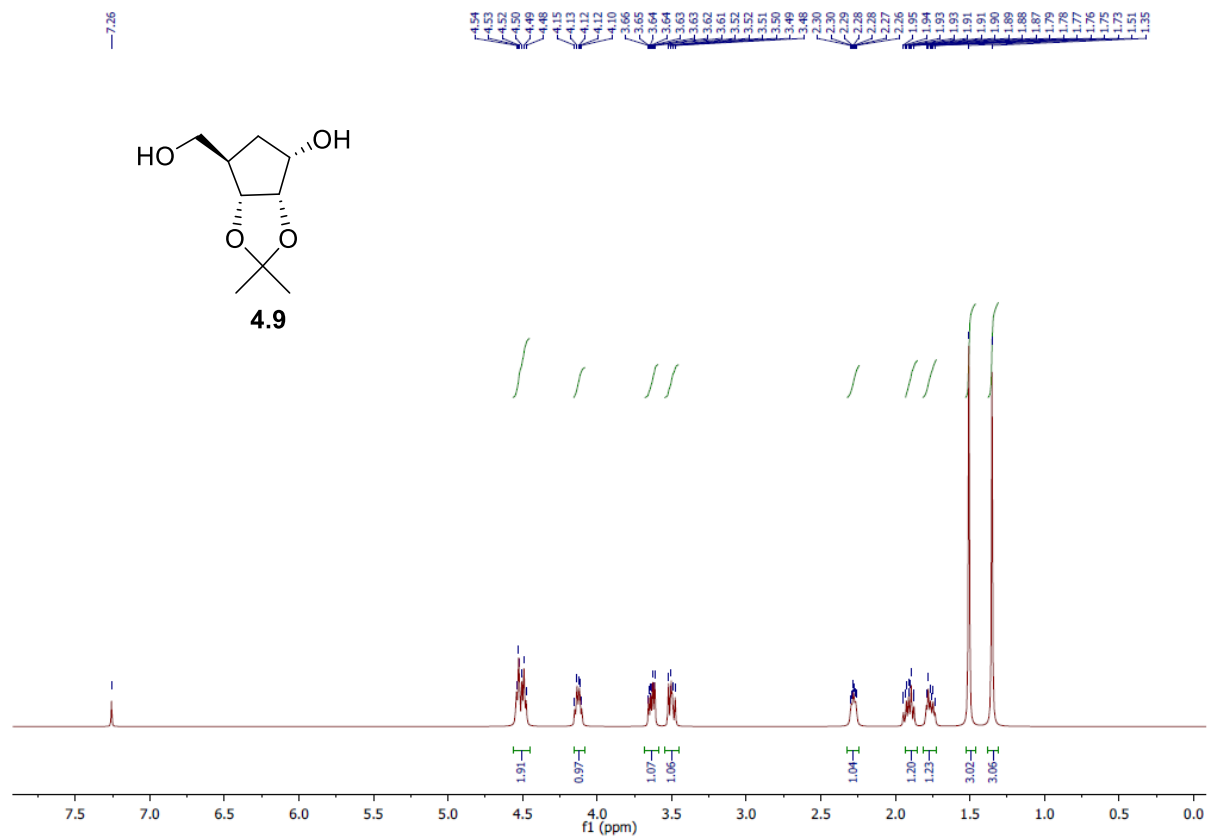


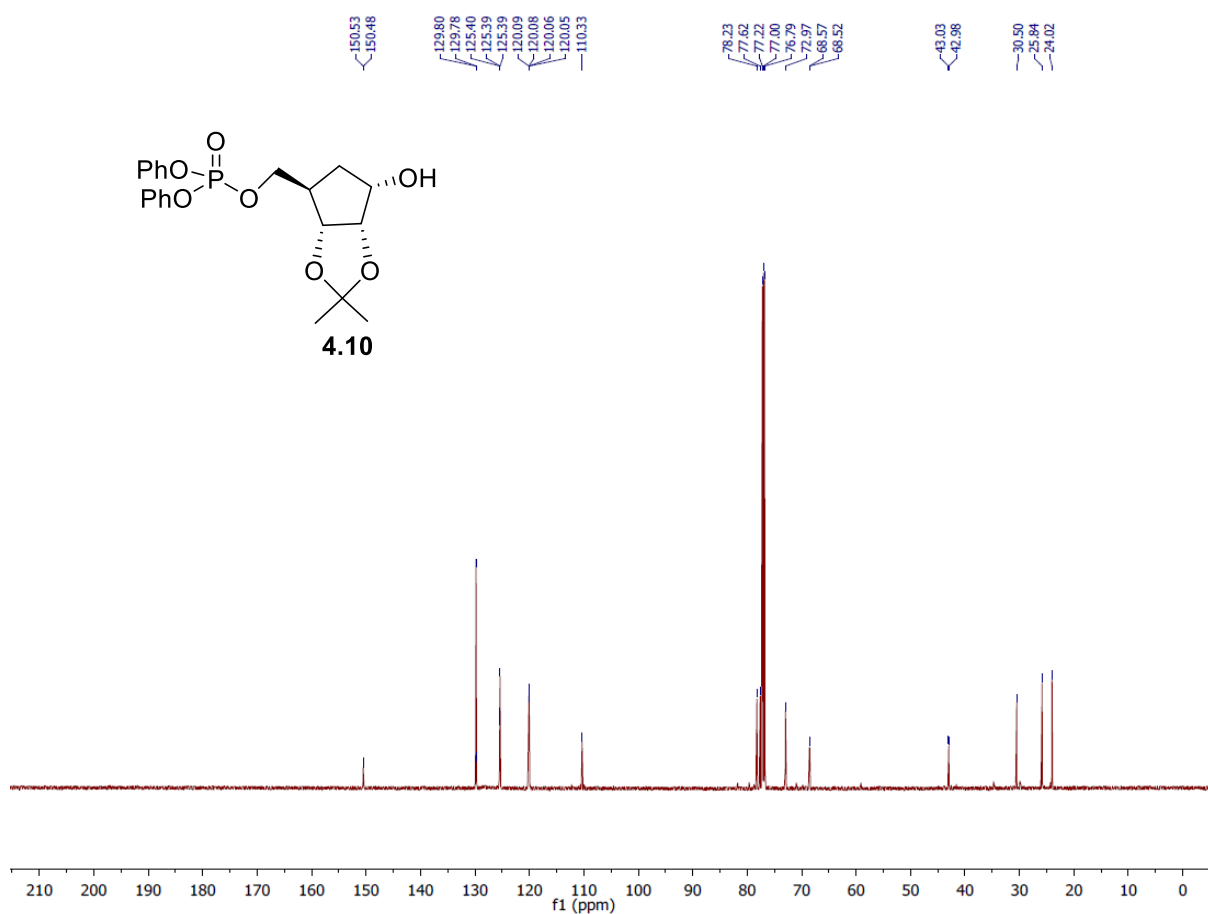
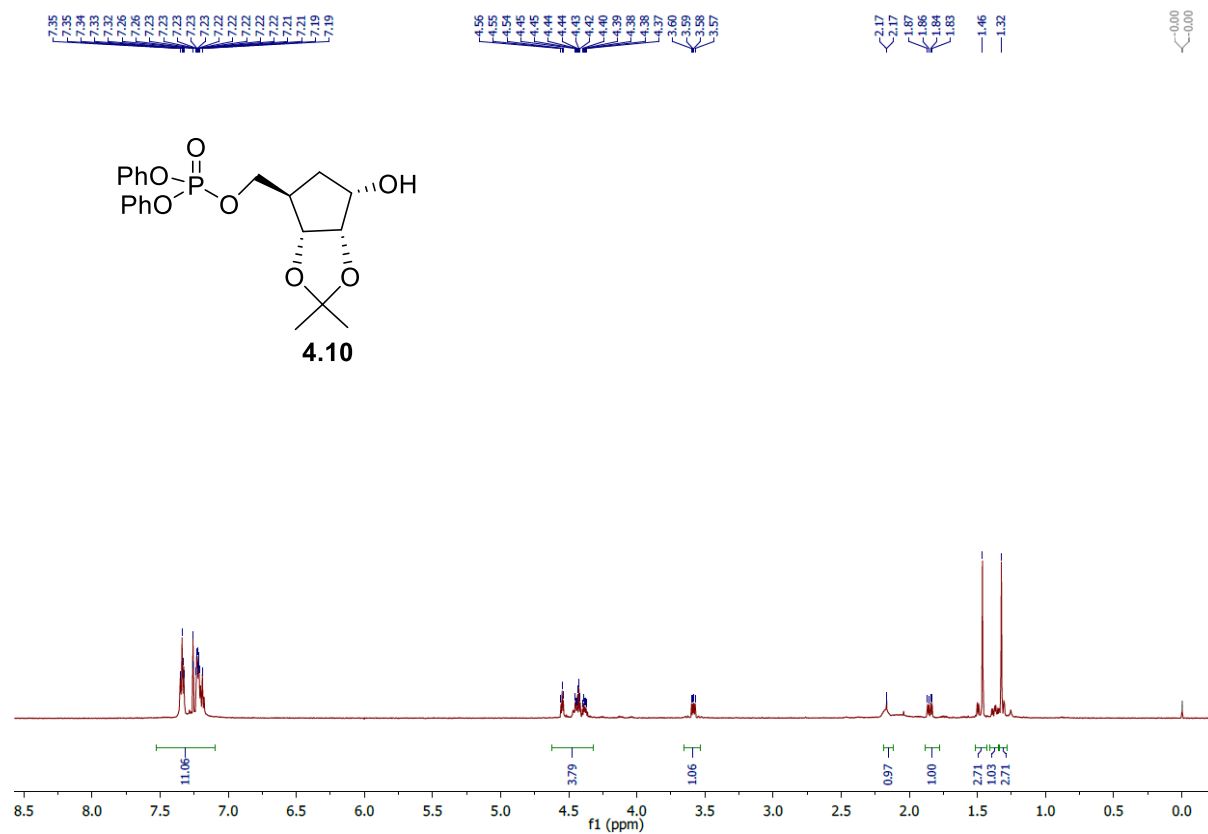


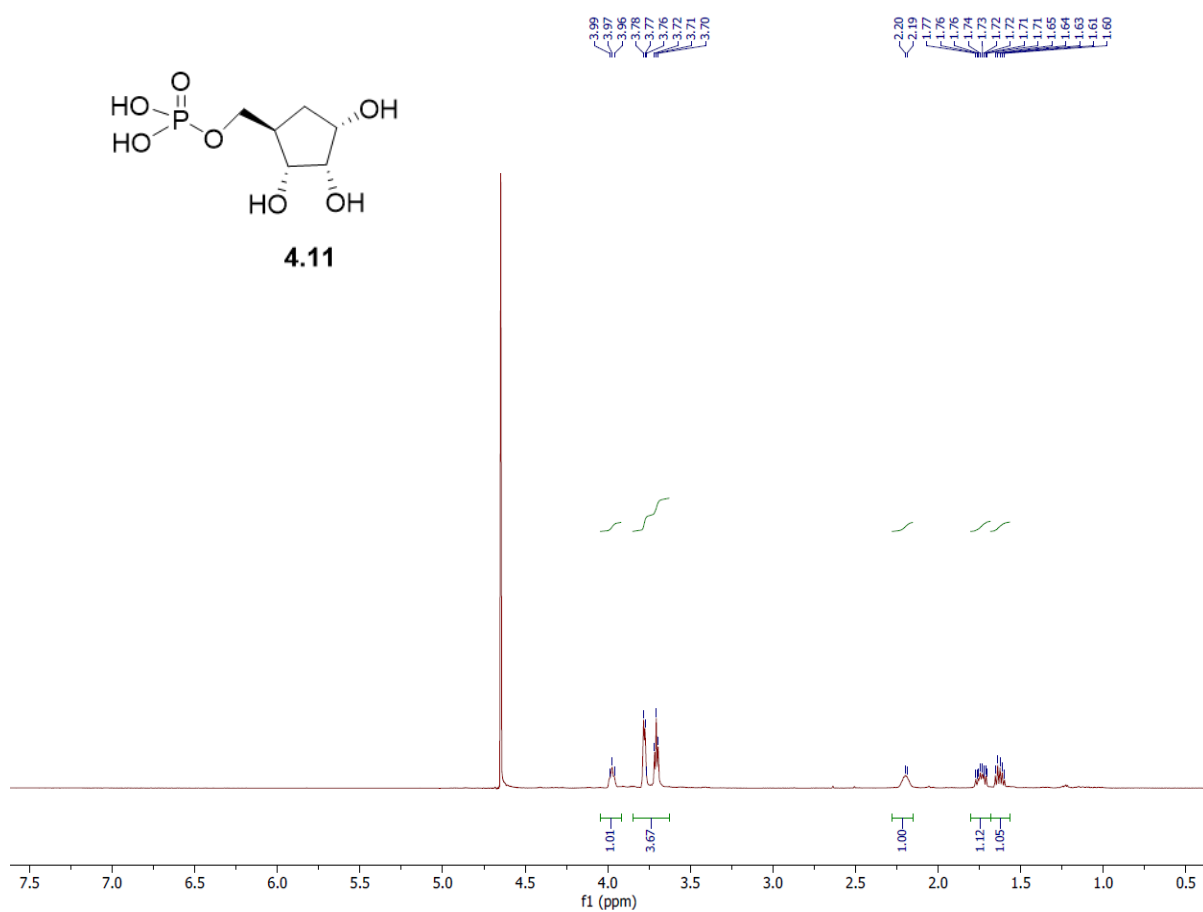
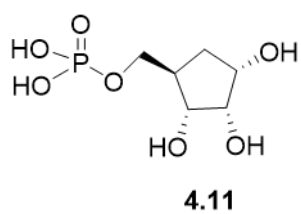
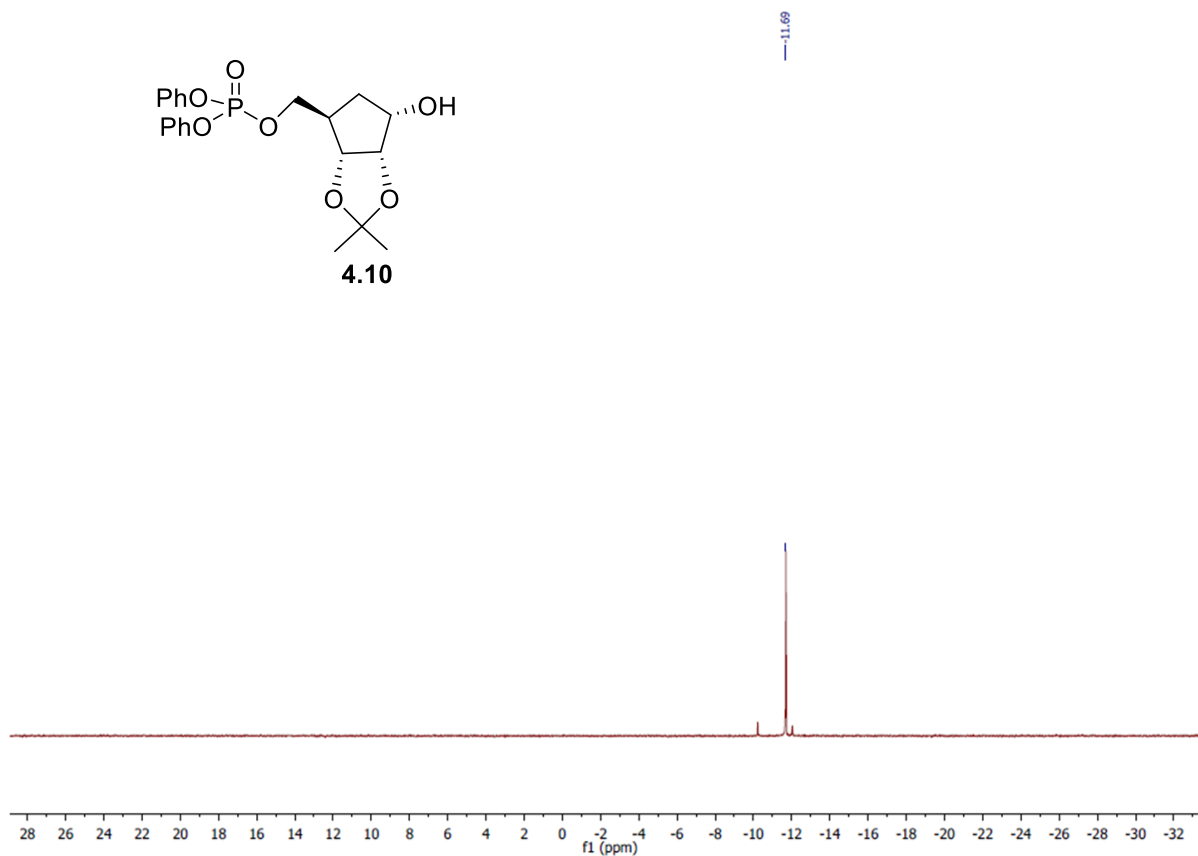
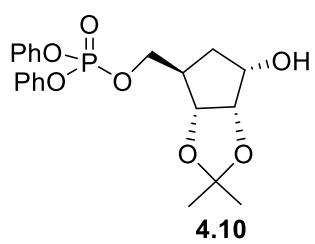


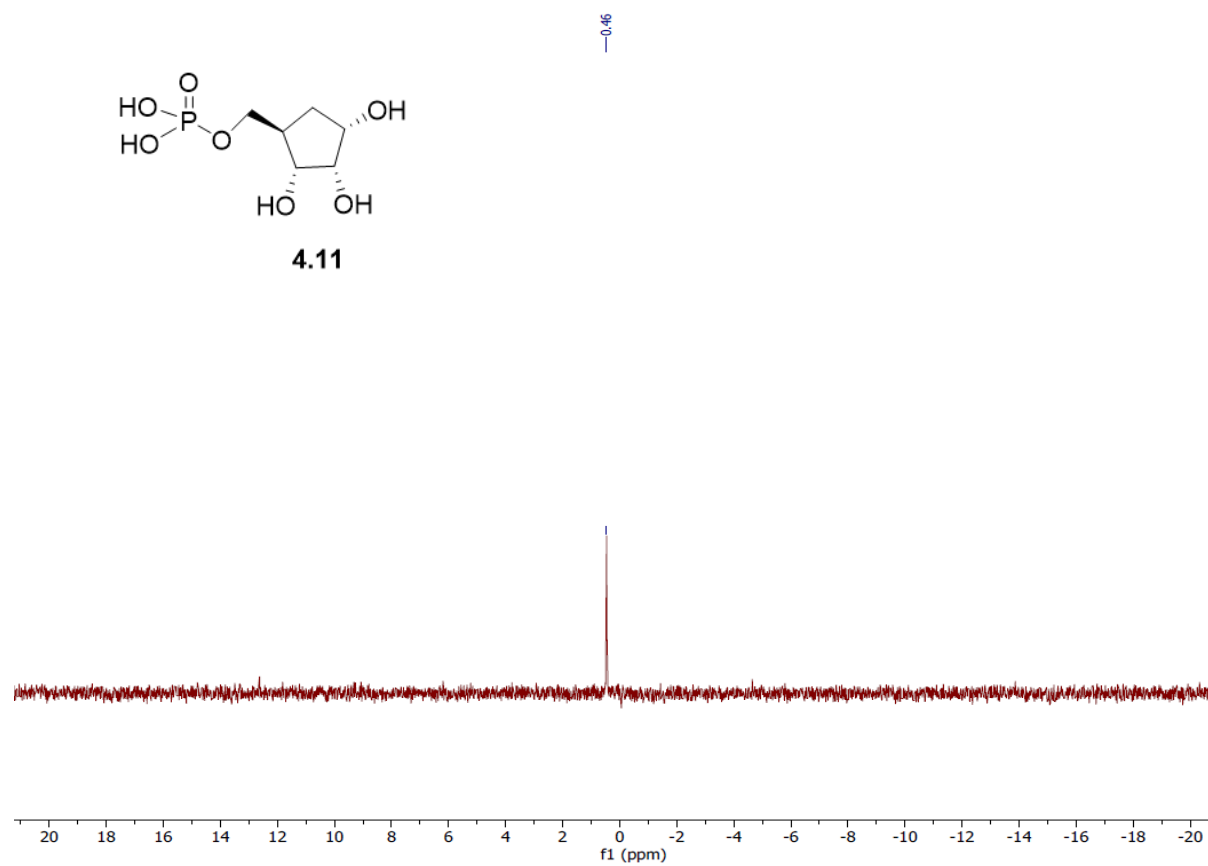
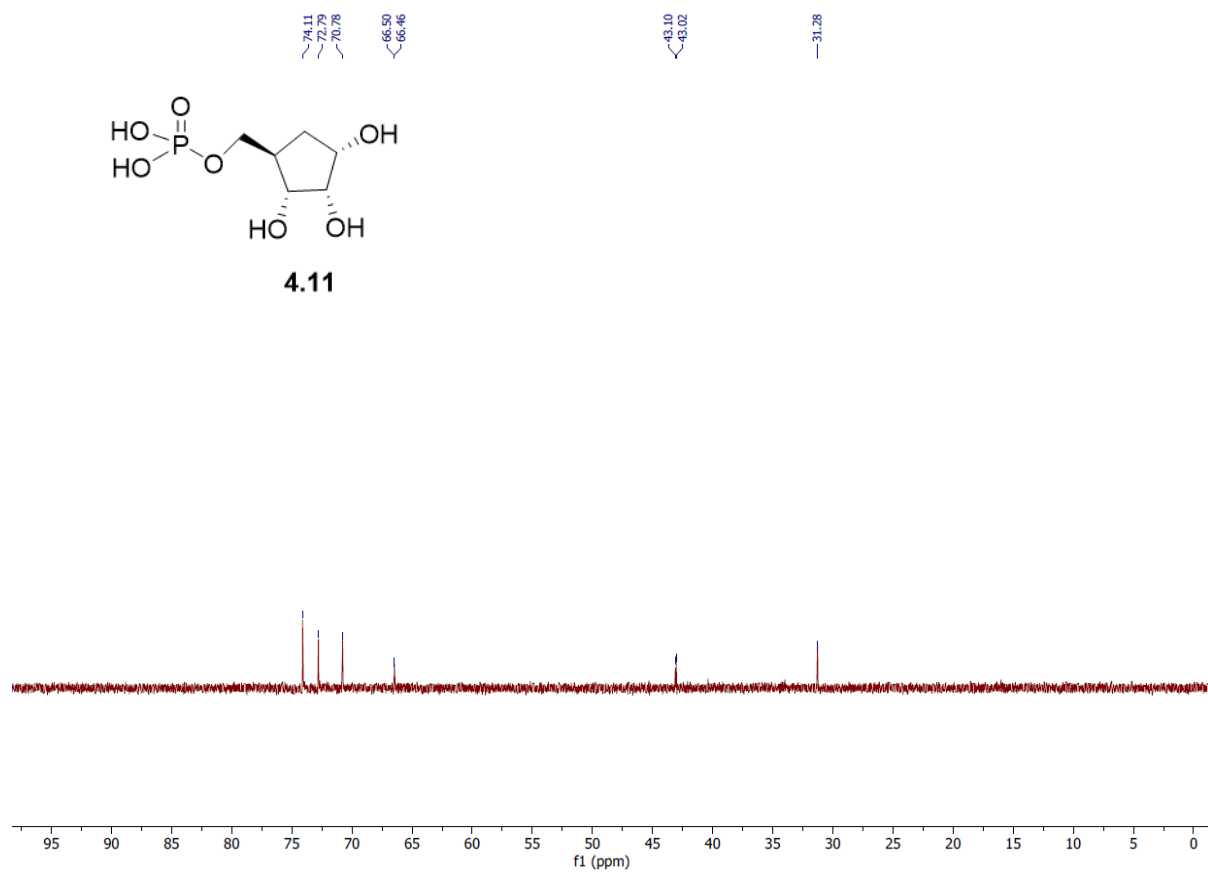


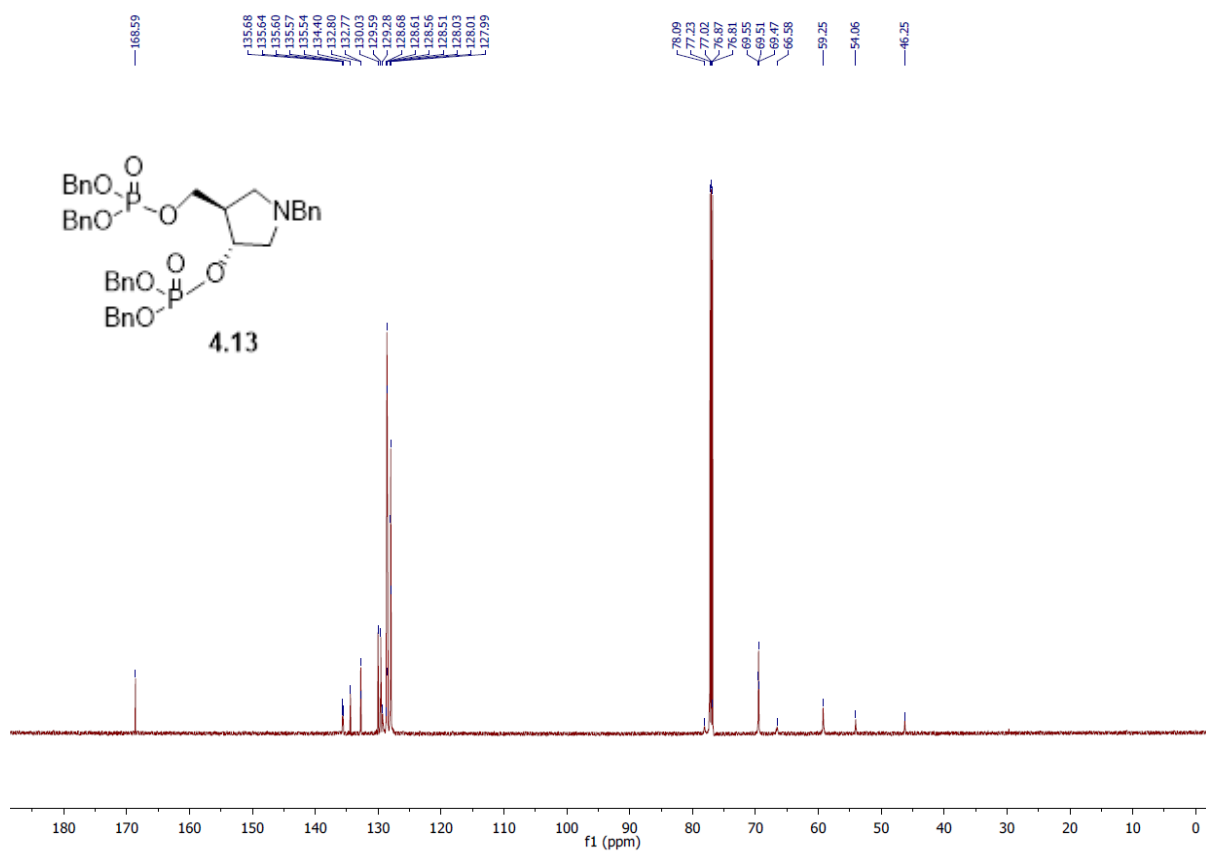
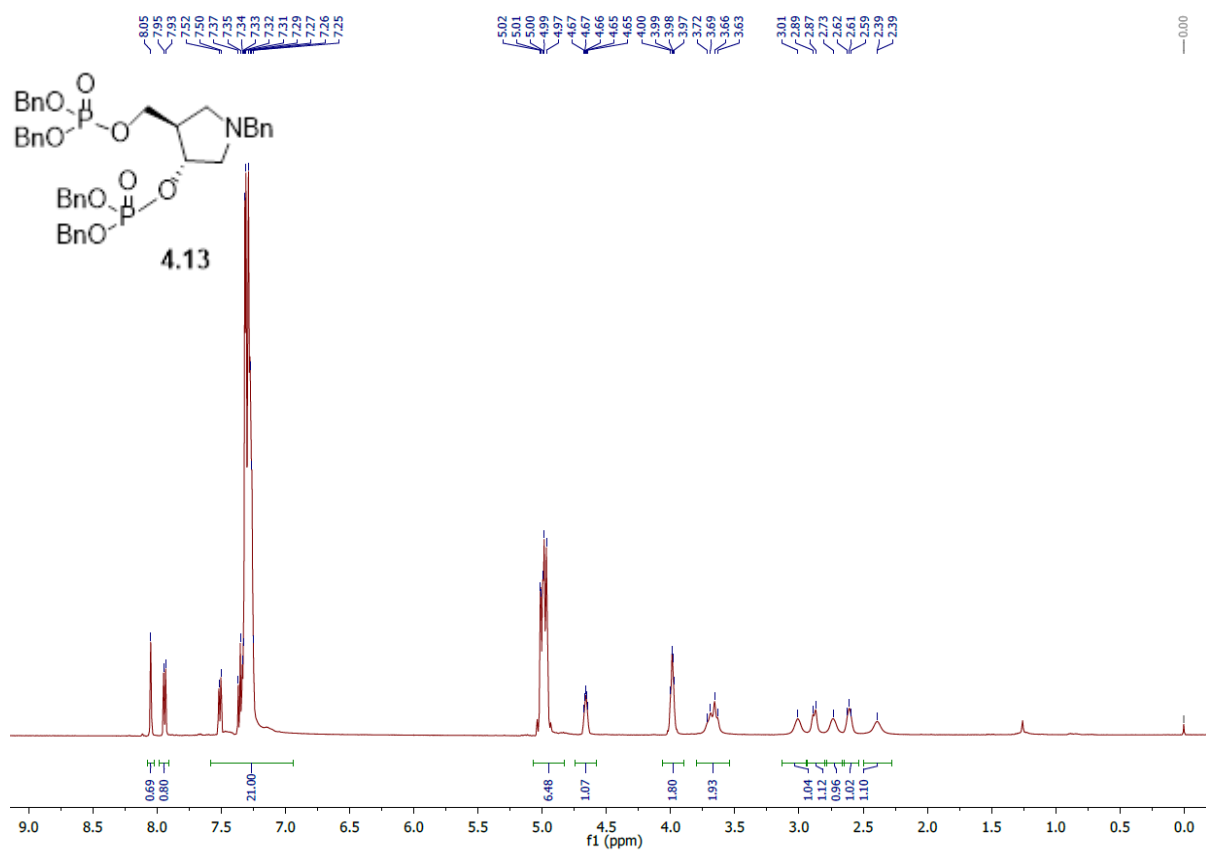


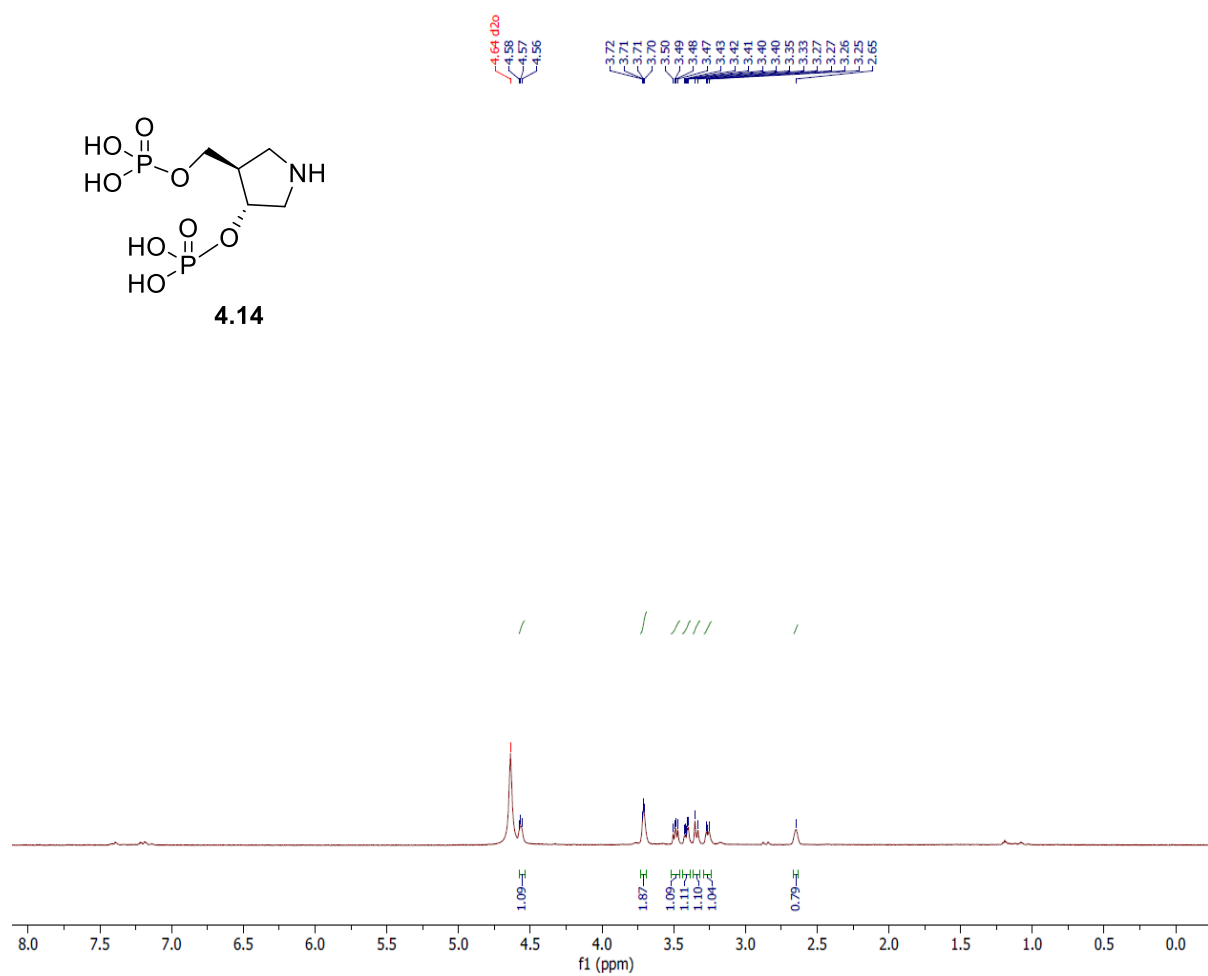
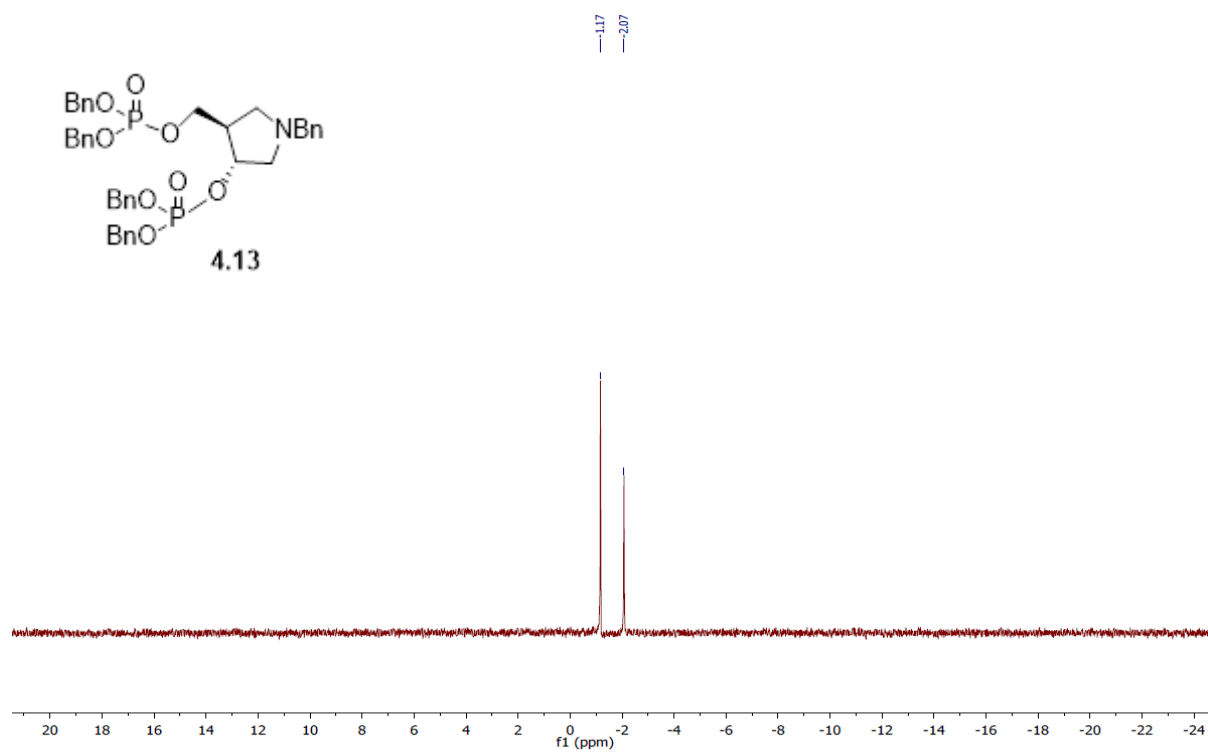


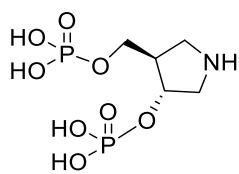






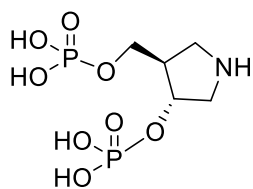
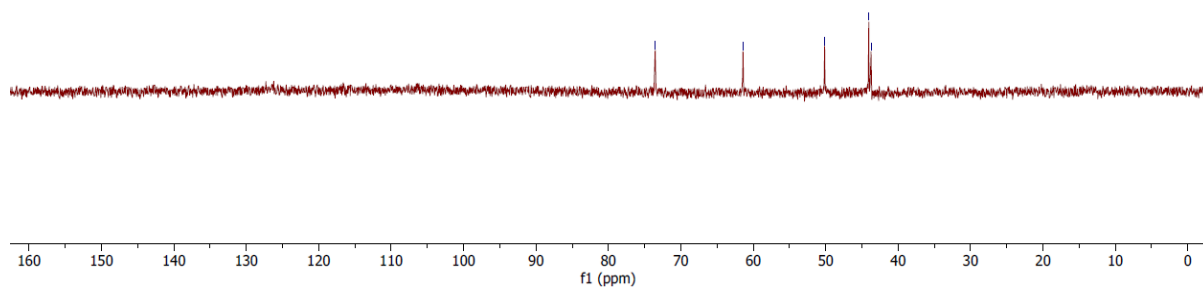






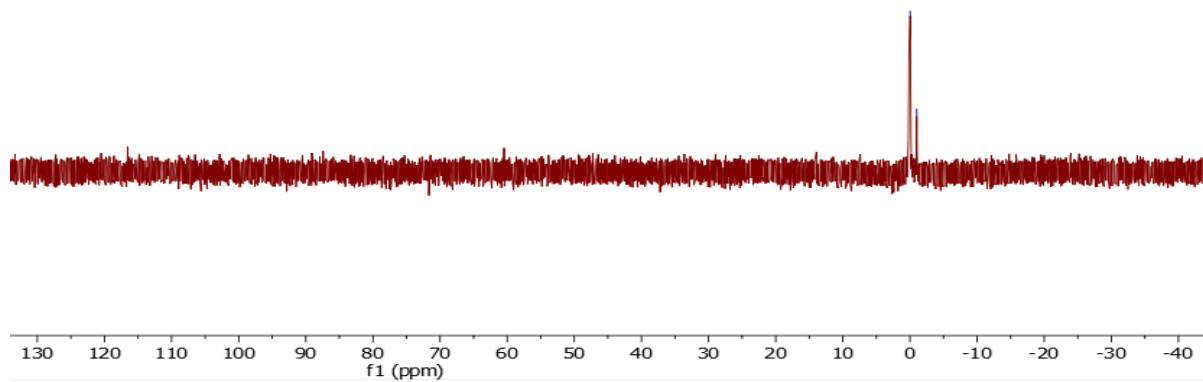
4.14

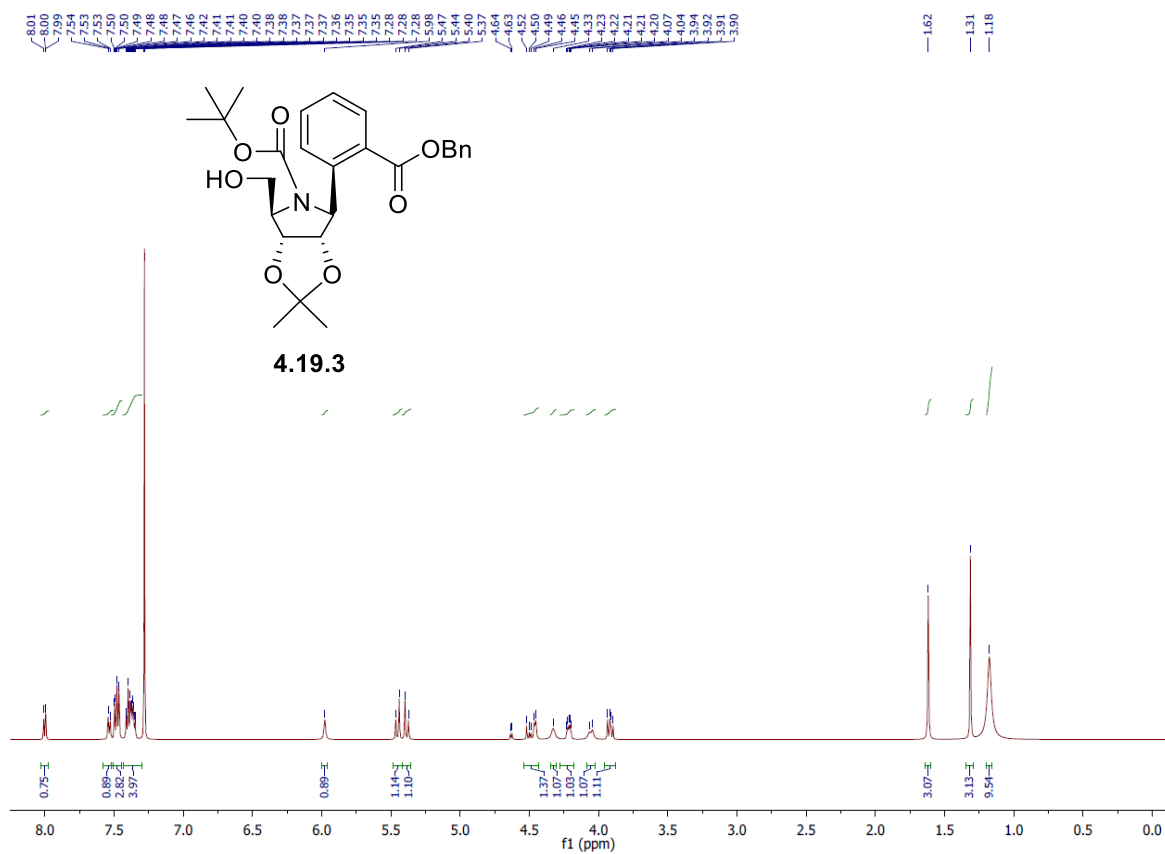
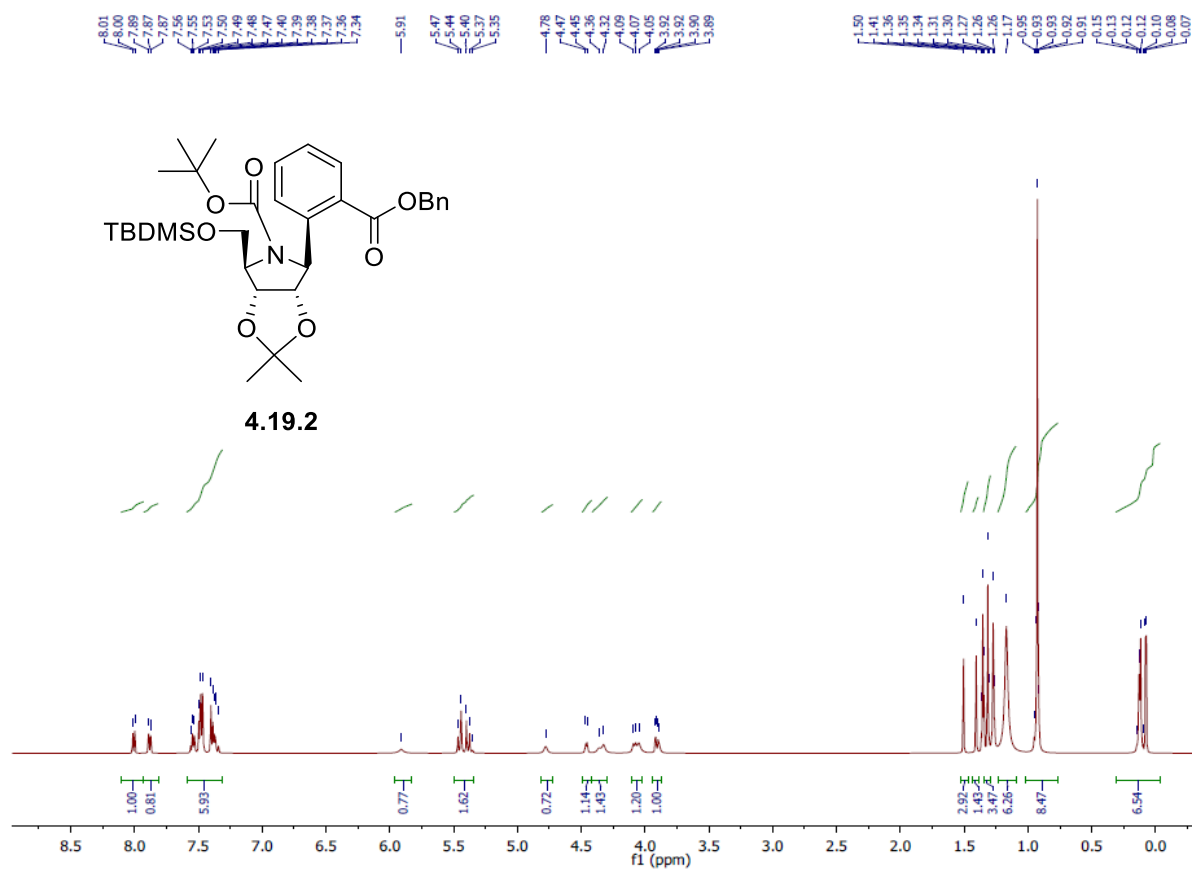
73.55
61.41
50.14
44.05
43.73

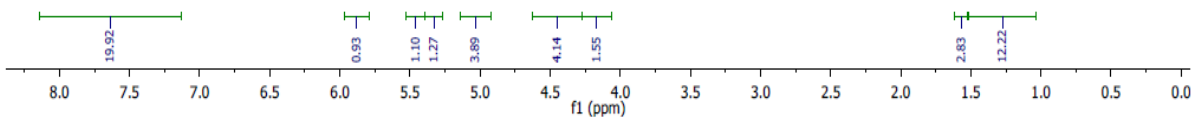


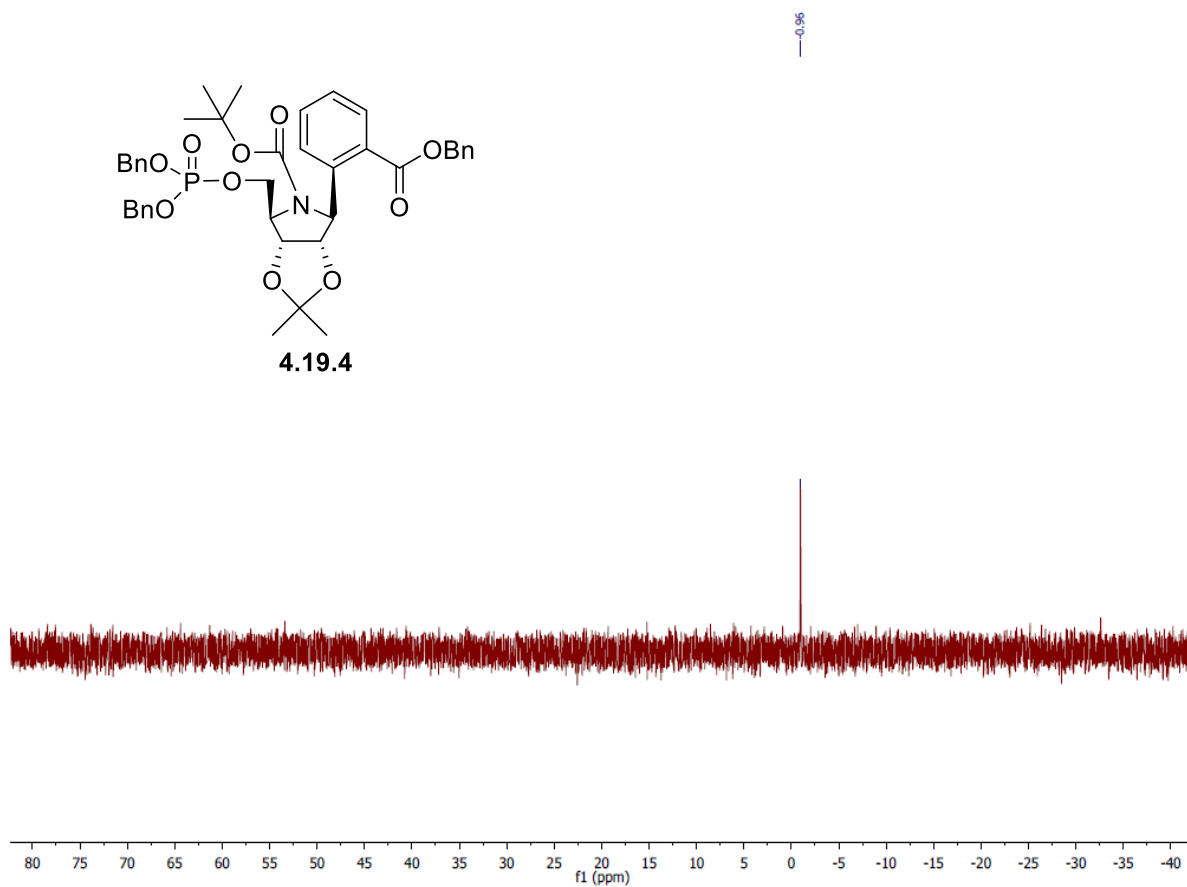
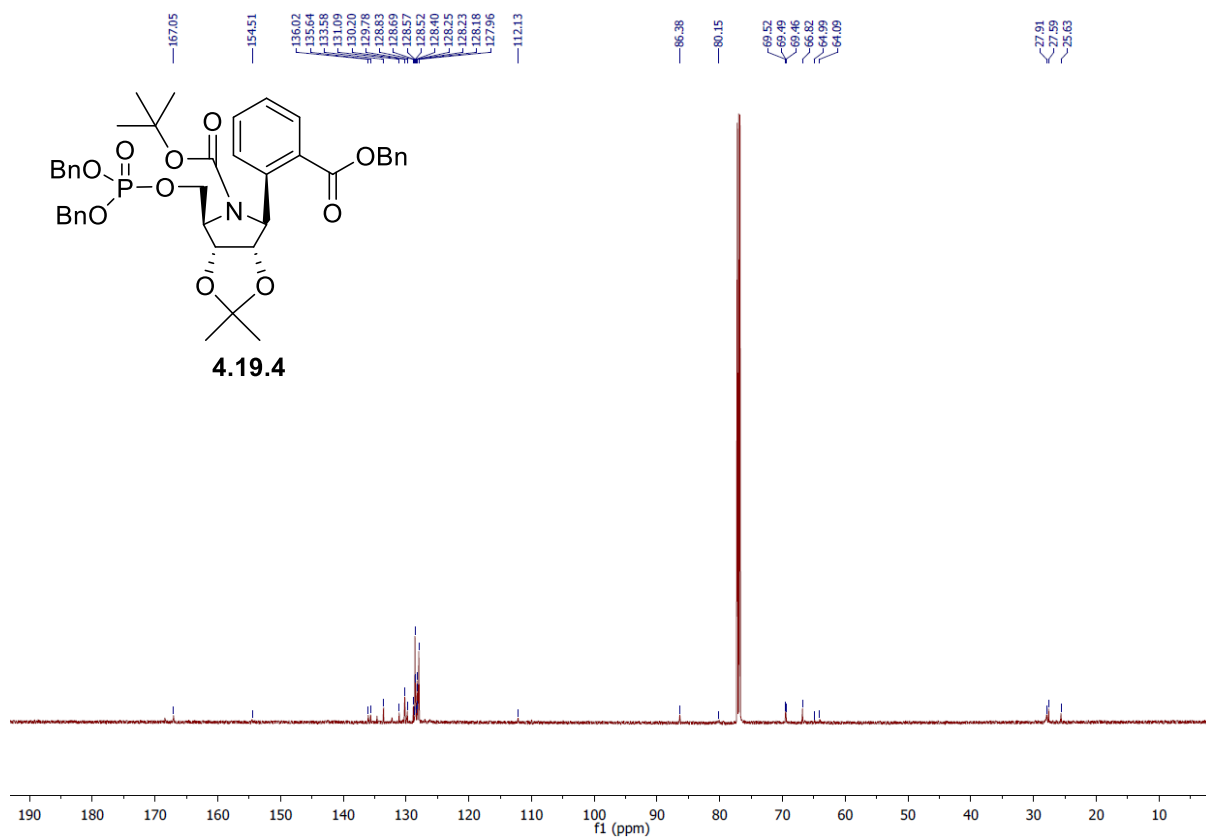
4.14

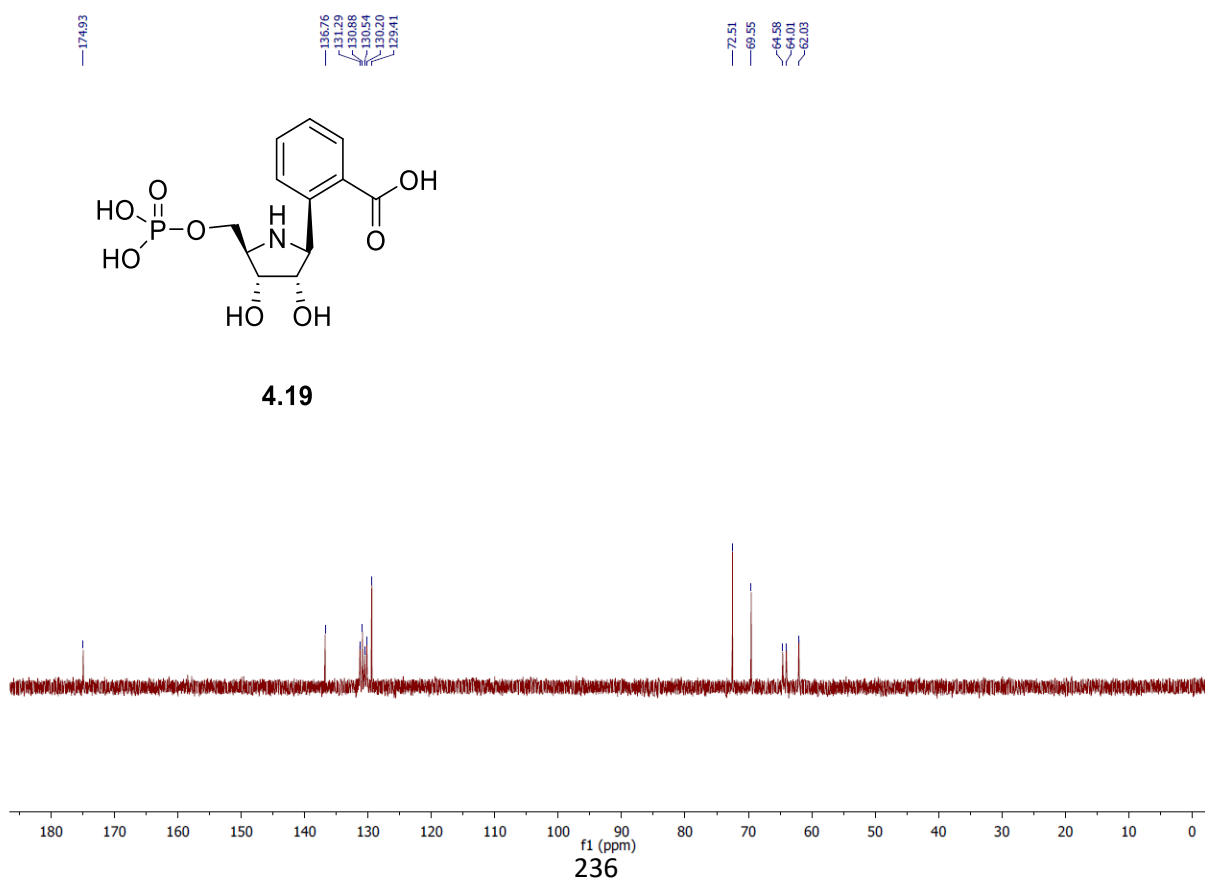
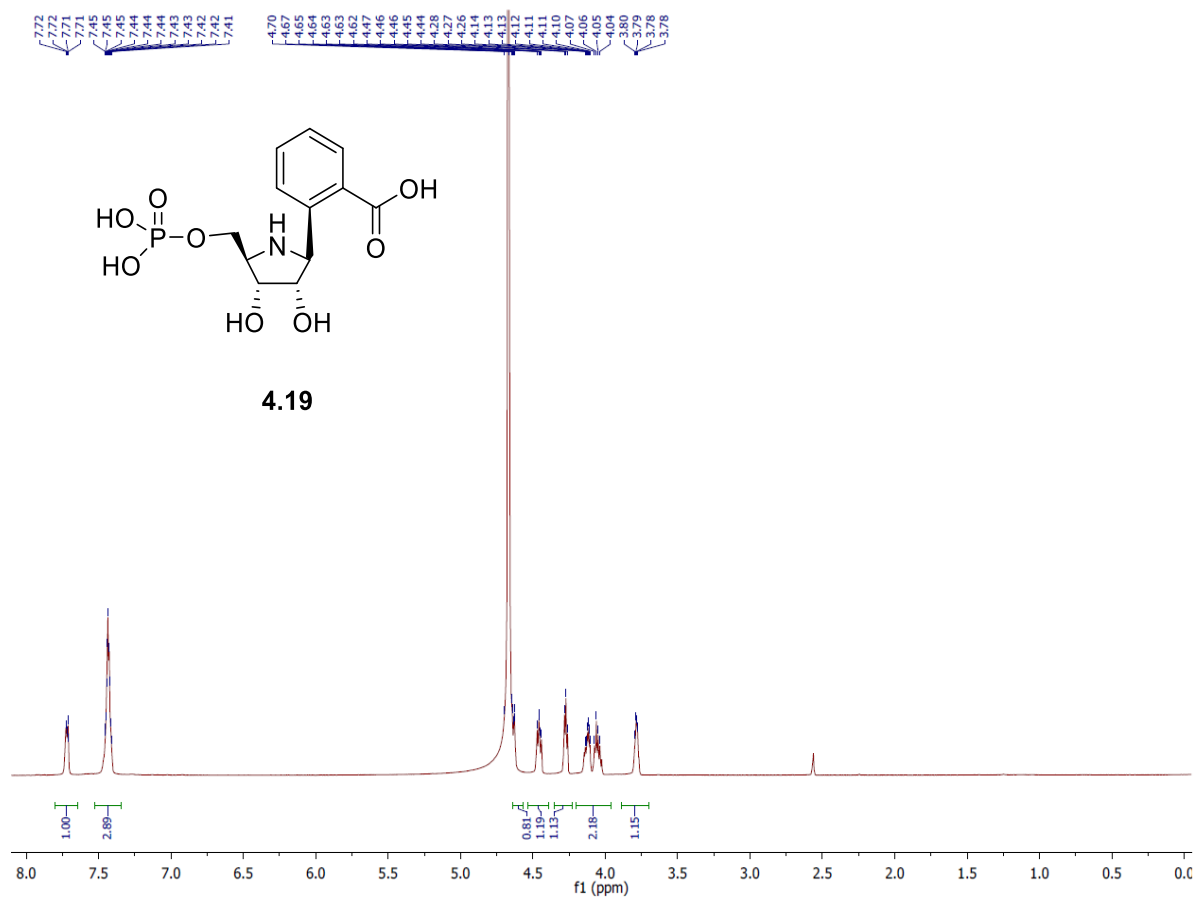
0.03
1.02

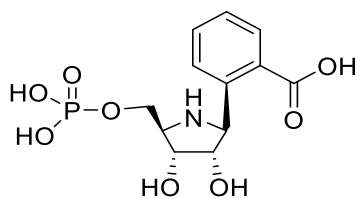




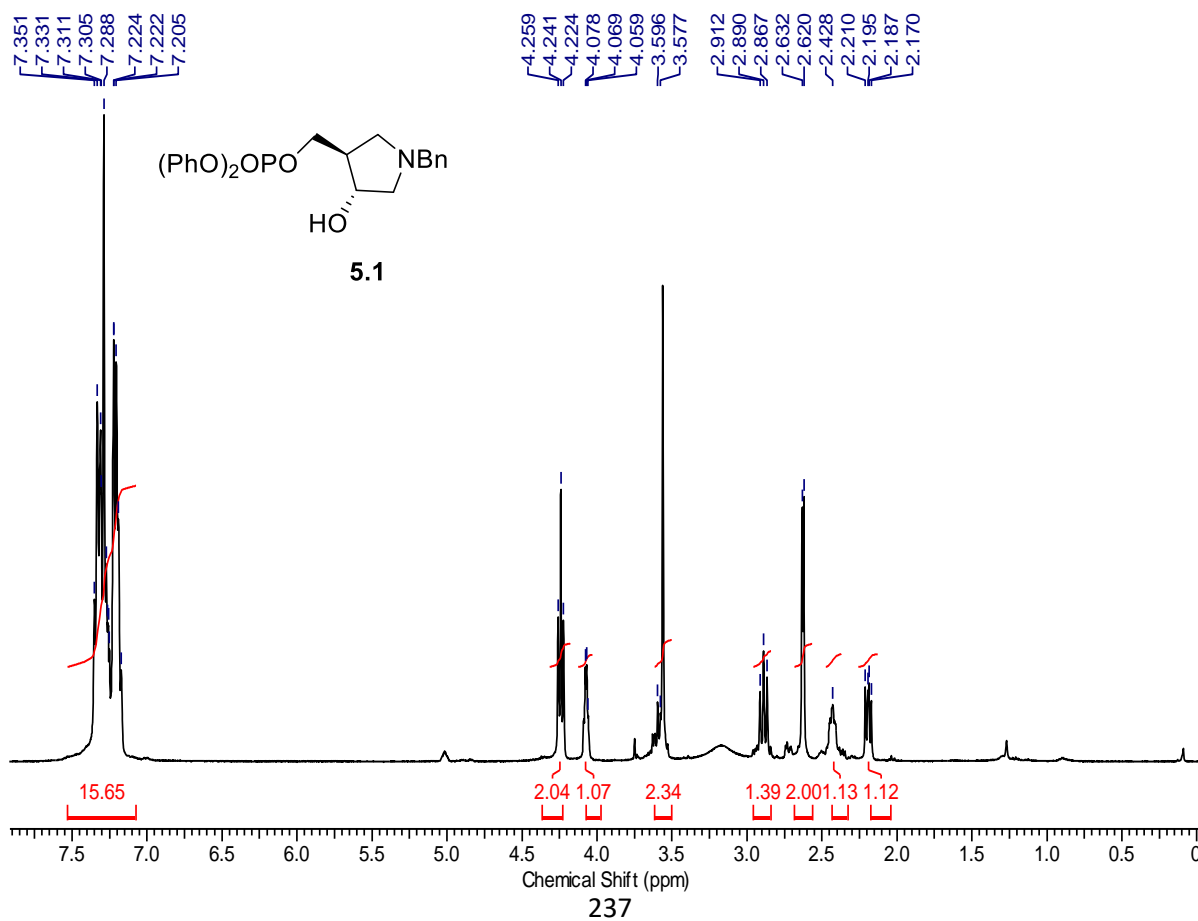
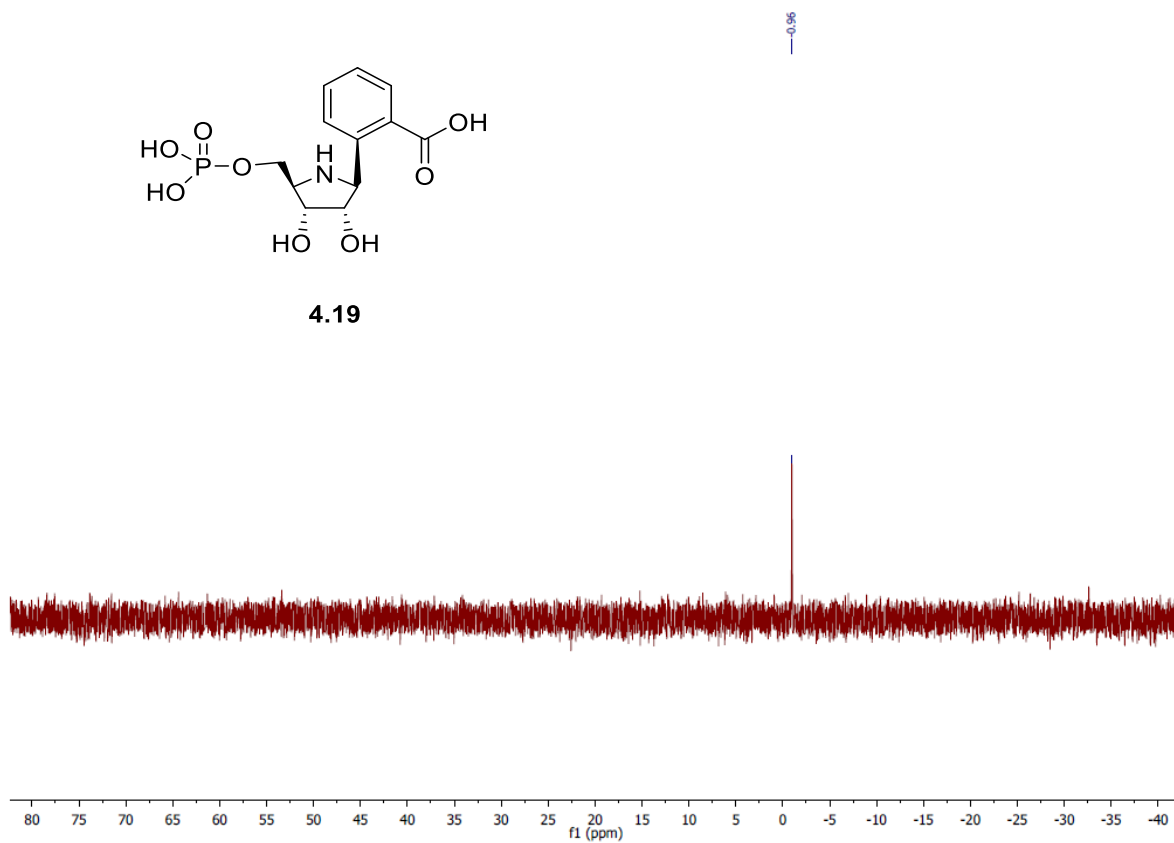


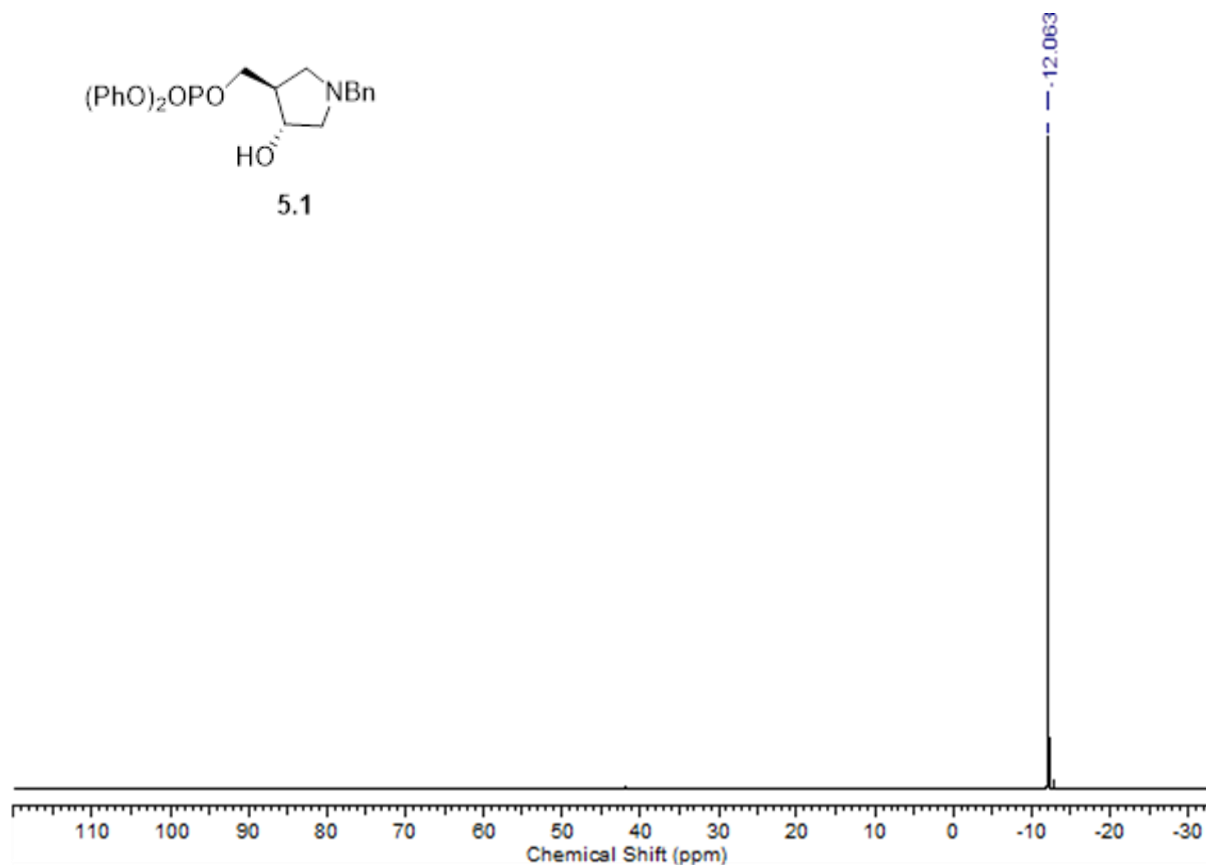
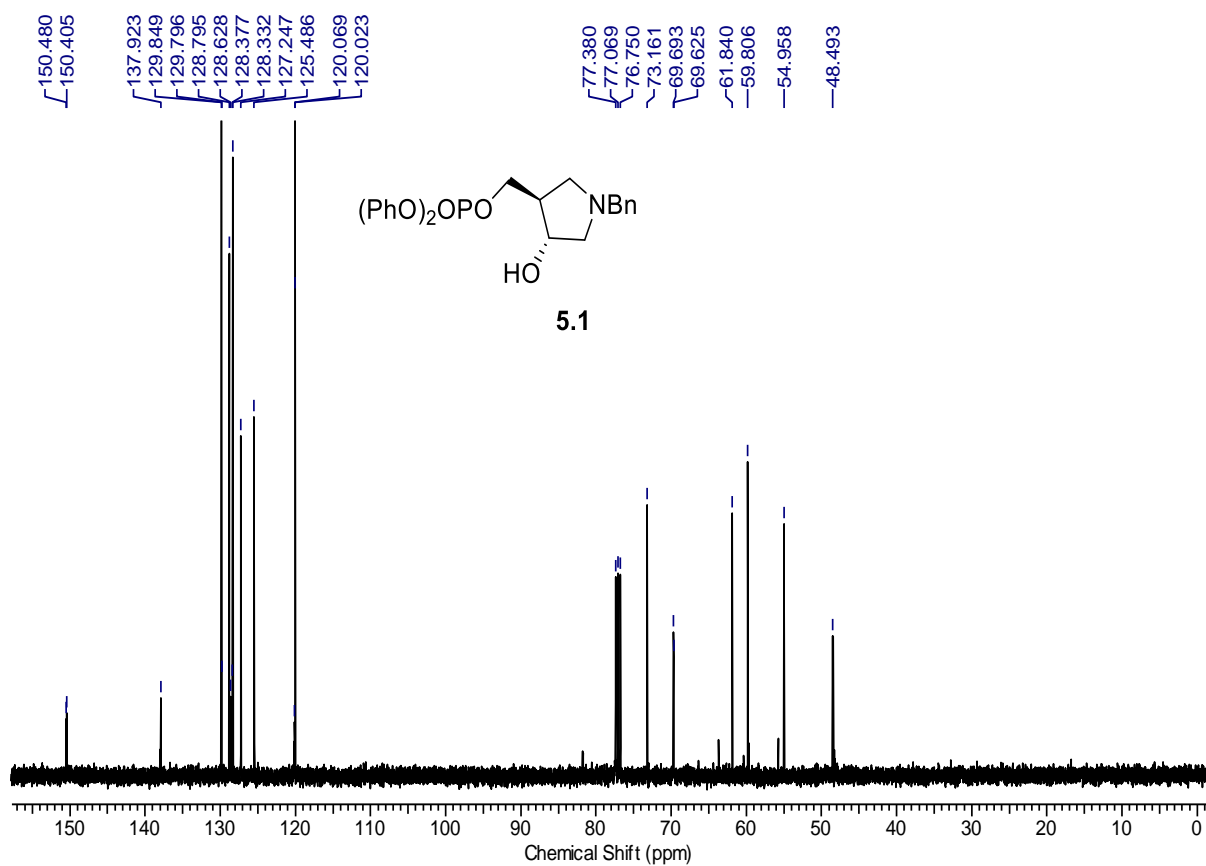


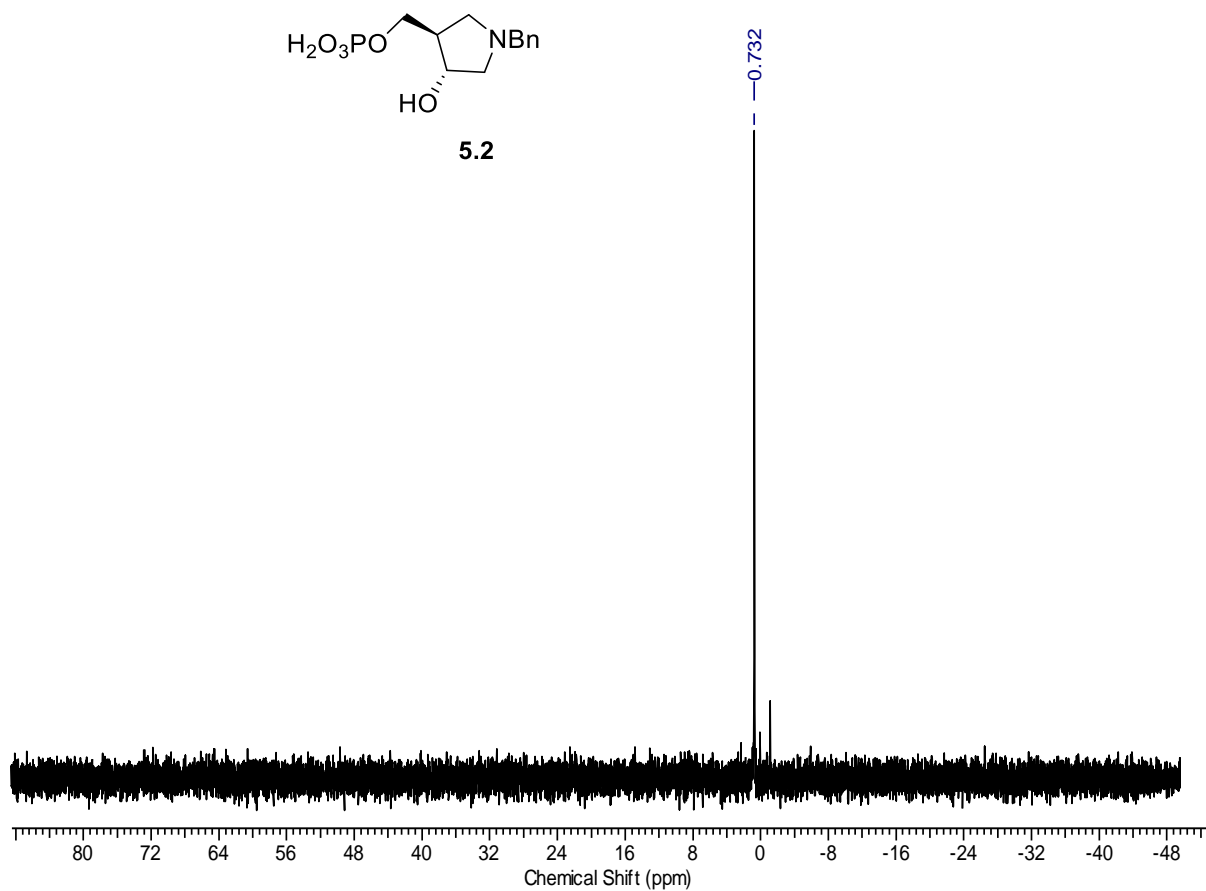
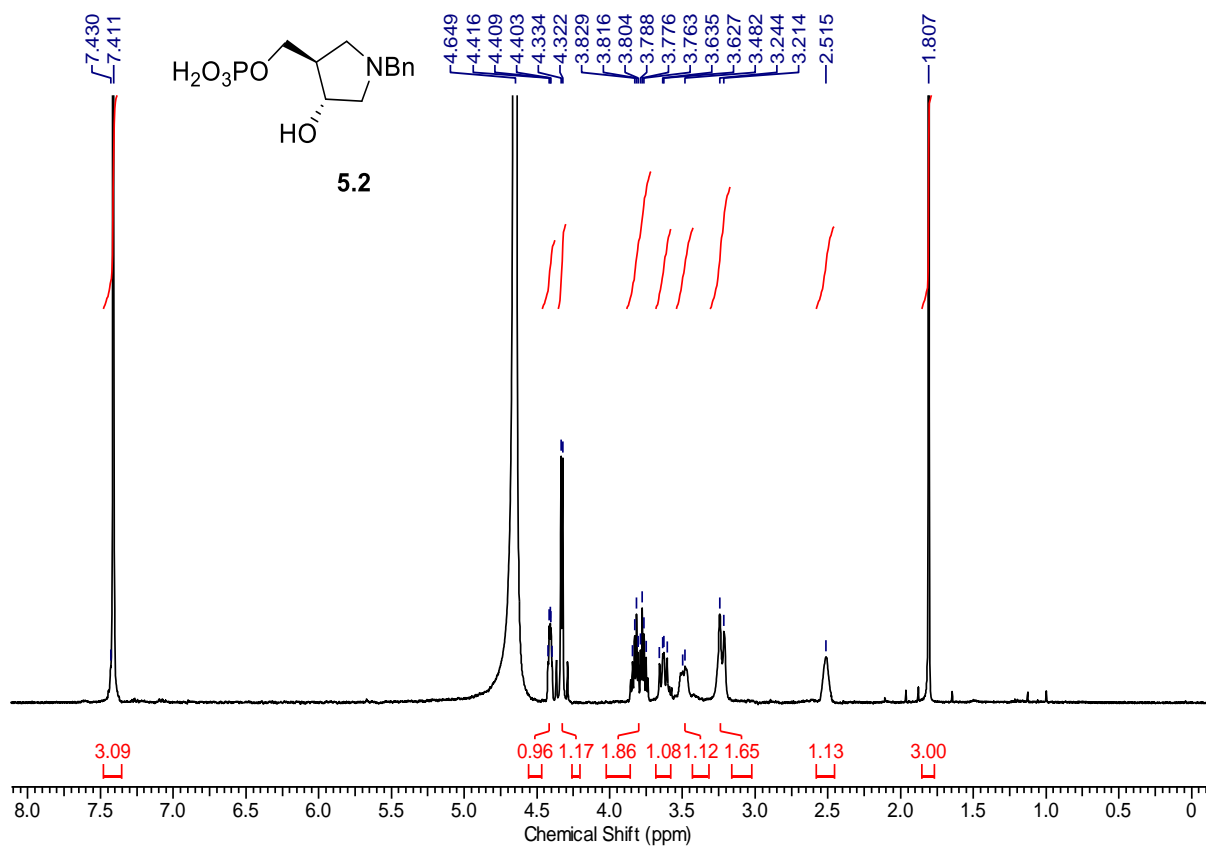


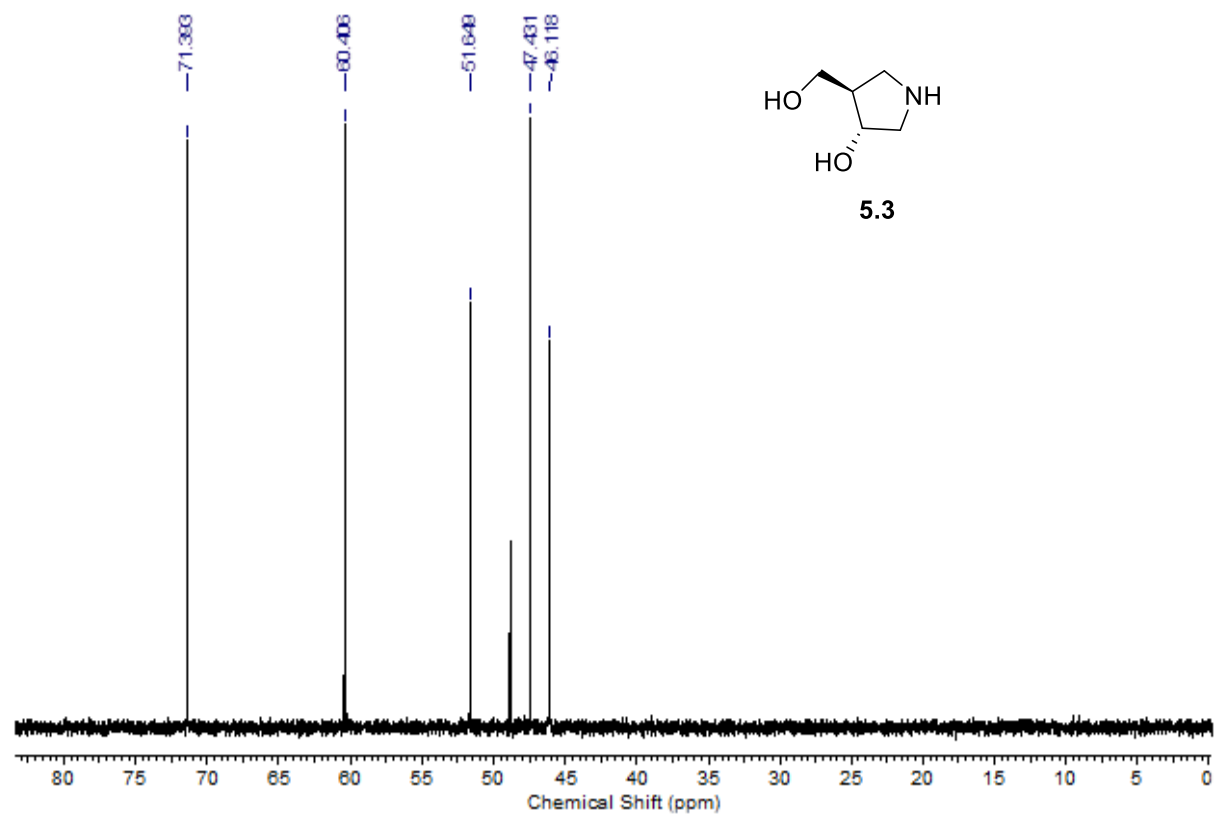
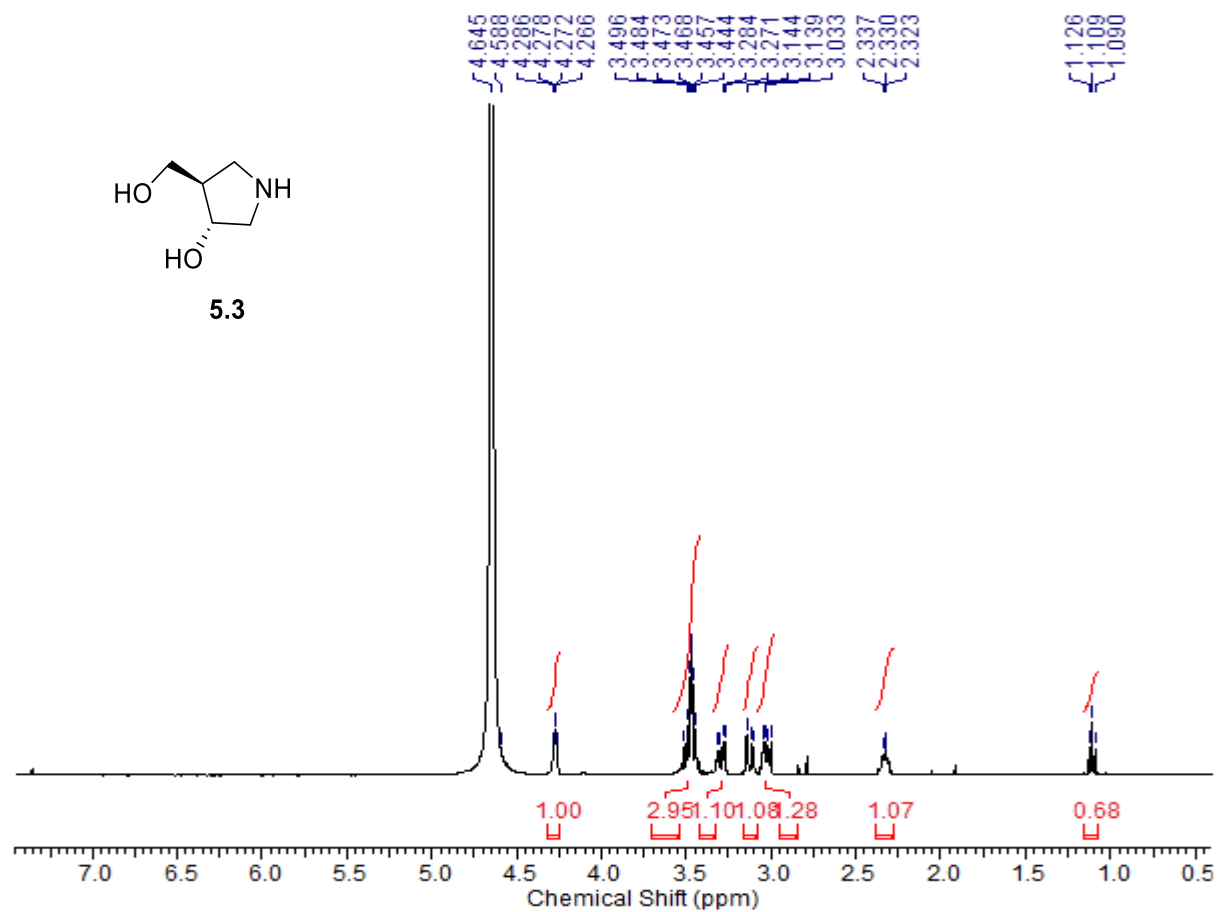


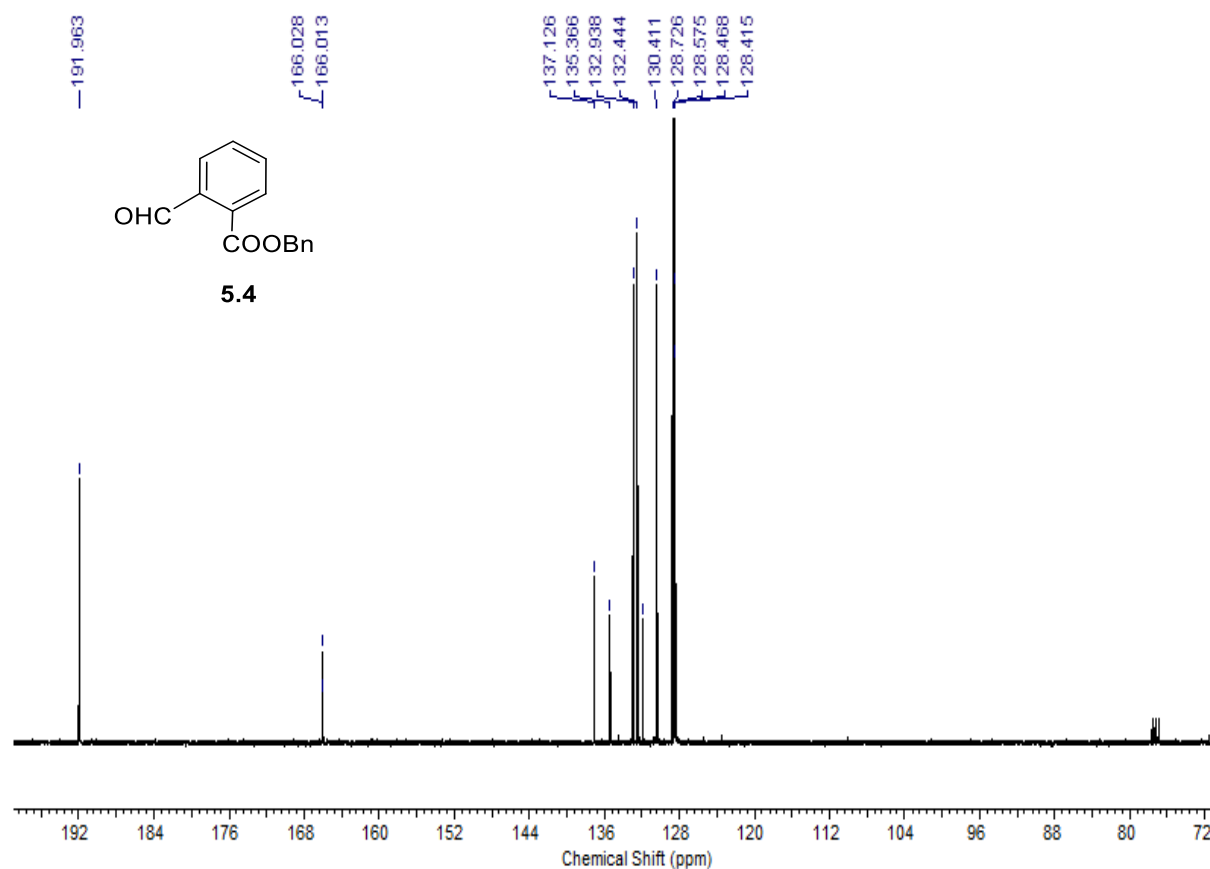
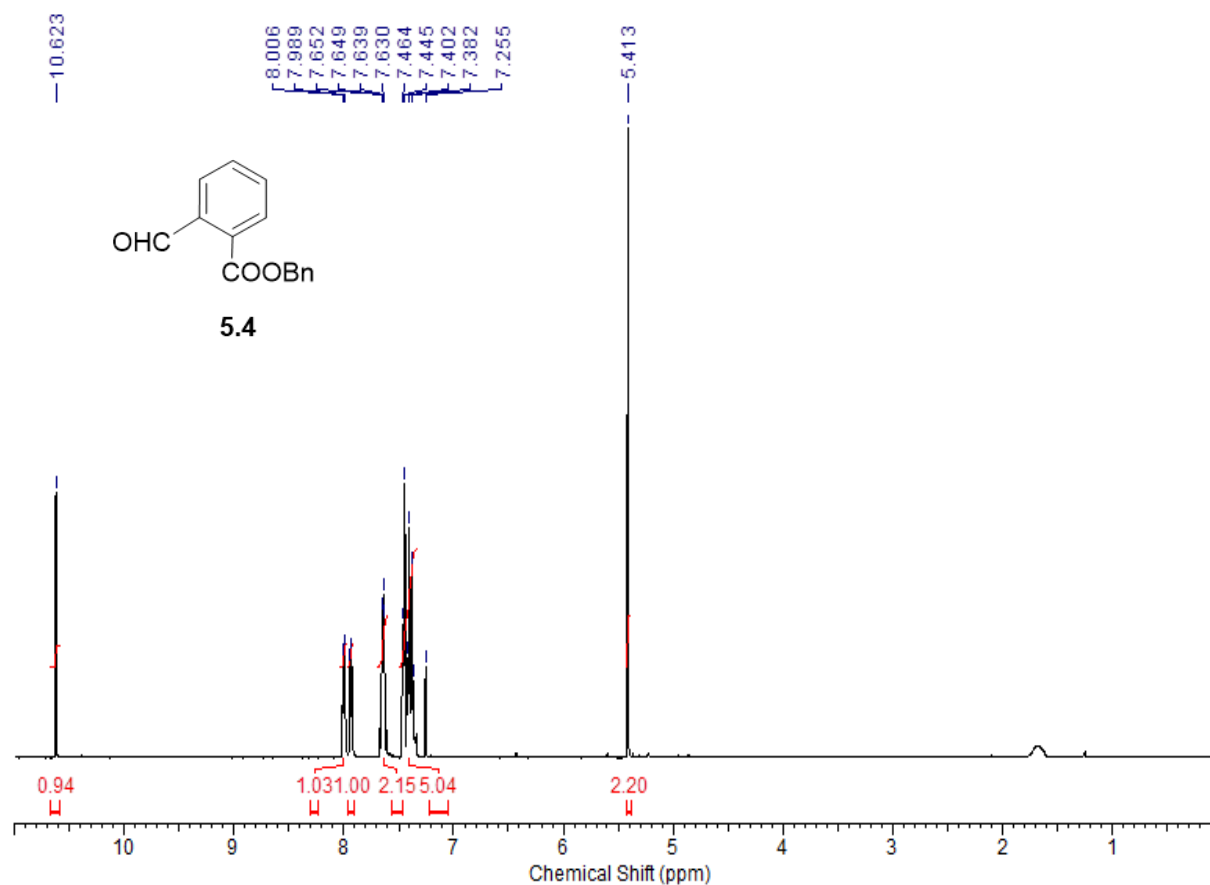
4.19

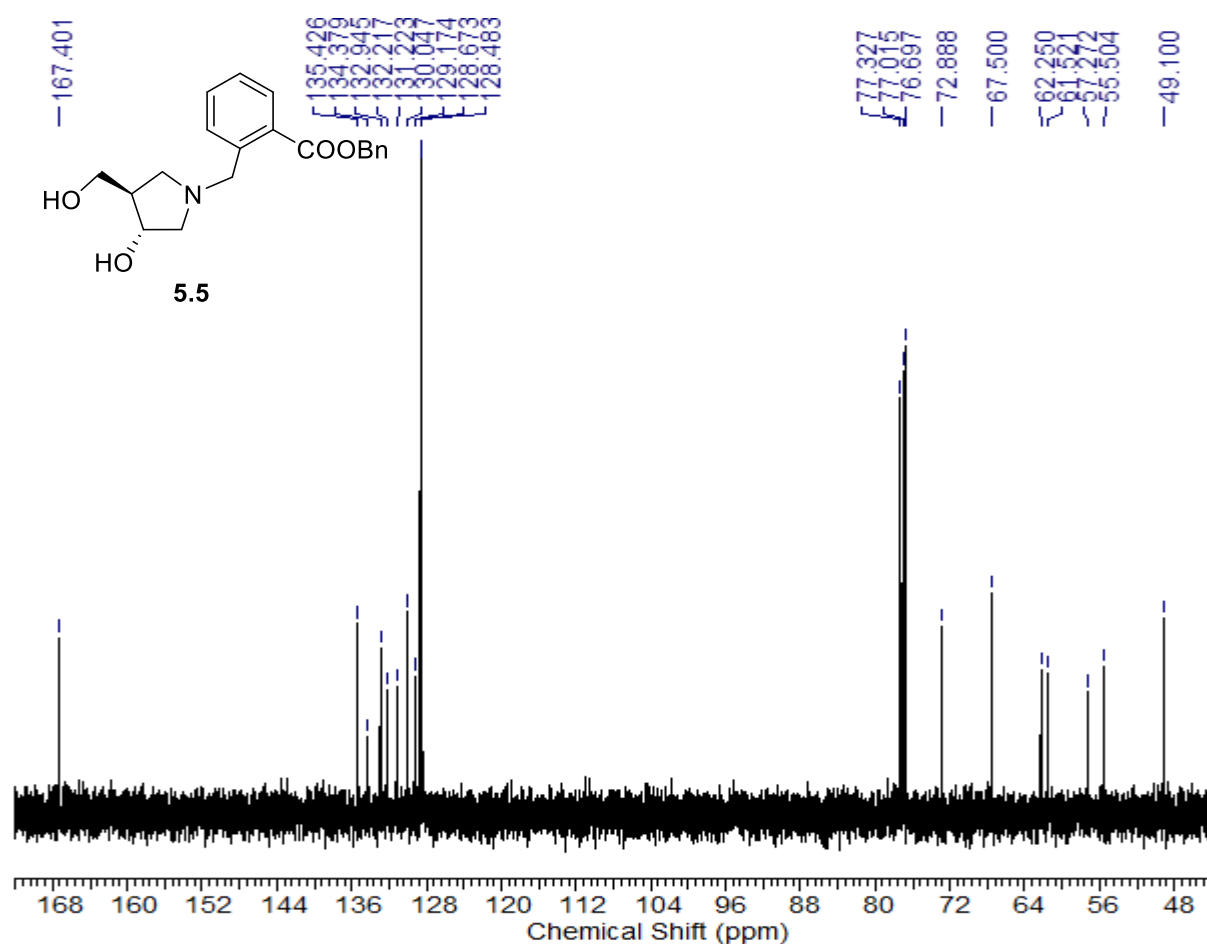
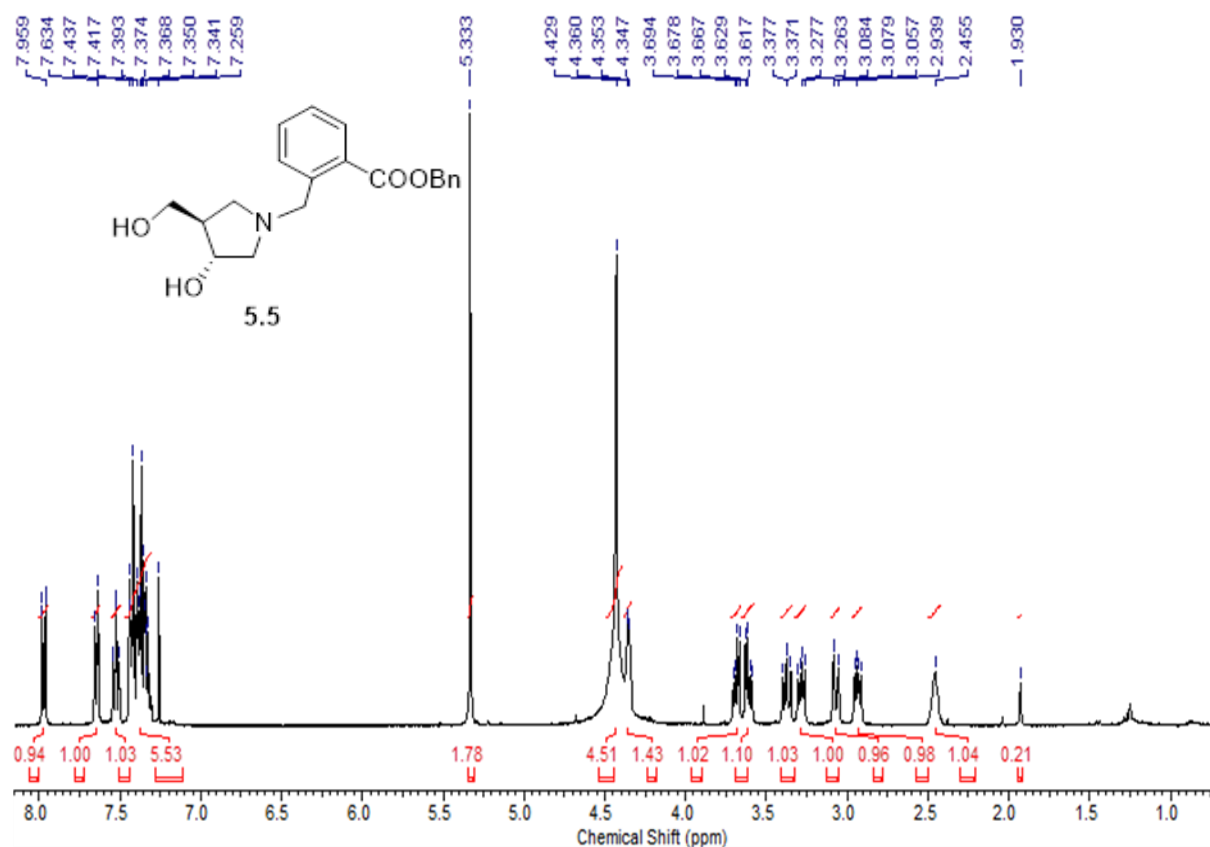


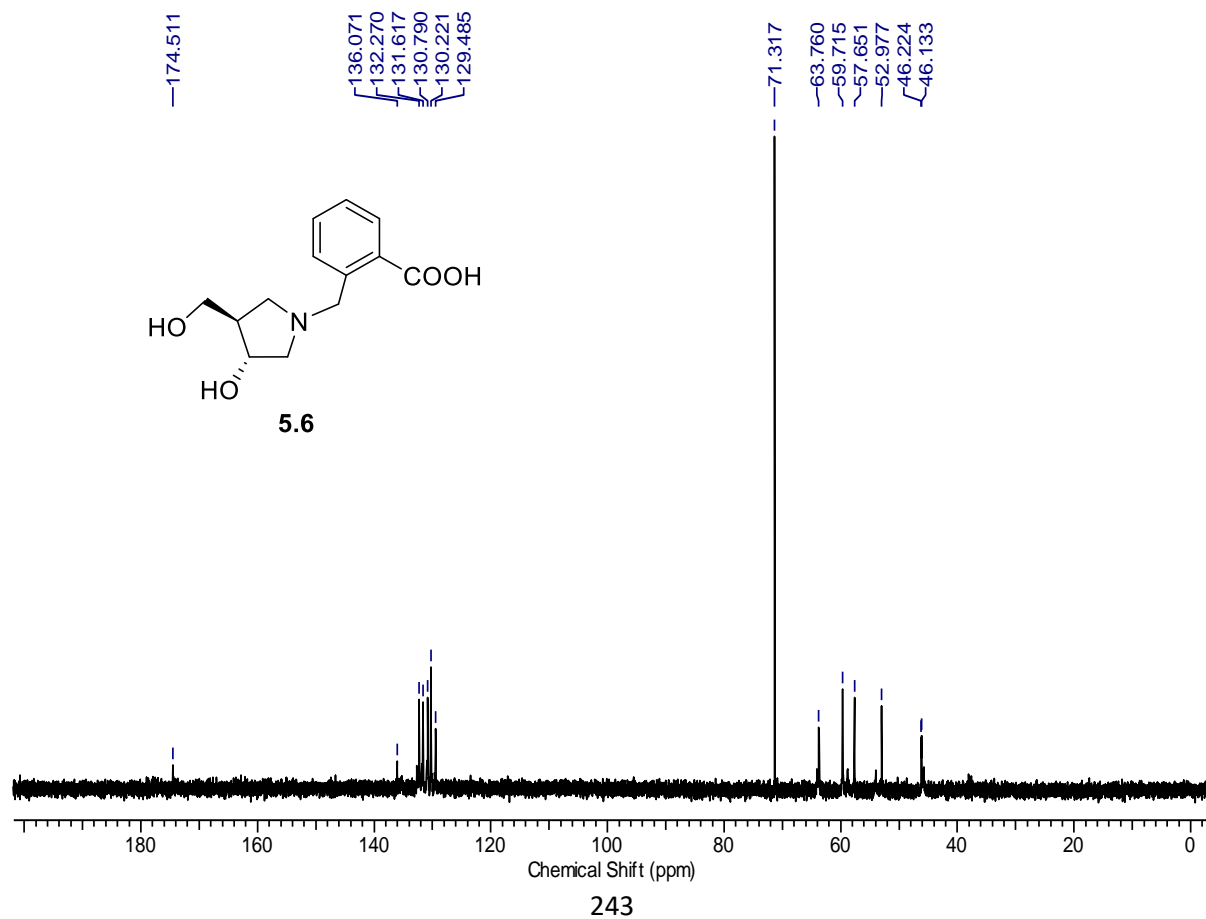
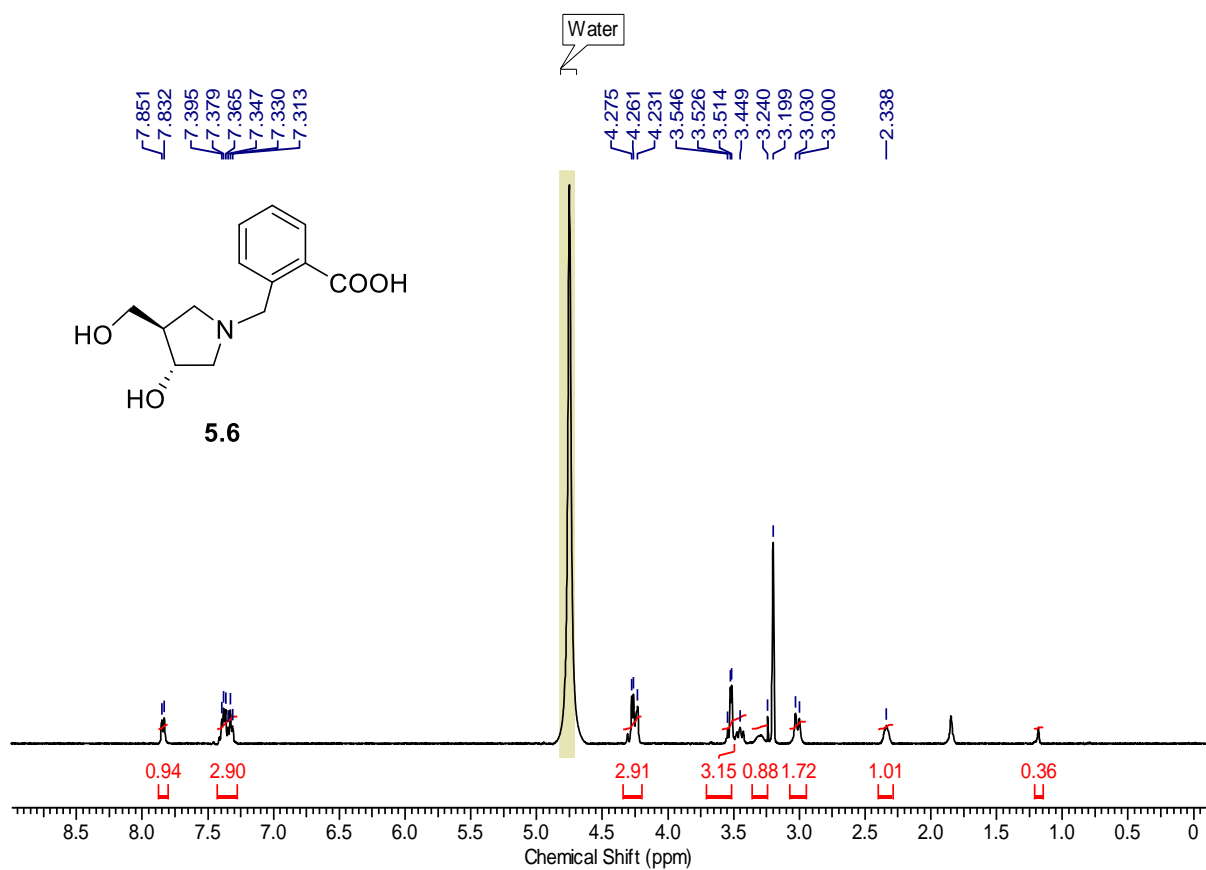


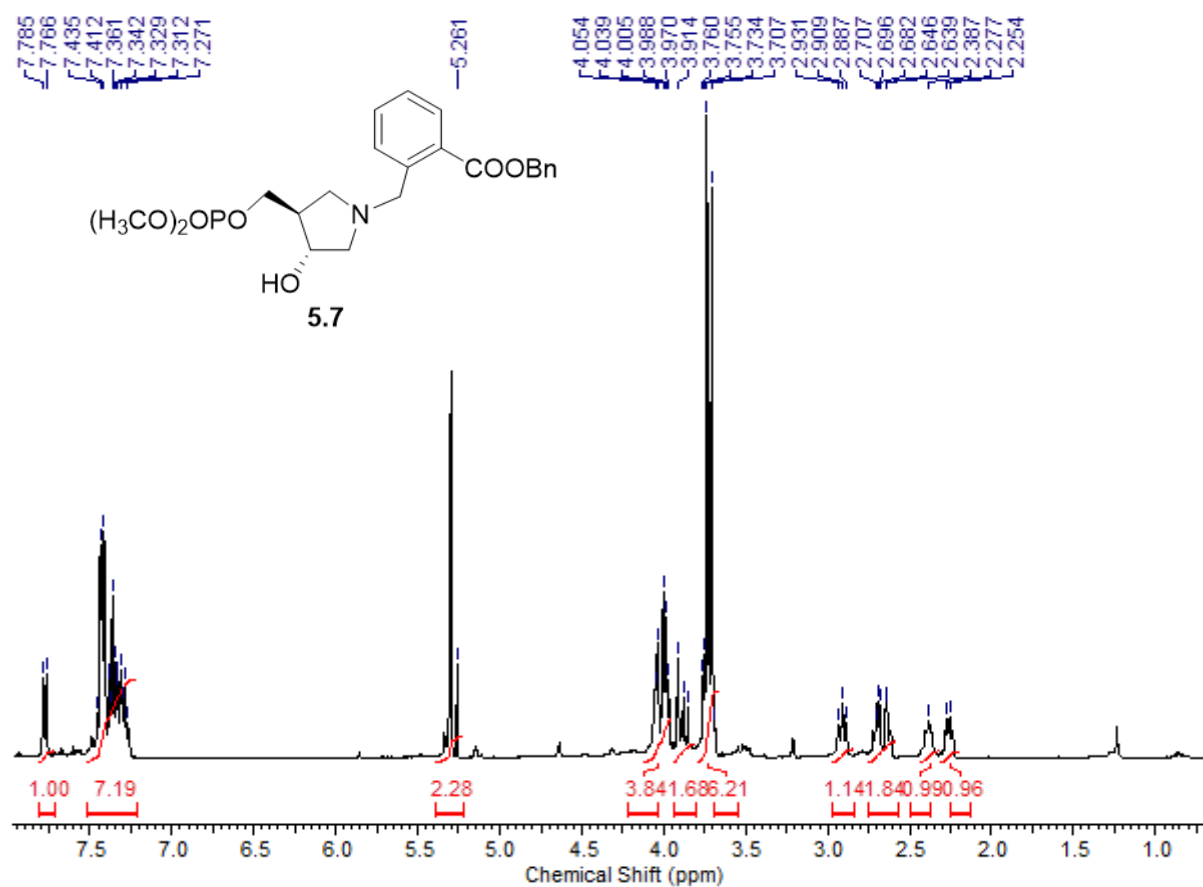
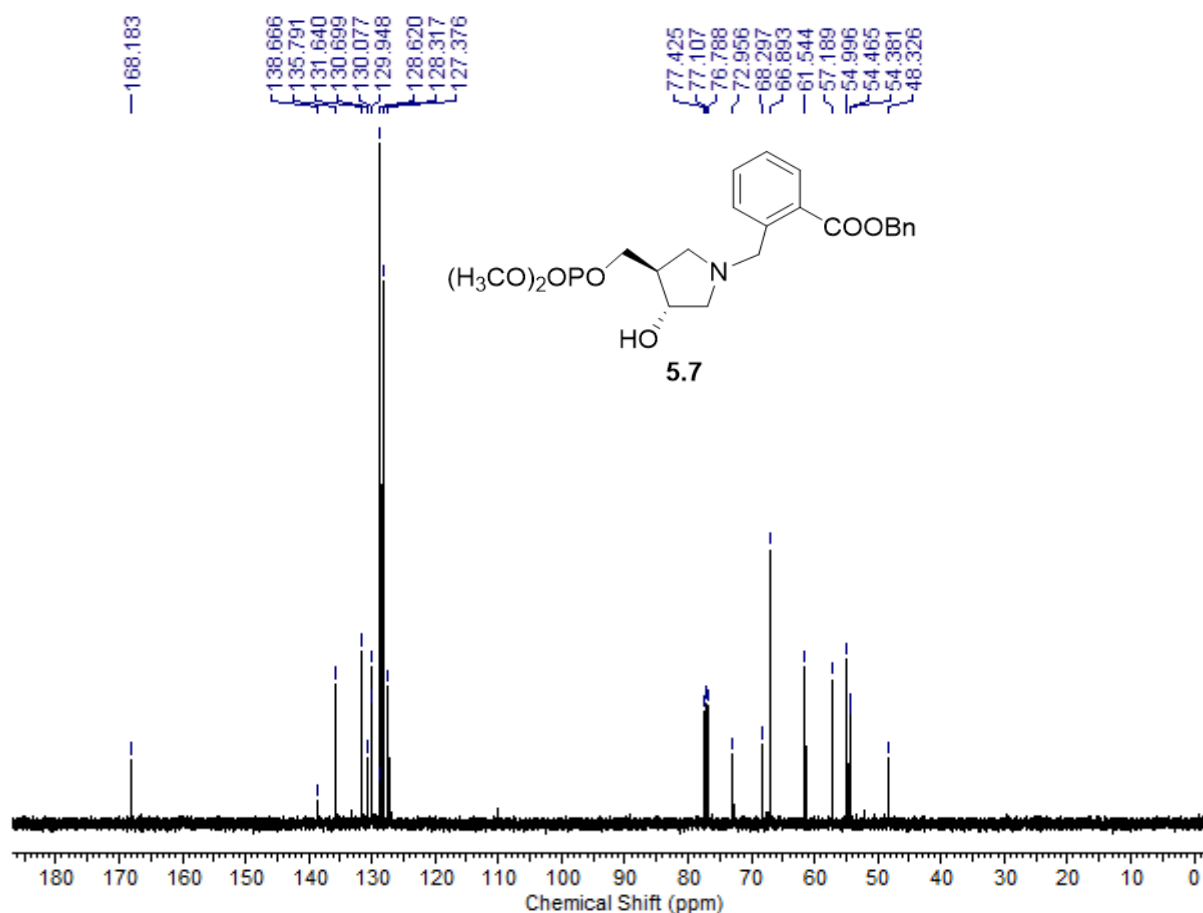


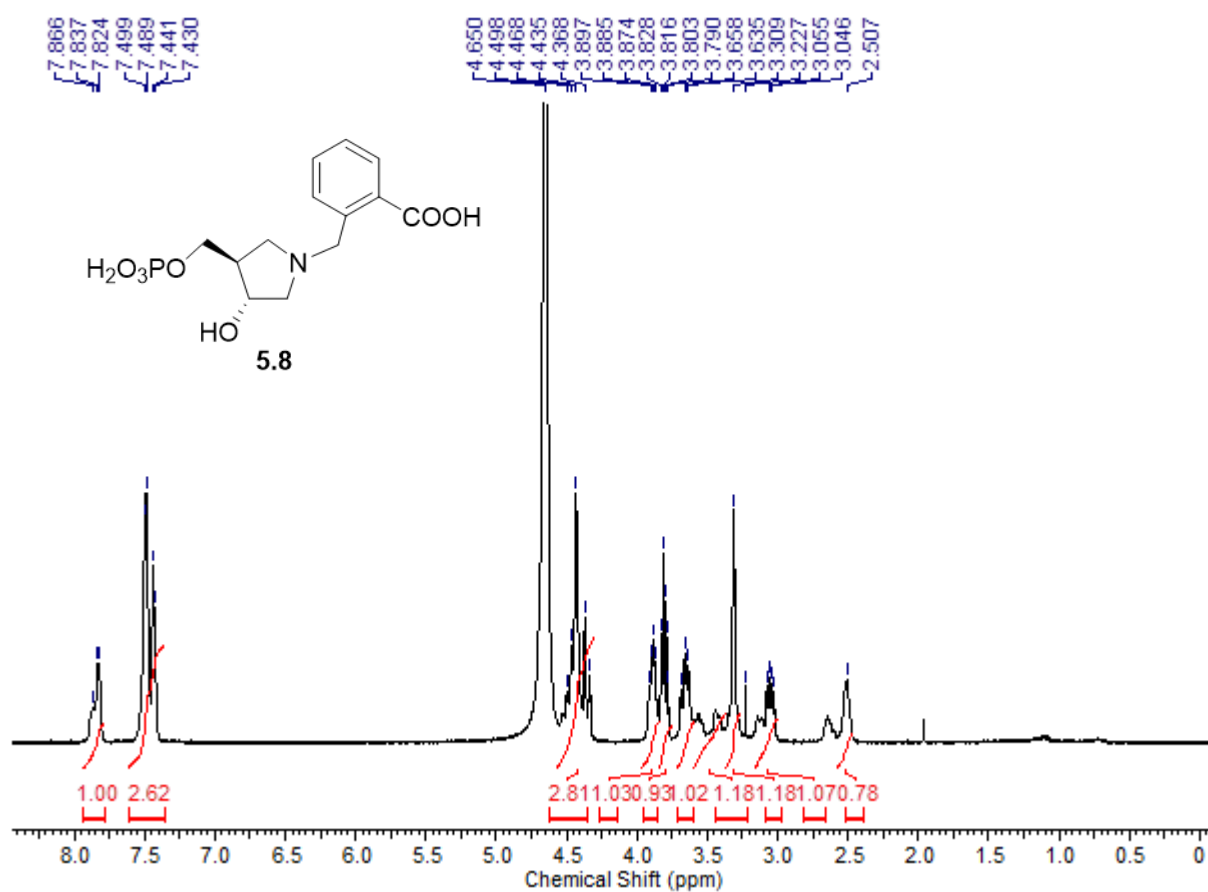
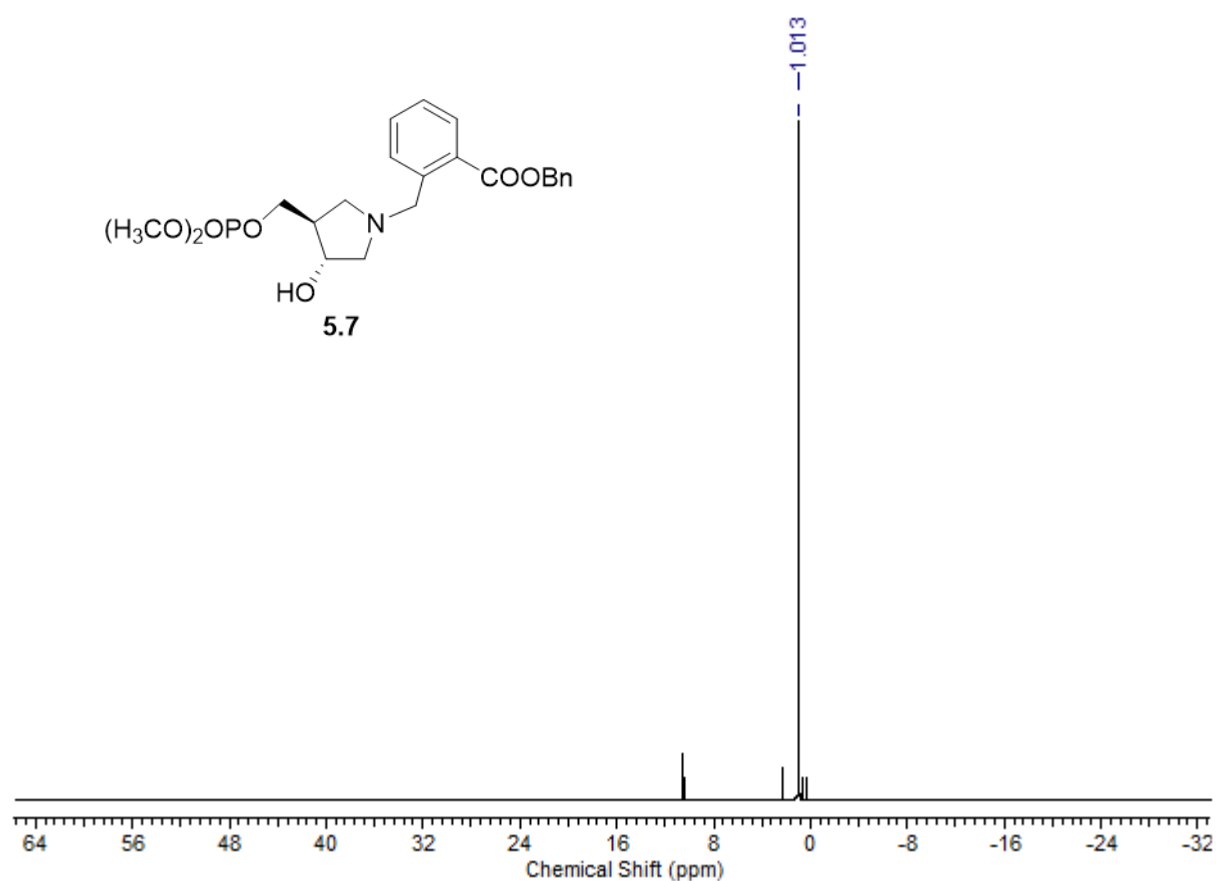


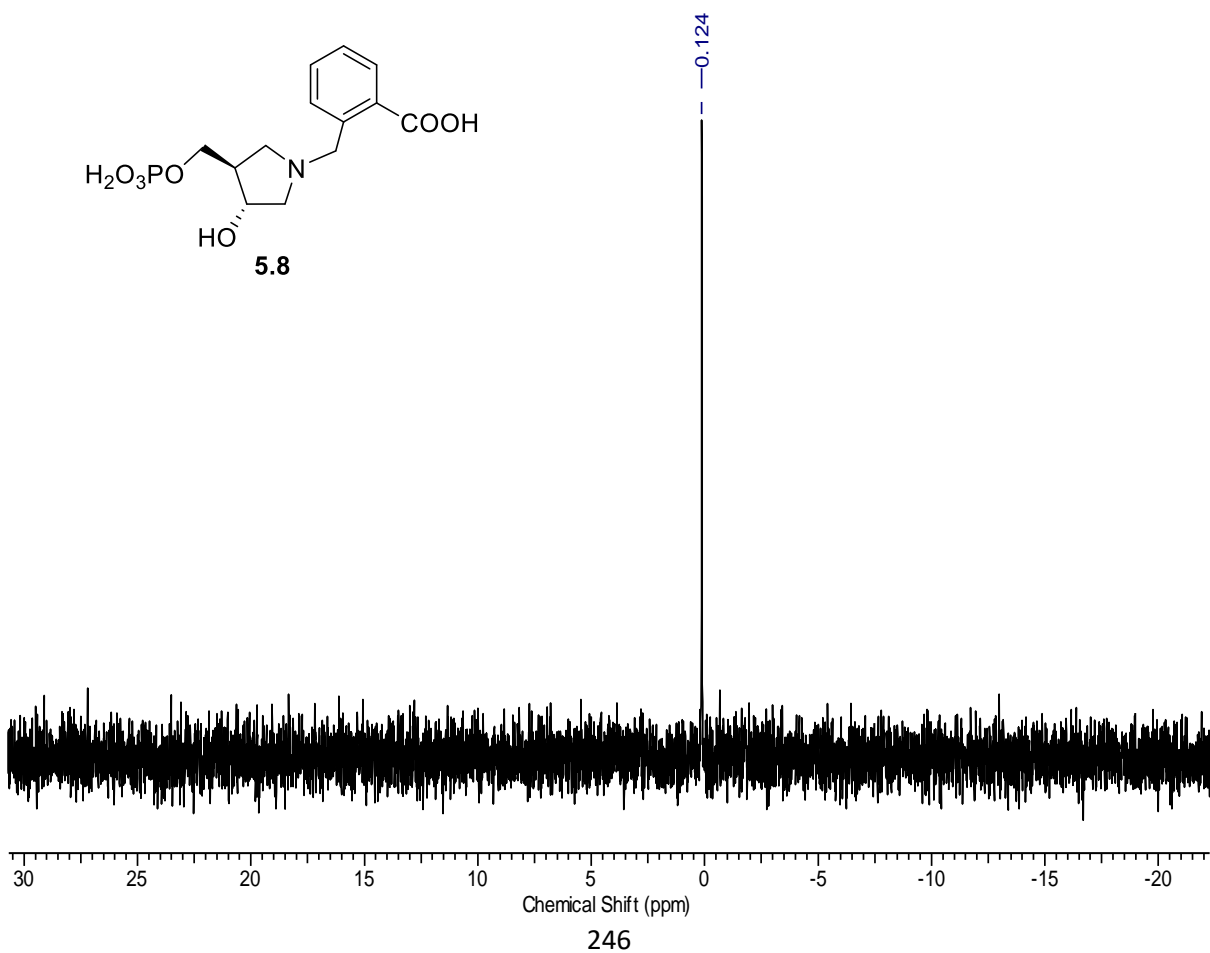
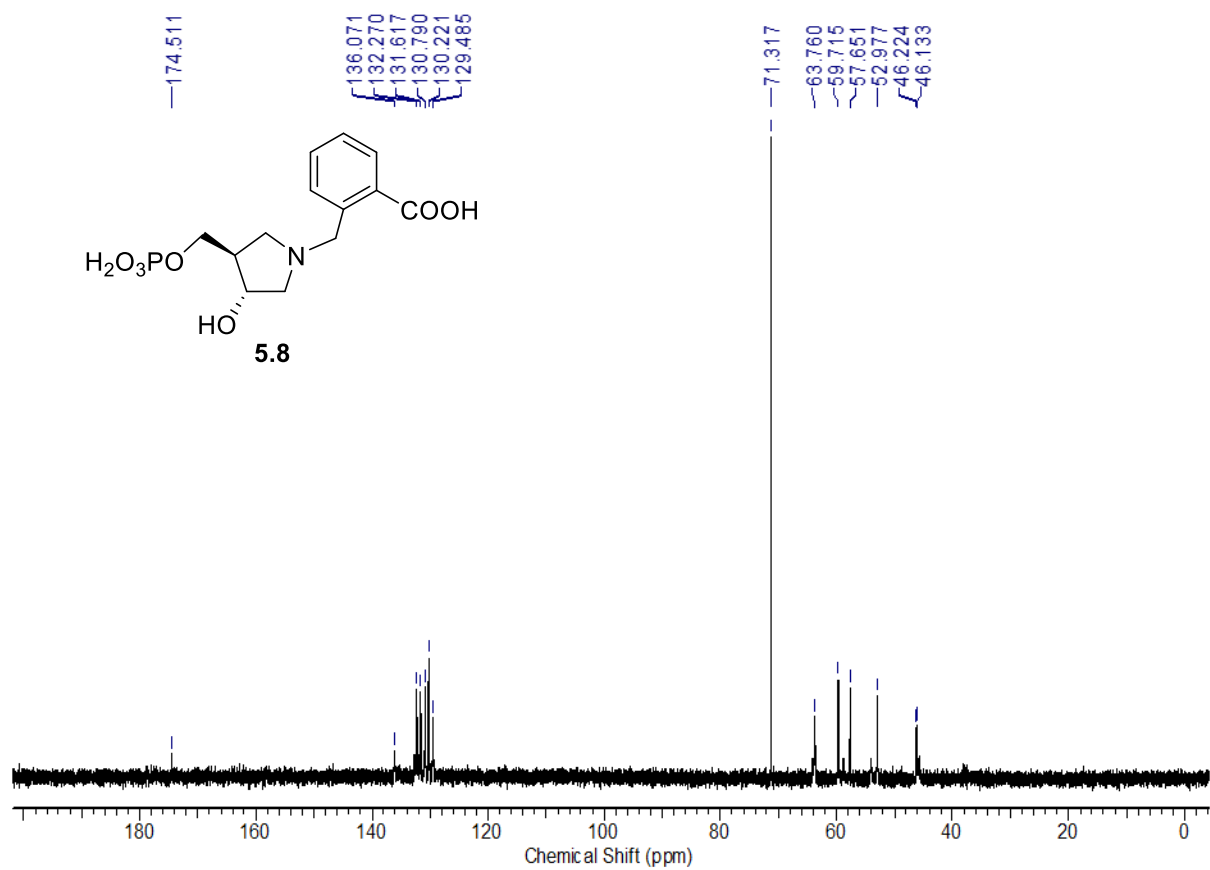












References

1. Fersht, A. Enzyme structure and mechanism. **99**, (1985).
2. Copeland, R. A. Enzyme reactions with multiple substrates. in *Enzymes* 350–366 (John Wiley & Sons, Inc., 2000).
3. Cornish-Bowden, A. & Cornish-Bowden, A. Fundamentals of enzyme kinetics. **510**, (2012).
4. Cole, S. T. Comparative and functional genomics of the *Mycobacterium tuberculosis* complex. *Microbiology* **148**, 2919–2928 (2002).
5. Talbot, E. A. & Raffa, B. J. Chapter 92 – *Mycobacterium tuberculosis*. *Mol. Med. Microbiol.* (2015).
6. Guzman, Juan, D. Antimycobacterials from natural sources: ancient times, antibiotic era and novel scaffolds. *Front. Biosci.* **17**, 1861 (2012).
7. Kumar, A., Farhana, A., Guidry, L., Saini, V., Hondalus, M. & Steyn, A. J. C. Redox homeostasis in *Mycobacteria*: the key to tuberculosis control? *Expert Rev. Mol. Med.* **13**, e39 (2011).
8. Alderwick, L. J., Harrison, J., Lloyd, G. S. & Birch, H. L. The mycobacterial cell wall—peptidoglycan and arabinogalactan. *Cold Spring Harb. Perspect. Med.* **5**, a021113 (2015).
9. World Health Organization Tuberculosis.
http://www.who.int/tb/publications/global_report/factsheet_global_2015.pdf?ua=1. (2016).
10. World Health Organization. *Global tuberculosis report 2018*. World Health Organization. <http://www.who.int/iris/handle/10665/274453>. (2018).

11. Cambau, E. & Drancourt, M. Steps towards the discovery of *Mycobacterium tuberculosis* by Robert Koch, 1882. *Clin. Microbiol. Infect.* **20**, 196–201 (2014).
12. Russell, D. G., Barry, C. E. & Flynn, J. L. Tuberculosis: What We Don't Know Can, and Does, Hurt Us. *Science* (80-.). **328**, 852–856 (2010).
13. Brennan, P. J. Structure, function, and biogenesis of the cell wall of *Mycobacterium tuberculosis*. *Tuberculosis* **83**, 91–97 (2003).
14. Nath, H. & Ryoo, S. First- and Second-Line Drugs and Drug Resistance. in *Tuberculosis - Current Issues in Diagnosis and Management* (InTech, 2013).
15. Dalton, T., Cegielski, P., Akksilp, S., Asencios, L., Caoili, J. C., Cho, S. N., Erokhin, V. V, Ershova, J., Gler, M. T. & Kazenny, B. Y. Prevalence of and risk factors for resistance to second-line drugs in people with multidrug-resistant tuberculosis in eight countries: a prospective cohort study. *Lancet* **380**, 1406–1417 (2012).
16. Lönnroth, K., Castro, K. G., Chakaya, J. M., Chauhan, L. S., Floyd, K., Glaziou, P. & Raviglione, M. C. Tuberculosis control and elimination 2010–50: cure, care, and social development. *Lancet* **375**, 1814–1829 (2010).
17. Koul, A., Arnoult, E., Lounis, N., Guillemont, J. & Andries, K. The challenge of new drug discovery for tuberculosis. *Nature* **469**, 483–490 (2011).
18. S., A. & C., P. Old and new TB drugs: mechanisms of action and resistance. *Understanding Tuberculosis - New Approaches to Fighting Against Drug Resistance* (InTech, 2012).
19. Rivers, E. C. & Mancera, R. L. New anti-tuberculosis drugs in clinical trials with novel mechanisms of action. *Drug Discov. Today* **13**, 1090–1098 (2008).
20. Protopopova, M., Hanrahan, C., Nikonenko, B., Samala, R., Chen, P., Gearhart, J., Einck, L. & Nacy, C. A. Identification of a new antitubercular drug candidate, SQ109, from a combinatorial library of 1,2-ethylenediamines. *J. Antimicrob. Chemother.* **56**, 968–974 (2005).

21. Sacksteder, K. A., Protopopova, M., Barry, C. E., Andries, K. & Nacy, C. A. Discovery and development of SQ109: a new antitubercular drug with a novel mechanism of action. *Future Microbiol.* **7**, 823–837 (2012).
22. Chen, P. Synergistic interactions of SQ109, a new ethylene diamine, with front-line antitubercular drugs in vitro. *J. Antimicrob. Chemother.* **58**, 332–337 (2006).
23. Gaurrand, S., Desjardins, S., Meyer, C., Bonnet, P., Argoullon, J. M., Oulyadi, H. & Guillemont, J. Conformational analysis of r207910, a new drug candidate for the treatment of tuberculosis, by a combined NMR and molecular modeling approach. *Chem. Biol. Drug Des. Des.* **68**, 77–84 (2006).
24. Lounis, N., Veziris, N., Chauffour, A., Truffot-Pernot, C., Andries, K. & Jarlier, V. Combinations of R207910 with drugs used to treat multidrug-resistant tuberculosis have the potential to shorten treatment duration. *Antimicrob. Agents Chemother.* **50**, 3543–3547 (2006).
25. Palomino, J. C. & Martin, A. TMC207 becomes bedaquiline, a new anti-TB drug. *Future Microbiol.* **8**, 1071–80 (2013).
26. Sasaki, H., Haraguchi, Y., Itotani, M., Kuroda, H., Hashizume, H., Tomishige, T., Kawasaki, M., Matsumoto, M., Komatsu, M. & Tsubouchi, H. Synthesis and antituberculosis activity of a novel series of optically active 6-Nitro-2,3-dihydroimidazo[2,1-b]oxazoles. *J. Med. Chem.* **49**, 7854–7860 (2006).
27. Kana, B. D., Karakousis, P. C., Parish, T. & Dick, T. Future target-based drug discovery for tuberculosis? *Tuberculosis* **94**, 551–556 (2014).
28. Matsumoto, M., Hashizume, H., Tomishige, T., Kawasaki, M., Tsubouchi, H., Sasaki, H., Shimokawa, Y. & Komatsu, M. OPC-67683, a nitro-dihydro-imidazooxazole derivative with promising action against tuberculosis in vitro and in mice. *PLOS Med.* **3**, e466 (2006).
29. Saliu, O. Y., Crismale, C., Schwander, S. K. & Wallis, R. S. Bactericidal activity of OPC-

- 67683 against drug-tolerant *Mycobacterium tuberculosis*. *J. Antimicrob. Chemother.* **60**, 994–8 (2007).
30. Sotgiu, G., Pontali, E., Centis, R., D'Ambrosio, L. & Migliori, G. B. Delamanid (OPC-67683) for treatment of multi-drug-resistant tuberculosis. *Expert Rev. Anti. Infect. Ther.* **13**, 305–315 (2015).
 31. Bentley, R. & Haslam, E. The shikimate pathway—a metabolic tree with many branches. *Crit. Rev. Biochem. Mol. Biol.* **25**, 307–384 (1990).
 32. Favrot, L. & Ronning, D. R. Targeting the mycobacterial envelope for tuberculosis drug development. *Expert Rev. Anti. Infect. Ther.* **10**, 1023–1036 (2012).
 33. Parish, T. Starvation survival response of *Mycobacterium tuberculosis*. *J. Bacteriol.* **185**, 6702–6706 (2003).
 34. Hondalus, M. K., Bardarov, S., Russell, R., Chan, J., Jacobs, W. R. & Bloom, B. R. Attenuation of and protection induced by a leucine auxotroph of *Mycobacterium tuberculosis*. *Infect. Immun.* **68**, 2888–2898 (2000).
 35. Sambandamurthy, V. K., Wang, X., Chen, B., Russell, R. G., Derrick, S., Collins, F. M., Morris, S. L. & Jacobs, W. R. A pantothenate auxotroph of *Mycobacterium tuberculosis* is highly attenuated and protects mice against tuberculosis. *Nat. Med.* **8**, 1171–1174 (2002).
 36. Gordhan, B. G. Construction and Phenotypic Characterization of an Auxotrophic Mutant of *Mycobacterium tuberculosis* Defective in L-Arginine Biosynthesis. *Infect. Immun.* **70**, 3080–3084 (2002).
 37. Priya, V. K., Sarkar, S. & Sinha, S. Evolution of tryptophan biosynthetic pathway in microbial genomes: a comparative genetic study. *Syst. Synth. Biol.* **8**, 59–72 (2014).
 38. Smith, L. K., Gomez, M. J., Shatalin, K. Y., Lee, H. & Neyfakh, A. A. Monitoring of gene knockouts: Genome-wide profiling of conditionally essential genes. *Genome Biol.* (2007).

39. Crawford, I. P. Evolution of a biosynthetic pathway: the tryptophan paradigm. *Annu. Rev. Microbiol.* **43**, 567–600 (1989).
40. Yanofsky, C., Platt, T., Crawford, I. P., Nichols, B. P., Christie, G. E., Horowitz, H., VanCleemput, M. & Wu, A. M. The complete nucleotide sequence of the tryptophan operon of *Escherichia coli*. *Nucleic Acids Res.* **9**, 6647–68 (1981).
41. Sterner, R., Dahm, A., Darimont, B., Ivens, A., Liebl, W. & Kirschner, K. (Beta alpha)8-barrel proteins of tryptophan biosynthesis in the hyperthermophile *Thermotoga maritima*. *EMBO J.* **14**, 4395–402 (1995).
42. Barona-Gómez, F. & Hodgson, D. A. Occurrence of a putative ancient-like isomerase involved in histidine and tryptophan biosynthesis. *EMBO Rep.* **4**, 296–300 (2003).
43. Jurgens, C., Strom, A., Wegener, D., Hettwer, S., Wilmanns, M. & Sterner, R. Directed evolution of a (beta alpha)8-barrel enzyme to catalyze related reactions in two different metabolic pathways. *Proc. Natl. Acad. Sci.* **97**, 9925–9930 (2000).
44. Sinha, S. The PRT protein family. *Curr. Opin. Struct. Biol.* **11**, 733–739 (2001).
45. Schumacher, M. A. Crystal structures of *Toxoplasma gondii* uracil phosphoribosyltransferase reveal the atomic basis of pyrimidine discrimination and prodrug binding. *EMBO J.* **17**, 3219–3232 (1998).
46. Scapin, G., Ozturk, D. H., Grubmeyer, C. & Sacchettini, J. C. The crystal structure of the orotate phosphoribosyltransferase complexed with orotate and α -D-5-phosphoribosyl-1-pyrophosphate. *Biochemistry* **34**, 10744–10754 (1995).
47. Eads, J. C., Scapin, G., Xu, Y., Grubmeyer, C. & Sacchettini, J. C. The crystal structure of human hypoxanthine-guanine phosphoribosyltransferase with bound GMP. *Cell* **78**, 325–334 (1994).
48. Jensen, K. F. & Mygind, B. Different oligomeric states are involved in the allosteric behaviour of uracil phosphoribosyltransferase from *Escherichia Coli*. *Eur. J. Biochem.* **240**, 637–645 (1996).

49. Chen, S., Tomchick, D. R., Wolle, D., Hu, P., Smith, J. L., Switzer, R. L. & Zalkin, H. Mechanism of the synergistic end-product regulation of *Bacillus subtilis* glutamine phosphoribosylpyrophosphate amidotransferase by nucleotides. *Biochemistry* **36**, 10718–10726 (1997).
50. Eads, J. C., Ozturk, D., Wexler, T. B., Grubmeyer, C. & Sacchettini, J. C. A new function for a common fold: the crystal structure of quinolinic acid phosphoribosyltransferase. *Structure* **5**, 47–58 (1997).
51. Chappie, J. S., Cànaves, J. M., Han, G. W., Rife, C. L., Xu, Q. & Stevens, R. C. The structure of a eukaryotic nicotinic acid phosphoribosyltransferase reveals structural heterogeneity among Type II PRTases. *Structure* **13**, 1385–1396 (2005).
52. Okuno, E., White, R. J. & Schwarcz, R. Quinolinic acid phosphoribosyltransferase: Purification and partial characterization from human liver and brain. *J. Biochem.* **103**, 1054–1059 (1988).
53. Castell, A., Short, F. L., Evans, G. L., Cookson, T. V. M., Bulloch, E. M. M., Joseph, D. D. A., Lee, C. E., Parker, E. J., Baker, E. N. & Lott, J. S. The substrate capture mechanism of mycobacterium tuberculosis anthranilate phosphoribosyltransferase provides a mode for inhibition. *Biochemistry* (2013).
54. Evans, G. L., Furkert, D. P., Abermil, N., Kundu, P., de Lange, K. M., Parker, E. J., Brimble, M. A., Baker, E. N. & Lott, J. S. Anthranilate phosphoribosyltransferase: Binding determinants for 5'-phospho-alpha-D-ribosyl-1'-pyrophosphate (PRPP) and the implications for inhibitor design. *Biochim. Biophys. Acta - Proteins Proteomics* **1866**, 264–274 (2018).
55. Marino, M., Deuss, M., Svergun, D. I., Konarev, P. V., Sterner, R. & Mayans, O. Structural and mutational analysis of substrate complexation by anthranilate phosphoribosyltransferase from *Sulfolobus solfataricus*. *J. Biol. Chem.* **281**, 21410–21421 (2006).
56. Kim, C., Xuong, N. H., Edwards, S., Madhusudan, Yee, M. C., Spraggon, G. & Mills, S. E.

- The crystal structure of anthranilate phosphoribosyltransferase from the enterobacterium *Pectobacterium carotovorum*. *FEBS Lett.* **523**, 239–46 (2002).
57. Cookson, T. V. M. Probing the active site of anthranilate phosphoribosyltransferase from *Mycobacterium tuberculosis* to facilitate novel drug development. (University Of Canterbury, 2013).
 58. Focia, P. J., Craig, S. P. & Eakin, A. E. Approaching the transition state in the crystal structure of a phosphoribosyltransferase. *Biochemistry* (1998).
 59. Sharma, V., Grubmeyer, C. & Sacchettini, J. C. Crystal structure of quinolinic acid phosphoribosyltransferase from *Mycobacterium tuberculosis*: a potential TB drug target. *Structure* **6**, 1587–1599 (1998).
 60. Lee, C. E., Goodfellow, C., Javid-Majd, F., Baker, E. N. & Shaun Lott, J. The crystal structure of TrpD, a metabolic enzyme essential for lung colonization by *Mycobacterium tuberculosis*, in complex with its substrate phosphoribosylpyrophosphate. *J. Mol. Biol.* **355**, 784–797 (2006).
 61. Champagne, K. S., Sissler, M., Larrabee, Y., Doublié, S. & Francklyn, C. S. Activation of the Hetero-octameric ATP Phosphoribosyl Transferase through Subunit Interface Rearrangement by a tRNA Synthetase Paralog. *J. Biol. Chem.* **280**, 34096–34104 (2005).
 62. Cho, Y., Sharma, V. & Sacchettini, J. C. Crystal structure of ATP phosphoribosyltransferase from *Mycobacterium tuberculosis*. *J. Biol. Chem.* **278**, 8333–9 (2003).
 63. Bovee, M. L., Champagne, K. S., Demeler, B. & Francklyn, C. S. The quaternary structure of the HisZ-HisG N-1-(5'-phosphoribosyl)-ATP transferase from *Lactococcus lactis*. *Biochemistry* **41**, 11838–46 (2002).
 64. Schlee, S., Deuss, M., Bruning, M., Ivens, A., Schwab, T., Hellmann, N., Mayans, O. & Sterner, R. Activation of anthranilate phosphoribosyltransferase from *Sulfolobus solfataricus* by removal of magnesium inhibition and acceleration of product release.

- Biochemistry* **48**, 5199–209 (2009).
65. Perveen, S., Rashid, N., Tang, X.-F., Imanaka, T. & Papageorgiou, A. C. Anthranilate phosphoribosyltransferase from the hyperthermophilic archaeon *Thermococcus kodakarensis* shows maximum activity with zinc and forms a unique dimeric structure. *FEBS Open Bio* **7**, 1217–1230 (2017).
 66. Cookson, T. V. M., Evans, G. L., Castell, A., Baker, E. N., Lott, J. S. & Parker, E. J. Structures of *Mycobacterium tuberculosis* anthranilate phosphoribosyltransferase variants reveal the conformational changes that facilitate delivery of the substrate to the active site. *Biochemistry* **54**, 6082–6092 (2015).
 67. Schwab, T., Skegro, D., Mayans, O. & Sterner, R. A rationally designed monomeric variant of anthranilate phosphoribosyltransferase from *Sulfolobus solfataricus* is as active as the dimeric wild-type enzyme but less thermostable. *J. Mol. Biol.* **376**, 506–16 (2008).
 68. Evans, G. L., Furkert, D. P., Abermil, N., Kundu, P., de Lange, K. M., Parker, E. J., Brimble, M. A., Baker, E. N. & Lott, J. S. Datasets, processing and refinement details for Mtb-AnPRT: inhibitor structures with various space groups. *Data Br.* **15**, 1019–1029 (2017).
 69. Evans, G. L., Gamage, S. A., Bulloch, E. M. M., Baker, E. N., Denny, W. A. & Lott, J. S. Repurposing the chemical scaffold of the anti-arthritis drug lobenzarit to target tryptophan biosynthesis in *Mycobacterium tuberculosis*. *ChemBioChem* **15**, 852–864 (2014).
 70. Zheng, H., Cooper, D. R., Porebski, P. J., Shabalin, I. G., Handing, K. B. & Minor, W. CheckMyMetal: a macromolecular metal-binding validation tool. *Acta Crystallogr. Sect. D Struct. Biol.* **73**, 223–233 (2017).
 71. Castell, A., Short, F. L., Evans, G. L., Cookson, T. V. M., Bulloch, E. M. M., Joseph, D. D. A., Lee, C. E., Parker, E. J., Baker, E. N. & Lott, J. S. The substrate capture mechanism of *Mycobacterium tuberculosis* anthranilate phosphoribosyltransferase provides a mode for inhibition. *Biochemistry* **52**, 1776–1787 (2013).

72. Zalkin, H. & Henderson, E. J. Tryptophan-mediated substrate inhibition of anthranilate-5-phosphoribosylpyrophosphate phosphoribosyltransferase. *Biochem. Biophys. Res. Commun.* **35**, 52–58 (1969).
73. Balderas-Hernandez, V. E., Sabido-Ramos, A., Silva, P., Cabrera-Valladares, N., Hernandez-Chavez, G., Baez-Viveros, J. L., Martinez, A., Bolivar, F. & Gosset, G. Metabolic engineering for improving anthranilate synthesis from glucose in *Escherichia coli*. *Microb. Cell Fact.* **8**, 19 (2009).
74. Cookson, T. V. M., Castell, A., Bulloch, E. M. M., Evans, G. L., Short, F. L., Baker, E. N., Lott, J. S. & Parker, E. J. Alternative substrates reveal catalytic cycle and key binding events in the reaction catalysed by anthranilate phosphoribosyltransferase from *Mycobacterium tuberculosis*. *Biochem. J.* **461**, 87–98 (2014).
75. Mayans, O., Ivens, A., Nissen, L. J., Kirschner, K. & Wilmanns, M. Structural analysis of two enzymes catalysing reverse metabolic reactions implies common ancestry. *EMBO J.* **21**, 3245–54 (2002).
76. Mushegian, A. R. & Koonin, E. V. Unexpected sequence similarity between nucleosidases and phosphoribosyltransferases of different specificity. *Protein Sci.* **3**, 1081–1088 (1994).
77. Fedorov, A., Shi, W., Kicska, G., Fedorov, E., Tyler, P. C., Furneaux, R. H., Hanson, J. C., Gainsford, G. J., Larese, J. Z., Schramm, V. L. & Almo, S. C. Transition state structure of purine nucleoside phosphorylase and principles of atomic motion in enzymatic catalysis. *Biochemistry* **40**, 853–860 (2001).
78. Tao, W., Grubmeyer, C. & Blanchard, J. S. Transition state structure of *Salmonella typhimurium* orotate phosphoribosyltransferase. *Biochemistry* **35**, 14–21 (1996).
79. Zhang, Y. J., Reddy, M. C., Ioerger, T. R., Rothchild, A. C., Dartois, V., Schuster, B. M., Trauner, A., Wallis, D., Galaviz, S., Huttenhower, C., Sacchettini, J. C., Behar, S. M. & Rubin, E. J. Tryptophan biosynthesis protects mycobacteria from CD4 T-Cell-mediated Killing. *Cell* (2013).

80. Lee, C. E. Structural and Biochemical Studies on Potential Drug Targets from *Mycobacterium tuberculosis*. (University of Auckland, 2007).
81. Gasteiger, E., Hoogland, C., Gattiker, A., Duvaud, S., Wilkins, M. R., Appel, R. D. & Bairoch, A. *Protein identification and analysis tools on the ExPASy server*. (Springer, 2005).
82. Ben-Bassat, A., Bauer, K., Chang, S. Y., Myambo, K., Boosman, A. & Chang, S. Processing of the initiation methionine from proteins: properties of the *Escherichia coli* methionine aminopeptidase and its gene structure. *J. Bacteriol.* **169**, 751–757 (1987).
83. Gonzalez, J. E. & Somerville, R. L. The anthranilate aggregate of *Escherichia coli* : kinetics of inhibition by tryptophan of phosphoribosyltransferase. *Biochem. Cell Biol.* **64**, 681–691 (1986).
84. Caligiuri, M. G. & Bauerle, R. Subunit communication in the anthranilate synthase complex from *Salmonella typhimurium*. *Science (80-.)*. **252**, 1845–1848 (1991).
85. Ivens, A., Mayans, O., Szadkowski, H., Wilmanns, M. & Kirschner, K. Purification, characterization and crystallization of thermostable anthranilate phosphoribosyltransferase from *Sulfolobus solfataricus*. *Eur. J. Biochem.* **268**, 2246–2252 (2001).
86. O’Sullivan, W. J. & Smithers, G. W. Stability constants for biologically important metal-ligand complexes. in *Methods in Enzymology* 294–336 (1979).
87. Berg, M., Van der Veken, P., Goeminne, A., Haemers, A. & Augustyns, K. Inhibitors of the purine salvage pathway: a valuable approach for antiprotozoal chemotherapy? *Curr. Med. Chem.* **17**, 2456–2481 (2010).
88. Smith, J. L. Forming and inhibiting PRT active sites. *Nature Structural Biology* (1999).
89. Keough, D. T., Hocková, D., Holý, A., Naesens, L. M. J., Skinner-Adams, T. S., Jersey, J. de & Guddat, L. W. Inhibition of hypoxanthine-guanine phosphoribosyltransferase by acyclic nucleoside phosphonates: a new class of antimalarial therapeutics. *J. Med.*

- Chem.* **52**, 4391–4399 (2009).
90. Hazleton, K. Z., Ho, M. C., Cassera, M. B., Clinch, K., Crump, D. R., Rosario, I., Merino, E. F., Almo, S. C., Tyler, P. C. & Schramm, V. L. Acyclic immucillin phosphonates: second-generation inhibitors of *Plasmodium falciparum* hypoxanthine-guanine-xanthine phosphoribosyltransferase. *Chem. Biol.* **19**, 721–730 (2012).
 91. Eng, W. S., Hocková, D., Špaček, P., Janeba, Z., West, N. P., Woods, K., Naesens, L. M. J., Keough, D. T. & Guddat, L. W. First crystal structures of *Mycobacterium tuberculosis* 6-oxopurine phosphoribosyltransferase: complexes with GMP and pyrophosphate and with acyclic nucleoside phosphonates whose prodrugs have antituberculosis activity. *J. Med. Chem.* **58**, 4822–4838 (2015).
 92. Collaborative Computational Project, N. 4. The CCP4 suite: programs for protein crystallography. *Acta Crystallogr. Sect. D Biol. Crystallogr.* **50**, 760–763 (1994).
 93. Evans, P. R. An introduction to data reduction: space-group determination, scaling and intensity statistics. *Acta Crystallogr. Sect. D Biol. Crystallogr.* **67**, 282–292 (2011).
 94. Lebedev, A. A. & Isupov, M. N. Space-group and origin ambiguity in macromolecular structures with pseudo-symmetry and its treatment with the program Zanuda. *Acta Crystallogr. Sect. D Biol. Crystallogr.* **70**, 2430–2443 (2014).
 95. Zwart, P. H., Grosse-Kunstleve, R. W., Lebedev, A. A., Murshudov, G. N. & Adams, P. D. Surprises and pitfalls arising from (pseudo)symmetry. *Acta Crystallogr. Sect. D Biol. Crystallogr.* **64**, 99–107 (2008).
 96. McCoy, A. J., Grosse-Kunstleve, R. W., Adams, P. D., Winn, M. D., Storoni, L. C. & Read, R. J. Phaser crystallographic software. *J. Appl. Crystallogr.* **40**, 658–674 (2007).
 97. Murshudov, G. N., Vagin, A. A. & Dodson, E. J. Refinement of macromolecular structures by the maximum-likelihood method. *Acta Crystallogr. Sect. D Biol. Crystallogr.* **53**, 240–255 (1997).
 98. Bajorath, J. Integration of virtual and high-throughput screening. *Nat. Rev. Drug Discov.*

- 1**, 882–894 (2002).
99. Walters, W. P., Stahl, M. T. & Murcko, M. A. Virtual screening—an overview. *Drug Discov. Today* **3**, 160–178 (1998).
100. Langer, T. & Hoffmann, R. Virtual screening an effective tool for lead structure discovery. *Curr. Pharm. Des.* **7**, 509–527 (2001).
101. Kitchen, D. B., Decornez, H., Furr, J. R. & Bajorath, J. Docking and scoring in virtual screening for drug discovery: methods and applications. *Nat. Rev. Drug Discov.* **3**, 935–949 (2004).
102. Gohlke, H. & Klebe, G. Approaches to the description and prediction of the binding affinity of small-molecule ligands to macromolecular receptors. *Angew. Chemie Int. Ed.* **41**, 2644–2676 (2002).
103. Wermuth, C. G. Strategies in the search for new lead compounds or original working hypotheses. in *The Practice of Medicinal Chemistry* 69–89 (Elsevier, 2003).
104. Smith, R. H., Jorgensen, W. L., Tirado-Rives, J., Lamb, M. L., Janssen, P. A. J., Michejda, C. J. & Kroeger Smith, M. B. Prediction of binding affinities for TIBO inhibitors of HIV-1 reverse transcriptase using Monte Carlo simulations in a linear response method. *J. Med. Chem.* **41**, 5272–5286 (1998).
105. Udier-Blagović, M., Tirado-Rives, J. & Jorgensen, W. L. Validation of a model for the complex of HIV-1 reverse transcriptase with nonnucleoside inhibitor TMC125. *J. Am. Chem. Soc.* **125**, 6016–6017 (2003).
106. Kroeger Smith, M. B., Hose, B. M., Hawkins, A., Lipchock, J., Farnsworth, D. W., Rizzo, R. C., Tirado-Rives, J., Arnold, E., Zhang, W., Hughes, S. H., Jorgensen, W. L., Michejda, C. J. & Smith, R. H. Molecular modeling calculations of HIV-1 reverse transcriptase nonnucleoside inhibitors: correlation of binding energy with biological activity for novel 2-Aryl-substituted benzimidazole analogues. *J. Med. Chem.* **46**, 1940–1947 (2003).
107. Capdeville, R., Buchdunger, E., Zimmermann, J. & Matter, A. Glivec (STI571, imatinib),

- a rationally developed, targeted anticancer drug. *Nat. Rev. Drug Discov.* **1**, 493–502 (2002).
108. Smithson, J. & Mitchell, P. B. Antidepressants. in *Side Effects of Drugs Annual* 11–20 (2018).
109. Repasky, M. P., Shelley, M. & Friesner, R. A. Flexible ligand docking with Glide. in *Current Protocols in Bioinformatics* (John Wiley & Sons, Inc., 2007).
110. Bhachoo, J. & Beuming, T. Investigating protein–peptide interactions using the Schrödinger computational suite. in *Methods in Molecular Biology* 235–254 (2017).
111. McGovern, S. L. & Shoichet, B. K. Information decay in molecular docking screens against holo, apo, and modelled conformations of enzymes. *J. Med. Chem.* **46**, 2895–2907 (2003).
112. Sterling, T. & Irwin, J. J. ZINC 15 – ligand discovery for everyone. *J. Chem. Inf. Model.* **55**, 2324–2337 (2015).
113. Engh, R. A. & Huber, R. Accurate bond and angle parameters for X-ray protein structure refinement. *Acta Crystallogr. Sect. A Found. Crystallogr.* **47**, 392–400 (1991).
114. Niesen, F. H., Berglund, H. & Vedadi, M. The use of differential scanning fluorimetry to detect ligand interactions that promote protein stability. *Nat. Protoc.* **2**, 2212–2221 (2007).
115. Waldron, T. T. & Murphy, K. P. Stabilization of proteins by ligand binding: application to drug screening and determination of unfolding energetics. *Biochemistry* **42**, 5058–5064 (2003).
116. Bruce, D., Cardew, E., Freitag-Pohl, S. & Pohl, E. How to stabilize protein: stability screens for thermal shift assays and nano differential scanning fluorimetry in the virus-X project. *J. Vis. Exp.* e58666 (2019).
117. Larsson, E. A., Jansson, A., Ng, F. M., Then, S. W., Panicker, R., Liu, B., Sangthongpitag,

- K., Pendharkar, V., Tai, S. J., Hill, J., Dan, C., Ho, S. Y., Cheong, W. W., Poulsen, A., Blanchard, S., Lin, G. R., Alam, J., Keller, T. H. & Nordlund, P. Fragment-based ligand design of novel potent inhibitors of Tankyrases. *J. Med. Chem.* **56**, 4497–4508 (2013).
118. Perozzo, R., Folkers, G. & Scapozza, L. Thermodynamics of protein–ligand interactions: history, presence, and future aspects. *J. Recept. Signal Transduct.* **24**, 1–52 (2004).
 119. Su, H. & Xu, Y. Application of ITC-based characterization of thermodynamic and kinetic association of ligands with proteins in drug design. *Front. Pharmacol.* **9**, (2018).
 120. FREIRE, E. Do enthalpy and entropy distinguish first in class from best in class? *Drug Discov. Today* **13**, 869–874 (2008).
 121. Silver, L. L. Challenges of Antibacterial Discovery. *Clin. Microbiol. Rev.* **24**, 71–109 (2011).
 122. Copeland, R. A., Harpel, M. R. & Tummino, P. J. Targeting enzyme inhibitors in drug discovery. *Expert Opinion on Therapeutic Targets* (2007). doi:10.1517/14728222.11.7.967
 123. Walsh, C. T. Suicide substrates, mechanism-based enzyme inactivators: recent developments. *Annu. Rev. Biochem.* **53**, 493–535 (1984).
 124. Pongdee, R. & Liu, H. Elucidation of enzyme mechanisms using fluorinated substrate analogues. *Bioorg. Chem.* **32**, 393–437 (2004).
 125. Smithers, G. W. & O’Sullivan, W. J. ³¹P nuclear magnetic resonance study of phosphoribosyldiphosphate and its interaction with magnesium ions. *J. Biol. Chem.* **257**, 6164–6170 (1982).
 126. Parry, R. J., Bums, M. R. & Jiralerspong, S. Synthesis of (+)-(1S)-1-Pyrophosphoryl-(2R, 3R)-2,3-dihydroxy-(4S)-4-(phosphoryloxymethyl)cyclopentane, a stable, optically-active carbocyclic analog of 5-Phosphoribosyl-1-pyrophosphate (PRPP). *Tetrahedron Lett.* **53**, 7077–7088 (1997).
 127. Ova, H., Lastdrager, B., Codée, J. D. C., van der Marel, G. A., Overkleeft, H. S. & van

- Boom, J. H. A flexible synthesis of cyclopentitol derivatives based on ring-closing metathesis of carbohydrate-derived 1,6-dienes. *J. Chem. Soc. Perkin Trans. 1* 2370–2377 (2002).
128. Moggré, G. J. The reaction mechanism and inhibition of ATP-PRTase enzymes. (University of Canterbury, 2016).
 129. Oxidation of alcohols by ‘activated’ dimethyl sulfoxide. a preparative, steric and mechanistic study. *Tetrahedron* **34**, 1651–1660 (1978).
 130. Benko, Z., Fraser-Reid, B., Mariano, P. S. & Beckwith, A. L. J. Conjugate addition of methanol to α -enones: photochemistry and stereochemical details. *J. Org. Chem.* **53**, 2066–2072 (1988).
 131. Parry, R. J., Burns, M. R., Skae, P. N., Hoyt, J. C. & Pal, B. Carbocyclic analogues of D-ribose-5-phosphate: Synthesis and behavior with 5-phosphoribosyl α -1-pyrophosphate synthetases. *Bioorg. Med. Chem.* **4**, 1077–1088 (1996).
 132. Yang, M., Ye, W. & Schneller, S. W. Preparation of carbocyclic S-adenosylazamethionine accompanied by a practical synthesis of (-)-aristeromycin. *J. Org. Chem.* **69**, 3993–6 (2004).
 133. Garegg, P. J., Konradsson, P., Oscarson, S. & Ruda, K. Synthesis of part of a proposed insulin second messenger glycosylinositol phosphate and the inner core of glycosylphosphatidylinositol anchors. *Tetrahedron* **53**, 17727–17734 (1997).
 134. Harris, L. D., Harijan, R. K., Ducati, R. G., Evans, G. B., Hirsch, B. M. & Schramm, V. L. Synthesis of bis-phosphate iminoaltritol enantiomers and structural characterization with adenine phosphoribosyltransferase. *ACS Chem. Biol.* **13**, 152–160 (2018).
 135. Taylor Ringia, E. A., Tyler, P. C., Evans, G. B., Furneaux, R. H., Murkin, A. S. & Schramm, V. L. Transition state analogue discrimination by related purine nucleoside phosphorylases. *J. Am. Chem. Soc.* **128**, 7126–7127 (2006).
 136. Evans, G. B., Furneaux, R. H., Lenz, D. H., Painter, G. F., Schramm, V. L., Singh, V. & Tyler,

- P. C. Second generation transition state analogue inhibitors of human 5'-methylthioadenosine phosphorylase. **48**, 4679–4689 (2005).
137. Zhang, Y., Evans, G. B., Clinch, K., Crump, D. R., Harris, L. D., Fröhlich, R. F. G., Tyler, P. C., Hazleton, K. Z., Cassera, M. B. & Schramm, V. L. Transition state analogues of *Plasmodium falciparum* and human orotate phosphoribosyltransferases. *J. Biol. Chem.* **288**, 34746–34754 (2013).
138. Clinch, K., Evans, G. B., Fröhlich, R. F. G., Gulab, S. a, Gutierrez, J. A., Mason, J. M., Schramm, V. L., Tyler, P. C. & Woolhouse, A. D. Transition state analogue inhibitors of human methylthioadenosine phosphorylase and bacterial methylthioadenosine/S-adenosylhomocysteine nucleosidase incorporating acyclic ribooxacarbenium ion mimics. *Bioorg. Med. Chem.* **20**, 5181–5187 (2012).
139. Laidler, K. J. & King, M. C. Development of transition-state theory. *J. Phys. Chem.* **87**, 2657–2664 (1983).
140. Truhlar, D. G., Garrett, B. C. & Klippenstein, S. J. Current status of transition-state theory. *J. Phys. Chem.* **100**, 12771–12800 (1996).
141. Wolfenden, R. Transition state analogues for enzyme catalysis. *Nature* **223**, 704–705 (1969).
142. Scholey, J. M. Compare and contrast the reaction coordinate diagrams for chemical reactions and cytoskeletal force generators. *Molecular Biology of the Cell* (2013). doi:10.1091/mbc.E12-07-0545
143. Dantus, M., Bowman, R. M., Baskin, J. S. & Zewail, A. H. Femtosecond real-time alignment in chemical reactions. *Chem. Phys. Lett.* **159**, 406–412 (1989).
144. Schramm, V. L. Transition states, analogues, and drug development. *ACS Chem. Biol.* **8**, 71–81 (2013).
145. Pauling, L. Molecular architecture and biological reactions. *Chem. Eng. News* **24**, 1375–1377 (1946).

146. Schramm, V. L. Transition states and transition state analogue interactions with enzymes. *Acc. Chem. Res.* **48**, 1032–1039 (2015).
147. Guo, H., Rao, N., Xu, Q. & Guo, H. Origin of tight binding of a near-perfect transition-state analogue by cytidine deaminase: implications for enzyme catalysis. *J. Am. Chem. Soc.* **127**, 3191–3197 (2005).
148. Wolfenden, R. Analog approaches to the structure of the transition state in enzyme reactions. *Acc. Chem. Res.* **5**, 10–18 (1972).
149. Wolfenden, R. Transition state analogue inhibitors and enzyme catalysis. *Annu. Rev. Biophys. Bioeng.* **5**, 271–306 (1976).
150. Luo, M., Li, L. & Schramm, V. L. Remote mutations alter transition-state structure of human purine nucleoside phosphorylase. *Biochemistry* **47**, 2565–2576 (2008).
151. Evans, G. B., Schramm, V. L. & Tyler, P. C. The transition to magic bullets – transition state analogue drug design. *Medchemcomm* **9**, 1983–1993 (2018).
152. Goldthwait, D. A. 5-Phosphoribosylamine, a precursor of glycinamide ribotide. *J. Biol. Chem.* **222**, 1051–1068 (1956).
153. Chu, A. M., Fettingner, J. C. & David, S. S. Profiling base excision repair glycosylases with synthesized transition state analogs. *Bioorg. Med. Chem. Lett.* **21**, 4969–4972 (2011).
154. Evans, G. B., Cameron, S. A., Luxenburger, A., Guan, R., Suarez, J., Thomas, K., Schramm, V. L. & Tyler, P. C. Tight binding enantiomers of pre-clinical drug candidates. *Bioorg. Med. Chem.* **23**, 5326–5333 (2015).
155. Abdel-Magid, A. F., Carson, K. G., Harris, B. D., Maryanoff, C. A. & Shah, R. D. Reductive amination of aldehydes and ketones with sodium triacetoxyborohydride. studies on direct and indirect reductive amination procedures 1. *J. Org. Chem.* **61**, 3849–3862 (1996).
156. Lane, C. F. Sodium cyanoborohydride - a highly selective reducing agent for organic

- functional groups. *Synthesis (Stuttg)*. **1975**, 135–146 (1975).
157. Stowell, J. K. & Widlanski, T. S. A new method for the phosphorylation of alcohols and phenols. *Tetrahedron Lett.* **36**, 1825–1826 (1995).
158. Olah, G. A. & Narang, S. C. Iodotrimethylsilane—a versatile synthetic reagent. *Tetrahedron* **38**, 2225–2277 (1982).
159. Coleman, R. S. Chemoselective cleavage of benzyl ethers, esters, and carbamates in the presence of other easily reducible groups. *Synthesis (Stuttg)*. **1999**, 1399–1400 (1999).
160. Felix, A. M., Heimer, E. P., Lambros, T. J., Tzougraki, C. & Meienhofer, J. Rapid removal of protecting groups from peptides by catalytic transfer hydrogenation with 1,4-cyclohexadiene. *J. Org. Chem.* **43**, 4194–4196 (1978).
161. Elamin, B., Anantharamaiah, G. M., Royer, G. P. & Means, G. E. Removal of benzyl-type protecting groups from peptides by catalytic transfer hydrogenation with formic acid. *J. Org. Chem.* **44**, 3442–3444 (1979).
162. Mallesha, N., Suhas, R., Rao, P. S. & Channe, G. D. A simple and convenient protocol for the selective mono debenzilation of dibenzylamines using 10% Pd/C and HCOONH₄. *Int. J. Chem. Res.* **2**, 26–28 (2011).
163. Ram, S. & Ehrenkaufer, R. E. Ammonium formate in organic synthesis: a versatile agent in catalytic hydrogen transfer reductions. *Synthesis (Stuttg)*. **1988**, 91–95 (1988).
164. Gowda, D. C. & Abiraj, K. Heterogeneous catalytic transfer hydrogenation in peptide synthesis. *Lett. Pept. Sci.* **9**, 153–165 (2002).
165. Bull, S. D., Davies, S. G., Mulvaney, A. W., Prasad, R. S., Smith, A. D. & Fenton, G. Chemoselective oxidative debenzilation of tertiary *N*-benzyl amines. *Chem. Commun.* 337–338 (2000).
166. Khurana, J. & Arora, R. Rapid chemoselective deprotection of benzyl esters by nickel boride. *Synthesis (Stuttg)*. **2009**, 1127–1130 (2009).

167. Schramm, V. L. Enzymatic transition states and transition state analog design. *Annu. Rev. Biochem.* **67**, 693–720 (1998).
168. Krissinel, E. Stock-based detection of biological assemblies in PISA software. *Acta Crystallogr. Sect. A Found. Adv.* **70**, C1745–C1745 (2014).
169. Reichau, S., Jiao, W., Walker, S. R., Hutton, R. D., Baker, E. N. & Parker, E. J. Potent inhibitors of a shikimate pathway enzyme from *Mycobacterium tuberculosis*: Combining mechanism- and modeling-based design. *J. Biol. Chem.* (2011).
170. Cowieson, N. P., Aragao, D., Clift, M., Ericsson, D. J., Gee, C., Harrop, S. J., Mudie, N., Panjikar, S., Price, J. R., Riboldi-Tunncliffe, A., Williamson, R. & Caradoc-Davies, T. MX1: a bending-magnet crystallography beamline serving both chemical and macromolecular crystallography communities at the Australian Synchrotron. *J. Synchrotron Radiat.* **22**, 187–190 (2015).
171. Aragão, D., Aishima, J., Cherukuvada, H., Clarken, R., Clift, M., Cowieson, N. P., Ericsson, D. J., Gee, C. L., Macedo, S., Mudie, N., Panjikar, S., Price, J. R., Riboldi-Tunncliffe, A., Rostan, R., Williamson, R. & Caradoc-Davies, T. T. MX2: a high-flux undulator microfocus beamline serving both the chemical and macromolecular crystallography communities at the Australian Synchrotron. *J. Synchrotron Radiat.* **25**, 885–891 (2018).
172. Kabsch, W. XDS. *Acta Crystallogr. Sect. D Biol. Crystallogr.* **66**, 125–132 (2010).
173. Evans, P. Scaling and assessment of data quality. *Acta Crystallogr. Sect. D Biol. Crystallogr.* **62**, 72–82 (2006).
174. Kabsch, W. Integration, scaling, space-group assignment and post-refinement. *Acta Crystallogr. Sect. D Biol. Crystallogr.* (2010).
175. Winn, M. D., Ballard, C. C., Cowtan, K. D., Dodson, E. J., Emsley, P., Evans, P. R., Keegan, R. M., Krissinel, E. B., Leslie, A. G. W., McCoy, A., McNicholas, S. J., Murshudov, G. N., Pannu, N. S., Potterton, E. A., Powell, H. R., Read, R. J., Vagin, A. & Wilson, K. S. Overview of the CCP 4 suite and current developments. *Acta Crystallogr. Sect. D Biol.*

- Crystallogr.* **67**, 235–242 (2011).
176. Vagin, A. & Teplyakov, A. MOLREP : an automated program for molecular replacement. *J. Appl. Crystallogr.* **30**, 1022–1025 (1997).
 177. Murshudov, G. N., Skubák, P., Lebedev, A. A., Pannu, N. S., Steiner, R. A., Nicholls, R. A., Winn, M. D., Long, F. & Vagin, A. A. REFMAC 5 for the refinement of macromolecular crystal structures. *Acta Crystallogr. Sect. D Biol. Crystallogr.* **67**, 355–367 (2011).
 178. Emsley, P., Lohkamp, B., Scott, W. G. & Cowtan, K. Features and development of Coot. *Acta Crystallogr. Sect. D Biol. Crystallogr.* **66**, 486–501 (2010).
 179. Davis, I. W., Leaver-Fay, A., Chen, V. B., Block, J. N., Kapral, G. J., Wang, X., Murray, L. W., Arendall, W. B., Snoeyink, J., Richardson, J. S. & Richardson, D. C. MolProbity: All-atom contacts and structure validation for proteins and nucleic acids. *Nucleic Acids Res.* (2007).
 180. Berman, H., Henrick, K. & Nakamura, H. Announcing the worldwide Protein Data Bank. *Nature Structural Biology* (2003). doi:10.1038/nsb1203-980
 181. Dolomanov, O. V., Bourhis, L. J., Gildea, R. J., Howard, J. A. K. & Puschmann, H. OLEX2 : a complete structure solution, refinement and analysis program. *J. Appl. Crystallogr.* **42**, 339–341 (2009).
 182. Sheldrick, G. M. Crystal structure refinement with SHELXL. *Acta Crystallogr. Sect. C Struct. Chem.* **71**, 3–8 (2015).
 183. Sugawara, E. & Nikaido, H. An alternative synthesis of (1*R*,2*S*,3*R*,4*R*)-2,3-dihydroxy-4-hydroxymethyl-1-cyclopentanamine, a synthetic intermediate of (–)-aristeromycin. *Tetrahedron Lett.* **28**, 2741–2744 (1987).
 184. Clinch, K., Evans, G. B., Furneaux, R. H., Lenz, D. H., Mason, J. M., Mee, S. P. H., Tyler, P. C. & Wilcox, S. J. A practical synthesis of (3*R*,4*R*)-*N*-tert-butoxycarbonyl-4-hydroxymethylpyrrolidin-3-ol. *Org. Biomol. Chem.* **5**, 2800 (2007).